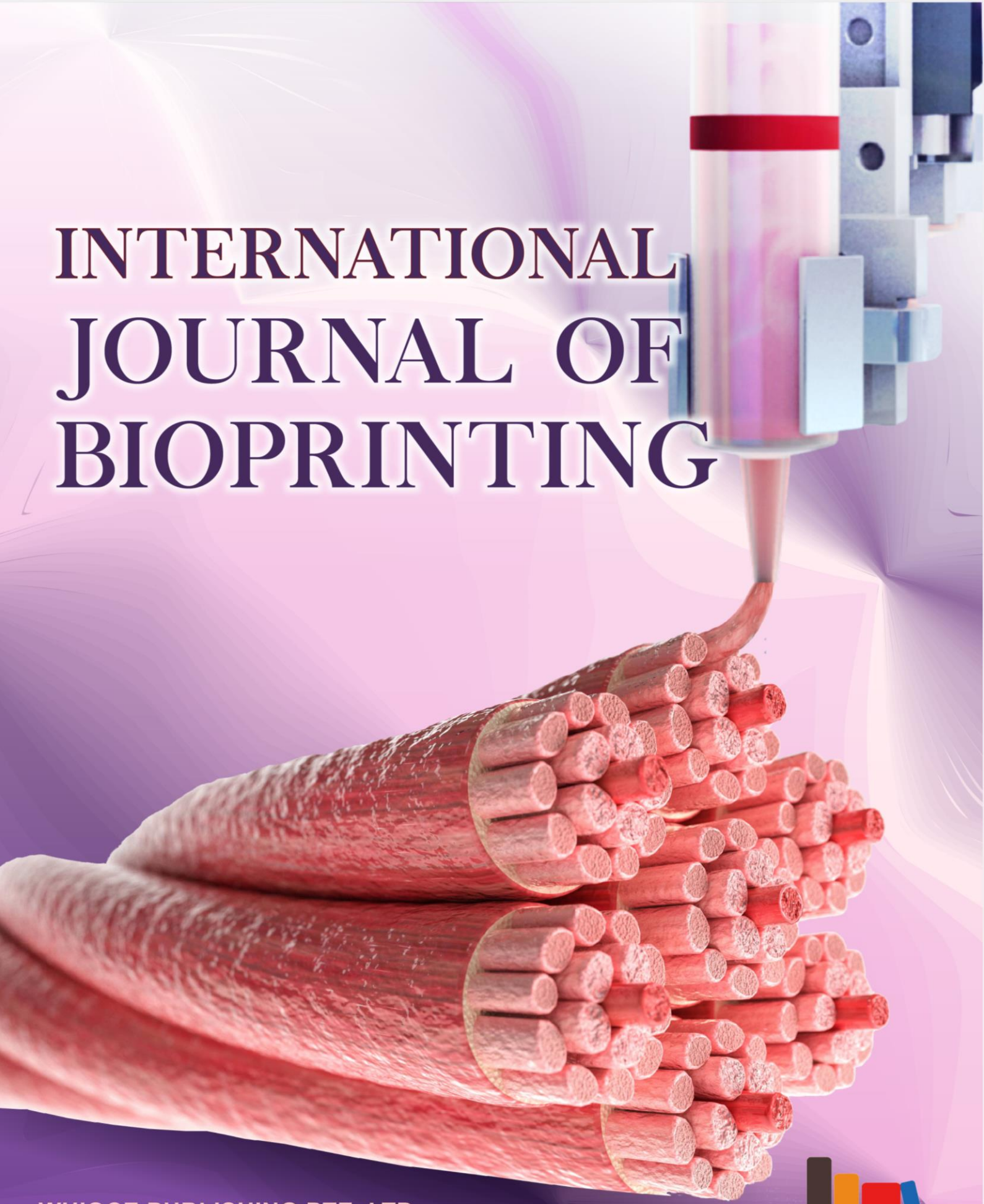
INTERNATIONAL JOURNAL OF BIOPRINTING



WHIOCE PUBLISHING PTE. LTD.
Volume 8 Issue 2, May 2022
ISSN: 2424-8002 (Online) ISSN: 2424-7723 (Print)

WHIOCE PUBLISHING PTE. LTD.

International Journal of Bioprinting

Print ISSN: 2424-7723

Online ISSN: 2424-8002

International Journal of Bioprinting is an international journal covering the technology, science and clinical application of the broadly defined field of Bioprinting. Bioprinting is defined as the use of 3D printing technology with materials that incorporate viable living cells or biological elements to produce tissue or biotechnological products. We are interested in the scientific topics spanning all stages of bioprinting process from concept creation to fabrication and beyond.



Scan to access website:

Scan to submit papers:

About Whioce Publishing

Whioce Publishing is a publishing company based in Singapore. We have in our portfolio a range of high-quality, open-access, peer-reviewed journals and books.

Contact Us

Managing Editor
Ian Wong, info@whioce.com

Editorial Assistant
Puvanesswaray Ramakrishnan, editor@whioce.com

Whioce Publishing
73 Upper Paya Lebar Road #07-02B-06 Centro Bianco Singapore 534818.

Editorial Office of *International Journal of Bioprinting*
34-2B, Jalan Puteri 1/2, Bandar Puteri, 47100 Puchong, Selangor, Malaysia.

Volume 8 Issue 2 • May 2022
ISSN 2424-7723 (print) ISSN 2424-8002 (online)

INTERNATIONAL JOURNAL OF BIOPRINTING

Editor-in-Chief

Chee Kai Chua

Singapore University of Technology and Design, Singapore

WHIOCE PUBLISHING PTE. LTD.

Full issue copyright © 2022 Whioce Publishing
All rights reserved. Without permission in writing from the publisher, this full issue publication in its entirety may not be reproduced or transmitted for commercial purposes in any form or by any means, electronic or mechanical, including photocopying, recording, or any information storage and retrieval system. Permissions may be sought from info@whioce.com.

Article copyright © Respective Author(s)
See articles for copyright year. All articles in this full issue publication are open-access. There are no restrictions in the distribution and reproduction of individual articles, provided the original work is properly cited. However, permission to reuse copyrighted materials of an article for commercial purposes is applicable if the article is licensed under Creative Commons Attribution-NonCommercial License. Check the specific license before reusing.

INTERNATIONAL JOURNAL OF BIOPRINTING

ISSN: 2424-7723 (print)
ISSN: 2424-8002 (online)

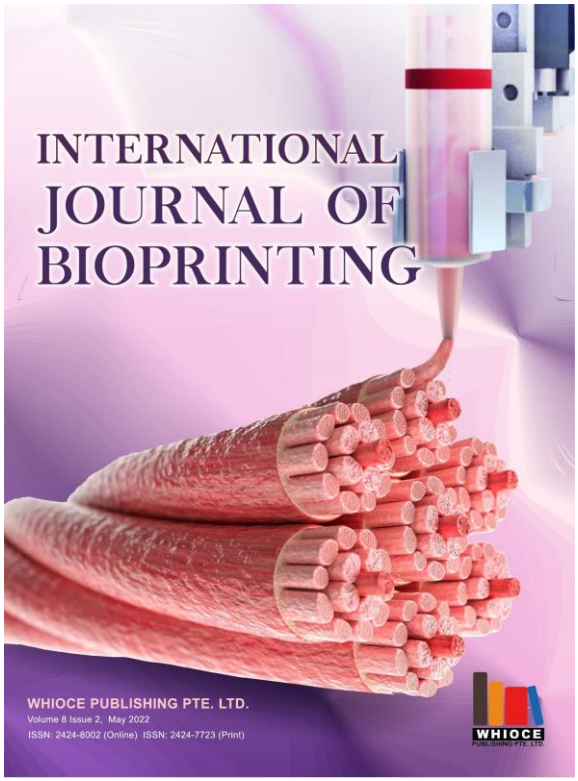
Editorial and Production Credits

Publisher - Whioce Publishing
Managing Editor - Ian Wong
Editorial Assistant - Puvanesswaray Ramakrishnan
Production Editors - Puvanesswaray Ramakrishnan, Ian Wong
Special Issue Commissioning Editor - Felicia Wang
Article Layout and Typeset - Sinjore Technologies (India)
Cover Design - BUTTON GRAPHIC DESIGN STUDIO (Malaysia)

For all advertising queries, contact info@whioce.com.

Supplementary file

Supplementary files of articles can be obtained at https://ijb.whioce.com/index.php/int-j-bioprinting/issue/view/36.



About the Cover

Bioprinting of muscle fiber in action

Disclaimer

Whioce Publishing is not liable to the statements, perspectives, and opinions contained in the publications. The appearance of advertisements in the journal shall not be construed as a warranty, endorsement, or approval of the products or services advertised and/or the safety thereof. Whioce Publishing disclaims responsibility for any injury to persons or property resulting from any ideas or products referred to in the publications or advertisements. Whioce Publishing remains neutral with regard to jurisdictional claims in published maps and institutional affiliations.

International Journal of Bioprinting

Editorial Board

Editor-in-Chief

Chee Kai Chua

Singapore University of Technology and Design, Singapore

Associate Editors

Wai Yee Yeong

Nanyang Technological University, Singapore

Jiankang He

Xi'an Jiaotong University, China

Liliang Ouyang

Tsinghua University, China

Assistant Editor

Jia An

Nanyang Technological University, Singapore

*Editorial Board Members**

Shweta Agarwala, *Denmark*

Mario Moisés Alvarez, *Mexico*

Richard James Bibb, *UK*

Martin Birchall, *UK*

Christian Celia, *Italy*

Boris Chichkov, *Germany*

Gianluca Ciardelli, *Italy*

Frederik Claeyssens, *UK*

Rui Domingues, *Portugal*

Eleonora Ferraris, *Belgium*

Maling Gou, *China*

Charlotte Hauser, *Saudi Arabia*

Mei He, *USA*

Jingchao Jiang, *China*

Qing Jiang, *China*

Ali Khademhosseini, *Japan*

Geun Hyung Kim, *South Korea*

Vladimir Mironov, *Russia*

Makoto Nakamura, *Japan*

Roger Narayan, *USA*

Joaquim Miguel Oliveira, *Portugal*

Aleksandr Ovsianikov, *Austria*

Ibrahim Tarik Ozbolat, *USA*

Michael Raghunath, *Switzerland*

Jin-Hyung Shim, *South Korea*

Cijun Shuai, *China*

Paulo Jorge Da Silva Bartolo, *Singapore*

Ergün Süleyman, *Germany*

Lay Poh Tan, *Singapore*

Savas Tasoglu, *Turkey*

Sanjairaj Vijayavenkataraman, *UAE*

Xiaohong Wang, *China*

Shoufeng Yang, *UK*

Yi Zhang, *China*

Yu Shrike Zhang, *USA*

Veronica MacChi, *Italy*

Shinji Sakai, *Japan*

Giovanni Vozzi, *Italy*

Swee Leong Sing, *Singapore*

Kedong Song, *China*

*Editorial Board Members as of May 12, 2022

May 2022 | Volume 8 | Issue 2 | Page 1 – 186 |

International Journal of Bioprinting

https://ijb.whioce.com/index.php/int-j-bioprinting

CONTENTS

1	**Enhanced Attachment and Collagen Type I Deposition of MC3T3-E1 Cells via Electrohydrodynamic Printed Sub-Microscale Fibrous Architectures** *Shugang Hu, Zijie Meng, Junpeng Zhou, Yongwei Li, Yanwen Su, Qi Lei, Mao Mao, Xiaoli Qu, Jiankang He, Wei Wang*	*RESEARCH ARTICLE*
13	**Bioprinted Gelatin-Recombinant Type III Collagen Hydrogel Promotes Wound Healing** *Jianghong Huang, Xiaoling Lei, Zhiwang Huang, Zhibin Rong, Haihang Li, Yixin Xie, Li Duan, Jianyi Xiong, Daping Wang, Shihui Zhu, Yujie Liang, Jianhao Wang, Jiang Xia*	*RESEARCH ARTICLE*
25	**Development of a 3D Individualized Mask for Neonatal Non-Invasive Ventilation** *Cristina Borràs-Novell, Mario García Causapié, Maria Murcia, Damien Djian, Óscar García-Algar*	*RESEARCH ARTICLE*
31	**3D-Printed β-Tricalcium Phosphate Scaffolds Promote Osteogenic Differentiation of Bone Marrow-Deprived Mesenchymal Stem Cells in an N6-methyladenosine-Dependent Manner** *Xin Jiao, Xin Sun, Wentao Li, Wenxiang Chu, Yuxin Zhang, Yiming Li, Zengguang Wang, Xianhao Zhou, Jie Ma, Chen Xu, Kerong Dai, Jinwu Wang, Yaokai Gan*	*RESEARCH ARTICLE*
45	**Computational Fluid Dynamics Assessment of the Effect of Bioprinting Parameters in Extrusion Bioprinting** *Rashik Chand, Beni Shimwa Muhire, Sanjairaj Vijayavenkataraman*	*RESEARCH ARTICLE*
61	**Validity of a Soft and Flexible 3D-Printed Nissen Fundoplication Model in Surgical Training** *Yangyi Zhang, Jianfu Xia, Jiye Zhang, Jinlei Mao, Hao Chen, Hui Lin, Pan Jiang, Xinzhong He, Xiaodong Xu, Mingzhu Yin, Zhifei Wang*	*RESEARCH ARTICLE*
70	**CNT-Type Dependent Cellular Adhesion on 3D-Printed Nanocomposite for Tissue Engineering** *Adam A. Mieloch, Julia A. Semba, Jakub D. Rybka*	*RESEARCH ARTICLE*
80	**3D-printed Bioresorbable Stent Coated with Dipyridamole-Loaded Nanofiber for Restenosis Prevention and Endothelialization** *Chengjin Wang, Yang Yang, Jingyuan Ji, Yongcong Fang, Liliang Ouyang, Lei Zhang, Wei Sun*	*RESEARCH ARTICLE*
95	**3D-Printing-Assisted Extraluminal Anti-Reflux Diodes for Preventing Vesicoureteral Reflux through Double-J Stents** *Jihun Lee, Jaebum Sung, Jung Ki Jo, Hongyun So*	*RESEARCH ARTICLE*
109	**Fabrication of Microstructured Calcium Phosphate Ceramics Scaffolds by Material Extrusion-Based 3D Printing Approach** *Peifang Dee, Sharlene Tan, Hortense Le Ferrand*	*RESEARCH ARTICLE*
124	**Fast Customization of Hollow Microneedle Patches for Insulin Delivery** *Rong Li, Xuan Liu, Xin Yuan, Shanshan Wu, Li Li, Xuebing Jiang, Bo Li, Xian Jiang, Maling Gou*	*RESEARCH ARTICLE*
136	**Laser-Induced Forward Transfer Printing on Microneedles for Transdermal Delivery of Gemcitabine** *Zoi Kanaki, Chrysoula Chandrinou, Ioanna-Maria Orfanou, Christina Kryou, Jill Ziesmer, Georgios A. Sotiriou, Apostolos Klinakis, Constantin Tamvakopoulos, Ioanna Zergioti*	*RESEARCH ARTICLE*
147	**Application of Bioprinting in Ophthalmology** *Yanfang Wang, Jiejie Wang, Ziyu Ji, Wei Yan, Hong Zhao, Wenhua Huang, Huan Liu*	*REVIEW ARTICLE*
159	**Novel High-Speed 3D Printing Method Using Selective Oil Sintering with Thermoplastic Polyurethane Powder Printing** *Jun Yi-Wu, Chih-Hua Hsieh, Zheng-Ying Lin*	*SHORT COMMUNICATION*

164 **Deep Learning-Assisted Nephrotoxicity Testing with Bioprinted Renal Spheroids** *SHORT COMMUNICATION*
Kevin Tröndle, Guilherme Miotto, Ludovica Rizzo, Roman Pichler, Fritz Koch, Peter Koltay, Roland Zengerle, Soeren S. Lienkamp, Sabrina Kartmann, Stefan Zimmermann

174 **Computer Vision-Aided 2D Error Assessment and Correction for Helix Bioprinting** *METHODS*
Changxi Liu, Jia Liu, Chengliang Yang,Yujin Tang, Zhengjie Lin, Long Li, Hai Liang, Weijie Lu, Liqiang Wang

RESEARCH ARTICLE

Enhanced Attachment and Collagen Type I Deposition of MC3T3-E1 Cells via Electrohydrodynamic Printed Sub-Microscale Fibrous Architectures

Shugang Hu[1,†], Zijie Meng[2,3,†], Junpeng Zhou[1], Yongwei Li[1], Yanwen Su[2,3], Qi Lei[2,3], Mao Mao[2,3], Xiaoli Qu[2,3], Jiankang He[2,3]*, Wei Wang[1]*

[1]Department of Bone and Joint Surgery, the Second Affiliated Hospital of Xian Jiaotong University, Xian Shaanxi, 710004, People's Republic of China
[2]State key laboratory for manufacturing systems engineering, Xi'an Jiaotong University, Xi'an, Shaanxi 710049, People's Republic of China
[3]NMPA Key Lab for Research and Evaluation of Additive Manufacturing Medical Devices, Xi'an Jiaotong University, Xi'an, 710049, China
†*These authors contributed equally to this work*

Abstract: Micro/sub-microscale fibrillar architectures of extracellular matrix play important roles in regulating cellular behaviors such as attachment, migration, and differentiation. However, the interactions between cells and organized micro/sub-microscale fibers have not been fully clarified yet. Here, the responses of MC3T3-E1 cells to electrohydrodynamic (EHD) printed scaffolds with microscale and/or sub-microscale fibrillar architectures were investigated to demonstrate their potential for bone tissue regeneration. Fibrillar scaffolds were EHD-fabricated with microscale (20.51 ± 1.70 μm) and/or sub-microscale (0.58 ± 0.51 μm) fibers in a controlled manner. The *in vitro* results showed that cells exhibited a 1.25-fold increase in initial attached cell number and 1.17-fold increase in vinculin expression on scaffolds with micro/sub-microscale fibers than that on scaffolds with pure microscale fibers. After 14 days of culture, the cells expressed 1.23 folds increase in collagen type I (COL-I) deposition compared with that on scaffolds with pure microscale fibers. These findings indicated that the EHD printed sub-microscale fibrous architectures can facilitate attachment and COL I secretion of MC3T3-E1 cells, which may provide a new insight to the design and fabrication of fibrous scaffolds for bone tissue engineering.

Keywords: Electrohydrodynamic printing; Micro/sub-microscale fibrous architectures; MC3T3-E1; Cell-scaffold interaction; Bone tissue engineering

*Correspondence to: Wei Wang, Department of Bone and Joint Surgery, the Second Affiliated Hospital of Xian Jiaotong, University, Xian Shaanxi, 710004, People's Republic of China; dr.wangwei@xjtu.edu.cn; Jiankang He, State key laboratory for manufacturing systems engineering, Xi'an Jiaotong University, Xi'an, Shaanxi 710049, People's Republic of China; jiankanghe@mail.xjtu.edu.cn

Received: December 6, 2021; **Accepted:** January 10, 2022; **Published Online:** February 11, 2022

Citation: Hu S, Meng Z, Zhou J, et al., 2022, Enhanced Attachment and Collagen Type I Deposition of Mc3t3-E1 Cells via Electrohydrodynamic Printed Sub-Microscale Fibrous Architectures. *Int J Bioprint,* 8(2):514. http://doi.org/10.18063/ijb.v8i2.514

1. Introduction

The extracellular matrix (ECM) of native bone exhibits filamentous nature, which consists of highly organized micro/nanoscale collagen fibers with hydroxyapatite and serves as crucial biophysical cues in regulating cellular behaviors for bone homeostasis[1-3]. Mimicking such fibrillar architectures in artificial implants is of great importance to restoring the biological functions of damaged bone tissues *in vitro*[4]. In this aspect, electrospinning technique has been widely utilized as a promising approach for the construction of bone tissue engineering scaffolds due to its unique capability in fabricating ECM-mimetic ultrafine fibers[5-7]. For example, Yao *et al*.[8] developed polycaprolactone (PCL) and polylactic acid composite fibrous scaffolds with

© 2022 Author(s). This is an Open Access article distributed under the terms of the Creative Commons Attribution License, permitting distribution and reproduction in any medium, provided the original work is properly cited.

the fiber diameter ranging from 250 nm to 1 μm using electrospinning, which were found to facilitate attachment and osteogenic differentiation of human mesenchymal stem cells (hMSCs) *in vitro*. Ren *et al*.[9] fabricated electrospinning nanofibers membranes with different ratios of PCL/gelatin for guided bone regeneration. They found the fibrous membranes prompted calcium deposition of MC3T3-E1 cells both in growth media and osteogenic media. Nevertheless, the random deposition of the micro/sub-microscale fibers increases the complexity of the fibrous structures, which makes it difficult to decouple and decipher the interactions between the cells and the ECM-mimetic fibers[10-12].

Electrohydrodynamic (EHD) printing is a newly emerging method for fabricating fibrous scaffolds with ultrafine fibers and user-defined organizations[13]. Due to its capability of depositing every single fiber in a highly controlled manner, there has been an increasing interest in the investigation of cell-scaffold interactions using EHD printing[14-16]. For example, Brennan *et al*.[17] EHD-printed PCL microscale fibrous scaffolds with a fiber diameter of 4.01 μm and a fiber space ranging from 100 μm to 300 μm, and they found the scaffolds with the fiber space of 100 μm enhanced collagen and mineral deposition of hMSCs. Eichholz *et al*.[18] proposed microscale fibrous scaffolds (fiber diameter of 10.4 μm) with four types of fiber orientation angles (90°, 45°, 10°, and random) using EHD printing, which were further used to culture human skeletal stem cells (hSSCs). Their results indicated that scaffolds with orthogonal architectures enhanced osteogenesis of hSSCs via prompting yes-associated protein nuclear translocation. Xie *et al*.[19] investigated the effect of fiber diameter (3 – 22 μm) on the spreading behaviors of bone marrow stem cells (BMSCs) and human umbilical vein endothelial cells. They found that the BMSCs (with a size of 200 μm) preferred to adhere and bridge between thick fibers, while HUVECs (with a size of 100 μm) can only adhere to the microfibers and form a circle to gradually fill the pore space. However, the existing EHD-printed fibers are usually in microscale, and few studies have been conducted to investigate the response of cells on EHD-printed sub-microscale ECM-mimetic fibers.

We previously developed a solution-based EHD printing method for the fabrication of sub-microscale fibrous architectures[20]. The effect of sub-microscale fibers (about 0.5 μm) on rat myocardial cells was preliminarily investigated, with the results indicating that sub-microscale fibers could enhance cellular adhesion and orientation, whereas the effect of EHD-printed sub-microscale fibrillar architectures on bone cells' adhesion patterns, spreading morphologies, growth, migration, and osteogenic differentiation was not clear. Furthermore, solution-based EHD printing also provides an unprecedented opportunity to incorporate functional nanomaterials into the organized fibrous architectures for enhanced bioactivity[21,22]. Especially for osteogenic differentiation, nano hydroxyapatite (nHA) exhibits a strong componential similarity to native bones, which has been proven to be good osteoconductive and osteoinductive material[23,24]. Many existing studies have demonstrated that fibrous architectures with nHA can facilitate osteogenic differentiation[25,26]. For example, Li *et al*.[27] fabricated nHA/methacrylate gelatin/poly (l-lactic acid) electrospinning membranes with nHA concentration of 1% (nHA/solvent, w/v), which showed superior osteoinductivity compared to the membranes without nHA. However, few studies have realized organized sub-microscale fibrous architectures with nHA. In this study, we investigated the effect of the scaffolds with microscale and/or sub-microscale fibers on behaviors of MC3T3-E1 *in vitro*. The cellular attachment and spreading patterns were investigated by staining with vinculin and F-action. The osteogenic differentiation of MC3T3-E1 on scaffolds with microscale and/or sub-microscale fibers, and sub-microscale fibers with nHA was evaluated by detecting collagen type I (COL-I) deposition and alkaline phosphatase (ALP) after 14 days of culture.

2. Materials and methods

2.1. Materials

Medical-grade PCL was bought from Jinan Daigang Biomaterial Co., Ltd (Mw = 80,000 g/mol, China). Polyethylene oxide (PEO) was bought from Aladdin Co. Ltd (Mw = 300,000 g/mol, Italy). nHA was bought from Aladdin Reagent Co., LTD (China). For solution-based EHD printing of the sub-microscale fibrous architectures, PCL-PEO or PCL-PEO-nHA were dissolved or dispersed in acetic acid solution, and the content of which was set as 5% (w/v) for PCL, 6% (w/v) for PEO, and 0.5% (w/v) for nHA, respectively.

2.2. Design and EHD printing of fibrous scaffolds with micro/sub-microfibers

Three types of scaffolds with different structural and compositional organizations were designed and fabricated using EHD printing techniques (**Figure 1A-C**). The microscale fibrous scaffold (M) was designed with a fiber spacing of 300 μm, a cross angle at 90°, and a fiber offset of 150 μm (**Figure 1D**). The micro/sub-microscale fibrous scaffold (MS) was designed based on the M scaffolds, which contained sub-microscale fibers with a spacing of 100 μm. For fabrication, a total of five layers' microscale fibers and five layers' sub-microscale fibers were alternately stacked in a layer-by-layer manner (**Figure 1E**). The sub-microscale fibrous scaffold with nHA (MSN) shares the same structural organizations

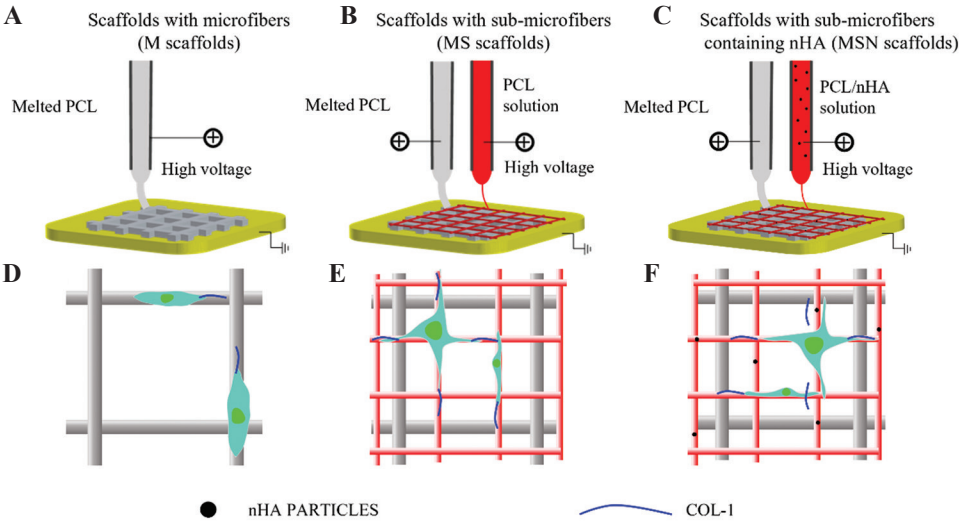


Figure 1. Schematic diagram for the fabrication and cellular responses on the fibrous scaffolds with different structural and componential organizations. Electrohydrodynamic printing of M scaffolds with microfibers (A), MS scaffolds with microscale and sub-microscale fibers (B), and MSN scaffolds with microscale and sub-microscale fibers containing nano hydroxyapatite (C). Illustration of cell morphology and COL-I secretion pattern on M (D), MS (E), and MSN (F) scaffolds are shown.

with MS scaffolds and contains 0.5% nHA in the sub-microscale fibers (**Figure 1F**).

To fabricate PCL microfibers, PCL raw materials were melted at 80°C in a glass syringe, and an ITO glass was used as the collecting substrate. The nozzle gauge was 20G and the nozzle to collector distance was set as 5 mm. The voltage, feeding rate, and stage moving speed were fixed at 4.6 kV, 30 μl/h, and 35 mm/s, respectively. To fabricate the sub-microscale fibrous architectures, solution-based EHD printing process was employed[20]. The nozzle gauge was 34G and the nozzle to collector distance was set as 2 mm. The voltage, feeding rate, and stage moving speed were fixed at 0.8 kV, 50 nl/min, and 150 mm/s, respectively.

After fabrication, the morphology of the micro/sub-microscale fibrous scaffolds was characterized by emission scanning electronic microscopy (SEM, SU8010, Hitachi, Japan). The fiber diameter was further measured by ImageJ software from the SEM images. The existence of nHA in the sub-microfibers was characterized by an energy-dispersive X-ray spectrometry with an elemental analyzer (EDS, Vario EL cube, ELEMENT, Germany).

2.3. MC3T3-E1 cell culture on fibrous scaffolds with micro/sub-microfibers

To investigate the responses of cells on the fibrous scaffolds with different fiber diameters for potential bone regeneration applications, the mouse pre-osteoblast cell line, MC3T3-E1 (Cell Bank of the Chinese Academy of Sciences, Shanghai, China) was used. The cells were cultured in an alpha-minimum essential media (α-MEM, Biological Industries, Israel) supplemented with 10% fetal bovine serum (Biological Industries, Israel) and 1% penicillin/streptomycin (Biological Industries, Israel). Before cell seeding, the scaffolds were punched to have a round shape with a diameter of 15 mm and placed into a 24-well culture plate, which were then fixed by glass rings and sterilized using 75% alcohol aqueous solution. Cells were then seeded at a density of 5×10^4 cells per scaffold and cultured in a humidified incubator with 5% CO_2 at 37°C.

2.4. Initial adhesion behaviors of MC3T3-E1 on scaffolds with micro/sub-microfibers

To investigate the effect of scaffolds with micro/sub-microscale fibers on the initial adhesion numbers of MC3T3-E1 cells, a live/dead viability/cytotoxicity kit (Invitrogen, USA) was used for staining the attached cells after 4 h of culture. Cell-scaffold constructs were washed with phosphate-buffered saline (PBS) for 3 times and then incubated in staining solutions for 30 min. An inverted laser confocal microscope (A1, Nikon, Japan) was employed to measure the living cell numbers attached on the scaffolds, which were further standardized by the image area to calculate the initial adhesion density of the fibrous scaffolds.

To further evaluate the MC3T3-E1 adhesion patterns on micro/sub-microscale fibers, the cell-scaffold constructs were fixed with 4% formaldehyde and then triple-stained with vinculin, F-actin, and nuclear after 24 h of culture. After permeabilized by 0.3% Triton X-100 and blocked by 5% bovine serum albumin (BSA), the cell-scaffold constructs were incubated with primary antibodies (Recombinant Anti-Vinculin antibody, ab129002, Abcam, USA) overnight at 4°C. Then the

constructs were further incubated with Alexa Fluor 488-conjugated goat anti-rabbit IgG H&L (ab150077, Abcam, USA) secondary antibodies for 60 min. Finally, F-actin was stained with Alexa Fluor 594 phalloidin for 30 min and cell nuclear was stained with DAPI for 5 min. Cells were visualized by laser confocal fluorescence microscope. For each sample, the fluorescence images were captured with a total thickness of 60 μm and a z-step of 5 μm. The fluorescence intensity was then measured on the maximum projection stacks of the vinculin channel by Image J software[7].

2.5. MC3T3-E1 morphology, migration on scaffolds with micro/sub-microfibers

Cell morphology and migration were visualized by staining cellular F-actin and nucleus with phalloidin and DAPI after 4 h, 24 h, 4 days, and 7 days of culture using previously described methods. The fluorescence images of the cells on the scaffolds were captured with a total thickness of 25 μm and a z-step of 5 μm. Cell projection area and cell aspect ratio were defined as critical parameters for the evaluation of cellular morphology. Cell projection area was measured by manually drawing the outlines of F-actin on the maximum projection stacks of the F-actin channel and cell aspect ratio was obtained by calculating the ratio of the major to minor axis of the cells[18]. The cell-scaffold constructs were gradually dehydrated by ethyl alcohol and the cellular morphology was further observed with SEM[28].

2.6. Osteogenic differentiation of MC3T3-E1 on scaffolds with micro/sub-microfibers

The osteogenic differentiation of MC3T3-E1 cells on scaffolds with micro/sub-microscale fibers was analyzed by COL-I immunofluorescence staining, ALP staining, and ALP activity. Cells were seeded at a density of 2×10^5 cells per scaffold and cultured for 14 days. Osteoblastic phenotypic maturation of MC3T3-E1 cells was analyzed by immunofluorescence staining of COL-I. After being fixed with 4% formaldehyde, followed by permeabilized by 0.3% Triton X-100 and blocked by 5% BSA, the cell-scaffold constructs were incubated with primary antibodies (COL1A1 (E8F4L) XP Rabbit mAb, 72026, and Cell Signaling Technology, USA) overnight at 4°C. Next, the samples were incubated with Alexa Fluor 555-conjugated anti-rabbit IgG H&L (4413, Cell Signaling Technology, USA) secondary antibodies for 60 min. Cell nucleus was stained with DAPI for 5 min. The COL-I was viewed using the confocal laser scanning microscope, and the amount of the deposited COL-I was quantified using Image J software[29].

ALP was stained using BCIP/NBT ALP color development kit (Beyotime, China) according to the manufacturer's protocol. Briefly, the cell-scaffold constructs were washed with PBS for 3 times and fixed with 4% formaldehyde for 30 min. Then the constructs were incubated in BCIP/NBT solutions for 60 min. For measuring the ALP activity, the cell-scaffold constructs were washed with cold PBS (4°C) for 3 times and lysed in RIPA lysis buffer (strong, without inhibitors, Beyotime, China). After centrifugation at 11,000 relative centrifugal force (rcf) for 20 min, the supernatant was collected and the amount of converted p-nitrophenol was measured using the p-nitrophenyl phosphate (PNPP) assay. The total amount of protein was evaluated by a bicinchoninic acid protein assay kit (BCA, Beyotime, China) with BSA serving as standard protein samples. The ALP activities of MC3T3-E1 cells were finally quantified by standardization of the amount of converted p-nitrophenol with the corresponding reaction time and the total amount of proteins.

2.7. Statistical analysis

The quantified and semi-quantified data were presented as mean ± standard deviation. Statistical analysis was performed using one-way statistical analysis of variance (ANOVA) followed by Tukey *post hoc* test with GraphPad software. $P < 0.05$ (*) was considered as statistical difference.

3. Results and discussion

3.1. Characterization of micro/sub-microscale fibrous scaffolds

Figure 2 shows the SEM images of EHD-printed M, MS, and MSN scaffolds with orthogonal microfibers (**Figure 2A**), microscale and sub-microscale fibers (**Figure 2B**) as well as microscale and sub-microscale fibers containing nHA (**Figure 2C**), respectively. It can be observed that the microfibers can be regularly deposited according to the designed trajectory with a smooth surface morphology in each type of scaffold. In contrast, the deposited sub-microscale fibers exhibited a less regular organization, as the ultrafine fibers are very tiny and extremely susceptible to electrostatic repulsion and attraction force derived from previously deposited fibers. Besides, the sub-microscale fibers with nHA possessed a larger diameter compared to PCL-PEO sub-microscale fibers (**Figure 2C**). The diameters of EHD-printed microfibers, sub-microscale fibers, and sub-microscale fibers with nHA were measured as 20.51 ± 1.70 μm, 0.58 ± 0.13 μm, and 0.62 ± 0.11 μm, respectively (**Figure 2D**). The size of the sub-microscale fibers with or without nHA showed no statistical differences and was close to the scale of collagen fibrils (<500 nm)[30]. The presence of nHA in sub-microscale fibers was further verified using EDS profiles. Calcium and phosphorus elements were detected in sub-microscale fibers with nHA

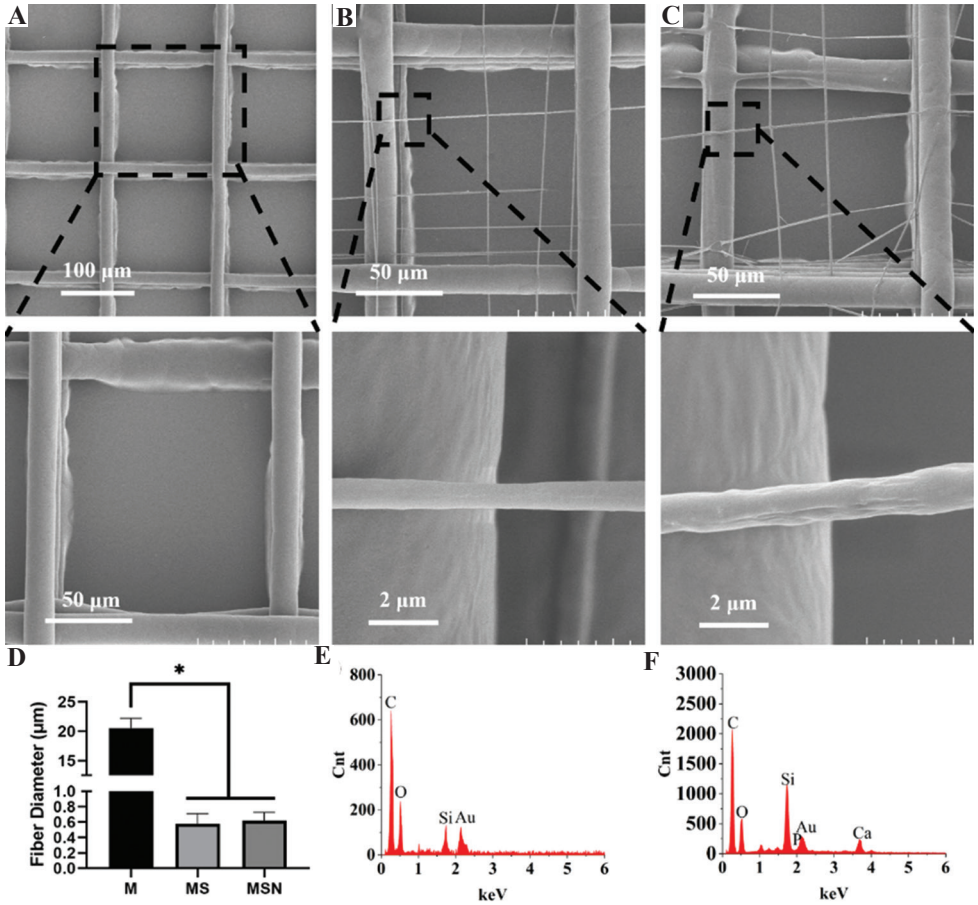


Figure 2. Characterization of the structure and component of scaffolds with microscale and sub-microscale fibers. (A–C) Scanning electronic microscopy images of M, MS, and MSN scaffolds, respectively. (D) Diameters of the electrohydrodynamic-printed microscale and sub-microscale fibers. (E) EDS spectrum of pure polycaprolactone sub-microscale fiber. (F) Sub-microscale fiber with nano hydroxyapatite. *$P < 0.05$.

(**Figure 2F**), which were absent in microscale fibrous PCL architectures (**Figure 2E**).

We also tried to print sub-microscale PCL fibers with a higher nHA concentration (e.g., 1%, 2%, and 4%). As shown in **Figure S1A**, nHA nanoparticles were found to sparely decorate in the sub-micron PCL fibers when the nHA concentration was 0.5%. The resultant fibers were continuous and showed smooth surface. By contrast, obvious nHA aggregates appeared in the fibers with the increase of the nHA concentration to 1%, 2%, and 4% (**Figure S1B-D**). These uneven distribution of nHA within PCL solutions resulted in non-uniform Coulomb force between the nHA aggregates in the polymer jet, which thus affected the stability of EHD printing. Meanwhile, the printed fibers exhibited a ribbon-like morphology with a larger feature size of 1.10 ± 0.31, 1.33 ± 0.45, and 2.16 ± 0.80 μm as the nHA concentration increased from 1% to 4%, respectively.

More importantly, we found that a higher concentration of nHA over 0.5% inside the PCL solution disturbed the stability of EHD printing process, causing fracture of ultrafine fibers at the intersection site of sub-microscale fibers and microfibers, as shown in the SEM images of **Figure S2**. This will further cause the instability and floating of tiny fibers during cell culture period. Therefore, the cell culture experiment was only conducted for the EHD-printed architectures with a nHA concentration of 0.5%.

3.2. MC3T3-E1 initial adhesion behaviors on scaffolds with micro/sub-microfibers

Figure 3A-C present the live/dead staining of the cells attached on the porous scaffolds after 4 h of culture. The attached MT3T3-E1 cell showed high viability on each type of scaffold, indicating good biocompatibility of the fibrous architectures. The cells were found to uniformly distribute on M scaffolds with only a few cells decorated on the microfibers (**Figure 3A**). By contrast, the cells can adhere on both microscale and sub-microscale fibers of MS and MSN scaffolds, resulting in a relatively high cellular density (**Figure 3B and C**). The numbers of

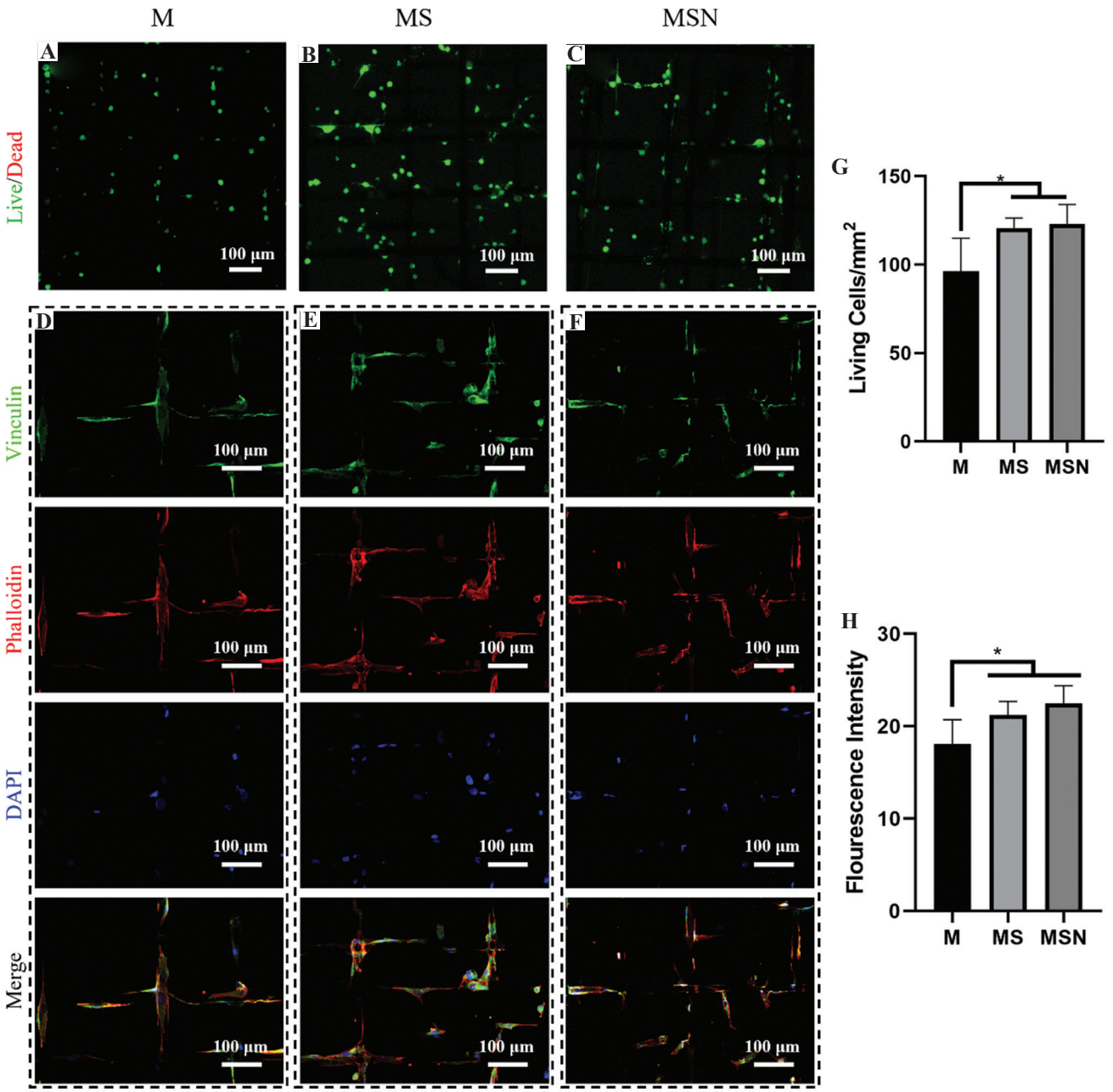


Figure 3. Effect of scaffolds with micro/sub-microscale fibers on MC3T3-E1 initial adhesion behaviors. (A–C) Live/dead staining of cells on M, MS, and MSN scaffolds, respectively. (D–F) Vinculin immunofluorescence staining of cells on M, MS, and MSN scaffolds, respectively. (G) Average living cell numbers on M, MS, and MSN scaffolds. (H) Semi-quantified results of vinculin fluorescence intensity. *$P < 0.05$.

attached living cells were then counted using ImageJ software and standardized by image area. As shown in **Figure 3G**, M, MS, and MSN scaffolds possessed a cellular density of 96.31 ± 18.58, 120.70 ± 5.62, and 122.80 ± 11.15 cells/mm^2, respectively. The cell numbers were almost the same on MS and MSN scaffolds, which were 1.25- and 1.28-fold higher than that on M scaffolds. This phenomenon is in good agreement with previous literature, which reported a higher number of attached cells on scaffolds with sub-microscale fibers than that on scaffolds with pure microfibers[31,32].

Focal adhesions are believed to be positively associated with cell attachment, morphology, migration, and mechanosensory[33,34]. In our study, vinculin, an intracellular component of focal adhesion that mediates the interaction between integrins and actin[35] was detected to investigate the adhesion patterns of cells on scaffolds with micro/sub-microscale fibers. As showed in **Figure 3D-F**, vinculin,

F-actin and nuclei of the MT3T3-E1 cells were represented with green, red, and blue fluorescence, respectively. The confluence of vinculin and F-actin confirmed the cytoplasm localization of vinculin, which were partially adhered on the microfibers (**Figure 3D**) and completely wrap the sub-microscale fibers (**Figure 3E and F**). This finding demonstrated that the cell exhibited a firm interaction with sub-microscale fibers. Semi-quantification of vinculin expression through measuring fluorescence intensity was further shown in **Figure 3H**. The fluorescence intensity of vinculin on MS and MSN scaffolds was 21.22 ± 0.90 and 22.47 ± 1.77, which were 1.17- and 1.24-fold higher than that on M scaffolds. However, no significant difference was observed between the mean fluorescence intensity on MS and MSN scaffolds. The improved cellular adhesion behaviors on the sub-microscale fibrous architectures can be attributed to the morphology of the ultrafine fibers, which provide unique contact cues for cell membrane to warp[31].

3.3. Cell spreading morphology on scaffolds with micro/sub-microfibers

We further analyzed the cell morphology on porous scaffolds with different fiber sizes and organizations.

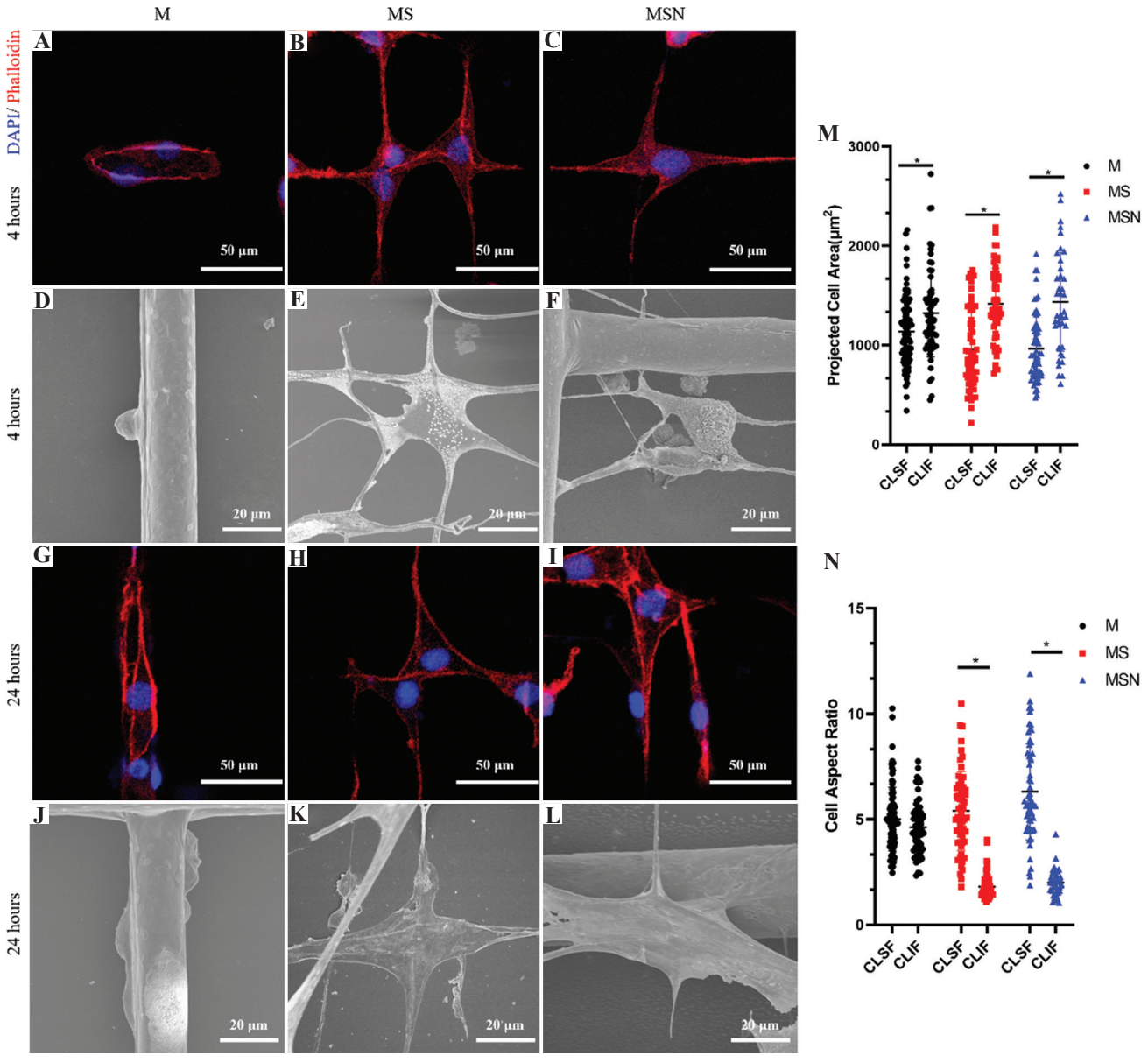


Figure 4. Cell spreading morphology on scaffolds with micro/sub-microscale fibers. F-actin staining of cells on M, MS, and MSN scaffolds after 4- (A–C) and 24- (G–I) hour of culture. SEM images of cells on M, MS, and MSN scaffolds after 4- (D–F) and 24- (J–L) hour of culture. Quantitative cell projection area (M) and aspect ratio (N) after 24 h of culture. CLSF, cells located at single fiber; CLIF, cells located at intersection of fibers. *$P < 0.05$.

Figure 4 shows fluorescent and SEM images of the cytoskeleton of the seeded MC3T3-E1 cells. After 4 h of culture, cells remained a round shape morphology on microfibers of M scaffolds (**Figure 4A and D**). By contrast, the cells were found to spread on sub-microscale fibers of MS (**Figure 4B and E**) and MSN scaffolds (**Figure 4C and F**). After cultured for 24 h, cells spread along both micro and sub-microfibers with an elongated morphology (**Figure 4G-L**). It is interesting to note that the cells exhibited different morphologies depending on fiber size and structural locations. At the intersection of sub-microfibers, cells were polygonal and showed a large cell projection area (**Figure 4M**). When the cells spread on a single sub-microfiber, they were fusiform with a high cell aspect ratio (**Figure 4N**). Similar phenomenon has also been observed when culturing mouse C2C12 cells on polystyrene nanofibers[36]. On the other hand, the cells exhibited oval shape on microfibers regardless of the location, which showed a relatively large projection area and small aspect ratio (**Figure 4M and N**).

3.4. MC3T3-E1 cells growth and migration on scaffolds with micro/sub-microfibers

Bone-related cells are recruited to the injured region during the tissue regeneration process[37], which requires the scaffolds to be well osteoconductive[38]. F-actin staining was used to track the distribution and migration of MC3T3-E1 cells on the scaffolds with micro/sub-microscale fibers (**Figure 5**). As shown in **Figure 5A**, MC3T3-E1 cells were found to spread on microfibers of the M scaffolds after 1 day of culture, which gradually proliferated and migrated along the microfibers on day 4 (**Figure 5D**). Some pores between the microfibers were found to be bridged and filled with cells on day 7 (**Figure 5G**). In contrast, cells on MS scaffolds can attach and spread on both microscale and sub-microscale fibers after cultured for 1 day (**Figure 5B**). With the guidance of sub-microscale fibers, the cells quickly migrated into the spacing between fibers on day 4 (**Figure 5E**) and finally formed interconnected cellular networks on day 7 (**Figure 5H**). Similar phenomena were also observed

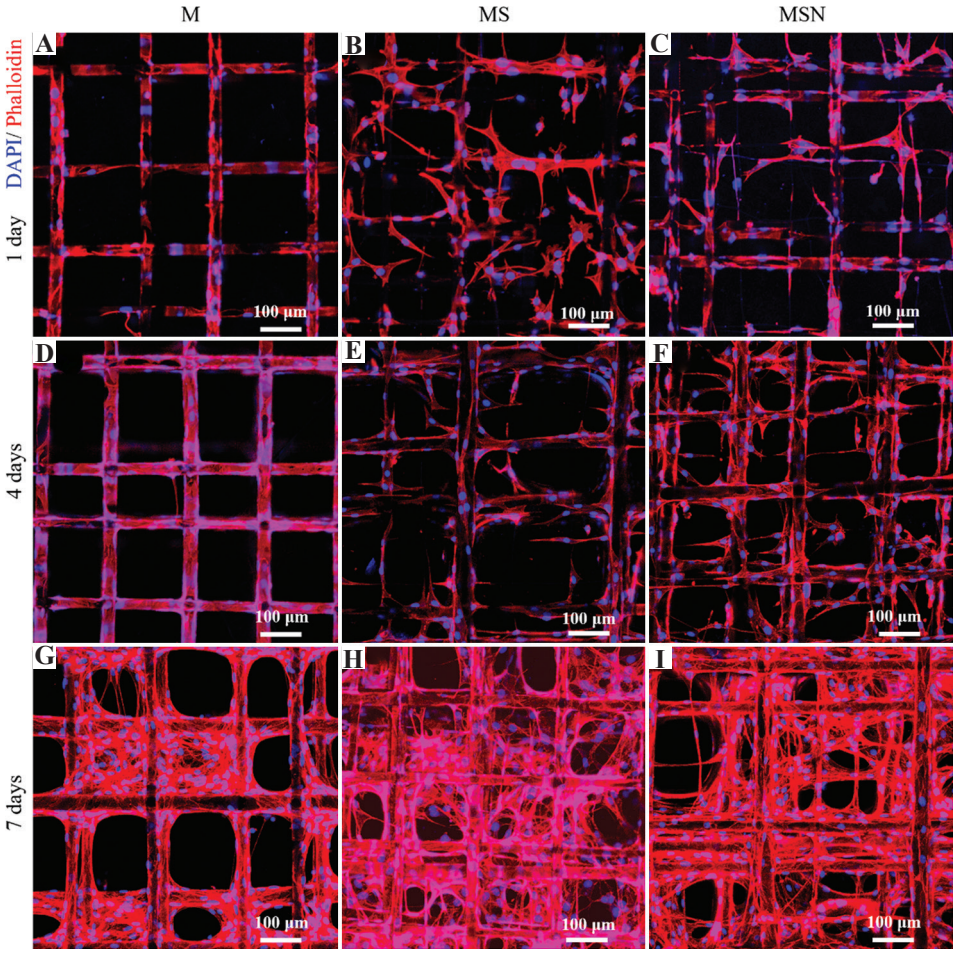


Figure 5. Effect of scaffolds with micro/sub-microscale fibers on MC3T3-E1 cells migration. Migration and distribution of cells on M, MS, and MSN scaffolds on day 1 (A–C), 4 (D–F), and 7 (G–I), respectively.

in MSN scaffolds (**Figure 5C, F and I**). These results evidenced that the scaffolds with sub-microscale fibers can facilitate the spreading and migration of cells to cover the whole scaffold, which resulted in a more uniform cellular distribution. In addition, these findings provide an innovative approach to designing tissue analogs with desirable cellular morphologies and distributions. For example, heterogeneous scaffolds with variable fiber size and controlled fibrous organizations can be fabricated for directing the cellular morphology, migration, and distribution to meet specific tissue demands.

3.5. Osteogenic differentiation of MC3T3-E1 on scaffolds with micro/sub-microfibers

As a major organic component of bone matrices, COL-1 is directly synthesized and secreted by bone cells during bone regeneration process[38]. In addition, ALP degrades phosphate-containing compounds to produce phosphate ions, which plays an essential role in the formation of hydroxyapatite crystals of bone matrices[39]. In this study, COL-I immunofluorescence staining, ALP staining, and ALP activity measurement were conducted on day 14 to evaluate the osteogenic differentiation of MC3T3-E1 cells. As shown in **Figure 6A-C**, COL-I was found around the MC3T3-E1 cells in all scaffolds. Obviously denser secretion of COL-I was observed on MS and MSN scaffolds, with the semi-quantified results showing 1.23- and 1.25-fold higher COL-I fluorescence intensity than that on M scaffolds (**Figure 6G**).

ALP staining of different scaffolds exhibited very similar trends (**Figure 6D-F**), which was further quantitatively analyzed in **Figure 6H**. It was found that the ALP activity increased to 8.68 ± 1.68 nmol/min/mg protein compared to that of M and MS scaffolds, which were 7.34 ± 1.34 and 6.89 ± 0.67 nmol/min/mg protein. However, the result showed no statistical difference. On the basis of these findings, the EHD-printed PCL scaffolds

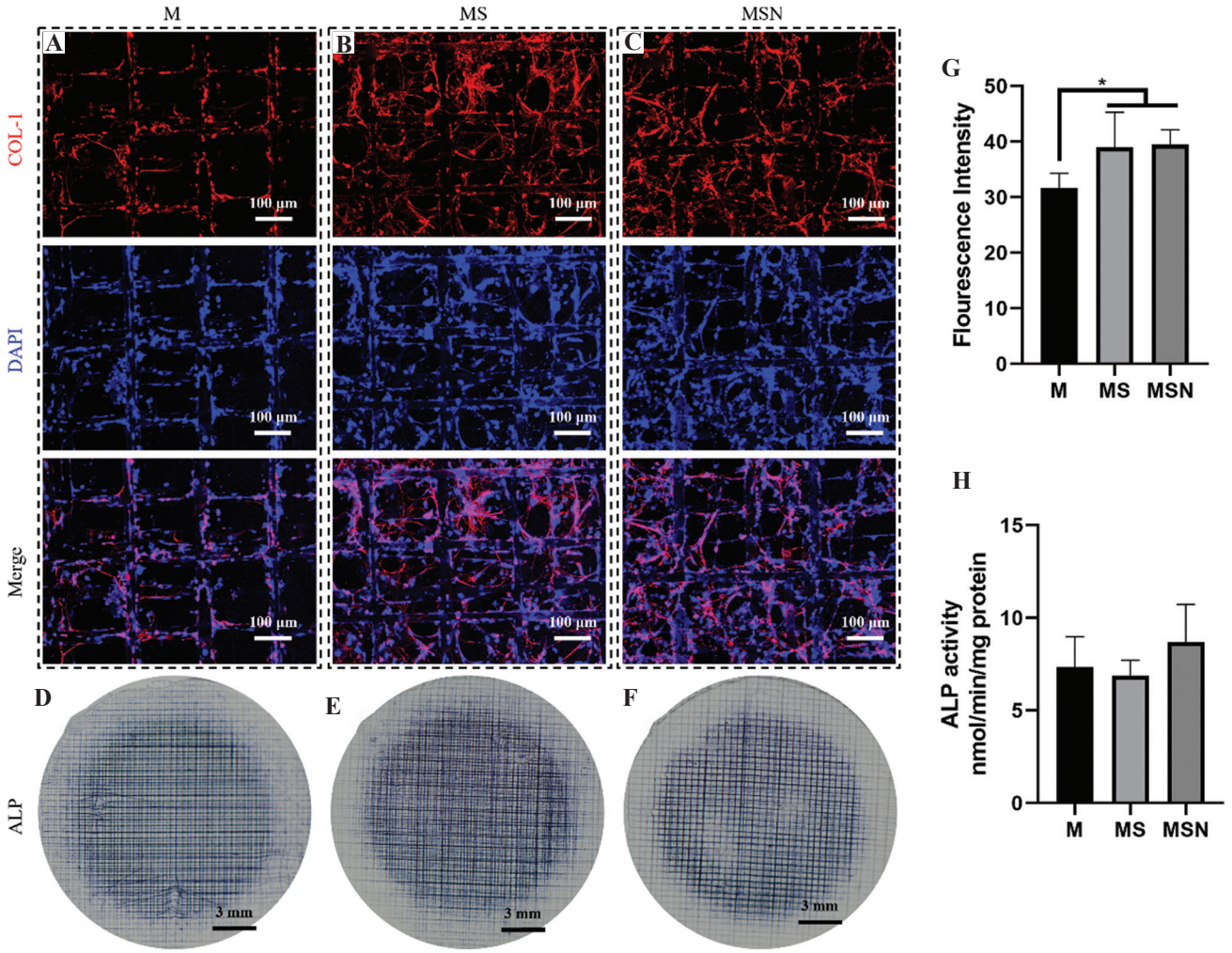


Figure 6. Effects of scaffolds with micro/sub-microscale fibers on MC3T3-E1 cells' osteogenic differentiation. (A–C) COL-I immunofluorescence staining of M, MS, and MSN scaffolds, respectively. (D–F) ALP staining of M, MS, and MSN scaffolds, respectively. Semi-quantified results of COL-1 fluorescence intensity (G) and normalized ALP activity (H) are shown. *$P < 0.05$.

with sub-microscale fibers can direct the osteogenic differentiation through prompting organic component deposition (COL-I), while the sub-microscale fibrillar architectures have little effect on ironic component formation.

A series of life activity of bone-related cells was involved during the regeneration of bone tissues. Namely, cells are recruited to the defect areas and then proliferate and differentiate to specific functional cell lines[40,41]. Here, we fabricated scaffolds with microscale and/or sub-microscale fibrillar architectures, and mouse pre-osteoblast cell line MC3T-E1 was used to demonstrate their potential for bone tissue regeneration. Cells initial adhesion behaviors on scaffolds were investigated since cellular migration is largely dependent on focal adhesion[34]. Our results showed that cells on scaffolds with sub-microscale fibers expressed more focal adhesion and can quickly spread and migrated into the spacing between fibers with the guidance of sub-microfibers. The differentiation of MC3T3-E1 cells were evaluated by ALP activity and COL-I expression, with the results showing that scaffolds with sub-microfibers prompted COL-I deposition while have little effect on ALP activities.

It should be noted that there are several limitations in this study. About 0.5% nHA was added to sub-microscale fibrous architectures successfully and we found that the ALP activity did increase to 8.68 ± 1.68 nmol/min/mg protein compared to that of micro/sub-microscale fibrous architecture without nHA (6.89 ± 0.67 nmol/min/mg protein). However, due to the small size of nHA (about 50 nm), most nHA particles were entrapped inside the sub-microscale PCL fibers (>500 nm), which might be the main reason for no significant statistical difference in the ALP results. One promising solution to improve bioactivity of the MS scaffolds in the future is to coat or self-assemble functional nanomaterials on the surface of micro/sub-microscale fibrous architectures. Furthermore, the effectiveness of the sub-microscale fibrous architectures to promote bone regeneration should be further evaluated *in vivo* for future clinical applications.

4. Conclusion

In the present study, we fabricated ECM-mimetic scaffolds with microscale and/or sub-microscale fibrillar architectures. The average diameter of microfibers and sub-microscale fibers is 20.51 ± 1.70 μm and 0.58 ± 0.51 μm, respectively. We found that the scaffolds with sub-microscale fibers could enhance MC3T3-E1 cell's initial attachment, regulate cell spreading morphology, facilitate cell migration, and prompt COL-I deposition *in vitro* compared to the scaffolds with pure microfibers. These results primarily demonstrated the potential capability of scaffolds with sub-microscale fibers for bone tissue engineering.

Acknowledgments

The authors sincerely thank Dr. Liying Liu at the Biomedical Experimental Center of Xi'an Jiaotong University Health Science Center for her assistance with cell culture and laser scanning confocal microscope experiments.

Funding

This work was financially supported by the National Natural Science Foundation of China (82072522, 52125501, and 31971272), the Integrated Traditional Chinese and Western Medicine Clinical Collaboration Innovation Project of Shaanxi Administration of Traditional Chinese Medicine (2020-ZXY-003), the Key Research Project of Shaanxi Province (2020GXLH-Y-001, 2020GXLH-Y-021, 2021GXLH-Z-028), Guangdong Basic and Applied Basic Research Foundation (2020B1515130002), The Youth Innovation Team of Shaanxi Universities and the Fundamental Research Funds for the Central Universities.

Conflict of interest

The authors declare no competing financial interest.

Author contributions

S.H., Z.M., Y.S., and X.Q. designed the experimental plan and conducted the experiments. S.H. wrote the manuscript with support from Z.M., J.H., and W.W. Detailed research results were collected and reviewed by J.Z., Y.L, Q.L, and M.M. J.H. and W.W. supervised the project and conceived the original idea.

References

1. Eliaz Nand Metoki N, 2017, Calcium Phosphate Bioceramics: A Review of Their History, Structure, Properties, Coating Technologies and Biomedical Applications. *Materials (Basel)*, 10:334.
https://doi.org/10.3390/ma10040334
2. Florencio-Silva R, Sasso G R, Sasso-Cerri E, *et al.*, 2015, Biology of Bone Tissue: Structure, Function, and Factors That Influence Bone Cells. *Biomed Res Int*, 2015:421746.
https://doi.org/10.1155/2015/421746
3. Lin X, Patil S, Gao Y G, *et al.*, 2020, The Bone Extracellular Matrix in Bone Formation and Regeneration. *Front Pharmacol*, 11:757.
https://doi.org/10.3389/fphar.2020.00757
4. Hogrebe NJ, Reinhardt JW, Gooch KJ, 2017, Biomaterial Microarchitecture: A Potent Regulator of Individual Cell Behavior and Multicellular Organization. *J Biomed MATER Res A*, 105:640–61.

https://doi.org/10.1002/jbm.a.35914

5. Xue J, Wu T, Dai Y, *et al.*, 2019, Electrospinning and Electrospun Nanofibers: Methods, Materials, and Applications. *Chem Rev*, 119:5298–415. https://doi.org/10.1021/acs.chemrev.8b00593
6. Nekounam H, Samadian H, Bonakdar S, *et al.*, 2021, Electro-Conductive Carbon Nanofibers Containing Ferrous Sulfate for Bone Tissue Engineering. *Life Sci*, 282:119602. https://doi.org/10.1016/j.lfs.2021.119602
7. Wu L, Gu Y, Liu L, *et al.*, 2020, Hierarchical Micro/Nanofibrous Membranes of Sustained Releasing VEGF for Periosteal Regeneration. *Biomaterials*, 227:119555. https://doi.org/10.1016/j.biomaterials.2019.119555
8. Yao Q, Cosme J G, Xu T, *et al.*, 2017, Three Dimensional Electrospun PCL/PLA Blend Nanofibrous Scaffolds with Significantly Improved Stem Cells Osteogenic Differentiation and Cranial Bone Formation. *Biomaterials*, 115:115–27. https://doi.org/10.1016/j.biomaterials.2016.11.018
9. Ren K, Wang Y, Sun T, *et al.*, 2017, Electrospun PCL/Gelatin Composite Nanofiber Structures for Effective Guided Bone Regeneration Membranes. *Mater Sci Eng C Mater Biol Appl*, 78:324–32. https://doi.org/10.1016/j.msec.2017.04.084
10. Bean AC, Tuan RS, 2015, Fiber Diameter and Seeding Density Influence Chondrogenic Differentiation of Mesenchymal Stem Cells Seeded on Electrospun Poly (Epsilon-Caprolactone) Scaffolds. *Biomed Mater*, 10:015018. https://doi.org/10.1088/1748-6041/10/1/015018
11. Shanmugasundaram S, Chaudhry H, Arinzeh TL, 2011, Microscale Versus Nanoscale Scaffold Architecture for Mesenchymal Stem Cell Chondrogenesis. *Tissue Eng Part A*, 17:831–40. https://doi.org/10.1089/ten.TEA.2010.0409
12. Sisson K, Zhang C, Farach-Carson MC, *et al.*, 2010, Fiber Diameters Control Osteoblastic Cell Migration and Differentiation in Electrospun Gelatin. *J Biomed Mater Res A*, 94:1312–20. https://doi.org/10.1002/jbm.a.32756
13. He J, Zhang B, Li Z, *et al.*, 2020, High-Resolution Electrohydrodynamic Bioprinting: A New Biofabrication Strategy for Biomimetic Micro/Nanoscale Architectures and Living Tissue Constructs. *Biofabrication*, 12:042002. https://doi.org/10.1088/1758-5090/aba1fa
14. Abbasi N, Abdal-hay A, Hamlet S, *et al.*, 2019, Effects of Gradient and Offset Architectures on the Mechanical and Biological Properties of 3-D Melt Electrowritten (MEW) Scaffolds. *ACS Biomater Sci Eng*, 5:3448–61. https://doi.org/10.1021/acsbiomaterials.8b01456
15. Abbasi N, Ivanovski S, Gulati K, *et al.*, 2020, Role of Offset and Gradient Architectures of 3-D Melt Electrowritten Scaffold on Differentiation and Mineralization of Osteoblasts. *Biomater Res*, 24:2. https://doi.org/10.1186/s40824-019-0180-z
16. Mao M, He J, Li Z, *et al.*, 2020, Multi-Directional Cellular Alignment in 3D Guided by Electrohydrodynamically-Printed Microlattices. *Acta Biomater*, 101:141–51. https://doi.org/10.1016/j.actbio.2019.10.028
17. Brennan CM, Eichholz KF, Hoey DA, 2019, The Effect of Pore Size within Fibrous Scaffolds Fabricated Using Melt Electrowriting on Human Bone Marrow Stem Cell Osteogenesis. *Biomed Mater*, 14:065016. https://doi.org/10.1088/1748-605X/ab49f2
18. Eichholz KF, Hoey DA, 2018, Mediating Human Stem Cell Behaviour Via Defined Fibrous Architectures by Melt Electrospinning Writing. *Acta Biomater*, 75:140–51. https://doi.org/10.1016/j.actbio.2018.05.048
19. Xie C, Gao Q, Wang P, *et al.*, 2019, Structure-Induced Cell Growth by 3D Printing of Heterogeneous Scaffolds with Ultrafine Fibers. *Mater Des*, 181:108092. https://doi.org/10.1016/j.matdes.2019.108092
20. Zhang B, He J, Lei Q, *et al.*, 2019, Electrohydrodynamic Printing of Sub-Microscale Fibrous Architectures with Improved Cell Adhesion Capacity. *Virtual Phys Prototyp*, 15:62-74. https://doi.org/10.1080/17452759.2019.1662991
21. He J, Xu F, Dong R, *et al.*, 2017, Electrohydrodynamic 3D Printing of Microscale Poly (Epsilon-Caprolactone) Scaffolds with Multi-Walled Carbon Nanotubes. *Biofabrication*, 9:015007. https://doi.org/10.1088/1758-5090/aa53bc
22. Vijayavenkataraman S, Thaharah S, Zhang S, *et al.*, 2019, 3D-Printed PCL/rGO Conductive Scaffolds for Peripheral Nerve Injury Repair. *Artif Organs*, 43:515–23. https://doi.org/10.1111/aor.13360
23. Zhou Hand Lee J, 2011, Nanoscale Hydroxyapatite Particles for Bone Tissue Engineering. *Acta Biomater*, 7:2769–81. https://doi.org/10.1016/j.actbio.2011.03.019
24. Turnbull G, Clarke J, Picard F, *et al.*, 2018, 3D Bioactive Composite Scaffolds for Bone Tissue Engineering. *Bioact Mater*, 3:278–314. https://doi.org/10.1016/j.bioactmat.2017.10.001
25. Wu X, Miao L, Yao Y, *et al.*, 2014, Electrospun Fibrous Scaffolds Combined with Nanoscale Hydroxyapatite Induce Osteogenic Differentiation of Human Periodontal Ligament

Cells. *Int J Nanomed*, 9:4135–43.
https://doi.org/10.2147/IJN.S65272

26. Ribeiro Neto WA, Pereira IH, Ayres E, *et al.*, 2012, Influence of the Microstructure and Mechanical Strength of Nanofibers of Biodegradable Polymers with Hydroxyapatite in Stem Cells Growth. Electrospinning, Characterization and Cell Viability. *Polym Degrad Stab*, 97:2037–51.
https://doi.org/10.1016/j.polymdegradstab.2012.03.048
27. Li B, Chen Y, He J, *et al.*, 2020, Biomimetic Membranes of Methacrylated Gelatin/Nanohydroxyapatite/Poly(l-Lactic Acid) for Enhanced Bone Regeneration. *ACS Biomater Sci Eng*, 6:6737–47.
https://doi.org/10.1021/acsbiomaterials.0c00972
28. Lei Q, He J, Li D, 2019, Electrohydrodynamic 3D Printing of Layer-Specifically Oriented, Multiscale Conductive Scaffolds for Cardiac Tissue Engineering. *Nanoscale*, 11:15195–205.
https://doi.org/10.1039/c9nr04989d
29. Xia J, Yuan Y, Wu H, *et al.*, 2020, Decoupling the Effects of Nanopore Size and Surface Roughness on the Attachment, Spreading and Differentiation of Bone Marrow-Derived Stem Cells. *Biomaterials*, 248:120014.
https://doi.org/10.1016/j.biomaterials.2020.120014
30. Gao C, Peng S, Feng P, *et al.*, 2017, Bone Biomaterials and Interactions with Stem Cells. *Bone Res*, 5:17059.
https://doi.org/10.1038/boneres.2017.59
31. Tian F, Hosseinkhani H, Hosseinkhani M, *et al.*, 2008, Quantitative Analysis of Cell Adhesion on Aligned Micro- and Nanofibers. *J Biomed Mater Res A*, 84:291–9.
https://doi.org/10.1002/jbm.a.31304
32. Huang B, Aslan E, Jiang Z, *et al.*, 2020, Engineered Dual-Scale Poly (ε-Caprolactone) Scaffolds using 3D Printing and Rotational Electrospinning for Bone Tissue Regeneration. *Addit Manuf*, 36:101452.
https://doi.org/10.1016/j.addma.2020.101452
33. Oakes PW, Gardel ML, 2014, Stressing the Limits of Focal Adhesion Mechanosensitivity. *Curr Opin Cell Biol*, 30:68–73.
https://doi.org/10.1016/j.ceb.2014.06.003
34. Paluch EK, Aspalter IM, Sixt M, 2016, Focal Adhesion-Independent Cell Migration. *Annu Rev Cell Dev Biol*, 32:469–90.
https://doi.org/10.1146/annurev-cellbio-111315-125341
35. Revach OY, Grosheva I, Geiger B, 2020, Biomechanical Regulation of Focal Adhesion and Invadopodia Formation. *J Cell Sci*, 133:jcs244848.
https://doi.org/10.1242/jcs.244848
36. Sheets K, Wunsch S, Ng C, *et al.*, 2013, Shape-Dependent Cell Migration and Focal Adhesion Organization on Suspended and Aligned Nanofiber Scaffolds. *Acta Biomater*, 9:7169–77.
https://doi.org/10.1016/j.actbio.2013.03.042
37. Fu X, Liu G, Halim A, *et al.*, 2019, Mesenchymal Stem Cell Migration and Tissue Repair. *Cells*, 8:784.
https://doi.org/10.3390/cells8080784
38. Abedin E, Lari R, Shahri NM, *et al.*, 2018, Development of a Demineralized and Decellularized Human Epiphyseal Bone Scaffold for Tissue Engineering: A Histological Study. *Tissue Cell*, 55:46–52.
https://doi.org/10.1016/j.tice.2018.09.003
39. Blair HC, Larrouture QC, Li Y, *et al.*, 2017, Osteoblast Differentiation and Bone Matrix Formation *In Vivo* and *In Vitro*. *Tissue Eng Part B Rev*, 23:268–80.
https://doi.org/10.1089/ten.TEB.2016.0454
40. Oryan A, Kamali A, Moshiri A, *et al.*, 2017, Role of Mesenchymal Stem Cells in Bone Regenerative Medicine: What Is the Evidence? *Cells Tissues Organs*, 204:59–83.
https://doi.org/10.1159/000469704
41. Iaquinta MR, Mazzoni E, Bononi I, *et al.*, 2019, Adult Stem Cells for Bone Regeneration and Repair. *Front Cell Dev Biol*, 7:268.
https://doi.org/10.3389/fcell.2019.00268

Publisher's note

Whioce Publishing remains neutral with regard to jurisdictional claims in published maps and institutional affiliations.

RESEARCH ARTICLE

Bioprinted Gelatin-Recombinant Type III Collagen Hydrogel Promotes Wound Healing

Jianghong Huang[1,2†], Xiaoling Lei[3†], Zhiwang Huang[1†], Zhibin Rong[4], Haihang Li[5], Yixin Xie[2], Li Duan[1], Jianyi Xiong[1], Daping Wang[1], Shihui Zhu[6], Yujie Liang[2,7*], Jianhao Wang[3*], Jiang Xia[2*]

[1]Department of Orthopedics, Shenzhen Intelligent Orthopaedics and Biomedical Innovation Platform, Guangdong Artificial Intelligence Biomedical Innovation Platform, Shenzhen Second People's Hospital, the First Affiliated Hospital of Shenzhen University Health Science Center, Shenzhen, 518035, China
[2]Department of Chemistry, the Chinese University of Hong Kong, Shatin, Hong Kong SAR, China
[3]School of Pharmacy, Changzhou University, Changzhou, Jiangsu 213164, China
[4]Shijiazhuang Maternity and Child Health Hospital, Shijiazhuang, Hubei, 050093, China
[5]Jiangsu Trautec Medical Technology Co., Ltd, No.28 Shuanglong Road, Jintan Development Zone, Changzhou, Jiangsu, 213200, China
[6]Department of Burn Surgery, Institute of Burns, the First Affiliated Hospital, Naval Medical University, Shanghai, 200433 China
[7]Shenzhen Kangning Hospital, Shenzhen Mental Health Center, Shenzhen, Guangdong, 518020, China
[†]*These authors contributed equally to this work.*

Abstract: Artificial skins are biomaterials that can replace the lost skin or promote the regeneration of damaged skin. Skin regenerative biomaterials are highly applauded because they can exempt patients with severe burns from the painful procedure of autologous skin transplantation. Notwithstanding decades of research, biocompatible, degradable, and printable biomaterials that can effectively promote skin regeneration as a transplantation replacement in clinical use are still scarce. Here, we report one type of all-protein hydrogel material as the product of the enzymatic crosslinking reaction of gelatin and a recombinant type III collagen (rColIII) protein. Doping the rColIII protein in gelatin reduces the inflammatory response as an implant underneath the skin. The all-protein hydrogel can be bioprinted as scaffolds to support the growth and proliferation of 3T3 fibroblast cells. The hydrogel used as a wound dressing promotes wound healing in a rat model of skin damage, showing a faster and healthier recovery than the controls. The rColIII protein in the hydrogel has been shown to play a critical role in skin regeneration. Altogether, this work manifests the development of all-protein gelatin-rColIII hydrogel and demonstrates its use in wound healing. The gelatin-collagen hydrogel wound dressing thereby may become a promising treatment of severe wounds in the future.

Keywords: Gelatin; Recombinant collagen; Hydrogel; Artificial skin; Wound healing

*Correspondence to: Yujie Liang, Department of Chemistry, the Chinese University of Hong Kong, Shatin, Hong Kong SAR, China; liangyjie@126.com; Jianhao Wang, School of Pharmacy, Changzhou University, Changzhou, Jiangsu 213164, China; minuswan@163.com; Jiang Xia, Department of Chemistry, the Chinese University of Hong Kong, Shatin, Hong Kong SAR, China; jiangxia@cuhk.edu.hk.

Received: November 18, 2021; **Accepted:** December 29, 2021; **Published Online:** February 24, 2022

Citation: Huang J, Lei X, Huang Z, *et al*, 2022, Bioprinted Gelatin Recombinant Type III Collagen Hydrogel Promotes Wound Healing. *Int J Bioprint,* 8(2):517. http://doi.org/10.18063/ijb.v8i2.517

1. Introduction

The skin is the largest organ of the human body. The skin serves multiple functions, including regulation of body temperature and transmission of sensations, and also acts as a barrier to safeguard the body from the invasion of microorganisms and the damaging effects of unwanted chemical and physical stimuli. The skin is also a fragile organ; it is difficult to replace when irreversibly damaged by severe burns, trauma, or disease[1-3]. Despite

© 2022 Author(s). This is an Open Access article distributed under the terms of the Creative Commons Attribution License, permitting distribution and reproduction in any medium, provided the original work is properly cited.

being the most common treatment for repairing severe skin defects, autologous skin transplantation has many disadvantages[4,5]. Skin from the patient's unburned area, including the dermis and epidermis, can be used to repair burned skin areas. For severe burns larger than 60% of total body surface area, multiple harvests from the donor site after healing are required. However, this procedure may increase the risk of infection and cause scarring and pigmentation changes of the donor site. In addition, patients need to endure for a long time to wait for the new skin to re-epithelize at the donor site.

At present, researchers are developing new biomaterials that can be used to replace skin for the short term or permanently; these skin substitutes are collectively called "artificial skin." To promote wound healing, the skin substitute must: (a) Adhere to the substrate, (b) has sufficient elasticity and the ability to withstand deformation, (c) allow water to evaporate at a typical rate similar to the stratum corneum, (d) has a microbial barrier, (e) promotes hemostasis and accelerates coagulation, (f) is easy to use, (g) be used immediately after injury, and (h) causes a "regeneration-like" reaction in the wound bed without causing inflammation or foreign bodies or non-self-immunologic reaction[6-8]. A successful example is given by Burke *et al*. who pioneered classical experiments of the development of dermal equivalents for biological replacement[6-8]. Briefly, starting from glutaraldehyde-cross-linked collagen, glycosaminoglycan was mixed to stimulate the synthesis of normal connective tissue matrix in the dermis without inflammation, foreign body reaction, or immunologic reaction. Years of work resulted in a product called Integra®, which contains collagen extracted from cowhide and chondroitin 6-sulfate extracted from shark cartilage to form a collagen-chondroitin-6-sulfate fiber. This product was approved the United States Food and Drug Administration for treating burn patients.

Notwithstanding the success Integra® achieved over the years, there is still much room to improve. Natural collagen purified from animal sources faces several limitations in clinical use[9-12]. For example, the quality control of collagen products from animal sources is often a challenge because of the heterogeneity of the natural collagen and the risk of pathogen contamination. The main ingredients of adult skin tissue are type I and type III collagen. In contrast, the proportion of type III collagen in fetal skin is significantly higher than that of adults[13,14]. It has been reported that the decrease of type III collagen is associated with the aging of the skin, leading to the lack of elasticity and renewability[15-18]. Supplementing the loss of type III collagen will reduce scar hyperplasia and promote skin regeneration[19]. In this regard, collagens from a natural animal source are often a mixture of different isotypes, making it difficult to delineate the role of each collagen isotype. We reason that a recombinant, pure form of type III collagen will be superior for skin regeneration[20]. This then inspired the use of recombinant technology and genetic tools to produce type III collagen *ex vivo*[21-24]. The recombinant human type III collagen (rColIII) has been used to treat full-thickness skin defects in pigs[25]. Since rColIII is highly soluble, to form a hydrogel for wound covering, we sought to use gelatin, the hydrolysate of collagen, to provide a framework of crosslinking. Gelatin has excellent biocompatibility, low immunogenicity, low toxicity, and high biodegradability. Therefore, gelatin is widely used in hemostatic wound dressings, vascular stents, drug carriers, tissue engineering stents, coating materials, etc.[26]. In this study, we synthesized gelatin-rColIII hydrogel (GRH) through enzymatic crosslinking and reported the therapeutic efficacy of the all-protein hydrogel in wound healing in a rat model of skin damage.

On the other hand, three-dimensional (3D) bioprinting is a manufacturing technology that can construct biomaterial scaffolds in a range of biomedical applications. 3D bioprinting of biomaterials can realize the precise assembly of the polymeric biomacromolecules, which provides a spatial framework for the growth of cell cultures and tissue engineering. Biomaterials amenable to 3D bioprinting should meet the following requirements[27-31]: (a) Excellent biocompatibility; (b) suitable biodegradability to allow substitution by the extracellular matrix and natural tissues; (c) suitable pore size and porosity to facilitate the exchange of oxygen, nutrients, and metabolites; (d) mechanical properties similar to the natural tissues; (e) low toxicity and immunogenicity; (f) strong plasticity; and (g) ease of processing. 3D bioprinting, in general, is achieved through several strategies including material extrusion[32,33], material jetting[34,35], and vat polymerization[36,37]. Among the three methods, extrusion-based 3D bioprinting strategies are now the most widely used for producing 3D tissue constructs. Here, we demonstrated that enzymatic crosslinking solidifies the GRH into the ink of 3D extrusion bioprinting[38]. The 3D GRH scaffold supports the growth of mouse embryonic fibroblasts.

2. Materials and methods

2.1. Materials and instruments

rColIII (purity >90%) was kindly provided by Jiangsu Chuangjian Medical Technology Co., Ltd. Dulbecco's modified Eagle's medium (DMEM) penicillin-streptomycin solution, fetal bovine serum (FBS), trypsin-EDTA, and gelatin were obtained from Sigma-Aldrich (USA). Aminoamidase was purchased from BOMEI Company (China). Cell counting kit-8 (CCK-8)

and cell live/dead staining kit were obtained from Dojindo Company (Japan). Other instruments include fluorescence microscope from Leica (Germany), scanning electron microscope (SEM) (TESCAN Company, Czech Republic), microplate reader (Thermo Company, USA), and CPD1 3D bioprinter (Shangpu Boyuan Company, China). Sprague Dawley rats were obtained from Top Biotech Biotechnology Co. Ltd. (Shenzhen, China) or Changzhou Cavens Biological Technology Co. Ltd. and allowed to acclimatize for 1 week in the laboratory.

2.2. 3D printing of the scaffolds

Gelatin and rColIII were mixed with the ratios of 1:0, 1:0.05, 1:0.1, 1:0.15, and 1:0.2 to form the hydrogel. A model was built by 3D CAD file (.stl file format). We set the wire spacing of the model at 1.5 mm and the layer height at 0.25 mm. Rectangular parallelepiped specimens with dimensions of 20 mm × 20 mm × 3 mm (length × width × height) were used. Briefly, gelatin and rColIII were sterilized by Co60 radiation. The gelatin powder was dissolved in ultrapure water (1 g gelatin and 10 ml ultrapure water are mixed to make a 10% solution, heated to 40°C, and stirred for 30 min), and rColIII was added in different proportions (0 g, 0.05 g, 0.10 g, 0.15 g, and 0.20 g). Before 3D printing, 1 ml of 10% transglutaminase aqueous solution was added for enzymatic crosslinking for 5 min. Then, 3D porous hydrogel scaffolds with a size of 20 mm × 20 mm × 3 mm were printed by a CPD1 3D printer.

2.3. Porosity measurement

Porosity is defined as the volume of the pores over the total volume of the scaffold. Ethanol occupation was used to estimate the volumes. The 3D scaffolds were lyophilized for 48 h, and the dry weight was measured. The scaffolds were then immersed in absolute ethanol and placed under a vacuum until all the pores were filled. The weight of ethanol that occupies the pores is calculated as M_p. The weight of ethanol that corresponds to the total volume of the scaffold is calculated as M_T. Porosity is then calculated as M_p/M_T. The samples were measured in triplets. The moisture content is calculated based on the weight loss of the stent after freeze-drying. The swelling curve of the material was calculated by measuring the water absorption of the freeze-dried scaffold at different time points.

2.4. SEM analysis

Scaffolds were sliced into samples of 4 mm × 4 mm × 3 mm sizes, fixed in 2.5% glutaraldehyde solution, dehydrated gradually from 50% up to 100% ethanol, displaced with isopropyl acetate, and freeze-dried for 48 h before being processed for SEM imaging.

2.5. Proliferation assay

NIH-3T3 cells were cultured in DMEM containing 10% FBS and 1% penicillin/streptomycin at 37°C under the ambience of 5% CO_2. Cells were seeded on the scaffold at a density of 1.0×10^5 per scaffold. In the control group, cells were grown on 48-well plates. Then, the CCK-8 kit was used to measure the number of cells at different time points.

2.6. Subcutaneous implantation assay

All the animal experiments have been approved by the ethics committee of Shenzhen Top Biotech Co. Ltd. (no. TOP-IACUC-2020-09-0007). Hydrogel samples were implanted subcutaneously in rats to evaluate biocompatibility *in vivo*. After the rats were anesthetized with 1.5% isoflurane, the dorsal region was disinfected, and an incision of about 2 cm was made. A sterile hydrogel cube of 1 cm in length and width and 3 mm in thickness was implanted. The incision was sutured with 4-0 sutures. After implantation for 4 weeks, the rats were anesthetized and killed. The back hydrogel and surrounding tissues were taken out together and fixed with 4% paraformaldehyde. After dehydration, they were embedded in paraffin and cut into pathological sections. The sections were stained with hematoxylin and eosin (HE), and immunohistochemical staining was applied to quantify the inflammatory factors such as CD68, interleukin (IL)-10, and tumor necrosis factor-alpha (TNF-α). Immunohistochemical staining was performed as previously reported[39]. The primary antibodies used in this experiment were anti-collagen I, anti-collagen III, anti-IL-10, anti-TNF-α, and anti-CD68 antibodies (Abcam, Cambridge, MA, UK).

2.7. Cell live-dead staining

NIH-3T3 cells were inoculated into the hydrogel for 1, 4, and 7 days in separate experiments. After inoculation, cells were then stained with calcein AM (2 μM) and propidium iodide (3 μM) for 20 min at 37°C before imaging under a fluorescence microscope.

2.8. Animal wound treatment

Briefly, male adult Sprague Dawley rats (180–220 g) were kept in polypropylene cages with free access to water and food. Animals were divided into four groups, and each group contained six animals: A, PBS control; B, GRH_0 group; C, GRH_{10} group; and D, GRH_{20} group. All rats were anesthetized with sodium phenobarbitone before surgery. Then, the dorsal surface of rats was surgically manipulated to remove one full-thickness skin wound (diameter = 2 cm) under aseptic conditions. A 2 ml hydrogel materials were then applied to the surface of the wounds and bandage, and the dressing was changed

every 2 days. Photographs of skin wound healing were taken on days 1, 3, 5, 7, 9, 11, and 13 to observe the skin recovery. The rats were sacrificed on days 1, 7, and 13 after the operation. The wound bed and the surrounding healthy skin were collected. Full-thickness skin samples, wound edges, and epithelialized wounds were prepared for tissue sections.

2.9. Histological evaluation of wound regeneration

For histological staining analysis, the wound skin tissues were taken out on days 1, 7, and 13. The excised skin samples were first fixed with 10% formalin, then dehydrated by ethanol gradient incubation, embedded in paraffin, and cut into sections with a thickness of 8 μm. As a part of the histopathological evaluation, tissue sections were stained with HE, Masson's trichrome stain, and Sirius red stain to determine collagen formation status.

3. Results and discussion

3.1. GRH scaffolds

Doping rColIII protein to gelatin at different ratios, followed by crosslinking by transglutaminase, gives a series of GRH materials amenable to 3D printing. We thereby constructed GRH scaffolds: GRH_0, GRH_5, GRH_{10}, GRH_{15}, and GRH_{20} with 0%, 5%, 10%, 15%, and 20% of rColIII in gelatin, respectively. These GRH materials were then printed into scaffolds with sizes of 20 mm × 20 mm × 3 mm and grids of about 1 mm (**Figure 1A**). SEM analysis showed that these materials had a rough surface amenable for cell adhesion (**Figure 1B**). All five GRHs were highly porous and rich in water (**Figure 2A** and **B**). The lyophilized GRHs reached the maximal water absorption after 4 h during the hydration process. An increasing amount of rColIII corresponded to the decreasing level of swelling in the solution (**Figure 2C**). The Fourier transform infrared (FTIR) spectra of the hydrogels show several characteristic bands of protein-based materials (**Figure S1**). The vibration of amide A bands at around 3290 cm^{-1} and 3300 cm^{-1} indicates hydrogen bonds. The amide I bands at 1638 cm^{-1} and 1633 cm^{-1} correspond to the vibration of the C=O bond, suggesting the existence of the secondary structure of the polypeptide in the protein material. The amide II bands appear at 1550 cm^{-1} and 1541 cm^{-1}, indicating the stretching vibration of the C-N bond and the bending vibration of the N-H bond, respectively. Amide III bands appear at 1239 cm^{-1} and 1238 cm^{-1}, indicating that the triple helix structure of gelatin molecules is still maintained in the hydrogel. The peak at 1450 cm^{-1} corresponds to the cis structure of the peptide bond. The infrared spectrum of the hydrogel has a strong serine side group C-O stretching vibration absorption peak near 1024 cm^{-1}, which is a characteristic peak of type III collagen.

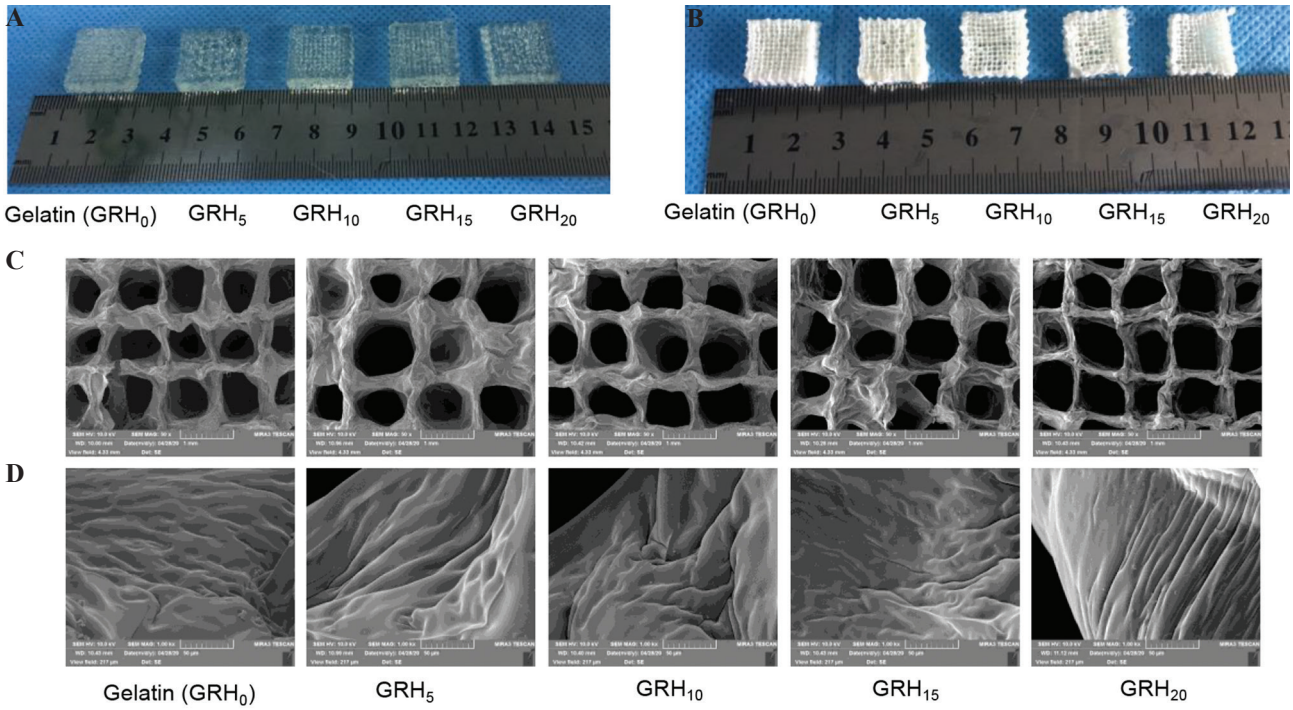


Figure 1. Morphology of gelatin rColIII hydrogel (GRH) scaffolds. Images of the GRH scaffolds in wet (A) and lyophilized form (B). Scanning electron microscope images of the GRH scaffolds in 50× (C) and 1000× (D).

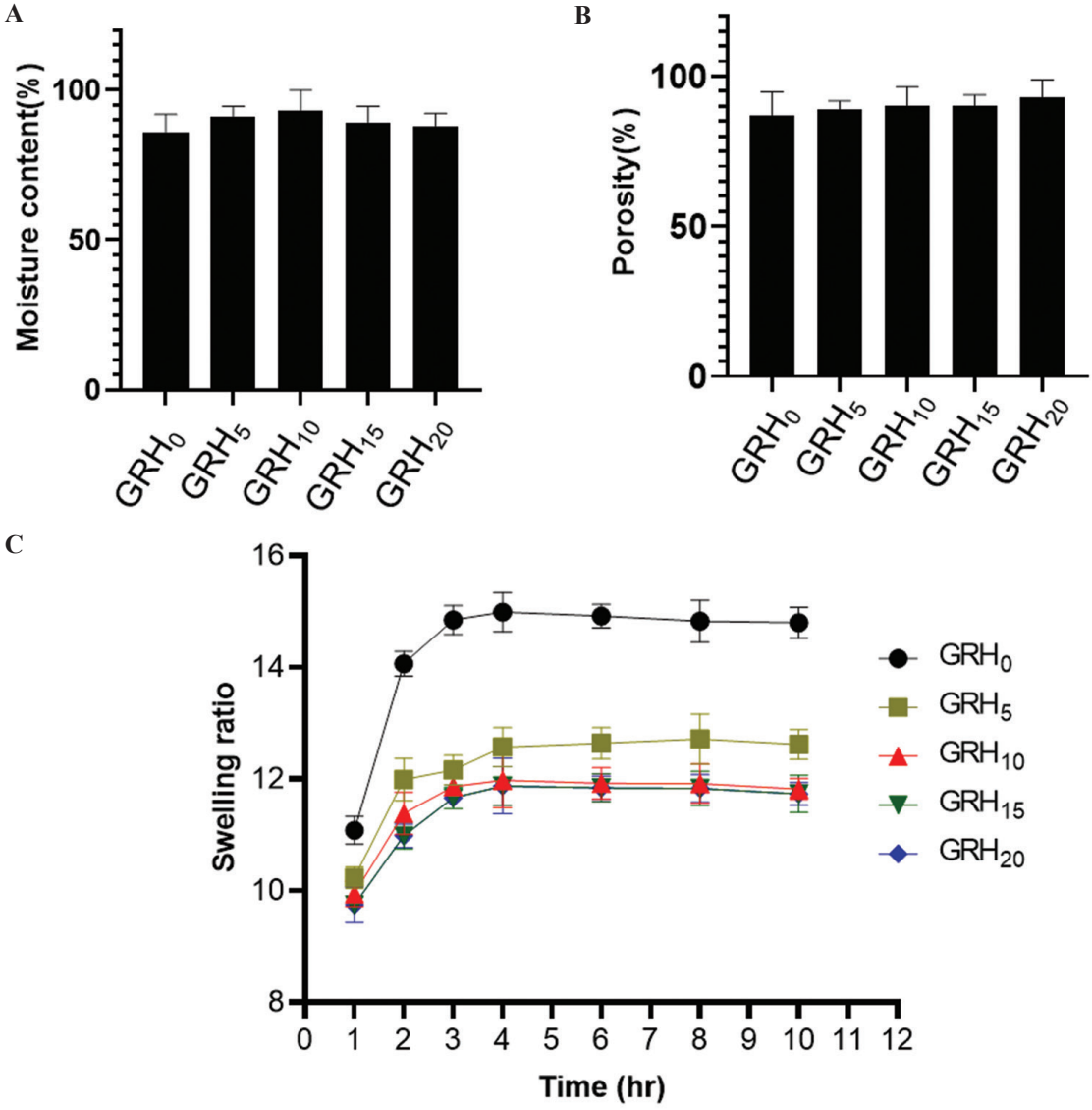


Figure 2. Physical properties of gelatin rColIII hydrogel. (A) Moisture content. (B) Porosity. (C) Swelling kinetics.

3.2. Biocompatibility of the GRHs

To study the material's biocompatibility *in vivo*, the stent was implanted subcutaneously in rats for 28 days. After the 28-day incubation, we explored the inflammatory response of the surrounding tissue by immunohistochemical analyses of IL-10, TNF-α, and CD68 (**Figure 3**). In the GRH_0 group, residual gelatin remained after the 28-day incubation, and the implant material was completely degraded in the other groups. HE staining of the GRH_{20} group showed that the number of monocytes and macrophages was reduced. GRH_{20} group also showed lower expression of the inflammatory factors such as IL-10, TNF-α, and CD68 (indicated by level of staining). We also observed that the GRH_{20} hydrogel was significantly degraded as compared to other samples (**Figure S2**). Therefore, the recombinant type III collagen (rColIII) protein may increase the absorption of GRH implant and alleviate the inflammatory response of the gelatin hydrogel.

3.3. Cell adhesion and proliferation on GRH scaffolds in vitro

We next explored whether the GRH scaffolds can support the adhesion and proliferation of NIH 3T3 cells, a cell line of mouse embryonic fibroblasts. All four GRH scaffolds support cell proliferation based on CCK8 analysis (**Figure S3**). We incubated the cells on the GRH scaffolds for 1, 4, and 7 days and stained them with calcein AM for the live cells (green fluorescence) and propidium iodide for the dead cells (red fluorescence) (**Figure 4**). Most cells grew on the scaffolds instead of in the cavities or on the bottom of

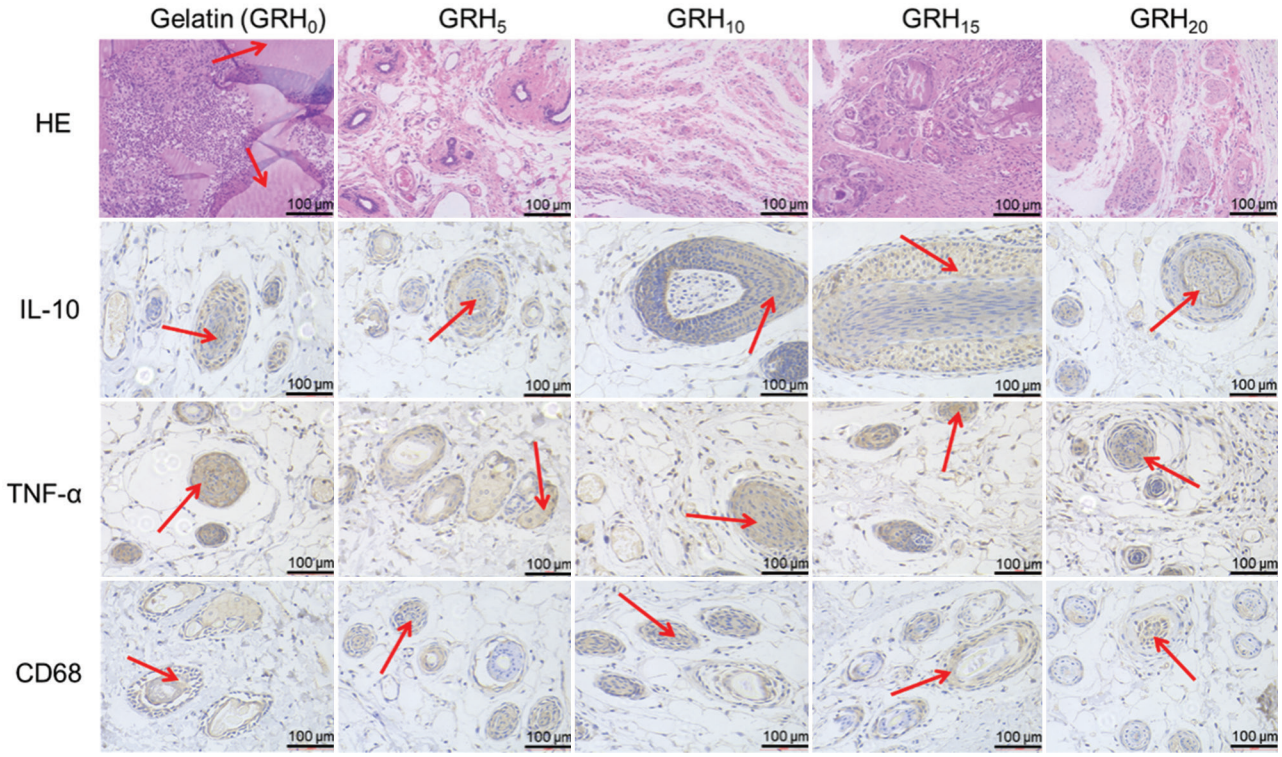


Figure 3. Immunohistochemical staining of tissues surrounding different implants. Arrows in the HE staining show the residual hydrogel material. Arrows in other panels show areas of interest where high staining signals are detected. Scale bar: 100 μm.

the cell culture dish. All five GRH scaffolds support the adhesion, proliferation, and migration of NIH 3T3 cells.

3.4. Promotion of wound healing in a rat model

Finally, we examined whether the GRH hydrogels can be used as dressing materials to promote wound healing in a rat model of skin damage. Briefly, full-thickness skin wounds (diameter = 2 cm) were created on the dorsal surface of rats, and hydrogel materials were then applied to the surface of the wounds. After a designated duration of incubation, the skin samples were removed and analyzed by various methods. First, the wound sizes in different groups were recorded. We observed a trend that the higher percentage of the type III collagen component corresponds with increasing wound healing rate, and in the GRH_{20} group, the wound healed almost completely after 13 days, which was significantly faster than all other groups (**Figure 5**).

The quality of the wound healing was then analyzed by various staining of the tissue samples at the wound areas. Rats were sacrificed on day 7 or 13, and the wound areas were dissected and stained by HE staining. In the control group in which rats were treated with PBS, the formation of scab and necrotic tissue agglomeration was observed in the absence of epidermis, hair follicles, or blood vessels on day 7. Only a small number of new collagen fibers were formed with disordered distributions on day 13 in this group (**Figure 6**). This shows that although adult rats can self-regenerate wounded skins to a certain degree, the regeneration process took longer than 2 weeks. All three GRH treatment groups showed promising healing results, and the higher concentration of rColIII corresponded to more complete skin regeneration. For example, on day 13, the wounds in PBS control and GRH_0 groups showed disorganized tissue structures. On the contrary, in both GRH_{10} and GRH_{20} groups, dense tissue structures with the ordered arrangement and obvious cuticle were seen (**Figure 6**), which is a sign of the emergence of healthy skin tissues.

The same tissue was also stained by Masson's trichrome; the blue marks represent collagen fibers, and the red marks represent muscle fibers. On day 7, scar formation or tissue hyperplasia, indicated by the predominant red color, occurred at the wound area in the PBS control and GRH_0 groups. In contrast, significantly higher level of collagen fibers was observed in the GRH_{10} and GRH_{20} groups (**Figure 7**). Consistently, this demonstrates healthy healing due to rColIII in the wound dressing material. The same trend was also observed in the staining images of the day 13 samples (**Figure 7**). Quantification of the staining signals highlighted the differences (**Figure 7B**).

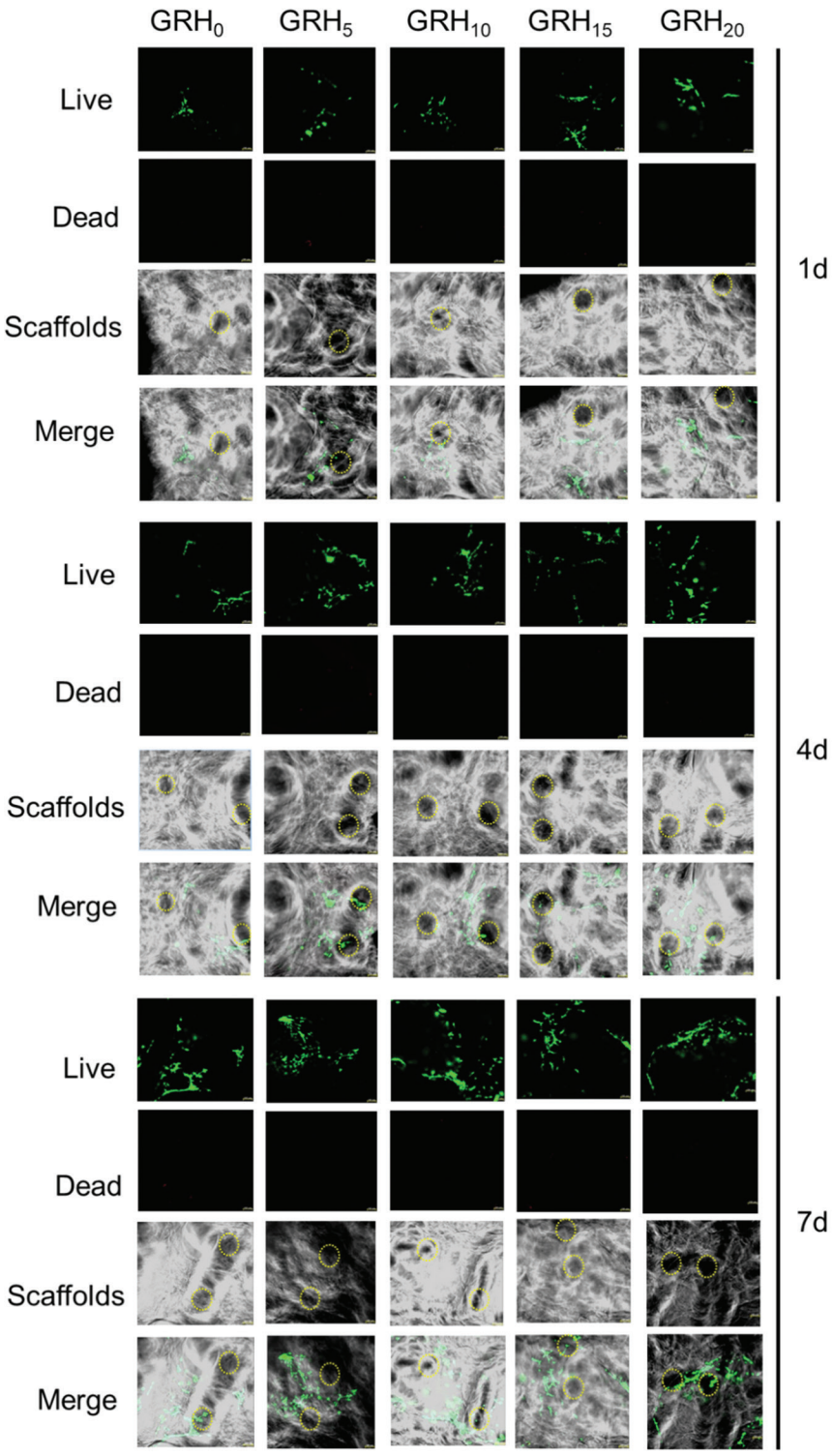


Figure 4. Cell proliferation on the scaffolds based on the live/dead staining. Images of 1d, 4d, and 7d are representative images of cell cultures incubated on the scaffold for 1 day, 4 days, and 7 days, representatively. The cavities of the scaffolds are marked. Scale bar: 100 μm.

Finally, after Sirius red staining of the tissue section can be seen as orange for type I collagen and type III collagen was stained orange and bright green for type III collagen, respectively, confirming collagen deposition at the wound. During the skin healing process, the collagen content of all groups increased. However, the PBS control group and GRH_0 group were dominated by the formation of type I collagen. On

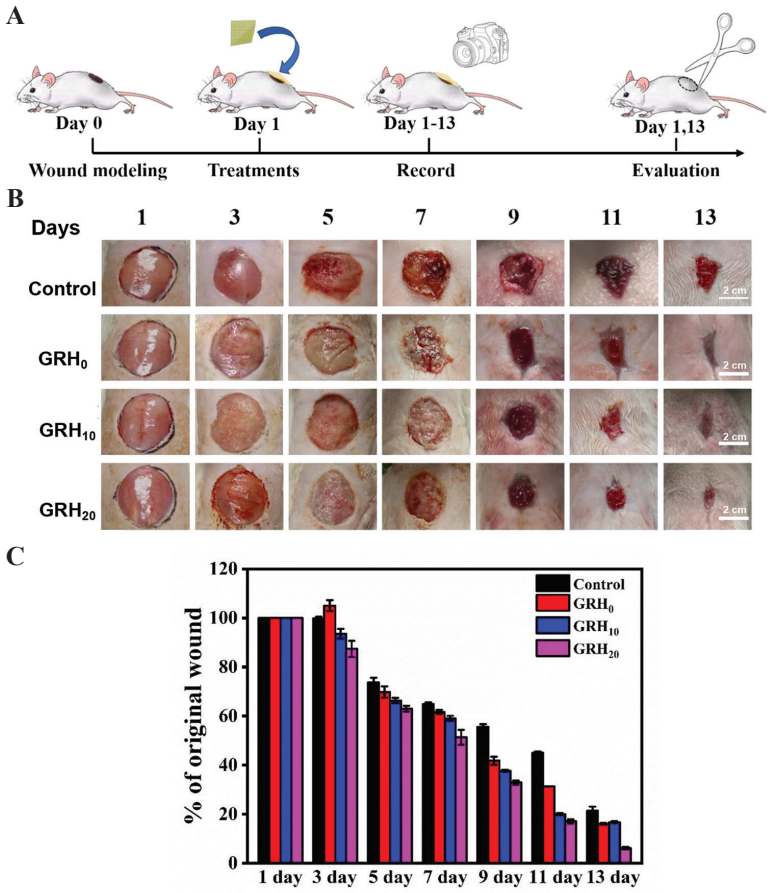


Figure 5. Gelatin rColIII hydrogel coating promotes wound closure. (A) Schematic illustration of the experimental procedure. (B) Representative photographs of wounds in four groups during the 13-day treatment. Scale bar: 2 cm. (C) Quantification of the relative sizes of the wounds (% of the original dimensions of the wounds). Data were expressed as standard deviations (n=6).

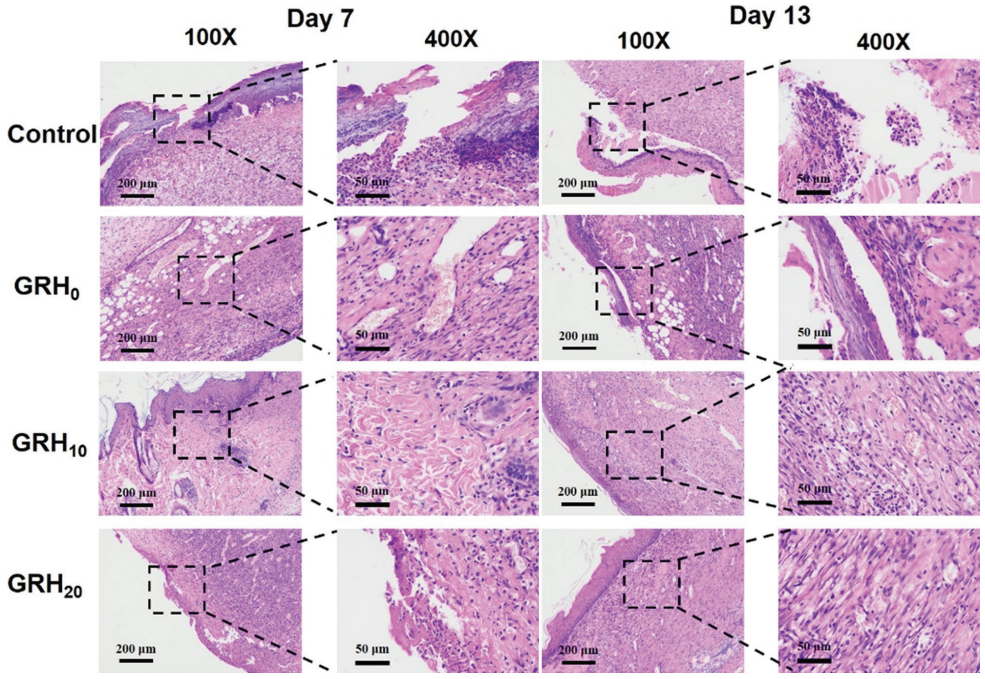


Figure 6. Representative HE staining images of the skin tissues of rat wounds in four different groups.

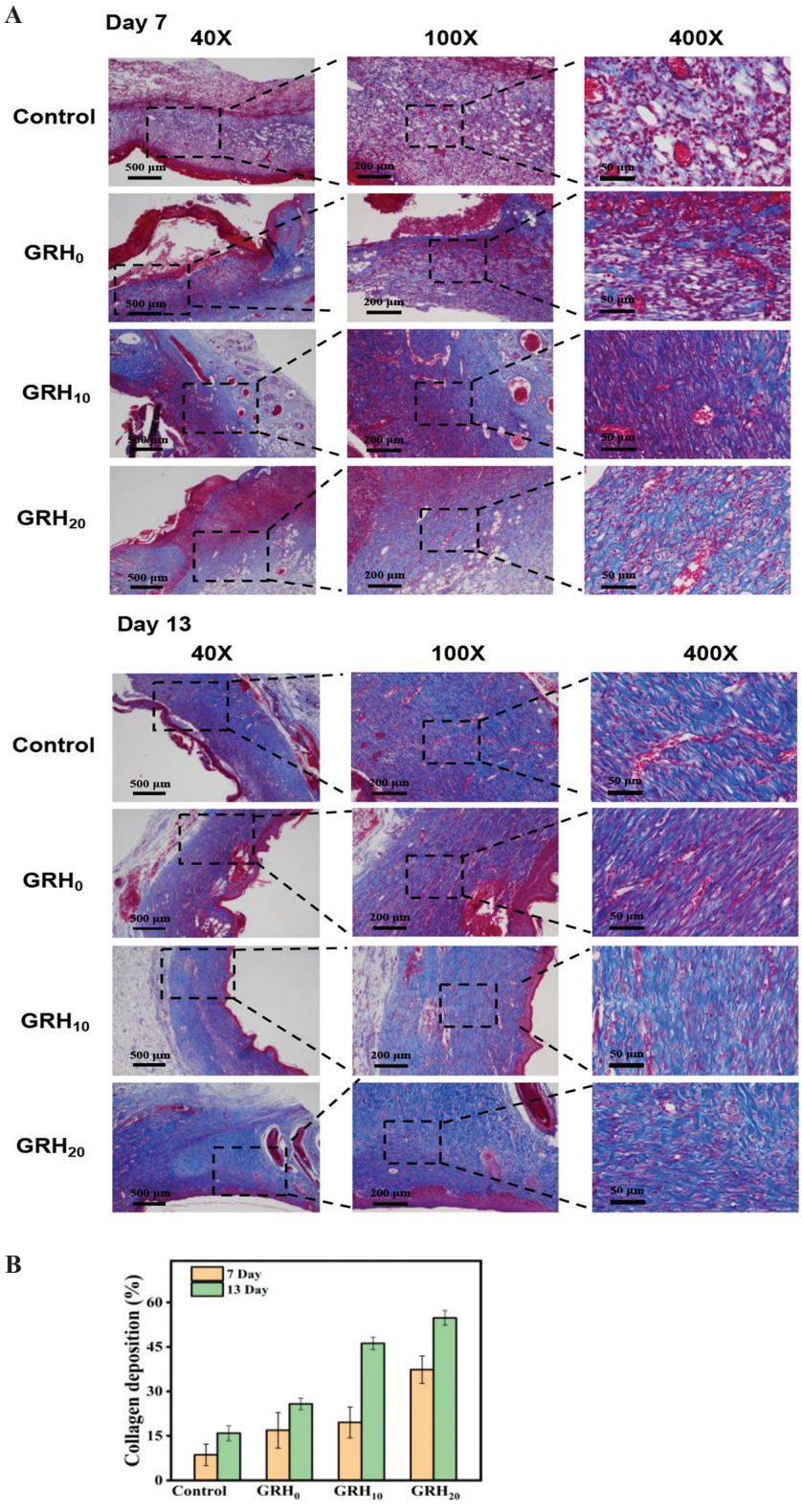


Figure 7. Masson's trichrome staining images and the corresponding quantification of the collagen deposition in four different groups.

the contrary, a significantly higher amount of type III collagen was observed in the GRH_{20} group (**Figure 8**), with less wound scar contracture and sclerosis. These findings altogether indicate that more advanced and

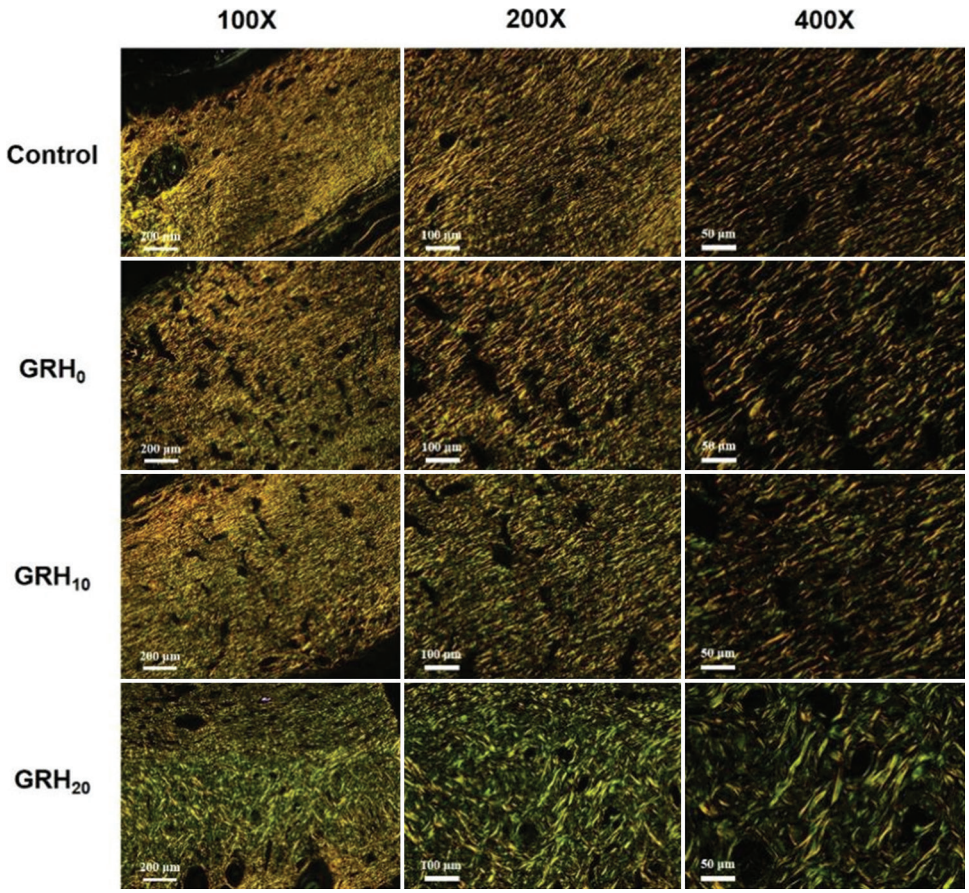


Figure 8. Sirius red staining images of the skin tissues of the rat wounds in four different groups on day 13. Scale bar: 200 μm.

high-quality wound healing was achieved in the GRH_{20} group compared to other groups.

4. Conclusion

Artificial skins as the wound covering materials that promote the regeneration of damaged skins can alleviate the pain of patients with severe skin damage. Yet, an optimal composition of the covering materials that lead to a high-quality, rapid wound healing has still not been found. In this study, we showed that gelatin alone is insufficient to provide an environment for damaged skin tissues to heal rapidly. The addition of rColIII can significantly accelerate the speed of wound healing and improve the quality of repair, as evidenced by a substantially smaller wound area, denser tissue structures with an ordered arrangement and obvious cuticle, a significantly higher amount of collagen fibers instead of muscle fibers, and a higher level of nascent collagens, especially the type III collagen. Taken together, we present an all-protein hydrogel material composed of gelatin and rColIII that can be used for wound healing in patients with severe skin damage.

Acknowledgments

We acknowledge funding supports by Jiangsu Key Research and Development Plan (Society Development, No. BE2018639), the Qinglan Project of Jiangsu Province, Shenzhen Science and Technology Projects (GJHZ20190820115203714, JSGG20191129094218565), Sanming Project of Medicine in Shenzhen (SZSM201612079), Shenzhen Fund for Guangdong Provincial High Level Clinical Key Specialties (No. SZGSP013, SZGSP007), and Shenzhen Key Medical Discipline Construction Fund (SZXK042 and SZXK049). This work was partially funded by the University Grants Committee of Hong Kong (GRF Grants N_CUHK422/18) and CUHK RSFS grant.

Conflicts of interest

No author has financial or other contractual disagreements that might cause conflicts of interest.

Author contributions

J.H., H.L., and J. Xia designed the research. J.H., X.L., Z.H., Z.R., and Y.X. performed the research. L.D., J.

Xiong, D.W., and Y.L. analyzed the data. X.L., Y.L., J.W., and J. Xia wrote the paper.

References

1. Martin P, 1997, Wound Healing--Aiming for Perfect Skin Regeneration. *Science*, 276:75–81. https://doi.org/10.1126/science.276.5309.75
2. Reinke JM, Sorg H, 2012, Wound Repair and Regeneration. *Eur Surg Res*, 49:35–43. https://doi.org/10.1159/000339613
3. Heng M, 2011, Wound Healing in Adult Skin: Aiming for Perfect Regeneration. *Int J Dermatol*, 50:1058–66. https://doi.org/10.1111/j.1365-4632.2011.04940.x
4. Fleischmann T, Nicholls F, Lipiski M, *et al*., 2019, Transplantation of Autologous Dermo-epidermal Skin Substitutes in a Pig Model. *Methods Mol Biol*, 1993:251–9. https://doi.org/10.1007/978-1-4939-9473-1_20
5. Herskovitz I, Hughes OB, Macquhae F, *et al*., 2016, Epidermal Skin Grafting. *Int Wound J*, 3:52–6. https://doi.org/10.1111/iwj.12631
6. Schulz JT 3rd, Tompkins RG, Burke JF, *et al*., 2020, Artificial Skin. *Annu Rev Med*, 51:231–44. https://doi.org/10.1146/annurev.med.51.1.231
7. Vig K, Chaudhari A, Tripathi S, *et al*., 2017, Advances in Skin Regeneration Using Tissue Engineering. *Int J Mol Sci*, 18:789. https://doi.org/10.3390/ijms18040789
8. Bhardwaj N, Chouhan D, Mandal BB, (2017) Tissue engineered skin and wound Healing: current strategies and future directions. *Curr Pharm Des*, 23:3455–82. https://doi.org/10.2174/1381612823666170526094606
9. Sorushanova A, Delgado LM, Wu Z, *et al*., 2019, The Collagen Suprafamily: From Biosynthesis to Advanced Biomaterial Development. *Adv Mater*, 31:e1801651. https://doi.org/10.1002/adma.201801651
10. Rodríguez MI, Barroso LG, Sánchez ML, 2018, Collagen: A Review on its Sources and Potential Cosmetic Applications. *J Cosmet Dermatol*, 17:20–6. https://doi.org/10.1111/jocd.12450
11. Davison-Kotler E, Marshall WS, García-Gareta E, 2019, Sources of Collagen for Biomaterials in Skin Wound Healing. *Bioengineering*, 6:56. https://doi.org/10.3390/bioengineering6030056
12. Browne S, Zeugolis DI, Pandit A, 2013, Collagen: Finding a Solution for the Source. *Tissue Eng Part A*, 19:1491–4. https://doi.org/10.1089/ten.TEA.2012.0721
13. Liu X, Hong WU, Byrne M, *et al*., 1997, Type III Collagen is Crucial for Collagen I Fibrillogenesis and for Normal Cardiovascular Development. *Proc Natl Acad Sci U S A*, 94:1852–6.
14. Clore JN, Cohen IK, Diegelmann RF, 1979, Quantitation of Collagen Types I and III during Wound Healing in Rat Skin. *Proc Soc Exp Biol Med*, 161:337–40. https://doi.org/10.3181/00379727-161-40548
15. Gay S, Vijanto J, Raekallio J, *et al*., 1978, Collagen Types in Early Phases of Wound Healing in Children. *Acta Chir Scand*, 144:205–11.
16. Mays PK, Bishop JE, Laurent GJ, 1988, Age-related Changes in the Proportion of Types I and III Collagen. *Mech Ageing Dev*, 45:203–12. https://doi.org/10.1016/0047-6374(88)90002-4
17. Podolsky MJ, Yang CD, Lizama C, *et al*., 2020, Age-dependent Regulation of Cell-mediated Collagen Turnover. *JCI Insight*, 5:e137519. https://doi.org/10.1172/jci.insight.137519
18. Wang C, Rong YH, Ning FG, *et al*., The Content and Ratio of Type I and III Collagen in Skin Differ with Age and Injury. *Afr J Biotechnol*, 10:2524–9.
19. Leung A, Crombleholme TM, Keswani SG, 2012, Fetal Wound Healing: Implications for Minimal Scar Formation. *Curr Opin Pediatr*, 24:371–8. https://doi.org/10.1097/MOP.0b013e3283535790
20. Chattopadhyay S, Raines RT, 2014, Review Collagen-based Biomaterials for Wound Healing. *Biopolymers*, 101:821–33. https://doi.org/10.1002/bip.22486
21. Báez J, Olsen D, Polarek JW, 2005, Recombinant Microbial Systems for the Production of Human Collagen and Gelatin. *Appl Microbiol Biotechnol*, 69:245–52. https://doi.org/10.1007/s00253-005-0180-x
22. Myllyharju J, Nokelainen M, Vuorela A, *et al*., 2000, Expression of Recombinant Human Type I-III Collagens in the Yeast Pichia pastoris. *Biochem Soc T*, 28:353–7.
23. Olsen D, Yang C, Bodo M, *et al*., 2003, Recombinant Collagen and Gelatin for Drug Delivery. *Adv Drug Deliv Rev*, 55:1547–67. https://doi.org/10.1016/j.addr.2003.08.008
24. Shoseyov O, Posen Y, Grynspan F, 2014, Human Collagen Produced in Plants: More than Just Another Molecule. *Bioengineered*, 5:49–52. https://doi.org/10.4161/bioe.26002
25. Liu T, Zheng X, Li H, *et al*., 2019, Effect of Recombinant Human Type-III Collagen Hydrogels on Wound Healing of Pig Full-thickness Skin Defects. *Chin J Injury Repair Wound Healing*, 14:97–102.
26. Echave MC, Burgo L, Pedraz JL, *et al*., 2017, Gelatin as Biomaterial for Tissue Engineering. *Curr Pharm Des*,

23:3567–84.
https://doi.org/10.2174/0929867324666170511123101

27. Skardal A, Atala A, 2015, Biomaterials for Integration with 3-D Bioprinting. *Ann Biomed Eng*, 42:730–46.
https://doi.org/10.1007/s10439-014-1207-1
28. Jungst T, Smolan W, Schacht K, *et al*., 2016, Strategies and Molecular Design Criteria for 3D Printable Hydrogels. *Chem Rev*, 116:1496–539.
https://doi.org/10.1021/acs.chemrev.5b00303
29. Blaeser A, Campos DF, Puster U, *et al*., 2016, Controlling Shear Stress in 3D Bioprinting is a Key Factor to Balance Printing Resolution and Stem Cell Integrity. *Adv Healthc Mater*, 5:326–33.
https://doi.org/10.1002/adhm.201500677
30. Billiet T, Vandenhaute M, Schelfhout J, *et al*., 2012, A Review of Trends and Limitations in Hydrogel-rapid Prototyping for Tissue Engineering. *Biomaterials*, 33:6020–41.
https://doi.org/10.1016/j.biomaterials.2012.04.050
31. Highley CB, Rodell CB, Burdick JA, 2015, Direct 3D Printing of Shear-Thinning Hydrogels into Self-Healing Hydrogels. *Adv Mater*, 27:5075–9.
https://doi.org/10.1002/adma.201501234
32. Zhang YS, Haghiashtiani G, Hübscher T, *et al*., 3D Extrusion Bioprinting. *Nat Rev Methods Primers*, 1:75.
33. Ramesh S, Harrysson OL, Rao PK, *et al*., 2021, Extrusion Bioprinting: Recent Progress, Challenges, and Future Opportunities. *Bioprinting*, 21:e00116.
34. Ng WL, Huang X, Shkolnikov V, *et al*., 2022, Controlling Droplet Impact Velocity and Droplet Volume: Key Factors to Achieving High Cell Viability in Sub-Nanoliter Droplet-based Bioprinting. *Int J Bioprinting*, 8:424.
35. Li X, Liu B, Pei B, *et al*., 2020, Inkjet Bioprinting of Biomaterials. *Chem Rev*, 120:10793–833.
36. Ng WL, Lee JM, Zhou M, *et al*., 2020, Vat Polymerization-based Bioprinting-process, Materials, Applications and Regulatory Challenges. *Biofabrication*, 12:022001.
37. Li W, Mille LS, Robledo JA, *et al*., 2020, Recent Advances in Formulating and Processing Biomaterial Inks for Vat Polymerization-Based 3D Printing. *Adv Healthc Mater*, 9:e2000156.
https://doi.org/10.1002/adhm.202000156
38. Huang J, Huang Z, Liang Y, *et al*., 2012. 3D Printed Gelatin/Hydroxyapatite Scaffolds for Stem Cell Chondrogenic Differentiation and Articular Cartilage Repair. *Biomater Sci*, 9:2620–30.
39. Akutsu T, Ikegaya H, Watanabe K, *et al*., 2019, Immunohistochemical Staining of Skin-expressed Proteins to Identify Exfoliated Epidermal Cells for Forensic Purposes. *Forensic Sci Int*, 303:109940.
https://doi.org/10.1016/j.forsciint.2019.109940

Publisher's note

Whioce Publishing remains neutral with regard to jurisdictional claims in published maps and institutional affiliations.

RESEARCH ARTICLE

Development of a 3D Individualized Mask for Neonatal Non-Invasive Ventilation

Cristina Borràs-Novell[1]*, Mario García Causapié[2], Maria Murcia[3], Damien Djian[4], Óscar García-Algar[1]

[1]Department of Neonatology. BCNatal – Center for Fetomaternal and Neonatal Medicine Barcelona. Hospital Clínic. Universitat de Barcelona. Barcelona, 08028, Spain
[2]Biomedical Engineering. Hospital Clínic. Universitat de Barcelona. Barcelona, 08036, Spain
[3]Elkem Siliconas España. Santa Perpetua de Mogoda, Spain
[4]Elkem Silicones France SAS. Saint Fons, France

Abstract: Non-invasive masks are designed based on generic facial models; therefore, difficulties in fitting patients' unique characteristics are common. A poor fit of the mask may have consequences such as air leaks or pressure ulcers. It is possible to optimize the fit of interfaces by adapting them to a patient's face. Our objective is to design an individualized silicone mask for non-invasive ventilation for a premature phantom using a three-dimensional (3D) scanner and bioprinter. The facial surface of the manikin was scanned with a 3D scanner in a supine position, in an incubator with a sliding mattress and in <2 min. We printed the tailor-made mask in 3 h with biocompatible and hypoallergenic silicone. When applied under a simulated clinical scenario, the mask possessed good structural reliability after post-processing and optimal mechanical features. We observed adequate thoracic excursion and 14% reduction in air leaks when the manikin was ventilated with the customized mask with a neonatal ventilator. We ink the edges of personalized and standard masks. After fitting them to phantoms, personalized mask showed better pressure distribution. Our subsequent research direction is to test the viability of personalizing non-invasive ventilation masks for very preterm infants of our department.

Keywords: Premature infant; Non-invasive ventilation; Mask; Pressure ulcer; 3D printing

*Correspondence to: Cristina Borràs-Novell, Department of Neonatology. BCNatal – Center for Fetomaternal and Neonatal Medicine Barcelona. Hospital Clínic. Universitat de Barcelona. Barcelona, 08028, Spain; cborrasn@clinic.cat

Received: November 18, 2021; **Accepted:** December 29, 2021; **Published Online:** February 24, 2022

Citation: Borràs-Novell, C., Causapié, M.G., Murcia, M, *et al.,* 2022, Development of a 3D Individualized Mask for Neonatal Non-Invasive Ventilation. *Int J Bioprint,* 8(2):516. http://doi.org/10.18063/ijb.v8i2.516

1. Introduction

The application of three-dimensional (3D) printing for medical purposes has become more common in recent years, and it's application has been further accelerated due to the coronavirus disease 2019 (COVID-19) pandemic[1]. 3D printing is a technology that allows printing solid objects in different materials by overlapping layers in cross sections. The 3D models can be created *de novo* or by replicating an existing object with the use of a 3D scanner.

Although the literature related to 3D printing in medicine remains scarce, disciplines such as dentistry, reconstructive surgery, neurosurgery, and orthopedic surgery are among the top disciplines that have proven the utility of 3D printing. Although the applications of 3D printing are still limited in neonatology, a specialty that has undergone a significant technological advancement in recent decades, it is expected that this technology will contribute to the individualization of neonatal care[2]. Recent publications have demonstrated the viability to create individualized masks for occupational health, aerosol therapy or non-invasive ventilation (NIV) in adults and children[3-7].

NIV is used in neonatology departments worldwide. NIV requires the use of an interface that connects the ventilator to the patient. There are different types of interfaces; one of the most used in neonatology is nasal mask. NIV masks are designed based on generic facial models; therefore, difficulties in fitting patients' unique facial

© 2022 Author(s). This is an Open Access article distributed under the terms of the Creative Commons Attribution License, permitting distribution and reproduction in any medium, provided the original work is properly cited.

characteristics are quite inevitable, especially in younger patients or in patients with peculiar facial features[3,8]. A poor fit of the mask may have relevant clinical consequences such as air leaks, making it difficult to achieve proper ventilation, and oxygenation[9]. The great diversity of human faces' geometries, especially in newborns during the 1st days of life or in growing infants, may represent a limitation for standardized masks[5]. An individualized mask was recently designed for the application of nocturnal continuous positive airway pressure (CPAP) in a pediatric patient with Treacher-Collins syndrome and obstructive sleep apnea[3]. With the use of this individualized mask, Morrison *et al*. described an air leakage reduction of 74% and a greater adherence of the patient to therapy compared to the standard mask.

In addition, skin in-contact with the mask can suffer pressure ulcers, especially if the mask does not fit properly. Mask-related pressure ulcers cause pain, discomfort and loss of function, resulting in extended hospital stays and increased costs[4], and are recognized as preventable adverse events in healthcare[10,11]. Despite the application of best practices to prevent medical device-related pressure ulcers, the Skin Adverse Events' Working Group of the Hospital Clínic reported an incidence of 30.7% of pressure ulcers related to the use of NIV masks in very preterm infants during the 1st week of life (65% of these patients will suffer from a recurrence)[12]. Other complications related to these ulcers can range from local/systemic infections to long-term scars.

More effective strategies to prevent pressure ulcers related to the use of medical devices are urgently needed[4]. There is no report regarding individualized neonatal masks for NIV. We believe that 3D printing can make an important contribution to a more personalized neonatal care in the near future.

Before a planned test with premature patients, we checked with the present work the feasibility of the process of creating and printing a 3D customized mask for NIV for a manikin. Our primary objective is to design an individualized prototype of a biocompatible silicone nasal mask for NIV for the Premature Anne manikin from Laerdel® using a 3D printer. The secondary objectives are:

(i) To assist the manikin achieve adequate thoracic excursion using the customized mask;
(ii) To compare the reduction in air leakage between the customized mask and standardized mask suitable for the aforementioned manikin; and
(iii) To compare the pressure distribution at the skin contact areas between the customized mask and standardized mask suitable for the aforementioned manikin.

2. Methods

This experimental observational study was carried out in the Neonatology Department of the Hospital Clínic Barcelona in 2020 and 2021.

The research team made up of two physicians and six nurses who are part of the Skin Adverse Events' Working Group of our hospital. The project was also a collaboration with an engineer from the Biomedical Engineering Department of the Hospital Clínic who is used to work on 3D printing models in resin for orthopedic and reconstructive surgery, and a collaboration with Avinent Implant System S.L.U. (Santpedor, Spain) and Elkem Silicones France SAS companies.

The followings steps were proposed to obtain the tailor-made mask:

(i) Image capture. Scan of the facial surface of the manikin was made using the 3D Peel 2 CAD scanner with LED light. The scanner has a mesh resolution of 0.25 mm and a scan area of 380 mm × 380 mm. This step necessitates the use of a device that does not need contact with the manikin, can be used inside the incubator and does not use harmful radiations.
(ii) Image processing. Once the points' cloud of the scanned surface was obtained, we converted it into a.STL file (standard data transmission format that transformed the scanned volumetric surface to a solid reconstruction using triangle-faces modeling). Next, we redesigned the standard mask model by adapting the part that is in contact with the manikin so that it matches the exact physiognomy of the scanned face.
(iii) 3D mask printing. The mask was printed using the Liquid Deposition Modeling technique, which consists of deposition by extrusion of liquid silicone at room temperature with a curing process. The printed mask had a resolution of 200 µm thick layer and was extruded through a nozzle orifice with diameter of 234 µm. Avinent Implant System S.L.U. (Santpedor, Spain) Company is the owner of the bioprinter. The chosen material for this purpose was from the AMSil™ Silicone Elastomers series. Elkem Silicones France SAS Company is the manufacturer of the silicone. In addition to the already known properties, other properties of silicone include resistance to oxidation processes, thermal stability, and resistance to compression and friction; these properties justify the wide application of silicone in the health sector. Moreover, the printable silicone is hypoallergenic when it is in contact with the skin.

We compared air leaks detected by the ventilator between the customized mask and the standard mask that corresponds to the size of the manikin according to our interface selection protocol for non-invasive neonatal ventilation. The standard mask used was the CareFusion® Infant Flow LP Nasal CPAP System. The manikin was modified to minimize leakage through the mouth.

The edges of both masks were marked with ink on the face of the manikin to qualitatively compare their support areas.

Since the current prototype was developed on a base and tested on the face of a mannequin, an ethical approval was not necessary and was therefore not sought from the ethics committee of our center.

3. Results

3.1. Image capture

The facial surface of the manikin was scanned with a 3D Peel 2 CAD scanner, as shown in **Figure 1**. The manikin was placed in a supine position, in an incubator with a sliding mattress and with three spatial reference points. The procedure lasted 10 min, with a direct light to manikin's eyes in 1.5 – 2 min.

3.2. Image processing

We use Mimics Medical 24.0 program from Materialize (approved for designing medical and surgical devices for medical use) to customize a mask that perfectly fits the geometry of the manikin with smooth contact boundaries. The customized mask was designed to rest on the nasal bone, nasolabial sulcus and philtrum, without contacting the alas of the nose nor obstructing the nostrils. In the manikin that was used to design the prototype of customized mask, its size would correspond to the XS–S size of commercial masks. The work related to image processing and subsequent design corrections under medical guidelines lasted 2 h (**Figure 2**).

3.3. 3D printing

The created design was sent for printing. The process of printing the mask with selected biocompatible and hypoallergenic silicone (AMSil™ Silbione™ 24501-50 TRS A-B) took 3 h and consumed about 2 g of the material. The first mask obtained, as shown in **Figure 3**, had no macroscopic defects. An adhesive silicone strip type Silbione RTGel 4642 A&B (which does not damage the skin after removal) was added to the edge of the mask in contact with the manikin to optimize its adherence.

The manikin was ventilated with non-invasive ventilator and the printed mask with adequate thoracic excursion.

Since air leakage percentage was not displayed on our neonatal non-invasive ventilators, we created a "leak-free circuit" with an invasive ventilator. For this purpose, the manikin leaks were blocked with a plasticine mold in the mouth and printed mask was connected to inspiratory and expiratory tubing. Under the same conditions, with a constant flow of air, invasive ventilator measured 78% of air leakage from standardized mask, and 64% from individualized mask.

For evaluating how the mask was fitted to the manikin's face, we marked with ink the edges of both masks. We fitted both mask to two manikin's face prints during 30 s. Pressure distribution is shown in **Figure 4**.

We estimated that the whole process might involve 6 h and cost 80 euros. This price also accounted for the time spent by the team of engineers, who designed the prototype and made the subsequent corrections under medical criteria, and the materials used.

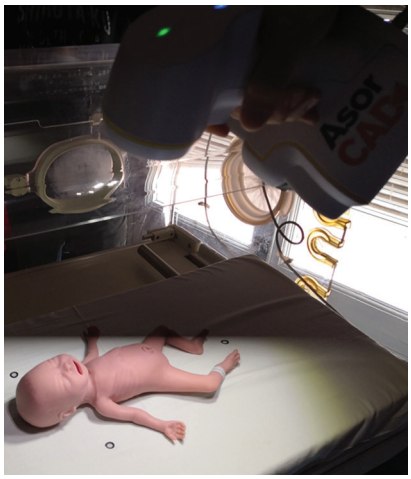


Figure 1. Scan of the facial surface of the manikin.

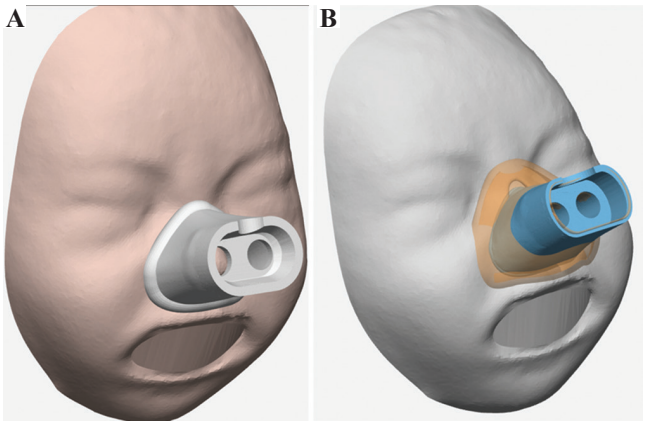


Figure 2. (A) Customized mask design. (B) Comparison of the contact surface with the standardized mask (in orange) and with the customized mask (in blue).

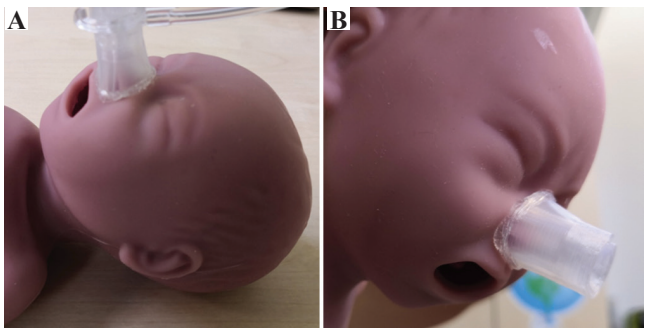


Figure 3. (A) Checking the fit of printed nasal mask on the face of the manikin (B) checking the adherence of printed nasal mask to the face (without subjection system).

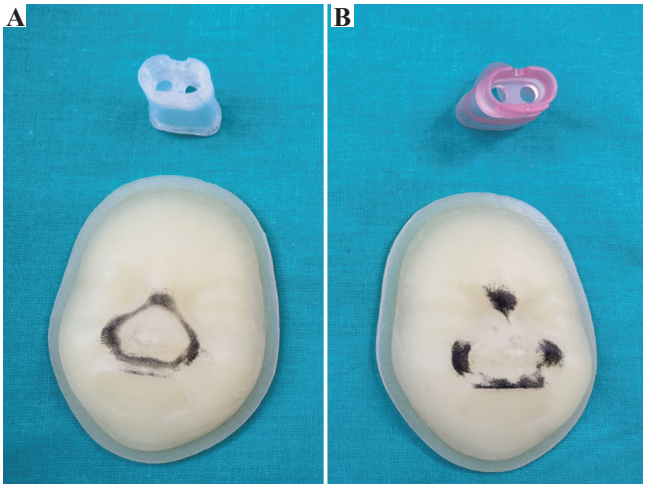


Figure 4. (A) Support areas of the personalized nasal mask. (B) Support areas of the standard nasal mask to two manikin's face prints. Material used for customized mask was AMSil™ Silbione™ 24501-50 TRS A-B from Elkem Silicones France SAS. Material used for standardized mask was Medical Grade Liquid Silicone Rubber from CareFusion ® and for printed faces was Agilus30Clear from Stratasys TM (PolyJet® technology).

4. Discussion

This is a pilot study that demonstrated that a customized NIV mask for a manikin (a manikin that emulates the size of an extremely premature patient) can be 3D printed using a 3D scanner imaging system. The customized nasal mask was designed to mimic existing nasal masks but has a tailor-made shape to fit the manikin's face. The evaluation of the process of designing a mask from scan data, the organization of its manufacture and the printing of the prototype described in this study are valuable experiences for future reference.

To the best of our knowledge, although this is not the first study that demonstrated effectiveness of 3D scanning and printing technology in healthcare[6,8], this is the first article reporting the manufacture of a 3D individualized mask for neonatal population and the application of silicone certified for medical use.

The use of NIV changed the way neonatologists treated patients with respiratory failure, thereby minimizing the risks and complications associated with endotracheal intubation and invasive ventilation. There are between 350,000 and 400,000 births each year in Spain; about 7 – 13% are preterm births[13]. The majority of very preterm infants (born before week 32 of gestation) need NIV, especially during the first few days or weeks of life. Around 100 very preterm infants are born in our hospital each year; more than 70% of them will require NIV for a mean period of 8 days. NIV needs an interface that links the ventilator with the patient. There are different types of interfaces, for example, prongs or nasal masks (the current project is based on nasal masks). Unfortunately, the use of these interfaces has raised other problems such as air leaks and pressure ulcers[14]. It is possible to optimize the fit of these interfaces by adapting them to the specific characteristics of each patient[6,15].

Given the vulnerability of the target population (very premature infants), the development conditions of the mask are very demanding. For this reason, we proposed a preliminary study in which we worked with a manikin (subject of the present publication).

Requested requirements for the first step of the described process, that is, facial image capture, were accomplished. We worked without touching the manikin (scanning the face instead of using a mold), keeping it inside the incubator (avoiding extra mobilizations), and without using harmful radiation or long light exposures (maximum 2 min). It is known that long or intense light exposures are detrimental to the neurodevelopment of premature patients[16]. AsorCAD Creafom gamma Academia 3D scanner has given us these advantages as well as an adequate image resolution for the size of the manikin's face. This step lasted less than 10 min, similar to that described by Willox *et al*. in their customized masks' tests on adult patients[8]. This form of facial image capture has a limitation that it can be affected by the patient's gestures, so a neutral posture of the face should be acquired[8].

The 3D printing of the mask has been made with a biocompatible and hypoallergenic silicone thanks to the participation of the companies Avinent Implant System S.L.U. (Santpedor, Spain) and Elkem Silicones France SAS. 3D printing with silicone is a strong point of our project, because despite its universal use in healthcare, the application of this material in 3D printing is quite novel. Its most notable characteristics are low allergenicity, durability, non-deformability and stability at high temperatures (in case of sterilization procedures). The transparency of the mask is a point to improve. A breakthrough in the field of 3D printing materials is expected in the near future.

The personalized mask perfectly fits the facial features of the manikin compared to standardized masks. We believe that this perfect fit reduces air leaks and avoids an excessively firm fixation as indicated in our results. If the mask is too tightly fitted, the pressure on the skin leads to the appearance of skin lesions. Through the qualitative tests with ink, we observed that the support area of the personalized mask on the face was homogeneous and the pressure was better distributed, but even so, there is no guarantee that the personalized mask will not cause pressure injuries in patients. This is an issue to be explored in further studies. The standardized mask discontinuously rested on manikin's face; high pressure points on the nasal bridge and the upper lip were detected. These areas are susceptible to frequent occurrence of pressure ulcers[12].

Finally, the physical characteristics of the 3D printed prototype allow the incorporation of an adhesive silicone strip in the contour that rests on manikin; this strip does not damage the skin when it is removed. This extra adherence may reduce damage caused by friction mechanisms, instead of pressure mechanisms. Willox *et al*. added *granuflexv* to their printed prototype to cushion the edges as the mask seems more rigid[8]. The adhesive silicone strip could also be used in commercially available masks.

The use of a resuscitation manikin in this study enabled us to connect a ventilation system to the manikin to check the correct thoracic excursion with the use of a tailor-made mask. However, due to such use of the phantom, other ventilatory parameters could not be tested.

3D printing can also become a potentially useful tool for both patients and health personnel in the background of the COVID-19 pandemic. Individualized printed masks represent an improvement in NIV therapies for patients affected by respiratory failure. On the other hand, customized masks could also play a role in the protection of healthcare personnel; some studies have demonstrated the application of 3D printing in the development of personal protective equipment and respiratory protective devices[7,17-19].

At the end of the study, we estimated that the price of making an individualized mask was 80 euros at the time. To prevent NIV-related skin ulcerations, our hospital's protocol recommends the alternative use of two generic nasal masks of different sizes in every infant (these masks need to be renewed every 5 days). The total NIV days in our department are around 600 days/year, corresponding to the use of approximately 250 standardized masks. This price is, in general terms, higher than that of standardized masks (in our case, it is 4 times higher), but we believe that the cost can be substantially reduced by automating the design phase and by having the printer available in the hospital. Potential clinical benefits from tailor-made masks can lead to a favorable cost/benefit ratio.

The next step of our research team is to test the viability of the process in very preterm infants admitted in our department. This will include the previously mentioned steps (3D facial scan, image processing, and 3D printing process) by following the same methodology. To make sure very preterm infants could eventually benefit from these tailor-made masks as soon as possible, the team is dedicated to shortening the time that it currently takes to produce each mask by automating the design phase. This new proposed project will be presented to the ethics committee of our hospital. Once ethical approval is granted by the research ethics committee, we will conduct a clinical study to test the resulting tailor-made, 3D-printed NIV masks and compare their effectiveness and safety versus the standardized masks. The key endpoints of the project are related to the ability of the tailor-made masks in optimizing patient's ventilation, and especially their ability to reduce skin ulcerations.

4. Conclusions

Our research team has tested and validated the technical viability of designing and printing silicone tailor-made 3D facial masks for NIV to a very preterm manikin (Anne Premature from Laerdel®). The customization of these non-invasive masks allows perfect fit of the specific anatomic features of any given patient's face. In near future, these tailor-made masks could reduce air leaks and allow for a homogeneous distribution of pressure on the skin, thereby optimizing NIV and reducing the risk for skin ulcers, respectively.

Acknowledgments

The authors would like to thank Avinent Implant System S.L.U. and Elkem Silicones France SAS, especially Lauriane Depernon (Technical Service Manager Skin Adhesives - Compentence Center – ATRiON), for their technological support and knowledge in the development of this project.

The authors would like also to thank to the Skin Adverse Events' Working Group of the Neonatology Department of Hospital Clínic for their collaboration, their expertise has been fundamental.

Funding

Our project was granted by research aid Adolfo Valls-Respisurf of the Spanish Society of Neonatology (edition 2018).

Conflict of interest

Authors Cristina Borràs-Novell, Mario García Causapié and Oscar García-Algar do not have conflicts of interest. Authors Maria Murcia and Damien Djian work in Elkem Company as Sales Manager HC&IAM Iberia and Sales Expert 3D printing Europa and R&I – Compentence Center – ATRiON respectively. The mentioned companies had altruist collaboration in the current project, within the framework of Research & Development.

Author contributions

C.B.N. literature review, image capture, prototype design corrections, prototype tests, data management, data interpretation, draft manuscript, consolidation of coauthor comments, and paper finalization. M.G.C. image capture, prototype design, prototype tests, data interpretation, and manuscript review. M.M prototype design and manuscript review. D.D. prototype design, prototype printing, and manuscript review. O.G.A. conceptualization, work coordination, and manuscript review.

References

1. Choong YY, Tan HW, Patel DC, *et al*., 2020, The Global Rise of 3D Printing During the COVID-19 Pandemic. *Nat Rev Mater*, 5:637–9.
2. Aufieri R, Picone S, Gente M, *et al*., 2015, 3D Printing in Neonatal Care. *Ital J Pediatr*, 41:A1. http://doi.org/10.1186/1824-7288-41-s1-a1
3. Morrison RJ, VanKoevering KK, Nasser HB, *et al*., 2015, Personalized 3D-Printed CPAP Masks Improve CPAP Effectiveness in Children with OSA and Craniofacial Anomalies Robert'. Conference: Combined Otolaryngology Spring Meetings, Boston. http://doi.org/10.13140/RG.2.1.2328.1687
4. Hsu DY, Cheng YL, Bien MY, *et al*., 2015, Development of a Method for Manufacturing Customized Nasal Mask Cushion for CPAP Therapy. *Australas Phys Eng Sci Med*, 38:657–66. http://doi.org/10.1007/s13246-015-0383-0
5. Sela M, Toledo N, Honen Y, *et al*., 2016, Customized Facial Constant Positive Air Pressure (CPAP) Masks. Available from: http://arxiv.org/abs/1609.07049 [Last accessed on 2021 Sep 23].
6. Shikama M, Nakagami G, Noguvhi H, *et al*., 2018, Development of Personalized Fitting Device with 3-Dimensional Solution for Prevention of Niv Oronasal Mask-Related Pressure Ulcers. *Respir Care*, 63:1024–32. http://doi.org/10.4187/respcare.05691
7. Makowski K, Okrasa M, 2019, Application of 3D Scanning and 3D Printing for Designing and Fabricating Customized Half-mask Facepieces: A Pilot Study. *Work*, 63:125–35. http://doi.org/10.3233/WOR-192913
8. Willox M, Metherall P, Jeays-Ward K, *et al*., 2020, Custom-made 3D Printed Masks for Children Using Non-invasive Ventilation: A Feasibility Study of Production Method and Testing of Outcomes in Adult Volunteers. *J Med Eng Technol*, 44:213–23. http://doi.org/10.1080/03091902.2020.1769759
9. Barker N, Willox M, Elphick H, 2018, A Review of the Benefits, Challenges and the Future for Interfaces for Long Term Non-Invasive Ventilation in Children. *Int J Respir Pulm Med*, 5:77. http://doi: 10.23937/2378-3516/1410077
10. Apold J, Rydrych D, 2012, Preventing Device-related Pressure Ulcers: Using Data to Guide Statewide Change. *J Nurs Care Qual*, 27:28–34. http://doi.org/10.1097/NCQ.0b013e31822b1fd9
11. Murray JS, Noonan C, Quigley S, *et al*., 2013, Medical Device-related Hospital-acquired Pressure Ulcers in Children: An Integrative Review. *J Pediatr Nurs*, 28:585–95. http://doi: 10.1016/j.pedn.2013.05.004
12. Gracia MC, Muñoz A, Vidal M, *et al*., 2021, Incidence and risk factors associated with the appearance of pressure injuries in premature less than 34 weeks with non-invasive ventilation. *Rev Enfer*m, 44:23–9.
13. InstitutoNacionaldeEstadística,2020,EstadísticadeNacimientos. Available from: https://www.ine.es/dyngs/INEbase/es/operacion.htm?c=Estadistica_C&cid=1254736177007&menu=ultiDatos&idp=1254735573002 [Last accessed on 2020 Jul 03].
14. Pittman J, Beeson T, Kitterman J, *et al*., 2015, Medical Device-related Hospital-Acquired Pressure Ulcers: Development of an Evidence-based Position Statement. *J Wound Ostomy Continence Nurs*, 42:151–4. http://doi.org/10.1097/WON.0000000000000113
15. Ma Z, Drinnan M, Hyde P, *et al*., 2018, Mask Interface for Continuous Positive Airway Pressure Therapy: Selection and Design Considerations. *Exp Rev Med Dev*, 15:725–33. http://doi.org/10.1080/17434440.2018.1525291
16. Santos J, Pearce SE, Stroustrup A, 2015, Impact of Hospital-based Environmental Exposures on Neurodevelopmental Outcomes of Preterm Infants. *Curr Opin Pediatr*, 27:254–60. http://doi.org/10.1097/MOP.0000000000000190
17. Celik H K, Kose O, Ulmeanu M, *et al*, 2020, Design and Additive Manufacturing of Medical Face Shield for Healthcare Workers Battling Coronavirus (COVID-19). *Int J Bioprint*, 6:286. http://doi.org/10.18063/ijb.v6i4.286
18. Sherborne C, Claeyssens F, 2021, Considerations Using Additive Manufacture of Emulsion Inks to Produce Respiratory Protective Filters Against Viral Respiratory Tract Infections Such as the COVID-19 Virus. *Int J Bioprint*, 7:316. http://doi.org/10.18063/ijb.v7i1.316
19. Bishop EG, Leigh SJ, 2020, Using Large-Scale Additive Manufacturing as a Bridge Manufacturing Process in Response to Shortages in Personal Protective Equipment during the COVID-19 Outbreak. *Int J Bioprint*, 6:281. http://doi.org/10.18063/ijb.v6i4.281

Publisher's note

Whioce Publishing remains neutral with regard to jurisdictional claims in published maps and institutional affiliations.

RESEARCH ARTICLE

3D-Printed β-Tricalcium Phosphate Scaffolds Promote Osteogenic Differentiation of Bone Marrow-Deprived Mesenchymal Stem Cells in an N6-methyladenosine-Dependent Manner

Xin Jiao[1†], Xin Sun[1†], Wentao Li[1†], Wenxiang Chu[2], Yuxin Zhang[3], Yiming Li[1], Zengguang Wang[1], Xianhao Zhou[1], Jie Ma[1], Chen Xu[1], Kerong Dai[1], Jinwu Wang[1*], Yaokai Gan[1*]

[1]Department of Orthopaedic Surgery, Shanghai Ninth People's Hospital, Shanghai JiaoTong University School of Medicine, No. 639 Zhi Zao Ju Road, Huangpu District, Shanghai, China
[2]Department of Orthopaedic Surgery, Changzheng Hospital, Naval Medical University, No. 415 Fengyang Road, Huangpu District, Shanghai, China
[3]Department of Rehabilitation Medicine, Shanghai Ninth People's Hospital, Shanghai JiaoTong University School of Medicine, No.639 Zhi Zao Ju Road, Huangpu District, Shanghai, China
[†]*These authors contribute equally to this work.*

Abstract: Bone defect is a serious orthopedic disease which has been studied for a long time. Alternative degradable biomaterials are required for bone repairing and regeneration to address the limitation of autogenous bone. β-tricalcium phosphate (β-TCP) is an alternative material with good cytocompatibility and has been used in bone defect treatment. However, whether β-TCP contributes to osteogenesis of bone marrow stem cells (BMSCs) through N6-methyladenosine (m6A) modification remains unknown. To address this issue, we verified the effects of β-TCP on osteogenesis of BMSCs. We also studied the expression of m6A-related enzymes in BMSCs after β-TCP treatment. Furthermore, the m6A level and stability of Runt-related transcription factor 2 (RUNX2) mRNA were investigated after β-TCP treatment. Finally, rat calvarial defect models were performed to detect expression level of osteogenic factors and m6A-related enzymes after the stimulation of three-dimension (3D)-printed β-TCP scaffolds. We found that β-TCP showed good biocompatibility and was osteoinductive. Meanwhile, methyltransferase-like 3 (METTL3) increased, causing the elevation of m6A level of RUNX2, results in stabler RUNX2 mRNA level. At last, based on the animal experiments, we demonstrated that the increase of RUNX2 and METTL3 levels was induced by β-TCP. These findings suggest that METTL3 increases the m6A level of RUNX2 mRNA after β-TCP induction, contributing to its stability, and the results in vivo also confirmed the osteogenic and bone-repair properties of β-TCP.

Keywords: β-tricalcium phosphate; Osteogenic differentiation; Bone marrow stem cells; Runt-related transcription factor 2; N6-methyladenosine

*Correspondence to: Jinwu Wang, Department of Orthopaedic Surgery, Shanghai Ninth People's Hospital, Shanghai JiaoTong University School of Medicine, No. 639 Zhi Zao Ju Road, Huangpu District, Shanghai, China; wangjw@sjtu.edu.cn; Yaokai Gan, Department of Orthopaedic Surgery, Shanghai Ninth People's Hospital, Shanghai JiaoTong University School of Medicine, No. 639 Zhi Zao Ju Road, Huangpu District, Shanghai, China; ganyk2004@126.com

Received: November 30, 2021; **Accepted:** February 5, 2022; **Published Online:** March 22, 2022

Citation: Jiao X, Sun X, Li W, *et al.,* 2022, 3D-Printed β-Tricalcium Phosphate Scaffolds Promote Osteogenic Differentiation of Bone Marrow-Deprived Mesenchymal Stem Cells in an N6-methyladenosine-Dependent Manner. *Int J Bioprint,* 8(2):544. http://doi.org/10.18063/ijb.v8i2.544

© 2022 Author(s). This is an Open-Access article distributed under the terms of the Creative Commons Attribution License, permitting distribution and reproduction in any medium, provided the original work is properly cited.

1. Introduction

Bone defect is one of the most common diseases encountered in the field of orthopedics. With the development of tissue engineering, allochthonous and autogenous bones have commonly been used for transplantation into the site of bone defects for therapeutic purposes[1]. However, this never addresses the problems, such as a shortage of bone sources and high infection rates. In view of the limitation of bone sources, degradable biomaterials such as hydroxyapatite (HA) and β-tricalcium phosphate (β-TCP) have become alternative choices for use in bone repair. β-TCP has been widely applied in clinical treatments due to their promising results. β-TCP has several beneficial properties in the aspects of biocompatibility, osteoconductivity, osteoinductivity, and biodegradability, and can be easily manufactured into porous structures, which further improves its biodegradability and makes it suitable as a bone substitute for clinical application. Numerous clinical trials have shown that β-TCP has a similar effect on bone repair as allografts[1]. Conventionally, β-TCP is used in the shape of disks or granules. Three-dimensional (3D) printing technology, as an emerging technology, has provided a new prospect in the treatment of bone defect. 3D printing can be used to make porous β-TCP, which is beneficial for ingrowth of new bone. In addition, β-TCP combined with bone marrow mesenchymal stem cells (bone marrow stem cells [BMSCs]) has shown significantly higher degree of new bone formation compared to β-TCP alone[2]. β-TCP/BMSCs combination could be used to treat bone defects, bone nonunion, and other orthopedic diseases requiring bone implantation, with a lower infection rate and a higher success rate of artificial bone implantation[3-7]. The osteoinductivity of β-TCP is probably related to the osteogenesis induced by BMSCs. It has been suggested that β-TCP promotes upregulation of osteocalcin (OCN), osteopontin (OPN), bone sialoprotein (BSP), and bone morphogenetic protein 2[8]. Moreover, Runt-related transcription factor 2 (RUNX2), the key transcription factor in osteogenesis of BMSCs, was also increased in expression level after 7 days of TCP stimulation[9]. However, the mechanism by which β-TCP contributes to the high expression of RUNX2 in BMSCs is not fully understood.

RUNX2 is an indispensable transcriptional factor for the commitment of mesenchymal stem cells toward the osteoblast lineage[10]. Knockout of RUNX2 causes osteogenesis blockage at the cartilage stage, suggesting that RUNX2 is a promoter of early mineralization[11]. Mechanistically, RUNX2, as a transcriptional factor, can activate a large number of bone-related genes, including OCN, OPN, bone sialoprotein, and alkaline phosphatase (ALP)[12]. The osteoblast differentiation program also requires the activation of the genes like osterix to encode a transcriptional factor downstream of RUNX2[13]. Notably, RUNX2 is also regulated by N6-methyladenosine (m6A) RNA methylation. Yan *et al*. discovered the dual signaling cascades of osteogenic pathways: (i) Methyltransferase-like 3 (METTL3) upregulates m6A methylation of RUNX2, which increases RUNX2 stability and level, and contributes to osteogenesis; and (ii) METTL3 increases m6A methylation of pre-miR-320, decreases miR-320 levels, upregulates RUNX2 levels, and improves osteogenesis[14]. The dual mechanism of m6A modification on osteogenic differentiation may be caused by high or low levels of m6A modification[15]. However, it is still unknown if the upregulation of RUNX2 after β-TCP stimulation is related to m6A modification.

M6A RNA methylation plays an important role in the regulation of numerous cell behaviors. M6A works through three mechanisms: (i) Writing, which is regulated by a methyltransferase complex consisting of METTL3, METTL14, Wilms tumor-1-associated protein (WTAP), and other methyltransferases, also known as writers[16-18]; (ii) erasing, which is regulated by demethylases fat mass and obesity-associated protein (FTO) and AlkB homolog 5 (ALKBH5), also known as erasers[19]; and (iii) reading, which is regulated by m6A-binding proteins, including YTH family proteins and IGF2BP family members, also known as readers. M6A also influences the osteogenic differentiation of BMSCs in different ways; however, there are contradictory opinions regarding the m6A regulation mechanism. Wu *et al*. found that parathyroid hormone (PTH)-induced osteogenic effects and the translation efficiency of parathyroid hormone receptor-1 (Pth1r) mRNA were decreased after the knockout of METTL3[20]. In contrast, METTL3 positively regulates myeloid differentiation primary response 88 (MYD88), activating the nuclear factor kappa B (NF-κB) signaling pathway, which is regarded as an inhibitor of osteogenesis. Meanwhile, the adverse effects of METTL3 can be reversed by ALKBH5[21]. M6A modification also regulates interaction between cell and extracellular matrix. For example, overexpression of METTL3 promotes accumulation of ECM in human Tenon's capsule fibroblasts[22]. However, the relationship between osteoinductivity of β-TCP and m6A modification remains unclear.

Therefore, the aim of this study is to prove that β-TCP might promote the osteogenesis of BMSCs by upregulating RUNX2 in an m6A-dependent manner, further providing new evidence to support the clinical use of β-TCP in bone defect treatment.

2. Materials and methods

2.1. 3D printing of β-TCP scaffolds

3D printing (REGENOVO, China) was utilized to make β-TCP scaffolds for implanting the β-TCP into Sprague-

Dawley (SD) rats. The β-TCP was mixed with Pluronic F-127 in an aqueous solution to obtain a β-TCP ink, and the mixture was then stirred until it was homogeneous. The ink was printed using a 22G needle, and the scaffolds were sintered at 1100°C for 3 h. The sintered β-TCP scaffolds were observed by scanning electron microscopy (SEM, USA). The scaffolds were then used for animal experiments.

2.2. Cell culture

Primary bone marrow mesenchymal stem cells were isolated after flushing the bone marrow of tibiae and femurs from 1-week-old SD rats. The BMSCs were cultured in α-minimum essential medium (α-MEM) (HyClone, SH30265.01, USA) supplemented with 10% fetal bovine serum (FBS; Gibco, 10099-141, USA), 1% penicillin/streptomycin (Gibco, 15140122, USA), and 0.4% gentamicin (Sangon Biotech, Shanghai, China), after which the cells were cultured at 37°C with 5% CO_2 and 95% humidity. The cell medium was changed every 3–4 days and the BMSCs were passaged when they were at nearly 80% confluence.

2.3. Preparation of β-TCP extract and characterization measurement of β-TCP extract

β-TCP powder was purchased from Kunshan Chinese Technology New Materials Co., Ltd (China). Two grams of the powder were incubated in 10 ml α-MEM at 37°C for 24 h to prepare β-TCP extract (200 mg/ml)[23-25]. Then, the mixture was centrifuged at 3000 ×g, and the supernatant was collected. The extract was sterilized through 0.22 μm filter membranes (Millipore, SLGPR33RB, USA) and stored at 4°C until further use. Size distribution and zeta potential were detected by Nano Sizer and Zeta potential Tester (Omni, USA). We diluted the β-TCP extract with α-MEM to concentrations of 1/32, 1/64, and 1/128. The concentrations of calcium (Ca) and phosphorus (P) ions in the three extracts with the concentrations of 1/32, 1/64, and 1/128 and α-MEM (control, ctrl) were detected using an inductively coupled plasma atomic emission spectrometer (ICP-AES; avio500, USA). The β-TCP extract at the three concentrations with α-MEM was used for cell experiments and supplemented with 10% FBS, 1% penicillin/streptomycin, 0.4% gentamicin, and osteogenic induction component (10 mM β-glycerophosphate, 50 μM ascorbic acid, and 10 nM dexamethasone). Cells in the control group were treated with α-MEM supplemented with 10% FBS, 1% penicillin/streptomycin, 0.4% gentamicin, and osteogenic induction component (10 mM β-glycerophosphate, 50 μM ascorbic acid, and 10 nM dexamethasone). The treatment lasted for 7 days.

2.4. Cytotoxicity assay

After being incubated in the above-mentioned extract with three replicates per group, BMSCs were seeded in 96-well plates at a density of 2.5×10^3 cells per well for cytotoxicity assay. Cell Counting Kit-8 (CCK-8) assay was performed on days 3 and 7 to assess the cytotoxicity of the β-TCP extract. The BMSCs were incubated in complete medium with 10% CCK-8 reagent (Dojindo, CK04-05, Japan) for 2 h at 37°C. The absorbance of the supernatant at 450 nm was measured using a microplate reader (Infinite M200 Pro, Tecan, Switzerland).

2.5. ALP staining

ALP staining was conducted on the BMSCs after incubation in the above extract for 7 days. BMSCs were washed 3 times with phosphate-buffered saline (PBS) and fixed with 4% paraformaldehyde (Beyotime, P0099, China) for 15 min. After that, the BMSCs were washed 3 times with PBS. An ALP kit (Hongqiao Lexiang, LRB-ALP, China) was used to perform ALP staining according to the manufacturer's instructions. The results were analyzed by ImageJ.

2.6. RNA extraction and quantitative real-time polymer chain reaction (PCR)

After a culture period of 7 days, the total RNA from the BMSCs seeded on 6-well plates, at a density of 2*10^5 cells per well, was extracted using TRIzol reagent (Invitrogen, 15596018, USA) following the manufacturer's instructions. The concentration of total RNA was measured using a NanoDrop ND-1000 Spectrophotometer (Thermo Fisher Scientific, USA), and 1000 ng of the extracted RNA was reverse transcribed to cDNA using PrimeScript Master Mix (TaKaRa, RR036A, Japan). For the qRT-PCR reaction, 2× SYBR Green qPCR Master Mix (Low ROX) (Bimake, B21703, China) and Applied Biosystems 7500 Real-Time PCR System (Applied Biosystems, Foster City, CA, USA) were used. Glyceraldehyde-3-phosphate dehydrogenase (GAPDH) was used as the quantitative control for normalization. The $2^{-\Delta\Delta Ct}$ method was used to calculate the relative mRNA levels. The primers used in this study are listed in **Table 1**.

2.7. Prediction of Runx2 m6A methylation sites

The prediction of possible sites modified by m6A was performed using SRAMP, a sequence-based m6A modification site predictor (www.cuilab.cn/sramp). The entire sequence of RUNX2 mRNA was imported onto the server. Then, the possible Runx2 m6A methylation sites were exported from the online tool automatically.

Table 1. Sequences of primers used in this study

Primer	Forward primer (5' to 3')	Reverse primer (5' to 3')
GAPDH	GGCAAGTTCAACGGCACAGT	GCCAGTAGACTCCACGACAT
METTL3	CAATGTGCAGCCCAACTGGATT	CACCATCTGGATACCTGTGCTT
WTAP	CTCGCCTCGTCTCTTCTGG	TGTTTCACTCAGTCGGACCTTT
ALKBH5	GGCTGCATCGTATCTCACGTA	AGCAGCATACCCACTGAGCAC
RUNX2	TCTTCCCAAAGCCAGAGCG	TGCCATTCGAGGTGGTCG
OPN	GAGGAGAAGGCGCATTACAG	AAACGTCTGCTTGTCTGCTG
BSP	TACGAACAAATAGGCAACGAGT	TTCGTCCTCATAAGCTCGGTAA
COL1	TGACTGGAAGAGCGGAGAGTA	GGGGTTTGGGCTGATGTACC

2.8. M6A-RT-PCR (MeRIP-qPCR)

After extraction with TRIzol, the total RNA was used for the m6A-IP-PCR (MeRIP-qPCR). Total RNA (1 μg) was taken out regraded as an input and was reverse transcribed to cDNA instantly. The remaining RNA (20 μg) was equally divided into RIP and IgG groups. The RNAs of the RIP and IgG groups were immunoprecipitated with 5 μg m6A antibody (Synaptic system, 202003, Germany) or anti-IgG (Cell Signaling Technology, 2729S, USA) in 500 μL IP buffer (150 mM NaCl, 0.1% NP-40, 10 mM Tris, pH 7.4, 100 U RNase inhibitor) at 4°C for 2 h. The liquid was then mixed with Pierce™ Protein A/G Magnetic Beads (Thermo Fisher Scientific, 88803, USA) and rotated for 2 h at 4°C after the beads were washed in 1 ml IP buffer twice. Afterward, the mixture was washed with 1 ml IP buffer 4 times and eluted twice with 50 μL elution buffer (5 mM Tris-HCl pH 7.5, 1 mM EDTA pH 8.0, 0.05% sodium dodecyl sulfate (SDS), 20 mg/ml Proteinase K) for 30 min. Then, the RNA was extracted with TRIzol and reverse transcribed to cDNA with random hexamers. cDNA (2 μL) from the RIP or IgG groups was used for qRT-PCR. Relative fold enrichment was calculated as $2^{-\Delta\Delta Ct}$. The primers for MeRIP-qPCR were as follows: Forward, 5' to 3', TGTACCACACAGGTCACGATT; reverse, 5' to 3', ATGAGGGGAGAAAATGCCAA.

2.9. RNA stability assays

To measure RNA stability, actinomycin D (Act-D; Sigma, A4262, USA) was added to the BMSCs at 5 μg/ml. After being incubated at 37°C for 0 h, 2 h, 4 h, and 6 h, the BMSCs were collected and RNA was extracted with TRIzol for qRT-PCR. GAPDH was used as an endogenous control.

2.10. Western blot analysis

The BMSCs were harvested using RIPA lysis buffer (Beyotime, P0013B, China) containing 1% protease and phosphatase inhibitor cocktail (100×) (Thermo Scientific, 78442, USA) and 1% phenylmethanesulfonyl fluoride (PMSF) (100 mM) (Beyotime, ST506, China) followed by centrifugation at 13,500 × g at 4°C for 15 min. The protein was mixed with SDS-PAGE protein loading buffer (Beyotime, P0286, China) and boiled at 99°C for 5 min. Equal amounts of protein lysates were subjected to SDS gel electrophoresis and transferred onto polyvinylidene fluoride (PVDF) membranes (Millipore, IPVH00010, USA). The membranes were then blocked in Tris-buffered saline Tween-20 containing 5% non-fat milk at room temperature for 1 h and incubated with a primary antibody at 4°C overnight. The membrane was incubated with a secondary antibody at room temperature for 1 h. Protein immunoreactivity was detected using LI-COR Odyssey Fluorescence Imaging System (LI-COR Biosciences, Lincoln, NE, USA) and the protein immunoreactive band intensity was measured using Image-Pro Plus 6.0. The antibodies used were as follows: METTL3 (1:1000; Proteintech, 15073-1-AP, USA), WTAP (1:6000; Proteintech, 60188-1-Ig, USA), ALKBH5 (1:6000; Proteintech, 16837-1-AP, USA), RUNX2 (1:1000; Cell Signaling Technology, 12556, USA), β-actin (1:6000; Proteintech, 66009-1-Ig, USA), anti-rabbit IgG (H+L) (DyLight™ 800 4X PEG Conjugate) (1:10,000; Cell Signaling Technology, 5151, USA), and anti-mouse IgG (H+L) (DyLight™ 800 4X PEG conjugate) (1:10,000; Cell Signaling Technology, 5257, USA).

2.11. Animal experiments

(1) Calvarial defect model

Eight-week-old SD rats were chosen for the animal experiments. All animal surgeries were performed under sterile conditions. The rats were anesthetized, and a 10 mm incision was made along the median line of the heads. Two calvarial defects with a diameter of 7 mm were made bilaterally using a circular bit. Then, the β-TCP scaffolds were implanted carefully into a random side, and the other side was used as a control. Subsequently, the skin was sutured and the wound was disinfected.

Animal experiments of this study were approved by the Ethics Committee of Shanghai Ninth People's Hospital, Shanghai JiaoTong University School of Medicine.

(2) Micro-computed tomography (micro-CT) analysis

Two months after the surgery, the SD rats were euthanized, and the skulls were collected. A micro-CT scanning

system (Bruker SkyScan 1176; Germany) was used to analyze the samples, which were scanned with a spot size of 10 μm, current of 250 μA, and maximum voltage of 40 kV. Then, the 3D images were reconstructed, and the bone volume fraction (BV/TV) and bone mineral density (BMD) were calculated using auxiliary software.

(3) Hematoxylin and eosin (H&E) staining and Masson staining

The skull samples were fixed with 4% paraformaldehyde and decalcified in 10% ethylenediaminetetraacetic acid. Then, the samples were embedded in paraffin and sectioned at a thickness of 5 μm. H&E staining and Masson's trichrome staining were performed as previously described[26].

(4) Immunohistochemistry

The sample sections were incubated with primary antibodies at 4°C overnight. The slides were then incubated with horseradish peroxidase (HRP)-conjugated secondary antibodies. Images were captured using a microscope and the numbers of positive cells were counted.

2.12. Statistical analysis

All results are expressed as mean ± standard deviation (SD). Error bars represent the SD. A two-tailed Student's *t*-test and one-way analysis of variance were used to analyze the difference between two groups and more than 2 groups, respectively; subsequently, Tukey's *post hoc* analysis was used to compare the differences between three or more groups. Statistical significance was set at $*P < 0.05$ and $**P < 0.01$.

3. Results

3.1. Characterization and biocompatibility of β-TCP extract

We prepared extract of β-TCP made of β-TCP powder. Size distribution analysis revealed a particle size smaller than 10,000 nm and mainly between 300 and 1000 nm (**Figure S1**). The zeta potential of β-TCP extract was −7.04 ± 0.69 mV (**Table S1**). Next, we diluted β-TCP extract into the ratios of 1/32, 1/64, and 1/128. The concentrations of Ca and P ions (Ctrl, 1/32, 1/64, and 1/128) were detected by ICP-AES, as shown in **Figure 1A**. The concentrations of Ca were 66.20 ± 1.53, 65.37 ± 0.81, 64.26 ± 0.97, and 65.79 ± 1.26 mg/L in Ctrl, 1/32, 1/64, and 1/128 dilutions, respectively, while the concentrations of P were 32.05 ± 1.64, 29.96 ± 0.65, 29.80 ± 0.96, and 30.99 ± 0.19 mg/L, respectively, which were consistent with a previous study and showed no significant difference in the concentrations of Ca and P[27].

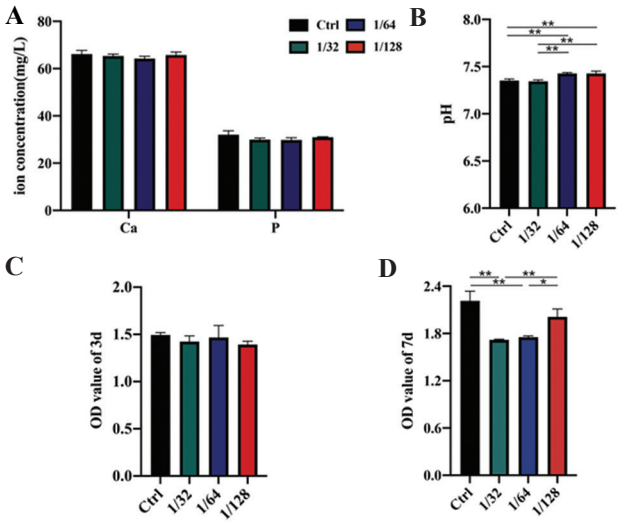


Figure 1. Characterization and biocompatibility of β-TCP extract. (A) Ion concentrations of Ca and P of α-MEM medium (Ctrl), α-MEM with 1/32 dilution of β-TCP extract (1/32), α-MEM with 1/64 dilution of β-TCP extract (1/64), and α-MEM with 1/128 dilution of β-TCP extract (1/128). (B) pH values of Ctrl, 1/32, 1/64, and 1/128 dilution groups. (C) OD values of BMSCs in Ctrl, 1/32, 1/64, and 1/128 dilution groups on day 3 by CCK-8. (D) OD values of BMSCs in Ctrl, 1/32, 1/64, and 1/128 groups on day 7 by CCK-8. $*P < 0.05$; $**P < 0.01$.

The pH values were 7.353 ± 0.012, 7.343 ± 0.012, 7.427 ± 0.009, and 7.427 ± 0.021, respectively (**Figure 1B**). The pH of the Ctrl and 1/32 dilution was significantly different from that of 1/64 and 1/128 dilutions ($P < 0.01$).

The cytotoxicity of the β-TCP extract was examined using the CCK-8 assay. It was found that BMSCs proliferated, and the cell numbers increased over time throughout the assay period. No significant difference was observed between the Ctrl and β-TCP extracts on day 3 after treatment, revealing no cytotoxicity of the β-TCP extract on day 3 (**Figure 1C**). On day 7 after treatment, however, the absorbance of 1/32 and 1/64 dilutions of β-TCP extract obviously decreased, showing a lower cell viability than the Ctrl and 1/128 dilution of β-TCP extract on day 7 (**Figure 1D**).

3.2. β-TCP promoted the osteogenic differentiation of BMSCs

We then tested the osteogenic differentiation of the BMSCs induced by β-TCP. As shown in **Figure 2A and B**, after induction for 7 days, all the groups treated with β-TCP extract showed approximately twice the ALP expression than those of the Ctrl. However, the expression among the three β-TCP groups showed no significant difference, suggesting that the β-TCP extract could induce osteogenic differentiation of BMSCs. We also examined the expression of bone formation-related genes. **Figures 2C-F** show that the levels of collagen type I

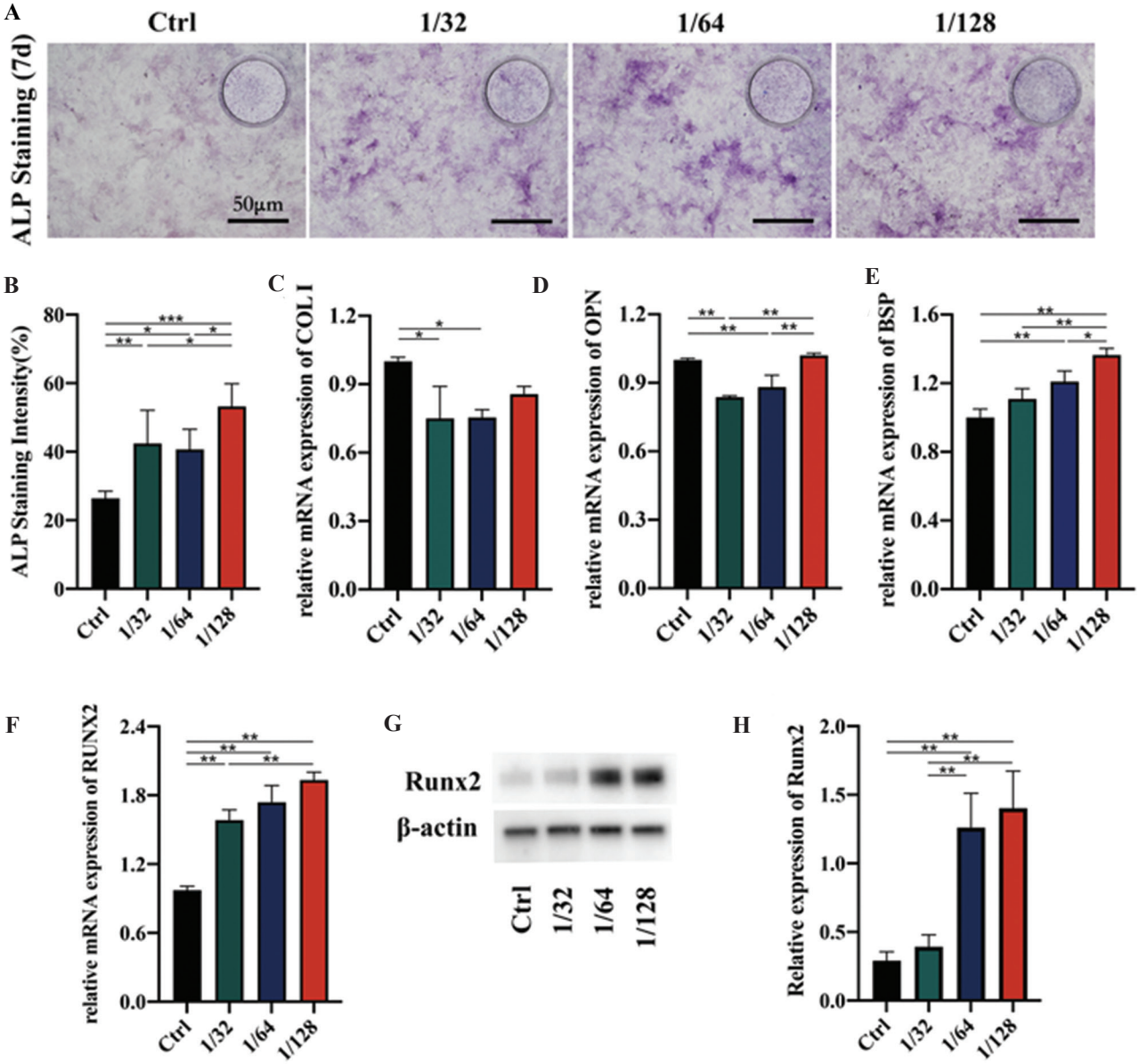


Figure 2. Osteogenesis effects of β-TCP on BMSCs. (A) ALP staining of BMSCs in Ctrl, 1/32, 1/64, and 1/128 groups. Top-right corner shows macroscopic pictures. Scale bars = 50 μm. (B) Quantitative results of (A). The mRNA expression levels of COL I (C), OPN (D), BSP (E), and RUNX2 (F) in Ctrl, 1/32, 1/64, and 1/128 dilution groups are illustrated in bar charts. The mRNA expression levels were determined by qRT-PCR. (G) The protein expression level of RUNX2 in Ctrl, 1/32, 1/64, and 1/128 dilution groups by Western blot. (H) The quantitative result of (G). *$P < 0.05$; **$P < 0.01$.

(COL I) and OPN, which represent late osteogenesis, in the β-TCP extract groups, were slightly lower than that of the Ctrl group, except for the 1/128 dilution of the β-TCP extract. Meanwhile, the levels of RUNX2 and BSP, which represent early osteogenesis, increased. Since RUNX2 was the key translation factor of osteogenesis, we further tested the expression of RUNX2 protein by Western blotting. The 1/64 and 1/128 dilutions of β-TCP extract showed higher expression of RUNX2 protein than the Ctrl (**Figure 2G and H**). These results demonstrated the excellent osteoinductivity of β-TCP. Considering the cytotoxicity and osteogenic differentiation assay results, we chose 1/128 dilutions of β-TCP extract for further experiments.

3.3. Expression level of m6A-related enzymes changed after β-TCP treatment

To study the effects of β-TCP on m6A-related enzymes such as "writers" and "erasers," we detected the mRNA and protein levels of several m6A-related enzymes. The results of the qRT-PCR analysis indicated that the

main m6A methyltransferases (METTL3, WTAP) and demethylases (ALKBH5) were significantly higher in the BMSCs after β-TCP induction at the mRNA level (**Figure 3A-C**). As determined by Western blotting, WTAP and ALKBH5 showed no statistically significant differences at protein level (**Figure 3D, F and G**). However, METTL3 expression was obviously increased (**Figure 3D and E**). All the results showed that β-TCP regulated the m6A-related enzymes, which might have an effect on the m6A level of osteogenesis-related genes.

3.4. RUNX2 showed higher m6A modification and the degradation of RUNX2 mRNA slowed down after β-TCP treatment

We further investigated the mechanism of RUNX2 increase after β-TCP treatment. First, we predicted the possible sites of RUNX2 that might be modified by m6A. As shown in **Figure 4A**, there were five sites that were likely to be modified by m6A with high possibility. We chose the 5279th site as the target site to design-specific primers (**Figure 4B**). It was found that the m6A level of RUNX2 in the BMSCs was significantly increased by β-TCP, which might lead to an increase in RUNX2 expression (**Figure 4C**). To explore the effects of the m6A level increase on the stability of RUNX2 mRNA, we used Act-D, an RNA polymerase II inhibitor, to detect the degradation of RUNX2 mRNA. The results showed that at 4 h and 6 h after the addition of Act-D, the degradation of RUNX2 mRNA treated with β-TCP significantly slowed down, that is, the half-life was prolonged (**Figure 4D**). All the data indicated that the m6A level of RUNX2 mRNA increased and the degradation of RUNX2 mRNA slowed down after the treatment with β-TCP.

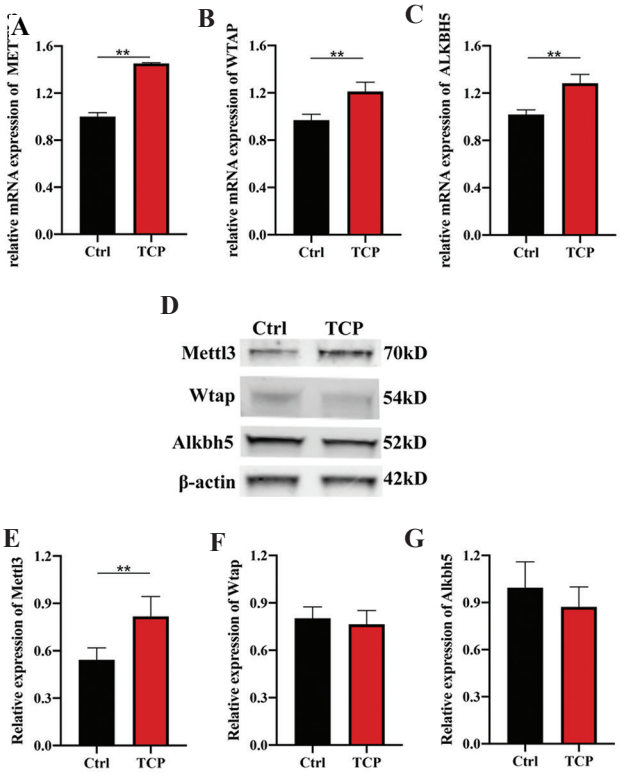


Figure 3. Expression level of m6A-related enzymes after β-TCP treatment. (A-C) The mRNA expression level of METTL3 (A), WTAP (B), and ALKBH5 (C) in the Ctrl and TCP (1/128 dilution) groups. The expression level was determined by qRT-PCR. (D) The protein expression level of METTL3, WTAP, and ALKBH5 in the Ctrl and TCP groups. (E-G) Quantitative results of (D). *$P < 0.05$; **$P < 0.01$.

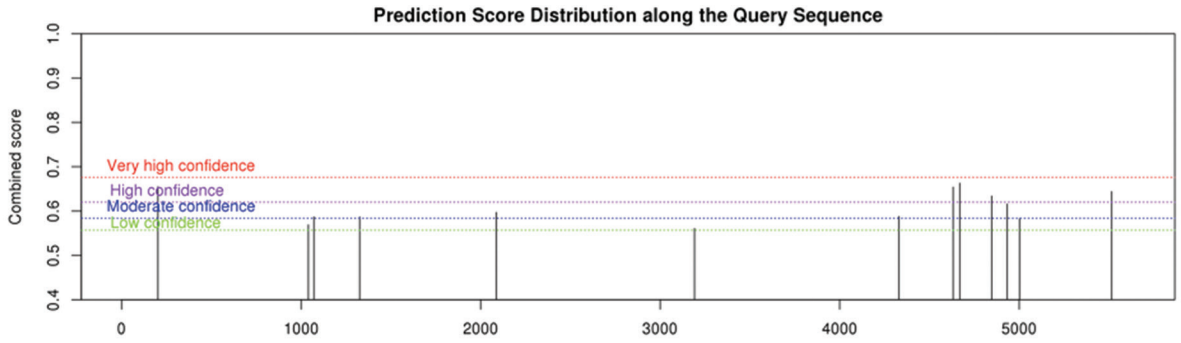
3.5. β-TCP-induced osteogenesis in vivo

We further verified the effects of the β-TCP on osteogenesis in vivo. β-TCP scaffolds were manufactured by 3D printer (**Figure 5A**), and the diameter of which was about 7 mm each (**Figure 5B**). The scaffolds were made porous so that they were beneficial for adhesion of BMSCs. The surface microstructure of β-TCP scaffolds was demonstrated by SEM. Microscopically, the surface of β-TCP scaffolds was also porous and rough, although some particles were sintered together (**Figure 5C**). To embed β-TCP into bone defect sites of rat cranial defect models (**Figure 5D**), we manufactured β-TCP scaffolds using 3D printing technology. Eight weeks after model construction, we sacrificed the rats to obtain the skull samples for micro-CT analyses. It was shown that some new bone was formed inside and outside the cranial defect (yellow section) (**Figure 5E**). Next, bone volume fraction (BV/TV) and BMD were evaluated to assess new bone formation. As shown in **Figure 5F** and **5G**, BV/TV and BMD in the β-TCP group increased approximately 2-fold compared to that in the Ctrl group. The above findings indicated that β-TCP-induced osteogenesis effectively and significantly. Next, H&E and Masson's trichrome staining were performed to analyze the proportion of osteogenic tissue. H&E staining showed that the bone defect site was filled with soft tissue in the Ctrl group but was surrounded by newly formed bone in the β-TCP group (**Figure 5H**). Consistent with the H&E staining, the Masson's trichrome staining showed that more new bone was present in the β-TCP group (**Figure 5I**). All the above data indicated that TCP induced new bone formation.

3.6. β-TCP increased the expression of METTL3 in vivo

Furthermore, we investigated the expression levels of a series of osteogenic factors and m6A-related enzymes in vivo. RUNX2, OCN, and OPN are the most common proteins involved in osteogenesis[3,26]. After β-TCP treatment, the expression levels of RUNX2, OCN, and OPN were significantly increased, indicating the osteoinductivity of TCP in vivo (**Figure 6A-D**).

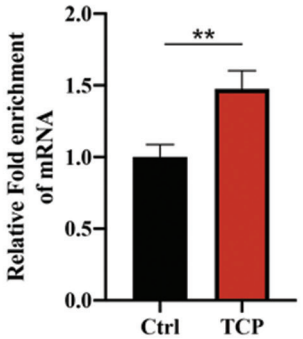
A



B

4094	UUUAC AAUAC AGUUA UUAAG GGACU AGAGG GGAUG CCUUA GUGCC	N/A	N/A	0.683	0.730	0.440	0.588	m^6A site (Moderate confidence)
4396	AAUGU CUUAA UACUC UCCUG GGACU GUUUU CGUGU ACAAA CUUCC	N/A	N/A	0.714	0.837	0.548	0.654	m^6A site (High confidence)
4433	AAACU UCCCU GGGCU UAGAU GGACA UGGUU CUCGA AGGAG CACAA	N/A	N/A	0.663	0.559	0.675	0.663	m^6A site (High confidence)
4611	GCACC CAGCC CAUAA UAGAA AGACU UACCA GAUUU AACUA GUUGG	N/A	N/A	0.732	0.551	0.511	0.634	m^6A site (High confidence)
4697	CAACA UCUCC ACAUC AUUAG AGACU GUCCA CAGUA GGUUC AGAAG	N/A	N/A	0.739	0.644	0.445	0.616	m^6A site (Moderate confidence)
4766	CUUGC UCCAA GGAAA GGCAC UGACU GACCU AGUUU UAGAG AACAG	N/A	N/A	0.612	0.475	0.557	0.583	m^6A site (Low confidence)
5279	GUUUA CUCUG AACUU CAAAG GGACU AUUUG UAUUG UAUGU UGCAA	N/A	N/A	0.734	0.647	0.521	0.644	m^6A site (High confidence)

C



D

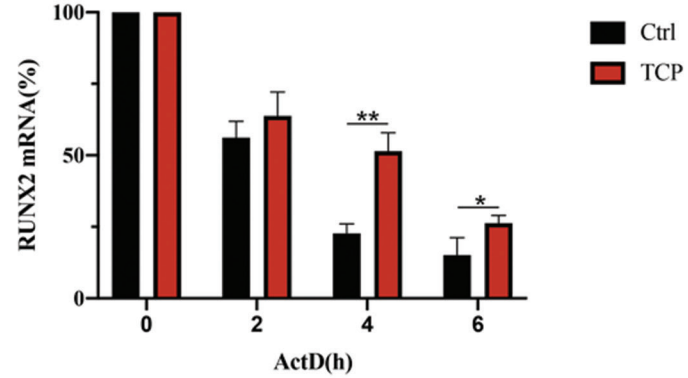


Figure 4. m6A level of RUNX2 mRNA and the stability of RUNX2 mRNA after TCP treatment. (A) Possible sites with m6A modification of RUNX2 mRNA. (B) Sequences of possible sites with m6A modification. (C) M6A level of RUNX2 mRNA in BMSCs in the Ctrl and TCP groups. (D) The decay of RUNX2 mRNA after TCP treatment at 0, 2, 4, and 6 h. * $P < 0.05$; ** $P < 0.01$.

Moreover, the expression levels of m6A-related enzymes were detected by immunohistochemistry. Identical to the in vitro results, the expression level of METTL3 on the TCP group was approximately 1.5-fold higher than that of the Ctrl group (**Figure 6E** and **F**). However, the expression levels of WTAP and ALKBH5 were not significantly different between the two groups, suggesting that METTL3 played a key role in the process of osteogenesis induced by β-TCP (**Figure 6E, G, H**). All the results indicated that β-TCP increased osteogenic proteins in calvarial defect models, and METTL3 other than WTAP or ALKBH5 promoted the osteogenesis.

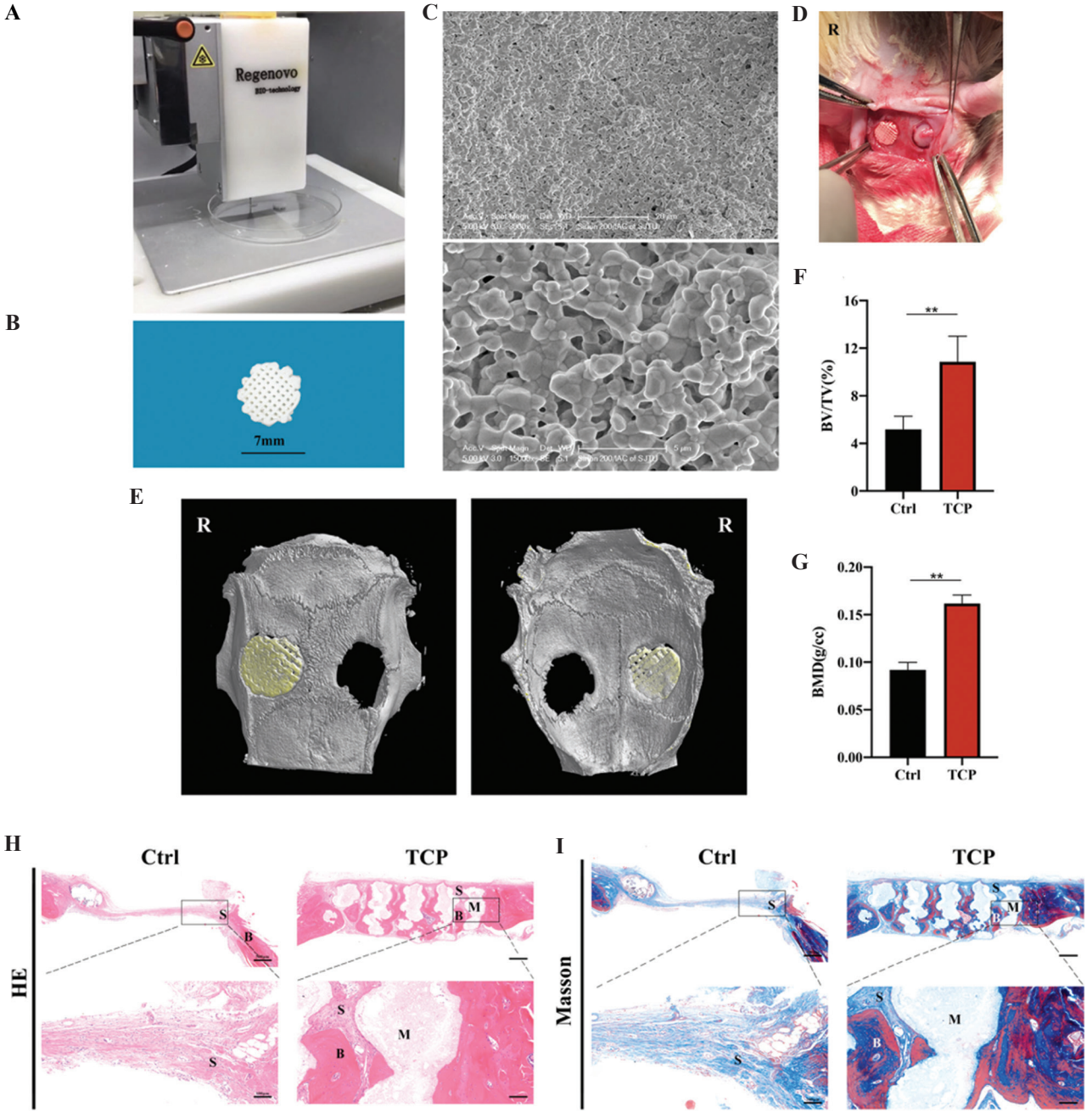


Figure 5. Osteogenesis effects of β-TCP scaffolds in vivo. (A) β-TCP scaffolds were made. (B) The appearance of β-TCP scaffolds with the diameter of around 7 mm. (C) SEM images of the surface microstructure of β-TCP scaffolds. (D) Rat cranial defect models were constructed. (E) 3D reconstruction of micro-CT images. (F) Quantitative analysis of BV/TV of micro-CT images. (G) Quantitative analysis of BMD of micro-CT images. (H) H&E staining of skull samples. Scale bars = 500 μm, 100 μm, respectively. (I) Masson staining of skull samples. Scale bars = 500 μm, 100 μm, respectively. S: Soft tissue; B: Bone; M: Material. *$P < 0.05$; **$P < 0.01$

4. Discussion

Collectively, our study demonstrated that β-TCP scaffolds made by 3D printing technology could induce osteogenic differentiation of BMSCs in vitro. Meanwhile, BMSCs stimulated by β-TCP extract had significantly higher expression of METTL3 in the β-TCP group than in the control group, which affected m6A modification of RNA in BMSCs. Mechanistically, the m6A level of RUNX2 in BMSCs increased after β-TCP treatment, leading to improved stability of RUNX2 mRNA and retardation of decay of RUNX2 mRNA, which indirectly facilitates an increase of RUNX2 mRNA and protein (**Figure 7**). According to the animal experiments, we found that β-TCP promoted new bone formation and increased

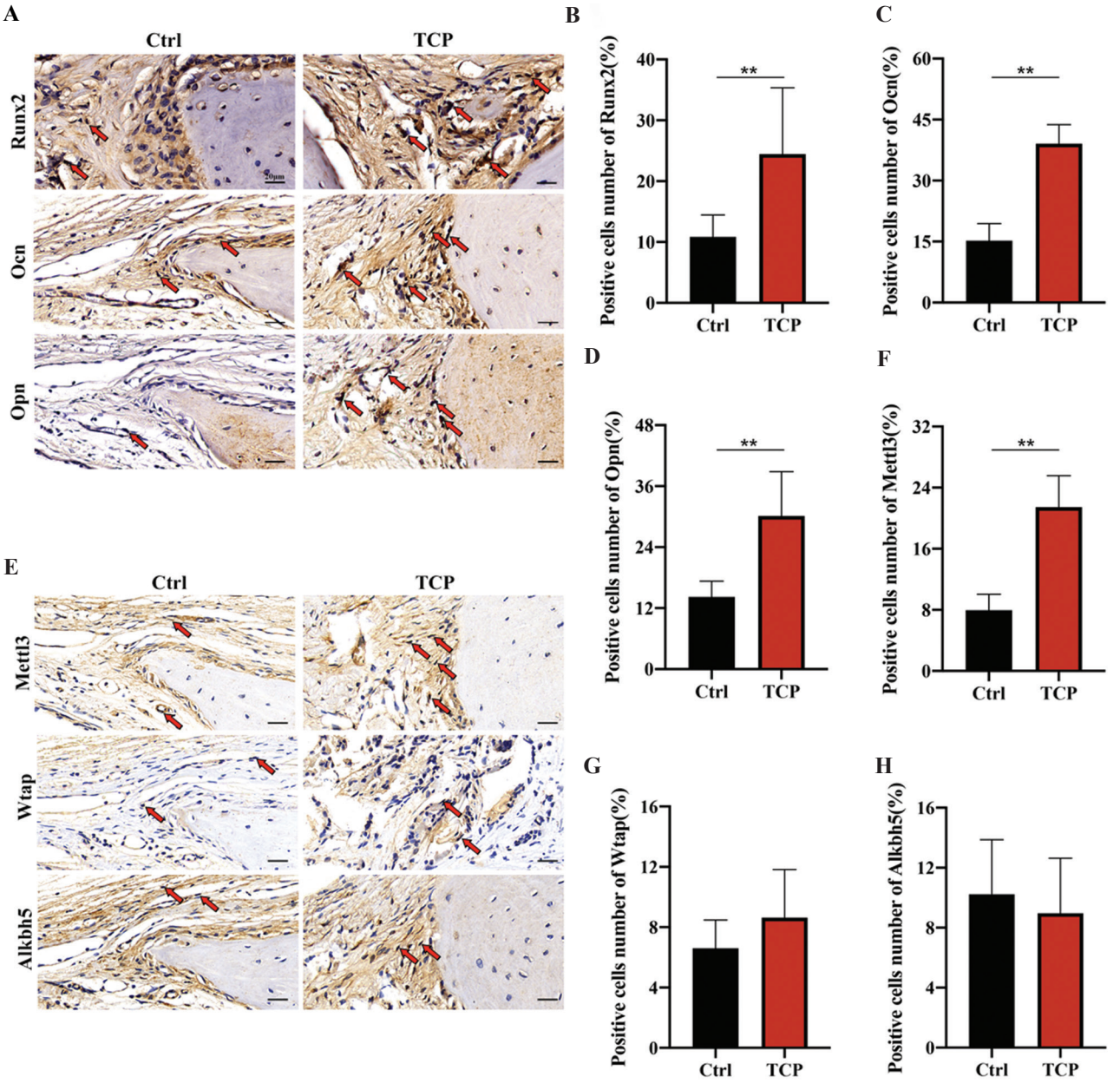


Figure 6. Immunohistochemistry analysis of osteogenic factors and m6A-related enzymes. (A) Immunohistochemistry analysis of Runx2, Ocn, and Opn in the Ctrl and TCP groups. Arrows represented positive cells. Scale bars = 20 μm. (B-D) Quantitative results of Runx2 (B), Ocn (C), and Opn (D). (E) Immunohistochemistry analysis of METTL3, WTAP, and ALKBH5 in the Ctrl and TCP groups. Arrows represented positive cells. Scale bars = 20 μm. (F-H) Quantitative results of METTL3 (F), WTAP (G), and ALKBH5 (H). *$P < 0.05$; **$P < 0.01$.

METTL3 expression. These results suggested that β-TCP could promote the osteogenic differentiation of BMSCs by increasing the m6A modification of RUNX2.

Bones have numerous key roles in the human body, such as acting as a framework to support the body, protecting internal organs from injury, enabling body movements, producing blood cells, and maintaining calcium homeostasis[28]. Bone tumors, injury, and other bone diseases are likely to lead to bone defects. For a long time, bone defects have been a serious orthopedic disease which downgrades the quality of life of patients[29]. In view of the limited bone repair capacity of autologous BMSCs, it is necessary to use natural or synthetic bone as a replacement in bone grafting[30]. In general, autogenous bone grafts are the gold standard material for bone substitutes[31]. Nevertheless, the inadequacies of allograft bone and finite autogenous bone resources impose restrictions on their clinical application[32].

The development of bone tissue engineering provides a new prospect for treating bone defects. The most important point is choosing feasible materials, which requires a balance between new bone formation and material

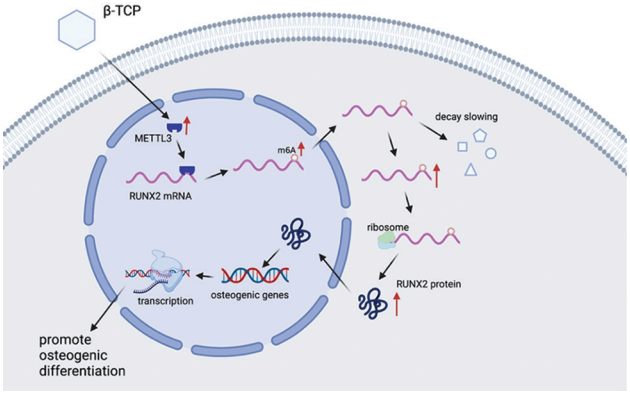


Figure 7. The mechanism of β-TCP contributing osteogenesis of BMSCs. β-TCP increases the expression of METTL3, which leads to an increase of m6A level of RUNX2 in BMSCs. The upregulation of m6A level helps stabilize the RUNX2 mRNA, which indirectly facilitates the increase of RUNX2 mRNA. As a consequence, more RUNX2 protein promotes the transcription of other osteogenic factors, launching the osteogenic differentiation of BMSCs. The illustration was made using BioRender (https://biorender.com/).

degradation. Being one of the most crucial components of the bone[33], HA was one of the materials studied in the early stage for its bone repair potential[34,35]. HA has been used in clinical treatment because of its good cytocompatibility[36]. Composites consisting of HA, such as polylysine-modified coral HA, collagen-HA-based scaffolds, and chitosan/curdlan/HA biomaterials, have been proven to improve osteogenesis[37,38]. TCP, which is composed of phosphate radicals and calcium ions in aqueous solution, is a new bone substitute for bone regeneration. It is known that calcium and phosphorus are the two fundamental elements of bones. Therefore, these two elements of β-TCP promote bone regeneration. Herein, we detected the release of calcium and phosphorus, which was also reported in a previous study[27]. No significant difference existing among the four groups was possibly linked to the precipitation of calcium phosphate. Since β-TCP extract showed alkalescence, which was identical to pH values of body fluids, it had good biocompatibility. Numerous studies have demonstrated the cytocompatibility and osteoinductivity of TCP and its composites[39]. Herein, our results suggested that β-TCP extract showed low cytotoxicity, which disappeared after the extract was diluted (in 1/128 dilution).

At the same time, the BMSCs stimulated by β-TCP tended to undergo osteogenic differentiation relative to the cells received no treatment; this was confirmed by ALP staining and determination of mRNA and protein expression of osteogenic factors. These results were consistent with those of the previous studies[40]. Among the osteogenic factors, RUNX2 has been proven to be a key transcriptional factor that triggers the activation of other factors and promotes osteogenic differentiation of BMSCs. Thus, RUNX2 was regarded as a target gene in this study.

The mechanism by which β-TCP contributes to osteogenesis is not well understood. To begin with investigating the mechanism, we note that the m6A modification shows strong association with osteogenesis, and METTL3 affects the osteogenic differentiation of BMSCs through the PI3K-Akt signaling pathway and the expression level of VEGF[41]. In C3H10T1/2 cells, FTO and p-AMPK form a positive feedback loop, stimulating endoplasmic reticulum (ER) stress and inducing osteogenic differentiation[42]. In view of the above, we investigated the mechanism by which β-TCP contributed to osteogenesis in terms of m6A modification. It was found that mRNA and protein levels of METTL3 both increased after β-TCP treatment, hinting at the significance of METTL3 in the process of osteogenesis induced by β-TCP. M6A RNA methylation is the most prevalent post-transcriptional modification in mammals[43]. Usually, m6A modification is regulated by methyltransferases and demethylases, and then is identified by "readers"[44]. Recently, a growing number of studies have focused on the effects of m6A modifications on osteogenesis. Zhang *et al*. found that METTL3 knockdown suppressed osteoblast differentiation and Smad-dependent signaling by stabilizing Smad7 and Smurf1 mRNA transcripts in a YTHDF2-dependent manner[45]. METTL3 is the most important methyltransferases. In our study, METTL3 also showed increase while the other m6A-related enzymes did not.

There are many ways that m6A modification can regulate mRNA in cells, depending on different m6A binding proteins. Recent studies have reported new findings on the m6A post-transcriptional modification in the regulation of RNA transcription[46], splicing[47], processing events[48], RNA stability[49], and translation[50]. Among these, cytoplasmic mRNA stability and reduction in mRNA stability are crucial for cell activities. Thus, we studied the mechanism of β-TCP osteoinductivity in detail. The results showed that β-TCP increased the m6A level of RUNX2 after β-TCP treatment by MeRIP-qPCR. Simultaneously, the m6A level increase also resulted in improved stability of RUNX2 mRNA induced by β-TCP, and increased the mRNA and protein expression of RUNX2, contributing to osteogenesis of BMSCs.

Finally, we verified the osteogenesis of β-TCP through animal experiments. The calvarial defect model is the most commonly used model for bone defects. The micro-CT results suggested that more new bone was formed after β-TCP induction. Likewise, the expression of RUNX2, OCN, and OPN showed similar tendency to those of the micro-CT. Besides, METTL3 expression level also increased in the β-TCP embedded side, implying that METTL3 exerted a vital influence on the osteogenesis process. We also performed immunohistochemistry analysis of m6A-related enzymes to study the effects

of β-TCP in vivo, which shed light on the mechanism of osteoinductivity of β-TCP from the perspective of epigenetic modifications.

5. Conclusions

In this study, we investigated the effect of β-TCP on osteogenic differentiation of BMSCs. The underlying mechanism is that β-TCP increases the expression of METTL3, leading to a higher m6A level of RUNX2. The rise of m6A level results in the retardation of decay and enhanced stability of RUNX2 mRNA, causing an increase of RUNX2 mRNA and protein levels. As a result, RUNX2 triggers the transcription of other osteogenic factors and promotes osteogenic differentiation of BMSCs.

Funding

This work was supported by the National Key Research and Development Program of China (2017YFC110390), National Natural Science Foundation of China (82172402), Funds of the Clinical Research Plan of SHDC (16CR3099B), and National Natural Science Foundation of China (82072412).

Conflicts of interest

All the authors declare no conflicts of interest.

Authors' contributions

Y.G. and J.W. designed the study. X.J. and X.S. performed the experiments. X.J. and W.L. interpreted data and wrote the manuscript. W.C., Y.Z., and Y.L. helped analyze the data. Z.W., X.Z., J.M., C.X., and K.D. provided experimental assistance. Y.G. supervised the project. All authors read and approved the manuscript.

References

1. Wang Z, Guo Z, Bai H, *et al.*, 2013, Clinical Evaluation of β-TCP in the Treatment of Lacunar Bone Defects: A Prospective, Randomized Controlled Study. *Mater Sci Eng C*, 33:1894–9. https://doi.org/10.1016/j.msec.2012.12.041
2. Seebach C, Henrich D, Kähling C, *et al.*, 2010, Endothelial Progenitor Cells and Mesenchymal Stem Cells Seeded onto β-TCP Granules Enhance Early Vascularization and Bone Healing in a Critical-Sized Bone Defect in Rats. *Tissue Eng Part A*, 16:1961–70. https://doi.org/10.1089/ten.tea.2009.0715
3. Chu W, Zhuang Y, Gan Y, *et al.*, 2019, Comparison and Characterization of Enriched Mesenchymal Stem Cells Obtained by the Repeated Filtration of Autologous Bone Marrow Through Porous Biomaterials. *J Transl Med*, 17:377. https://doi.org/10.1186/s12967-019-02131-y
4. Chu W, Gan Y, Zhuang Y, *et al.*, 2018, Mesenchymal Stem Cells and Porous β-tricalcium Phosphate Composites Prepared through Stem Cell Screen-enrich-combine (Biomaterials) Circulating System for the Repair of Critical Size Bone Defects in Goat Tibia. *Stem Cell Res Ther*, 9:157. https://doi.org/10.1186/s13287-018-0906-1
5. Chu W, Wang X, Gan Y, *et al.*, 2019, Screen-enrich-combine Circulating System to Prepare MSC/β-TCP for Bone Repair in Fractures with Depressed Tibial Plateau. *Regener Med*, 14:555–69. https://doi.org/10.2217/rme-2018-0047
6. Wang X, Chu W, Zhuang Y, *et al.*, 2019, Bone Mesenchymal Stem Cell-Enriched β-Tricalcium Phosphate Scaffold Processed by the Screen-Enrich-Combine Circulating System Promotes Regeneration of Diaphyseal Bone Non-Union. *Cell Transplant*, 28:212–23. https://doi.org/10.1177/0963689718818096
7. Masaoka T, Yoshii T, Yuasa M, *et al.*, 2016, Bone Defect Regeneration by a Combination of a β-Tricalcium Phosphate Scaffold and Bone Marrow Stromal Cells in a Non-Human Primate Model. *Open Biomed Eng J*, 10: 2-11. https://doi.org/10.2174/1874120701610010002
8. Barradas AM, Monticone V, Hulsman M, *et al.*, 2013, Molecular Mechanisms of Biomaterial-driven Osteogenic Differentiation in Human Mesenchymal Stromal Cells. *Integr Biol*, 5:920–31. https://doi.org/10.1039/c3ib40027a
9. Liu J, Zhao L, Ni L, *et al.*, 2015, The Effect of Synthetic α-tricalcium Phosphate on Osteogenic Differentiation of Rat Bone Mesenchymal Stem Cells. *Am J Transl Res*, 7:1588–601.
10. Rittipakorn P, Thuaksuban N, Mai-Ngam K, *et al.*, 2021, Bioactivity of a Novel Polycaprolactone-Hydroxyapatite Scaffold Used as a Carrier of Low Dose BMP-2: An In Vitro Study. *Polymers* (*Basel*), 13:466. https://doi.org/10.3390/polym13030466
11. Hesse E, Saito H, Kiviranta R, *et al.*, 2010, Zfp521 Controls Bone Mass by HDAC3-dependent Attenuation of Runx2 Activity. *J Cell Biol*, 191:1271–83. https://doi.org/10.1083/jcb.201009107
12. Liu JC, Lengner CJ, Gaur T, *et al.*, 2011, Runx2 Protein Expression Utilizes the Runx2 P1 Promoter to Establish Osteoprogenitor Cell Number for Normal Bone Formation. *J Biol Chem*, 286:30057–70. https://doi.org/10.1074/jbc.M111.241505
13. Kronenberg HM, 2004, Twist Genes Regulate Runx2 and Bone Formation. *Dev Cell*, 6:317–8. https://doi.org/10.1016/S1534-5807(04)00069-3

14. Yan G, Yuan Y, He M, *et al.*, 2020, m6A Methylation of Precursor-miR-320/RUNX2 Controls Osteogenic Potential of Bone Marrow-Derived Mesenchymal Stem Cells. *Mol Ther Nucleic Acids*, 19:421–36. https://doi.org/10.1016/j.omtn.2019.12.001
15. Chen J, Tian Y, Zhang Q, *et al.*, 2021, Novel Insights into the Role of N6-Methyladenosine RNA Modification in Bone Pathophysiology. *Stem Cells Dev*, 30:17–28. https://doi.org/10.1089/scd.2020.0157
16. Lee M, Kim B, Kim VN, 2014, Emerging Roles of RNA Modification: m 6 A and U-Tail. *Cell*, 158:980–7. https://doi.org/10.1016/j.cell.2014.08.005
17. Zhao BS, Roundtree IA, He C, 2017, Post-transcriptional Gene Regulation by mRNA Modifications. *Nat Rev Mol Cell Biol*, 18:31–42. https://doi.org/10.1038/nrm.2016.132
18. He C, 2010, Grand Challenge Commentary: RNA epigenetics? *Nat Chem Biol*, 6:863–65. https://doi.org/10.1038/nchembio.482
19. Yang Y, Hsu PJ, Chen YS, *et al.*, 2018, Dynamic Transcriptomic m6A Decoration: Writers, Erasers, Readers and Functions in RNA Metabolism. *Cell Res*, 28:616–24. https://doi.org/10.1038/s41422-018-0040-8
20. Wu Y, Xie L, Wang M, *et al.*, 2018, Mettl3-mediated m6A RNA Methylation regulates the fate of bone marrow mesenchymal stem cells and osteoporosis. *Nat Commun*, 9:4772. https://doi.org/10.1038/s41467-018-06898-4
21. Yu J, Shen L, Liu Y, *et al.*, 2020, The m6A Methyltransferase METTL3 Cooperates with Demethylase ALKBH5 to Regulate Osteogenic Differentiation through NF-κB Signaling. *Mol Cell Biochem*, 463:203–10. https://doi.org/10.1007/s11010-019-03641-5
22. Liu Y, Gu C, Li X, *et al.*, 2021, Involvement of METTL3/m6Adenosine and TGFβ/Smad3 Signaling on Tenon's Fibroblasts and in a Rabbit Model of Glaucoma Surgery. *J Mol Histol*, 52:1129–44. https://doi.org/10.1007/s10735-021-10028-8
23. Liu L, Yu F, Li L, *et al.*, 2021, Bone Marrow Stromal Cells Stimulated by Strontium-substituted Calcium Silicate Ceramics: Release of Exosomal miR-146a Regulates Osteogenesis and Angiogenesis. *Acta Biomater*, 119:444–57. https://doi.org/10.1016/j.actbio.2020.10.038
24. Zhou P, Xia D, Ni Z, *et al.*, 2021, Calcium Silicate Bioactive Ceramics Induce Osteogenesis through Oncostatin M. *Bioact Mater*, 6:810–22. https://doi.org/10.1016/j.bioactmat.2020.09.018
25. Huang Y, Jin X, Zhang X, *et al.*, 2009, *In Vitro* and *In Vivo* Evaluation of Akermanite Bioceramics for Bone Regeneration. *Biomaterials*, 30:5041–8. https://doi.org/10.1016/j.biomaterials.2009.05.077
26. Sun X, Ma Z, Zhao X, *et al.*, 2021, Three-dimensional Bioprinting of Multicell-laden Scaffolds Containing Bone Morphogenic Protein-4 for Promoting M2 Macrophage Polarization and Accelerating Bone Defect Repair in Diabetes Mellitus. *Bioact Mater*, 6:757–69. https://doi.org/10.1016/j.bioactmat.2020.08.030
27. Zheng M, Weng M, Zhang X, *et al.*, 2021, Beta-tricalcium Phosphate Promotes Osteogenic Differentiation of Bone Marrow-derived Mesenchymal Stem Cells through Macrophages. *Biomed Mater*, 16:025005. https://doi.org/10.1088/1748-605X/abdbdc
28. El-Rashidy AA, Roether JA, Harhaus L, *et al.*, 2017, Regenerating Bone with Bioactive Glass Scaffolds: A Review of *In Vivo* Studies in Bone Defect Models. *Acta Biomater*, 62:1–28. https://doi.org/10.1016/j.actbio.2017.08.030
29. Wu D, Wang Z, Wang J, *et al.*, 2018, Development of a Micro-tissue-mediated Injectable Bone Tissue Engineering Strategy for Large Segmental Bone Defect Treatment. *Stem Cell Res Ther*, 9:331. https://doi.org/10.1186/s13287-018-1064-1
30. Stevens MM, 2008, Biomaterials for Bone Tissue Engineering. *Mater Today*, 11:18–25. https://doi.org/10.1016/S1369-7021(08)70086-5
31. Baldwin P, Li DJ, Auston DA, *et al.*, 2019, Autograft, Allograft, and Bone Graft Substitutes: Clinical Evidence and Indications for Use in the Setting of Orthopaedic Trauma Surgery. *J Orthop Trauma*, 33:203–13. https://doi.org/10.1097/BOT.0000000000001420
32. Prakash J, Prema D, Venkataprasanna KS, *et al.*, 2020, Nanocomposite Chitosan Film Containing Graphene Oxide/Hydroxyapatite/Gold for Bone Tissue Engineering. *Int J Biol Macromol*, 154:62–71. https://doi.org/10.1016/j.ijbiomac.2020.03.095
33. Kaushik N, Nguyen LN, Kim JH, *et al.*, 2020, Strategies for Using Polydopamine to Induce Biomineralization of Hydroxyapatite on Implant Materials for Bone Tissue Engineering. *Int J Mol Sci*, 21:E6544. https://doi.org/10.3390/ijms21186544
34. Take Y, Mae T, Yoneda M, *et al.*, 2020, On-lay Grafting of a Calcium Hydroxyapatite Bone Substitute: A Preliminary Animal Experimental Study. *J Orthop Sci*, 25:1101–6. https://doi.org/10.1016/j.jos.2019.12.012

35. Sathiyavimal S, Vasantharaj S, Oscar FL, *et al.*, 2019, Biosynthesis and Characterization of Hydroxyapatite and its Composite (Hydroxyapatite-gelatin-chitosan-fibrin-bone Ash) for Bone Tissue Engineering Applications. *Int J Biol Macromol*, 129:844–52. https://doi.org/10.1016/j.ijbiomac.2019.02.058

36. Beuriat PA, Lohkamp LN, Szathmari A, *et al*., 2019, Repair of Cranial Bone Defects in Children Using Synthetic Hydroxyapatite Cranioplasty (CustomBone). *World Neurosurg*, 129:e104–13. https://doi.org/10.1016/j.wneu.2019.05.052

37. Zhang H, Zhou Y, Yu N, *et al.*, 2019, Construction of Vascularized Tissue-engineered Bone with Polylysine-modified Coral Hydroxyapatite and a Double Cell-sheet Complex to Repair a Large Radius Bone Defect in Rabbits. *Acta Biomater*, 91:82–98. https://doi.org/10.1016/j.actbio.2019.04.024

38. Przekora A, Kazimierczak P, Wojcik M, 2021, *Ex Vivo* Determination of Chitosan/Curdlan/Hydroxyapatite Biomaterial Osseointegration with the Use of Human Trabecular Bone Explant: New Method for Biocompatibility Testing of Bone Implants Reducing Animal Tests. *Mater Sci Eng C Mater Biol Appl*, 119:111612. https://doi.org/10.1016/j.msec.2020.111612

39. Putri TS, Hayashi K, Ishikawa K, 2020, Bone Regeneration Using β-tricalcium Phosphate (β-TCP) block with Interconnected Pores Made by Setting Reaction of β-TCP Granules. *J Biomed Mater Res A*, 108:625–32. https://doi.org/10.1002/jbm.a.36842

40. Zhang D, Gao P, Li Q, *et al.*, Engineering Biomimetic Periosteum with β-TCP Scaffolds to Promote Bone Formation in Calvarial Defects of Rats. *Stem Cell Res Ther*, 8:134. https://doi.org/10.1186/s13287-017-0592-4

41. Tian C, Huang Y, Li Q, *et al.*, 2019, Mettl3 Regulates Osteogenic Differentiation and Alternative Splicing of Vegfa in Bone Marrow Mesenchymal Stem Cells. *Int J Mol Sci*, 20:551. https://doi.org/10.3390/ijms20030551

42. Son HE, Min HY, Kim EJ, *et al.*, 2020, Fat Mass and Obesity-Associated (FTO) Stimulates Osteogenic Differentiation of C3H10T1/2 Cells by Inducing Mild Endoplasmic Reticulum Stress via a Positive Feedback Loop with p-AMPK. *Mol Cells*, 43:58–65.

43. Zhang C, Chen Y, Sun B, *et al.*, 2017, m6A Modulates Haematopoietic Stem and Progenitor Cell Specification. *Nature*, 549:273–6. https://doi.org/10.1038/nature23883

44. Zhang B, Wu Q, Li B, *et al.*, 2020, m6A Regulator-Mediated Methylation Modification Patterns and Tumor Microenvironment Infiltration Characterization in Gastric Cancer. *Mol Cancer*, 19:53. https://doi.org/10.1186/s12943-020-01170-0

45. Zhang Y, Gu X, Li D, *et al.*, 2019, METTL3 Regulates Osteoblast Differentiation and Inflammatory Response via Smad Signaling and MAPK Signaling. *Int J Mol Sci*, 21:199. https://doi.org/10.3390/ijms21010199

46. Barbieri I, Tzelepis K, Pandolfini L, *et al.*, 2017, Promoter-bound METTL3 Maintains Myeloid Leukaemia by m6A-dependent Translation Control. *Nature*, 552:126–31. https://doi.org/10.1038/nature24678

47. Dominissini D, Moshitch-Moshkovitz S, Schwartz S, *et al.*, 2012, Topology of the Human and Mouse m6A RNA Methylomes Revealed by m6A-seq. *Nature*, 485:201–6. https://doi.org/10.1038/nature11112

48. Bartosovic M, Molares HC, Gregorova P, *et al.*, 2017, N6-methyladenosine Demethylase FTO Targets pre-mRNAs and Regulates Alternative Splicing and 3'-end Processing. *Nucleic Acids Res*, 45:11356–70. https://doi.org/10.1093/nar/gkx778

49. Geula S, Moshitch-Moshkovitz S, Dominissini D, *et al.*, 2015, Stem Cells. m6A mRNA Methylation Facilitates Resolution of Naïve Pluripotency toward Differentiation. *Science*, 347:1002–6. https://doi.org/10.1126/science.1261417

50. Kennedy EM, Bogerd HP, Kornepati AV, *et al.*, 2017, Posttranscriptional m6A Editing of HIV-1 mRNAs Enhances Viral Gene Expression. *Cell Host Microbe*, 22:830. https://doi.org/10.1016/j.chom.2017.11.010

Publisher's note

Whioce Publishing remains neutral with regard to jurisdictional claims in published maps and institutional affiliations.

RESEARCH ARTICLE

Computational Fluid Dynamics Assessment of the Effect of Bioprinting Parameters in Extrusion Bioprinting

Rashik Chand[1], Beni Shimwa Muhire[2], Sanjairaj Vijayavenkataraman[1,3]*

[1]The Vijay Lab, Division of Engineering, New York University Abu Dhabi, Abu Dhabi, United Arab Emirates
[2]Department of Mechanical Engineering, United Arab Emirates University, Al Ain, United Arab Emirates
[3]Department of Mechanical and Aerospace Engineering, Tandon School of Engineering, New York University, Brooklyn, NY 11201, USA.

Abstract: Wall shear stress is the most critical factor in determining the viability of cells during the bioprinting process, and controlling wall shear stress remains a challenge in extrusion bioprinting. We investigated the effect of various bioprinting parameters using computational simulations on maximum wall shear stress (MWSS) in the nozzle to optimize the bioprinting process. Steady-state simulations were done for three nozzle geometries (conical, tapered conical, and cylindrical) with varying nozzle diameters (0.1 mm–0.5 mm) at different inlet pressure (0.025 MPa–0.25 MPa) as inlet conditions. Non-Newtonian power law was used to model the bioink rheology and four different bioinks with power-law constants ranging from 0.0863 to 0.5050 were examined. To capture the dynamic behavior of the bioink and the thread profile of the extruded bioink, transient simulations were carried out. Our results indicate that although the MWSS is lowest in the cylindrical nozzle, this stress condition lasts for a longer portion of the nozzle and for the same inlet pressure and nozzle diameter, the mass flow rate is lower compared to the tapered conical and conical nozzle, contributing to lower cell viability.

Keywords: Computational fluid dynamics; Non-Newtonian fluid; Power-law fluid model; Extrusion bioprinting; Bioprinting parameters

*Correspondence to: Sanjairaj Vijayavenkataraman, Global Network Assistant Professor of Mechanical Engineering, Experimental Research Building (C1-039), NYU Abu Dhabi, Saadiyat Campus P.O. Box 129188 Abu Dhabi, United Arab Emirates; vs89@nyu.edu

Received: December 5, 2021; **Accepted:** January 20, 2022; **Published Online:** March 22, 2022

Citation: Chand R, Muhire BS, Vijayavenkataraman S., 2022, Computational Fluid Dynamics Assessment of the Effect of Bioprinting Parameters in Extrusion Bioprinting. *Int J Bioprint,* 8(2):545. http://doi.org/10.18063/ijb.v8i2.545

1. Introduction

Bioprinting refers to the biofabrication involving specially designed three-dimensional (3D) bioprinters that deposit bioinks in a controlled manner to create tissues and biocompatible structures. Bioinks are composed of living cells suspended in a biocompatible polymer (hydrogel) in the presence of other additives, such as differentiation and growth factors, or other biomaterials. Bioprinting is increasingly being considered an ideal tool for biofabricating rejection-free tissues and organs for transplantation[1].

Bioprinting can be categorized into four main technologies: Micro-extrusion, inkjet, laser assisted, and stereolithography. Among these categories, extrusion-based bioprinting is the most used due to its relative simplicity, affordability, and scalability as high viscous materials with high cell density can be used. In extrusion bioprinting, continuous bioink filaments are deposited layer by layer on a surface mechanically by displacement of a piston or screw or using pneumatic pressure[2]. In contrast, inkjet bioprinting is comparable to conventional two-dimensional (2D) printing and cannot generate a continuous flow, whereas in laser-assisted bioprinting, a high-intensity laser is used to deposit the bioink without applying direct force to the cell and finally, stereolithography makes use of light-sensitive polymer material[3]. While the advantage of extrusion-based bioprinting is that it can create more clinically relevant printed structures using bioink with higher viscosity, cell viability in extrusion bioprinting ranges from 40 to 80% which is lower compared to >85% in inkjet-based bioprinting and >95% in laser-assisted bioprinting[4,5].

© 2022 Author(s). This is an Open-Access article distributed under the terms of the Creative Commons Attribution License, permitting distribution and reproduction in any medium, provided the original work is properly cited.

Nozzles are very important in determining the printability of bioinks and survivability of cells; therefore, the nozzle design is critical and takes into consideration various aspects, including viscosity of bioink, shear-thinning property, and shear stress induced during the printing process. Cells are exposed to various mechanical forces, and among these, shear stress is regarded as especially significant since it is the main cause of cell damage and death. These forces are directly proportional to the inlet pressure of the nozzle and an increased pressure corresponds to an increased shear stress endured by the cells. The cells near the wall experience greater shear stress compared to the cells in the center of the nozzle, and the cell viability decreases in an exponential manner as shear stress increases[6]. On the other hand, an overly low inlet pressure will result in no or little bioink being deposited, whereas a pressure too high will result in excess bioink being deposited[7].

The behavior of the bioink flowing inside a nozzle is an important aspect to determine, but is difficult to achieve with experimental tests, mainly due to the small size of the nozzles, which make it harder to directly probe without interfering with the measurements. Experimental tests of bioink behavior are usually focused on bioprinting results, such as printability, shape fidelity, or cell viability, but studies on influential bioprinting parameters, such as shear stress, pressure, and velocity, are not as common experimentally[8]; therefore, computational simulations are increasingly being used to address this gap.

Computational fluid dynamics (CFD) can provide key insights into the effect of specific bioprinting parameters that cannot be measured while running an experiment. For instance, using CFD, we can calculate microfluidics inner parameters, such as velocity, pressure, or shear stress, which are experimentally difficult to measure[7]. Experimental tests focus on bioprinting results (printability, shape fidelity, or cell viability) but require a large number of iterations, thereby increasing the cost, especially if the bioink is prepared using expensive materials. CFD can reduce such iterations, thereby making the process cost and time efficient. As previously mentioned, doing a measurement itself can affect the parameters since the measurement devices have a non-negligible size compared to the conditions of the experiment[7]. CFD is widely used to obtain flow behavior in simple or more complicated designs and can pinpoint the exact spatial coordinates where forces are exerted on the cells, facilitating bioprinter optimization for complex geometries.

In recent years, several papers have discussed optimizing extrusion bioprinting using computational simulations. Magalhães *et al.*[2] looked at optimizing nozzle geometry through CFD simulation using wall shear stress as a measure of cell viability and concluded that convergence angle of the nozzle and exit diameter had the greatest effect on printability and cell viability. Emmermacher *et al.*[9] used computational simulations and analytical calculations to predict mechanical stress, pressure gradient, and flow rate for optimizing the bioprinting process and developing new bioinks. Göhl *et al.*[10] simulated the flow of bioink from a nozzle onto a printing plate using a proprietary CFD simulation tool IPS IBOFlow to evaluate the effect of bioprinting parameters, such as printing speed and nozzle height, on the printed strand resolution. Gómez-Blanco *et al.*[11] investigated the effect of inlet velocity, which is proportional to flow rate and can affect the extent of pressure endured by cells during the bioprinting process. Reina-Romo *et al.*[12] studied the effect of conical and blunted nozzle geometry on cell viability through computational simulations and conducted additional comparisons with experimental results. Most computational studies are limited by the fact that they are specific to certain bioinks and/or nozzle geometries and some by the use of proprietary software that hinders reproducibility. Our study aims to not only characterize holistically the effect of bioprinting parameters but also investigate whether the trends in the results observed for a particular bioink are transferable to and reproducible in other bioinks.

In this paper, we will use CFD to provide an overview of the effects of dispensing pressure, nozzle diameter, and nozzle geometry, which are bioprinting parameters known to greatly affect the shear stress experienced by cells in bioink[6]. Using the wall shear stress as a measure of cell viability, we will analyze the effect of these parameters taking into consideration the rheological properties of the bioinks. We also investigate the impact of printing speed and dynamic behavior of the extruded bioink through transient simulations.

2. Materials and methodology

2.1. Modeling

We adapted the procedure outlined by Magalhães *et al.*[2] using three distinct nozzle geometries, namely, tapered conical, conical, and cylindrical, as shown in **Figure 1.** Three-dimensional models were created for each of the nozzle designs using 3D Computer-Aided Design software, Solidworks. The inlet diameter (D_{in}) was kept constant at 10.0 mm across all three nozzle geometries, whereas the outlet diameter (D_{out}) was varied as 0.1 mm, 0.3 mm, and 0.5 mm, which correspond to the nominal inner diameter of 32G, 24G, and 21G commercial nozzles commonly used in bioprinting, respectively. The angle of convergence was noted as a driven variable. The complete specification of the nozzles is provided in **Table 1**. The 3D models were imported into Ansys Fluent® 2021 R1

Academic License for the CFD simulations. Meshes were generated in Fluent for each nozzle using a hex dominant method with default element size (1.4 mm). In hindsight, sweep mesh method could have been used. All meshes had average element quality >0.50 and orthogonal quality >0.60. For the transient simulation, adaptive mesh sizing with a resolution of 6 was used for the nozzle, and sizing of 0.1 mm was used for the bottom environment half of the mesh.

2.2. Bioinks

Four different bioinks whose viscous behavior was described by the power-law viscosity model for non-Newtonian fluids (Equation 1) were chosen from existing literature, and the power-law parameters along with the density are tabulated in **Table 2**.

$$\eta = K.\gamma^{n-1} \quad (1)$$

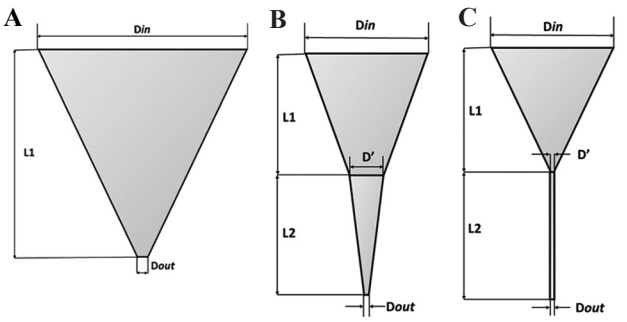


Figure 1. Diagram of selected nozzle geometry. (A) Tapered conical nozzle. (B) Conical nozzle. (C) Cylindrical nozzle.

Where, η is the viscosity (Pa s), n is the power-law constant (unitless), γ is the shear strain rate (s^{-1}), and K is the flow consistency index (Pa s). The initial viscosity of the bioink is given by K and is related to the extrudability of bioinks, with lower values indicating higher extrudability[13]. Based on the flow behavior index, n: if $0 < n < 1$, then, the fluid shows pseudo-plastic or shear-thinning behavior, with a smaller value of n meaning a greater degree of shear-thinning. If $n = 1$, the fluid shows Newtonian behavior, and if $n > 1$, the fluid shows dilatant or shear-thickening behavior with a higher value of n resulting in greater thickening[14].

Several studies have previously used the shear-dependent power-law to simulate the flow of non-Newtonian bioinks in different nozzle geometries using empirically obtained K and n values from curve approximation[2,8,15-17]. In addition, Markstedt *et al.*[18] used a linear PTT model in IPS IBOFlow, whereas Emmermacher *et al.*[9] used a model based on Herschel-Bulkley law to simulate the fluid flow inside the nozzle. The Herschel-Bulkley and Carreau-Yasuda model were considered but the value for required parameters was not readily available for chosen bioink, whereas n and K values were more readily available in the literature. All the chosen bioinks exhibit shear thinning, that is, viscosity decreases when shear rate increases. Shear-thinning is a desirable property in bioinks as it is crucial in determining printability by preventing clogging of nozzle and reducing shear stress, leading to greater cell survivability[19]. The bioinks were added into ANSYS Fluent® as user-

Table 1. Nozzle parameters for the three nozzle geometries

Nozzles	D_{in}(mm)	D'' (mm)	D_{out}(mm)	L1 (mm)	L2 (mm)	α1	α2
Tapered conical	10		0.1	10		26.84	
Tapered conical	10		0.3	10		25.87	
Tapered conical	10		0.5	10		25.41	
Conical	10	3	0.1	10	10	19.29	8.25
Conical	10	3	0.3	10	10	19.29	7.69
Conical	10	3	0.5	10	10	19.29	7.13
Cylindrical	10	0.1	0.1	10	10	26.34	
Cylindrical	10	0.3	0.3	10	10	25.87	
Cylindrical	10	0.5	0.5	10	10	25.41	

Table 2. Power law parameters and density of bioinks

Bioink	K (Pa.s)	*n*	Density (kg/m³)	Reference
Ink 6040 (NFC/alginate)	109.73	0.154	998.2	Dharmadasa[16]
CELLINK Bioink	102.53	0.170	1000	Gómez-Blanco, Mancha-Sánchez, Marcos[8]
Alginate-Sulfate Nanocellulose	56.503	0.0863	~1000	Müller, Öztürk, Arlov[17]
CM-cellulose + Alginate + κ-carrageenan + Gelatin	24.943	0.505	1039.8	Pössl[20]

defined materials with the density and power-law parameters enlisted in **Table 2**.

2.3. Simulations

Steady-state simulations were run in ANSYS Fluent® with each of the bioinks comprising the fluid domain. The boundary conditions were set to 0-gauge pressure at the outlet and six different values for inlet pressure were chosen: 0.025 MPa, 0.050 MPa, 0.10 MPa, 0.15 MPa, 0.20 MPa, and 0.25 MPa, similar to values found in the literature[20-22]. For the printing speed, multiphase volume of fluid transient simulations were run for 1000 timesteps with step size of 0.01 s, giving a flowtime of 10 s. The inlet condition was chosen as a constant mass flow rate of 0.0015 kgs^{-1} and ink6040 was used as the extruded bioink. The substrate was set as a moving wall condition with the desired translational speed (1 mms^{-1}, 5 mms^{-1}, and 10 mms^{-1}) corresponding to the printing speed, whereas the nozzle position was stationary. As described by Talluri[23], the movement of the nozzle is proportional to the movement of the substrate (bottom wall), and acceleration is approximately 0. This means that the simulation with moving substrate is equivalent to the simulation with moving nozzle. The pressure-implicit with splitting of operators (PISO) method was used as pressure-velocity coupling, and either the first- or second-order upwind was used to discretize momentum. PISO was chosen because solution convergence was obtained within acceptable computational time without having to use even smaller timestep and lower iteration per timestep.

There are some inherent assumptions made while using computational simulations to reduce the complexity of the simulations. It was assumed that (a) there was no slip between the bioink and the wall of the nozzle boundary condition of the nozzle wall; (b) the flow of bioink is incompressible, meaning its density is constant; and (c) the flow of the fluid is laminar.

3. Results and discussion

3.1. Nozzle geometry

In general, as shown in **Figure 2,** the tapered conical nozzle has a lower value for maximum wall shear stress (MWSS) than the conical nozzle, except for a dispensing pressure equal to 0.025 MPa for a given outlet diameter. The cylindrical nozzle with an outlet diameter of 0.5 mm has greater MWSS than the corresponding conical and tapered conical nozzle for inlet pressure >0.15 MPa. Besides this, the MWSS is lower in the cylindrical than the tapered conical and conical nozzles for all other combinations. This indicates that the cells would have higher survivability in the cylindrical nozzle. However, on examining the contours of MWSS for the three nozzles of outlet diameter 0.30 mm at 0.2 MPa presented in **Figure 3**, the region where the most wall shear stress is experienced by the cell is confined closer to just the outlet region of the tapered conical (**Figure 3A**) and conical nozzle (**Figure 3B**), which agrees with the findings of Liu *et al.*[24] and Gómez-Blanco *et al.*[8]. In contrast, for the cylindrical nozzle, the entirety of the cylindrical portion of the nozzle experiences a greater wall shear stress **(Figure 3C)**. While this particular combination was chosen as a representative condition to demonstrate where the region of MWSS occurred across the three nozzles, similar characteristic contours were

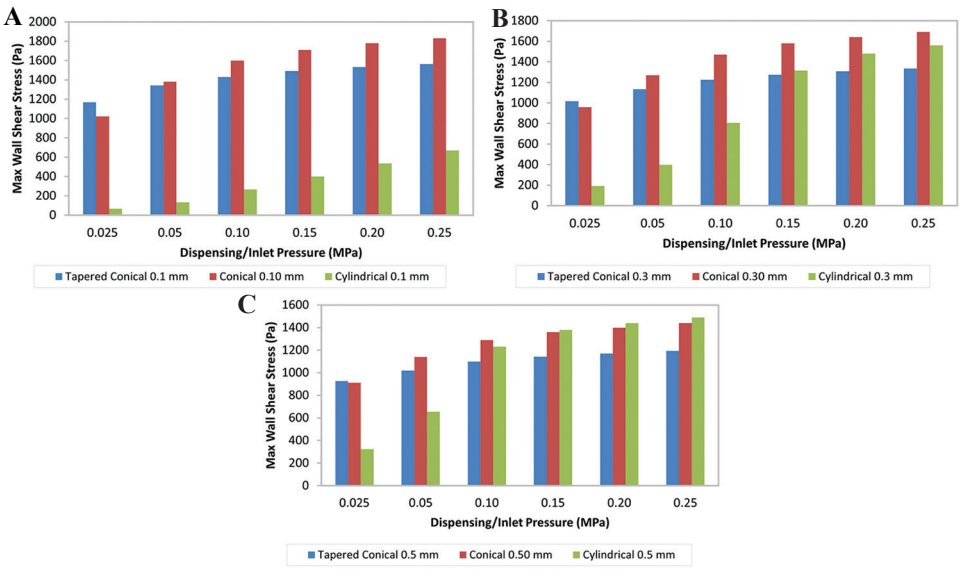


Figure 2. Variation of maximum wall shear stress with respect to different nozzle geometry at constant pressures. (A) 0.1 mm. (B) 0.3 mm. (C) 0.5 mm.

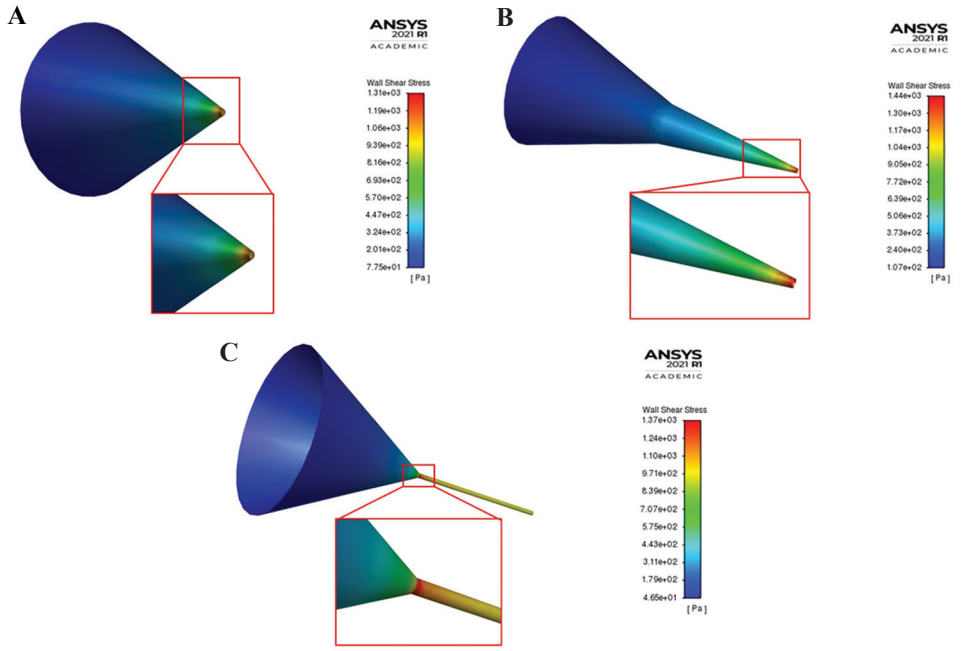


Figure 3. Contour of wall shear stress for (A) tapered conical, (B) conical, and (C) cylindrical nozzle with outlet diameter 0.3 mm at inlet pressure 0.20 MPa with regions of MWSS emphasized.

attained for other combination of outlet diameter and pressure. The region of maximum shear stress is longer in cylindrical nozzle because it has a uniform radius and requires a constant pressure throughout for extrusion in contrast to conical needles where high pressure is only needed at the tip of the nozzle[25]. Billiet *et al.*[15] also compared conical and cylindrical nozzle of internal diameter 200 mm at 1 bar inlet pressure and noted that the conical nozzle experienced greater shear stress for approximately 1 mm near the outlet, but the cylindrical nozzle experienced lower shear stress for >16 mm from the nozzle. This meant that cell death was higher in the cylindrical nozzle due to the higher passage time in the high shear stress region. This observation is indicative of the reduced cell viability in tubular (cylindrical) nozzles compared to conical nozzles, as shown by experimental observations[26,27].

The cylindrical nozzles that have a smaller volumetric footprint compared to the conical nozzle are ideal for printing in confined spaces and can reduce wastage of bioink, which is an added benefit while using expensive biomaterials or cells[7]. Although the MWSS in the cylindrical nozzle is much lower, the mass flow rate is comparatively lower than the tapered conical and conical nozzle for the same nozzle diameter and pressure, as shown in **Figure 4**. Since the flow rate is proportional to the applied pressure, increased pressure translates to an increased flow rate[28]. This means that to achieve the same flow rate in the cylindrical nozzle as in the conical and tapered conical nozzle, a greater pressure would be

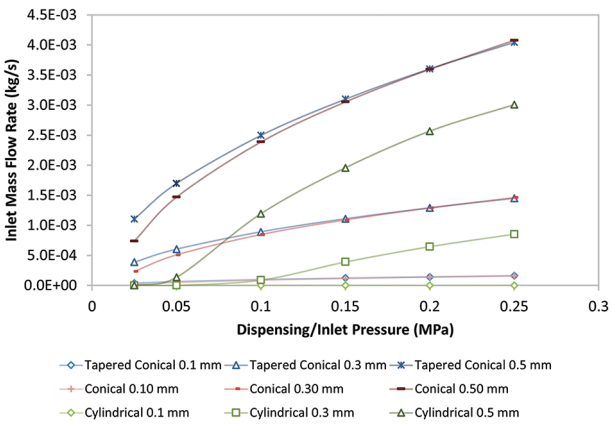


Figure 4. Graph of inlet mass flow rate with respect to pressure for different nozzles.

required, which consequently increases shear stress[17]. In our simulations, an inlet mass flow rate >0.003 kg/s was obtained in a cylindrical nozzle with an outlet diameter of 0.50 mm only at 0.25 MPa inlet pressure with a corresponding MWSS of 1490 Pa. In contrast, an inlet mass flow rate >0.003 kg/s was obtained in a tapered conical and conical nozzle with outlet diameter 0.50 mm at 0.15 MPa inlet pressure with a corresponding MWSS of 1142 Pa and 1360 Pa, respectively. The difference in mass flow rate was more drastic at lower inlet pressure values; for instance, the mass flow rates were 0.0017 kg/s and 0.0015 kg/s for tapered conical and conical nozzles, respectively, but the mass flow

rate for the cylindrical nozzle was 0.00014 kg/s at an inlet pressure of 0.05 MPa. Consequently, at equivalent flow rates, cell damage was lower in a tapered needle compared to a cylindrical one[27].

3.2. Nozzle diameter

As shown in **Figure 5**, for both tapered conical and conical nozzles, our findings agree that as the nozzle diameter increases from 0.1 mm to 0.5 mm, the MWSS decreases under constant pressure, possibly leading to greater cell viability. As shown in **Table 3**, the decrease of the diameter from 0.5 mm to 0.1 mm increases the MWSS by approximately 30% for the tapered conical nozzle and by 25% for the conical nozzle at a given pressure. However, for the cylindrical nozzle, the MWSS is the lowest for nozzle diameter 0.1 mm, and the maximum shear stress increases as outlet nozzle diameter increases. In addition, while the cylindrical nozzle with a diameter of 0.3 mm has a lower shear stress than the cylindrical nozzle with a diameter of 0.5 mm, for pressures higher than 0.2 MPa, the wall shear stress is greater in the cylindrical nozzle with outlet diameter 0.3 mm. One explanation for these deviations from the expected result for the cylindrical nozzles can be accounted to the choice of inlet condition as constant pressure. There is a significant increase in the flow rate, as evident in **Figure 6**, to maintain a constant pressure difference, which leads to the increased MWSS in the nozzle with the largest outlet diameter[12].

Cell survivability is crucial in the bioprinting process. As such, several studies have indicated the adverse effect on cell survivability with the decrease in nozzle diameter due to the increased shear forces experienced by the cells[29-31]. Conversely, an increase in nozzle diameter reduces the velocity gradient and thus reduces shear stress, in turn, increasing the cell survivability[22]. Although a larger outlet diameter increases flow rate and reduces shear stress, it also results in lower resolution; a smaller outlet diameter with higher inlet pressure gives higher resolution[2]. It is crucial to balance both cell survivability and printing resolution to obtain an optimum result.

Table 3. Percentage increase in maximum wall shear stress (Pa) on decreasing diameter of nozzle outlet from 0.5 mm to 0.1 mm

Pressure (MPa)	Tapered conical	Conical	Cylindrical
0.025	26.1	11.9	−79.4
0.050	31.7	21.1	−79.6
0.100	30.1	24.0	−78.2
0.150	30.5	25.7	−70.9
0.200	30.9	27.1	−62.8
0.250	30.9	27.1	−55.0

3.3. Dispensing pressure

Cells are exposed to various mechanical forces while moving through the nozzles; this generates internal pressures that can damage the cells[7]. These forces are directly proportional to the dispensing pressure as it determines the force with which the extruded material is being pushed. Increasing the dispensing pressure also increases the MWSS, much like decreasing the nozzle diameter. Nair *et al.*[31] suggested that the effect of increasing the inlet pressure has a more prominent negative effect on cell viability than nozzle diameter. However, taking into consideration, the maximum percentage increase in wall shear stress on increasing the pressure by 5 times (**Table 4**) and decreasing the outlet diameter by a factor of 5 at constant pressure (**Table 3),** our results do not conclusively show the more pronounced effect of inlet pressure. At a given outlet diameter, our findings suggest that on increasing the pressure from 0.05 MPa to 0.25 MPa, the increase in MWSS is highest in the cylindrical nozzle followed by the conical and finally tapered conical nozzle. Furthermore, the variation of the overall percentage increase in MWSS is lower for tapered conical and conical nozzles as compared to the cylindrical nozzle of different outlet diameter, as shown in **Table 4**.

In addition, a very low inlet pressure will result in no or little bioink being deposited, whereas a very high pressure will result in excess bioink being deposited[7]. It is very important to obtain a higher volumetric flow because it leads to a faster dispensing speed so as to shorten the time for the cells under pressure. However, the overall volumetric flow cannot be fully controlled by the dispensing pressure alone as it depends on the fluid viscosity and the inner geometry where the fluid flows[8]. Thus, the optimum dispensing pressure varies for different nozzles.

From **Figure 7**, the best pressure ranges are in the regions where there is a linear relationship between the pressure and the shear stress with a gentle slope. In these regions, it is easier to control the cell viability and volumetric flow. As we can see, these regions are different for all the nozzles. When determining the optimum working pressure, it is recommended to choose the lower pressures from the pressure ranges to reduce the risk of cell damage, but one must also consider the flow rate and choose the best compromise.

Table 4. Percentage increase in maximum wall shear stress (Pa) on increasing pressure from 0.05 MPa to 0.25 MPa for different outlet nozzle diameter

Diameter (mm)	Tapered conical	Conical	Cylindrical
0.1	16.5	32.6	401.9
0.3	17.9	33.1	290.3
0.5	17.2	26.3	127.5

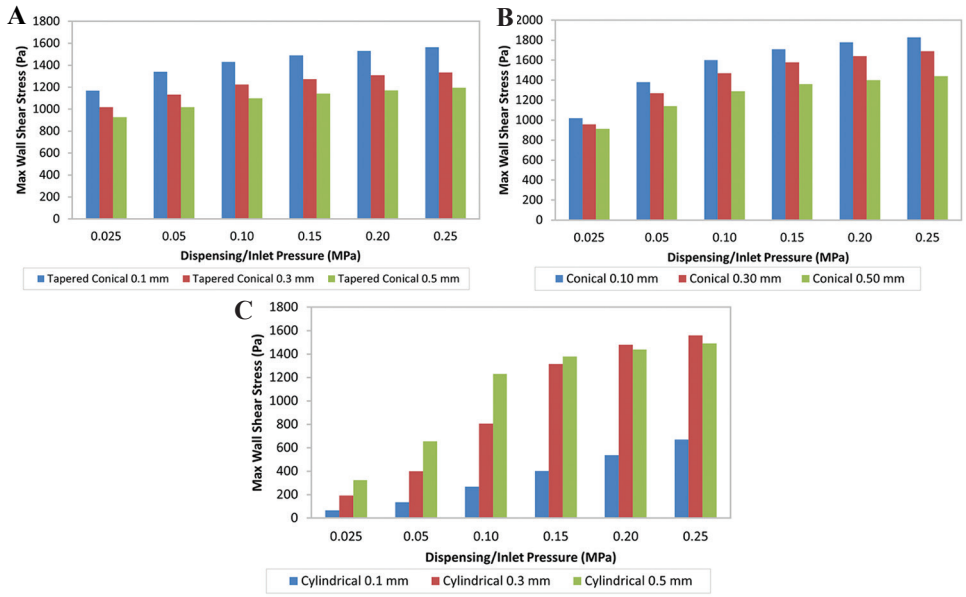


Figure 5. Variation of maximum wall shear stress with respect to different nozzle diameters at constant pressures for (A) tapered conical, (B) conical, and (C) cylindrical nozzles.

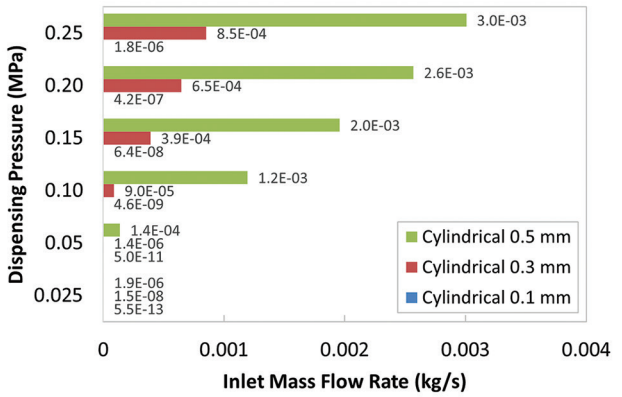


Figure 6. Inlet mass flow rate at specified pressures for cylindrical nozzles.

3.4. Bioink rheology

During extrusion bioprinting, bioinks go from a resting state to a high shear stress condition in the nozzle and then go back to a resting state. The decrease in the viscosity caused by the shear-thinning property of the bioink facilitates the deposition of the bioink and leads to high printing fidelity as shear stress is drastically reduced as the ink exits the nozzle[32]. The power-law constant (n) is representative of the bioink's shear thinning behavior. Bioinks with lower value of n exhibit a more shear thinning behavior, that is, an increase in shear rate causes a greater decrease in the viscosity of the bioink. **Figure 8** shows the results of the MWSS obtained for each of the nozzles with an outlet diameter of 0.3 mm using the four different bioinks at varying inlet pressure. Alginate-sulfate nanocellulose bioink with the lowest power-law constant value (n = 0.0863), that is, the highest shear thinning behavior experiences the lowest maximum shear stress. Ink6040 (n = 0.154) and CELLINK bioink (n = 0.170), both of which have similar n-value, show the same trend in MWSS with similar values. This is further supported by the fact that the viscosity is determined by the polymer concentration and molecular weight and both ink6040 and CELLINK bioink are made up of similar concentrations of nano-fibrillated cellulose and alginate, in the ratios of 60:40 and 80:20, respectively. In general, the results follow the expected trend, except for the inlet pressure value of 0.05–0.15 MPa in the cylindrical nozzle where the bioink with the highest n-value (0.5050) has a lower MWSS than the ink6040 and CELLINK bioink. When we look at the outlet mass flow rate for the four bioinks in the cylindrical nozzle, as shown in **Figure 9**, the flow rate of the CM-cellulose + Alginate + κ-carrageenan + Gelatin bioink (n = 0.5050) has an almost negligible mass flow rate, indicating that the bioink is not extrudable at the lower values of dispensing pressure due to its weaker shear-thinning properties. The trend in the values of MWSS is similar for all the four bioinks in the tapered conical and conical nozzles, suggesting that the aforementioned observations and inferences for ink6040 with respect to dispensing pressure, nozzle geometry, and outlet diameter would hold for the three other bioinks. With that said, the effect of the power-law constant is confounded by the difference in the consistency index value (K) in the power-law equation.

3.5. Printing speed

The 2D thread profiles for ink6040 in the conical nozzle with outlet diameter 0.3 mm obtained through transient simulations at printing speed 5 mms^{-1} for 10 s with an

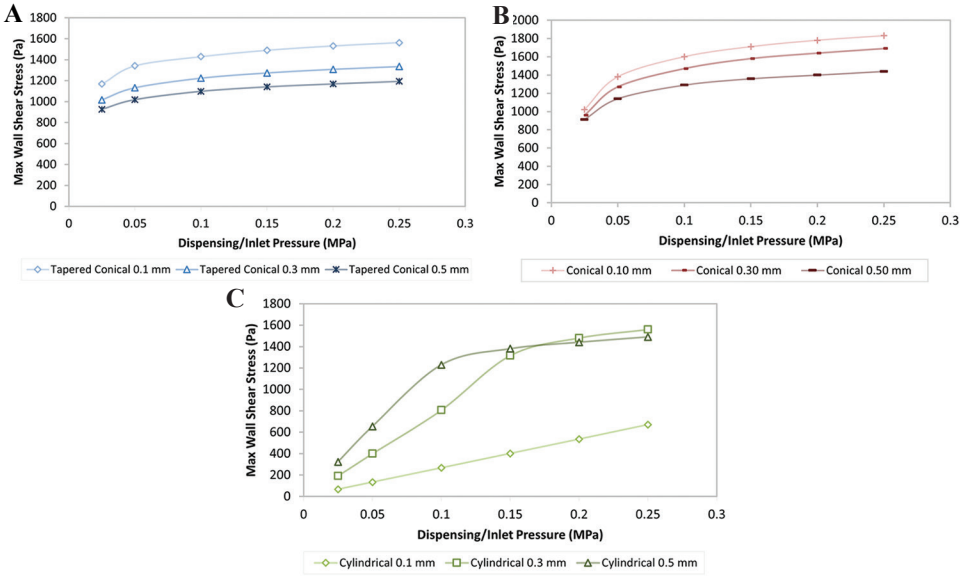


Figure 7. Variation of maximum wall shear stress of different nozzle diameters at different pressures. (A) Tapered conical. (B) Conical. (C) Cylindrical.

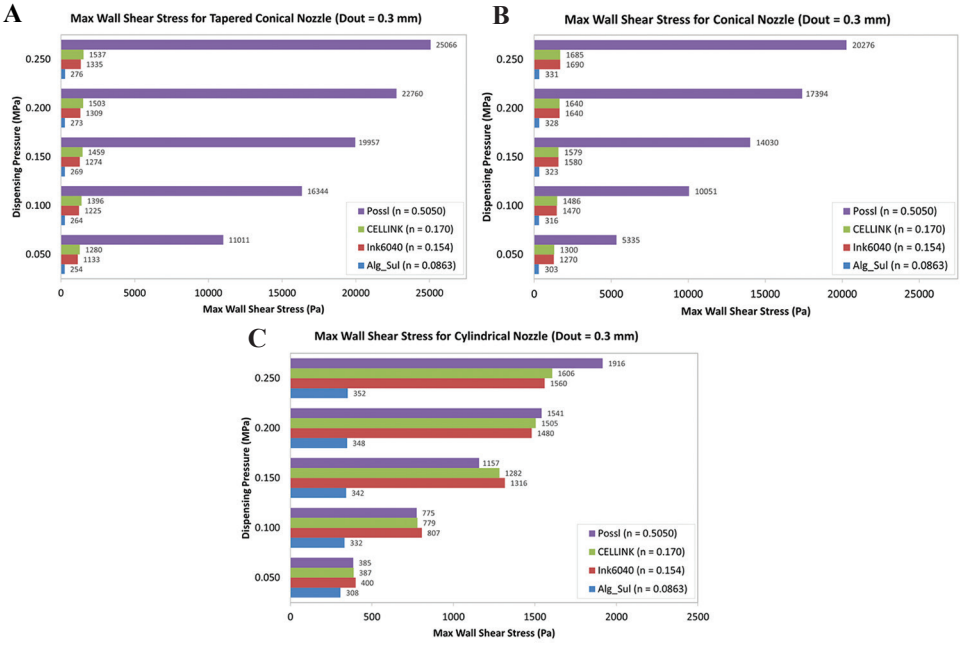


Figure 8. Graph of maximum wall shear stress at varying inlet pressure for bioinks with different power-law constant using (A) tapered conical nozzle (D_{out} = 0.3 mm), (B) conical nozzle (D_{out} = 0.3 mm), and (C) cylindrical nozzle (D_{out} = 0.3 mm).

interval of 2 s are shown in **Figure 10**. The thread profiles for the other nozzles at varied printing speeds (1 mms^{-1}, 5 mms^{-1}, and 10 mms^{-1}) at the same time intervals are shown in the **Appendix Figures 1-9**. Quantitative assessment of the thread profile using volume fraction of the bioink across all three nozzles shows that at lower printing speed, the strand of extruded bioink is continuous and uniform, but at higher printing speeds, the strand is discontinuous and smaller in width. Furthermore, the ideal printing speed seems to be the same regardless of the chosen nozzle geometry for a constant diameter at a constant inlet mass flow rate. A change in the strand width results in decreased accuracy of the printed strand at higher printing speed as observed experimentally[22]. As such, using CFD to simulate the effect of printing speed can assist in identifying the ideal printing speed for a given bioink in a particular system.

As shown in **Figure 11A**, in general, the conical nozzle has the lowest outlet velocity, whereas the cylindrical nozzle

has the highest outlet velocity. This result is contrary to the result expected from the steady-state simulations, but it can be explained by the choice of constant inlet mass flow rate used for the transient simulations contrary to the constant inlet pressure for the steady simulations. For the lower printing speed (1 mms^{-1} and 5 mms^{-1}), the outlet velocity plateaued at a constant velocity throughout the simulation across all three nozzles. However, the variation in velocity was greater for the higher printing speed especially in the latter half of the simulations. A similar trend was observed in the case of the outlet pressure across the three nozzles, as shown in **Figure 11B**. These variations can be explained by looking at the strand profile for the individual simulations. Due to the higher translational velocity of the bottom wall, the strands moved further away from the nozzle, causing the thread profile to move upwards. For instance, in the case of the conical nozzle at 10 mms^{-1} (Appendix, **Figure 3E**), the strand was broken and caused coagulation at the outlet, which caused the fluctuation. In practical applications, the variations in the velocities are in terms of a fraction of millimeters, so it is unlikely that it would make a significant difference.

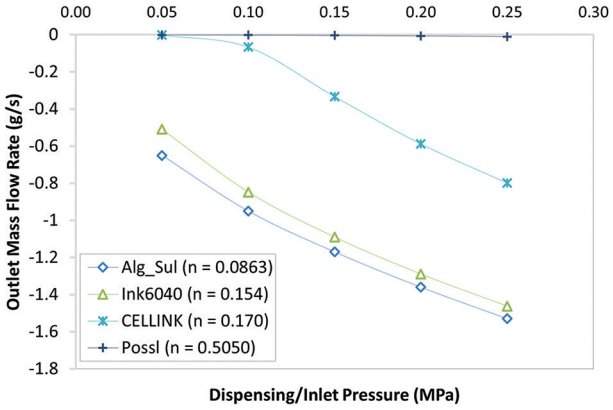


Figure 9. Line graph of outlet mass flow rate against inlet pressure for the four bioinks.

3.6. Empirical relationship

As cell viability and survivability are closely related to the shear stress experienced by the cell in the nozzle, predicting the amount of shear stress experienced by the cell can serve to increase cell viability. Nair *et al.*[31] developed an empirical model from experimental data to predict the degree of survivability of cells as a function of inlet pressure and outlet diameter. Since the dispensing pressure and diameters are independent variables, a complete second-order model with two independent variables can be expressed as shown in Equation 2[31].

$$(x, y) = \beta_0 + \beta_1 x_1 + \beta_2 x_2 + \beta_3 x_1 x_2 + \beta_4 x_1^2 + \beta_5 x_2^2 \qquad (2)$$

Based on this, we fitted a second-degree curve to the results of our computational simulations to get an empirical relationship for ink6040 and estimate the MWSS (z) experienced in the nozzle as a function of the inlet pressure (x) used for extrusion and the outlet diameter of the nozzle (y). Empirical equations can be calculated similarly for other bioinks and could be used to compare the MWSS and, in turn, survivability of cells in different bioinks.

The surface plot for the observed relationship is shown in **Figure 12** and the empirical relation is given by Equations 3, 4, and 5 for the tapered conical, conical, and cylindrical nozzles, respectively. For the cylindrical

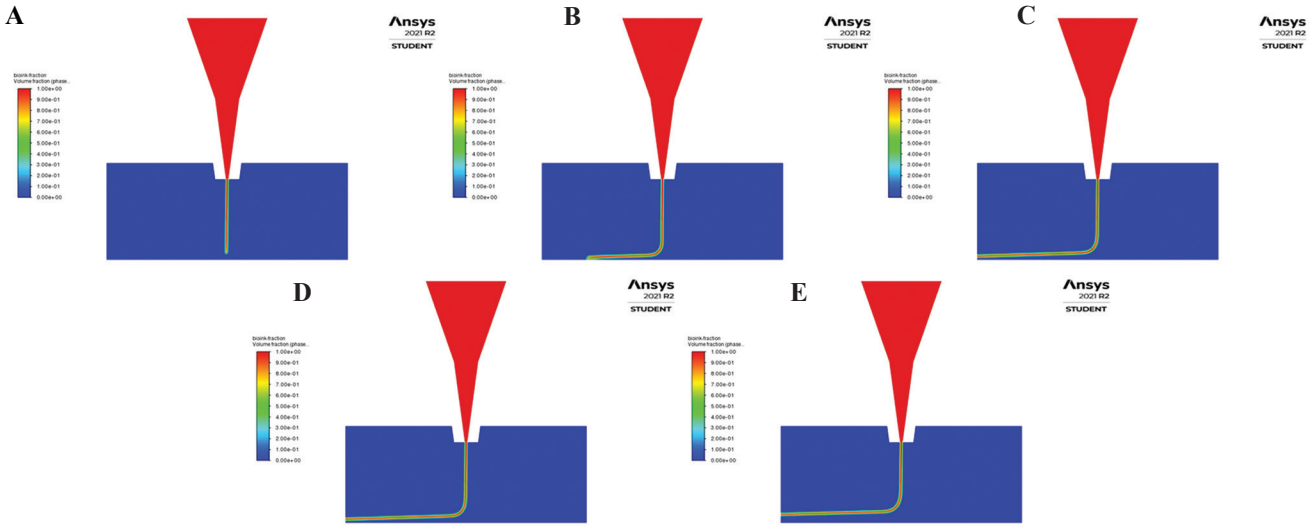


Figure 10. Contour of volume fraction for extruded bioink in conical nozzle with printing speed 5 mms−1 at (A) 2 s, (B) 4 s, (C) 6 s, (D) 8 s, and (E) 10 s.

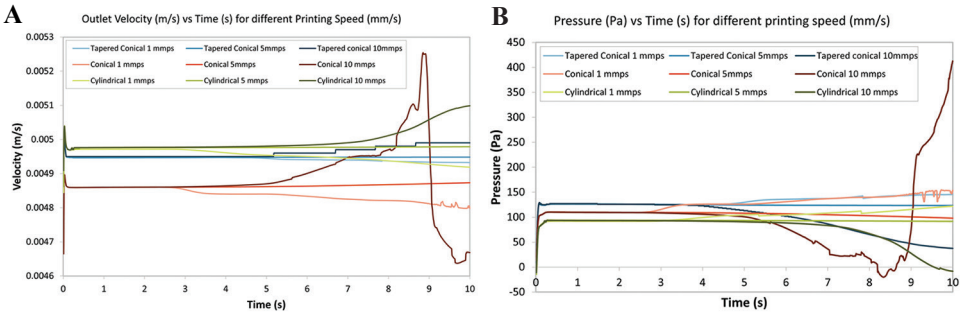


Figure 11. Variation of (A) outlet velocity (m/s) and (B) outlet pressure (Pa) in the nozzle against time (s) for different printing speeds through transient simulation.

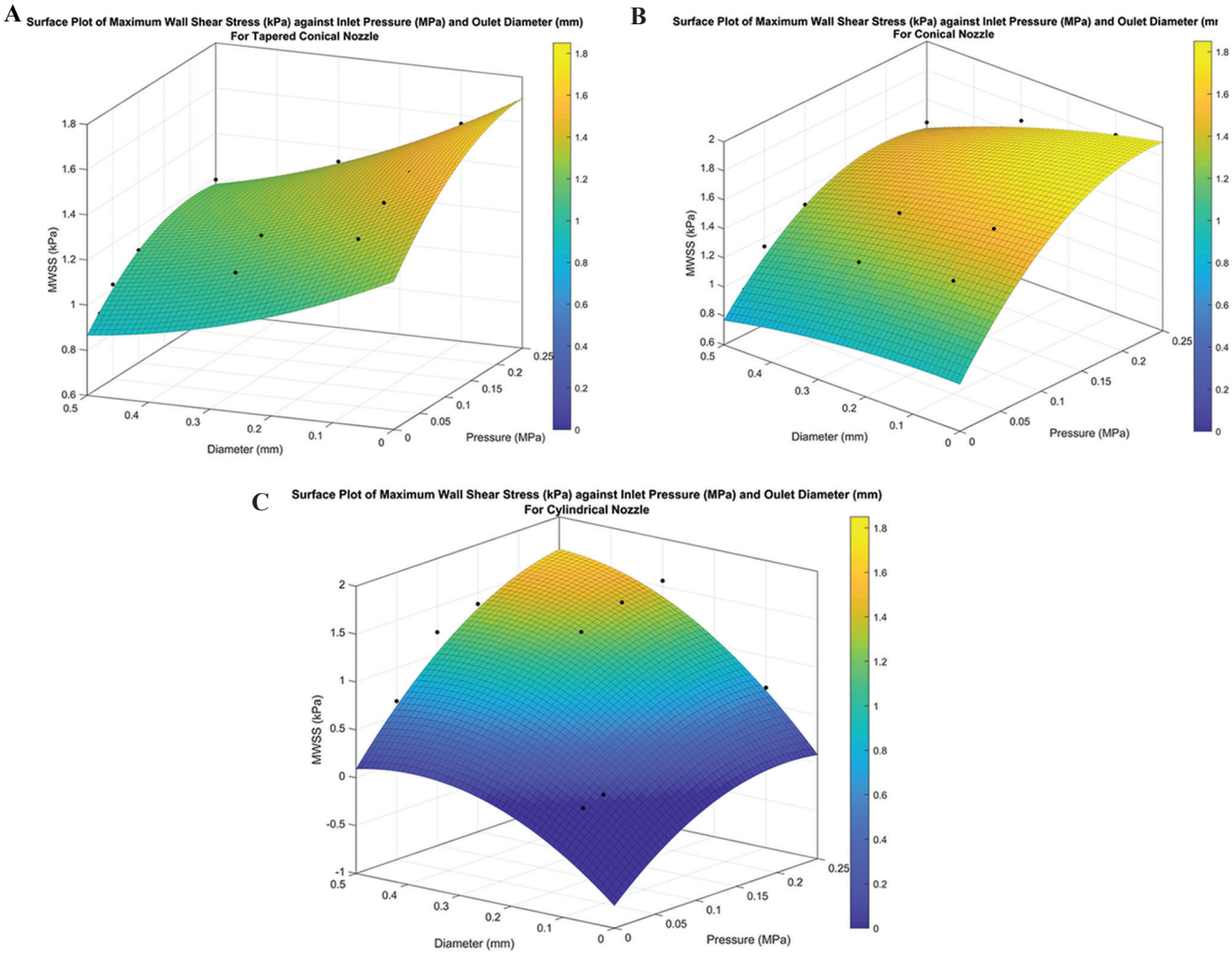


Figure 12. Surface plot for maximum wall shear stress (in kPa) for (A) tapered conical, (B) conical, and (C) cylindrical nozzles.

nozzle, the computational relationship suffers due to the wide variations in the MWSS (abbreviated as MWSS in the following equations) due to the effect of a drastic increase in flow rate to maintain the constant inlet pressure condition. As such, at low values of pressure and diameter, the model predicts a negative MWSS, as shown in **Figure 12C**.

$$MWSS_{tapered} = 1.26 + 3.56x - 1.29y - 7.11x^2 - 1.12xy + 1.02y^2 \quad (3)$$

$$MWSS_{conical} = 0.92 + 8.27x + 0.059y - 17.48x^2 - 2.76xy - 0.74y^2 \quad (4)$$

$$MWSS_{cylindrical} = -0.76 + 8.37x + 4.75y - 19.94x^2 + 5.74xy - 6.07y^2 \quad (5)$$

4. Conclusions

Our aim was to investigate the effect of crucial bioprinting parameters – nozzle geometry, nozzle diameter, inlet pressure, and bioink rheology, specifically, shear-thinning properties – on the MWSS and thus cell viability through computational simulation. In addition, we simulated the effect of printing speed on the thread profile along with outlet velocity and pressure. The main conclusions of our study can be summarized as follows:

- In general, the MWSS for the tapered conical nozzle is lower than the conical nozzle, and the cylindrical nozzle has the lowest MWSS. However, the cells experience higher shear stress for a greater portion of the nozzle length in the cylindrical nozzle.
- The flow rate of bioink is crucial in the investigation of shear stress. Higher pressure needs to be applied in the cylindrical nozzle to attain the same flow rate as the other two nozzles, resulting in higher shear stress. Increasing the pressure is a possible confounding factor because it increases mass flow rate which decreases the time spent by the cell under high shear stress.
- Increasing the nozzle diameter increases mass flow rate and decreases the wall shear stress, but it may negatively affect the printing resolution.
- Our findings do not suggest that increasing the inlet pressure has a more prominent negative effect than decreasing the outlet diameter.
- We demonstrated that computational simulations can be used to generate a thread profile of printed strand and our simulations suggest that the ideal printing speed is independent of nozzle geometry for a constant nozzle diameter at a constant inlet mass flow rate.
- We presented empirical relationships based on our simulations, which would facilitate comparisons amongst different bioinks and experimental setups.

Most importantly, the effects of these bioprinting parameters are in constant interplay with each other and they need to be considered as a whole to fully understand their effect in the bioprinting process. With CFD simulations, we could even observe the effect of these bioprinting parameters, which would not be possible in an experimental setup. It provides insights that may assist in optimizing the bioprinting parameters, developing and comparing different bioinks and experimental setups, and reducing the number of trial iterations required while bioprinting. As such, the efficiency of bioprinting processes can be increased and the development of novel approaches can be furthered.

The results for the cylindrical nozzle were confounded due to the drastic changes in mass flow rate, and hence, further simulations with a constant mass flow rate are needed. Three-dimensional simulations of the bioink thread profile under experimental conditions, simulations involving cells, and experimental verification of the results to validate the usefulness of the computational simulation are proposed as future work.

Acknowledgments

Beni Shimwa Muhire acknowledges NYU Abu Dhabi's Virtual Summer 2021 Visiting Undergraduate Research Program for the opportunity to work on this project.

Funding

This research received no specific grant from any funding agency in the public, commercial, or not-for-profit sectors.

Conflicts of interest

The authors declare no conflicts of interest.

Authors' contributions

R.C. carried out design of experiment, ran steady and transient simulation, and drafted and revised the manuscript. B.M. ran steady simulation and cowrote the manuscript. S.V. was responsible for ideation, manuscript review and editing, as well as overall supervision.

References

1. Vijayavenkataraman S, Yan WC, Lu WF, *et al*., 2018, 3D Bioprinting of Tissues and Organs for Regenerative Medicine. *Adv Drug Deliv Rev*, 132:296–332. https://doi.org/10.1016/j.addr.2018.07.004
2. Magalhães IP, Oliveira PM, Dernowsek J, *et al*., 2019, Investigation of the Effect of Nozzle Design on Rheological Bioprinting Properties Using Computational Fluid Dynamics. *Matéria* (*Rio de Janeiro*), 24:714. https://doi.org/10.1590/s1517-707620190003.0714
3. Wang Z, Abdulla R, Parker B, *et al*., 2015, A Simple and High-resolution Stereolithography-based 3D Bioprinting System Using Visible Light Crosslinkable Bioinks. *Biofabrication*, 7:045009. https://doi.org/10.1088/1758-5090/7/4/045009
4. Zhang J, Wehrle E, Rubert M, *et al*., 2021, 3D Bioprinting of Human Tissues: Biofabrication, Bioinks, and Bioreactors. *Int J Mol Sci*, 22:3971. https://doi.org/10.3390/ijms22083971
5. Biazar E, Najafi SM, Heidari KS, *et al*., 2018, 3D Bio-printing Technology for Body Tissues and Organs Regeneration.

J Med Eng Technol, 42:187–202.
https://doi.org/10.1080/03091902.2018.1457094

6. Boularaoui S, Al Hussein G, Khan KA, *et al*., 2020, An Overview of Extrusion-based Bioprinting with a Focus on Induced Shear Stress and its Effect on Cell Viability. *Bioprinting*, 20:e00093.
7. Bahrd A, 2017, Computational Fluid Dynamics and Quantitative Cell Viability Measurements in Dispensing-Based Biofabrication. p. 37.
8. Gómez-Blanco JC, Mancha-Sánchez E, Marcos AC, *et al*., Bioink Temperature Influence on Shear Stress, Pressure and Velocity Using Computational Simulation. *Processes*, 8:865.
9. Emmermacher J, Spura D, Cziommer J, *et al*., 2020, Engineering Considerations on Extrusion-based Bioprinting: Interactions of Material Behavior, Mechanical Forces and Cells in the Printing Needle. *Biofabrication*, 12:025022.
10. Göhl J, Markstedt K, Mark A, *et al*., 2018, Simulations of 3D Bioprinting: Predicting Bioprintability of Nanofibrillar Inks. *Biofabrication*, 10:034105.
https://doi.org/10.1088/1758-5090/aac872
11. Gómez-Blanco JC, Mancha-Sánchez E, Ortega-Morán JF, *et al*., 2020, Computational Fluid Dynamics Study of Inlet Velocity on Extrusion-Based Bioprinting. in XV Mediterranean Conference on Medical and Biological Engineering and Computing MEDICON 2019. Cham: Springer International Publishing.
12. Reina-Romo E, Mandal S, Amorim P, *et al*., 2021, Towards the Experimentally-Informed *In Silico* Nozzle Design Optimization for Extrusion-Based Bioprinting of Shear-Thinning Hydrogels. *Front Bioeng Biotechnol*, 9:701778.
https://doi.org/10.3389/fbioe.2021.701778
13. Gillispie G, Prim P, Copus J, *et al*., 2020, Assessment Methodologies for Extrusion-Based Bioink Printability. *Biofabrication*, 12:022003.
https://doi.org/10.1088/1758-5090/ab6f0d
14. Rapp BE, 2016, Fluids, in Microfluidics: Modeling, Mechanics and Mathematics. Amsterdam, Netherlands: Elsevier. p. 250–51.
15. Billiet T, Gevaert E, De Schryver R, *et al*., 2014, The 3D Printing of Gelatin Methacrylamide Cell-laden Tissue-engineered Constructs with High Cell Viability. *Biomaterials*, 35:49–62.
https://doi.org/10.1016/j.biomaterials.2013.09.078
16. Dharmadasa V, 2016, Investigation of Cell-viability in the Bioprinting Process. In: Department of Mechanics. Sweden: KTH Royal Institute of Technology. p. 54.
17. Müller M, Öztürk E, Arlov O, *et al*., 2017, Alginate Sulfate-Nanocellulose Bioinks for Cartilage Bioprinting Applications. *Ann Biomed Eng*, 45:210–23.
https://doi.org/10.1007/s10439-016-1704-5
18. Markstedt K, Mantas A, Tournier I, *et al*., 2015, 3D Bioprinting Human Chondrocytes with Nanocellulose-Alginate Bioink for Cartilage Tissue Engineering Applications. *Biomacromolecules*, 16:1489–96.
19. Wu Y, Wenger A, Golzar H, *et al*., 2020, 3D Bioprinting of Bicellular Liver Lobule-mimetic Structures via Microextrusion of Cellulose Nanocrystal-incorporated Shear-thinning Bioink. *Sci Rep*, 10:77146.
https://doi.org/10.1038/s41598-020-77146-3
20. Pössl A, 2021, A Targeted Rheological Bioink Development Guideline and its Systematic Correlation with Printing Behavior. *Biofabrication*, 13:035021.
21. Paxton N, Smolan W, Böck T, *et al*., 2017, Proposal to Assess Printability of Bioinks for Extrusion-based Bioprinting and Evaluation of Rheological Properties Governing Bioprintability. *Biofabrication*, 9:044107.
https://doi.org/10.1088/1758-5090/aa8dd8
22. Webb B, Doyle BJ, 2017, Parameter Optimization for 3D Bioprinting of Hydrogels. *Bioprinting*, 8, 8–12.
23. Talluri DJ, 2021, Numerical Modeling of the Fiber Deposition Flow in Extrusion-Based 3D Bioprinting. Rowan University, Ann Arbor. p. 103.
24. Liu W, Heinrich MA, Zhou Y, *et al*., 2017, Extrusion Bioprinting of Shear-Thinning Gelatin Methacryloyl Bioinks. *Adv Healthc Mater*, 6:1601451.
https://doi.org/10.1002/adhm.201601451
25. Kraynak J, 2021, Minimizing Cell Death During the Extrusion Bioprinting of Gelatin-Alginate Bioinks. Temple University, Libraries.
26. Anandan A, Courtial EJ, Lemarié L, *et al*., 2020, Rheology, Simulation and Data Analysis toward Bioprinting Cell Viability Awareness. *Bioprinting*, 21:e00119.
https://doi.org/10.1016/j.bprint.2020.e00119
27. Li M, Tian X, Schreyer DJ, *et al*., 2011, Effect of Needle Geometry on Flow Rate and Cell Damage in the Dispensing-based Biofabrication Process. *Biotechnol Prog*, 27:1777–84.
https://doi.org/10.1002/btpr.679
28. Udofia E, Zhou W, 2018, Microextrusion Based 3D Printing a Review. In: Solid Freeform Fabrication 2018: Proceedings of the 29th Annual International Solid Freeform Fabrication Symposium an Additive Manufacturing Conference, Austin, TX.
29. Blaeser A, Campos DF, Puster U, *et al*., 2016, Controlling Shear Stress in 3D Bioprinting is a Key Factor to Balance

Printing Resolution and Stem Cell Integrity. *Adv Healthc Mater*, 5:326–33.
https://doi.org/10.1002/adhm.201500677

30. Chang R, Sun W, 2008, Effects of Dispensing Pressure and Nozzle Diameter on Cell Survival from Solid Freeform Fabrication-based Direct Cell Writing. *Tissue Eng Part A*, 14:41–48.
https://doi.org/10.1089/ten.a.2007.0004

31. Nair K, Gandhi M, Khalil S, *et al*., 2009, Characterization of Cell Viability during Bioprinting Processes. *Biotechnol J*, 4:1168–77.
https://doi.org/10.1002/biot.200900004

32. Hölzl K, Lin S, Tytgat L, *et al*., 2016, Bioink Properties before, during and after 3D Bioprinting. *Biofabrication*, 8:032002.
https://doi.org/10.1088/1758-5090/8/3/032002

Publisher's note

Whioce Publishing remains neutral with regard to jurisdictional claims in published maps and institutional affiliations.

Appendix

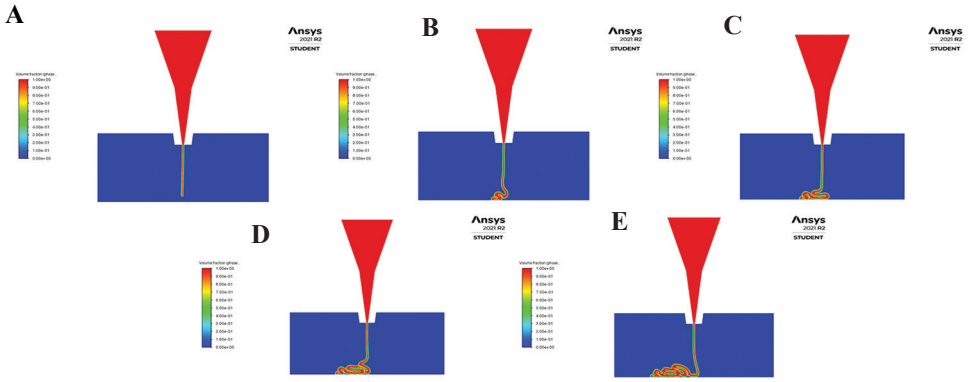


Figure 1. Contour of volume fraction for extruded bioink in conical nozzle with printing speed 1 mms^{-1} at (A) 2 s, (B) 4 s, (C) 6 s, (D) 8 s, and (E) 10 s.

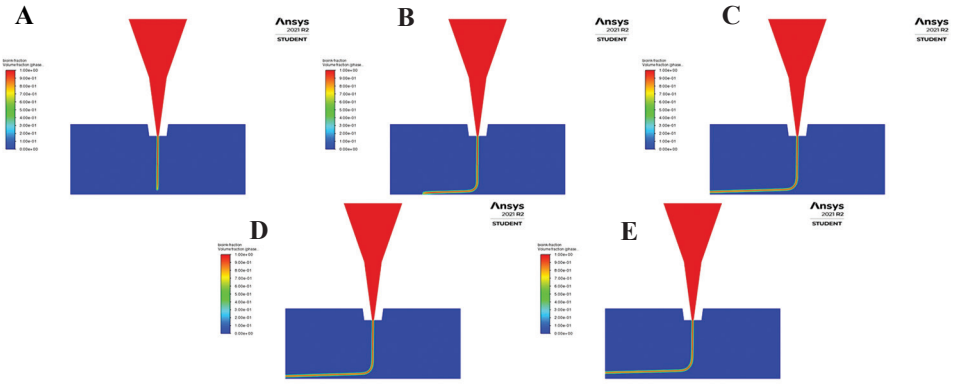


Figure 2. Contour of volume fraction for extruded bioink in conical nozzle with printing speed 5 mms^{-1} at (A) 2 s, (B) 4 s, (C) 6 s, (D) 8 s, and (E) 10 s.

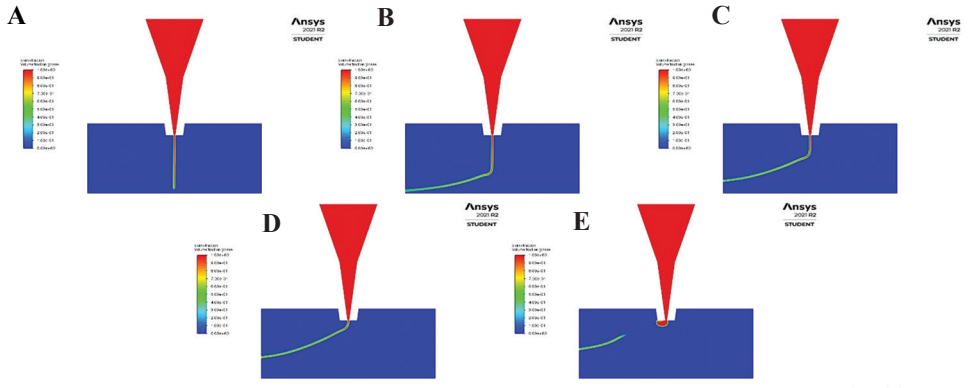


Figure 3. Contour of volume fraction for extruded bioink in conical nozzle with printing speed 10 mms^{-1} at (A) 2 s, (B) 4 s, (C) 6 s, (D) 8 s, and (E) 10 s.

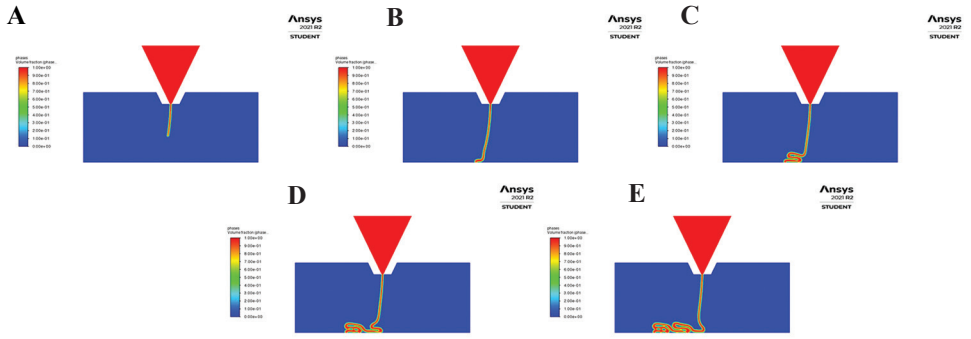


Figure 4. Contour of volume fraction for extruded bioink in tapered conical nozzle with printing speed 1 mms^{-1} at (A) 2 s, (B) 4 s, (C) 6 s, (D) 8 s, and (E) 10 s.

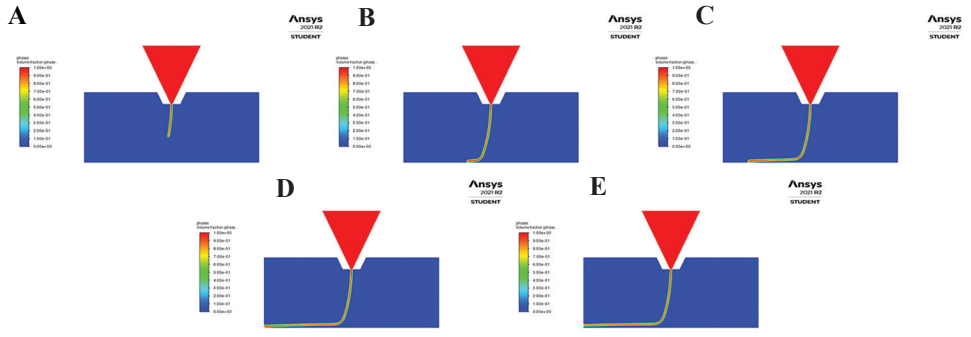


Figure 5. Contour of volume fraction for extruded bioink in tapered conical nozzle with printing speed 5 mms^{-1} at (A) 2 s, (B) 4 s, (C) 6 s, (D) 8 s, and (E) 10 s

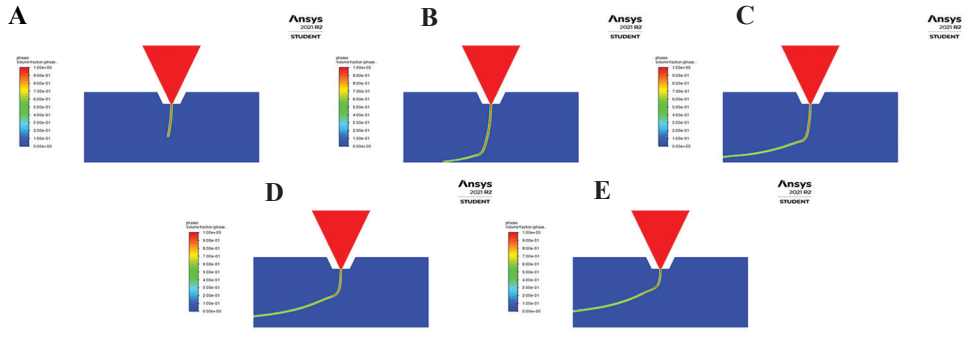


Figure 6. Contour of volume fraction for extruded bioink in tapered conical nozzle with printing speed 10 mms^{-1} at (A) 2 s, (B) 4 s, (C) 6 s, (D) 8 s, and (E) 10 s.

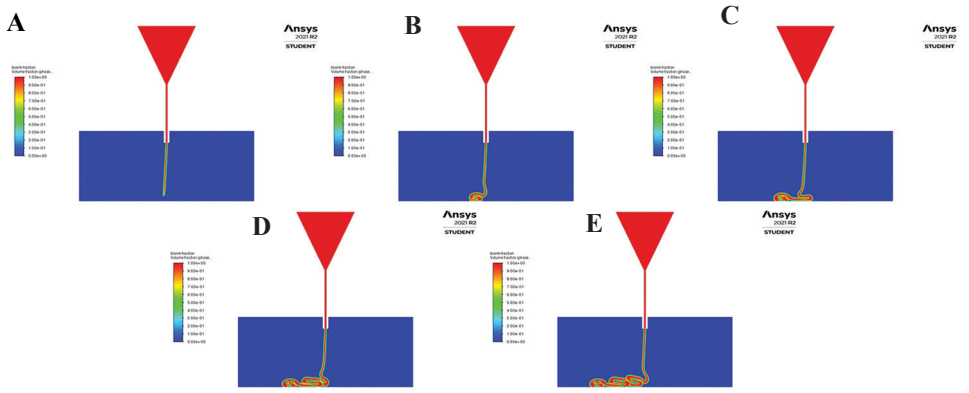


Figure 7. Contour of volume fraction for extruded bioink in cylindrical nozzle with printing speed 1 mms^{-1} at (A) 2 s, (B) 4 s, (C) 6 s, (D) 8 s, and (E) 10 s.

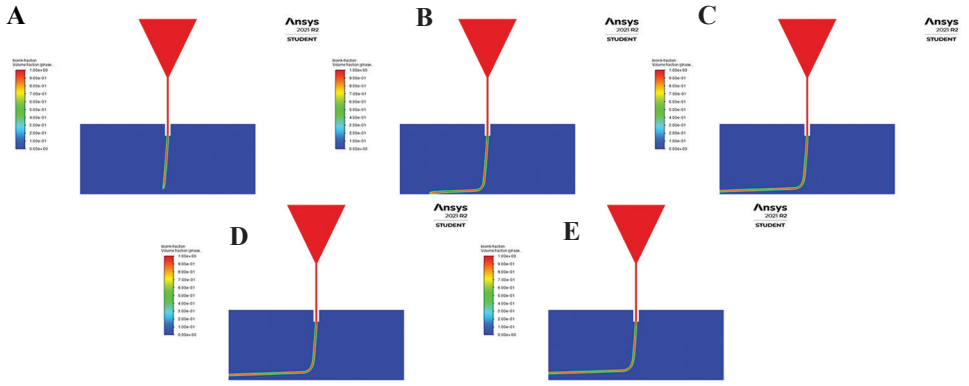


Figure 8. Contour of volume fraction for extruded bioink in cylindrical nozzle with printing speed 5 mms^{-1} at (A) 2 s, (B) 4 s, (C) 6 s, D) 8 s, and (E) 10 s.

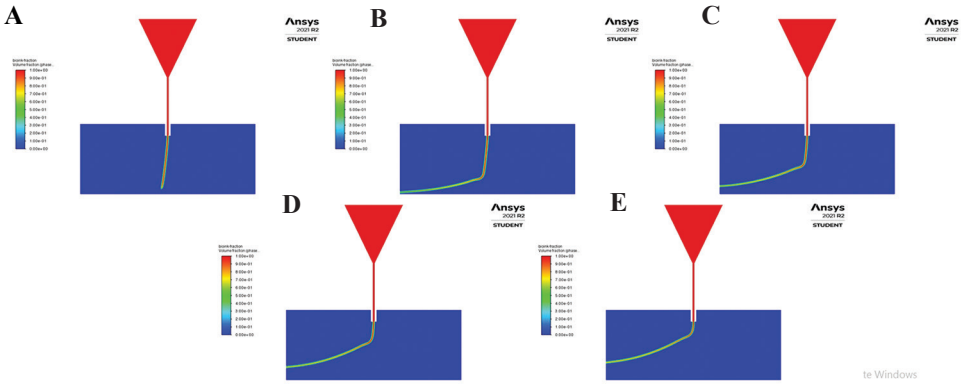


Figure 9. Contour of volume fraction for extruded bioink in cylindrical nozzle with printing speed 10 mms^{-1} at (A) 2 s, (B) 4 s, (C) 6 s, (D) 8 s, and (E) 10 s.

RESEARCH ARTICLE

Validity of a Soft and Flexible 3D-Printed Nissen Fundoplication Model in Surgical Training

Yangyi Zhang[1†], Jianfu Xia[2,3†], Jiye Zhang[4], Jinlei Mao[5], Hao Chen[6], Hui Lin[7], Pan Jiang[8], Xinzhong He[9], Xiaodong Xu[10], Mingzhu Yin[1*], Zhifei Wang[11*]

[1]Department of Dermatology, Hunan Engineering Research Center of Skin Health and Disease, Hunan Key Laboratory of Skin Cancer and Psoriasis, Xiangya Hospital, Central South University, Changsha, 410000, China
[2]Department of General Surgery, The Second Affiliated Hospital of Shanghai University (Wenzhou Central Hospital), Wenzhou, Zhejiang, 325000, China
[3]Soochow University, Soochow, Jiangsu, 215000, China
[4]Department of General Surgery, Yueqing Hospital Affiliated to Wenzhou Medical University (Yueqing People's Hospital), Yueqing, Zhejiang, 325600, China
[5]The Second Clinical Medical College, Zhejiang Chinese Medical University, Hangzhou, Zhejiang, 310000, China
[6]The Second Clinical Medical College, Zhejiang Chinese Medical University, Hangzhou, Zhejiang, 310000, China
[7]Department of General Surgery, Sir Run Run Shaw Hospital, Zhejiang University School of Medicine, Hangzhou, Zhejiang, 310000, China
[8]State Key Laboratory of Solid Lubrication, Lanzhou Institute of Chemical Physics, Chinese Academy of Sciences, Lanzhou 730000, China
[9]Department of Hepatobiliary and Pancreatic Surgery, The First People's Hospital of Tongxiang, Tongxiang, Zhejiang, 314500, China
[10]College of Materials Science and Engineering, Zhejiang University of Technology, Hangzhou, Zhejiang, 310014, China
[11]Department of Hepatobiliary and Pancreatic Surgery and Minimally Invasive Surgery, Zhejiang Provincial People's Hospital, Affiliated People's Hospital, Hangzhou Medical College, Hangzhou, Zhejiang, 310000, China
[†]*These authors contributed equally to this work*

Abstract: Rapid development of three-dimensional (3D) printing technique has enabled the production of many new materials for medical applications but the dry laboratory surgical training model made of soft and flexible materials is still insufficient. We established a new 3D-printed Nissen fundoplication training model of which materials simulate the real mechanical properties. In this study, 16 participants were divided into two groups: Experimental group and control group. The validity of model was tested using Likert scale by the experts and the experimental group. To evaluate the efficacy, performances of the experimental group were scored at the first, fourth, and eighth training by OSATS system and the duration of procedure was compared through the use of recorded video. Meanwhile, an *ex vivo* model was used to compare the performance of the experiment group and control group after the training in the same way. Our results showed that the 3D-printed model can support the future surgical applications, help improve surgical skills, and shorten procedure time after training.

Keywords: 3D-printed model; Nissen fundoplication; Surgical training; Soft materials

*Correspondence to: Mingzhu Yin, Department of Dermatology, Hunan Engineering Research Center of Skin Health and Disease, Hunan Key Laboratory of Skin Cancer and Psoriasis, Xiangya Hospital, Central South University, Changsha, 410000, China; yinmingzhu2008@126.com; Zhifei Wang, Department of Hepatobiliary and Pancreatic Surgery and Minimally Invasive Surgery, Zhejiang Provincial People's Hospital, Affiliated People's Hospital, Hangzhou Medical College, Hangzhou, Zhejiang, 310000, China; wangzhifei1973@zju.edu.cn

Received: November 28, 2021; **Accepted:** February 14, 2022; **Published Online:** March 23, 2022

Citation: Zhang Y, Xia J, Zhang J, *et al*., 2022, Validity of a Soft and Flexible 3D-Printed Nissen Fundoplication Model in Surgical Training. *Int J Bioprint,* 8(2):546. http://doi.org/10.18063/ijb.v8i2.546

© 2022 Author(s). This is an Open-Access article distributed under the terms of the Creative Commons Attribution License, permitting distribution and reproduction in any medium, provided the original work is properly cited.

1. Introduction

Three-dimensional (3D) printing is a technique that could enable the production of anatomically matched or patient-specific device and allow high on-demand fabrication of products for medical application in highly cost-effective manner[1]. Highly accurate products derived from patient's radiological imaging data were reportedly used in pre-operative planning, counseling with patients, training of students and residents, surgical training, intraoperative navigation, and templates or guides for specific task[2]. 3D-printed models range from hard tissues such as bones to soft-tissue structures such as heart, liver, lung, and vasculature are used in surgical simulation for different surgical procedures training. Compared to studies about hard tissues, however, studies about 3D-printed soft tissue for surgical training are scarce. Unlike fabrication of hard tissue, simulations using soft tissues are limited by the simulation of mechanical properties, which vary between organs or individuals[3,4]. There are several types of methods in 3D printing available for soft-tissues fabrication, including material extrusion (fused deposition modeling and [FDM] and direct ink writing), vat photopolymerization (VP), material jetting, and powder jet fusion[4,5]. Different printing materials and techniques are chosen depending on their benefits and limitations, especially in 3D bioprinting area, considering that the unique living or bioactive materials (bioink) used and the type of methods used are usually determined by the desired materials[6]. Various requirements, including appearance similarities, mechanical properties similarities, and simulations of true organ environment, should be taken into consideration when researchers or companies select the appropriate printing strategies[7]. As one of the methods used in early phase, material jetting is low cost and has high printing speed, but this technique demands high criteria and standards for bioinks used, especially in viscosity and clotting issue. Material extrusion, a process driven by pressure, allows the use of viscous liquid, such as cell suspension at a high density, but has a relatively slow printing speed and low resolution. Powder jet fusion was also an economic choice for fast and stable printing of soft tissue, while may more effort in post-processing modification is needed due to residual powder that leads to low surface accuracy and deficient structure. VP, including stereolithography, digital light processing, and two-photon polymerization, allows a relatively quick and precise fabrications of sophisticated internal or external anatomical structures[8-11]. Polyurethane, silicone gel, and hydrogels are some of the most commonly used materials in soft-tissue printing. Polyurethane can be combined with other hydroxyl or amine polymers, offering a changeable designation of chemical backbone, which can achieve different mechanical performances, but these can be a concern of toxicity and flammability. Despite low solubility in other solvents, silicone gel is widely used in industry because of its excellent elasticity and resilience, chemical stability, thermal and electrical resistance, biocompatibility, and low permeability compared with other polymer systems. Hydrogel is an attractive material used in medications attributed to its capability of absorbing and desorbing solvents in response to its environment; however, this property of absorbing and desorbing solvents depends on restricted environmental conditions, such as low humidity. With the availability of advanced materials and printing technique, there has been a growing number of surgical simulation models of soft tissues that are generated from different systems. The surgical models, including anatomical model and disease model, of liver and kidney are well-established; however, the studies on fabricating a stomach model are still scarce although researchers had attempted to simulate mechanical properties in an anthropomorphic gastric model[7,12,13]. The structures and organs in human have specific physical properties (for dissection), which differ from one other. For example, the texture of liver is softer than stomach, although they are both made of soft tissue. This should be considered in the process of creating an organ or disease model. Tissue response to surgical insults also should be considered. For example, the materials used should respond well during dissection by harmonic scalper[14].

Laparoscopic Nissen fundoplication (LNF) is a surgical treatment option for gastroesophageal reflux disease (GERD). GERD is a common disease with typical symptoms of acid regurgitation and heartburn, and complications including esophagitis, peptic strictures, and Barrett esophagus. The application of LNF requires high levels of expertise and training[15]. Developed by Dr. Rudolf Nissen, the use of LNF started as early as 1955 and was well established in Western countries, whereas at the same time, its application was still at its initial stage in China[16]. Relatively low prevalence (1.9–7%) in China coupled with delayed developments of surgical treatment of GERD had limited training or practicing opportunities of laparoscopic anti-reflux surgery for residents or attendings[17]. Nissen fundoplication was not included in the national textbook for medical college student until 2018; therefore, most of the Chinese students are unfamiliar about this surgical technique. Watching recorded video or direct observation of surgery are how most surgeons are trained but in the absence of practices.

Cadaver model, animal model, and *ex vivo* organ model are common wet laboratory models used in laparoscopic surgery training[14,18]. However, due to the concerns of high cost, social stress, and biosafety issue, the need for more proper alternatives to the wet laboratory models is emerging[19,20]. At present, animals such as swine, rats, or mouse are still the most widely used models

for anti-reflux surgery training[21-23]. Therefore, a lack of alternative models for anti-reflux surgery has driven us to generate a new dry laboratory model. A 3D-printed pancreaticojejunostomy model for use in robotic-assisted surgery training was generated in our previously work[24]. To extend the application of 3D-printed model in surgical training, we designed a new LNF model with a curriculum that incorporates the key steps in Nissen fundoplication to address the key issues related to failure during LNF, and conducted a trial to estimate the validity and efficacy of this model[25].

2. Methods

2.1. Model establishment

(1) Mold print

Anonymized Digital Imaging and Communication in Medicine files were obtained using Mimic 23.0 system from 3D computed tomography scans of disease-free human esophageal-gastric fundus and extracted/remodeling anatomy models of esophagus, stomach, diaphragm, spleen, and surrounding tissues. STL file abstracted was imported to Magic 24. The model was repaired to obtain a watertight structure. Then, OBJ files were exported from Magic 24 and imported to Zbush for further modification. Mold designations were completed by NX 1899 and either positive mold or negative mold was designed depending on the shape of organs. The STL files of designed mold were imported to Magic 24 for further designation of support structure and positioning. Next, FDM 3D printer was used to print the mold based on the sliced data, which would be given surface treatment and support structure removement after printing.

(2) Model formation

Resembled mold was treated with Vaseline on the build face to ensure smooth removal of the models from the mold. Silicone gel was poured into the mold from vacuum bin and cured under 25°C for 1 h. Finally, a model was obtained by removing the mold after solidification. Additional changes after initial palpation (by percentages) of silicon oil in silicone materials were implemented to manually adjust the texture until all experts agreed on the texture of the model.

(3) Model properties

The silicone material used for the stomach was pink, with modulus of elasticity of 0.15 MPa and a tensile strength of 0.95 MPa. The silicone material used for diaphragm was red, with modulus of elasticity of 0.18 MPa and a tensile strength of 0.82 MPa. The 3D-printed box simulates the abdomen, with 2 mm perforated silicone gel for the placement of laparoscopy and 5 mm silicone gel layer simulating the abdominal wall. The printed organs inside the box include: (i) Diaphragm, simulated by a silicone gel of 3 mm layer, which was made into a curved shape to simulate the shape of crus in real surgery, coupled with a hole with 5 cm diameter through which the esophageal part of the stomach can be pulled, simulating the hiatal hernia; (ii) stomach; (iii) liver; and (iv) mesentery, the surrounding connective part of esophagus and stomach, attaching both side of curvature of stomach and linking diaphragm with the angle of His. In compliance with the suturing requirements, we used a square-shaped mesh during the simulation surgery and removed a U-shaped piece from the mesh. In this study, we assume that the model needs mesh and manual suture although it is optional in real situation **(Figure 1)**.

2.2. Criteria for selecting participants

The present study was approved by Zhejiang Provincial People's Hospital to carry out experiments within its facilities. All procedures followed were in accordance with the ethical standards of the responsible committee on human experimentation (institutional and national) and with the Helsinki Declaration of 1975, as revised in 2000. All volunteers were PYG-3 residents from the standardized training program of general surgery department from June 2020 to March 2021. All selected participants had individually performed more than 30 laparoscopic cholecystectomy cases but never participated or preformed any laparoscopic fundoplication. Participants' performance was evaluated by two experts. Sixteen residents were assigned into the experimental group (n = 8) and control group (n = 8) based on their basic conditions, such as age, gender, and number of laparoscopic surgeries they have attended **(Table 1)**.

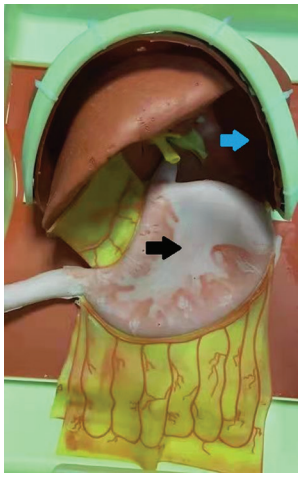


Figure 1. 3D-printed Nissen fundoplication training model. Blue arrow: Diaphragm; black arrow: Stomach.

2.3. Training curriculum

Operators were required to finish following steps: (i) Operators cut open silicone gel layer around the esophagus using ultrasonic scalpel to establish posterior esophagus tunnel **(Figure 2B)**; (ii) operators perform interrupted suture 2–3 times to close bilateral diaphragmatic crura with 2-0 non-absorbable Ethilon thread to close hiatal hernia **(Figure 2D-E)**; (iii) operators flatten the mesh and 6–8 suture on due spot for fixation of mesh on diaphragm **(Figure 2F-G)**; (iv) in Nissen fundoplication, operators

Table 1. General information of participants

	Experimental group	Control group	*P*-value
Age	28.13	29	>0.9999
Gender	M (7/8), F (1/8)	M (7/8), F (1/8)	
Hand dominance	R (8/8), L (0/8)	R (8/8), L (0/8)	
PGY level	PGY-3 8/8	PGY-3 8/8	
Average no. of basic laparoscopic procedures	95.63	99.38	>0.9999
Average no. of intermediate laparoscopic procedures	0.25	0.375	0.5598
Average no. of advanced laparoscopic procedures	0	0	
Average no. of laparoscopic bariatric procedures	0	0	
Box training experience	Y (8/8) N (0/8)	Y (8/8) N (0/8)	
VR experience	Y (0/8) N (8/8)	Y (0/8) N (8/8)	
3D printing model experience	Y (0/8) N (8/8)	Y (0/8) N (8/8)	
Ex vitro animal experience	Y (0/8) N (8/8)	Y (0/8) N (8/8)	
Live animal experience	Y (0/8) N (8/8)	Y (0/8) N (8/8)	
Average no. of laparoscopic cholecystectomy (LC)	42.38	46.88	0.3113
Psychomotor skills (OSATS SCORE)	23.00	22.13	>0.9999
Average knowledge test score	8.125	8.625	>0.9999

M: Male; F: Female; Y: Yes; N: No; VR: Virtual reality.

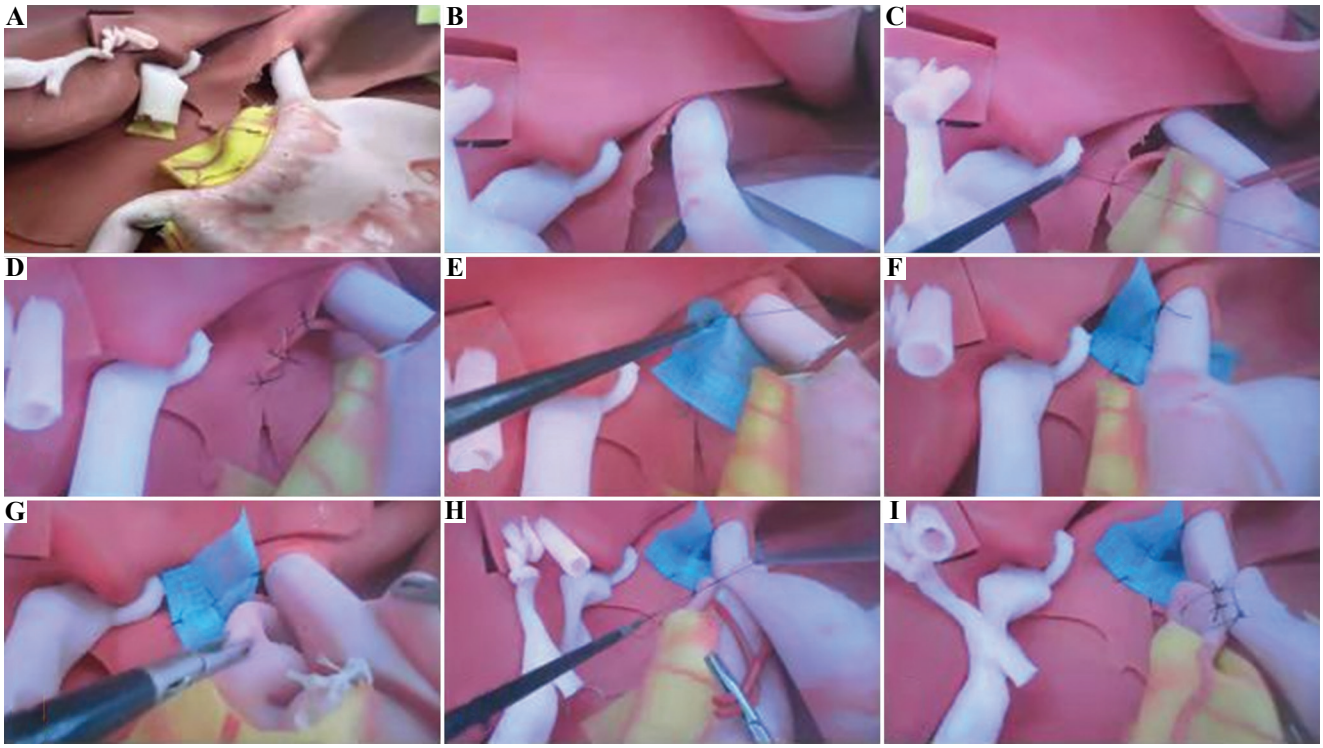


Figure 2. Model Nissen fundoplication procedure. (A) An overview of model under laparoscopy on simulation platform. (B) Established posterior esophagus tunnel. (C) Interrupted suture on hiatal hernia. (D) Enclosed hiatal hernia. (E) A step of placing mesh and fixation suture on diaphragm. (F) Fixed mesh. (G) Fundoplication through shoeshine maneuver. (H) Making a wrap using interrupted suture. (I) Forming a wrap.

incubate esophagus with 44F bougie tube and perform fundoplication through shoeshine maneuver of the fundus before making a ~3 cm wrap around the esophagus by 3–4 interrupted sutures **(Figure 2H-I)**.

2.4. Training method

Pathogenesis mechanism, symptoms, Nissen fundoplication, and surgical indications of GERD were introduced and explained to all participants at the beginning of the trial through recorded video. Questions from participants were answered by two experts. All participants were required to recap the surgical procedure and details after the introductory demonstration. No further training was given to control group in addition to their rotations. Participants in the experimental group were trained using the 3D-printed anti-reflux surgery model under a laparoscopic platform twice a week, and the training concluded after eight sessions. Videos were recorded for evaluation by two experts using OSATS score system.

2.5. Face validity and content validity

The validity of model was assessed using the 5-grade Likert scale by five experts and the experimental group (5: strongly agree; 4: agree; 3: neither agree nor disagree; 2: disagree; and 1, strongly disagree). This assessment involved nine parameters as follows: (i) The model is similar with real tissue or organ (experimental group skipped this parameter); (ii) the model is easy to use; (iii) using the model in surgical training is reasonable (experimental group skipped this parameter); (iv) training using the model can help reduce surgical risk to patient; (v) the model can help participants concentrate in learning; (vi) the model can help boost confidence in future surgery; (vii) the model can enhance tactile feedback; and (viii) the model is recommended for use in the training of anti-reflux surgery (experimental group skipped this parameter).

2.6. Construct validity

Performance of the experimental group was assessed by two experts who independently evaluated the recorded video using the global surgical and technical skills assessment tool (OSATS). Faces and voices of participants were not recorded in video. Seven aspects with five different levels each (35 points in total) were included in OSATS. The average of scores given by the two experts was the final score, and duration of the procedure was recorded at the same time.

2.7. Evaluation of efficacy of 3D model training

After 4 weeks of training, we compared the performances of laparoscopic anti-reflux surgery on *ex vivo* swine organs between two groups to assess the efficacy of model training **(Figure 3)**. Assessment method was the same as mentioned above.

2.8. Statistics analysis

In this study, *t*-test was used in parametric test. No non-parametric test was used in this study. SPSS 20.0.0 and GraphPad Prism 8.3.0 were used for statistical analysis and figure plotting. $P < 0.05$ was considered statistically significant.

3. Results

3.1. Model assessment

The validity of the model used by the experimental group was assessed by experts **(Table 2)**. All experts confirmed that (i) the model organs or tissues are similar to the real ones, the model training for anti-reflux surgery is reasonable, and (iii) the model can be applicable to anti-reflux surgery. This model was considered easy to handle, able to reduce the risk to patient, and able to improve skill, boost confidence, and tactile feedback of participants.

3.2. OSATS score and procedure duration in different training sessions

All participants of the experimental group had successfully completed eight training sessions. OSATS score was increasing whereas the procedure duration was reducing as the training was progressing **(Figure 4)**. The OSATS score was improved and the procedure duration was shortened as the training progressed **(Table 3)**.

3.3. Model training validity and efficacy assessment

Participants of the experimental and control groups performed Nissen fundoplication on *ex vivo* swine organs after 8 weeks of training. All participants (eight out of eight) of the experimental groups successfully finished the surgery while six out of eight participants of the control group completed the surgery with the helps from experts. OSATS of the experimental group (26.25 ± 1.67) was higher than that of the control group (17.50 ± 2.07, $t = 9.31$). Procedure duration of the experimental group (76.25 ± 2.49) was lower compared to the control group (110.13 ± 3.36, $t = 22.92$) (**Table 4** and **Figure 5)**.

4. Discussion

In China, it is very common that surgeons learn how to perform laparoscopic anti-reflux surgery by watching video or observing during surgery. Furthermore, the lack of practice is attributed to very limited number of medical centers that are equipped to perform this type of surgery. Laparoscopic fundoplication is a expertise demanding procedure, and surgeons who perform laparoscopic fundoplication should be sufficiently trained given the

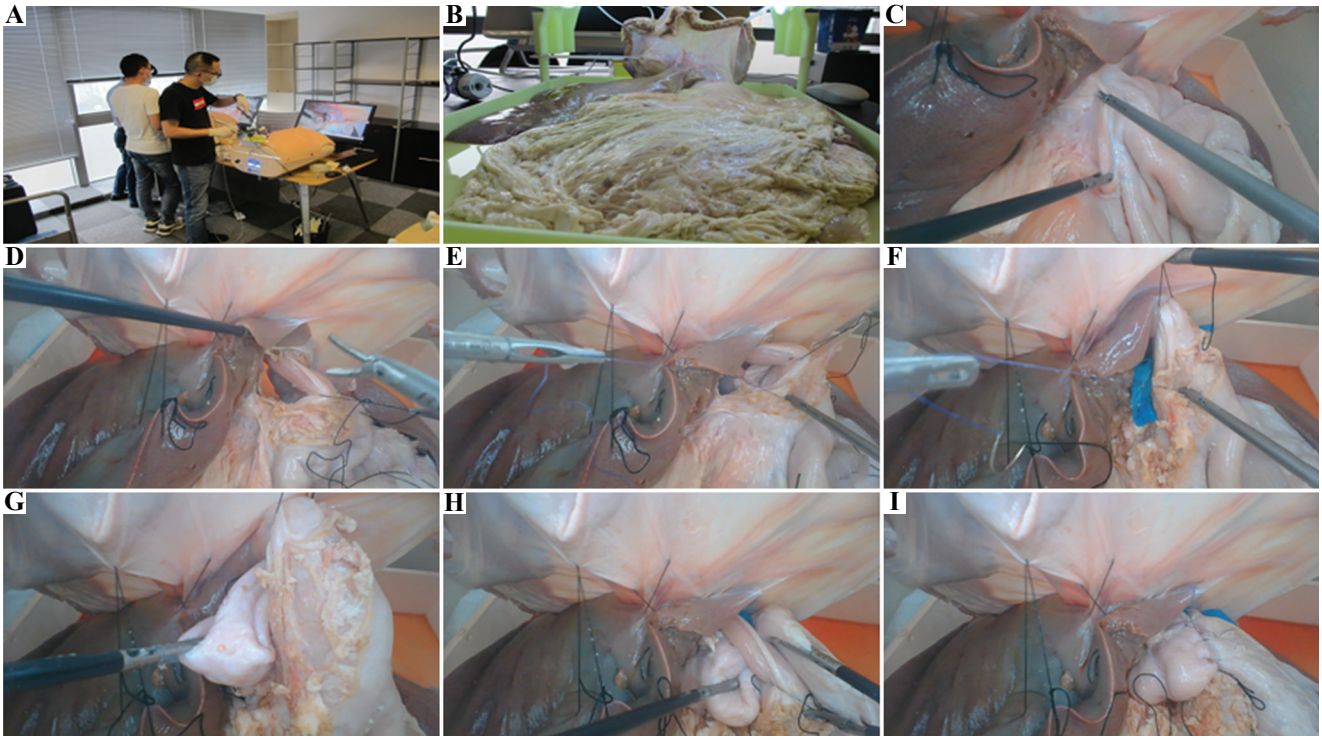


Figure 3. *Ex vivo* Nissen fundoplication procedure. (A) Participants were practicing on laparoscopic surgery platform. (B) *Ex vivo* swine organ. (C) Dissociation of lesser omental sac. (D) Establishment posterior esophagus channel. (E) Hiatal hernia closure. (F) Fixation mesh on diaphragm. (G) Fundoplication through esophagus. (H) Shoeshine maneuver. (I) Making a wrap using interrupted suture.

Table 2. Likert scale results of experts and experimental group

Parameters	Experts	Experimental group
The model is similar with real tissue or organ.	4.36±0.50	-
The model is easy to use.	4.52±0.50	4.24±0.12
Using model in surgical training is reasonable.	4.80±0.45	-
The model can help improve surgical skills.	4.28±0.08	4.76±0.16
Training using the model can help reduce surgical risk to patient.	4.36±0.23	4.66±0.11
The model can help participants concentrate in learning.	4.32±0.46	4.29±0.18
The model can help boost confidence in future surgery.	4.24±0.19	4.73±0.15
The model can enhance tactile feedback.	4.28±0.19	4.63±0.17
The model is recommended for use in the training of anti-reflux surgery.	4.80±0.45	-

Data are expressed as mean±standard variation.

anatomical complexities of esophagogastric junction, possibilities of disruption, herniation or slippage of wrap due to dynamical mechanical stress, and difficulty in reestablishment of anti-reflux barrier which prevents the wrap from being too tight or too loose[15]. Being unfamiliar with the key procedure during surgery can cause severe iatrogenic complications[26]. According to a study involving 2655 patients, 4.1% of patients developed complications within 30 days, including infection (1.1%), bleeding (0.9%), and iatrogenic esophageal perforation (0.9%). The recurrence rate of GERD was 17.7%[27]. Cadaver model or animal models are still the most commonly used training models for this procedure in China; however, these models are expensive and may raise ethical concerns, and thus, an alternative model for Nissen fundoplication training is now in a great demand in China[14,18].

3D printing is an appropriate alternative technique for fabricating models to be used in surgical training. 3D-printed products can be developed rapidly and become commonly used as biomaterials and applied in the fields of medicine and surgery[1,28]. Different types of surgical simulation models offer an economic-friendly way to multiple medical approaches[3]. However, despite significant progress, the mechanical simulation of soft tissue is not optimized yet, which greatly hampers its application in surgical training (for example, the mostly common techniques applied in surgery, such as suturing and dissecting). In our study, we attempted to generate a soft and flexible surgical training model for Nissen fundoplication procedure which considers

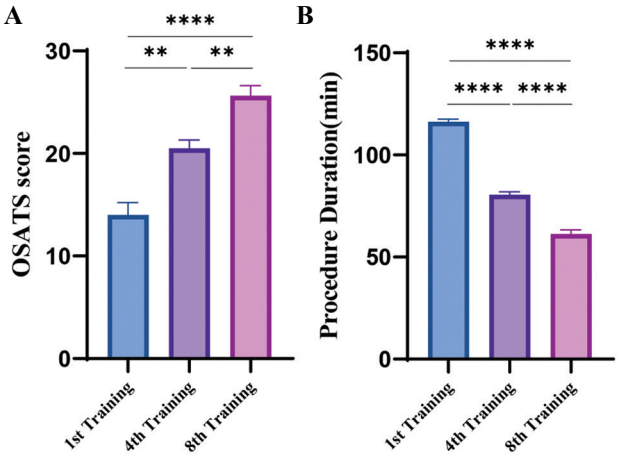


Figure 4. OSATS score and procedure duration of the experimental group in different training sessions. (A) OSATS score and (B) procedure duration (min) at the first training, fourth training, or eighth training. $^{**}P < 0.005$, $^{****}P < 0.0001$.

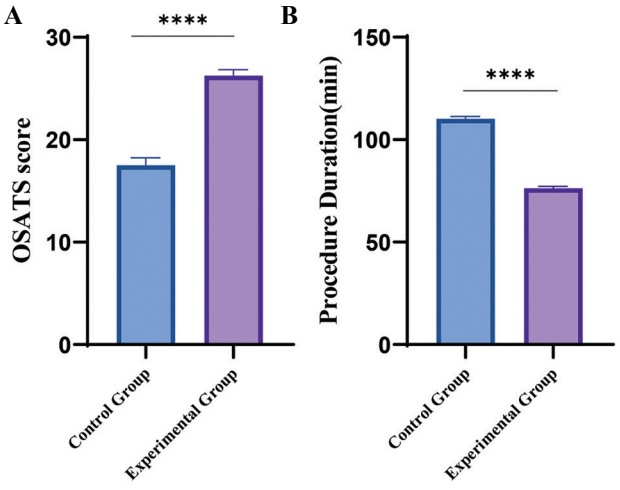


Figure 5. OSATS score and procedure duration of *ex vivo* Nissen fundoplication surgery. (A) OSATS score and (B) procedure duration (min) of the control group and experimental group. $^{****}P < 0.0001$.

Table 3. OSATS score and procedure duration in different training session

	First training	Fourth training	Eighth training
OSATS score	14.0±3.46	20.5±2.27[c]	25.63±2.77[a,b]
Procedure duration (min)	116.25±3.54	80.50±4.21[c]	61.25±5.95[a,b]

[a]P<0.005 compared to first training, [b]P<0.0001 compared to fourth training, [c]P<0.005 compared to first training. Data are expressed as mean±standard variation

not only the anatomical relations and resemblance to the original tissue or organ in appearance but also the mechanical properties. All organs used in our training curriculum are required to be soft and flexible, especially

Table 4. OSATS score and procedure duration of *ex vivo* experiments

	Control group	Experimental group
OSATS score	17.50±2.07	26.25±1.67[a]
Procedure duration (min)	110.13±3.36	76.25±2.49[a]

[a]P<0.0001 compared to the control group.

when fundoplication is performed. Thus, silicon gels were used to manufacture the model considering its excellent resilience and elasticity together with toxicity concern of polyurethane and strict ambient environment requirement for hydrogels[5]. Instead of performing a direct printing of the model, we chose to use an indirect printing method, which printed the mold by FDM in the first place that is relatively low cost and is able to manufacture the model in high throughput, considering that some of the molds could be reused for several times irrespective of the changes in materials and this method can be used in industrial productions in the future. Although several parameters related to the texture of the materials to simulate the organ tissue should be taken into consideration, it should be noted that the complex anatomical and histological aspects are not easy to be replaced in 3D printing, rendering the model imitation ineffective.

3D-printed models are superior to the conventional animal models in simulation and offer more individual-specific anatomic details of organs and tissues before surgery. They can also help enhance our understanding to a disease, enhance familiarity to the surgical procedure, improve surgical skills, reduce procedure duration, or predict underlying risk and complications[20]. A growing line of evidence shows that with a low quantum of investment and running cost, 3D-printed model can help reduce surgery time and blood loss[29]. After the first version of the model was produced, several engineers and surgeons worked together to modify the texture and tactility of the model through adjusting the ratio of silicon gel and silicon oil used. We tested different conditions until all surgeons agreed that the texture and tactile feedback of the model were similar to those of real organs. Participants of the experimental group considered that using 3D model could effectively improve surgical skills, level of confidence, and tactile feedback.

Our model training modules contained four parts which included the principal and difficult procedure of the anti-reflux surgery[25]. Residents (the participants) could understand the whole procedure and connections between each step using the 3D-printed model. The efficacy of 3D-printed model in anti-reflux surgery training was evaluated through comparing OSATS score and procedure duration after training between the experimental group and control group[30]. In the control group, only two out of eight participants were able to complete whole procedure by themselves, and six out of eight participants needed

extra help in using ultrasonic scalpel as well as establishing posterior esophagus tunnel and suture under laparoscope. However, all participants in the experimental group were able to finish the *ex vivo* organ procedure by themselves, and they scored higher in OSATS and completed the procedure in shorter duration. Interestingly, we found that the duration of the procedure on *ex vivo* organs was longer than that on 3D-printed model. We speculate that a large amount of adipose tissue accumulation within lessor omental bursa **(Figure 3C)**, which varies among patients, increased the difficulty of dividing lessor omental bursa by harmonic scalpel while the participants of the experimental group were performing the procedure on *ex vivo* organ. According to the results, the training efficacy using 3D-printed model was promising and the model we generated in this study attained a good face validity that all experts agreed that this model was vividly constructed with anatomic structures seen in a LNF surgery; therefore, this model is recommended for application in anti-reflux surgery in the future. 3D-printed models can be reusable for 20–30 times. Hence, the application of 3D-printed models incurs lower costs compared to the application of animal models.

However, our model does not take into consideration some important or unique anatomical details which might be encountered in surgery, such as greater omentum, endothoracic fascia, endoabdominal fascia, infracardiac bursa, mesoesophagus, and vagus nerve. Another limitation is that the objective assessment of the face and content validity of our model is lacking. We recommend that more participants with different levels of clinical practice experiences should be included in similar studies to validate the model. In addition, we will follow up with the participants of this study to learn more about their LNF performances in clinical practice.

6. Conclusion

Through this study, we manufactured a new 3D-printed model that mimics the anatomical details of patient and manifests similar mechanical properties. We also showed that the 3D-printed model for Nissen fundoplication surgery training could help accelerate the learning curves of surgical residents.

Funding

This work was supported by the fund of Subproject of the Key R&D Program of the Ministry of Science and Technology (2018YFB1107104) and Xinjiang Uygur Autonomous Region Regional Cooperative Innovation Program (2019E0287).

Conflict of interest

The authors declare no known conflicts of interest.

Authors' contributions

Z.W. and M.Y. reviewed related articles and designed the study, Y.Z drafted the article and did the statistics, J.X. recruited the surgeons and organized the training, J.Z, J.M, H.C., H.L., X.X., J.P. and X.H. participated in the designing of the model and modified it into the final edition.

References

1. Liaw CY, Guvendiren M, 2017, Current and Emerging Applications of 3D Printing in Medicine. *Biofabrication*, 9:024102. https://doi.org/10.1088/1758-5090/aa7279
2. Pugliese L, Marconi S, Negrello E, *et al*., 2018, The Clinical Use of 3D Printing in Surgery. *Updates Surg*, 70:381–88. https://doi.org/10.1007/s13304-018-0586-5
3. Ganguli A, Pagan-Diaz G J, Grant L, *et al.*, 2018, 3D Printing for Preoperative Planning and Surgical Training: A Review. *Biomed Microdevices*, 20:65. https://doi.org/10.1007/s10544-018-0301-9
4. Yap YL, Sing SL, Yeong WY, 2020, A Review of 3D Printing Processes and Materials for Soft Robotics. *Rapid Prototyp J*, 26:1345–61. https://doi.org/10.1108/Rpj-11-2019-0302
5. Wallin TJ, Pikul J, Shepherd RF, 2018, 3D Printing of Soft Robotic Systems. *Nat Rev Mater*, 3:84–100. https://doi.org/10.1038/s41578-018-0002-2
6. Stratton S, Manoukian OS, Patel R, *et al.*, 2018, Polymeric 3D Printed Structures for Soft-Tissue Engineering. *J Appl Polym Sci*, 135:45569. https://doi.org/10.1002/app.45569
7. Jin Z, Li Y, Yu K, *et al.*, 2021, 3D Printing of Physical Organ Models: Recent Developments and Challenges. *Adv Sci* (*Weinh*), 8:e2101394. https://doi.org/10.1002/advs.202101394
8. Li X, Liu B, Pei B, *et al.*, 2020, Inkjet Bioprinting of Biomaterials. *Chem Rev*, 120:10793–833. https://doi.org/10.1021/acs.chemrev.0c00008
9. Jiang T, Munguia-Lopez JG, Flores-Torres S, *et al.*, 2019, Extrusion Bioprinting of Soft Materials: An Emerging Technique for Biological Model Fabrication. *Appl Phys Rev*, 6:011310. https://doi.org/10.1063/1.5059393
10. Ng WL, Lee JM, Zhou MM, *et al.*, 2020, Vat Polymerization-based Bioprinting-Process, Materials, Applications and Regulatory Challenges. *Biofabrication*, 12(2):022001. https://doi.org/10.1088/1758-5090/ab6034
11. Li WL, Mille LS, Robledo JA, *et al.*, 2020, Recent Advances in Formulating and Processing Biomaterial Inks for Vat Polymerization-Based 3D Printing. *Adv Healthc Mater*,

9(15):2000156.
https://doi.org/10.1002/adhm.202000156

12. Pietrabissa A, Marconi S, Negrello E, *et al.*, 2020, An Overview on 3D Printing for Abdominal Surgery. *Surg Endosc Other Intervent Tech*, 34(1): 1-13.
https://doi.org/10.1007/s00464-019-07155-5
13. Kwon J, Choi J, Lee S, *et al.*, 2020, Modelling and Manufacturing of 3D-printed, Patient-specific, and anthropomorphic gastric phantoms: A pilot study. *Sci Rep*, 10:18976.
https://doi.org/10.1038/s41598-020-74110-z
14. Ratinam R, Quayle M, Crock J, *et al.*, 2019, Challenges in Creating Dissectible Anatomical 3D Prints for Surgical Teaching. *J Anat*, 234:419–37.
https://doi.org/10.1111/joa.12934
15. Yadlapati R, Hungness ES, Pandolfino JE, 2018, Complications of Antireflux Surgery. *Am J Gastroenterol*, 113:1137–47.
https://doi.org/10.1038/s41395-018-0115-7
16. Wu JM, Chen D, 2020, The Evolution and Expectation of Surgical Options for Gastroesophageal Reflux Disease. *Zhonghua Wai Ke Za Zhi*, 58:677–82.
https://doi.org/10.3760/cma.j.cn112139-20200229-00162
17. Xiao YL, Zhou LY, Hou XH, *et al.*, 2021, Chinese Expert Consensus on Gastroesophageal Reflux Disease in 2020. *J Dig Dis*, 22:376–89.
https://doi.org/10.1111/1751-2980.13028
18. La Torre M, Caruso C, 2013, The Animal Model in Advanced Laparoscopy Resident Training. *Surg Laparosc Endosc Percutan Tech*, 23:271–5.
https://doi.org/10.1097/SLE.0b013e31828b895b
19. Daly SC, Wilson NA, Rinewalt DE, *et al.*, 2014, A Subjective Assessment of Medical Student Perceptions on Animal Models in Medical Education. *J Surg Educ*, 71:61–4.
https://doi.org/v10.1016/j.jsurg.2013.06.017
20. Tanaka H, Yoshino H, Kobayashi E, *et al.*, 2004, Molecular Investigation of Hepatitis E Virus Infection in Domestic and Miniature Pigs Used for Medical Experiments. *Xenotransplantation*, 11:503–10.
https://doi.org/10.1111/j.1399-3089.2004.00170.x
21. Copaescu C, Dragomirescu C, 2009, The Pig Model for the Laparoscopic Antireflux Surgery Training. *Chirurgia* (*Bucur*), 104:309–15.
22. He J, Fang Y, Chen X, 2015, Surgical Models of Gastroesophageal Reflux with Mice. *J Vis Exp*, 102:e53012.
https://doi.org/10.3791/53012
23. Filho EV, Goldenberg A, Costa HO, 2005, Experimental Model of Gastroesophageal Reflux in Rats. *Acta Cir Bras*, 20:437–44.
https://doi.org/10.1590/s0102-86502005000600008
24. Wei F, Xu M, Lai X, *et al.*, 2019, Three-dimensional Printed dry Lab Training Models to Simulate Robotic-assisted Pancreaticojejunostomy. *ANZ J Surg*, 89:1631–5.
https://doi.org/10.1111/ans.15544
25. Horgan S, Pohl D, Bogetti D, *et al.*, 1999, Failed Antireflux Surgery what have we Learned from Reoperations? *Arch Surg*, 134:809–15.
https://doi.org/10.1001/archsurg.134.8.809
26. Lundell L, 2004, Complications after Anti-reflux Surgery. *Best Pract Res Clin Gastroenterol*, 18:935–45.
https://doi.org/10.1016/j.bpg.2004.08.004
27. Maret-Ouda J, Wahlin K, El-Serag HB, *et al.*, 2017, Association Between Laparoscopic Antireflux Surgery and Recurrence of Gastroesophageal Reflux. *JAMA*, 318:939–46.
https://doi.org/10.1001/jama.2017.10981
28. Lin HH, Lonic D, Lo LJ, 2018, 3D Printing in Orthognathic Surgery a literature review. *J Formos Med Assoc*, 117:547–58.
https://doi.org/10.1016/j.jfma.2018.01.008
29. Weidert S, Andress S, Suero E, *et al.*, 2019, 3D Printing in Orthopedic and Trauma Surgery Education and Training: Possibilities and Fields of Application. *Unfallchirurg*, 122:444–51.
https://doi.org/10.1007/s00113-019-0650-8
30. Hatala R, Cook DA, Brydges R, *et al.*, 2015, Constructing a Validity Argument for the Objective Structured Assessment of Technical Skills (OSATS): A Systematic Review of Validity Evidence. *Adv Health Sci Educ Theory Pract*, 20:1149–75.
https://doi.org/10.1007/s10459-015-9593-1

Publisher's note

Whioce Publishing remains neutral with regard to jurisdictional claims in published maps and institutional affiliations.

RESEARCH ARTICLE

CNT-Type Dependent Cellular Adhesion on 3D-Printed Nanocomposite for Tissue Engineering

Adam A. Mieloch[1]*, Julia A. Semba[1,2], Jakub D. Rybka[1]*

[1]Center for Advanced Technology, Adam Mickiewicz University, Poznan, Poland
[2]Faculty of Biology, Adam Mickiewicz University, Poznan, Poland

Abstract: At present, one of the main limitations of three-dimensional (3D) bioprinting in tissue engineering stems from a scarcity of biomaterials tailored for specific applications. Widely used hydrogels offer an optimal printability and a suitable environment for cell growth; however, they lack the mechanical strength required for non-soft tissues, for example, cartilage, tendons, and meniscus. This work investigated the physicochemical, mechanical, and biological characteristics of a 3D-printed polycaprolactone (PCL) reinforced with multiwalled carbon nanotubes (MWCNT) and "bamboo-like" carbon nanotubes (BCNT) with the following w/w % concentrations: 0.005%, 0.01%, 0.02%, and 0.2%. The materials were analyzed with subsequent techniques: Scanning electron microscopy, nanoindentation, parallel plate rheometry, and differential scanning calorimetry. Biological evaluations were performed with normal human articular chondrocytes by confocal microscopy and proliferation assay. The study revealed that the carbon nanotubes (CNT) addition improved the rheological properties of the material by increasing the setting temperature. Moderate enhancement was observed in terms of mechanical properties. The most significant difference was noted in cell adhesion and proliferation. Pure PCL did not facilitate cell growth and mainly apoptotic cells were observed on its surface. The addition of 0.01% MWCNT resulted in enhanced adhesion and proliferation; however, the morphology of the cells remained spherical, signifying a suboptimal surface for proliferation. Interestingly, PCL reinforced with 0.02% BCNT displayed excellent facilitation of cellular adhesion and proliferation, which is uncharacteristic of pure PCL. In summary, this study investigated the potential of CNT-reinforced PCL for 3D bioprinting and tissue engineering, highlighting key physicochemical, mechanical, and biological aspects of this biomaterial.

Keywords: 3D bioprinting; Polycaprolactone; Carbon nanotubes; Tissue engineering nanocomposite

*Correspondence to: Jakub D. Rybka, Center for Advanced Technology, Adam Mickiewicz University, Poznan, Poland; jrybka@amu.edu.pl; Adam A. Mieloch, Center for Advanced Technology, Adam Mickiewicz University, Poznan, Poland; amieloch@amu.edu.pl

Received: December 7, 2021; **Accepted:** January 15, 2022; **Published Online:** March 29, 2022

Citation: Mieloch AA, Semba JA, Rybka JD, 2022, CNT-Type Dependent Cellular Adhesion on 3D-Printed Nanocomposite for Tissue Engineering. *Int J Bioprint,* 8(2):548. http://doi.org/10.18063/ijb.v8i2.548

1. Introduction

Polycaprolactone (PCL) is a semicrystalline biodegradable polyester with a melting temperature of ~60°C. It is FDA-approved for use in surgical implants and drug delivery devices and is widely studied for applications in tissue engineering and regenerative medicine[1]. Due to its low melting temperature and proven biocompatibility, it is the most commonly used thermoplastic polymer for three-dimensional (3D) bioprinting[2-5]. However, its mechanical and bioadhesive properties are suboptimal for non-soft tissue engineering and can be improved on by implementing additives. Carbon nanotubes (CNT) are an excellent additive candidate, supplementing both inadequacies of the PCL. Structurally, CNT can be viewed as sheets of graphene rolled into cylinders. There are several morphologically distinct forms of CNT, resulting in varying physicochemical properties. Nonetheless, CNT are one of the strongest materials in nature with Young's modulus on the order of 270 – 950 GPa and tensile strength of 11 – 63 GPa[6]. In terms of biocompatibility, they have been extensively studied for tailored biomaterial engineering of tissues such as cardiac tissue, neural tissue, bone, and cartilage[7-10]. In addition, a significant body of work regarding CNT-reinforced nanocomposites and their characteristics can be found in

© 2022 Author(s). This is an Open Access article distributed under the terms of the Creative Commons Attribution License, permitting distribution and reproduction in any medium, provided the original work is properly cited.

the literature[11-13]. For the purpose of this study, two types of CNT were selected: "bamboo-like" CNT (BNCT) and multiwalled CNT (MWCNT). "Bamboo-like" CNT (BCNT) resemble the cup-in-cup structure characteristic of the bamboo stem, with a high presence of surface defects. This type of CNT is comparatively inexpensive as its imperfect morphology does not require stringent synthesis conditions. MWCNT are composed of multiple single-walled CNT with diminishing diameters, arranged concentrically. Due to the diminished quantity of structural defects in comparison to BCNT, MWNCT can be used for tissue engineering applications requiring electrical conductivity[14]. In recent years, a lot of research has been devoted to electrospun PCL/CNT nanocomposites for tissue engineering purposes, indicating a growing interest in biopolymers with CNT additives[15-19]. In regard to PCL/CNT composites, a staggering amount of variables, such as CNT aspect ratios, purity, defects, functionalizations, entanglement within a polymer matrix, and interfacial interactions reduce any predictive attempts of resulting properties to an educated guess. In addition, the potential cytotoxicity of a nanocomposite material depends on the biodegradation rate and subsequent gradual release of the nanofiller into the tissue environment. Therefore, despite a plethora of relevant research, a specific application-driven design of CNT-reinforced polymers still requires extensive laboratory work. This work aimed to evaluate mechanical and biological properties of PCL reinforced with BCNT and MWCNT from a 3D bioprinting and tissue engineering point of view.

2. Materials and methods

2.1. Materials

CNT were purchased from NanoLab Inc. (USA, MA). MWCNT have a purity >85%, diameter 10 – 30 nm, and length 5 – 20 μm. BCNT have a purity >85%, diameter 10 – 30 nm, and length 5 – 20 μm. PCL used in this work was in powder (~50 000 MW, Polysciences Europe GmbH). LIVE/DEAD Viability/Cytotoxicity Kit for mammalian cells (Invitrogen) was also used in this study.

2.2. Cell culture

Human knee articular chondrocytes (NHAC-kn, Cat No: CC-2550, LONZA) were cultured in DMEM/F12 with L-glutamine (Corning) supplemented with 10% fetal bovine serum (FBS), 50 μg/mL 2-phospho-L-ascorbic acid, 50 U/ml penicillin, and 50 μg/ml streptomycin at standard culture conditions. The medium was changed every 3 days. Cells were subcultured at 80 – 90% confluence with the TrypLE Express Enzyme (Gibco). Chondrocytes up to the ninth passage and with cell viability above 95% were used for cell experiments.

2.3. Material preparation

The PCL and CNT powders were mixed in 15 ml Falcon tubes by shaking until a visually homogeneous powder was obtained. Subsequently, the powder was placed on a glass Petri dish and heated on a magnetic stirrer until melting occurred. The melt was cooled down and folded several times to improve the homogeneity of the material. Finally, the melt was cut into pellet-like pieces, which were suitable for the thermoplastic printhead.

2.4. 3D printing

3D printing was performed with the Cellink BioX printer. In the process, the thermoplastic printhead was utilized. The 3D model of the grid was prepared by manual writing of a.gcode file. The printing was performed with the following parameters: printhead nozzle diameter, 0.4 mm; printhead temperature, 180°C; printing speed, 4 mm/s; and extrusion pressure, 510 kPa.

2.5. Nanoindentation

The nanoindentation study was performed on a G200 (Agilent) nanoindenter equipped with a DCM head. Each sample was subjected to 12 indentations of 2000 nm in-depth, with a Berkovich-type probe, at room temperature. Analyses were performed at 500 – 1800 nm depth. Due to the uneven topography of the surface, extreme results were excluded from further analysis.

2.6. Parallel plate rheometry

The rheology study was performed with the Discovery Hybrid HR20 Rheometer (TA instruments). A 20 mm aluminum parallel plate was used for the measurements. A temperature sweep analysis was performed in two ranges: 120 – 40°C and 50 – 80°C. For both ranges, the temp. step was set to 2°C, 1% strain, and angular frequency at 10 rad/s. The soak time was set to 30 s. A flow sweep analysis was performed at three temperatures: 180°C, 120°C, and 60°C. The range of shear rate was set from 1×10^{-3} 1/s to 500.0 1/s, at logarithmic step. Data were analyzed using TA Instruments TRIOS Software version 5.1.1.46572.

2.7. Differential scanning calorimetry (DSC)

DSC analysis was performed on a DSC 8500 apparatus (Perkin Elmer) in the temperature range of −90 – 180°C, with nitrogen flow (20 ml/min). The temperature change rate was set at 10°C/min. The thermal history of the raw material was erased before measurement. 3D-printed grids were not subjected to thermal history erasure.

2.8. LIVE/DEAD viability/cytotoxicity kit for mammalian cells

3D-printed grids were cut and sterilized by ultraviolet (UV) light (30 min on each side). This experiment was carried out on 24-well Ultra-Low Attachment plates (Corning) in three biological replications. The chondrocytes were seeded on the grids at a density of 2×10^4 cells per well. The culture medium was changed every three days. The assay was carried out after 2 weeks of culture under standard conditions. The final concentrations of calcein-AM and EthD-1 were 2 and 4 μM, respectively. The labeled cells were visualized under confocal microscopy (Olympus XI83).

2.9. Cell Titer-Glo 2.0 cell viability assay

To investigate the potential toxicity of the materials, 3D-printed PCL grids were cut and sterilized with UV light (30 min on each side). This experiment was carried out on 24-well plates in three biological replications. Chondrocytes were seeded at a density of 2×10^4 cells per well. Positive control was cells seeded without the grid. After 3 and 6 days, the CellTiter-Glo 2.0 cell viability assay was carried out according to the manufacturer's manual with slight modifications. Briefly, 500 μl of fresh medium was added to each well, equilibrated to room temperature, followed by the addition of the CellTiter reagent. The plates were mixed for 2 min and incubated for 10 min at room temperature. Then, 200 μl of the solution was transferred to 96-well opaque-walled plates in at least two technical repeats. The luminescence was recorded using the Infinite 200 PRO plate reader (TECAN).

2.10. Statistical analysis

Statistical analysis was performed using GraphPad Prism ver. 8.0.1.

3. Results

3.1. Scanning electron microscopy (SEM) imaging

SEM imaging of the printed constructs revealed that the addition of CNT, regardless of their type and concentration, resulted in a much smoother surface in comparison to the pure PCL (**Figure S1**). The initial assumption was that the decrease in surface roughness will result in diminished cell attachment.

3.2. Parallel plate rheometry

Rheological properties are crucial from the standpoint of 3D printing and polymer manufacturing. It also provides valuable insight into the supramolecular interactions present within a material. The materials were subjected to the temperature sweep in the 120 – 40°C range, followed by a 50 – 80°C range sweep. Subsequently, flow sweep analysis was performed at three temperatures: 180°C, 120°C, and 60°C. Exemplary results of a pure PCL are presented in **Figure 1**.

The rest can be found in Supplementary File (**Figures S2-S4**). From the temperature sweep analysis, a point of modulus cross-over was obtained. The modulus cross-over signifies a temperature at which a change of the dominant modulus occurs. If the storage modulus (G') dominates, a material presents more elastic (solid-like) behavior. Conversely, if the loss modulus (G'') dominates, the material presents a more viscous (liquid-like) behavior. From the flow sweep analysis, zero-rate viscosity was calculated. The results are presented in **Table 1.**

The addition of CNT resulted in elevated temperature of modulus cross-over during cooling, regardless of CNT type. The highest increase was observed for 0.2% addition of BCNT and 0.2% MWCNT: 6.3°C and 5.2°C increase, respectively, in comparison to pure PCL. The temperature of modulus cross-over during heating was not pronouncedly affected by CNT addition. These observations indicate that CNT influence the solidification of PCL, but not melting. This led us to the suspicion that CNT may affect the crystallization of PCL either by acting as nucleation centers or by facilitating heat transfer through the polymer. Such phenomena have been described previously[20-22]. Regarding zero-rate viscosity, 0.01% addition of BCNT and MWCNT increased the polymer's viscosity. Interestingly, at the highest concentrations, a decrease in zero-rate viscosity was observed instead. Congruous data were obtained for all three temperatures. This result could be attributed to a gradual shift in dominant interactions between the CNT and PCL chains. At 0.01%, PCL/CNT interactions may predominate over PCL/PCL and CNT/CNT. With increasing CNT concentrations, the balance shifts toward CNT/CNT interactions, resulting in a decrease in zero-rate viscosity. The best fit flow analysis of viscosity vs. strain curve confirmed the pseudoplastic behavior of all tested materials. In most cases, the Carreau-Yasuda model was attributed to the experimental data[23,24]. Regardless of CNT addition, all samples showed similarity in viscosity vs. strain curve (**Figure S4**). At 60°C, the Newtonian plateau persisted until the shear rate of c.a. 6 1/s, where the transition region occurred. Due to limitations of the apparatus, further measurements beyond this point were unattainable. At 120°C, a prolonged Newtonian plateau was observed, followed by a well-pronounced transition region starting at c.a. 25 1/s, and a precipitous drop in viscosity, signifying the power-law region. At 180°C, the Newtonian plateau extended to the shear viscosity of c.a. 100 1/s. The transition region and the power-law were, in general, more flattened in comparison to 120°C.

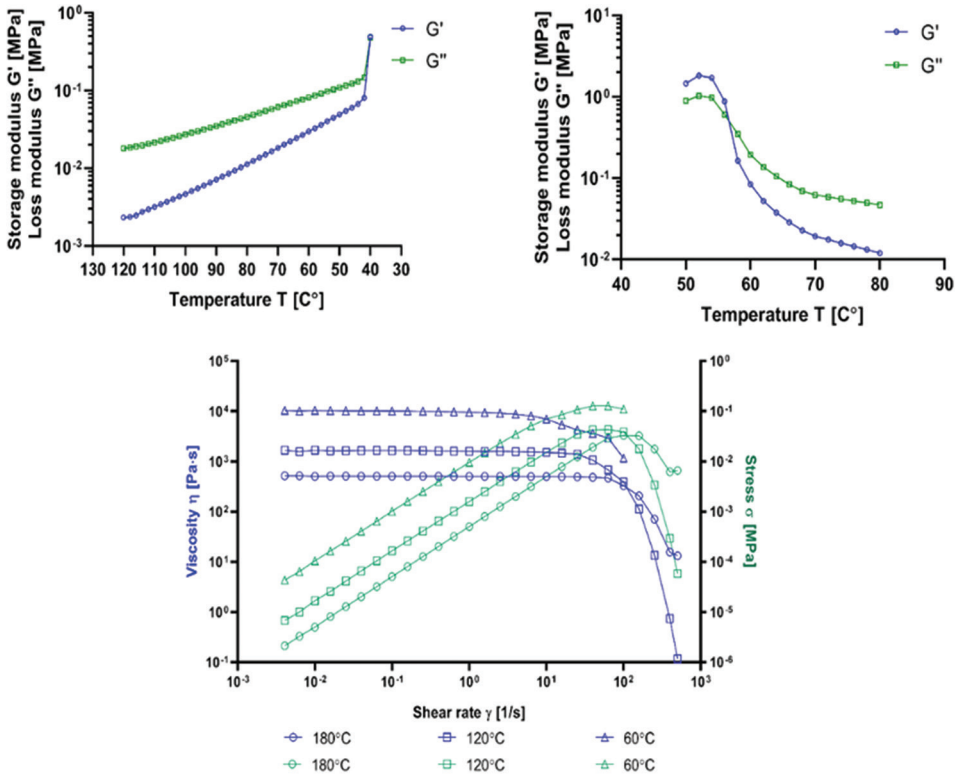


Figure 1. Example results of the temperature sweep and the flow sweep analysis (pure PCL).

Table 1. The modulus cross-over and zero-rate viscosity of the PCL at various CNTs concentrations.

	CNT content (w/w)	Modulus cross-over (°C)		Zero-rate viscosity (Pa·s)		
		120-40°C	50-80°C	180°C	120°C	60°C
PCL	0%	40.0	56.7	502.2	1579.6	10162.1
BCNT	0.005%	44.0	56.8	542.3	1662.8	10762.9
	0.01%	44.0	57.1	605.8	1892.9	10694.7
	0.02%	44.4	56.9	573.7	1775.7	9027.3
	0.2%	46.3	57.4	485.6	1536.2	7090.8
MWCNT	0.005%	42.8	57.0	555.4	1655.7	9729.2
	0.01%	42.6	56.9	579.7	1825.2	10252.4
	0.02%	44.0	57.1	569.8	1718.9	9377.6
	0.2%	45.2	57.2	452.6	1394.2	8445.1

In blue – minimum values; in red – maximum values. Zero-rate viscosity was calculated using best fit flow (viscosity vs. flow).

Obtained data indicates that the CNT addition does not affect the dynamics of shear-thinning behavior, displaying comparable viscosity versus strain curves across all samples at given temperatures. From this perspective, 120°C seems to be the most optimal for 3D printing of PCL, as it allows to fully utilize its shear-thinning behavior.

3.3. DSC

First, a DSC analysis was performed to assess the crystallinity of the raw material and the 3D 3D-printed grids. From the standpoint of a material investigation, it was vital to differentiate which factors affect crystallinity, namely, CNT addition or the 3D printing process. Therefore, the analysis of 3D printed grids was run without erasing the thermal history of the material, retaining its crystalline structure. The degree of crystallinity was calculated based on the heat of melting as:

$$\chi(\%) = \frac{\Delta H_m}{\Delta H_{m^0}} \cdot 100\%$$

where:

ΔH_m – the heat of melting (J/g)

$\Delta H_m{}^0$ – the heat of melting (J/g) for 100% crystalline polymer

The melting heat for 100% crystalline PCL is 139.5 J/g, which was adopted from the literature[25]. The results are summarized in **Table 2**.

The analysis revealed that the CNT addition does not affect substantially the overall crystallinity of the PCL. Interestingly, the process of 3D printing itself was much more influential, providing an 8.7% mean increase of crystallinity. Second, DSC analysis was utilized to investigate the crystallization dynamics of PCL + CNT blends. The rheological behavior of the samples suggests that the addition of CNT accelerates the solidification of the melts, which is associated with the crystallization of the material. The results confirmed the observations from the rheological analysis. The addition of CNT increases the temperature of crystallization onset (Tc) and the Tc (**Figure 2**). BCNT addition resulted in a mean increase of 4.0°C in the Tc onset and 6.9°C in the Tc. MWCNT addition provided a 2.9°C mean increase in the Tc onset and a 5.1°C mean increase in the Tc (**Table 3**). Despite not increasing overall crystallinity, CNT addition did enhance the crystallization rate of the PCL, calculated as Tc onset - Tc.

Table 2. The degree of crystallinity of the PCL at various CNTs concentrations.

	CNT content (w/w)	Degree of crystallinity (%)	
		Raw material	Grids
PCL	0%	50.75	59.00
BCNT	0.005%	51.38	59.94
	0.01%	50.68	60.20
	0.02%	50.14	60.26
	0.2%	50.91	61.92
MWCNT	0.005%	51.52	57.64
	0.01%	51.31	58.89
	0.02%	51.11	59.81
	0.2%	49.77	58.24

In blue – minimum values; in red – maximum values.

Table 3. The Tc and Tc onset the PCL at various CNTs concentrations.

	CNTs content (w/w)	Tc onset (°C)	Tc (°C)	Tc onset - Tc (°C)
PCL	0%	32.89	25.3	7.6
BCNT	0.005%	36.22	32.29	3.9
	0.01%	35.97	31.27	4.7
	0.02%	37.25	32.69	4.6
	0.2%	38.13	32.38	5.8
MWCNT	0.005%	33.66	27.93	5.7
	0.01%	35.43	29.65	5.8
	0.02%	36.54	31.91	4.6
	0.2%	37.62	32.01	5.6

In blue – minimum values; in red – maximum values.

3.4. Nanoindentation

Mean elastic modulus and mean hardness were measured via the nanoindentation method (**Figure 3**). Measurement was performed only on raw materials, as the curvature of 3D printed grids hinders reliable measurement. Therefore, we were unable to assess the effects of increased crystallinity on the mechanical properties of PCL reinforced with CNTs. The sole addition of CNTs did improve the mechanical properties of the material, however, in a nonlinear fashion. The highest increase in mean elastic modulus and hardness was observed for PCL with a concentration of 0.02% MWCNT.

3.5. LIVE/DEAD viability/cytotoxicity assay

Normal human knee articular chondrocytes (NHAC-kn) were seeded on the 3D printed grids and cultured for 2 weeks in standard conditions on non-adherent culture plates. After 2 weeks, cells were dyed with the LIVE/DEAD assay (**Figure 4**). The addition of CNTs did significantly affect the biocompatibility of the PCL. Chondrocytes seeded on pure PCL were mostly dead, while even the smallest concentration of 0.005% BCNT enhanced the viability. The enhancement was observed up to 0.02% concentration. At the highest tested concentration, BCNT decreased the viability of the chondrocytes in comparison to lower concentrations. The biocompatibility enhancement effect was less pronounced for PCL/MWCNT. A visible improvement was observed for the concentration of 0.01% MWCNT; however, it was still markedly worse compared to BCNT. Interestingly, BCNT addition facilitated a proper, elongated morphology of the chondrocytes, while this effect was absent in MWCNT-containing samples. In addition, the elongation occurred in parallel to the printhead movement, suggesting extrusion-driven topography alterations, dictating the direction of filopodia elongation. Cells on the PCL/MWCNT grids remained spherical and were rather loosely attached.

3.6. Cell Titer-Glo 2.0 cell viability assay

PCL is a biodegradable polymer; therefore, there is a risk of CNT-mediated cytotoxicity elicited by free-floating CNT, which are released from the polymer. To provide a quantitative analysis of cell viability, the CellTiter-Glo 2.0 Cell Viability assay was performed after three and 6 days of culture. In this experiment, cells were seeded on standard culture plates with inserted grids. After 3 days of culture, a slight increase of viability was observed for 0.01% MWCNT samples (**Figure 5**). On the other hand, 0.2% BCNT samples displayed markedly lower viability. As expected, the highest concentrations of CNT significantly decreased cell viability after 6 days of culture. Compared to control samples, 0.005 – 0.01%

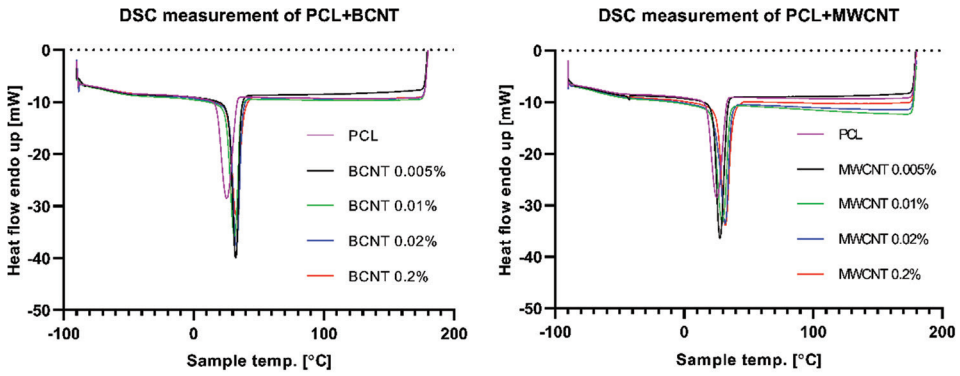


Figure 2. DSC measurement. Cooling step of raw materials (after thermal history erasure).

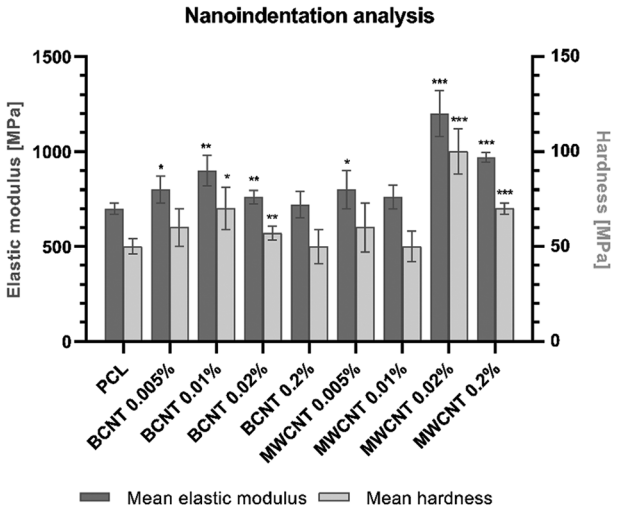


Figure 3. Mean elastic modulus and mean hardness of raw materials measured through nanoindentation. Statistical analysis was performed using one-way ANOVA and *post hoc* Dunnett's T3 multiple comparisons test. The mean of each column was compared to the mean of PCL column. CI = 95%, *P* value: 0.12 (ns), 0.033(*), 0.002 (**), <0.001 (***).

concentration range of both CNT types provided no statistically significant differences in viability. Pure PCL grids did have a minor effect on cell viability. The statistical significance of differences between samples against pure PCL was presented in the Supplementary File (**Table S1**).

4. Discussion

The data presented highlights several physicochemical, mechanical, and biological characteristics of PCL reinforced with CNT for 3D printing and tissue engineering. It is important to underline that the polymer mixing methodology most likely resulted in nonhomogeneous CNT dispersions within the polymer matrix, contributing to various characteristics of the resulting biomaterial. For an extensive overview of CNT/polymer nanocomposites and their interfacial characteristics, see the following article[26]. In our study, the addition of CNT resulted in a smoothened surface of the 3D-printed grids in comparison to pure PCL. As the data suggest, this effect cannot be explained by changes in viscosity or crystallinity of the samples. It could, however, be a result of an increased rate of crystallization, calculated as Tc onset - Tc. Presumably, CNT facilitate heat transfer through the polymer providing uniform temperature distribution, preventing local tensions arising from a nonequal rate of crystallization due to regional temperature differences. Contrary to this hypothesis, low concentrations of a thermoconductive filler are believed to facilitate phonons scattering at the filler/polymer interfaces, resulting in the "interface thermal resistance" phenomenon[27,28]. At this point, the mechanism of surface smoothening remains unsettled. However, taking into consideration the increase of the modulus cross-over temperature, Tc and Tc onset, with concomitant lack of increased overall crystallinity for CNT-reinforced PCL, supports the notion of enhanced thermal transfer.

Rheology analysis provided insight into the properties of the CNT/polymer interface. The initial increase of zero-rate viscosity at low to medium concentrations of CNT suggests that the strength of polymer/polymer interface interactions is lower than the polymer/CNT. However, at high CNT concentrations, zero-rate viscosity decreased below pure PCL, signifying the CNT/CNT interface being weaker in comparison to the polymer/polymer interface. Furthermore, the lack of increased viscosity at lower shear rates indicates that the CNT-filled PCL does not behave like a yield stress fluid (represented by the Herschel-Bulkley model)[29]. Therefore, it can be concluded that the CNT do not form cross-linked networks with the polymer chains. Moreover, it suggests that CNT do not act as nucleation centers for PCL crystallization, as was demonstrated for other polymers[30-32]. This finding is corroborated by the DSC data, revealing that the degree of crystallinity was not significantly affected by the CNT addition. Interestingly,

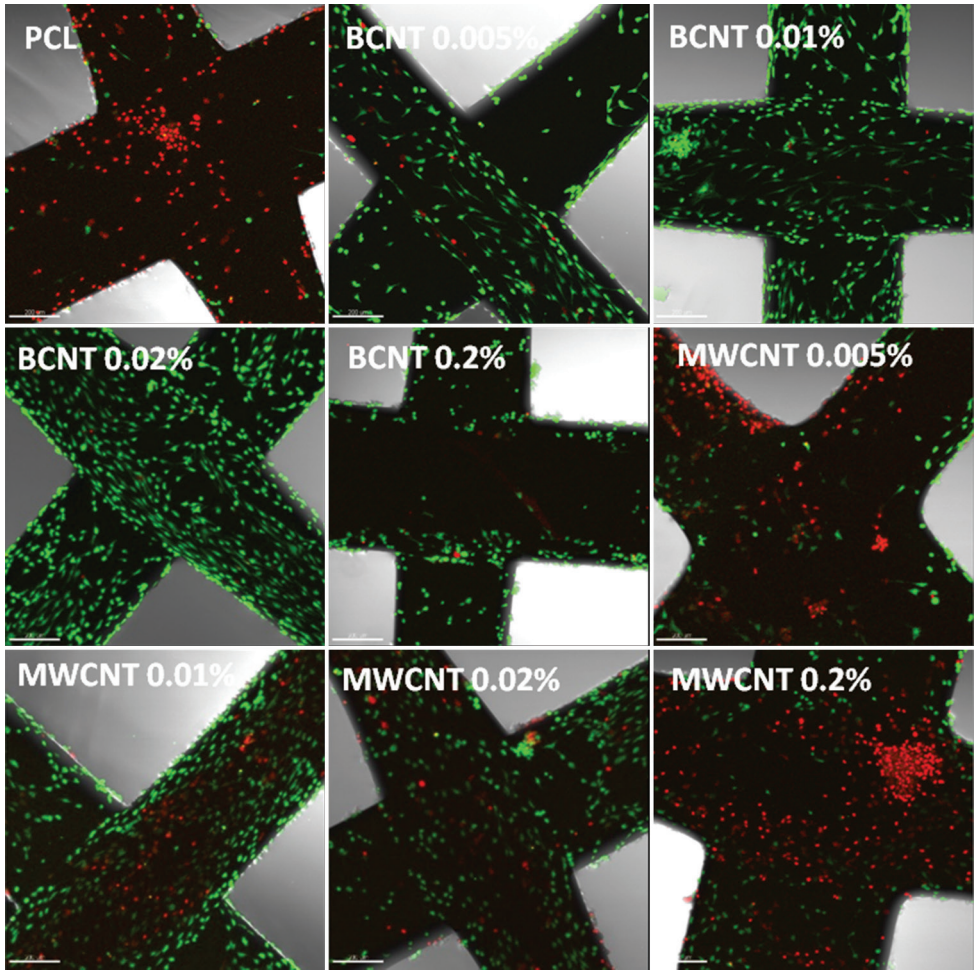


Figure 4. Confocal microscopy of LIVE/DEAD assay. Normal human knee articular chondrocytes (NHAC-kn) cultured for 2 weeks in standard conditions. Scale bars represent 200 μm.

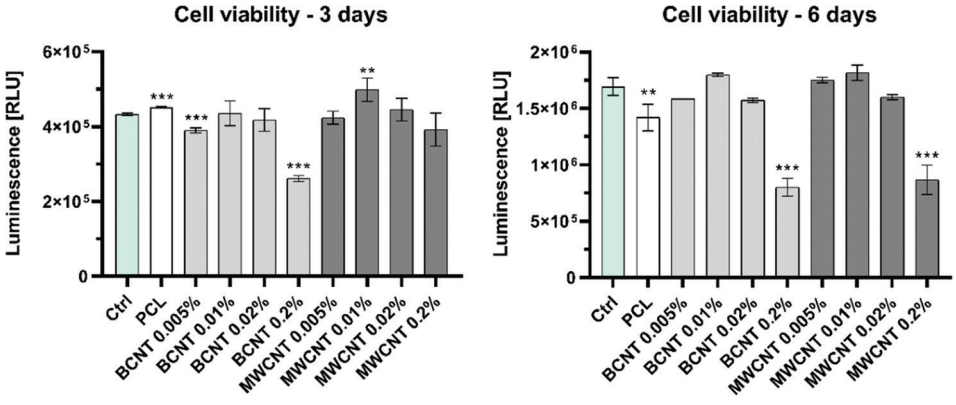


Figure 5. CellTiter-Glo 2.0 cell viability assay. Statistical analysis was performed using one-way ANOVA and *post hoc* Dunnett's T3 multiple comparisons test. The mean of each column was compared to the mean of the control (Ctrl) column. CI = 95%, *P* value: 0.12 (ns), 0.033(*), 0.002 (**), <0.001 (***).

the 3D printing process itself resulted in a significantly increased crystallinity compared to the raw material.

Regarding the mechanical properties assessed by nanoindentation, the addition of CNT did increase the hardness and elastic modulus of the PCL. The effect was the most pronounced for high concentrations of MWCNT. As mentioned previously, the main limitation of the study was the inability to measure 3D-printed grids

due to the cylindrical shape of the sample, which was unsuitable for nanoindentation. This obstacle prevented the comparison between more crystalline 3D-printed grids and raw material. Another factor that has to be taken into consideration is the nonhomogeneous dispersion of the nanotubes, which may form clusters within the material, potentially affecting the measurement.

Biological assessment of the materials revealed an extraordinary improvement in human knee chondrocyte proliferation and viability after the addition of BCNT. At 0.02 w/w% BCNT concentration, cells displayed an optimal morphology and enhanced proliferation. Interestingly, MWCNT addition also enhanced proliferation in comparison to pure PCL; however, cell morphology remained spherical, signifying nonoptimal adhesion to the surface. We suspect two potential mechanisms responsible for the observed effect: (i) Alterations of the surface zeta potential; and (ii) CNT protrusion from the polymer matrix, providing additional anchoring for the cells. In addition, the 3D printing process forces the alignment of CNT along the principal axis of the polymer extrusion, which coincides with the direction of the chondrocytes' filopodia projection, supporting the latter hypothesis. Unfortunately, no direct cause of the enhanced adhesion/proliferation has been found.

As mentioned previously, PCL is a biodegradable polymer, which entails a risk of gradual release of a filler into the environment[33-35]. Our cell viability assay performed after six days of culture showed a significant decrease in cell viability for the highest concentrations of CNT. The rate of biodegradation is a crucial factor, especially for potentially cytotoxic fillers. In theory, however, this could be mitigated by rapid extracellular matrix production, counteracting PCL degradation, and subsequently preventing CNT from being released into the environment.

5. Conclusions

Our study evaluated BCNT and MWCNT as fillers for PCL nanocomposites, dedicated for 3D bioprinting and tissue engineering. The following summary statements could be derived from this study: (i) CNT decreases the roughness of the 3D-printed constructs; (ii) CNT increases the temperature of modulus crossover, Tc, and Tc onset; (iii) the degree of crystallinity depends on the process of 3D printing rather than the CNT addition; (iv) BCNT addition favors cell growth and proliferation of human chondrocytes, facilitating their natural morphology; and (v) at high concentrations, CNT elicit cytotoxic effect and render the material rather unsuitable for tissue engineering purposes. In summary, this work provides novel aspects of PCL-based nanocomposites reinforced with CNT for 3D printing and tissue engineering.

Acknowledgments

The authors would like to thank Itedale Namro Redwan, Volodymyr Kuzmenko and Micheal Giersig for scientific support. Open access was cofounded by Excellence Initiative - Research University program, Call No. 040 "Open Access," grant 040/08/POB2/0001.

Funding

This work was supported by the National Center for Research and Development TECHMATSTRATEG-III/0027/2019-00 the National Science Centre UMO-2016/23/B/NZ7/01288 grants.

Conflict of interest

The authors declare no competing interests.

Author contributions

J.D.R. guided and supervised the project. A. A. M. designed and supervised the experiments. A. A. M., J.A.S., and J.D.R. conducted experiments and contributed intellectually to the scientific design of the project. A.A.M. and J.D.R. mentored the technical part of the project; manuscript preparation A.A.M and J.A.S.; manuscript edition J.D.R.

References

1. Li L, LaBarbera DV, 2017, 3D High-Content Screening of Organoids for Drug Discovery. In: Comprehensive Medicinal Chemistry III. Vol. 2-8. Amsterdam, Netherlands: Elsevier, p388–415.
2. Ramasamy S, Davoodi P, Vijayavenkataraman S, *et al*., 2021, Optimized Construction of a Full Thickness Human Skin Equivalent using 3D Bioprinting and a PCL/Collagen Dermal Scaffold. *Bioprinting*, 21:e00123. https://doi.org/10.1016/j.bprint.2020.e00123
3. Hassanajili S, Karami-Pour A, Oryan A, *et al*., 2019, Preparation and Characterization of PLA/PCL/HA Composite Scaffolds Using Indirect 3D Printing for Bone Tissue Engineering. *Mater Sci Eng C*, 104:109960. https://doi.org/10.1016/j.msec.2019.109960
4. Zhang W, Ullah I, Shi L, *et al*., 2019, Fabrication and Characterization of Porous Polycaprolactone Scaffold Via Extrusion-Based Cryogenic 3D Printing for Tissue Engineering. *Mater Des*, 180:107946. https://doi.org/10.1016/j.matdes.2019.107946
5. Duymaz BT, Erdiler FB, Alan T, *et al*., 2019, 3D Bio-Printing of Levan/Polycaprolactone/Gelatin Blends for Bone Tissue Engineering: Characterization of the Cellular Behavior. *Eur Polym J*, 119:426–37. https://doi.org/10.1016/j.eurpolymj.2019.08.015

6. Yu MF, Lourie O, Dyer MJ, *et al*., 2000, Strength and Breaking Mechanism of Multiwalled Carbon Nanotubes Under Tensile Load. *Science,* 287:637–40. https://doi.org/10.1126/science.287.5453.637
7. Szymański T, Mieloch AA, Richter M, *et al*., 2020, Utilization of Carbon Nanotubes in Manufacturing of 3D Cartilage and Bone Scaffolds. *Materials (Basel)*, 13:4039.
8. Patel DK, Dutta SD, Ganguly K, *et al*., 2021, Enhanced Osteogenic Potential of Unzipped Carbon Nanotubes for Tissue Engineering. *J Biomed Mater Res A*, 109:1869–80. https://doi.org/10.1002/jbm.a.37179
9. Edwards SL, Werkmeister JA, Ramshaw JA, 2009, Carbon Nanotubes in Scaffolds for Tissue Engineering. *Expert Rev Med. Dev*, 6:499–505.
10. Haniu H, Saito N, Matsuda Y, *et al*., 2012, Basic Potential of Carbon Nanotubes in Tissue Engineering Applications. *J Nanomater*, 2012:343747.
11. Soni SK, Thomas B, Kar VR, 2020, A Comprehensive Review on CNTs and CNT-Reinforced Composites: Syntheses, Characteristics and Applications. *Mater Today Commun*, 25:101546.
12. Stocco TD, Antonioli E, Romagnolli ML, *et al*., 2020, Aligned Biomimetic Scaffolds Based on Carbon Nanotubes-Reinforced Polymeric Nanofibers for Knee Meniscus Tissue *Eng Mater Lett*, 264:127351. https://doi.org/10.1016/j.matlet.2020.127351
13. Lebedev SM, 2020, PCL-CNT Nanocomposites Prepared by Melt Compounding and Evaluation of Their Basic Properties. *Polym Compos*, 41:1830–40. https://doi.org/10.1002/pc.25501
14. Abdal-Hay A, Taha M, Mousa HM, *et al*., 2019, Engineering of Electrically-Conductive Poly(E-Caprolactone)/Multi-Walled Carbon Nanotubes Composite Nanofibers for Tissue Engineering Applications. *Ceram Int*, 45:15736–40. https://doi.org/10.1016/j.ceramint.2019.04.206
15. Zadehnajar P, Akbari B, Karbasi S, *et al*., 2019, Preparation and Characterization of Poly ε-Caprolactone-Gelatin/Multi-Walled Carbon Nanotubes Electrospun Scaffolds for Cartilage Tissue Engineering Applications. *Int J Polym Mater Polym Biomater*, 69:326–37. https://doi.org/10.1080/00914037.2018.1563088
16. Jahanmard F, Eslaminejad MB, Amani-Tehran M, *et al*., 2020, Incorporation of F-MWCNTs into Electrospun Nanofibers Regulates Osteogenesis Through Stiffness and Nanotopography. *Mater Sci Eng C,* 106:110163. https://doi.org/10.1016/j.msec.2019.110163
17. Zadehnajar P, Karbasi S, Akbari B, *et al*., 2020, Incorporation of Multi-Walled Carbon Nanotubes Into Electrospun PCL/Gelatin Scaffold: The Influence on the Physical, Chemical and Thermal Properties and Cell Response for Tissue Engineering. *Mater Technol*, 35:39–49. https://doi.org/10.1080/10667857.2019.1651539
18. Wu T, Chen X, Sha J, *et al*., 2019, Fabrication of Shish-Kebab-Structured Carbon Nanotube/Poly(E-Caprolactone) Composite Nanofibers for Potential Tissue Engineering Applications. *Rare Met*, 38:64–72. https://doi.org/10.1007/s12598-017-0965-y
19. Zou Y, Zhang C, Wang P, *et al*., 2020, Electrospun Chitosan/Polycaprolactone Nanofibers Containing Chlorogenic Acid-Loaded Halloysite Nanotube for Active Food Packaging. *Carbohydr Polym*, 247:116711. https://doi.org/10.1016/j.carbpol.2020.116711
20. Yu W, Liu C, Fan S, 2021, Advances of CNT-Based Systems in Thermal Management. *Nano Res*, 14:2471–90.
21. Konstantopoulos G, Maroulas P, Dragatogiannis DA, *et al*., 2021, The Effect of Interfacial Resistance and Crystallinity on Heat Transfer Mechanism in Carbon Nanotube Reinforced Polyethylene. *Mater Des*, 199:109420. https://doi.org/10.1016/J.MATDES.2020.109420
22. Avramenko TG, Khutoryanskaya NV, Naumenko SM, *et al*., 2019, Effect of Carbon Nanofillers on Processes of Structural Relaxation in the Polymer Matrixes. In: Proceedings of the Springer Proceedings in Physics. Vol. 221. Cham: Springer, p293–305.
23. Carreau PJ, 1972, Rheological Equations from Molecular Network Theories. *Trans Soc Rheol,* 16:99–127. https://doi.org/10.1122/1.549276
24. Yasuda K, 1979, Investigation of the Analogies between Viscometric and Linear Viscoelastic Properties of Polystyrene Fluids, Massachusetts Institute of Technology.
25. Pitt CG, Chasalow FI, Hibionada YM, *et al*., 1981, Aliphatic Polyesters. I. The Degradation of Poly(ϵ-Caprolactone) *In Vivo*. *J Appl Polym Sci*, 26:3779–87. https://doi.org/10.1002/app.1981.070261124
26. Chen J, Liu B, Gao X, *et al*., 2018, A Review of the Interfacial Characteristics of Polymer Nanocomposites Containing Carbon Nanotubes. *RSC Adv*, 8:28048–85.
27. Evans W, Prasher R, Fish J, *et al*., 2008, Effect of Aggregation and Interfacial Thermal Resistance on Thermal Conductivity of Nanocomposites and Colloidal Nanofluids. *Int J Heat Mass Transf*, 51:1431–8. https://doi.org/10.1016/j.ijheatmasstransfer.2007.10.017
28. Klonos PA, Peoglos V, Bikiaris DN, *et al*., 2020, Rigid Amorphous Fraction and Thermal Diffusivity in

Nanocomposites Based on Poly(L-Lactic Acid) Filled with Carbon Nanotubes and Graphene Oxide. *J Phys Chem C*, 124:5469–79.
https://doi.org/10.1021/acs.jpcc.9b11843

29. Zhu H, Kim YD, de Kee D, 2005, Non-Newtonian Fluids with a Yield Stress. *J Nonnewton Fluid Mech*, 129:177–81.
https://doi.org/10.1016/j.jnnfm.2005.06.001
30. Wurm A, Herrmann A, Cornelius M, *et al*., 2015, TEMPERATURE dependency of Nucleation Efficiency of Carbon Nanotubes in Pet and PBT. *Macromol Mater Eng*, 300:637–49.
https://doi.org/10.1002/mame.201400405
31. Schawe JE, Pötschke P, Alig I, 2017, Nucleation Efficiency of Fillers in Polymer Crystallization Studied by Fast Scanning Calorimetry: Carbon Nanotubes in Polypropylene. *Polymer (Guildf)*, 116:160–72.
https://doi.org/10.1016/j.polymer.2017.03.072
32. Zhang S, Minus ML, Zhu L, *et al*., 2008, Polymer Transcrystallinity induced by Carbon Nanotubes. *Polymer (Guildf)*, 49:1356–64.
https://doi.org/10.1016/j.polymer.2008.01.018
33. Sun H, Mei L, Song C, *et al*., 2006, The *In Vivo* Degradation, Absorption and Excretion of PCL-Based Implant. *Biomaterials,* 27:1735–40.
https://doi.org/10.1016/j.biomaterials.2005.09.019
34. Goodwin DG, Boyer I, Devahif T, *et al*., 2018, Biodegradation of Carbon Nanotube/Polymer Nanocomposites Using a Monoculture. *Environ Sci Technol*, 52:40–51.
https://doi.org/10.1021/acs.est.7b02062
35. Frank BP, Goodwin DG, Bohutskyi P, *et al*., 2020, Influence of Polymer Type and Carbon Nanotube Properties on Carbon Nanotube/Polymer Nanocomposite Biodegradation. *Sci Total Environ*, 742:140642.
https://doi.org/10.1016/j.scitotenv.2020.140512

Publisher's note

Whioce Publishing remains neutral with regard to jurisdictional claims in published maps and institutional affiliations.

RESEARCH ARTICLE

3D-printed Bioresorbable Stent Coated with Dipyridamole-Loaded Nanofiber for Restenosis Prevention and Endothelialization

Chengjin Wang[1,2,3], Yang Yang[1,2,3], Jingyuan Ji[1,2,3], Yongcong Fang[1,2], Liliang Ouyang[1,2,3], Lei Zhang[1,2,3]*, Wei Sun[1,2,3,4]*

[1]Biomanufacturing Center, Department of Mechanical Engineering, Tsinghua University, Beijing 100084, China
[2]Biomanufacturing and Rapid Forming Technology Key Laboratory of Beijing, Beijing 100084, China
[3]"Biomanufacturing and Engineering Living Systems" Innovation International Talents Base (111 Base), Beijing 100084, China
[4]Department of Mechanical Engineering, Drexel University, Philadelphia, PA 19104, USA

Abstract: Intimal hyperplasia and restenosis caused by excessive proliferation of smooth muscle cells (SMC) are the main factors for the failure of stent implantation. Drug-eluting stents carried with antiproliferative drugs have emerged as a successful approach to alleviate early neointimal development. However, these agents have been reported to have an undesirable effect on re-endothelialization. In this study, we proposed an integrated bioresorbable stent coated with dipyridamole (DP)-loaded poly(D,L-lactide) (PDLLA) nanofibers. Three-dimensional (3D) bioresorbable stents were fabricated by printing on a rotation mandrel using polycaprolactone (PCL), and the stents were further coated with PDLLA/DP nanofibers. The in vitro degradation and drug release evaluation illustrated the potential for long-term release of DP. Stents coated with PDLLA/DP nanofibers showed excellent hemocompatibility. The cell viability, proliferation, and morphology analysis results revealed that stents coated with PDLLA/DP nanofibers could prevent the proliferation of SMC and have no adverse effects on endothelial cells. The in vivo implantation of stents coated with PDLLA/DP nanofibers showed initial patency and continuous endothelialization and alleviated neointimal formation. The attractive in vitro and in vivo performance indicated its potential for restenosis prevention and endothelialization.

Keywords: Bioresorbable stent; Nanofiber; Dipyridamole; Anti-restenosis; Endothelialization

*Correspondence to: Lei Zhang, Biomanufacturing Center, Department of Mechanical Engineering, Tsinghua University, Beijing 100084, China; stoneszhang@mail.tsinghua.edu.cn; Wei Sun, Biomanufacturing Center, Department of Mechanical Engineering, Tsinghua University, Beijing 100084, China; weisun@mail.tsinghua.edu.cn

Received: January 13, 2022; **Accepted:** February 19, 2022; **Published Online:** February 19, 2022

(This article belongs to the *Special Issue: Composite/Multi-component Biomaterial Inks and Bioinks*)

Citation: Wang, C., Yang, Y., Ji, J., *et al*., 2022, 3D-Printed Bioresorbable Stent Coated with Dipyridamole-Loaded Nanofiber for Restenosis Prevention and Endothelialization. *Int J Bioprint,* 8(2):543. http://doi.org/10.18063/ijb.v8i2.543

1. Introduction

In recent years, metallic drug-eluting stents (DES) have become an effective clinical treatment for coronary artery disease, which work by introducing antiproliferative drug-loaded polymer coatings that can inhibit smooth muscle cell (SMC) proliferation and alleviate neointimal development[1,2]. However, residual metallic stents as foreign objects would cage the vessel permanently, leading to late stent thrombosis, impaired coronary vasomotion, and prolonged dual antiplatelet therapy[3,4]. Moreover, antiproliferative agents loaded in the polymer coating of DES, such as sirolimus and paclitaxel, have been reported to have an undesirable effect on re-endothelialization, which may result in long-term endothelial dysfunction[5,6].

To overcome the inherent drawbacks of permanently existing metallic stents, bioresorbable stents have been developed to provide temporary support with tunable degradation rates of stent materials[7]. Bioresorbable

© 2022 Author(s). This is an Open Access article distributed under the terms of the Creative Commons Attribution License, permitting distribution and reproduction in any medium, provided the original work is properly cited.

stents have been demonstrated to facilitate the recovery of vasomotion and reduce the risk of late thrombosis[8,9]. Laser cutting is the conventional manufacturing technique for metal stents and bioresorbable polymeric stents. However, laser processing as a thermal process will cause heat-affected zones and microcracks and reduce a stent's fatigue life, especially for polymeric stents[10]. In our previous study[11], we developed a custom-made four-axis three-dimensional (3D) printing system with a novel mini-screw extruder and a rotation mandrel to realize precise extrusion of polymer filaments. We successfully developed a novel stent with a zero Poisson's ratio structure to address the longitudinal foreshortening problem of conventional metal stents. Moreover, bioresorbable polycaprolactone (PCL) stents with adjustable stent structures and shapes were fabricated by 3D printing.

To alleviate the limitations of antiproliferative agents on endothelialization, drugs that could impede SMC proliferation and have no detrimental effect on endothelial cell viability have been explored as coatings for vascular stents. Dipyridamole (DP), an antithrombotic and antithrombogenic drug used in the clinic, can impede the proliferation of SMCs by hindering the uptake of adenosine[12]. More importantly, DP has been reported to facilitate the proliferation and endothelialization of vascular endothelial cells[13]. Therefore, it is reasonable to develop a biodegradable polymer coating with the combination of versatile DP to address the dilemma of current antiproliferative agent-loaded DES. Various approaches, including dip coating[14], spray coating[15,16], and electrospinning[17], have been explored to achieve polymer/drug coating with stents. Among them, electrospinning has been reported to be a versatile and economical technology to produce nanofibers for biomedical applications[18]. Compared to DES, stents coated with drug-loaded nanofibers might introduce additional benefits. For example, drug-loaded nanofibers mimic the microenvironment of the native extracellular matrix and provide a high surface-to-volume ratio, which is beneficial for cell adhesion and proliferation, more uniform drug release, and higher doses of agents[19]. In addition, it is flexible to select different polymers as the carrier of agents[20]. Punnakitikashem *et al*.[21] reported a biodegradable vascular graft with nanofibrous structures electrospun by mixing polyurethane with DP, achieving sustained release of DP for more than 91 days. Liu *et al*.[22] fabricated bare-metal stents coated with poly(l-lactide-co-caprolactone) nanofibers loaded with both heparin and rosuvastatin using coaxial electrospinning for the treatment of aneurysms. This study demonstrated that nanofibers with shell-core structures could load different drugs with adjustable ratios and spatial distribution, suggesting the flexibility and compatibility of electrospun nanofibers for drug release. The release rate and drug loading capacity could be easily tuned by using various combinations of polymer nanofibers and structural designs.

Despite the progress of metal stents coated with drug-loaded nanofibers, the performance of drug-loaded nanofibers based on bioresorbable stents has not been well investigated. Accordingly, to overcome the challenges associated with DES, such as permanent metallic stents and the limitations of antiproliferative agents on endothelialization, we propose a strategy to combine bioresorbable stents with DP-loaded nanofiber coatings that could prevent in-stent restenosis and promote neo-endothelialization. As depicted in **Figure 1**, we developed an integrated stent with the combination of biodegradable polymers as the backbone material of 3D-printed stents and DP-loaded nanofibers as the coating. 3D bioresorbable stents were fabricated by printing on a rotation mandrel using PCL, and the stents were further coated with DP-loaded poly(D,L-lactide) (PDLLA) nanofibers by electrospinning. The surface morphology and radial strength of the stents were characterized by scanning electron microscopy (SEM) and radial compression tests, respectively. The in vitro drug release, degradation, and Fourier transform infrared (FTIR) characterization of PDLLA/DP nanofibers were investigated and a long-term sustained release of DP drug over 120 days was achieved. In addition, the in vitro hemocompatibility and biocompatibility results suggested that stents coated with DP-loaded nanofibers significantly inhibited the proliferation of SMCs and facilitated the endothelializtion of vascular endothelial cells. Moreover, in vivo evaluation of stent implantation was carried out using a porcine coronary artery model. After implantation for 28 days, the arteries implanted with DP-loaded stents showed reduced in-stent restenosis and initial endothelialization.

2. Materials and methods

2.1. Materials

PCL (average Mn 80000) and DP were purchased from Sigma-Aldrich (St. Louis, USA). 1,1,1,3,3,3-hexafluoro-2-propanol (HFIP, 99+%) was supplied by Aladdin Co., Ltd. (Shanghai, China). PDLLA (Mn = 10 kDa) was purchased from Jinan Daigang Biomaterial Co., Ltd. (Jinan, China).

2.2. 3D-printed PCL stents coated with PDLLA/DP nanofibers

A custom-made four-axis 3D printing system with a novel mini-screw extruder and a rotation mandrel reported in our previous study was applied to fabricate tubular PCL stents[11]. As illustrated in **Figure 1A(i)**, the PCL material was molten and extruded through the nozzle into filaments and further deposited on the rotating mandrel. Stents with an inner diameter of 3 mm and a length of 10 mm were fabricated. Subsequently, as illustrated in **Figure 1A(ii)**, PDLLA nanofibers loaded with DP were randomly deposited onto

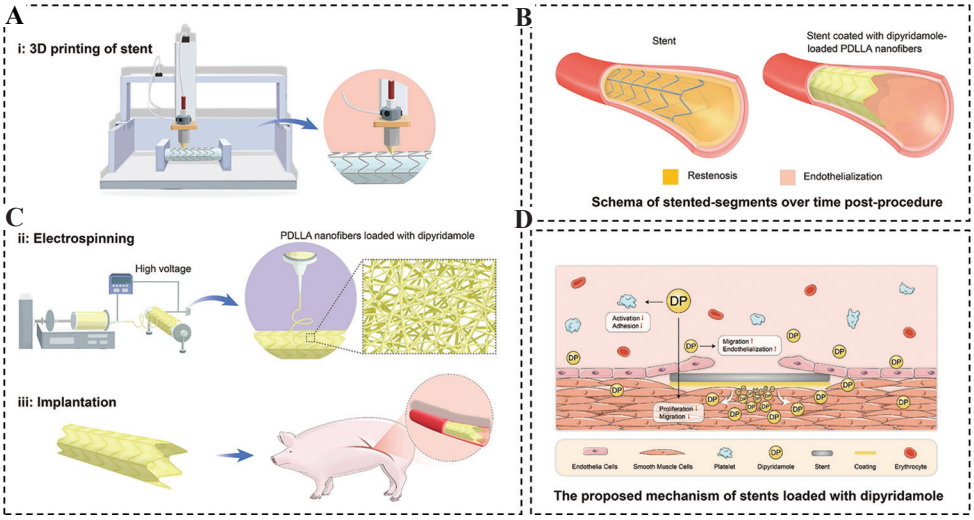


Figure 1. Fabrication of a 3D-printed bioresorbable stent coated with dipyridamole (DP)-loaded nanofiber and its mechanism for restenosis prevention and endothelialization. (A) Fabrication and implantation of stents coated with DP-loaded dipyridamole-loaded poly(D,L-lactide) (PDLLA) nanofibers, (i) 3D-printed stents were prepared using a 3D printing system with a rotation mandrel, (ii) PDLLA nanofibers loaded with DP were randomly deposited onto 3D-printed stents, and (iii) stents were implanted into porcine coronary arteries for in vivo evaluation. (B) The artery segment implanted with the bare stent exhibited more severe in-stent restenosis, while the artery implanted with DP-loaded stents showed initial endothelialization. (C) The proposed mechanism of stents coated with DP-loaded nanofibers for antiplatelet adhesion, the inhibition of smooth muscle cells proliferation, and enhanced endothelial cell growth.

3D-printed PCL stents. A similar electrospinning process was introduced in our previous work[23]. With the rotation of the mandrel, PDLLA/DP nanofibers were uniformly deposited onto 3D-printed stents. Thus, 3D-printed PCL stents coated with PDLLA/DP nanofibers were accomplished. To further demonstrate the function of PDLLA/DP nanofibers, bare stents and stents coated with only PDLLA nanofibers (without DP) were prepared as control groups.

2.3. Morphological and mechanical characterization of stents

The surface morphology of 3D-printed PCL stents, stents coated with only PDLLA nanofibers, and stents coated with PDLLA/DP nanofibers was characterized by SEM (ZEISS GeminiSEM 300, Germany). To further observe the morphology of the inside view of stents, stents were cut in half from the middle before SEM characterization. In this study, the crush resistance test using parallel plates was conducted by a mechanical test instrument (BOSE 3230, Germany). The stents used in this test possessed an inner diameter of 3 mm and a length of 10 mm. The stent was placed between two plates and compressed to a displacement of 1.5 mm (half of the stent inner diameter) at a constant moving speed of 1 mm/min. For each group, three samples were used to record the "Force-Displacement" curve.

2.4. Morphological and FTIR characterization of electrospun nanofibers

The morphology of PDLLA and PDLLA/DP nanofibers was obtained by SEM observation. The chemical bonding of DP, PDLLA nanofibers, and PDLLA/DP nanofibers was examined by FTIR spectroscopy (Bruker V70, Germany). The scanning wavenumber range was from 4000 cm^{-1} to 600 cm^{-1}.

2.5. Electrical conductivity

The electrical conductivity of different polymer solutions was measured using a conductometer (DDS-11A, INESA Scientific Instrument Co., Ltd., Shanghai, China). 5 mL of each polymer solution was measured at 25°C. Three samples (n = 3) from each group were used.

2.6. In vitro drug release and degradation

To investigate the in vitro drug release behavior of DP from PDLLA/DP nanofibers, weighted electrospun nanofiber mats were immersed in 10 ml of phosphate-buffered saline (PBS, pH 7.4). The samples (n = 6) were incubated at 37°C. At predefined time points, 10 mL of PBS solution with the released drug was collected, and 10 mL of fresh PBS was replenished. The absorbance value of PBS with released DP was recorded at 284 nm by an ultraviolet-visible spectrophotometer (HITACHI U3900, Japan). To plot the standard curve of DP concentration versus absorbance in PBS, the absorbance of different solutions with concentrations from 1 μg/mL to 100 μg/mL was measured. To obtain the whole drug release result, the absorbance value was accumulated based on the previous values.

To determine the in vitro degradation behavior, PDLLA/DP nanofibers were immersed in PBS, and

then samples were kept at 37°C. PBS was replaced at weekly intervals. At predefined time points, samples were weighed to record the residual mass after rinsing and vacuum drying. SEM observation of nanofibers after degradation was performed to analyze fiber morphology and integrity. Three replicates of each group were used at each time point.

2.7. In vitro hemocompatibility evaluation

In this study, the in vitro hemocompatibility evaluation was performed following the International Standard (ISO 10993-4) and National Standard of the People's Republic of China (GB/T 16886.4). To evaluate the hemocompatibility of different stents, male Sprague-Dawley rats (8 weeks old) were applied to obtain fresh whole blood.

(1) Platelet adhesion

To collect platelet-rich plasma (PRP), fresh whole blood was centrifuged at 1500 rpm for 10 min. As a previous study reported[24], 3D-printed bare PCL stents, stents coated with PDLLA nanofibers, and stents coated with PDLLA/DP nanofibers were incubated in PRP for 30 min at 37°C and washed 3 times in PBS. The samples were fixed, dehydrated, air-dried in sequence, and then observed by SEM.

(2) Hemolysis analysis

As reported in the previous studies[24,25], the hemolysis rate was measured by detecting hemoglobin release. Briefly, 3D-printed bare PCL stents, stents coated with PDLLA nanofibers, and stents coated with PDLLA/DP nanofibers were soaked in 10 mL of normal saline at 37°C for 60 min. Fresh whole blood (4 mL) was diluted by adding 5 mL of normal saline, and then 0.2 mL of diluted blood was added to these centrifuge tubes. Similarly, 10 mL of deionized water and normal saline solution were set as positive and negative controls, respectively. After incubation at 37°C for 60 min, all samples were centrifuged for 5 min at 3000 rpm to collect the supernatant. The optical density (OD) of the supernatant was recorded at 545 nm by a spectrophotometer (NanoDrop 2000, Thermo, USA).

2.8. In vitro biocompatibility assessment

In this study, rat aortic SMC (RASMCs) were purchased from Shanghai Zhong Qiao Xin Zhou Biotechnology Co., Ltd. (Shanghai, China), and human umbilical vein endothelial cells (HUVECs) were obtained from American Type Culture Collection (ATCC, USA). RASMCs were cultured in Dulbecco's modified eagle medium (DMEM) supplemented with 10% fetal bovine serum and 1% penicillin-streptomycin. HUVECs were cultured in endothelial cell growth medium-2 (EGM-2, Lonza, Switzerland).

(1) Cytotoxicity analysis

To collect the extracts of different groups, bare PCL stents, stents coated with PDLLA nanofibers, and stents coated with PDLLA/DP nanofibers were immersed in a culture medium of RASMCs and HUVECs at 37°C for 24 h, respectively. The cell suspensions of RASMCs and HUVECs were added to 96-well plates at densities of 5.0×10^3/100 μL in each well. The plates were incubated at 37°C with 5% CO_2. After 24 h of incubation, the cell culture medium was replaced by extracts of different groups. After culturing in extracts for 48 h, 10 μL of cell counting kit-8 (CCK-8, Dojindo Laboratories, Japan) per 100 μL of culture medium was slowly instilled into each well, and then the plates were incubated for 3 h at 37°C with 5% CO_2. Subsequently, the absorbance value for each well was recorded at 450 nm using a microplate reader (Multiskan, Thermo, USA). Cell viability was calculated in detail elsewhere[11].

(2) Cell viability and proliferation

RASMCs and HUVECs were seeded in different stents to assess biocompatibility via cell viability and proliferation experiments, respectively. Before seeding the cells, the specimens were sterilized in 75% ethanol for 5 h, washed 3 times in PBS, irradiated with UV for 1 h, and then incubated in culture medium overnight. Stents were transferred into a new 24-well plate, and then RASMCs and HUVECs were seeded onto the inside surface of stents at densities of 5.0×10^4 and 1.0×10^5 cells per well, respectively. All samples were incubated at 37°C with 5% CO_2. The cell culture medium was changed every 2 days. For cell-seeded stents, cell viability was analyzed by a cell live/dead staining assay kit (Dojindo, Japan) on days 1 and 7, according to the manufacturer's instructions. Samples were observed using a laser confocal microscope (Nikon A1, Japan). In addition, CCK-8 was applied to evaluate cell proliferation on days 1, 4, and 7.

(3) Cell morphological analysis

To further observe the cell morphology of the RASMCs and HUVECs on different stents, cytoskeletal staining and SEM analysis were conducted after culture for 7 days. Samples for immunostaining and SEM observation were treated with the same process as reported in our previous work[23].

2.9. In vivo evaluation of stent implantation

Six healthy white minipigs weighing 30 ± 5 kg were used in this study. All experimental procedures were carried out with approval by the Animal Ethics Committee of Nongnong Life Science and Technology Company (Beijing, China). 3D-printed bare PCL stents and stents coated with PDLLA/DP nanofibers (inner diameter:

3 mm, length: 15 mm) were prepared and sterilized using 15 kGy of gamma radiation before implantation. Six white minipigs were divided into two groups (group one and group two). Stents coated with PDLLA/DP nanofibers (n = 3) were implanted into group one, while PCL bare stents (n = 3) were implanted into group two as the control group.

Stents were positioned into the coronary arteries of pigs. Balloons with crimped stents were dilated with 10 atm for 30 s to realize a stent-to-artery diameter ratio of 1.2:1. Coronary angiography was recorded after implantation for days 1 and 28. After stents were implanted for 28 days, pigs were euthanized to harvest the stented artery samples. Then, samples were fixed in 10% formalin for 24 h, dehydrated and embedded in paraffin for cross-section slicing. Hematoxylin and eosin (H&E) and Masson staining were performed for histological analysis.

2.10. Statistical analysis

Experimental data are presented as the mean ± standard deviation (SD). The statistical analysis software GraphPad Prism 8.0 was used for Student's *t*-test.

3. Results

3.1. Fabrication and characterization of PDLLA/DP nanofibers

The diameter of electrospun fibers typically ranges from tens of nanometers to several micrometers[26]. The morphology of electrospun fibers was influenced by the polymer solution composition and processing parameters. We first optimized the electrospinning process with the base polymer PDLLA. The morphology of PDLLA nanofibers was investigated using different concentrations of PDLLA/HFIP solutions (100, 150, 200, and 250 mg/mL) and flow rates (0.5, 1.0, and 2.0 mL/h). As shown in **Figure S1**, in general, PDLLA fibers became more uniform with the increase of PDLLA concentration. The formation of beads was observed and gradually became unapparent at concentrations of 100, 150, and 200 mg/mL, while uniform nanofibers with smooth surfaces were achieved at concentrations of 250 mg/mL (**Figure S1A**). Fong *et al*.[27] reported that a higher viscosity of polymer solutions could facilitate the formation of fibers without beads, which was confirmed by our results. Thus, the PDLLA/HFIP polymer solution concentration was set as 250 mg/mL in the present work. The effect of the flow rate of polymer solution on the nanofiber morphology was further evaluated. As presented in **Figure S1B**, there was no obvious difference in the morphology of PDLLA fibers prepared with flow rates of 0.5, 1.0, and 2.0 mL/h. To achieve a more compact structure, we selected a higher flow rate (2.0 mL/h) in the following studies.

Electrospun fibers loaded with DP have been reported to realize sustained release for up to weeks. Punnakitikashem *et al*.[21] developed a nanofibrous scaffold with a higher DP content (10%), which inhibited SMC proliferation and showed no adverse effect on endothelial cells. A similar concentration of DP in the solution was also used to prepare drug-loaded nanofibers to achieve the antiplatelet effect[28,29]. Here, DP was dissolved in PDLLA/HFIP solution at a concentration of 10% to PDLLA. Thus, the concentration of DP in polymer solution was 25 mg/mL. PDLLA/DP nanofibers with an average diameter of 247.01 ± 44.65 nm showed a relatively uniform morphology and compact diameter distribution, as shown in **Figure 2A(i)**. In contrast, plain PDLLA nanofibers exhibited an average diameter of 685.54 ± 252.23 nm and possessed a bimodal distribution of fiber diameter, as depicted in **Figure S1C**.

Subsequently, FTIR characterization was performed to investigate the chemical structure of DP, PDLLA nanofibers, and PDLLA/DP nanofibers. Since the concentration of DP in the mixture of PDLLA/DP was only 10%, these peaks with low absorbance in the FTIR spectra of DP were not obvious in the spectra of PDLLA/DP. Therefore, we mainly focused on the characteristic peaks in each spectrum. As shown in **Figure 2B**, the most obvious peak in the spectra of DP was detected at 1527 cm^{-1}, which was correlated to C=N bonding and absent in the spectra of PDLLA. Similarly, peaks at approximately 1750 cm^{-1} (C=O), 1185 cm^{-1}, and 1085 cm^{-1} (C-O-C) were detected in the spectra of PDLLA but absent in the spectra of DP. After the loading of DP into PDLLA fibers, all peaks that were obvious in the spectra of DP or PDLLA were retained in the spectra of PDLLA/DP. These results indicated that the PDLLA/DP nanofibers maintained their chemical stability.

The morphologies of PDLLA/DP fibers at different degradation times were investigated. As presented in **Figure 2A(i)**, fibers possessed a uniform and centralized diameter distribution (247.01 ± 44.65 nm) before degradation (0 week). After degradation for 8 weeks, the diameter of the fibers slightly decreased (234.73 ± 80.48 nm), and the diameter distribution of the PDLLA/DP fibers flattened (**Figure 2A(ii)**). When the degradation lasted for 16 weeks, the diameter of the PDLLA/DP fibers showed an obvious decrease to 145.70 ± 66.87 nm compared to that after 8 weeks of degradation (**Figure 2D**). In addition, broken fibers were observed due to accelerated degradation (**Figure 2A(iii)**). Furthermore, the representative release curve of DP from PDLLA/DP nanofibers is presented in **Figure 2C**, which shows sustained and long-term drug release. In the initial 7 days, the release maintained a relatively fast rate, especially in the first 24 h. The release rate gradually stabilized in the following days. Approximately 60% of

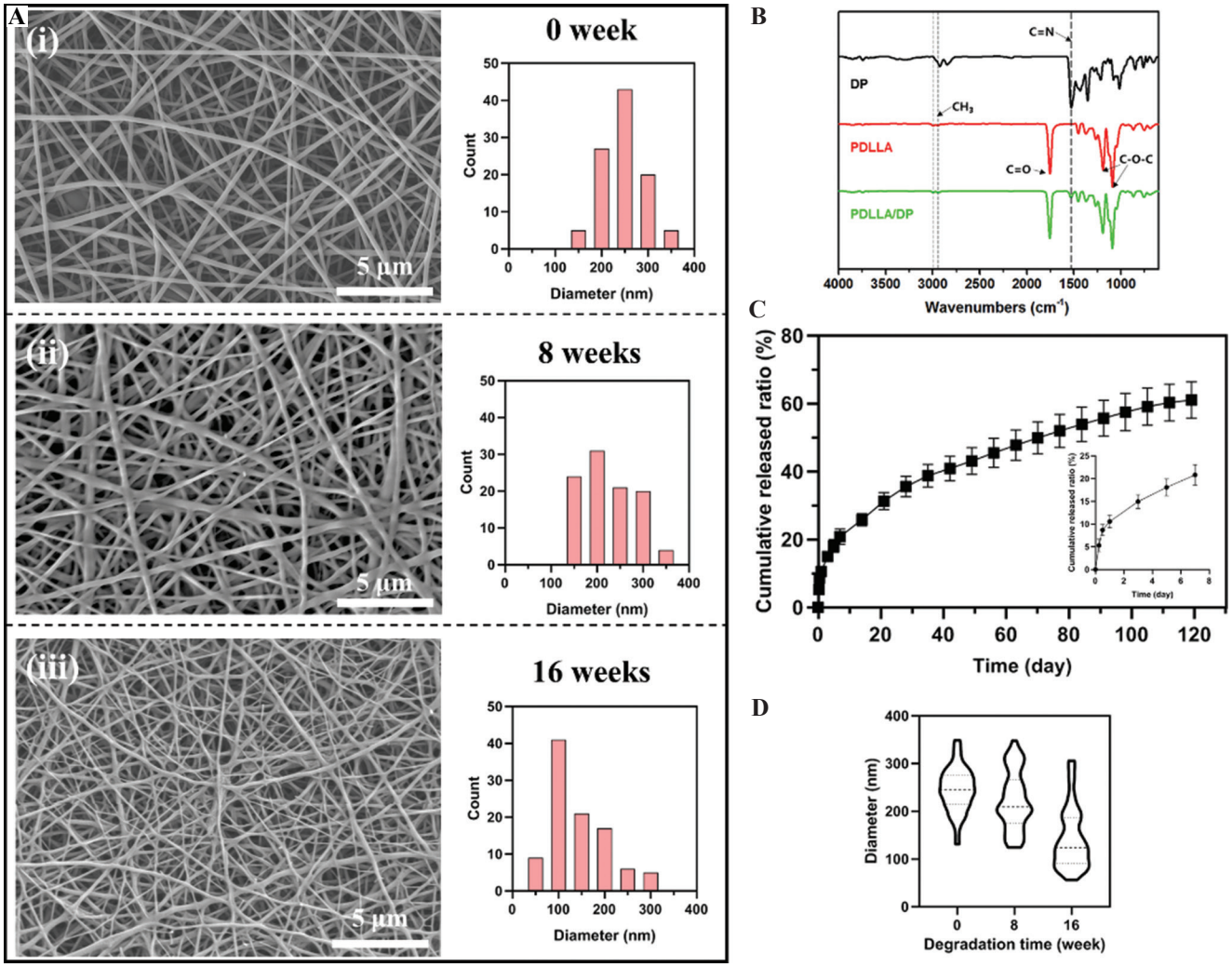


Figure 2. Morphology, drug release, and degradation of dipyridamole-loaded poly(D,L-lactide) (PDLLA)/DP nanofibers. (A) Scanning electron microscopy (SEM) images and distribution of fiber diameter of PDLLA/DP nanofibers before degradation at different degradation times: (i): 0 week, (ii) 8 weeks, and (iii) 16 weeks. (B) Fourier transform infrared spectra of DP, PDLLA nanofibers, and PDLLA/DP nanofibers. (C) In vitro DP release curve showed long-term drug release up to 120 days. (D) The average fiber diameters of PDLLA/DP nanofibers at different degradation times. Six samples (n = 6) from each group were used in the drug release test. The average diameters of PDLLA/DP nanofibers at different degradation times were obtained from 100 measurements using three SEM images for each time point.

DP was released during the 120-day long-term sustained release.

3.2. Fabrication and characterization of 3D-printed PCL stents coated with PDLLA/DP nanofibers

3D printing has emerged as a desirable technology for personalized customization and medical applications. To realize the development of customizable bioresorbable stents, we developed a four-axis 3D printing system with a novel mini-screw extruder and a rotation mandrel and fabricated 3D-printed PCL stents. The 3D model, 3D-printing trajectory strategy, and fabrication process of 3D-printed stents are presented in **Figure 3A** and **3B**. The surface morphologies of the stents with different magnifications and views are shown in **Figure 3C-E** (inside view) and **Figure S3** (outside view). Both the outside and inside surfaces of the stents showed smooth morphology. Furthermore, PDLLA/DP nanofibers prepared by the electrospinning technique were deposited onto 3D-printed PCL stents. For the control group, stents coated with PDLLA nanofibers were fabricated. SEM images of stents coated with PDLLA or PDLLA/DP nanofibers are illustrated in **Figure 3** and **Figure S3**. To better differentiate the three types of stents, the bare 3D-printed bare PCL stent, stent coated with PDLLA nanofibers, and stent coated with PDLLA/DP nanofibers were depicted as the "Stent" group, "Stent + Nano-PDLLA" group, and "Stent + Nano-PDLLA-DP" group,

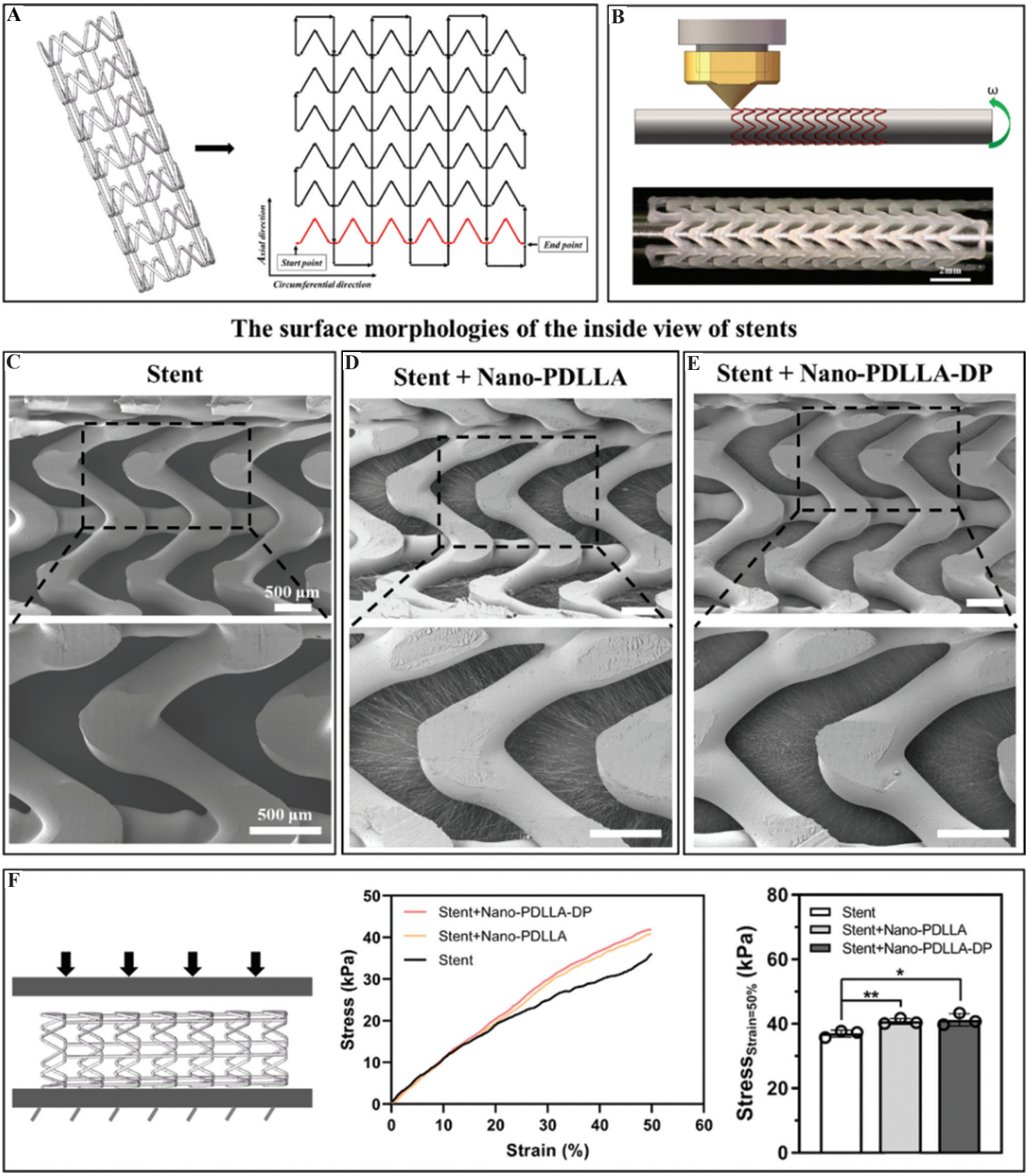


Figure 3. Fabrication and characterization of different stents. (A) 3D-printing trajectory strategy. (B) Schematic of the stent fabrication process. (C-E) The surface morphologies of the inside view of stents, (C) 3D-printed polycaprolactone stents, (D) stents coated with dipyridamole-loaded poly(D,L-lactide) (PDLLA) nanofibers, and (E) stents coated with PDLLA/DP nanofibers. (F) The radial compression test of different stents. Three samples (n = 3) from each group were used in the radial compression test. *$P < 0.05$, **$P < 0.01$.

respectively. In accordance with the results of electrospun fibers in **Figure 2** and **Figure S1**, PDLLA/DP fibers possessed a more compact structure and relatively uniform morphology compared to PDLLA fibers.

The radial crush resistance property is an essential indicator to respond the ability of stents to resist radial deformation. A parallel plate compression test was accomplished to record the load and displacement in the compression process. Stents with a length of 10 mm and a diameter of 3 mm were applied in this test. Stents were compressed until a radical deformation of 1.5 mm, and the load and displacement were continuously recorded in this process. As presented in **Figure 3F**, the stress–strain behavior suggested that the radial strength of stents with added nanofibers was slightly enhanced compared to that of the bare stent group. There was no significant difference between the "Stent + Nano-PDLLA" group and the "Stent + Nano-PDLLA-DP" group. The quantitative analysis of the stress value when the strain was 50% further corroborated the above results.

3.3. In vitro hemocompatibility evaluation

Thrombosis caused by platelet adhesion is a complication of stent implantation[30]. Thus, it is necessary to assess the hemocompatibility of stents. The platelet adhesion test was accomplished in the current study to evaluate the hemocompatibility of vascular implants. The surface morphology of adhered platelets on different stents is presented in **Figure 4A**. The red circles indicate the positions of adhered platelets, and the area of the red circles is proportional to the number of platelets inside. Compared to the bare PCL stents, stents coated with PDLLA nanofibers showed extensively increased platelet adhesion. Remarkably, compared with the "Stent + Nano-PDLLA" group, the number of adherent platelets in the "Stent + Nano-PDLLA-DP" group was significantly reduced due to the addition of DP agents.

Moreover, a hemolysis test can indicate whether samples destroy the structure of erythrocytes. As presented in **Figure 4B**, the hemolysis ratios of the three groups were less than the safe value (5%). In particular, the "Stent + Nano-PDLLA-DP" group could intensively reduce the hemolysis ratio to 1.00 ± 0.42%, compared with the hemolysis ratio of 2.91 ± 0.44% for the bare PCL stents, and 2.76 ± 0.41% for the stents coated with PDLLA nanofibers.

3.4. In vitro biocompatibility assessment

Here, RASMCs and HUVECs were selected to investigate the biocompatibility of stents. In particular, we investigated the effect of DP agents released from stents on cytotoxicity, cell viability and proliferation, and cell morphology.

(1) In vitro *cytotoxicity testing*

Cytotoxicity is an essential biological indicator in the toxicity evaluation of medical devices[31]. According to ISO 10993- 5:2009[32], the extract test method was applied to determine the in vitro cytotoxicity of stents. According to the value of relative cell viability, the cytotoxicity of the medical devices or materials was graded as none (>100%), slight (80 – 99%), mild (50 – 79%), moderate (30 – 49%), and severe (0 – 29%). Samples were considered to have cytotoxic effects, as relative cell viability was <80%. As depicted in **Figure S5**, the cell viability of RASMCs cultured in the extract of the "Stent + Nano-PDLLA-DP" group (48.92 ± 2.05%) showed a significant decrease, compared to the "Stent" group (96.14 ± 6.21%) and "Stent + Nano-PDLLA" group (90.40 ± 3.86%). In contrast, there was no significant difference in the cell viability of HUVECs among the three groups (all >90%), and all specimens showed no obvious cytotoxic function.

(2) Cell proliferation and morphology analysis of RASMCs seeded on stents

To further demonstrate the cell morphology of RASMCs and HUVECs on different stents, cytoskeletal immunofluorescence staining and SEM observation were carried out. Fluorescent phalloidin was used to bind to F-actin, which is a key cytoskeletal component and could help to identify the overall shape and structure of the cell. However, because of the opaque characteristic of the PCL thick fibers of stents, only cells attached between adjacent V-shaped struts could be observed in immunofluorescence staining images. Thus, SEM characterization was accomplished to show the overall distribution of cells.

As shown in **Figure 5A** and **5B**, RASMCs seeded on the "Stent + Nano-PDLLA" group showed a significantly higher cell proliferation rate than those seeded on the bare stent group. Compared to the "Stent + Nano-PDLLA" group, the "Stent + Nano-PDLLA-DP" group showed significantly decreased cell proliferation. In addition, the proliferation of RASMCs on day 7 showed no significant difference between the bare stents and stents with PDLLA/DP nanofibers. As shown in **Figure 5C** and **5D**, the surface of bare PCL stents and stents coated with PDLLA nanofibers was sufficiently covered with RASMCs after culture for 7 days. In the bare PCL stent group (**Figure 5C(i)** and **5D(i)**), RASMCs were only closely deposited on the surface of the PCL struts and exhibited powerful proliferation ability, despite the limited contact area and microenvironment. Remarkably, RASMCs crazily overspread the surface of stents coated with PDLLA nanofibers (**Figure 5C(ii)** and **5D(ii)**). As depicted in **Figure 5C(iii)** and 5D**(iii)**, the proliferation of RASMCs in the "Stent + Nano-PDLLA-DP" group was significantly suppressed compared with that of stents coated with only PDLLA nanofibers. It is worth mentioning that DP is a pyrimidine derivative and has a similar structure to thymine (one of the four constituent bases of nucleic acids), leading to the reaction between DAPI and DP. Thus, the cell nuclei of cells seeded in the "Stent + Nano-PDLLA-DP" group were absent in the

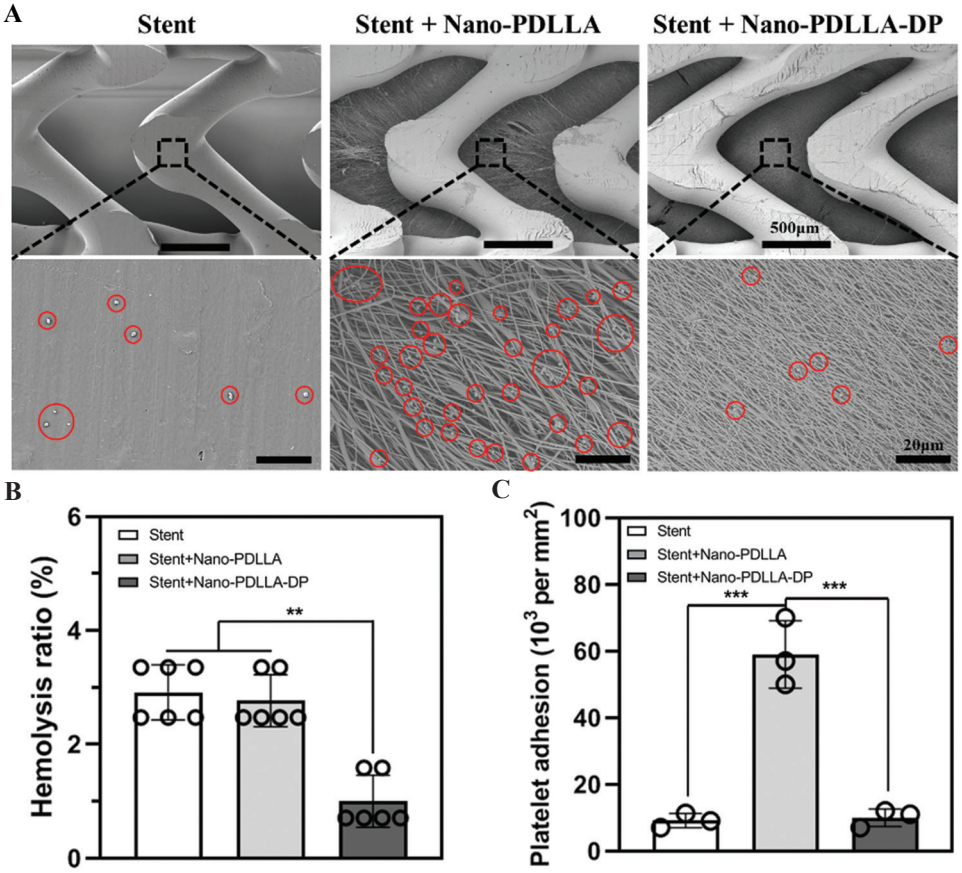


Figure 4. In vitro hemocompatibility evaluation of stents with different structures and compositions. (A) Scanning electron microscopy images of adhered platelets on different stents, and the red circles indicate the positions of adhered platelets. (B) Hemolysis ratios of different stents. (C) The number of adherent platelets on different stents. Six samples (n = 6) from each group were used in the hemolysis evaluation. Three samples (n = 3) of each group were used in the platelet adhesion test. $^{**}P < 0.01$. $^{***}P < 0.001$.

immunofluorescence staining images (**Figure 5C(iii)** and **6C(iii)**), due to the rapid combination of DAPI and DP.

(3) Cell proliferation and morphology analysis of HUVECs seeded on stents

Likewise, cell viability and morphological analyses were performed for HUVEC-seeded stents. As illustrated in **Figure 6**, compared to stents coated with nanofibers, HUVECs seeded on bare PCL stents showed unfavorable cell adhesion and cell proliferation due to the limited attachment area and the bare surface of PCL struts. As shown in **Figure 6D(i)**, sparse HUVECs adhered to the surface of bare PCL fibers, while RASMCs were spread over PCL fibers (**Figure 5D(i)**). HUVECs seeded on the "Stent + Nano-PDLLA" and "Stent + Nano-PDLLA-DP" groups presented enhanced cell adhesion and proliferation (**Figure 6A** and **6B**) and showed well-spread cellular morphologies (**Figure 6C(ii)**, **6C(iii)**, **6D(ii)**, and **6D(iii)**). The cell proliferation of HUVECs in the "Stent + Nano-PDLLA-DP" group was approximate to that of the "Stent + Nano-PDLLA" group, and the surface of the "Stent + Nano-PDLLA-DP" group was also adequately overspread with HUVECs.

3.5. In vivo stent implantation

To further demonstrate that DP-loaded nanofiber-coated stents could alleviate the formation of restenosis, in vivo implantation of stents was carried out. Coronary angiography of the stented artery section was performed to observe the patency of vessels on day 0 and day 28 post-implantation. As shown in **Figure S6**, the angiographic results indicated that arteries implanted with the bare stents showed an obvious reduction in the luminal area compared to arteries implanted with the "Stent + Nano-PDLLA-DP" group. Furthermore, the H&E staining and Masson staining images verified that arteries implanted with bare stents exhibited more severe in-stent restenosis (**Figure 7A-D**). As shown in **Figure 7A** and **7C**, the bare stent group revealed extensive proliferation of SMCs and consequent more serious lumen area loss. Stents

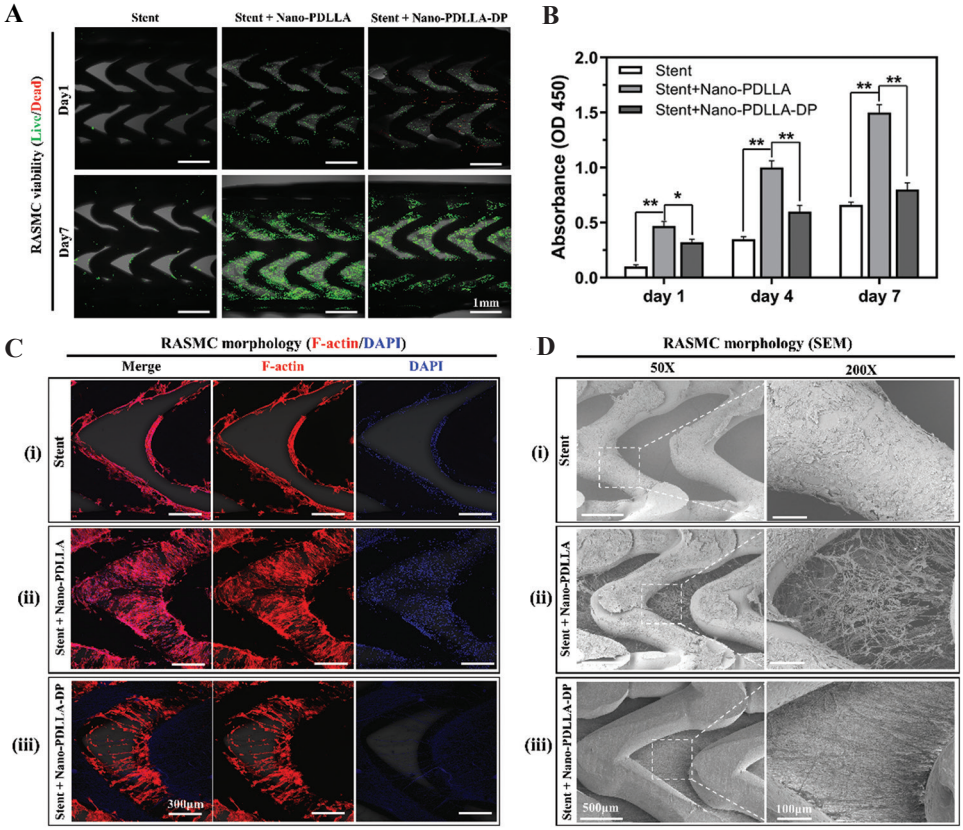


Figure 5. Cell proliferation and morphology analysis of RASMCs seeded on different stents. (A) Live/dead staining images of RASMC-seeded stents after culture for 1 day and 7 days. (B) Cell proliferation of RASMCs after seeding on stents for days 1, 4 and 7. (C) F-actin (phalloidin, red) and DAPI (blue) staining of RASMCs after seeding on (C(i)) bare stents, (C(ii)) stents coated with dipyridamole-loaded poly(D,L-lactide) (PDLLA) nanofibers, and (C(iii)) stents coated with PDLLA/DP nanofibers for 7 days. (D) SEM images of RASMCs after seeding on (D(i)) bare stents, (D(ii)) stents coated with PDLLA nanofibers, and (D(iii)) stents coated with PDLLA/DP nanofibers for 7 days. Three samples (n = 3) from each group were used for cell proliferation evaluation. $*P < 0.05$, $**P < 0.01$.

coated with DP-loaded nanofibers significantly reduced the thickness of intimal hyperplasia compared with bare stents, from 506 ± 153 μm to 288 ± 31 μm (**Figure 7E**). Meanwhile, the average neointimal area of stents with DP-loaded coating was decreased by 54% compared to that of the bare stent group, decreasing from 2.14 ± 0.31 mm^2 to 0.98 ± 0.15 mm^2 (**Figure 7F**). The average neointimal stenosis ratio of stents with DP-loaded coating was remarkably lower (42% vs. 65%) than that of the bare stent group (**Figure 7G**). As shown in **Figure 9**, after implantation for 28 days, CD31 expression around the bare PCL stents was lower than that around the DP-loaded nanofibers coated stents.

4. Discussion

Ideally, following the implantation of stents into the arteries, the sustained release of the drug should induce the inhibition of SMC proliferation and allow initial endothelialization with the rapid degradation of the coating polymer material. Subsequently, as the backbone materials slowly degrade, the stent gradually disappears, causing blood vessels to return to a more natural state and recover normal vasomotion[1,3,33]. DP-loaded nanofibers showed the potential for long-term drug release and could prevent SMC proliferation and have no detrimental effect on endothelial cells[21]. Therefore, it is a promising idea to develop a drug-loaded bioresorbable stent by coating 3D-printed biodegradable stents with DP-loaded nanofibers.

To achieve the desired stent degradation and drug elution, polymers with appropriate degradation rates and biocompatibility are essential to act as backbone materials and polymeric coatings. PCL has been widely applied in biomedical applications because of its excellent biocompatibility, flexible printability, suitable mechanical properties, and appropriate degradation rate (24 – 36 months)[34]. PDLLA has been widely used as a drug delivery carrier because of its excellent biocompatibility and suitable degradation rate (9 – 24 months)[35,36]. Hence, PCL and PDLLA were selected to act as the backbone material of the stent and the coating polymer in the present work.

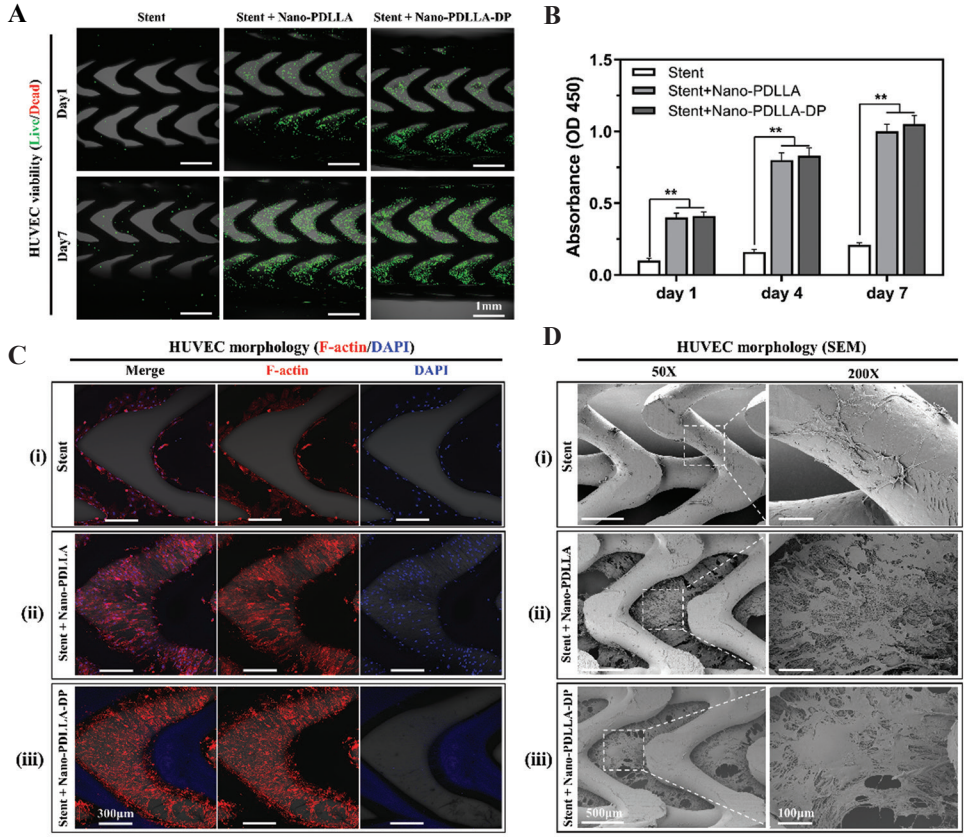


Figure 6. Cell proliferation and morphology analysis of HUVECs seeded on different stents. (A) Live/dead staining images of HUVEC-seeded stents after culture for 1 day and 7 days. (B) Cell proliferation of HUVECs after seeding on stents for days 1, 4 and 7. (C) F-actin (phalloidin, red) and DAPI (blue) staining of HUVECs after seeding on (C(i)) bare stents, (C(ii)) stents coated with dipyridamole-loaded poly(D,L-lactide) (PDLLA) nanofibers, and (C(iii)) stents coated with PDLLA/DP nanofibers for 7 days. (D) SEM images of HUVECs after seeding on (D(i)) bare stents, (D(ii)) stents coated with PDLLA nanofibers, and (D(iii)) stents coated with PDLLA/DP nanofibers for 7 days. Three samples (n = 3) from each group were used for cell proliferation evaluation. *$P < 0.05$, **$P < 0.01$.

As shown in **Figure S1** and **Figure 2**, PDLLA/DP nanofibers showed more uniform morphology and reduced average diameter compared to the plain PDLLA nanofibers, which is a result of the differentiation in the solution's electrical conductivity. The electrical conductivity of plain PDLLA/HFIP was 3.64 ± 0.02 μS/cm, while that of solution dissolved with 25 mg/mL of DP was significantly increased to 68.71 ± 0.39 μS/cm. According to the previous works[37], DP molecules added in the polymer solutions exist in an ionic form that could contribute to the electrostatic charge build-up during electrospinning. As the jet exits the tip of the nozzle, it reinforces the effect of the electric field, resulting in thinner fibers. The in vitro drug release and degradation of DP-loaded nanofibers suggested that 120-day long-term sustained release could be achieved accompanied by the degradation of PDLLA fibers. As shown in **Figure 2**, the changes in the distribution and average value of fiber diameter reflected the advancement of fiber degradation. Simultaneously, the drug was continuously released into PBS solution.

Subsequently, we developed 3D-printed PCL stents coated with DP-loaded PDLLA nanofibers, which showed smooth and integral morphology through SEM observation (**Figure 3** and **Figure S3**). Besides, compared to similar stents in the previous studies, stents fabricated in this work exhibited superior radial strength[38,39]. In detail, when the radial deformation was 50%, the stress of the stents in this study was approximately 40 kPa, while that of the stents in the previous studies was approximately 15 kPa. Platelet adhesion and hemolysis tests were performed to assess the hemocompatibility of stents. As presented in **Figure 4**, stents coated with PDLLA nanofibers showed extensively increased platelet adhesion, which was attributed to the introduction of electrospun fibers and the accompanying increasing contact area between the samples and PRP solution. Conversely, the "Stent + Nano-PDLLA-DP" group showed significantly reduced adherent platelets and hemolysis ratio. Hence, the "Stent + Nano-PDLLA-DP" group could prevent platelet adhesion and counteract the adverse effect of increased contact area due to the benefits of DP.

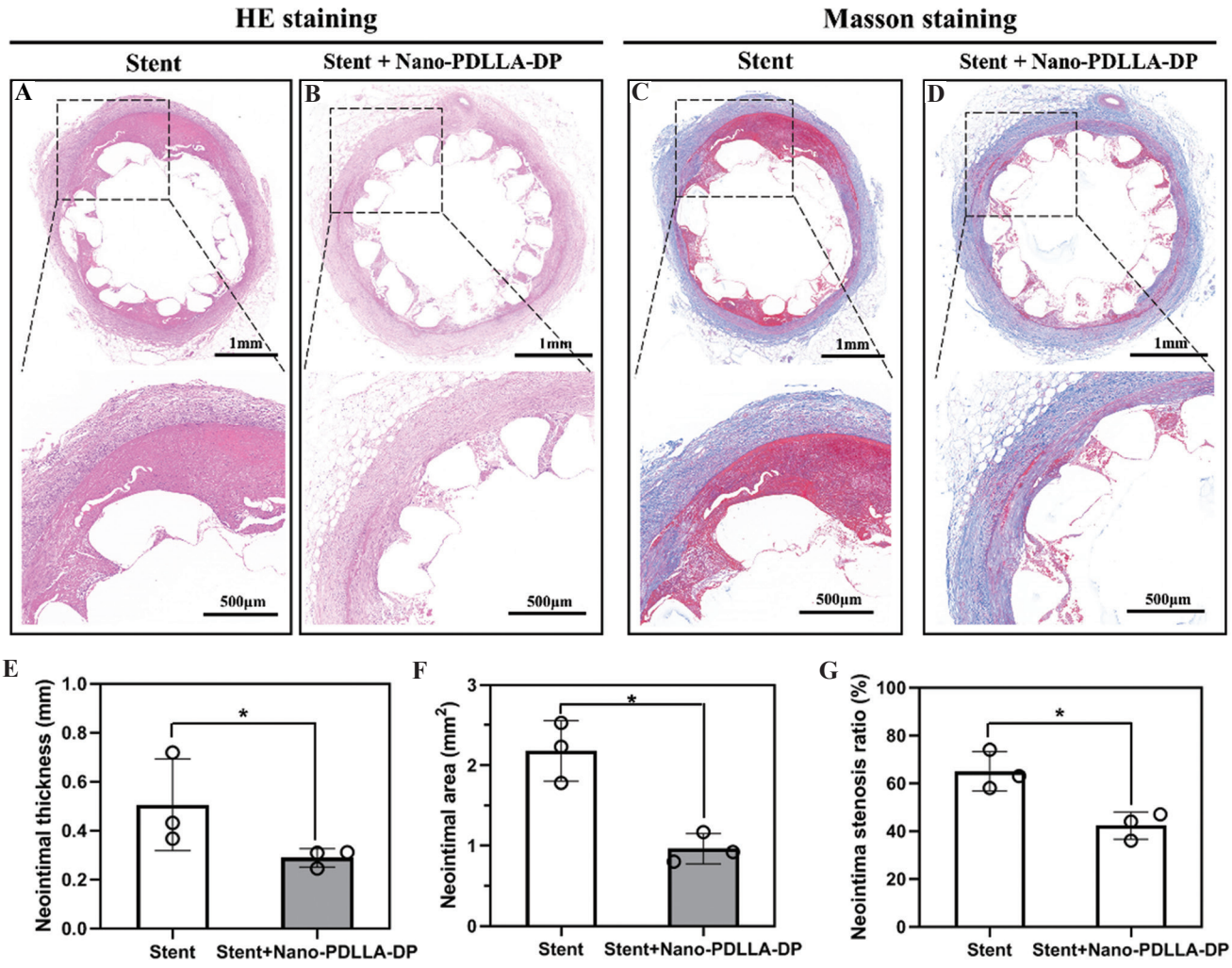


Figure 7. In vivo implantation evaluation of the bare stents and stents coated with dipyridamole-loaded poly(D,L-lactide) (PDLLA)/DP nanofibers. H&E staining images of (A) bare stents and (B) stents coated with PDLLA/DP nanofibers. Masson staining images of (C) bare stents and (D) stents coated with PDLLA/DP nanofibers. Quantitative analysis of (C) neointimal thickness, (D) neointimal area, and (E) neointimal stenosis ratio. Three samples (n = 3) from each group were used to analyze neointimal development *$P < 0.05$.

The native arteries consist of three structural layers: intima, media, and adventitia. The intima includes a monolayer of endothelial cells, and the media is composed of abundant vascular SMCs[40]. Adverse reactions after stent implantation are closely related to cellular biological changes in endothelial cells and SMCs. As presented in **Figure S5**, **Figure 5**, and **Figure 6**, both RASMCs and HUVECs seeded on the "Stent + Nano-PDLLA" group showed a significantly higher cell proliferation rate than cells seeded on the bare stents, benefiting from the introduction of nanofibers and an increased contact area for cell attachment and migration. Different cell behaviors of RASMCs and HUVECs were observed in the "Stent + Nano-PDLLA-DP" group. Compared to the "Stent + Nano-PDLLA" group, the cell proliferation of RASMCs seeded on the "Stent + Nano-PDLLA-DP" group showed an obvious decrease due to the continuous release of DP (**Figure 5C(iii)** and **5D(iii)**). In contrast, HUVECs were adequately overspread on the surface of the "Stent + Nano-PDLLA-DP" group, which indicated that the release of DP showed no adverse effects on the cell proliferation and morphology of endothelial cells (**Figure 6C(iii)** and **6D(iii)**). Therefore, it can be determined that 3D-printed stents coated with DP-loaded nanofibers (the "Stent + Nano-PDLLA-DP" group) could obviously prevent the proliferation of SMCs seeded onto stents and have no detrimental effects on the cell viability of endothelial cells.

The in vivo implantation assessment was conducted to further verify the performance of DP-loaded stents. The detriments of stents without drug delivery have been well demonstrated[1-3,8,9]. We believe that PDLLA nanofiber-coated stents without drugs cannot cope with the above-mentioned intimal hyperplasia. Therefore, in this study,

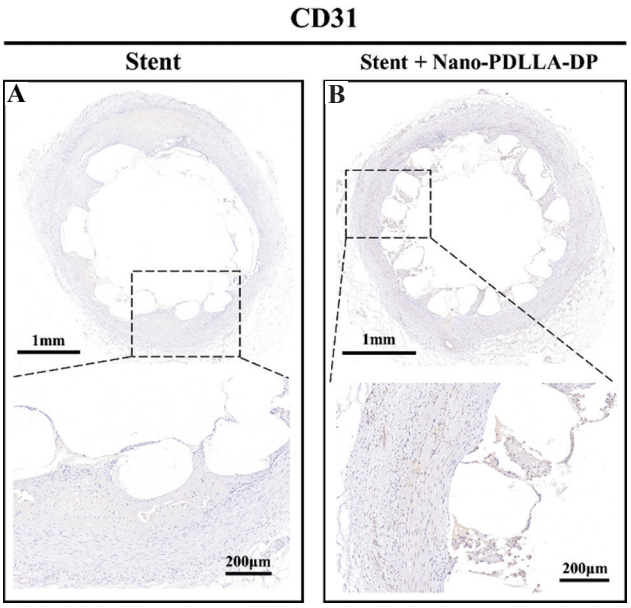


Figure 8. Immunohistochemical analysis of the stented arterial segments for CD31 after implantation for 28 days. (A) Bare stents and (B) stents coated with dipyridamole-loaded poly(D,L-lactide)/DP nanofibers.

with the guidance of the 3Rs principle (replace, reduce, and refine), we only retained the "Stent" group as a control group to reduce the number of experimental animals as much as possible. After implantation for 28 days, arteries implanted with DP-loaded stents were observed with a reduction in intimal hyperplasia, the average neointimal area, and the neointimal stenosis ratio (**Figure 7 and Figure S6**). These results suggest that stents coated with DP-loaded nanofibers could effectively inhibit neointimal development. Endothelialization is a hallmark of vascular healing and is important for the prevention of thrombus formation. As presented in **Figure 8**, the neointimal on bare stents showed deficient CD31 expression, indicating the delayed repair of the endothelium. Moreover, continuous initial endothelialization was observed in the inner surface of stents coated with DP-loaded nanofibers, which was a positive signal for long-term vascular patency.

5. Conclusions

In this study, we developed an integrated stent with the combination of 3D-printed PCL stents and DP-loaded electrospun nanofibers. Stents coated with nanofibers presented precise structures and possessed enhanced radial strength. The in vitro degradation and drug release evaluation showed a long-term sustained release of DP drug from PDLLA nanofibers over 120 days. With the introduction of DP in fibers, the stents also showed excellent in vitro hemocompatibility. The cell viability and morphological analysis results indicated that stents coated with PDLLA/DP nanofibers could inhibit the proliferation of SMC and had no detrimental effects on endothelial cells in vitro. Furthermore, the in vivo implantation of stents coated with PDLLA/DP nanofibers showed initial patency and continuous endothelialization and alleviated neointimal formation compared to bare stents. Collectively, the integrated stents coated with DP-loaded PDLLA nanofibers showed great potential for restenosis prevention and endothelialization. In future research, the decrease in strut thickness and the long-term in vivo implantation of improved stents will be further explored.

Acknowledgments

The authors acknowledge funding support from the Tsinghua University Initiative Scientific Research Program (20197050024) and the 111 Project (B17026).

Conflicts of interest

No conflict of interest was reported by all authors.

Author contributions

C. W., L. Z., and W. S. proposed the integrated stent design and prepared the manuscript. C. W., Y. Y., and J. J. conducted the experiments. Y. F. and L. O. helped to revise the manuscript. All authors have given approval to the final version of the manuscript.

References

1. Wiebe J, Nef HM, Hamm CW, 2014, Current Status of Bioresorbable Scaffolds in the Treatment of Coronary Artery Disease. *J Am Coll Cardiol*, 64:2541–51. https://doi.org/10.1016/j.jacc.2014.09.041
2. Wessely R, 2010, New Drug-eluting Stent Concepts. *Nat Rev Cardiol*, 7:194–203. https://doi.org/10.1038/nrcardio.2010.14
3. Ang H Y, Bulluck H, Wong P, *et al.*, 2017, Bioresorbable Stents: Current and Upcoming Bioresorbable Technologies. *Int J Cardiol*, 228:931–9. https://doi.org/10.1016/j.ijcard.2016.11.258
4. Joner M, Finn AV, Farb A, *et al.*, 2006, Pathology of Drug-Eluting Stents in Humans. Delayed Healing and Late Thrombotic Risk. *J Am Coll Cardiol*, 48:193–202. https://doi.org/10.1016/j.jacc.2006.03.042
5. Capranzano P, Dangas G, 2012, Late Stent Thrombosis: The Last Remaining Obstacle in Coronary Interventional Therapy. *Curr Cardiol Rep*, 14:408–17. https://doi.org/10.1007/s11886-012-0283-9
6. Inoue T, Croce K, Morooka T, *et al.*, 2011, Vascular

Inflammation and Repair: Implications for Re-endothelialization, Restenosis, and Stent Thrombosis. *JACC: Cardiovasc Interv*, 4:1057–66. https://doi.org/10.1016/j.jcin.2011.05.025

7. Jinnouchi H, Torii S, Sakamoto A, *et al.*, 2019, Fully bioresorbable vascular scaffolds: lessons learned and future directions. *Nat Rev Cardiol*, 16:286–304. https://doi.org/10.1038/s41569-018-0124-7
8. Onuma Y, Ormiston J, Serruys PW, 2011, Bioresorbable Scaffold Technologies. *Circ J*, 75:509–20. https://doi.org/10.1253/circj.CJ-10-1135
9. Iqbal J, Onuma Y, Ormiston J, *et al.*, 2014, Bioresorbable Scaffolds: Rationale, Current Status, Challenges, and Future. *Eur Heart J*, 35:765–76. https://doi.org/10.1093/eurheartj/eht542
10. Toong DW, Ng JC, Huang Y, *et al.*, 2020, Bioresorbable Metals in Cardiovascular Stents: Material Insights and Progress. *Materialia*, 12:100727. https://doi.org/10.1016/j.mtla.2020.100727
11. Wang C, Zhang L, Fang Y, *et al.*, 2021, Design, Characterization, and 3D Printing of Cardiovascular Stents with Zero Poisson's Ratio in Longitudinal Deformation. *Engineering*, 7:979–90. https://doi.org/10.1016/j.eng.2020.02.013
12. Zhuplatov SB, Masaki T, Blumenthal DK, *et al.*, 2006, Mechanism of Dipyridamole's Action in Inhibition of Venous and Arterial Smooth Muscle Cell Proliferation. *Basic Clin Pharmacol Toxicol*, 99:431–9. https://doi.org/10.1111/j.1742-7843.2006.pto_516.x
13. Mattfeldt T, Mall G, 1983, Dipyridamole-induced Capillary Endothelial Cell Proliferation in the Rat Heart a Morphometric Investigation. *Cardiovasc Res*, 17:229–37. https://doi.org/10.1093/cvr/17.4.229
14. Lamichhane S, Gallo A, Mani G, 2014, A Polymer-free Paclitaxel Eluting Coronary Stent: Effects of Solvents, Drug Concentrations and Coating Methods. *Ann Biomed Eng*, 42:1170–84. https://doi.org/10.1007/s10439-014-1003-y
15. Chen MC, Liang HF, Chiu YL, *et al.*, 2005, A Novel Drug-eluting Stent Spray-coated with Multi-layers of Collagen and Sirolimus. *J Control Release*, 108:178–89. https://doi.org/10.1016/j.jconrel.2005.07.022
16. Huang Y, Subbu SS, Boey FY, *et al.*, 2010, In vitro and In vivo Performance of a Dual Drug-eluting Stent (DDES). *Biomaterials*, 31:4382–91. https://doi.org/10.1016/j.biomaterials.2010.01.147
17. Oh Band Lee CH, 2013, Advanced Cardiovascular Stent Coated with Nanofiber. *Mol Pharm*, 10:4432–42. https://doi.org/10.1021/mp400231p
18. Tan GZ, Zhou Y, 2019, Electrospinning of Biomimetic Fibrous Scaffolds for Tissue Engineering: A Review. *Int J Polym Mater Polym Biomater*, 69:947–60. https://doi.org/10.1080/00914037.2019.1636248
19. Oh B, Lee CH, 2013, Nanofiber for Cardiovascular Tissue Engineering. *Expert Opin Drug Deliv*, 10:1565–82.
20. Hu X, Liu S, Zhou G, *et al.*, 2014, Electrospinning of Polymeric Nanofibers for Drug Delivery Applications. *J Control Release*, 185:12–21. https://doi.org/10.1016/j.jconrel.2014.04.018
21. Punnakitikashem P, Truong D, Menon JU, *et al.*, 2014, Electrospun Biodegradable Elastic Polyurethane Scaffolds with Dipyridamole Release for Small Diameter Vascular Grafts. *Acta Biomater*, 10:4618–28. https://doi.org/10.1016/j.actbio.2014.07.031
22. Liu P, Liu Y, Li P, *et al.*, 2018, Rosuvastatin-and Heparin-Loaded Poly(l-lactide- co-caprolactone) Nanofiber Aneurysm Stent Promotes Endothelialization via Vascular Endothelial Growth Factor Type A Modulation. *ACS Appl Mater Interf*, 10:41012-41018. https://doi.org/10.1021/acsami.8b11714
23. Wang C, Xu Y, Xia J, *et al.*, 2021, Multi-scale Hierarchical Scaffolds with Aligned Micro-fibers for Promoting Cell Alignment. *Biomed Mater* (*Bristol*), 16:ac0a90. https://doi.org/10.1088/1748-605X/ac0a90
24. Lin S, Ran X, Yan X, *et al.*, 2019, Corrosion Behavior and Biocompatibility Evaluation of a Novel Zinc-based Alloy Stent in Rabbit Carotid Artery Model. *J Biomed Mater Res Part B Appl Biomater*, 107:1814–1823. https://doi.org/10.1002/jbm.b.34274
25. Im SH, Kim CY, Jung Y, *et al.*, 2017, Biodegradable Vascular Stents with High Tensile and Compressive Strength: A Novel Strategy for Applying Monofilaments Via Solid-state Drawing and Shaped-annealing Processes. *Biomater Sci*, 5:422–31. https://doi.org/10.1039/c7bm00011a
26. Xue J, Wu T, Dai Y, *et al.*, 2019, Electrospinning and Electrospun Nanofibers: Methods, Materials, and Applications. *Chem Rev*, 119:5298–415. https://doi.org/10.1021/acs.chemrev.8b00593
27. Fong H, Chunand I, Reneker DH, 1999, Beaded Nanofibers Formed during Electrospinning. *Polymer*, 40:4585–92.
28. Qin Y, Liu R, Zhao Y, *et al.*, 2016, Preparation of Dipyridamole/Polyurethane Core-shell Nanofibers by Coaxial Electrospinning for Controlled-release Antiplatelet

Application. *J Nanosci Nanotechnol*, 16:6860–6. https://doi.org/10.1166/jnn.2016.11386

29. Repanas A, Wolkers WF, Gryshkov OP, *et al.*, 2015, Pcl/Peg Electrospun Fibers as Drug Carriers for the Controlled Delivery of Dipyridamole. *J In Silico* In vitro *Pharmacol*, 1:1–10. https://doi.org/10.21767/2469-6692.10003
30. Ruggeri ZM, Mendolicchio GL, 2007, Adhesion Mechanisms in Platelet Function. *Circ Res*, 100:1673–85. https://doi.org/10.1161/01.RES.0000267878.97021.ab
31. Li W, Zhou J, Xu Y, 2015, Study of the In vitro Cytotoxicity Testing of Medical Devices. *Biomed Rep*, 3:617–20. https://doi.org/10.3892/br.2015.481
32. 10993-5:2009 I, Biological Evaluation of Medical Devices Part 5: Tests for In vitro Cytotoxicity. Technical Committee.
33. Wu X, Wu S, Kawashima H, *et al.*, 2021, Current Perspectives on Bioresorbable Scaffolds in Coronary Intervention and other Fields. *Expert Rev Med Dev*, 18:351–65. https://doi.org/10.1080/17434440.2021.1904894
34. Woodruff MA, Hutmacher DW, 2010, The Return of a Forgotten Polymer Polycaprolactone in the 21st Century. *Prog Polym Sci* (*Oxford*), 35:1217–56. https://doi.org/10.1016/j.progpolymsci.2010.04.002
35. Kim K, Yu M, Zong X, *et al.*, 2003, Control of Degradation Rate and Hydrophilicity in Electrospun Non-woven Poly(D,L-lactide) Nanofiber Scaffolds for Biomedical Applications. *Biomaterials*, 24:4977–85. https://doi.org/10.1016/S0142-9612(03)00407-1
36. Ulery BD, Nair LS, Laurencin CT, 2011, Biomedical Applications of Biodegradable Polymers. *J Polym Sci Part B Polym Phys*, 49:832–64. https://doi.org/10.1002/polb.22259
37. Repanas A, Glasmacher B, 2015, Dipyridamole Embedded in Polycaprolactone Fibers Prepared by Coaxial Electrospinning as a Novel Drug Delivery System. *J Drug Deliv Sci Technol*, 29:132–42. https://doi.org/10.1016/j.jddst.2015.07.001
38. Qiu T, Jiang W, Yan P, *et al.*, 2020, Development of 3D-Printed Sulfated Chitosan Modified Bioresorbable Stents for Coronary Artery Disease. *Front Bioeng Biotechnol*, 8:462. https://doi.org/10.3389/fbioe.2020.00462
39. Lei D, Luo B, Guo Y, *et al.*, 2019, 4-Axis Printing Microfibrous Tubular Scaffold and Tracheal Cartilage Application. *Sci China Mater*, 62:1910–20. https://doi.org/10.1007/s40843-019-9498-5
40. Martinez-Lemus LA, 2012, The Dynamic Structure of Arterioles. *Basic Clin Pharmacol Toxicol*, 110:5–11. https://doi.org/10.1111/j.1742-7843.2011.00813.x

Publisher's note

Whioce Publishing remains neutral with regard to jurisdictional claims in published maps and institutional affiliations.

RESEARCH ARTICLE

3D-Printing-Assisted Extraluminal Anti-Reflux Diodes for Preventing Vesicoureteral Reflux through Double-J Stents

Jihun Lee[1], Jaebum Sung[1], Jung Ki Jo[2]*, Hongyun So[1,3]*

[1]Department of Mechanical Engineering, Hanyang University, Seoul 04763, South Korea
[2]Department of Urology, College of Medicine, Hanyang University, Seoul 04763, South Korea
[3]Institute of Nano Science and Technology, Hanyang University, Seoul 04763, South Korea

Abstract: This paper presents novel umbrella-shaped flexible devices to prevent vesicoureteral reflux along double-J stents, which is a backward flow of urine from the bladder to the kidney and is a critical issue in patients with urinary stones. The anti-reflux devices were designed to mechanically attach to the stent and were manufactured using three-dimensional (3D) printing and polymer casting methods. Based on the umbrella shapes, four different devices were manufactured, and the anti-reflux efficiency was demonstrated through in vitro experiments using a urination model. Consequently, penta-shaped devices exhibited the best anti-reflux performance (44% decrease in reflux compared to the stent without the device), and maximum efficiency occurred when the device was attached near the bladder-ureter junction. In addition, a disadvantage of 3D printing (i.e., unwanted rough surface) helped the device strongly adhere to the surface of the stent during the insertion operation. Finally, long-term soaking experiments revealed that the fabricated devices were mechanically robust and chemically stable (safe) even being soaked in urine for 4 weeks. The findings of this study support the use of additive manufacturing to make various flexible and biocompatible urological devices to mitigate critical issues in patients with urinary stones.

Keywords: Vesicoureteral reflux; Double-J stent; 3D printing; Anti-reflux diode; Urology

*Correspondence to: Jung Ki Jo, Department of Urology, College of Medicine, Hanyang University, Seoul 04763, South Korea; victorjo38@hanyang.ac.kr; Hongyun So, Department of Mechanical Engineering, Hanyang University, Seoul 04763, South Korea; hyso@hanyang.ac.kr

Received: December 21, 2021; **Accepted:** February 7, 2022; **Published Online:** February 7, 2022

Citation: Lee J, Sung J, Jo JK, *et al*., 2022, 3D-Printing-Assisted Extraluminal Anti-Reflux Diodes for Preventing Vesicoureteral Reflux Through Double-J Stents. *Int J Bioprint,* 8(2):549. http://doi.org/10.18063/ijb.v8i2.549

1. Introduction

Most urological procedures and treatments, such as lithotripsy, ureteroscopic procedures, prevention of ureteral stenosis, relief of hydronephrosis, and reduction in urological complications, require double-J (DJ) stents[1-7]. In general, these DJ stents are thin and hollow tubes with side holes composed of polyurethane material, and both ends are rolled up to hold the stent in the ureter[8]. The DJ stents are located in the ureter to enable urine drainage from the kidney into the bladder and to prevent contraction of the ureter after the removal of urinary stones[5,9]. In addition, ureteral stents are used during renal transplantation to reduce urological complications, such as anastomotic stricture or urine leakage after operation[6,7]. Thus, DJ stents are necessary medical tools for urologists during various urological procedures and treatments[10]. Despite the advantages of using DJ stents, the inserted DJ stents can cause side effects in patients. For example, hematuria, dysuria, irritative urination, and urinary tract infection can result from inserted DJ stents[4-7,9-13]. In addition, vesicoureteral reflux (VUR) is a side effect that frequently occurs because the stents preclude the complete closure of the bladder-ureter junction (vesicoureteric junction [VUJ]) during urination[14-16]. VUR is a significant problem that leads to flank pain, pyelonephritis, renal scar formation, and renal failure[15,17-20]. In particular, VUR induced by inserted stent can cause severe flank pain during urination or upper urinary tract infection, which has a potential hazard of pyelonephritis[15,19-21]. In addition, occurrence of

© 2022 Author(s). This is an Open Access article distributed under the terms of the Creative Commons Attribution License, permitting distribution and reproduction in any medium, provided the original work is properly cited.

reflux along the stents was reported in 51.4% of patients even after immediate insertion of ureteral stents[22]. Although VUR associated with DJ stents would not require an immediate treatment or surgery to relieve the symptoms, repetitive VUR may adversely affect patients who require long-term placement of ureteral stents[21,23]. Thus, for the quality of patients' life, the prevention of VUR is significantly important, and therefore, anti-reflux medical devices compatible with the DJ stents must be developed; this remains as a challenge in urology.

Once a DJ stent is inserted in the ureter, urine can flow either through the inner wall or outer surface of the stent (more specifically, the space between the outer stent wall and the inner wall of the ureter)[24]. Due to the dilated VUJ, reflux can flow not only in the intraluminal space but also in the extraluminal space[15,16]. To decrease the VUR, various types of anti-reflux devices integrated with DJ stents have been investigated for intraluminal reflux[15,21,23,25-27]. For example, polymeric flap valves and collapsed valves have been demonstrated as intraluminal anti-reflux devices[15,21,25,26]. For polymeric flap valve devices, in vitro experiments using hydrostatic pressure indicated that volumetric backflow rates were decreased by up to 8 times under 50 cm-H_2O pressure compared to a bare DJ stent with no valve. The membrane-type anti-reflux valves at distal end of the stent have also been studied and shown to reduce VUR degrees and frequencies[23,27]. However, the valves were large, inducing discomfort and irritation symptoms in patients during the insertion and therapeutic period. Although the devices described in previous studies were effective in preventing intraluminal reflux, they could not prevent extraluminal reflux alongside the stent, which accounts for the majority of the overall reflux. In addition, from a clinical point of view, there is also be a concern that extraluminal reflux may occur[15,21]. To the best of our knowledge, there is currently no published study about the prevention of extraluminal reflux alongside the stent. Therefore, the development of small, flexible, biocompatible, and reliable anti-reflux devices with less irritation is still required to prevent extraluminal reflux alongside the stent.

In the last decade, additive manufacturing has been widely used to develop various medical devices such as bio-microfluidic chips[28], dental implants[29,30], custom prosthetics[31,32], and even ureteral stents[33]. In particular, casting processes using three-dimensional (3D)-printed molds have been utilized in a variety of fields because they allow the use of diverse materials, which differ from 3D-printed materials. For example, in medical devices, flexible or biocompatible materials, such as silicone, epoxy, and polydimethylsiloxane, were utilized as the casting material poured in 3D-printed molds[34-36]. Among the various types of 3D-printing methods, the fused deposition modeling (FDM)-type printing method has been commonly used owing to its simplicity, low cost, and fast printing speed[37,38]. Moreover, products can be designed using computer-aided design (CAD) software to create the desired shape. The FDM method deposits a filament (e.g., polylactic acid or acrylonitrile butadiene styrene) layer-by-layer; however, the resulting product has a poor surface roughness[38,39]. Recent studies have revealed that this drawback (i.e., rough surface) can be intentionally utilized for various applications such as (super) hydrophobic surfaces[40], micro-drilling devices[41], microchannels[42], and non-sticky surfaces[43].

In this study, we fabricated and demonstrated attachable extraluminal anti-reflux diodes (EADs) based on an umbrella shape, which can effectively prevent extraluminal reflux from the bladder into the kidney while allowing urine drainage from the kidney into the bladder. The EADs were based on four different types of polygonal shapes and were fabricated by a casting process using an FDM-type 3D printer. The Ecoflex elastomer was utilized as the main body material due to its good flexibility and biocompatibility[44,45]. To demonstrate the diode performance, the devices were characterized using an in vitro voiding (urination) model to measure the maximum reflux height. In addition, the attached position of the diode on the DJ stent and the number of diodes were considered to investigate the maximum performance. The disadvantage of 3D printing (i.e., rough surface patterns) was intentionally used to effectively attach the diode onto the stent, and the mechanical properties were compared to those without rough surface patterns. To further investigate the health safety and durability of the devices in urine, Fourier transform infrared (FTIR) spectroscopy was conducted to observe changes in the chemical structures of devices immersed in artificial urine for 4 weeks.

2. Design and fabrication

Figure 1A shows an overall schematic of the EAD, which is an anti-reflux device integrated with the DJ stent in the ureter. Since the material of the EAD is Ecoflex, which is flexible, its shape can be easily deformed by pressure. **Figure 1B** presents the operational mechanisms for the forward flow (urine drainage) and backward flow (urine reflux). The mechanism is based on the change in the cross-sectional area (internal area) of the EAD with respect to the flow direction. During forward flow, the urine flows and pushes the outer wall of the EAD. As the EAD is pushed toward the stent, the internal area decreases and the external area (i.e., the area between the outer wall of the EAD and inner wall of the ureter) increases. Consequently, urine can readily flow along the external area in a forward direction. In contrast, during backward flow, the urine flows and pushes the inner wall of the EAD. Thus, the EAD expands and increases the internal area.

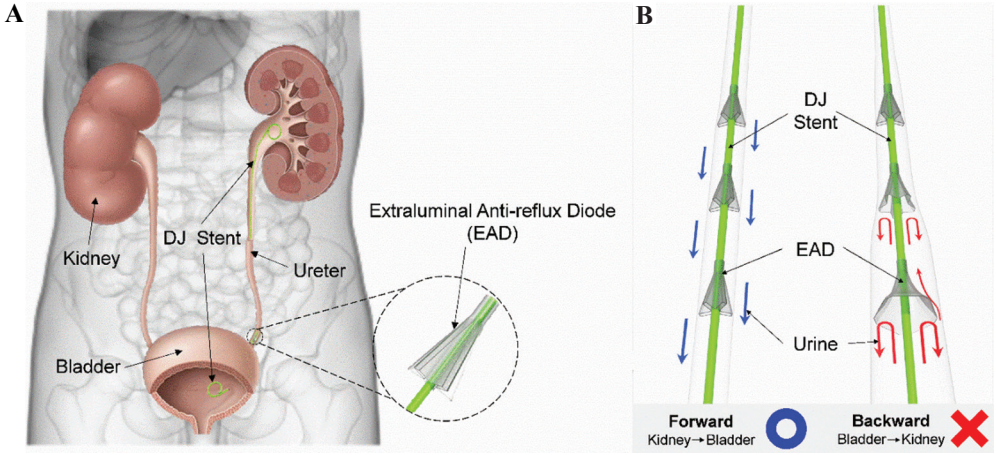


Figure 1. Conceptual illustration of the extraluminal anti-reflux diodes (EADs). (A) Schematic of the inserted EAD with the DJ stent in the urinary organs. (B) Working mechanism of the EADs for forward and backward flows.

Consequently, the external area is significantly reduced, and the flow resistance increases, such that reflux rarely occurs. Because the urine must pass through the inner space of the EAD in response to the applied reflux, the anti-reflux performance of the EAD highly depends on the cross-sectional (area) shapes. Hence, in this study, four different types of EADs (quadra-, penta-, hexa-, and octa-shaped) were fabricated and used to investigate the effect of the device shape on the anti-reflux performance.

To estimate the fluidic properties of the anti-reflux device with velocity and pressure fields across the EAD, a computer-aided engineering simulation was conducted using COMSOL Multiphysics, as shown in **Figure 2**. The penta-shaped EAD was used for the simulation. For forward flow (i.e., flow from the kidney to the bladder), the inlet pressure was set to 18 cm-H_2O owing to the renal pelvis pressure being approximately 15 – 18 cm-H_2O hydrostatic pressure when the stent was inserted in the ureter. For backward flow (i.e., flow from the bladder to the kidney), the inlet pressure was set to be 50 cm-H_2O of intravesical pressure on voiding[16,21]. **Figures 2A and C** show the velocity streamline fields across the penta-shaped device under forward and backward flows, respectively. **Figures 2B and D** show the pressure distribution of the cross-sectional area observed in the forward and backward flow directions, respectively. Based on the simulation, for forward flow, the pressure of the external area was higher than that of the internal area, as shown in **Figure 2B**. This implies that the EAD can be contracted toward the stent because of its flexibility. Conversely, for backward flow, the fluid (i.e., urine) can be trapped inside the EAD, thus inducing high pressure in the internal area. This high pressure inside the internal area can push the penta-shaped membrane toward the ureter, as shown in **Figure 2D**. This result implies that the EAD can expand toward the ureter because of the pressure gradient in the ureter wall direction. Thus, the designed anti-reflux device can rectify the desired urine flow in response to the flow direction.

The overall manufacturing procedure was based on casting methods using a 3D printer. The overall schematic of the fabrication process for the penta-shaped EAD is shown in **Figure 3**. FDM-type 3D printer (GUIDER II, FlashForge Co.) with polylactic acid (PLA) filament, which is a widely utilized filament for FDM printing, was employed to print casting mold and die (**Figure 3A**). The printing parameters, namely the extruder temperature, platform temperature, printing speed, layer height, and printing density, were set to 220°C, 40°C, 60 mm/s, 0.18 mm, and 15%, respectively. It should be noted that the shape of the PLA mold and die can be adjusted with respect to the final shape of the EAD (i.e., quadra, penta, hexa, and octa). After the PLA mold and die were printed, the prepared elastomer Ecoflex (00-50 type, Smooth-On Inc.), which was mixed in a 1:1 (part A: part B) ratio, was poured onto the printed PLA mold (**Figure 3B**). The poured Ecoflex was then degassed in a vacuum chamber for 10 min to eliminate air bubbles trapped in the liquid elastomer. After the degassing process, the printed PLA die was pushed into the mold; thus, a thin membrane of the Ecoflex could be formed in the clearance between the mold and die (**Figure 3C**). The Ecoflex was then baked on a heater at 50°C for 20 min for the curing process (**Figure 3D**). They can also be baked at high temperatures for fast curing. However, here, the shapes of the PLA mold and die can be deformed by a baking temperature higher than the glass transition temperature of the PLA. Consequently, the PLA mold and die maintained their original shapes at the baking temperature (50°C) as this temperature was below the glass transition temperature of the PLA (55 – 70°C)[46,47]. Next, to separate the three parts (i.e., mold, cured Ecoflex, and die), they were immersed in acetone for 12 h to delaminate the PLA (**Figure 3E**)[48], and subsequently, they were easily separated by hand

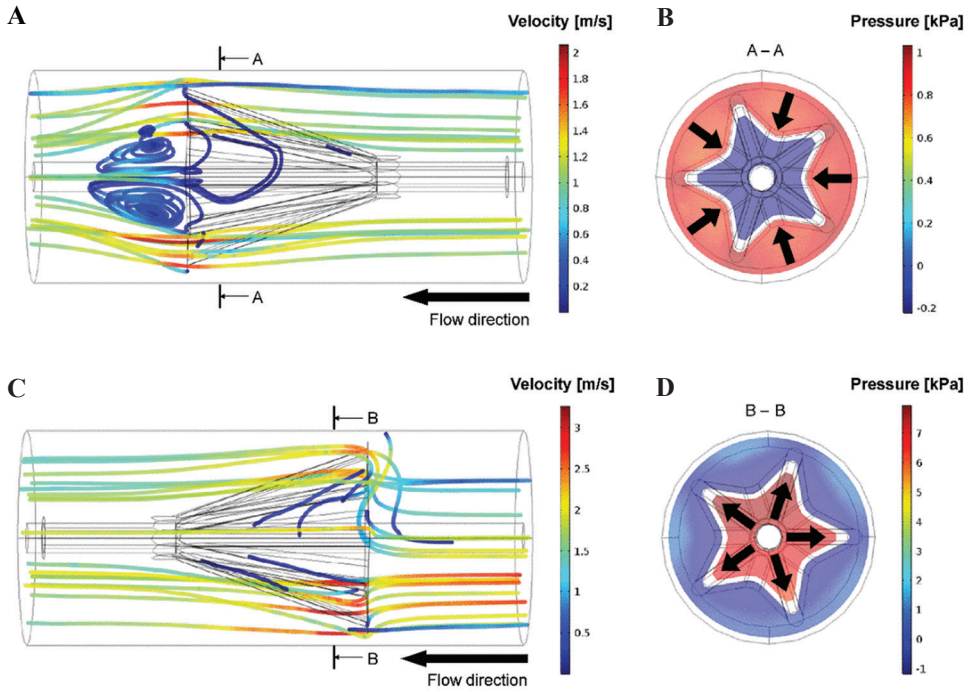


Figure 2. Simulation results for the penta-shaped extraluminal anti-reflux diode (EAD) under initial pressures of 18 cm-H_2O (1765 Pa) and 50 cm-H_2O (4903 Pa) for forward and backward directions, respectively. (A) Streamline in the forward direction. (B) Cross-section of pressure distribution in the forward direction. (C) Streamline in the backward direction. (D) Cross-section of pressure distribution in the backward direction.

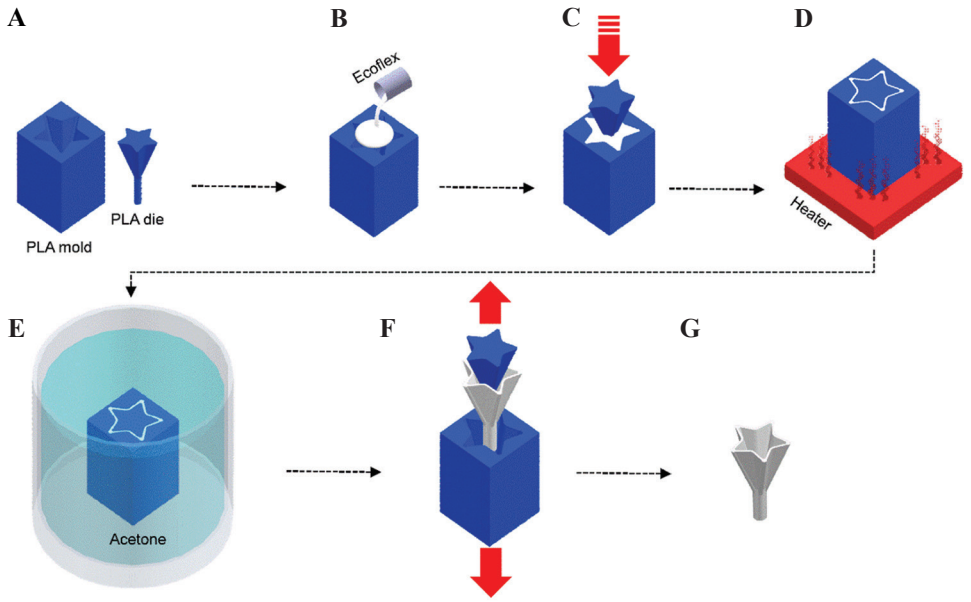


Figure 3. Schematic of the entire fabrication process. (A) Printing of the polylactic acid (PLA) mold and die using a 3D printer; (B) pouring of the Ecoflex onto the printed PLA mold; (C) pressing of the die into the mold after degassing process; (D) baking on a heater to cure the Ecoflex; (E) delamination of the PLA to separate the cured Ecoflex from the mold and die by immersing in acetone; (F) separation of the Ecoflex by hand; and (G) finalization of the fabrication of the extraluminal anti-reflux diode.

(**Figure 3F**). Finally, various types of anti-reflux devices were created (**Figure 3G**).

Figure 4 shows the optical and scanning electron microscopy (SEM) images of each manufactured EAD and integrated with the DJ stent. The fabricated EADs can be divided into three parts (rib, canopy, and joining part), as shown in **Figures 4A1 and A2**. The rib parts prevent the EAD from being turned inside out, similar

to the ribs of an umbrella. The canopy parts (i.e., flexible membranes) can expand their shapes against the fluidic resistance during the reflux, which are similar to fabric panels of an umbrella. Furthermore, the joining parts allow the EAD to be assembled with the DJ stent. The optical images of the cross-sectional area of each type of EAD, i.e., quadra, penta, hexa, and octa, are presented in **Figures 4A1, B1, C1, and D1**, respectively. The rib and canopy thickness of each device were set to 1 and 0.4 mm, respectively, on CAD software. Because the rib is slightly thicker than the canopy, the device can avoid rollover (overturn) during the reflux. **Figures 4A2, B2, C2, and D2** show each standing EAD with a length of 2 cm. The length, inner diameter, and thickness of the joining part were 5, 1.8, and 0.4 mm, respectively. In this study, a DJ stent (6Fr, 22 cm, C. R. Bard Inc.) with a 2-mm outer diameter was used. Since the inner diameter of the joining part is slightly smaller than the outer diameter of the DJ stent, the EADs can be assembled mechanically with the DJ stent through press fit. **Figures 4A3, B3, C3, and D3** present the SEM images of the outer walls of each EAD with detailed rough surfaces. It should be noted that the uniform rough patterns of each EAD were formed due to the layer-by-layer printed mold. Furthermore, because the printed PLA die was printed layer-by-layer, the inner wall of each EAD also had the same rough surface. **Figure 4E** shows a combination of the penta-shaped EAD and the DJ stent. Before the EAD and the DJ stent were assembled, they were placed in water for 5 min to allow for the mechanical friction of the joining part of the EAD to be reduced during the hand assembly that may induce cracks or rupture in the EAD. Therefore, the EAD can be located in the desired positions along the DJ stent without damage. In this study, we demonstrated the anti-reflux efficiency of each fabricated EAD using an experimental model. To investigate the best reflux prevention performance, parameters such as the shape of EAD, attaching position, and the number of attached devices were considered. Since the EAD and the DJ stent are assembled mechanically, the surface feature (roughness) is also important to decide attachment forces. Therefore, we utilized rough surfaces with patterns, which were formed by layer-by-layer deposition and compared them with smooth surfaces without patterns. Finally, to further demonstrate the safety and durability of EADs in the urine, surface deformation and chemical structure changes of EADs were observed using artificial urine.

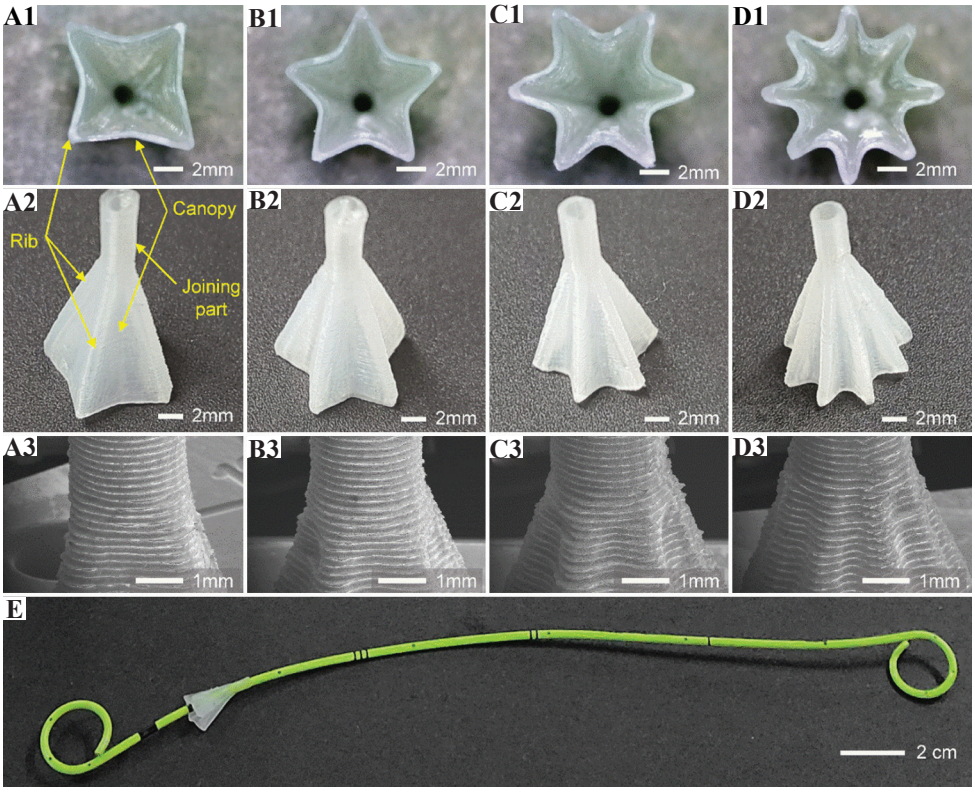


Figure 4. Optical images of cross-section of extraluminal anti-reflux diodes (EADs) with four different shapes: (A1) quadra, (B1) penta, (C1) hexa, and (D1) octa. Optical images of the standing EADs: (A2) quadra, (B2) penta, (C2) hexa, and (D2) octa. Tilted view of scanning electron microscopy images of each EAD: (A3) quadra, (B3) penta, (C3) hexa, and (D3) octa. (E) Optical image of the EAD integrated with the DJ stent.

3. Results and discussion

3.1. Anti-reflux performance

Figure 5 presents an experimental setup to characterize the anti-reflux performance of the EAD. To demonstrate and compare the anti-reflux performance of each EAD, a voiding (urination) model, which is designed for urination and reflux circumstances, was prepared using a 3D printer, transparent polycarbonate (PC) pipes, and silicone rubber. The designed voiding model is classified into three parts: 3D-printed bladder part where urine flows by urination pressure, urethra line in the bladder where urine is secreted, and ureter line where the reflex occurs along the inserted DJ stent. The bladder model was printed to have three different holes: 7-mm inner diameter for the urethra line, 10-mm inner diameter for the connection of the ureter line, and 30-mm inner diameter for 50-cm long PC pipe to provide the 50 cm-H_2O hydrostatic pressure and urine, as shown in **Figure 5A**. The bladder model and ureter line were connected using silicone rubber with a 10-mm inner diameter. To mimic the bladder pressure and urine simultaneously, hydrostatic pressure (i.e., 50 cm-H_2O) was used in this study[21]. The PC pipe was filled with deionized water dyed in red color up to a length of 50 cm and assembled with the bladder model. Although water was filled in the PC pipe up to the 50-cm height to represent voiding pressure, the actual initial pressure was 48 cm-H_2O because some portion of the inner volume of the bladder model was filled with water in this experiment. The water flowed into the urethra and the ureter due to reflux when the stop valve was removed to apply pressure on the bladder model. Using this experimental model, in vitro experiments were conducted to determine the efficiency of EADs of various shapes, which were inserted into the ureter after being assembled with the DJ stent. **Figure 5B** shows the urination state with reflux when the stop valve was removed. It was noticed that the canopy membrane of the EAD was expanded by the reflux pressure compared to normal EAD. This result is consistent with the simulation result (**Figure 2D**). The maximum height (indicated as H_{max} in **Figure 5B**) at which the reflux urine can rise in the ureter differs in response to the anti-reflex performance. Therefore, the efficiency of anti-reflux was characterized by measuring the maximum reflux height (H_{max}) of the water along the ureter line when pressure was applied. The lower the H_{max} measured, the better the anti-reflux efficiency.

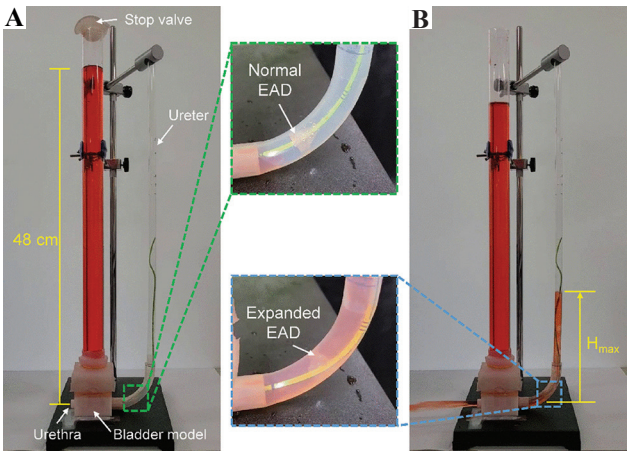


Figure 5. Experimental setup to characterize the anti-reflux efficiency. (A) Urination model with the extraluminal anti-reflux diode (EAD) and the DJ stent before the bladder pressure was applied with the zoomed-in image of normal EAD. (B) Urination state after the removal of the stop valve with the zoomed-in image of expanded EAD. Maximum height in the backflow (H_{max}) can be varied in response to the anti-reflux efficiency.

Figure 6A shows the measured H_{max} with respect to the types of EADs and attached positions along the DJ stent using a urination model. The positions are presented in **Figures 6B-D**, and only one device was attached to the DJ stent during this experiment. Five types (without EAD and with quadra-, penta-, hexa-, and octa-shaped EADs) of a single device were evaluated 5 times with respect to each position (Position #1, Position #2, and Position #3). Accordingly, the penta-shaped EAD exhibited the best anti-reflux performance at Position #1 (H_{max} =220.6 mm) with a 44% decrease in the maximum reflux height compared to that without EAD (H_{max} =394 mm). Moreover, the penta-shaped device showed the best efficiency compared to the other types of EADs at the same attached position along the DJ stent, as shown in **Figure 6A**. Thus, the penta-shaped EAD was beneficial in significantly mitigating the urine reflux in this study. It was noticed that the anti-reflux efficiency of the devices showed the same tendency at each attached position. The efficiency decreased in the order of penta-, octa-, hexa-

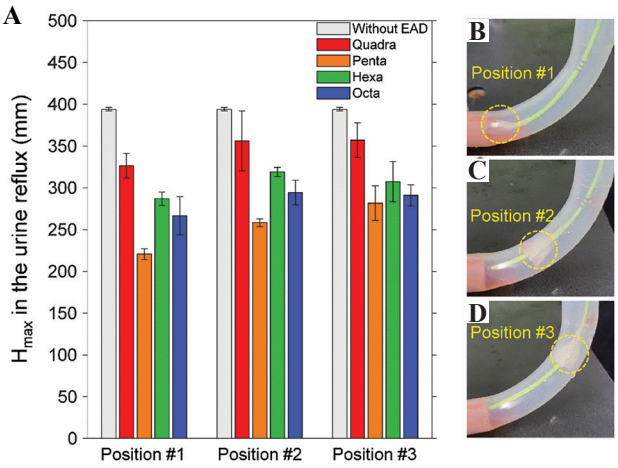


Figure 6. (A) Average values of the maximum height in the urine reflux without and with four different types of extraluminal anti-reflux diodes (quadra-, penta-, hexa-, and octa-shaped) with respect to the attached position along the DJ stent. (B) Position #1, (C) Position #2, and (D) Position #3.

, and quadra-shaped EADs. This tendency can possibly be attributed to the difference in the internal area, where urine can flow during the reflex. When the internal areas of each EAD were measured using the CAD model, the penta-, quadra-, octa-, and hexa-shaped EADs showed areas of 46.53, 46.01, 45.94, and 44.94 mm^2, respectively. As the internal area increased, the EAD has the potential to be expanded because more urine flow can be trapped inside the EAD when initial reflux occurs. In addition, the external area (i.e., the spatial area between the expanded EAD wall and the inner wall of the ureter) will decrease as the internal area of EAD increases, thus increasing the flow resistance in the ureter, which results in reduced H_{max}. Although the internal area of the quadra-shaped EAD is larger than that of the hexa- and octa-shaped EADs, its anti-reflux efficiency is lower than that of the others. Here, the quadra-shaped EAD was flipped (overturned) during the reflux because the number of ribs was not enough to maintain the overall shape against reflex pressure. Therefore, the quadra-shaped EAD showed the worst anti-reflux efficiency in this study.

To further characterize the anti-reflux effectiveness with respect to the number of attached EADs, an experiment was performed using an increasing number of penta-shaped EADs, which exhibited the best performance in the previous experiments. **Figures 7A-C** show the number of attached EADs (single, double, and triple) at the various positions. The joining part of the EAD was located close to the side hole of the DJ stent to avoid covering the side hole, and then the position was determined. Due to the unequal distance between the side holes, the distance between the positions also differed slightly. The distances between Positions #1 and #2 and Positions #2 and #3 were 17.5 and 22 mm, respectively, as shown in **Figures 7B and C**. Four experimental conditions (without EAD and with single, double, and triple penta-shaped EADs) were tested 5 times for each case. Consequently, the average values of H_{max} were measured to be 394, 220.6, 223.2, and 228.8 mm for the DJ stent without EAD and with single, double, and triple penta-shaped EADs, respectively, as shown in **Figure 7D**. The results showed that no significant variations existed in H_{max} between the single, double, and triple EADs. This might be because the pressure gradient, which helps the EAD expand, was significantly decreased across the EAD at Position #1. Due to the decreased pressure gradient, the subsequent EADs (i.e., EADs at Positions #2 and #3) did not fully expand to sufficiently block the ureter line. Thus, water flowed in the external area, and the EADs at Positions #2 or #3 may not work. This also indicated that a single EAD attached at Position #1 (near the VUJ) sufficed to mitigate urine reflux in the ureter line. From the results shown in **Figures 6 and 7**, a single penta-shaped EAD at Position #1 had the best performance in preventing reflux, and the anti-reflux performance did not change significantly depending on the number of attached EADs. In summary, the device with the highest effectiveness and least irritation to patients was found to be a single penta-shaped EAD at Position #1 in this study.

Table 1 shows a comparison of anti-reflex devices between this study and previous literature to reduce the VUR. It was noteworthy that previous studies have focused on intraluminal reflux issues whereas this study developed the anti-reflux device to prevent the extraluminal reflux. In addition, because the material used in this study (i.e., Ecoflex) is inherently biocompatible[44,45], additional processes such as parylene C coating were not required on the anti-reflex devices to enhance the biocompatibility. To characterize the anti-reflux performance, flow rate under the driven pressure was measured through the intraluminal anti-reflux devices. However, because urine can reach the renal pelvis for a long time and the pressure was continuously supplied during experiments[21,23], these methods could

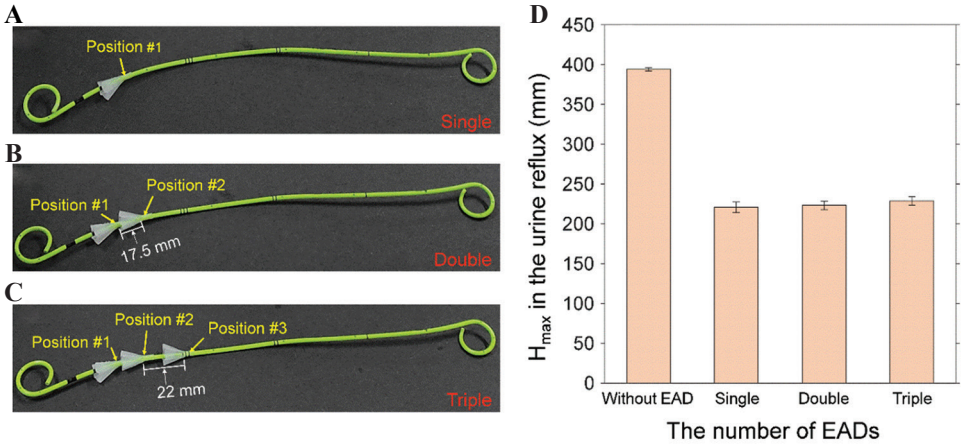


Figure 7. DJ stent assembled with (A) single penta-shaped extraluminal anti-reflux diode (EAD) at Position #1, (B) double penta-shaped EADs at Positions #1 and #2, and (C) triple penta-shaped EADs at Positions #1, #2, and #3. (D) Average values of maximum height in the urine reflux with respect to the number of EADs.

not present suitable voiding situations compared to this study. Nonetheless, to demonstrate the use of the EAD in the human body, further *in vivo* or clinical trial studies are needed. Although intraluminal reflux was not considered in this study, various intraluminal anti-reflux devices have been demonstrated and cone-shaped anti-reflux devices are commercially available[15]. When the EAD is combined with these intraluminal anti-reflux devices, the overall efficiency of reflux prevention alongside the stents will be dramatically increased. Consequently, patients are expected to be free from the urological complications caused by the VUR.

3.2. Mechanical adhesion and friction test

It is important to avoid easy separation (disassembly) of the EAD from the DJ stent during insertion into the ureter line. Because of the features of the FDM-printing method, a rough surface with regular patterns appeared both inside and outside the joining part, as shown in **Figures 4A3, B3, C3, and D3**. In this work, we utilized these unique patterns of the joining parts for stable and robust mechanical bonding with the DJ stent by enhancing the friction effect. To demonstrate the benefit of a rough surface, the tensile (pulling) load at the interface between the joining part and stent surface was measured using a tensile testing machine (MCT-2150, A&D Co.). To investigate the effect of the patterned surface, two types of specimens were prepared, that is, with and without patterned rough surfaces of the joining part; these specimens had a length, inner diameter, and thickness of 5, 1.8, and 0.4 mm, respectively. Casting fabrication methods (**Figure 3**) were also used in fabricating the specimens with and without a rough surface. In this study, an acrylonitrile butadiene styrene (ABS) filament was used to create the joining part without patterns. Since ABS melts in acetone, the rough surface of the ABS die was polished by acetone while maintaining the same diameter of the PLA die (**Figure S1** in Supplementary File). After assembly with the DJ stent, adhesion forces were measured by holding the DJ stent and pulling it at a speed of 50 mm/min and up to a displacement of 40 mm using a tensile testing machine (**Figure S2** in Supplementary File). In this experiment, three different specimens for each joining part with and without patterns were prepared and evaluated to measure the adhesion forces.

Figure 8A shows the measured tensile load (i.e., adhesion force) of each specimen with respect to the displacement at a pulling speed of 50 mm/min. Consequently, the characteristics of surface types (with and without patterns) were distinctly divided into "slip" and "miss" behaviors. For the joining part with rough patterns, the joining part was well attached on the surface of the DJ stent up to the pulling displacement of 20 – 25 mm, as confirmed from the linearly increased load. When the pulling displacement exceeded 25 mm, the measured load gradually decreased, meaning the joining part started slipping from the surface of the stent. In contrast, the joining part without rough patterns showed a relatively low load and a sudden drop in pulling load near a pulling displacement of 25 mm. This indicated that the joining part was suddenly separated (missed) from the stent. The joining part without rough patterns was also torn before separation from the DJ stent. Thus, a smooth surface is more dangerous because the EAD can be broken away from the stent during insertion. In summary, this result implies that the rough surface with patterns formed by FDM printing exhibited relatively durable adhesion and longer attaching time with the DJ stent than the smooth surface without patterns.

Figure 8B shows the average maximum load for the joining parts with rough and smooth surfaces. Consequently, specimens with and without surface patterns showed maximum tensile loads of 1274.4 and 1005.6 mN, respectively. The maximum average load of the rough surface with patterns was 26.7% higher than that of the smooth surface without patterns. A higher maximum load might be caused by the water (or urine) between the grooved patterns and the surface of the stent. The frictional force increased with the contact area when the same normal pressure was applied. Therefore, the applied load of a specimen with a smooth surface was assumed to be larger than that of a rough surface. However, if water is present between the smooth surface and the surface of the DJ stent, the actual contact area at the interface significantly decreases due to the thin liquid film, thus considerably reducing the frictional stress. In

Table 1. Comparison of the anti-reflux devices

Reflux type	Material	Dimensions	Method	Measurement	Ref.
Intraluminal	Polyurethane	N/A	Clinical trial	Questionnaire	[15]
Intraluminal	Tango Plus with parylene C coating	2.8 mm×5.3 mm	In vitro	Flow rate	[21]
Intraluminal	Silicone sleeve	15 mm×26 mm	In vitro/ Clinical trial	Flow rate/ Cystogram	[23]
Intraluminal	Tango Plus with parylene C coating	2.8 mm×5.3 mm	In vivo	VUR grade	[25]
Intraluminal	Polyurethane with hydrogel coating	N/A	Clinical trial	Questionnaire	[27]
Extraluminal	Ecoflex	10 mm × 20 mm	In vitro	Reflux height	This work

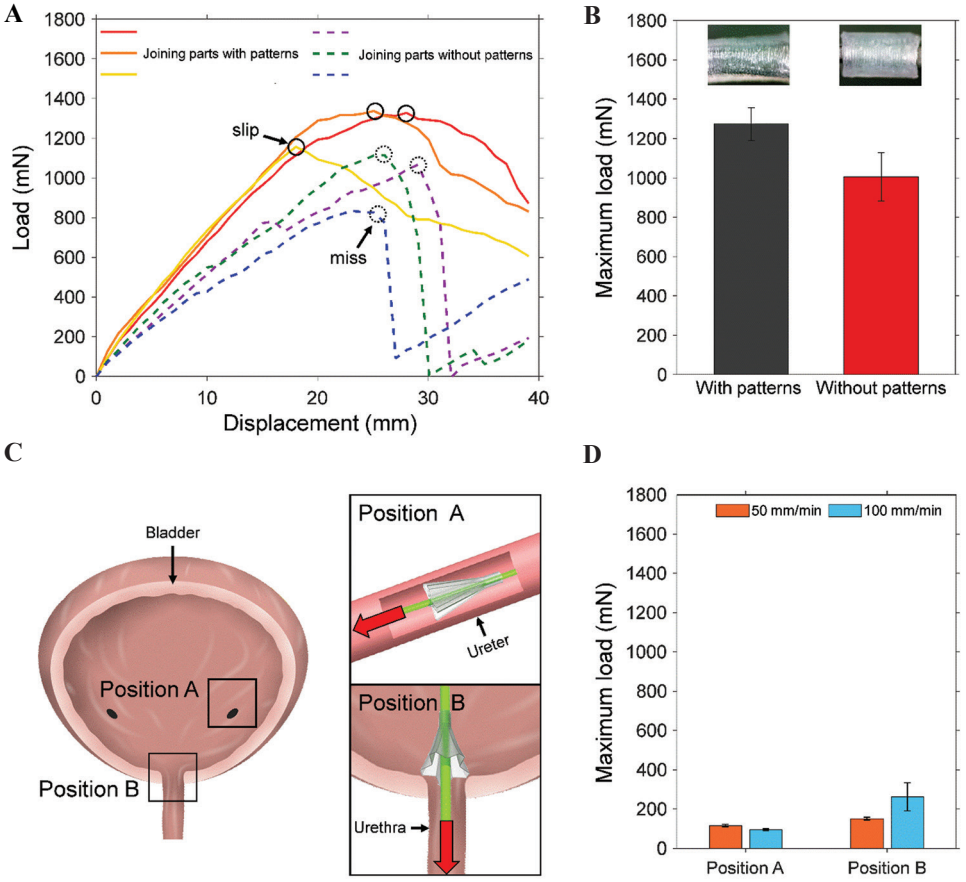


Figure 8. Mechanical properties of the extraluminal anti-reflux diode (EAD) with the DJ stent during insertion and removal. (A and B) Adhesion forces of joining parts with the DJ stent with a pulling speed of 50 mm/min. Comparison between rough surface (with patterns) and smooth surface (without patterns). (A) Applied load of specimens with respect to displacement. (B) Maximum average load of each joining part. Inset: inner surface of the joining parts (with and without patterns). (C) Schematic illustration of removal of the DJ stent with respect to the positions. Position A is path where the EAD is removing from the ureter to the bladder. Position B is path where the EAD is removing from the bladder to the urethra. (D) Friction forces between the EAD and silicone rubber with pulling speeds of 50 and 100 mm/min. Maximum average load at each position with respect to the pulling speed.

contrast, at the interface between grooved patterns and the surface of the stent, the water can be trapped in the grooved patterns, and the tips of the grooved patterns can still contact the stent surface, leading to an increase in friction[49]. This may lead to a higher maximum load of friction in a rough surface with patterns than a smooth surface without patterns. Taken together, the EAD with the patterned joining part is more beneficial for strong adhesion to the DJ stent compared to that with the joining part without patterns when the stent is inserting into the ureter. Based on this experiment, it was confirmed that a rough surface with patterns is more advantageous for mechanical coupling between the EAD and DJ stent. Hence, the disadvantage (rough surface) of the FDM-type 3D printer was utilized as a beneficial property in this study.

To use the EAD to the patients in practical, the ureter should not be injured when clinicians remove the DJ stents. For this reason, a friction test was additionally conducted to demonstrate that the EAD does not damage the ureteral mucosa during the removal of DJ stent. While removing the DJ stent, the EAD passes through ureter, bladder, and urethra, successively. In this study, friction forces between the EAD and silicone rubber, which emulate urinary organs (i.e., ureter and urethra) wall, were measured using in vitro experiment. **Figure 8C** shows the Positions A and B that represent different moving paths from the ureter to the bladder and from the bladder to the urethra, respectively. Positions A and B were implemented in the experimental setup, as shown in **Figure S3** in Supplementary File. Because the EAD is fully surrounded by the ureter at Position A during removal, silicone rubber covered whole EAD, as shown in **Figures S3A1 and A2**. To mimic the removal through Position B, the EAD was initially placed outside of silicone rubber (i.e., bladder) and pulled back through silicone rubber (i.e., urethra), as shown in **Figures S3B1 and B2**. It was noteworthy that the EAD was flipped over when

the DJ stent was pulled from the outside to the inside of silicone rubber, as shown in **Figure S3B2**. Friction forces for each case were measured by pulling the DJ stent up along a displacement of 40 mm using a tensile testing machine. The experiments were conducted with pulling speeds of 50 and 100 mm/min, and repeated 3 times.

Figure 8D shows the averaged maximum load between the EAD and inner wall of silicone rubber with respect to Positions A and B. Position A showed maximum tensile load 116.65 and 96.04 mN at a pulling speed of 50 and 100 mm/min, respectively. Position B showed maximum tensile load 157.74 and 263.34 mN at a pulling speed of 50 and 100 mm/min, respectively. Although the friction forces were present during the removal of DJ stent, these forces were considerably lower than the threshold force that can injure the inner wall of the ureter (2.9 N)[50]. The averaged maximum load at Position B showed higher values than those at Position A, but still negligible compared to the threshold force of 2.9 N. This was because more load was required to flip the EAD at Position B, thus increasing the friction force simultaneously. However, it was noteworthy that once the EAD was flipped, the EAD was easily removed in the silicone rubber with lower friction forces. Consequently, the fabricated EAD is expected not to damage or injure the inner wall (mucosa) of the ureter and urethra during both insertion and removal operations.

3.3. Safety and durability test in urine

To investigate the safety and durability of EADs made of Ecoflex (biocompatible) materials, the changes in the surface and chemical structure of the EADs were thoroughly examined in four types of artificial urine (Biozoa Biological Supply Co.): low-pH, normal-pH, high-pH, and glucose urine. The chemical composition of each artificial urine sample is presented in **Table 2**. For the long-term experiment, the penta-shaped EADs were immersed in each artificial urine sample in a vial and kept in a water bath at 36.5°C (body temperature) for 4 weeks. After 4 weeks, the EADs were washed with deionized (DI) water to investigate whether the EAD was physically damaged or chemically corroded by urine. **Figures 9A1, B1, C1, and D1** show the SEM images of the EADs surface washed after immersion in low-pH, normal-pH, high-pH, and glucose urine, respectively. No physical damage or solidified residues of urine were observed after rinsing with DI water. This characteristic is clearly distinct from the surfaces of the unwashed EADs. **Figures 9A2, B2, C2, and D2** show SEM images of the surfaces of unwashed EADs after immersion in low-pH, normal-pH, high-pH, and glucose urine for 4 weeks, respectively. Each unwashed EAD was dried at 36.5°C for 12 h without being rinsed with deionized water. The surfaces of the unwashed EADs showed adhered urinary stones for EADs immersed in low-pH, normal-pH, and high-pH urine, and solidified glucose residues for the EAD immersed in glucose urine. These results imply that the washing process can remove residues of urine effectively, and thus the EADs are reusable without physical damage after being washed with water.

To further demonstrate the chemically stable structures of the EADs in urine, FTIR (Nicolet iS50, Thermo Fisher Scientific Inc.) analysis was performed, as shown in **Figure 10**. The absorbance with respect to the wavenumber was measured to compare the chemical structures of the EADs before and after immersion in artificial urine. For the bare EAD before immersion in urine, the absorbance bands were observed at wavenumbers of 2963, 1260, 1089, 1018, and

Table 2. Chemical composition and pH of artificial low-pH, normal-pH, high-pH, and glucose urine

Ingredients (g/L)	Artificial urine type			
	Low-pH (pH 5)	Normal-pH (pH 7)	High-pH (pH 9)	Glucose (pH 7)
Calcium Chloride	0.49	0.49	0.49	0.49
Magnesium Chloride	0.3	0.3	0.3	0.3
Potassium Chloride	1.6	1.6	1.6	1.6
Potassium Phosphate	2.8	2.8	2.8	2.8
Ammonium Chloride	1.0	1.0	1.0	1.0
Sodium Sulfate	2.3	2.3	2.3	2.3
Sodium Chloride	2.5	2.5	2.5	2.5
Urea	2.5	2.5	2.5	2.5
Creatine	1.1	1.1	1.1	1.1
Sodium Hydroxide	1.0	-	1.0	-
Potassium Biphthalate	10	-	-	-
Boric Acid	-	-	3.0	-
Glucose	-	-	-	0.5

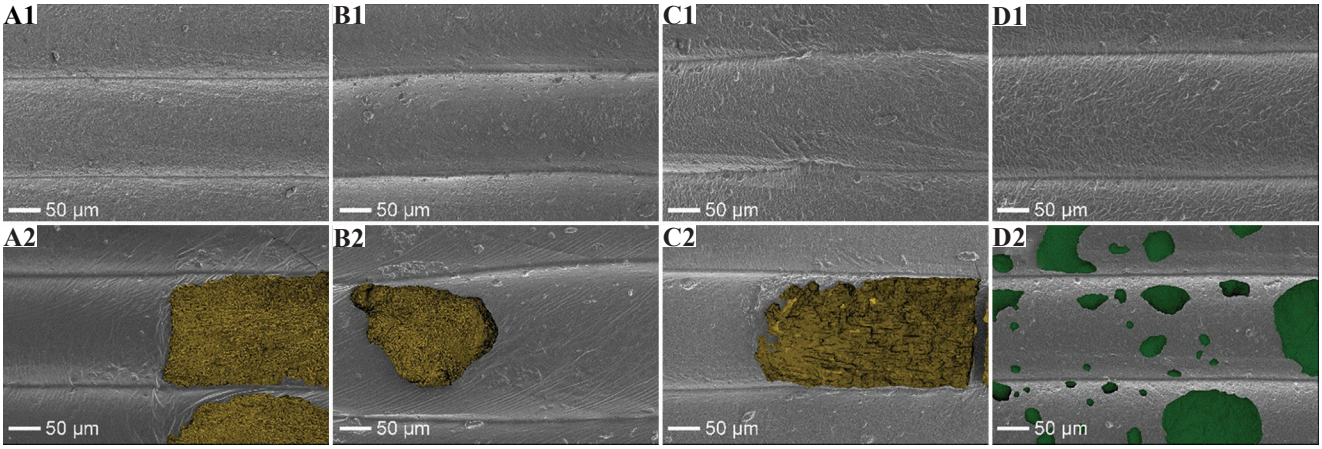


Figure 9. SEM images of the surfaces of extraluminal anti-reflux diodes immersed in artificial urine for 4 weeks. The surface rinsed using DI water after immersing in artificial (A1) low-pH, (B1) normal-pH, (C1) high-pH, and (D1) glucose urine. The unwashed surface after immersion in artificial (A2) low-pH, (B2) normal-pH, (C2) high-pH, and (D2) glucose urine. (A2), (B2), (C2) Urinary stones are overlaid with yellow color for visualization. (D2) Solidified glucose residues are overlaid with green color for visualization.

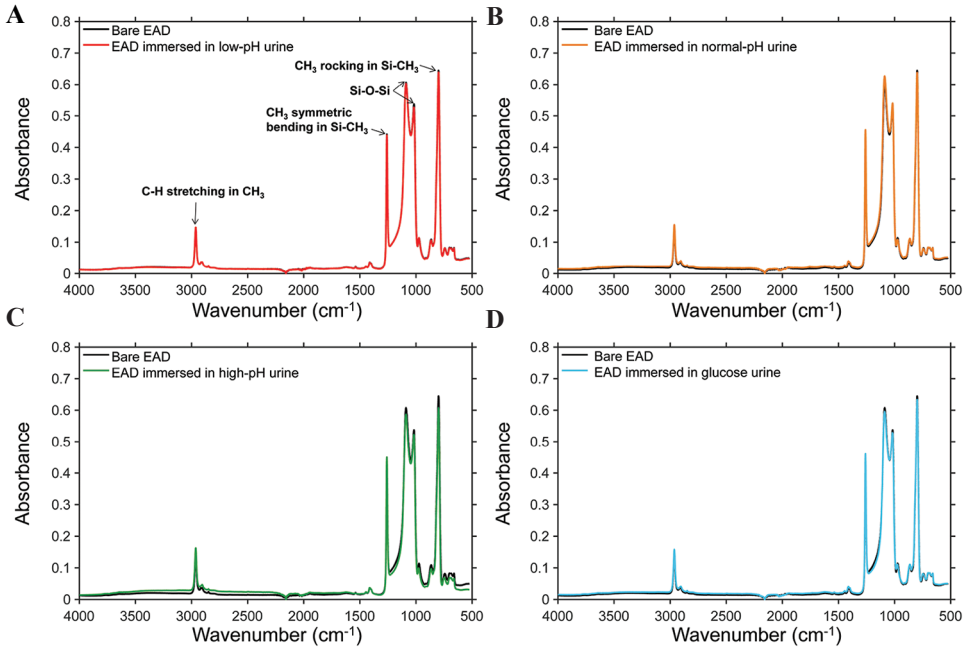


Figure 10. FTIR spectra of extraluminal anti-reflux diodes before and after immersion in (A) low-pH urine, (B) normal-pH urine, (C) high-pH urine, and (d) glucose urine for 4 weeks.

799.8 cm^{-1}, which represented C-H stretching in CH_3, CH_3 symmetrical bending in Si-CH_3, asymmetric stretching of Si-O-Si, symmetric stretching of Si-O-Si, and CH_3 rocking in Si-CH_3, respectively[51,52]. The FTIR peaks of the absorbance bands exactly overlapped with those of the EADs immersed in low-pH, normal-pH, high-pH, and glucose urine, as shown in **Figures 10A, B, C, and D**, respectively. This implied that the chemical structures of the Ecoflex EADs were not affected by urine[53]. These results also demonstrated that the fabricated EADs were mechanically and chemically stable, even after long-term soaking in urine. Therefore, it is noteworthy that the EADs are mechanically and chemically safe in the ureter line and reusable as long as they are washed with water.

4. Conclusion

In this study, anti-reflux devices based on an umbrella shape and with a DJ stent were successfully fabricated and demonstrated to prevent VUR and provide facile drainage. The working mechanisms are based on the change in the internal area of the EAD as it deforms under fluid pressure. To estimate the feasibility of the rectification performance through the EAD, a

computational simulation was conducted for forward and backward urine flows. Consequently, the difference in the cross-sectional pressure fields of the penta-shaped EAD could expand the canopy membrane along the rib structures of the EAD. For the fabrication of the EADs, 3D printing and casting methods were utilized. The printed PLA mold and die were tailored to create four different umbrella shapes with flexible and biocompatible Ecoflex. Among the fabricated devices, the penta-shaped EAD showed the best anti-reflux performance compared to the other types. The maximum anti-reflux efficiency was observed when the EAD was attached near the bladder-ureter junction, and an approximately 44% decrease in reflux was demonstrated in the ureter line using a voiding model. In addition, the anti-reflux efficiency did not show significant changes depending on the number of EADs attached to the DJ stent. Thus, a single EAD sufficed to minimize reflux of urine with minimal discomfort to patients. A disadvantage of the FDM-type 3D printer (i.e., rough surface with grooved patterns) was intentionally used for mechanically robust adhesion between the EAD and DJ stent. Finally, a long-term soaking test in artificial urine with different pH values was performed to demonstrate the safety, mechanical durability, and chemical stability of the device in urine for at least 4 weeks. Although *in vivo* and parametric studies on the length, shape, and thickness of the EAD are required to enhance the rectification performance, the findings of this study support the use of 3D printing methods to manufacture various medical devices with flexibility, biocompatibility, mechanical durability, and chemical stability for urological applications.

Funding

This work was supported by the National Research Foundation of Korea (NRF), funded by the Ministry of Science and ICT of the Republic of Korea (No. NRF-2021R1C1C1010836).

Conflict of interest

The authors declare that there is no conflict of interest.

Author contributions

J. L. Conceptualization, methodology, formal analysis, investigation, data curation, validation, visualization, writing - original draft, writing - review and editing. J. S. Conceptualization, methodology, investigation, data curation, validation, writing - review and editing. J. K. J. Conceptualization, methodology, formal analysis, investigation, supervision, writing - review and editing. H. S. Conceptualization, methodology, resources, supervision, writing - review and editing, funding acquisition.

References

1. Pengfei S, Min J, Jie Y, *et al*., 2011, Use of Ureteral Stent in Extracorporeal Shock Wave Lithotripsy for Upper Urinary Calculi: A Systematic Review and Meta-analysis. *J Urol*, 186:1328–35. https://doi.org/10.1016/j.juro.2011.05.073
2. Hübner WA, Plas EG, Trigo-Rocha F, *et al*., 1993, Drainage and Reflux Characteristics of Antireflux Ureteral Double-J Stents. *J Endourol*, 7:497–9. https://doi.org/10.1089/end.1993.7.497
3. Dyer RB, Chen MY, Zagoria RJ, *et al*., 2002, Complications of Ureteral Stent Placement. *Radiographics*, 22:1005–22. https://doi.org/10.1148/radiographics.22.5.g02se081005
4. Irani J, Siquier J, Pirès C, *et al*., 1999, Symptom Characteristics and the Development of Tolerance with Time in Patients with Indwelling Double-pigtail Ureteric Stents. *BJU Int*, 84:276–9. https://doi.org/10.1046/j.1464-410x.1999.00154.x
5. Auge BK, Preminger GM, 2002, Ureteral stents and their use in endourology. *Curr Opin Urol*, 12:217–22. https://doi.org/10.1097/00042307-200205000-00007
6. Sarier M, Demir M, Duman I, *et al*., 2017, Evaluation of Ureteral Stent Colonization in Live-Donor Renal Transplant Recipients. *Transplant Proc*, 49:415–9. https://doi.org/10.1016/j.transproceed.2017.01.004
7. Sarier M, Seyman D, Tekin S, *et al*., 2017, Comparision of Ureteral Stent Colonization Between Deceased and Live Donor Renal Transplant Recipients. *Transplant Proc*, 49:2082–5. https://doi.org/10.1016/j.transproceed.2017.09.028
8. Kim HH, Kim KW, Choi YH, *et al*., 2020, Numerical Analysis of Urine Flow with Multiple Sizes of Double-J Stents. *Appl Sci*, 10:4291. https://doi.org/10.3390/app10124291
9. Seymour H, Patel U, 2000, Ureteric Stenting-current Status. *Semin Intervent Radiol*, 17:351–65. https://doi.org/10.1055/s-2000-13148
10. Damiano R, Oliva A, Esposito C, *et al*., 2002, Early and Late Complications of Double Pigtail Ureteral Stent. *Urol Int*, 69:136–40. https://doi.org/10.1159/000065563
11. Leibovici D, Cooper A, Lindner A, *et al.*, 2005, Ureteral Stents: Morbidity and Impact on Quality of Life. *Isr Med Assoc J*, 7:491–4.
12. Al-Marhoon MS, Shareef O, Venkiteswaran KP, 2012, Complications and Outcomes of JJ Stenting of the Ureter in Urological Practice: A Single-centre Experience. *Arab J Urol*, 10:372–7.

https://doi.org/10.1016/j.aju.2012.08.004

13. Joshi HB, Okeke A, Newns N, *et al*., 2002, Characterization of Urinary Symptoms in Patients with Ureteral Stents. *Urology*, 59:511–6. https://doi.org/10.1016/s0090-4295(01)01644-2
14. de la Cruz JE, Fernández I, Sanz-Migueláñez JL, *et al*., 2021, Assessment of the Grades of Vesicoureteral Reflux in Stented Ureters: An Experimental Study. *Urol Int*, 105:554–9. https://doi.org/10.1159/000515613
15. Ritter M, Krombach P, Knoll T, *et al*., 2012, Initial Experience with a Newly Developed Antirefluxive Ureter Stent. *Urol Res*, 40:349–53. https://doi.org/10.1007/s00240-011-0415-5
16. Cummings LJ, Waters SL, Wattis JAD, *et al*., 2004, The Effect of Ureteric Stents on Urine Flow: Reflux. *J Math Biol*, 49:56–82. https://doi.org/10.1007/s00285-003-0252-4.
17. Vahidi B, Fatouraee N, 2012, A Biomechanical Simulation of Ureteral Flow During Peristalsis using Intraluminal Morphometric Data. *J Theor Biol*, 298:42–50. https://doi.org/10.1016/j.jtbi.2011.12.019
18. Peters C, Rushton HG, 2010, Vesicoureteral Reflux Associated Renal Damage: Congenital Reflux Nephropathy and Acquired Renal Scarring. *J Urol*, 184:265–73. https://doi.org/10.1016/j.juro.2010.03.076
19. Chew BH, Lange D, 2016, Advances in Ureteral Stent Development. *Curr Opin Urol*, 26:277–82. https://doi.org/10.1097/MOU.0000000000000275
20. Chew BH, Seitz C, 2016, Impact of Ureteral Stenting in Ureteroscopy. *Curr Opin Urol*, 26:76–80. https://doi.org/10.1097/MOU.0000000000000234
21. Park CJ, Kim HW, Jeong S, *et al*., 2015, Anti-reflux Ureteral Stent with Polymeric Flap Valve using Three-dimensional Printing: An in vitro Study. *J Endourol*, 29:933–8. https://doi.org/10.1089/end.2015.0154
22. Korkes F, Baccaglini W, Silveira MA, 2019, Is Ureteral Stent an Effective Way to Deliver Drugs Such as Bacillus Calmette-Guérin to the Upper Urinary Tract? An experimental study, *Ther Adv Urol*, 11:1–7. https://doi.org/10.1177/1756287219836895
23. Yamaguchi O, Yoshimura Y, Irisawa C, *et al.*, 1992, Prototype of a Reflux-preventing Ureteral Stent and its Clinical Use. *Urology*, 40:326–9. https://doi.org/10.1016/0090-4295(92)90381-6
24. Clavica F, Zhao X, ElMahdy M, *et al*., 2014, Investigating the Flow Dynamics in the Obstructed and Stented Ureter by Means of a Biomimetic Artificial Model. *PLoS One*, 9:e87433. https://doi.org/10.1371/journal.pone.0087433
25. Kim HW, Park CJ, Seo S, *et al*., 2016, Evaluation of a Polymeric Flap Valve-attached Ureteral Stent for Preventing Vesicoureteral Reflux in Elevated Intravesical Pressure Conditions: A Pilot Study Using a Porcine Model. *J Endourol*, 30:428–32. https://doi.org/10.1089/end.2015.0711
26. Liu Z, Liu N, Zhao C, *et al*., 2020, Preliminary Assessment of the Effectiveness of an Anti-reflux Ureteral Stent with a Novel Device in a Swine Model. *Int J Clin Exp Med*, 13:141–7.
27. Ecke TH, Bartel P, Hallmann S, *et al.*, 2010, Evaluation of Symptoms and Patients' Comfort for JJ-ureteral Stents With and Without Antireflux-membrane Valve. *Urology*, 75:212–6. https://doi.org/10.1016/j.urology.2009.07.1258
28. Urrios A, Parra-Cabrera C, Bhattacharjee N, *et al*., 2016, 3D-printing of Transparent Bio-microfluidic Devices in PEG-DA. *Lab Chip*, 16:2287–94. https://doi.org/10.1039/c6lc00153j
29. Schweiger J, Beuer F, Stimmelmayr M, *et al*., 2016, Histo-anatomic 3D Printing of Dental Structures. *Br Dent J*, 221:555–60. https://doi.org/10.1038/sj.bdj.2016.815
30. Jeong YG, Lee WS, Lee KB, 2018, Accuracy Evaluation of Dental Models Manufactured by CAD/CAM Milling Method and 3D Printing Method. *J Adv Prosthodont*, 10:245–51. https://doi.org/10.4047/jap.2018.10.3.245
31. Yoshikawa M, Sato R, Higashihara T, *et al*., 2015, Rehand: Realistic Electric Prosthetic Hand Created with a 3D Printer. *Proc Annu Int Conf IEEE Eng Med Biol Soc*, 2015:2470–3. https://doi.org/10.1109/EMBC.2015.7318894
32. Burn MB, Ta A, Gogola GR, 2016, Three-dimensional Printing of Prosthetic Hands for Children. *J Hand Surg Am*, 41:e103–9. https://doi.org/10.1016/j.jhsa.2016.02.008
33. Del Junco M, Okhunov Z, Yoon R, *et al*., 2015, Development and Initial Porcine and Cadaver Experience with Three-dimensional Printing of Endoscopic and Laparoscopic Equipment. *J Endourol*, 29:58–62. https://doi.org/10.1089/end.2014.0280
34. He Y, Xue GH, Fu JZ, 2014, Fabrication of Low Cost Soft Tissue Prostheses with the Desktop 3D Printer. *Sci Rep*, 4:1–7. https://doi.org/10.1038/srep06973
35. Bégin-Drolet A, Dussault MA, Fernandez SA, *et al*., 2017, Design of a 3D Printer Head for Additive Manufacturing of Sugar Glass for Tissue Engineering Applications. *Addit Manuf*, 15:29–39. https://doi.org/10.1016/j.addma.2017.03.006
36. Salentijn GI, Oomen PE, Grajewski M, *et al*., 2017, Fused

Deposition Modeling 3D Printing for (Bio)analytical Device Fabrication: Procedures, Materials, and Applications. *Anal Chem*, 89:7053–61. https://doi.org/10.1021/acs.analchem.7b00828

37. Skowyra J, Pietrzak K, Alhnan MA, 2015, Fabrication of Extended-release Patient-Tailored Prednisolone Tablets Via Fused Deposition Modelling (FDM) 3D Printing. *Eur J Pharm Sci*, 68:11–7. https://doi.org/10.1016/j.ejps.2014.11.009
38. He Y, Wu Y, Fu JZ, *et al*., 2016, Developments of 3D Printing Microfluidics and Applications in Chemistry and Biology: A Review. *Electroanalysis*, 28:1658–78. https://doi.org/10.1002/elan.201600043
39. Lalehpour A, Janeteas C, Barari A, *et al*., 2018, Surface Roughness of FDM Parts After Post-processing with Acetone Vapor Bath Smoothing Process. *Int J Adv Manuf Technol*, 95:1505–20. https://doi.org/10.1007/s00170-017-1165-5
40. Kang B, Sung J, So H, 2021, Realization of Superhydrophobic Surfaces Based on Three-Dimensional Printing Technology. *Int J Precis Eng Manuf Green Technol*, 8:47–55. https://doi.org/10.1007/s40684-019-00163-9
41. Park S, Ko B, Lee H, *et al*., 2021, Rapid Manufacturing of Micro-drilling Devices using FFF-Type 3D Printing Technology. Sci Rep, 11.1-9. https://doi.org/10.1038/s41598-021-91149-8
42. He Y, Qiu J, Fu J, *et al*., 2015, Printing 3D Microfluidic Chips with a 3D Sugar Printer, *Microfluid Nanofluidics*, 19:447–56. https://doi.org/10.1007/s10404-015-1571-7
43. Sung J, So H, 2021, 3D Printing-assisted Fabrication of Microgrid Patterns for Flexible Antiadhesive Polymer Surfaces. *Surf Interfaces*. 23:100935. https://doi.org/10.1016/j.surfin.2021.100935
44. Amjadi M, Yoon YJ, Park I, 2015, Ultra-stretchable and Skin-mountable Strain Sensors using Carbon Nanotubes-ecoflex Nanocomposites. *Nanotechnology*, 26:375501. https://doi.org/10.1088/0957-4484/26/37/375501
45. Ghassami E, Varshosaz J, Jahanian-Najafabadi A, *et al*., 2018, Pharmacokinetics and in vitro/*In Vivo* Antitumor Efficacy of Aptamer-targeted Ecoflex® Nanoparticles for Docetaxel Delivery in Ovarian Cancer. *Int J Nanomed*, 13:493–504. https://doi.org/10.2147/IJN.S152474
46. Chen CC, Chueh JY, Tseng H, *et al*., 2003, Preparation and Characterization of Biodegradable PLA Polymeric Blends. *Biomaterials*, 24:1167–73. https://doi.org/10.1016/s0142-9612(02)00466-0
47. Chuensangjun C, Pechyen C, Sirisansaneeyakul S, 2013, Degradation Behaviors of Different Blends of Polylactic Acid Buried in Soil. *Energy Proc*, 34:73–82. https://doi.org/10.1016/j.egypro.2013.06.735
48. Erokhin KS, Gordeev EG, Ananikov VP, 2019, Revealing Interactions of Layered Polymeric Materials at Solid-liquid Interface for Building Solvent Compatibility Charts for 3D Printing Applications. *Sci Rep*, 9:20177. https://doi.org/10.1038/s41598-019-56350-w
49. Yashima S, Takase N, Kurokawa T, *et al*., 2014, Friction of Hydrogels with Controlled Surface Roughness on Solid Flat Substrates. *Soft Matter*, 10:3192–9. https://doi.org/10.1039/c3sm52883a
50. Kaler KS, Lama DJ, Safiullah S, *et al*., 2019, Ureteral Access Sheath Deployment: How Much Force is Too Much? Initial Studies with a Novel Ureteral Access Sheath Force Sensor in the Porcine Ureter. *J Endourol*, 33:712–8. https://doi.org/10.1089/end.2019.0211
51. Lancastre JJ, Fernandes, N, Margaça FM, *et al*., 2012, Study of PDMS Conformation in PDMS-based Hybrid Materials Prepared by Gamma Irradiation. *Radiat Phys Chem*, 81:1336–40. https://doi.org/10.1016/j.radphyschem.2012.02.016
52. Lee J, Kim J, Kim H, *et al*., 2013, Effect of Thermal Treatment on the Chemical Resistance of Polydimethylsiloxane for Microfluidic Devices. *J Micromech Microeng*, 23:035007. https://doi.org/10.1088/0960-1317/23/3/035007
53. Zhao Y, Zhu B, Wang Y, *et al*., 2019, Effect of Different Sterilization Methods on the Properties of Commercial Biodegradable Polyesters for Single-use, Disposable Medical Devices. *Mater Sci Eng C*, 105:110041. https://doi.org/10.1016/j.msec.2019.110041

Publisher's note

Whioce Publishing remains neutral with regard to jurisdictional claims in published maps and institutional affiliations.

RESEARCH ARTICLE

Fabrication of Microstructured Calcium Phosphate Ceramics Scaffolds by Material Extrusion-Based 3D Printing Approach

Peifang Dee[1,2], Sharlene Tan[1], Hortense Le Ferrand[1,2,3]*

[1]School of Mechanical and Aerospace Engineering, Nanyang Technological University, Singapore 639798, Singapore
[2]Singapore Centre for 3D Printing, Nanyang Technological University, Singapore 639798, Singapore
[3]School of Materials Science and Engineering, Nanyang Technological University of Singapore, 50 Nanyang Avenue, Singapore 639798, Singapore

Abstract: Natural materials such as bone and enamel have intricate microstructures with inorganic minerals oriented to perform multiple mechanical and biological functions. Current additive manufacturing methods for biominerals from the calcium phosphate (CaP) family enable fabrication of custom-shaped bioactive scaffolds with controlled pore structures for patient-specific bone repair. Yet, these scaffolds do not feature intricate microstructures similar to those found in natural materials. In this work, we used direct material extrusion to 3D print water-based inks containing CaP microplatelets, and obtained microstructured scaffolds with various designs. To be shear-thinning and printable, the ink incorporated a concentration of 21 – 24 vol% CaP microplatelets of high aspect ratio. Good shape retention, print fidelity and overhanging layers were achieved by simultaneous printing and drying. Combined with the 3D design, versatile CaP microstructured objects can be built, from porous scaffolds to bulk parts. Extruded filaments featured a core-shell microstructure with graded microplatelet orientations, which was not affected by the printing parameters and the print design. A simple model is proposed to predict the core-shell microstructure according to the ink rheology. Given the remaining open porosity after calcination, microstructured scaffolds could be infiltrated with an organic phase in future to yield CaP biocomposites for hard tissue engineering.

Keywords: Robocasting; Calcium phosphate; Microstructure

*Correspondence to: Le Ferrand Hortense, School of Mechanical and Aerospace Engineering, Nanyang Technological University, Singapore 639798, Singapore; hortense@ntu.edu.sg

Received: December 23, 2021; **Accepted:** February 26, 2022; **Published Online:** February 26, 2022

Citation: Dee P, Tan S, Le Ferrand H., 2022, Fabrication of Microstructured Calcium Phosphate Ceramics Scaffolds by Material Extrusion-Based 3D Printing Approach. *Int J Bioprint,* 8(2):551. http://doi.org/10.18063/ijb.v8i2.551

1. Introduction

Natural materials such as bone and enamel possess highly complex microstructures featuring calcium phosphate (CaP) rods or platelets oriented in multiple directions[1,2]. These complex microstructural patterns are thought to contribute to the outstanding mechanical and functional properties of these natural materials[3,4]. In bone, for example, the local alignment of CaP anisometric nanoplatelets in an organic phase results in a combination of toughening mechanisms that increase crack resistance and prevent brittle fracture[4]. Indeed, using the tension-shear chain model, fracture mechanics theoretically predicts that high aspect ratio CaP platelets with nanoscale thickness do not break, but experience pull-out from the protein-matrix[3]. At present, numerous bone repair materials have been developed, including bioactive glasses, hydroxyapatite composites, bone cements, and polymers[5-7]. Among these, CaP-based scaffolds are promising due to similar chemical composition with natural bone. Furthermore, additive manufacturing, also called three-dimensional (3D) printing, is now extensively used to fabricate 3D scaffolds enabling vascularization, cell invasion, and bone growth[8,9]. However, these synthetic bone implant materials lack the complex microstructures

© 2022 Author(s). This is an Open-Access article distributed under the terms of the Creative Commons Attribution License, permitting distribution and reproduction in any medium, provided the original work is properly cited.

found on their natural counterparts[10,11]. Developing 3D printed CaP scaffolds with a complex microstructure could induce more biomimetic properties. For example, the microstructure could be designed to increase crack resistance and impart anisotropic mechanical properties to CaP scaffolds. Therefore, new 3D printing strategies are needed to allow the fabrication of CaP materials with controlled shape and design as well as an internal microstructure.

Conventional fabrication methods to synthesize microstructured CaP include biotemplating, freeze-casting, and lamination. In biotemplating, natural porous microstructured materials such as cuttlefish bone[12] or rattan wood[13-16] are decellularized then remineralized with CaP by a hydrothermal treatment. Through this way, the original porous hierarchical microstructure of the natural material is preserved in the synthetic material. In freeze-casting, also called ice-templating, the microstructure is induced by the directional growth of ice dendrites during freezing[17-19]. When subjecting slurries containing ceramic particles to freeze-casting, the growing ice dendrites push and shear the particles, leading to the increase in local packing of particles. When the particles are anisometric, self-assembly and particle alignment are also reported[20]. After removing the ice dendrites by sublimation, a lamellar ceramic scaffold with elongated pores oriented in desired directions is obtained. This method can be combined with external fields or temperature gradients to control the microstructure and shape. For example, bidirectional freezing of a hydroxyapatite suspension produced a biomimetic, nacre-like microstructure with enhanced mechanical properties[21]. Besides, microstructured CaP materials can be built using lamination from sheets of CaP platelets or whiskers. For example, a nacre-like composite was made by laminating alginate films containing CaP microplatelets[22]. A twisted plywood or Bouligand microstructure could also be made using CaP microfibers, leading to significant enhancement in the toughness of the composite[23]. Unfortunately, these methods are not yet easily compatible with 3D printing, which is required to provide patient-adapted shapes and tunable designs of internal pore structures[10,24].

3D printed CaP scaffolds have demonstrated promising osteogenic ability for bone tissue engineering and research has been growing[10,24]. In particular, direct material extrusion (or robocasting) and indirect vat photopolymerization-based techniques have been the most extensively used for CaPs. In an interesting example which applied photopolymerization after material extrusion with cell seeding, an ultraviolet (UV)-curable hydrogel scaffold was bioprinted with only up to 30 wt% nanocrystalline CaPs formed by *in situ* precipitation, which contributed to the scaffold's compressive strength through electrostatic interaction with the polymers and were not cytotoxic to fibroblasts[25]. Although there has been no 3D printed microstructured CaP scaffolds, 3D printing of other microstructured ceramics have been reported, often using alumina microplatelets of high aspect ratio. Digital light processing (DLP) was used to create various architectures from alumina microplatelets suspended in a UV-curable resin using magnetic alignment[26]. The alumina microplatelets were pre-coated with iron oxide nanoparticles so that the microplatelet orientation could be controlled by magnetic fields applied during DLP. While the local control over the alumina microstructure was precise, the composite had a low mineral content of only 15 vol%)[26]. Alternatively, direct extrusion of alumina microplatelets was used to induce alignment by shear[27,28]. Alumina filaments with a core-shell microstructure were robocast to form a twisted plywood structure[27]. The pluronic-based gel containing 31 vol% alumina microplatelets and microparticles produced green bodies with 36 vol% residual porosity after drying and isostatic pressing[27]. Higher sintering temperatures could further reduce the final porosity through templated grain growth, whereby the surrounding alumina nanoparticles enhanced grain growth and densification of the aligned alumina platelets without affecting the microstructure[28,29]. While vat photopolymerization-based approaches such as DLP achieve higher resolution and better surface finish than direct extrusion[10,30], the volume fraction of particles which can be suspended in the photocurable resin is limited by the increase in viscosity. In vat photopolymerization, the low ceramic content makes printed parts prone to cracking and shrinkage during debinding and sintering[10,30]. Direct material extrusion, on the other hand, can yield higher concentrations of solid particles in the green body. Continuous filament extrusion could therefore be applied to an ink composition containing anisometric CaP minerals with the microstructure controlled using shear stresses. Along with the microstructure, controllable macroscopic porosity as found in conventional bone scaffolds would also be required in 3D printed structures to allow vascularization and cell invasion. Such porous structures have not been reported with the microstructured alumina printing.

In this work, we 3D print microstructured CaP parts by direct ink writing (DIW), based on line-by-line material extrusion. The microstructure is created by orienting synthesized brushite ($CaHPO_4 \cdot 2H_2O$) microplatelets suspended in a water-based ink using shear stresses that develop in the printing nozzle. The ink is designed to allow simultaneously efficient particle alignment and high solid loading after printing, of about 23 vol%. The strategy to create complex shapes is to simultaneously dry while depositing the ink onto a porous gypsum substrate that sucks out water from the deposited ink through capillary

forces. The CaP parts could later be consolidated with the microstructure retained by calcination at a temperature lower than the sintering temperature. First, we study the rheological properties of aqueous inks at various solid loadings of brushite and assess the printability to obtain a good print resolution. Then, we analyze the microstructure of extruded filaments and use a simple model to relate the microstructure to the rheology of the ink. Finally, we demonstrate that complex, porous or bulk 3D shapes can be obtained with our approach, such as scaffolds or bone plates. This work is anticipated to be of interest for fabricating patient-adapted implants with more biomimetic microstructure to enable enhanced properties. Future work could tackle infiltration of the 3D printed CaP scaffolds with a biomimetic polymeric matrix to study the mechanical properties and the cellular response.

2. Materials and methods

2.1. Synthesis and characterization of brushite microplatelets

Brushite microplatelets were prepared using a method described by Gao *et al*.[22] and Mandel and Tas[31]. Briefly, 6.062 g of calcium chloride ($CaCl_2$) (anhydrous, ≥97%, Sigma) dissolved in 0.4 L of deionized water was rapidly added to a beaker with 1.650 g of potassium dihydrogen phosphate (KH_2PO_4) (anhydrous, ≥99% ACS, VWR Chemicals, Singapore) and 6.026 g of disodium hydrogen phosphate (Na_2HPO_4) (anhydrous, ≥99% ACS, VWR Chemicals, Singapore) dissolved in 1.4 L of deionized water. After stirring at room temperature for 1 h, the white precipitate was collected by vacuum filtration and dried in a 45°C oven for 2 days. 6.062 g $CaCl_2$ in 1.8 L reaction mixture produced a yield of ~7.0 g brushite. The synthesis is easily scalable, with a yield of ~10.6 g brushite collected from 2.7 L reaction mixture using 9.093 g $CaCl_2$. The powder was stored in a dry box until use.

The synthesized powder was sputtered with gold and examined under a field emission scanning electron microscope (SEM) (JEOL 6340F) to determine its dimensions. The powder was grinded using mortar and pestle and characterized using powder X-ray diffraction (XRD) with Bragg-Brentano geometry (Panalytical X'Pert Pro, Cu K_α 0.1541874 nm, scanning range 2θ from 10° to 60°, step size 0.017°). The scanned material was checked against the PDF-4+ database (2021) using Match! (version 3.6, Crystal Impact). Reference CIF files obtained from the Inorganic Crystal Structure Database (ICSD, FIZ Karlsruhe) was used for analysis in TOPAS (version 6, Bruker AXS). Energy dispersive spectroscopy (EDS) was performed on coated powder in a thermionic SEM (JEOL 5500LV) with Oxford Inca 200 detector, 20 kV accelerating voltage) to measure the calcium/phosphorus atomic ratio.

2.2. Preparation and characterization of the brushite ink

The aqueous brushite ink consisted of various volume fraction Φ of brushite microplatelets, an anionic surfactant Dolapix CE 64 (Zschimmer & Schwarz, Germany) as the dispersant, and polyvinylpyrrolidone (PVP) of average molecular weight ~360,000 (Sigma-Aldrich) as the binder. Synthesized brushite powder was slowly added to deionized water containing 0.1 wt% Dolapix CE 64 with respect to brushite, frequently mixing with vortex and probe sonicator (Bandelin), resting 2 s between every 1 s of low amplitude ultrasonic pulse to prevent overheating. 20 w/v% PVP stock solution was added to the suspension to give a final concentration of 7 w/v% PVP with respect to water. The brushite ink was homogenized by mixing with vortex and probe sonicator before use.

The rheological properties of the inks were measured using a rheometer (Bohlin, Malvern Instruments) and 15 mm serrated plates. All measurements were performed at room temperature with a gap of 1000 μm. An amplitude sweep from 0.1 Pa to 1000 Pa was carried out in oscillatory mode at 1 s^{-1}. Rotational measurements were carried out from 0.01 s^{-1} to 100 s^{-1}. All measurements were repeated at least three times.

2.3. Drying of brushite ink

The possibility of drying extruded brushite inks by solvent removal through a water-absorbent print substrate was studied using gypsum, also known as plaster of Paris. Gypsum is an abundant, safe, and easily moldable material. Gypsum was prepared by mixing 6 parts water to every 10 parts gypsum casting powder (Cera-Mix Standard Plaster Casting Compound) by weight. To obtain a flat gypsum substrate, the gypsum slurry was cast onto a non-stick surface and mechanically smoothed at the top by pressing with a flat surface while wet, then left overnight to set.

A 5 μL droplet of 21 vol% brushite ink was deposited on the gypsum slab with a micropipette. A digital microscope (Dino-Lite Edge AM7915MZTL) was used to record videos of the droplet drying on the gypsum substrate. The droplet size and contact angle were measured from the video snapshots using ImageJ. The experiment took place at an ambient temperature of ~22°C and relative humidity ~74%.

2.4. Direct material extrusion of brushite

For 3D printing, the brushite ink was filled into a 10 mL Luer-lock syringe (Terumo) of inner diameter 14.3 mm. Cone-shaped polyethylene nozzles (Nordson EFD Optimum SmoothFlow) were used. The syringe was fitted to a clay printer (3D Potterbot Micro 8, USA) using a custom adapter to enable mechanical extrusion of

filaments by pushing the plunger down, and the plunger speed was measured. The printer stage moved in the $-x$ direction at the printing speed v. To print the first layer, the nozzle tip was set at 0.6 mm (z_1) above the print substrate. The nozzle tip moved up by 0.5 mm (z_2) every subsequent layer. A spirit level was used to ensure the print substrate was level. The setup is shown in **Figure 1** and the printing parameters are described in **Table 1**.

When building structures taller than 3 mm, a hot plate may be secured on the printer stage directly under the print substrate to enable quick drying of the water-based ink during printing. The print substrate surface was heated to 85 – 95°C.

2.5. Post-processing of 3D printed parts and chemical characterization

The printed parts were left to dry in ambient conditions overnight before detaching them from the gypsum substrate from one edge by sliding in a sharp blade.

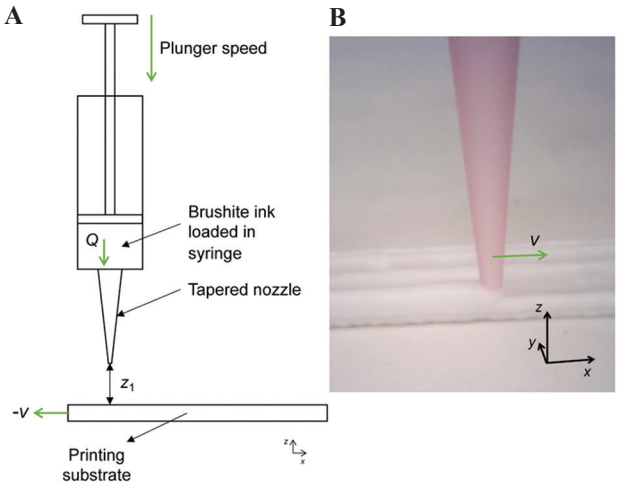


Figure 1. (A) 3D printing setup and parameters, as described in **Table 1.** (B) Close-up photograph near the nozzle tip (d = 0.58 mm).

Alternatively, elective pre-treatment in a 200°C oven for 4 h may be performed before detaching the print from the substrate. The green parts underwent debinding at 500°C for 2 h and calcination at 900°C for 6 h in a box furnace (Nabertherm, Germany) using a heating ramp of 5°C/min. The samples were left to cool in the furnace to prevent cracking during shrinkage. To determine the crystallographic phase transformation of the CaP after calcination, the material was crushed into powder and analyzed by XRD using the same procedure as previously described in section **2.1**.

2.6. Characterization of the prints

Cross-section surfaces of calcined parts exposed by brittle fracture were observed under thermionic SEM (JEOL 5500LV) after coating with gold. Alternatively, calcined parts were embedded in resin and polished to examine the microstructure under the SEM. The microplatelet orientations in the prints were determined by image analysis using ImageJ v1.53g.

3. Results and discussion

3.1. 3D printing approach

Our 3D printing approach (**Figure 2**) utilizes CaP microplatelets of high aspect ratio suspended in an aqueous slurry, which is extruded onto a porous water-absorbent substrate for drying and consolidation. The bioceramic chosen in the water-based ink is brushite ($CaHPO_4 \cdot 2H_2O$), a type of CaP also known as dicalcium phosphate dihydrate (DCPD). Brushite microplatelets can be synthesized in scalable quantities and yield a bioresorbable material, calcium pyrophosphate, after calcination[32] (**Supplementary file: Section 1.1** for details about the crystallographic phase). Here, the aspect ratio of the synthesized brushite was large, with microplatelets of ~10 μm length and ~13.8 nm

Table 1. Printing parameters descriptions and settings used

Printing parameter	Description	Settings used
Q	Volumetric flow rate of ink extrusion	Plunger speed multiplied by the cross-sectional area of the syringe
d	Inner diameter of nozzle tip	0.41, 0.58, 0.84, 1.19, and 1.60 mm
f	Multiplier for ink flow rate Q	500 and 800%
v	Speed of nozzle relative to the printing substrate in the x-direction	1, 5, and 10 mm/s
I_f	Infill density controlling how densely the part volume is filled with ink	30%, 50%, 70%, and 90%
Extrusion width	Multiplier for extruded filament width	Fixed at 100%
z_1	Initial stand-off distance of nozzle tip above printing substrate	0.6 mm (first layer)
z_2	Height increment of nozzle tip	Fixed at 0.5 mm (subsequent layers)

thickness (see **Supplementary file: Section 1.2**). These dimensions were chosen because microplatelets with nanoscopic thickness are thought to be optimal to achieve platelet pull-out instead of brittle fracture in bioinspired microstructured composites[3]. The ink solvent was water to allow good dispersion and high concentration of brushite microplatelets. An anionic surfactant was used as dispersant and PVP was used as the binder to strengthen the green part after drying. The printed parts were dried overnight before calcination at 900°C for a dwell time of 6 h to yield a stiff, consolidated part. The arrangement of microplatelets within the printed filaments remained intact as the low calcination temperature of 900°C prevented necking and shrinkage, while ensuring complete phase transformation into β-calcium pyrophosphate (β-CPP, $Ca_2P_2O_7$)[32] (**Supplementary file: Section 1.1**). After printing, drying, and calcinating, the CaP material has a relative density of about 23 vol%.

The key to enabling extrusion at the nozzle, microstructuring and high relative density in the final material resides in the optimization of the brushite solid content in the ink, whereas the realization of complex, 3D shapes is governed by the fast drying of the ink on the porous substrate. How to determine the ink composition and its printability are detailed in the following section.

3.2. Rheology and printability of brushite inks

The rheological properties of inks were tested to determine the required brushite solid loading Φ (**Figure 3**). The primary property that had to be achieved is flowability to enable extrusion through a nozzle. To this aim, brushite inks with solid loadings from 16 to 27 vol% were tested in viscometry (**Figure 3A**). As expected, the apparent viscosity of the inks increased with the concentration of brushite. In particular, the ink with 27 vol% brushite was paste-like, with an increased viscosity at rest of 600 Pa·s (see **Supplementary file: Section 2**). Furthermore, the ink gradually shifted from a zero-shear viscosity profile at lower solid loadings to a yield stress profile at the highest solid loading of Φ = 27 vol% (**Figure 3A**). The inks were modeled as Herschel-Bulkley fluids and their flow profiles from 10 s^{-1} to 100 s^{-1} were fitted with:

$$\tau = \tau_y + K\gamma^n \tag{3.1}$$

where τ is the shear stress (Pa), τ_y the yield stress (Pa), the shear rate (s^{-1}), K the consistency index and n the flow index[28,33]. All inks had a flow index $n < 1$, confirming their shear-thinning properties, which is necessary for the extrusion (**Figure 3B**). Also as expected, the consistency increased with solid loading, denoting less fluidity as more brushite particles are loaded in the ink. These data suggest that all inks can be extruded through a nozzle. However, a yield stress of 100 ~ 800 Pa is typically reported as one of the printability criteria for extruded filaments to support their own weight and avoid sagging[34]. From Equation 3.1, only the ink containing 27 vol% CaP microplatelets exhibits a yield stress. Another important rheological property is the stiffness of the ink at rest indicated by G'_{eq}, which is the plateau value of the storage modulus before the yield point[28,34]. Printable ceramic inks typically have G'_{eq} at rest ranging from 25 to 200 kPa and a damping factor at rest G''_{eq}/G'_{eq} ranging from 0.1 to 0.3[34]. These properties are key to realizing shape fidelity. The viscoelastic properties of brushite inks at various solid loadings were thus measured. In all of our brushite inks, liquid-like behavior generally dominated with damping factor $G''/G' > 1$, even for 27 vol% which

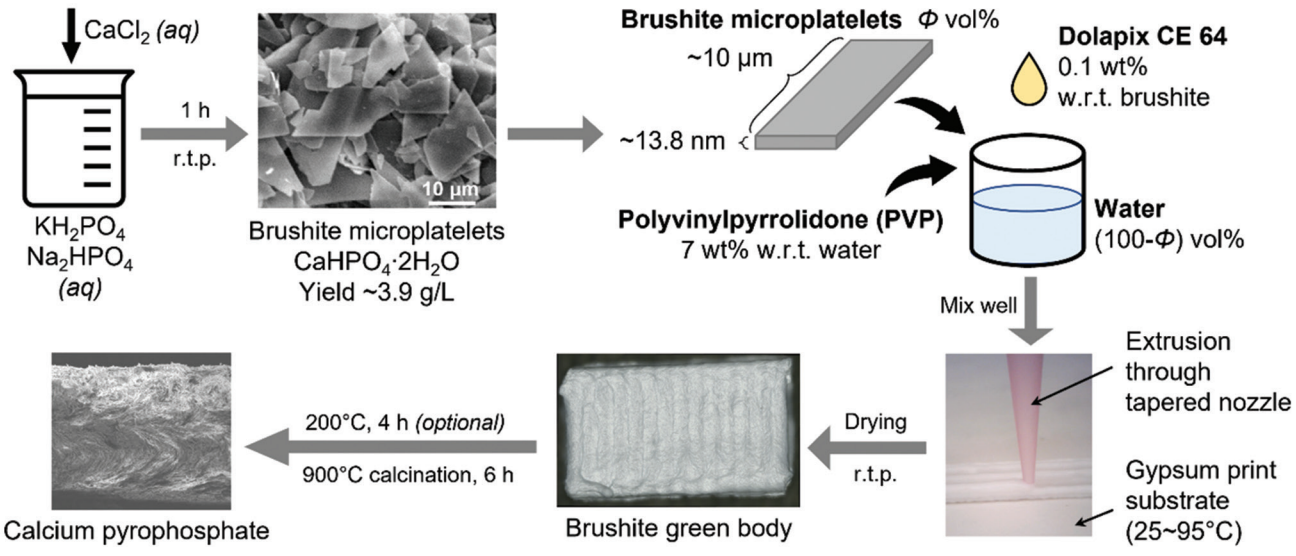


Figure 2. Schematic of the 3D printing strategy: scalable synthesis of brushite microplatelets of high aspect ratio loaded into an aqueous-based ink. The ink is 3D printed by direct extrusion onto porous substrate, before drying and calcination to yield a solid, microstructured part.

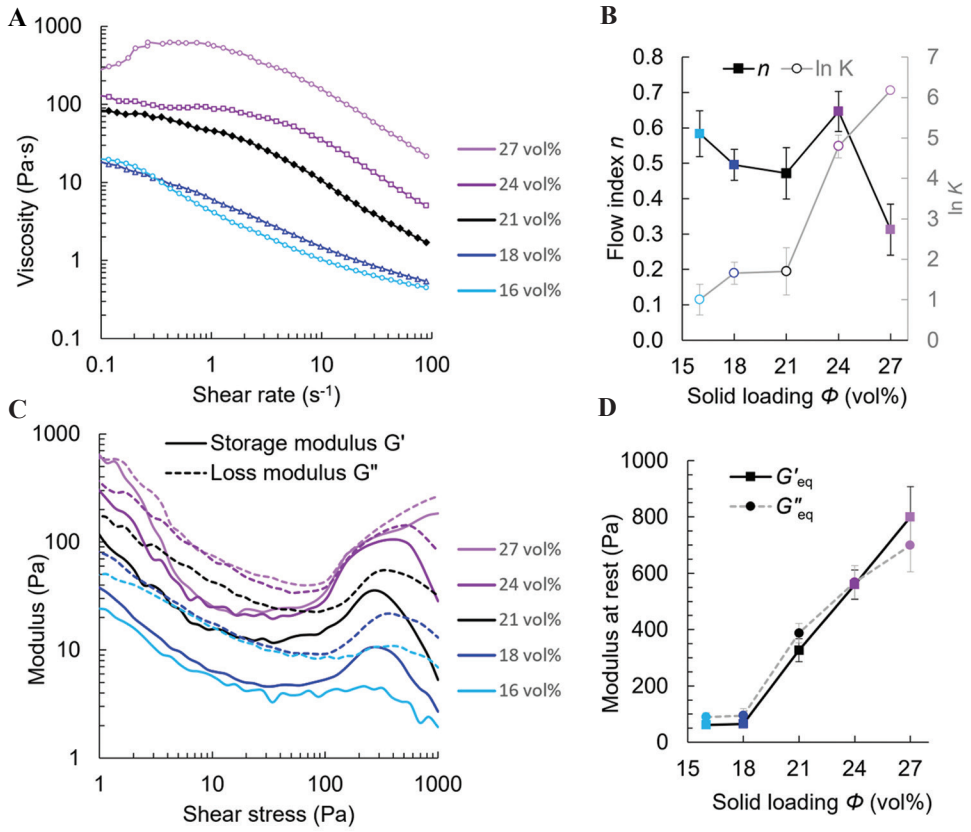


Figure 3. Rheological properties of brushite inks with solid loading Φ = 16 to 27 vol%. (A) Representative viscosity profile as a function of the shear rate. (B) Flow index n and ln K as a function of brushite solid loading. (C) Representative storage modulus G' and loss modulus G'' as a function of the shear stress. (D) G'_{eq} and G''_{eq} as a function of the brushite solid loading.

had a paste-like consistency (**Figure 3C**). The initial G'_{eq} at rest increased with Φ but remained below 1 kPa for all inks (**Figure 3D**). This suggests that none of the inks presents the rheological properties typically required for direct extrusion.

To overcome the absence of yield stress and the low stiffness of the inks, the printing strategy involves drying the ink as it is printed by using a porous print substrate. This approach is inspired from ceramic slip casting where a liquid slurry, generally water-based, is poured into a porous substrate that sucks out the water by capillary action[35]. Using the brushite ink with solid loading of 21 vol%, we demonstrated that drying is a good approach for shape retention and fidelity. The drying was carried out by placing a porous flat slab of gypsum, similar to those used in slip casting, as a water-absorbent print substrate. On extrusion onto the gypsum substrate, the water from the ink is rapidly absorbed by capillary action, increasing the solid loading of the printed filament and maintaining its shape, as illustrated with the droplet of 21 vol% brushite ink (**Figure 4A**). Furthermore, shape retention was achieved: on depositing the sessile droplet, the contact angle remained high at about 111 – 113°, while the droplet dries. The use of the gypsum substrate indeed restricts the spreading of liquid ink, thereby enabling shape fidelity. Besides, the drying of the ink droplets at ambient room temperature and >70% relative humidity typically leveled off after about half a minute, hence enabling sufficiently fast 3D printing of under one minute per layer.

Testing the inks of various solid loadings, we found that inks with $\Phi \leq 18$ vol% were not easily extrudable with uniform thickness and often produced discontinuous filaments (**Figure 4B**). We also found that the ink containing 27 vol% brushite tended to clog nozzles and exhibited more print defects compared to the other concentrations. 21 and 24 vol% brushite inks are therefore adequate. In the remainder of the paper, the brushite ink containing 21 vol% brushite will be used to study the microstructure development in the 3D printed scaffolds. The results can be extrapolated for the ink containing 24 vol% brushite, if needed.

3.3. Filament size and microstructure

(1) Filament shape fidelity and size

The microstructure in the 3D printed materials built from 21 vol% brushite ink was characterized after consolidating the print by calcination at 900°C. The effects of the print

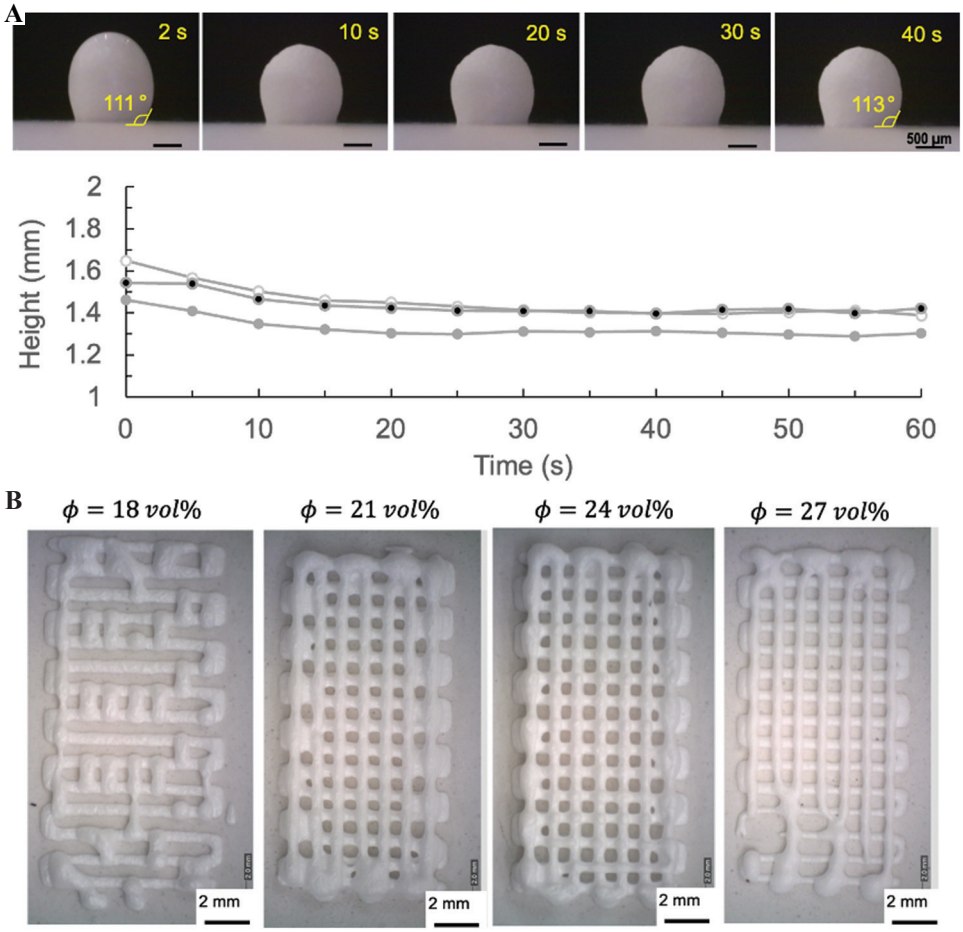


Figure 4. (A) Optical images showing the drying of a 5 µL droplet of 21 vol% brushite ink on gypsum substrate and measurement of the height of the droplets as a function of time. Contact angle remains almost unchanged during drying. Scale bar is the same on all images (0.5 mm). (B) Optical images of printed structures using the inks with various solid loadings at room temperature.

parameters on the shape fidelity and microstructure were first studied on single printed lines, which are also referred to as "filaments." Single filaments were extruded through nozzles of different sizes at a flow rate multiplier f = 500% or f = 800% and a printing speed v = 1 mm/s to 10 mm/s. The size of the nozzle was the primary parameter studied since it is known that the flow through a pipe is laminar and has a parabolic profile along the diameter of the pipe:

$$v(r) = v_c \cdot \left(1 - \left(\frac{r}{d}\right)^2\right) \quad (3.2)$$

where v is the flow in a pipe of diameter d, v_c is the flow at the center of the pipe and r is the position along the diameter. The flow rate multiplier was also tuned as it controlled the volume flow rate of the fluid through the nozzle, whereas the printing speed was maintained constant to allow for 3D printing of continuous lines. After calcination, filament cross-sections were examined under SEM to measure their dimensions and their microstructure (width, w, area of filament, A and area of filament core, C) (**Figure 5**). The shape of the cross-section of filaments extruded on gypsum typically resembled the outline of the ink droplet dried on gypsum shown in **Figure 4A**. A high contact angle and a round-like shape were obtained (**Figure 5A**). Looking at the cross-section, a core-shell microstructure appeared with a core region C showing disordered microplatelets, whereas the shell had microplatelets aligned along the border of the filament (**Figure 5A and B**).

The cross-section area of an extruded brushite filament is expected to exceed the area of the nozzle tip due to the pressure drop experienced by the ink on exiting the nozzle[36]. The cross-section area A of the calcined filament was observed to increase linearly with nozzle diameter d (**Figure 5C**). A also scales linearly with the flow rate f. In addition, the final filament width w was found to have a linear relationship with $\sqrt{d \times f}$ (**Figure 5D**). Although these relationships are empirical, they are convenient as they permit simple adjustment of the flow rate multiplier f according to the desired resolution, for a given nozzle size.

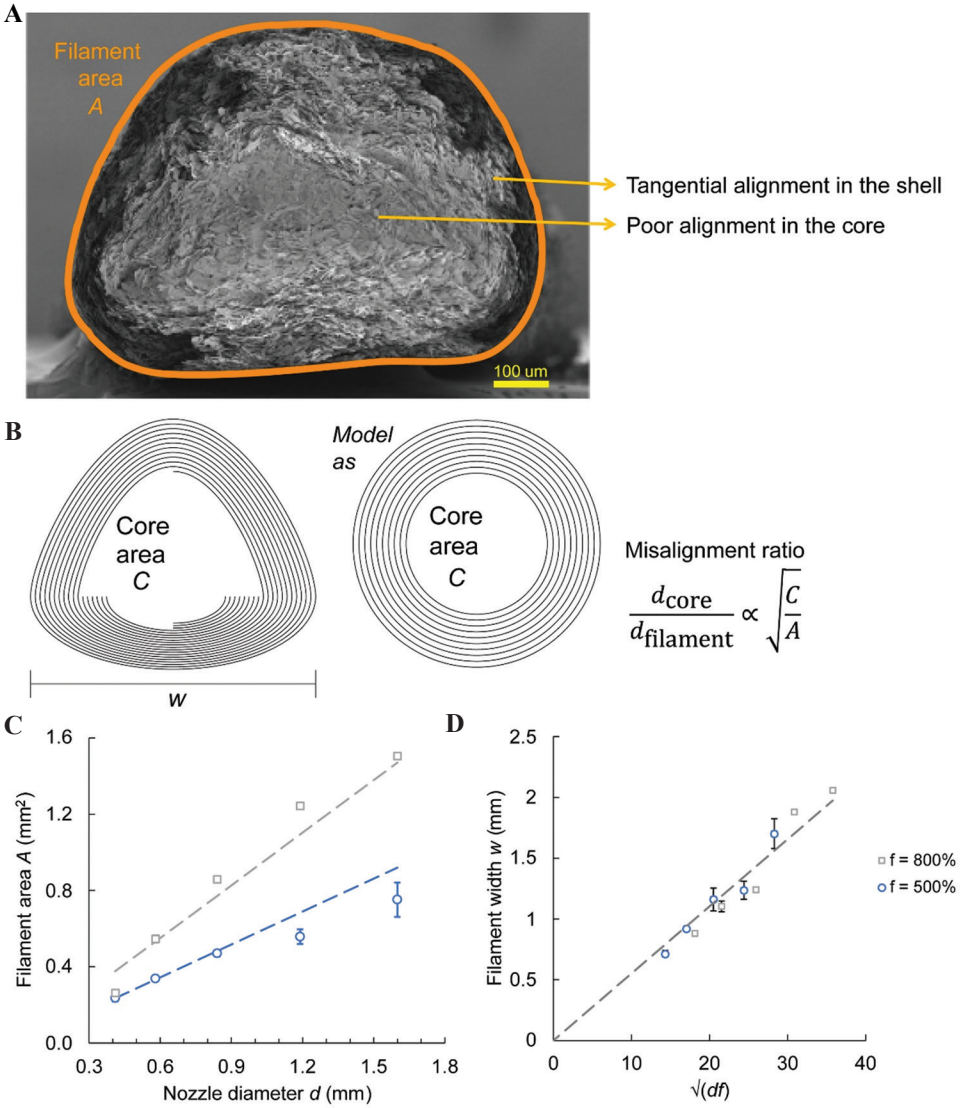


Figure 5. (A) Electron micrographs of the cross-section of a filament extruded though 0.58 mm nozzle at f = 500% after calcination, showing cross-section area A (orange) and the core-shell microstructure. Scale bar: 100 µm. (B) Schematic showing the idealized model of a typical filament cross-section. Post-calcination dimensions of filaments extruded through different nozzle diameters d at f = 500% and at f = 800%. (C) Cross-section area A of filaments extruded from different sized nozzles. (D) Width w of final filaments. Dashed line shows prediction that w is proportional to $\sqrt{(df)}$.

(2) Filament microstructure

After looking into the effect of the print parameters on the print resolution, the core-shell microstructure is analyzed (**Figure 6**). Near the filament edge, the microplatelets were aligned tangentially forming a distinctive "shell," whereas the microplatelets at the filament "core" exhibited poor alignment (**Figure 5A and B**). These observations share similarities with previous works on extrusion of alumina platelets through straight nozzles[24,25]. During extrusion, the shear stresses in the nozzle aligned the microplatelets tangentially, especially those close to the filament edge where the stresses are higher. In this way, the characteristic core-shell microstructure as observed from the y-z cross-section is produced. The area of the filament core region C was measured from electron micrographs (**Figure 5A and 5C**). The relative core radius to filament radius after calcination is approximated by $\sqrt{C/A}$, hereby called the misalignment ratio. We used the area instead of the height or width as the filament obtained did not have a perfectly round cross-section (**Figure 5B**). Despite variations in the filament diameter, the misalignment ratio of CaP filaments remained approximately constant at about 0.68 with the nozzle size d, flow rate multiplier f, and printing speed v (**Figures 6A and B**). Unchanged misalignment ratio at different nozzle diameter has also been reported in

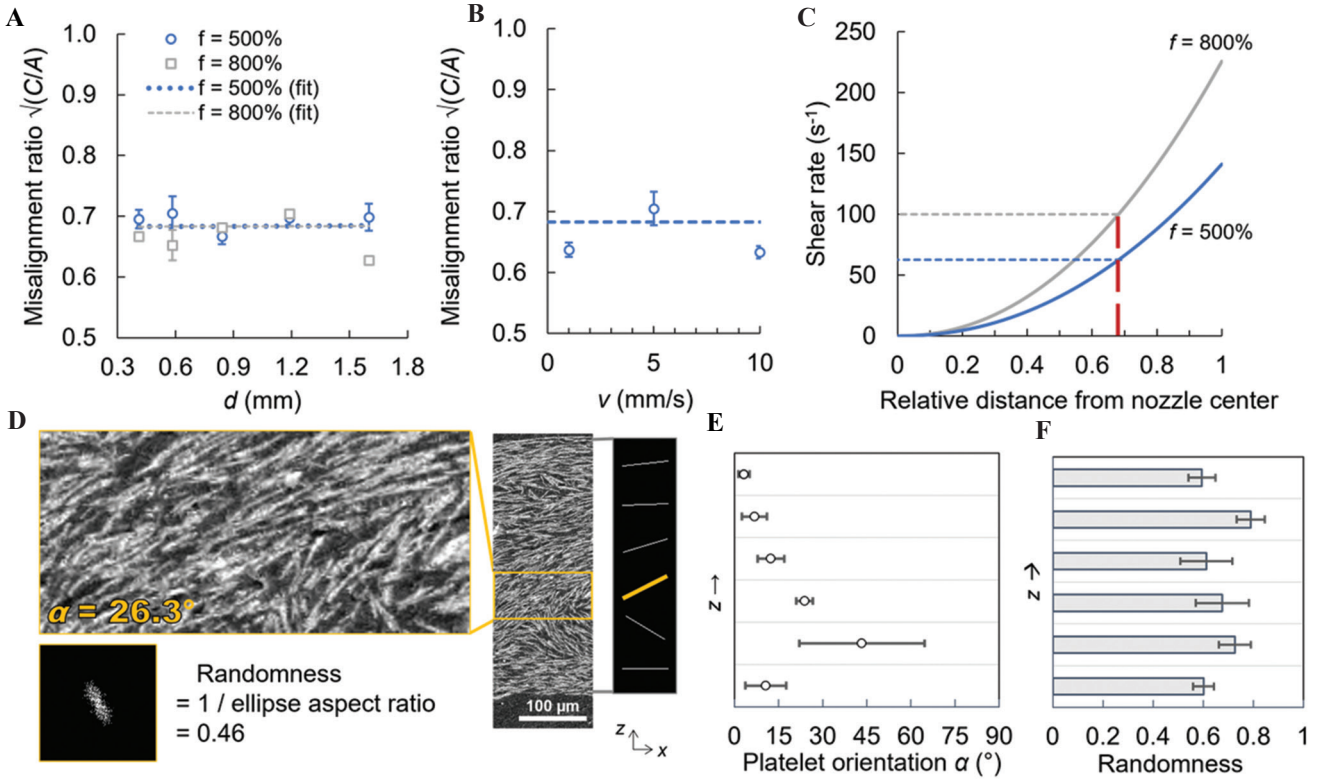


Figure 6. (A) Misalignment ratio $\sqrt{C/A}$ as a function of the nozzle diameter *d*. *v* = 5 mm/s. (B) Misalignment ratio $\sqrt{C/A}$ as a function of the printing speed *v*. *d* = 0.58 mm, *f* = 500%. (C) When the flow rate multiplier *f* is increased from 500% to 800%, the misalignment ratio remains unchanged as shown by the red dashed line. (D) Scanning electron micrograph of the filament cross-section in *x*-*z* plane after calcination (*d* = 0.58 mm, *f* = 500%, *v* = 5 mm/s). Applying FFT to each segment gives the dominant platelet orientation *α* and the randomness of alignment. The six lines on the right represent the typical platelet orientation in the six segments. (E) Dominant platelet orientation *α* in each of the six segments, taken as a positive value from the x-axis, along the height *z* of the filament. (F) Randomness of platelet alignment in each segment along the height (1 = completely random).

alumina ink[27]. This indicates that the platelet alignment process during printing is predictable and independent from the printing parameters. To study this, the ink can be simplified to rigid disc-shaped particles suspended in an incompressible Newtonian fluid undergoing laminar flow down a long pipe. Here, the nozzle is modeled as a long pipe relative to the particle size. The Newtonian fluid refers to the 7% PVP solution, while the brushite ink is non-Newtonian. As the ink flows down the nozzle, the particles nearest to the nozzle wall experience the maximum shear rate, following[33]:

$$\dot{\gamma}_{wall} = \frac{32Q}{\pi d^3} \tag{3.3}$$

while the particles at the nozzle center experience zero shear stress. The volumetric flow rate Q was determined experimentally by measuring the plunger speed. For a given printing speed v, Q increases linearly with the nozzle size d and the flow rate multiplier f (**Supplementary File: Section 3.1**). The time taken for the ink to travel down the nozzle was also calculated from the plunger speed. Then, the higher the shear rate experienced by a particle in the pipe, the shorter the time it takes to reach the equilibrium orientation, in this case tangential to the nozzle wall. This alignment time t_a is inversely proportional to the shear rate $\dot{\gamma}_a$ [37], following:

$$t_a \propto \frac{1}{\dot{\gamma}_a} \tag{3.4.}$$

Since this approximation in Equation 3.4 holds for particles at high solid loadings and low shear rate[37], the relationship in Equation (3.4) can be applied to brushite ink. Given that the shear stress τ decreases linearly from τ_{wall} at the nozzle wall to zero at the nozzle center, the shear stress at any position along the nozzle diameter can now be determined[28,37]. We then used the misalignment ratio $\sqrt{(C/A)}$, which estimates the relative core radius, to determine the shear stress τ at the core-shell border.

$$\tau_a = \sqrt{\frac{C}{A}} \times \tau_{wall} \tag{3.5}$$

Through the Herschel-Bulkley relation, the minimum shear rate required to align brushite microplatelets is hence determined.

$$\dot{\gamma}_a = \left(\frac{\tau_a - \tau_y}{K} \right)^{\frac{1}{n}} \quad (3.6.)$$

Platelets in the core experienced $\dot{\gamma} < \dot{\gamma}_a$ in the nozzle and hence remained disordered upon extrusion, while platelets in the shell experienced $\dot{\gamma} > \dot{\gamma}_a$ and preferentially aligned to the nozzle wall. Indeed, our observations of the misalignment ratio at different print parameters obey the model described by Equation 3.4 (**see Supplementary File: Section 1.2 and 3.2** for details on the model). Furthermore, our experimental results showed that $t_a \propto 1/d$ (see **Supplementary File: Section 3.2**) and we therefore obtain the following relation:

$$\dot{\gamma}_a \propto \frac{1}{t_a \times d} \quad (3.7)$$

Although changing the print parameters such as flow rate multiplier *f* or the nozzle diameter *d* changes the volume flow rate *Q* and shear stress, the misalignment ratio remains constant since t_a changes at the same time. For example, when *f* is increased from 500% to 800% (**Figure 6C**), the increase in *Q* leads to the higher shear stress and shear rate experienced by the platelets in the nozzle, so the required alignment time t_a is reduced. At the same time, the increased ink extrusion rate provides less time for platelets to rotate and align to the equilibrium orientation, resulting in an unchanged misalignment ratio when *f* increased. Therefore, the filament microstructure is unaffected by printing parameters and is expected to depend solely on the ink's rheology. For a given ink, this enables design flexibility at the macro-level (print resolution and print speed) without affecting the core-shell microstructure. Furthermore, with the help of the model and the possibility to relate the rheological properties to the microstructure, it should be possible to design inks to obtain specific microstructures. For example, to tune the misalignment ratio, the viscosity could be modified by fine tuning the concentration in PVP in the ink, without modifying the concentration of CaP microplatelets.

To confirm the platelet orientation inside a printed filament, SEM micrographs of the *x-z* cross-section of those filaments were examined (**Figure 6D**). Gradient changes in the platelet orientation from the bottom of the filament to the middle and from the middle to the top were observed, as expected from the gradient increase in shear stress towards the filament edges due to the laminar flow. To quantify the change in platelet orientation, the electron micrographs of each filament were divided into six segments of equal height from bottom to top, and the platelet orientation and the degree of alignment in each segment were quantified by Fast Fourier Transformation (FFT). The FFT results for filaments extruded at d = 0.58, f = 500%, v = 5 mm/s in the +*x* direction are presented in **Figures 6D-F**. Taking the representative platelet orientation α of each segment; we can visualize the gradient platelet orientation in a typical filament. At the bottom of the filament, CaP platelets were oriented close to 0°, almost parallel to the print substrate (**Figure 6E**). The angle α increased sharply to 45° before decreasing gradually to ~0° near the top. Indeed, the platelets preferentially aligned with the extrusion direction, especially near the nozzle wall where the shear stresses are highest. Platelets at the bottommost and topmost segments also displayed the most uniform alignment (**Figure 6F**). Filaments extruded at different print parameters are expected to exhibit similar trends since their misalignment ratio is about the same.

Having studied the microstructure within one single printed filament, we now look at complex 3D prints to show how our 3D printing approach can be used to construct multi-layered bulk or porous, overhanging structures, while retaining the core-shell microstructure.

3.4. Building microstructured multi-layered structures

(1) Buildability of microstructured CaP

Moving from single filaments, we explored the capability of the printing strategy to build microstructured multi-layered structures. Thanks to the drying method, good buildability of multi-layered structures from 21 vol% brushite ink was possible at room temperature. **Figure 7A** shows that multi-layered parts have the core-shell microstructure like in single filaments (**Figure 5A**). The post-calcination layer height is ~0.5 mm using the nozzle of 0.58 mm diameter at f = 500% (**Figure 7A**).

Since solvent removal by capillary action starts at the substrate surface, it can be expected that there is a maximum height above which the drying takes too long to build more layers with good filament shape fidelity. In practice, this issue can be circumvented through combination with evaporative drying using a fan, heating gun, infrared lamp, or in an environment with controlled temperature. **Figure 7B** shows a thin wall 6 layers tall printed at room temperature at v = 5 mm/s. By heating gypsum on a hot plate, a 20-layer tall thin wall can be built at v = 1 mm/s (**Figure 7C**). In **Figure 7D**, a small jigsaw piece ten layers thick was printed on heated gypsum, showing the construction of intricate parts for custom repairs. Indeed, print fidelity on heated gypsum enables near net shape fabrication of ceramics.

(2) Porosity and print resolution

β-CPP has similar osteoinductivity as hydroxyapatite, and a biodegradability rate between hydroxyapatite and β-tricalcium phosphate (β-TCP and Ca_3PO_4)[38]. The resorption rate is dependent on the crystallographic structure which could be altered by sterilization and other

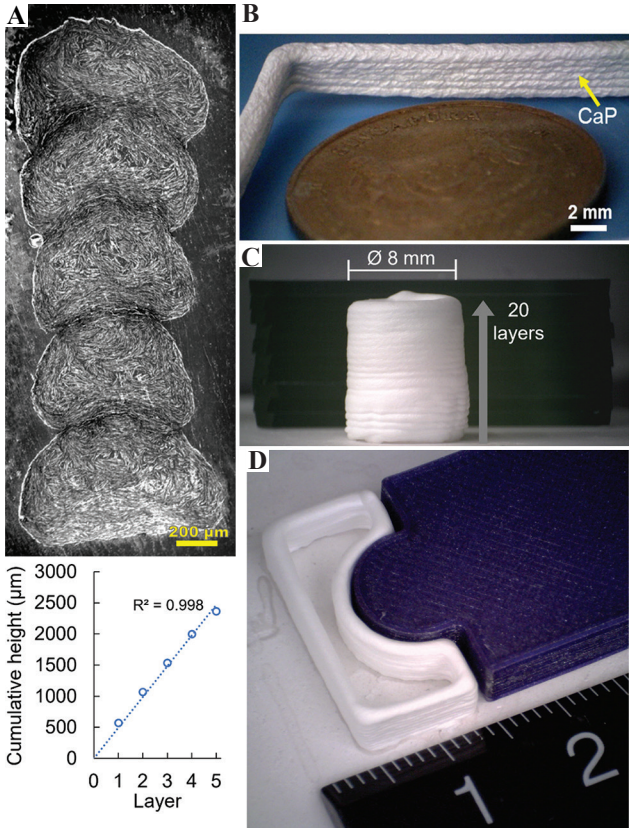


Figure 7. (A) Electron micrograph of the cross-section of a 5-layer print, scale bar: 200 µm. Height of calcined parts, printed at room temperature, d = 0.58 mm, f = 500%, v = 5 mm/s. Dashed line shows linear fit. (B) Optical photograph of a 6 layer-print after debinding, placed next to a Singapore 5-cent coin 16.75 mm in diameter. (C) Optical photograph of a 20-layer brushite cylindrical shell printed on heated gypsum. Background contains a stack of ten microscope glass slides 10.25 mm tall. (D) 10-layer brushite jigsaw piece printed on heated gypsum (left). 5 mm thick jigsaw piece printed from PLA by FDM (right). Ruler in centimeters.

processes[39]. Implantation in sheep tibiae found that the addition of 28 wt% CPP to brushite bone cement promoted bone mineralization *in vivo* as osteoblasts hydrolyzed pyrophosphate into orthophosphate ions[40]. Better osseointegration of bioceramics with pyrophosphate and bone mineralization in humans have also been clinically reported[39]. Prolonged exposure to pyrophosphate was found to stimulate osteoblast differentiation *in vitro*[39]. The bioactivity of β-CPP makes it a potential material in applications such as porous bone scaffolds, bone screws, bone coatings or bone plates. Osseointegration of CaP-based bone plates could potentially eliminate the need for surgical removal of metallic internal fixation.

To demonstrate various biomedical applications requiring different macro-porosity, multi-layered structures were designed with different infill density. In the first example, a 16 mm diameter scaffold resembling commonly robocast porous cancellous bone scaffolds was printed on heated gypsum (**Figure 8A**). At 30% infill density, filaments were widely spaced apart, which is expected to be favorable for vascularization (**Figure 8B**, **left**). In the second example, a higher infill density of 50% was used to print a six-layer thick portion of a bone plate at room temperature (**Figure 8B, right**). The outer surface finish appeared rough, as further discussed in **Supplementary File: Section: 4.2.** Post-processing would be required to improve the surface finish although surface roughness could promote cell attachment and bone growth[7]. Micro-porosity could be further explored using sacrificial organic material or foaming agents, for example. The effects of the scaffold microstructure and surface roughness on osteoinductivity, cell differentiation and proliferation, and bone remodeling remains to be explored.

Furthermore, our approach also permitted the printing of overhanging filaments that support their own weight. In our buildability test modified from Ribeiro *et al.* (2018)[41], underlying supports of three layers tall were extruded at spacing's ranging from 1.0 mm to 3.0 mm (**Figure 8C**). The fourth and topmost layer of filaments spanned across the supports below. Filaments extruded through 0.58 mm nozzle at f = 500% could be continuously extruded across supports up to 2.8 mm apart reliably. The topmost layer was able to support the weight of additional filaments without collapse and the filaments did not show deformation (see **Figure S6** in **Supplementary File**). Besides, the rectangular shape of majority of the pores as seen from the top view also points to good print accuracy and print fidelity[42]. 24 vol% brushite ink with higher storage modulus is expected to bridge wider spans[43].

For a 0.58 mm nozzle using flow rate of 500%, filament fusion occurred for center-to-center spacing of 1.0 mm (**Figure 8C**). The post-calcination filament width is 0.92 ± 0.03 mm. The horizontal print resolution is limited by the filament thickness after extrusion, which has a minimum of 0.7 mm in the green body for a nozzle diameter of 0.41 mm and flow rate of 400%. Although line-by-line robocasting is generally not well-suited for printing dense monolithic structures due to voids between printed filaments[30,36,44], we could make use of filament fusion to minimize porosity in bulk structures by careful tuning of the infill density I_f. At infill density I_f = 30%, there was no overlap between adjacent filaments. At $I_f \geq$ 70%, the overlap between adjacent filaments caused the layer height to increase unevenly, leading to deviation from the print design (**Figure 8D and E**). Infill density ~50% could be chosen to print bulk structures with minimal porosity and good interfilament interface (**Figure 8F**), It is also notable that the calcination step of the multi-layered bulk parts did not cause defects such as microcracks or delamination due to the consolidation without shrinkage. Anisotropic ceramic materials present a tendency to exhibit strong anisotropic shrinkage. This is

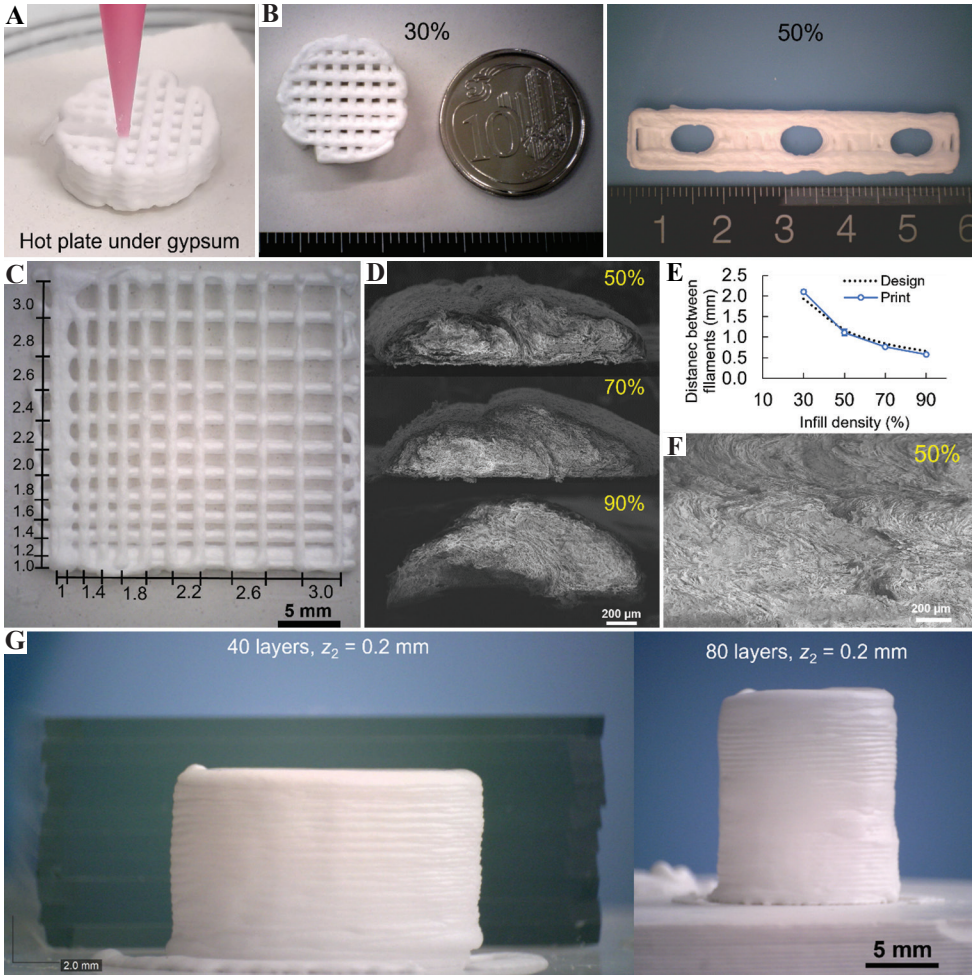


Figure 8. (A) Printing of 16 mm diameter scaffold on heated gypsum at v = 1 mm/s. (B) Brushite green body of 16 mm diameter scaffold next to a coin 18.5 mm in diameter (left). Brushite green body six layers thick resembling part of a bone plate (right). Ruler in centimeters. (C) Green body of 4-layer tall print on gypsum. Top layer of filaments spans across underlying supports at various distances apart (labeled in black in mm). d = 0.58 mm, f = 500%. (D) Cross-section of adjacent filaments printed at different infill density I_f. Scale bar: 200 µm. (E) Deviation of printed green body from design at different infill density. (F) Electron micrograph of dense bulk part printed at infill density of 50%. Scale bar: 200 µm. (G) Brushite cylindrical shells printed on heated gypsum at d = 1.19 mm, $z_1 = z_2$ = 0.2 mm, and v = 1 mm/s. Left: 40 layers tall. Background contains ten microscope slides 10.25 mm tall. Scale bar: 2 mm. Right: 80 layers tall. Scale bar: 5 mm.

mitigated here by the use of a mild heating and cooling ramp.

Replacing the 0.58 mm nozzle with a 1.19 mm nozzle, the layer height is reduced from ~0.5 mm (**Figure 7A and B**) to just ~0.2 mm (**Figure 8G**). In this way, the vertical resolution and side profile surface finish may be further improved by adjusting print parameters to reduce the layer height, with potential trade-offs in horizontal print resolution.

Our results demonstrate the ability to 3D print porous microstructured scaffolds from our CaP ink, which is a desired feature for biomedical applications. The dimensions are comparable to robocast CaP scaffolds, with a layer thickness 0.15~0.35 mm and a macro-pore width of 0.1~0.5 mm commonly reported[45]. Closed porosity does not contribute to a scaffold's nutrient exchange and generally weakens bulk ceramics exponentially. Notably, printing 21 vol% CaP ink at infill density ~50% eliminated internal voids, which are inevitable in conventional robocasting, while still being sufficiently printable. With our 3D printing method, it is, therefore, possible to design and print various complex 3D shapes, with well-controlled macroscopic porosity locally.

CaP materials like β-CPP are inherently brittle in the bulk, monolithic form, despite high stiffness of microplatelets at the nano-scale. Debinding and calcination at high temperatures removes all organic matter, so microstructured CaP scaffolds are fragile and brittle due to the absence of intermolecular forces or polymer chains bridging the CaP microplatelets. To induce toughening mechanisms, the residual open porosity obtained after calcination could be infiltrated

with a polymer having good interfacial strength with CaP. Based on the tension-shear chain model, the ceramic composite is expected to absorb energy as the polymer deforms until eventual platelet pull-out[3].

In addition, microstructure design is often used to toughen such ceramic composites. The periodic orientation of microplatelets in the printed multi-layered CaP (**Figure 8F**) bears resemblance to the periodic structures in highly tough natural materials often employed in biomimetic materials for toughness enhancement, such as the Bouligand structure[46]. We indeed found that the graded orientation of the microplatelets was effective and driving the crack along curved path, following the orientation of the planes of the microplatelets (see **Supplementary File: Section 5** for images of an unusual, curved crack path).

4. Conclusion

In this paper, we have developed an ink composition and 3D printing strategy to build complex shaped microstructured CaP-based materials. Aqueous inks containing CaP microplatelets were developed and their rheology studied. These inks were being dried upon deposition onto gypsum while simultaneously extruding the structure. We found that a concentration of 21 – 24 vol% CaP microplatelets was optimum for printing and studied the microstructure obtained in single filaments after calcination. In each filament, a core-shell microstructure with graded orientation of the microplatelets was obtained. Using a simple model to fit our results, we correlated the rheology of the ink to the microstructure so that it can be possible to further tune the ink composition to attain the desired core-shell microstructure. We also demonstrated porous scaffolds bridging 2.8 mm spans, as well as microstructured multi-layer structures. Such microstructured 3D printed green parts produce a bioresorbable material which make them interesting for biomedical applications such as hard tissue engineering. Micro-porosity could be further explored using sacrificial organic particles or polymer, or foaming agents, for example. Introduction of biological components and cell seeding post-calcination could be explored. Microstructure control is often used to toughen ceramic composites and previous work extruding water-based CaP ink without rheological modifiers did not produce microstructured filaments[47]. Polymer infiltration into the calcium pyrophosphate after calcination could enable toughening mechanisms in the resultant ceramic composite, such as crack bifurcation, platelet pull-out or polymer deformation. Thanks to this 3D printing method, it is now possible to build bulk microstructured CaP from low viscosity inks with a wide range of porosity. To enable CaP materials to be 3D printed into custom-shaped bioactive implants, scaffold macro-porosity will be tuned by computer-aided design (CAD) to study the influence of the CaP microstructure design on the mechanical properties of the infiltrated CaP composites.

Acknowledgments

The authors thank Chan Xin Ying for customizing the 3D printer. The authors would like to acknowledge the Facility for Analysis, Characterisation, Testing and Simulation, Nanyang Technological University, Singapore, for use of their electron microscopy and X-ray facilities.

Funding

This work was supported by the National Research Foundation, Singapore, with the Fellowship NRFF12-2020-0006.

Conflict of interest

The authors declare no conflict of interest.

Author contributions

D.P. and T.S. prepared the samples. T.S. performed experiments and SEM imaging. D.P. analyzed the data and drafted the manuscript. L.F.H. supervised the project, designed the experiments, and reviewed the manuscript

References

1. Reznikov N, Bilton M, Lari L, *et al.*, 2018, Fractal-like Hierarchical Organization of Bone Begins at the Nanoscale. *Science*, 360:eaao2189. https://doi.org/10.1126/science.aao2189
2. Beniash E, Stifler CA, Sun CY, *et al.*, 2019, The Hidden Structure of Human Enamel. *Nat Commun*, 10:1–13. https://doi.org/10.1038/s41467-019-12185-7
3. Gao H, 2006, Application of fracture mechanics concepts to hierarchical biomechanics of bone and bone-like materials. *Int J Fract*, 138:101–137. https://doi.org/10.1007/s10704-006-7156-4
4. Wegst UG, Bai H, Saiz E, *et al.*, 2015, Bioinspired Structural Materials. *Nat Mater*, 14:23–36. https://doi.org/10.1038/nmat4089
5. Yousefi AM, 2019, A Review of Calcium Phosphate Cements and Acrylic Bone Cements as Injectable Materials for Bone Repair and Implant Fixation. *J Appl Biomater Funct Mater*, 17:2280800019872594. https://doi.org/10.1177/2280800019872594
6. Jia W, Lau GY, Huang W, *et al.*, 2015, Bioactive Glass for Large Bone Repair. *Adv Healthc Mater*, 4:2842–2848. https://doi.org/10.1002/adhm.201500447

7. Marques A, Miranda G, Silva F, *et al.*, 2021, Review on Current Limits and Potentialities of Technologies for Biomedical Ceramic Scaffolds Production. *J Biomed Mater Res Part B Appl Biomater*, 109B:1–17. https://doi.org/10.1002/jbm.b.34706
8. Li T, Chang J, Zhu Y, *et al.*, 2020, 3D Printing of Bioinspired Biomaterials for Tissue Regeneration. *Adv Healthc Mater*, 9:1–17. https://doi.org/10.1002/adhm.202000208
9. Wen Y, Xun S, Haoye M, *et al.*, 2017, 3D Printed Porous Ceramic Scaffolds for Bone Tissue Engineering: A Review. *Biomater Sci*, 5:1690–8. https://doi.org/10.1039/C7BM00315C
10. Lin K, Sheikh R, Romanazzo S, *et al.*, 2019, 3D Printing of Bioceramic Scaffolds Barriers to the Clinical Translation: From Promise to Reality, and Future Perspectives. *Materials*, 12:2660. https://doi.org/10.3390/ma12172660
11. Le Ferrand H, Athanasiou CE, 2020, A Materials Perspective on the Design of Damage-Resilient Bone Implants Through Additive/Advanced Manufacturing. *JOM*, 72(3):1195–210. https://doi.org/10.1007/s11837-019-03999-3
12. Rogina A, Antunović M, Milovac D, 2019, Biomimetic Design of Bone Substitutes Based on Cuttlefish Bone-derived Hydroxyapatite and Biodegradable Polymers. *J Biomed Mater Res Part B Appl Biomater*, 107B:197–204. https://doi.org/10.1002/jbm.b.34111
13. Bigoni D, Cavuoto R, Misseroni D, *et al.*, 2020, Ceramics with the Signature of Wood: A Mechanical Insight. *Mater Today Bio*, 5:100032. https://doi.org/10.1016/j.mtbio.2019.100032
14. Sprio S, Panseri S, Montesi M*, et al.*, 2020, Hierarchical porosity inherited by natural sources affects the mechanical and biological behaviour of bone scaffolds. *Journal of the European Ceramic Society*, 40: 1717-1727. https://doi.org/10.1016/j.jeurceramsoc.2019.11.015
15. Tampieri A, Sprio S, Sandri M, *et al.*, 2011, Mimicking Natural Bio-mineralization Processes: A New Tool for Osteochondral Scaffold Development. *Trends Biotechnol*, 29:526–35. https://doi.org/10.1016/j.tibtech.2011.04.011
16. Ruffini A, Sprio S, Tampieri A, 2013, Study of the Hydrothermal Transformation of Wood-derived Calcium Carbonate into 3D Hierarchically Organized Hydroxyapatite. *Chem Eng J*, 217:150–8. https://doi.org/10.1016/j.cej.2012.11.107
17. Cheng Q, Huang C, Tomsia AP, 2017, Freeze Casting for Assembling Bioinspired Structural Materials. *Adv Mater*, 29:1703155. https://doi.org/10.1002/adma.201703155
18. Nelson I, Naleway SE, 2019, Intrinsic and Extrinsic Control of Freeze Casting. *J Mater Res Technol*, 8:2372–85. https://doi.org/10.1016/j.jmrt.2018.11.011
19. Deville S, Saiz E, Tomsia AP, 2006, Freeze Casting of Hydroxyapatite Scaffolds for Bone Tissue Engineering. *Biomaterials*, 27:5480–9. https://doi.org/10.1016/j.biomaterials.2006.06.028
20. Bouville F, Portuguez E, Chang Y, *et al.*, 2014, Templated Grain Growth in Macroporous Materials. *J Am Ceram Soc*, 97:1736–42. https://doi.org/10.1111/jace.12976
21. Bai H, Walsh F, Gludovatz B, *et al.*, 2016, Bioinspired Hydroxyapatite/Poly(methyl methacrylate) Composite with a Nacre-Mimetic Architecture by a Bidirectional Freezing Method. *Adv Mater*, 28:50–6. https://doi.org/10.1002/adma.201504313
22. Gao HL, Chen SM, Mao LB, *et al.*, 2017, Mass Production of Bulk Artificial Nacre with Excellent Mechanical Properties. *Nat Commun*, 8:287. https://doi.org/10.1038/s41467-017-00392-z
23. Chen SM, Gao HL, Zhu YB, *et al.*, 2018, Biomimetic Twisted Plywood Structural Materials. *Natl Sci Rev*, 5:703–14. https://doi.org/10.1093/nsr/nwy080
24. Kumar A, Kargozar S, Baino F, *et al.*, 2019, Additive Manufacturing Methods for Producing Hydroxyapatite and Hydroxyapatite-Based Composite Scaffolds: A Review. *Front Mater*, 6:1–20. https://doi.org/10.3389/fmats.2019.00313
25. Chen S, Jang TS, Pan HM, *et al.*, 2020, 3D Freeform Printing of Nanocomposite Hydrogels through in situ Precipitation in Reactive Viscous Fluid. *Int J Bioprint*, 6:29–49. https://doi.org/10.18063/ijb.v6i2.258
26. Martin JJ, Fiore BE, Erb RM, 2015, Designing Bioinspired Composite Reinforcement Architectures via 3D Magnetic Printing. *Nat Commun*, 6:1–7. https://doi.org/10.1038/ncomms9641
27. Feilden E, Ferraro C, Zhang Q, *et al.*, 2017, 3D Printing Bioinspired Ceramic Composites. *Sci Rep*, 7:1–9. https://doi.org/10.1038/s41598-017-14236-9
28. Fu Z, Freihart M, Wahl L, *et al.*, 2017, Micro-and Macroscopic Design of Alumina Ceramics by Robocasting. *J Eur Ceram Soc*, 37:3115–24. https://doi.org/10.1016/j.jeurceramsoc.2017.03.052
29. Le Ferrand H, 2020, Pressure-Less Processing of Ceramics with Deliberate Elongated Grain Orientation and Size. In:

Minerals, Metals and Materials Series. Berlin/Heidelberg: Springer. p45–56.
https://doi.org/10.1007/978-3-030-36552-3_5

30. Zocca A, Colombo P, Gomes CM, *et al.*, 2015, Additive Manufacturing of Ceramics: Issues, Potentialities, and Opportunities. *J Ame Ceram Soc*, 98:1983–2001.
https://doi.org/10.1111/jace.13700
31. Mandel S, Tas AC, 2010, Brushite ($CaHPO_4 \cdot 2H_2O$) to Octacalcium Phosphate ($Ca_8(HPO_4)_2(PO_4)_4 \cdot 5H_2O$) Transformation in DMEM Solutions at 36.5 °C. *Mater Sci Eng C*, 30:245–54.
https://doi.org/10.1016/j.msec.2009.10.009
32. Anastasiou AD, Thomson CL, Hussain SA, *et al.*, 2016, Sintering of calcium phosphates with a femtosecond pulsed laser for hard tissue engineering. *Mater Des*, 101:346–54.
https://doi.org/10.1016/j.matdes.2016.03.159
33. M'Barki A, Bocquet L, Stevenson A, 2017, Linking Rheology and Printability for Dense and Strong Ceramics by Direct Ink Writing. *Sci Rep*, 7:1–10.
https://doi.org/10.1038/s41598-017-06115-0
34. del-Mazo-Barbara L, Ginebra MP, 2021, Rheological Characterisation of Ceramic Inks for 3D Direct Ink Writing: A Review. *J Eur Ceram Soc*, 41:18–33.
https://doi.org/10.1016/j.jeurceramsoc.2021.08.031
35. Adcock D, McDowall I, 1957, The Mechanism of Filter Pressing and Slip Casting. *J Am Ceram Soc*, 40:355–60.
https://doi.org/10.1111/j.1151-2916.1957.tb12552.x
36. Hu F, Mikolajczyk T, Pimenov DY, *et al.*, 2021, Extrusion-based 3d Printing of Ceramic Pastes: Mathematical Modeling and *In Situ* Shaping Retention Approach. *Materials*, 14:1–22.
https://doi.org/10.3390/ma14051137
37. Hausmann MK, Rühs PA, Siqueira G, *et al.*, 2018, Dynamics of Cellulose Nanocrystal Alignment during 3D Printing. *ACS Nano*, 12:6926–37.
https://doi.org/10.1021/acsnano.8b02366
38. Windarti T, Taslimah, Haris A, *et al.*, 2017, Synthesis of β-Calcium Pyrophosphate by sol-gel method. *IOP Conf Ser Mater Sci Eng*, 172:012058.
https://doi.org/10.1088/1757-899X/172/1/012058
39. Pujari-Palmer M, Pujari-Palmer S, Lu X, *et al.*, 2016, Pyrophosphate Stimulates Differentiation, Matrix Gene Expression and Alkaline Phosphatase Activity in Osteoblasts. *PLoS One*, 11:e0163530.
https://doi.org/10.1371/journal.pone.0163530
40. Grover LM, Wright AJ, Gbureck U, *et al.*, 2013, The Effect of Amorphous Pyrophosphate on Calcium Phosphate Cement Resorption and Bone Generation. *Biomaterials*, 34:6631–7.
https://doi.org/10.1016/j.biomaterials.2013.05.001
41. Ribeiro A, Blokzijl MM, Levato R, *et al.*, 2018, Assessing Bioink Shape Fidelity to Aid Material Development in 3D Bioprinting. *Biofabrication*, 10:14102.
https://doi.org/10.1088/1758-5090/aa90e2
42. Schwab A, Levato R, D'Este M, *et al.*, 2020, Printability and Shape Fidelity of Bioinks in 3D Bioprinting. *Chem Rev*, 120:11028–55.
https://doi.org/10.1021/acs.chemrev.0c00084
43. Smay JE, Cesarano J, Lewis JA, 2002, Colloidal Inks for Directed Assembly of 3-D Periodic Structures. *Langmuir*, 18:5429–37.
https://doi.org/10.1021/la0257135
44. Li Z, Hojati M, Wu Z, *et al.*, 2020, Fresh and Hardened Properties of Extrusion-based 3D-printed Cementitious Materials: A Review. *Sustainability* (*Switzerland*), 12:1–33.
https://doi.org/10.3390/su12145628
45. Liu Q, Lu WF, Zhai W, 2021, Toward Stronger Robocast Calcium Phosphate Scaffolds for Bone Tissue Engineering: A Mini-review and Meta-analysis. *Mater Sci Eng C*, 107:2411–502.
https://doi.org/10.1016/j.msec.2021.112578
46. Behera RP, Le Ferrand H, 2021, Impact-resistant Materials Inspired by the Mantis Shrimp's Dactyl Club. *Matter*, 4:2831–49.
https://doi.org/10.1016/j.matt.2021.07.012
47. Houmard M, Fu Q, Saiz E, *et al.*, 2012, Sol-gel Method to Fabricate CaP Scaffolds by Robocasting for Tissue Engineering. *J Mater Sci Mater Med*, 23:921–30.
https://doi.org/10.1007/s10856-012-4561-2
48. Huang H, Lu X, 2017, An Ellipsoidal Particle in Tube Poiseuille Flow. *J Fluid Mech*, 822:664–88.
https://doi.org/10.1017/jfm.2017.298

Publisher's note

Whioce Publishing remains neutral with regard to jurisdictional claims in published maps and institutional affiliations.

RESEARCH ARTICLE

Fast Customization of Hollow Microneedle Patches for Insulin Delivery

Rong Li[1], Xuan Liu[1], Xin Yuan[1], Shanshan Wu[2], Li Li[1], Xuebing Jiang[1], Bo Li[1], Xian Jiang[3], Maling Gou[1]*

[1]State Key Laboratory of Biotherapy and Cancer Center, West China Hospital, Sichuan University, Chengdu, 610041, China
[2]Department of Ophthalmology, West China Hospital, Sichuan University, Chengdu, 610041, China
[3]Department of Dermatology, West China Hospital, Sichuan University, Chengdu 610041, China

Abstract: Hollow microneedle patches (HMNPs) have great promise for efficient and precise transdermal drug delivery in a painless manner. Currently, the clinical application of HMNPs is restricted by its complex manufacturing processes. Here, we use a new three-dimensional (3D) printing technology, static optical projection lithography (SOPL), for the fast fabrication of HMNPs. In this technology, a light beam is modulated into a customized pattern by a digital micromirror device (DMD) and projected to induce the spatial polymerization of monomer solutions which is controlled by the distribution of the light intensity in the monomer solutions. After an annulus picture is inputted into the DMD via the computer, the microneedles with hollow-cone structure can be precisely printed in seconds. By designing the printing pictures, the personalized HMNPs can be fast customized, which can afford the scale-up preparation of personalized HMNPs. Meanwhile, the obtained hollow microneedles (HMNs) have smooth surface without layer-by-layer structure in the commonly 3D-printed products. After being equipped with a micro-syringe, the HMNPs can efficiently deliver insulin into the skin by injection, resulting in effective control of the blood glucose level in diabetic mice. This work demonstrates a SOPL-based 3D printing technology for fast customization of HMNPs with promising medical applications.

Keywords: Microneedle; Three-dimensional printing; Hollow microneedle patches; Fabrication; Drug delivery

*Correspondence to: Maling Gou, State Key Laboratory of Biotherapy and Cancer Center, West China Hospital, Sichuan University, Chengdu, 610041, China; goumaling@scu.edu.cn

Received: January 24, 2022; **Accepted:** March 8, 2022; **Published Online:** March 8, 2022

Citation: Li R, Liu X, Yuan X, *et al*., 2022, Fast Customization of Hollow Microneedle Patches for Insulin Delivery. *Int J Bioprint,* 8(2):553. http://doi.org/10.18063/ijb.v8i2.553

1. Introduction

Microneedles are micron-sized needles, capable of perforating stratum corneum painlessly and delivering drugs into the body. The primary superiority of microneedles is that they combine the potential delivery ability of a hypodermic needle with the user-friendly benefits of a percutaneous patch. Based on the application characteristics of microneedles, they can be divided into solid microneedles, coated microneedles, dissolving microneedles, porous microneedles, and hollow microneedles (HMNs). The pretreatment of skin with solid microneedles in advance promotes the permeation of transdermal preparations (*e.g.*, ointments, gels, and emulsions). Solid microneedles can also be used to destroy the skin cell structures and induce the expression and deposition of elastin and collagen. Coated microneedles deliver the drugs coated on the surface of microneedles into the skin. Dissolving microneedles are made of dissolvable materials and release the drugs after microneedle dissolution. Porous microneedles release the drug into the skin through the pores of the needle body, such as swelling hydrogel-forming microneedle[1], and other porous microneedles[2-4]. HMNs can be regarded as scaled-down traditional hypodermic needles with a micron-level length and diameter. When connected to a syringe or device, they have the potential to replace syringe-based administration that usually causes fear in the user. Compared with the other four types of microneedles, HMNs have major advantages, such as

© 2022 Author(s). This is an Open Access article distributed under the terms of the Creative Commons Attribution License, permitting distribution and reproduction in any medium, provided the original work is properly cited.

rapid drug delivery directly into the body without a time-consuming slow penetration and release process, and a higher drug utilization rate. By combining with the minimally invasive, painless, and convenient delivery of microneedles, HMNs have been used for transdermal drug delivery of insulin[5,6], vaccine[7,8], lidocaine,[9] etc.

HMN patches (HMNPs) are commonly fabricated using microelectromechanical systems (MEMS) techniques, including photolithography[10,11], etching[12,13], laser direct writing,[14] etc. In these methods, a thin substrate film is firstly created by chemical, physical vapor deposition, or spin coating. Next, the two-dimensional master pattern of the required material is transferred from the original photomask to the photosensitive film on the substrate by photolithography technology. Finally, microneedles are made by wet or dry (plasma-based) etching[15]. However, MEMS techniques cannot achieve the high-precision manufacturing of HMNs with fine structures. In addition, MEMS techniques can hardly be used for customization and large-scale manufacturing because of the cumbersome, time-consuming, and costly manufacturing processes. Therefore, the translation of HMNPs to clinical applications is challenging and novel techniques for rapid fabrication of HMNPs are urgently needed.

Recently, three-dimensional (3D) printing technology has been used to flexibly customize with intricate structures, and the manufacturing period has been decreased to dozens of minutes[14,16-18]. For example, laser stereolithography (SLA) can be used to fabricate cone- and pyramid-shaped HMNs and basic syringe-shaped needle arrays (12.5 min are needed for the generation of each device)[17]. Liquid crystal display vat polymerization and digital light processing (DLP) have an improved molding speed when constructing HMNs[16,19]. These 3D printing technologies shorten the fabrication period and simplify the production processes of customized HMNs. However, layer-by-layer additive manufacturing always resulted in a layered structure, which affects the mechanical properties of the microneedle and potentially causes needle break and penetration failure during use. The layer-by-layer structure can be improved by high printing precision, such as high-precision two-photon polymerization (TPP). Moreover, TPP enables the fabrication of HMNs with various straightforward shapes and small openings[20] as well as in-plane and out-of-plane microneedles with different aspect ratios[18,21]. However, it requires a long period to prepare microneedle arrays (10 min per needle) by TPP[14], leaving considerable room for improvement in terms of fabrication speed. Together, it remains a challenge to rapidly fabricate high-quality HMNs. Nonetheless, our group developed a 3D printing technology, namely static optical projection lithography (SOPL), for rapid customizing high-quality solid microneedle arrays[22]. The obtained solid microneedles do not have the stair-like surface and layer-by-layer structure that are associated with the common 3D-printing technologies.

Herein, we innovatively use the SOPL technique for rapid customization of HMNPs within 5 s. In this technology, the digital light is modulated by a digital micromirror device (DMD) and projected to induce spatial polymerization controlled by the distribution of the light intensity in the monomer solutions. After an annulus picture is inputted into the DMD via the computer, the microneedles with hollow-cone structure can be precisely printed in seconds. By adjusting printing pictures, various structures of HMNs can be customized. The obtained HMNs have smooth surfaces and good mechanical properties. After being equipped with a micro-syringe, the HMNP enables the quantitative, minimally invasive, and pain-free insulin injection, which greatly reduces physical pain and mental anguish.

2. Materials and methods

2.1. Materials

Photosensitive resin was purchased from Ausbond (China). Cell-Counting Kit-8 was purchased from SUNBAO BIOTECH (China). Quick-drying adhesive was obtained from ergo (Switzerland). Agarose gel was purchased from Bioweste (Spain). Insulin injection was purchased from Jiangsu Wanbang Biochemical Medicine Co., Ltd (China). Streptozocin (STZ) was purchased from BioFroxx (Germany). All chemical reagents were of analytical grade. C57BL/6 mice were provided by Chengdu Dossy Experimental Animals Co., LTD. Animal studies were in compliance with the guidelines for the ethical use of animals and were conducted at State Key Laboratory of Biotherapy, Sichuan University, China.

2.2. HMNPs customized by SOPL

The main modules for SOPL equipment to prepare HMNPs are excitation light source, DMD chip, high magnification micromirror, and reservoir. Printing picture is one of the key points of this technology. The printing picture of a HMN, made of Adobe Photoshop CC 2019, consists of two non-concentric circles, which can be regarded as an annulus. Its small inner circle represents the unexposed area, while the large outer circle represents the exposed area. Large circle and small circle are overlaid to form an annular pattern of the exposure area. The size of the large white circle represents the bottom size of the HMN. The size of the small black circle and the relative position to the large circle represent the opening size and opening position of the HMN, respectively.

The preparation of the HMN was as follows: First, the printing picture of the HMN was inputted into a DLP LightCrafter 4500 Control Software. Second, a light beam

(405 nm) was modulated into the customized pattern of the HMN by DMD on the basis of the aforementioned printing picture. Thirdly, digital light projected from DMD was adjusted by a high magnification microlens to improve the printing resolution. Finally, the resin in the reservoir was solidified according to the special spatial distribution of digital light in the monomer solutions and a 3D structure was formed. In addition, various structures of HMNs were prepared by adjusting printing pictures.

HMNPs were fabricated to prepare HMN syringes. The printing picture of the HMN array and substrate were drawn respectively. Multiple annular pictures were arranged to form a printing picture of the HMN array. The printing picture of the substrate was set as a rectangular picture with large white circles of HMNs turned to nonexposed area. The glass slide was placed on a photosensitive resin bath before printing. The HMNP was printed consecutively in two steps. First, the photosensitive resin underwent polymerization under the first projected light pattern originating from the printing picture of HMN array and HMNs formed. Then, the second projected light pattern from the printing picture of the substrate was exposed in turn, and the substrate of the HMNP was printed and the HMMP was obtained.

The morphology of 3D-printed HMNs and HMNPs were observed by the camera and scanning electron microscope (SEM) (JSM-7500F) at 15 kV.

2.3. Simulation of the HMN formation process

To visualize the diffractive lithography by microlens effect and the complicated diffracted intensity distribution within the photosensitive resin in our fabrication, numerical simulation was implemented using an electromagnetic wave beam envelope module in COMSOL Multiphysics software. The ultraviolet (UV) light electric field when $z = 0$ (the surface of liquid resin), namely, E (r', 0) was introduced as uniform distribution propagating along the positive z-direction. The original intensity at $z = 0$ was set as $I_0 = 30\ mW.cm^{-2}$, according to the UV power measurement and the attenuation coefficients along needle growing direction were set as C_0=0.9627, C_1=0, and C_2=0.002878, respectively[23,24].

2.4. Post-treatment of HMNPs

The printed HMNPs were separated from the glass slide with a sharp blade. Since there were residual uncured materials on the printed products, HMNPs were soaked in anhydrous ethanol 3 times (each with 2 min) to completely remove the residual resin on the surface and in the cavity of microneedles. HMNPs were then dried. To enhance the mechanical properties of printed objects, HMNPs were exposed to UV-visible radiation at 450 nm under a light-emitting diode, LED lamp for 3 min to polymerize remaining uncured resin. They were successively soaked in 75% ethanol for 24 h and ×1 phosphate-buffered saline (PBS) for 24 h to improve the biocompatibility of HMNPs. The resultant HMNPs were dried at room temperature before used.

2.5. In vitro biocompatibility of HMNPs

In accordance with EN ISO 10993-12:2012 guidelines, the *in vitro* biocompatibility of HMNPs was conducted using six 1 cm^3 cubes with the same printing materials and post-processing as HMNPs. The cubes were soaked in 6 ml of PBS for 24 h to obtain the extract of printing materials[25'26]. Skin cells of human adult low calcium high temperature (HaCaT, human-immortalized keratinocytes) and human dermal fibroblast (HDF) were used to assess the toxicity of the printed HMNPs. Cells were cultured in each well of 96-well microtiter plates, treated with 180 µl of fresh culture medium plus 20 µl of the extract for each well. The negative control was incubated with 180 µl of fresh culture medium and 20 µl of sterile PBS. After incubated for 24 h (day 1) and 72 h (day 3), CCK-8 assay was used to analyze cell viability with an absorbance wavelength of 450 nm.

2.6. Mechanical strength testing of HMNs

Compression test of a single HMN was performed to investigate the mechanical property of HMNs by a dynamic mechanical analysis (DMA) (Q800 TA Instruments). In brief, a single HMN was placed on the test stage positioned vertically and a metal probe was moved to the point where it touched the tip of HMN. The metal probe was then moved vertically downward at a compressive force of 2.5 N/min. The deformation process of the HMN during compression tests was captured by a camera. The relationship between compression displacement and static force was recorded by TA Instruments Universal Analysis 2000 (software of DMA). The fracture (failure) force was the turning point of static force on the curve.

2.7. Puncture experiment and skin healing experiment

Puncture experiment was applied on the skin of mice to evaluate the skin insertion ability of HMNPs. The hair on the back of mouse was shaved and depilated immediately after death by over anesthesia of the mouse and then wiped clean with saline. HMNPs were inserted into the dorsal skin of mice for 3 min to check their puncture ability. Then, the treated skin was fixed with formalin for 48 h and rinsed with running water for 2 h. Samples were then dehydrated before they were embedded in paraffin. Five-micrometer-thick cross-sections were cut from the samples followed by hematoxylin-eosin (H&E) staining. In addition, we applied HMNPs to the mouse skin for 3 min, and then removed them to verify whether the skin

would quickly heal after microneedle treatment. The skin of mice was observed with the naked eye at 0, 10, 20, 30, 60, and 120 min after the HMNP application. Pictures were taken with a camera for recording them.

2.8. Preparation of HMN syringe

A 3D-printed HMNP was pasted after post-treatment on the punched steel plate with quick-drying adhesive. The punched steel plate had the same size as HMNP, and the holes in the plate correspond to the cavities of microneedles. The HMN syringe was then formed by connecting HMNP at one end of the converter and a micro-syringe at the other end. The converter was customized by 3D printing technology of SLA to match HMNPs and micro-syringes.

2.9. Delivery ability of HMN syringe *in vitro*

The agarose gel was used as an *in vitro* skin model and rhodamine as the model drug to assess the *in vitro* drug delivery ability of the HMN syringe. According to the literature[27], agarose powder was added with distilled water (0.0265 g/mL), heated to 100°C until completely dissolved, and then poured into the mold for cooling and molding for later use. Rhodamine was slowly injected into the above skin model using the HMN syringe, and the delivery process was photographed under an optical microscope.

2.10. Mouse models of diabetes

C57BL/6 mice were placed in a pathogen-free room with a 12 h light-dark cycle. The diabetic mouse was induced by STZ. Generally, male C57BL/6 mice (6 – 8 weeks old) were intraperitoneally injected with 2% STZ (150 mg/kg) after overnight fasting. Mice were then fed with a normal diet. One week later, the experiment was carried out in the morning where diabetic mice had fasted for 12 h. The blood was collected from tail clipping, and blood glucose levels were monitored with a glucometer of Yuwell. Fasting blood glucose higher than 16.7 mmol/L (or 300 mg/dl) were confirmed as type 1 diabetic mice and were used for further experiment[28].

2.11. Blood glucose control study in type 1 diabetic mice

The experiment began in the morning with diabetic mice fasted for 12 h. The hair of mice was partially shaved the day before the experiment to facilitate the injection. The initial blood glucose levels of the diabetic mice were measured at first. Diabetic mice with similar blood glucose were randomly divided into three groups (n = 5 for each group) with untreated diabetic mice as the negative control group, commercial insulin syringe as the positive control group, and HMN syringe group. The insulin injection dose of two IU/kg was selected for the positive control group and experimental group to avoid hypoglycemia. The blood glucose levels were then monitored at 0, 0.5, 1, 2, and 4 h after insulin injection. In the negative control group, mice received no other treatment except that blood was collected at the same time to monitor blood glucose levels.

2.12. Ethics statement

The experimental procedures were approved by the Institutional Animal Care and Use Committee of West China Hospital of Sichuan University (20211424A) and were performed in accordance with the guidelines and regulations of the Sichuan University Committee on Animal Research and Ethics.

2.13. Statistical/data analysis

All data were analyzed and arranged using GraphPad Prism 8 (GraphPad Software Inc., CA, USA). The significance of the data was calculated using Student's t-test or one-way ANOVA methods. Results were presented as means with standard error of the mean and a $P < 0.05$ was considered statistically significant.

3. Results

3.1. HMNPs customized by SOPL

Schematic diagram for fabricating HMNPs via SOPL is depicted in **Figure 1**. During the printing process, according to the printing picture, a light beam was modulated into a customized pattern by a DMD and then passed through a high magnification microlens, which significantly improved the printing resolution to 5 μm. An annulus consisting of two non-concentric circles, namely a large white circle and a small black circle was designed in the printing picture to customize the HMN. The white circle represented the area exposed by the digital light, and the black circle was the unexposed area. The formation principle of HMNs was based on the spatial intensity distribution of projected annulus light. On the one hand, the light intensity distribution of circle light gradually weakened from the center of the focal plane to the outside and resembled an inverted cone. The small black circle represented nonexposed area, thus forming a hollow-cone structure. On the other side, the light intensity was greatly reduced after being absorbed by photosensitive resin according to the Beer-Lambert Law. The unique distribution of light intensity enabled the formation of HMNs accordingly. In addition, we simulated the light propagation and light intensity distribution during printing (see video in Supplementary File) to visualize the formation process of the HMN. It can be observed that the hollow-cone light intensity distribution was adjusted with the curing of the monomer solution, and finally, the HMN was formed.

HMNs with three different opening sizes were obtained (**Figure 2B and C)** by adjusting the size of small black circles in printing pictures (**Figure 2A**). The opening sizes of HMNs enlarged with the increase of small black circles in size, and the bottom of HMNs remained unchanged when keeping large white circles unchanged. HMNs with five different opening positions are formed by adjusting the relative position of small black circles (**Figure 3**). The HMNs in **Figure 3A-C** had holes at the bottom; while HMNs in **Figure 3D and E** had no holes at the bottom. This is mainly due to the different intensity distribution of digital light in photosensitive resin. When the small black circle is too close to the edge of the large white circle, the exposure area at the edge is small and the light intensity is not enough to support the closed loop at the bottom of the HMN. When the small black circle is too close to the center of the large white circle, the stronger annular light will be scattered in the solution,

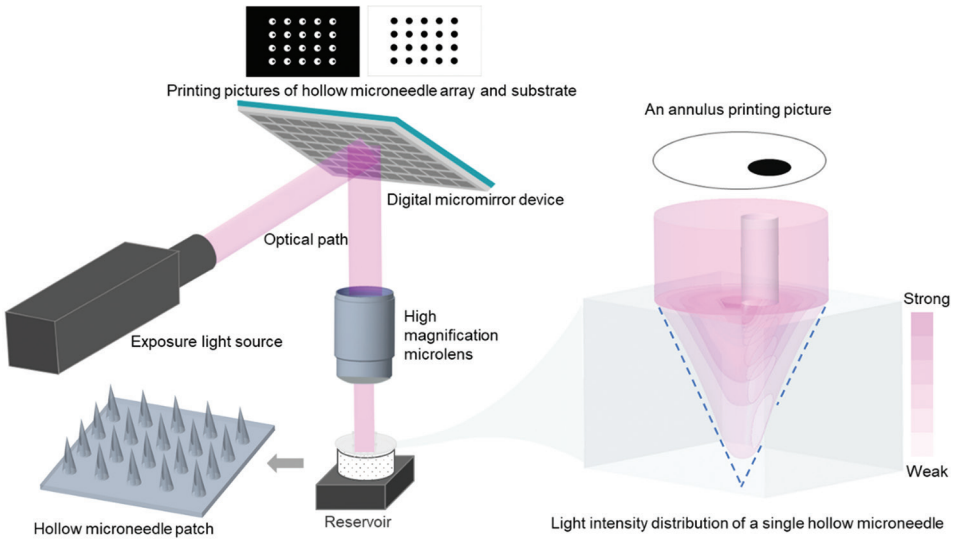


Figure 1. Schematic diagram of fabrication principle of hollow microneedle patches (HMNPs) via static optical projection lithography.

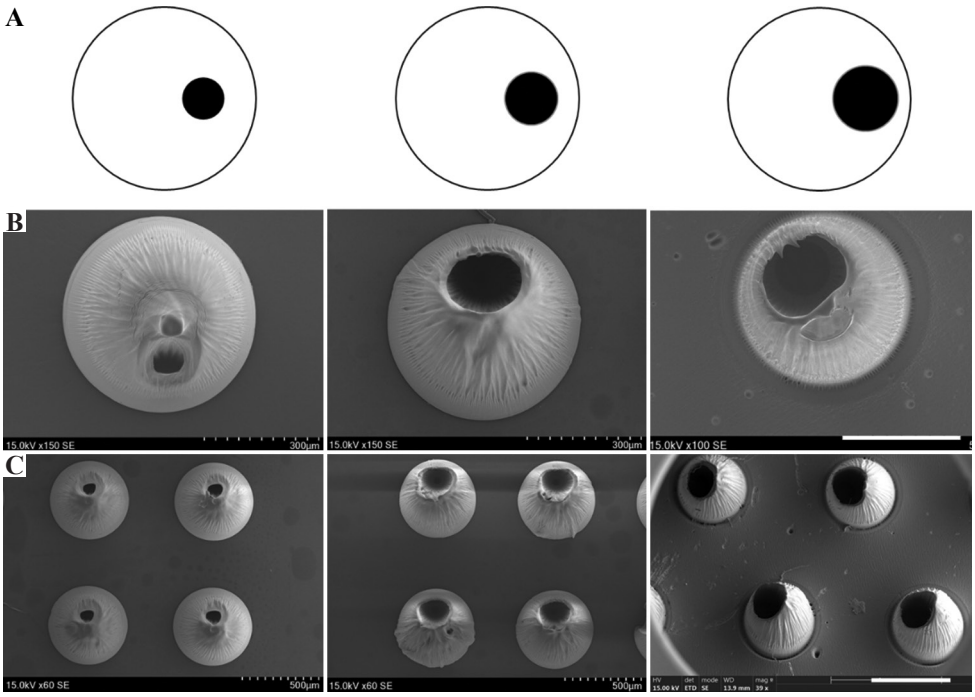


Figure 2. The morphologies of hollow microneedles (HMNs) observed by scanning electron microscope (SEM). As the size of small black circles in printing pictures increased, the opening sizes of HMNs were enlarged. (A) Printing pictures. (B) HMNs with different opening sizes (Scale bar: 300 μm). (C) HMN arrays with different opening sizes (Scale bar: 500 μm).

thus blocking the cavity of the microneedle. All the HMNs can be fabricated by a single exposure within 5 s. These results indicate that SOPL technology can flexibly and rapidly customize HMNs with various structures, which may have broader applications. For instance, HMNs with large openings can be made into coated HMNs, which would increase drug loading efficiency[29].

HMNPs can be fabricated by sequentially exposing printing pictures of HMN arrays and substrates. SOPL technique can customize HMN arrays with various alignments by designing printing pictures. For example, HMNPs with the aligned arrangement and dislocated arrangement were portrayed in **Figure 4A and B,** respectively. As shown in **Figure 4A**, a 5 × 8 aligned HMNP could be obtained by exposing the specific printing pictures of the HMN array and the substrate in sequence. The dislocation-arranged HMNP could be prepared by changing the arrangement of the printing pictures (**Figure 4B)**. It was worth noting that the printing picture of the substrate should be consistent with the arrangement of the large white circles. A 10 × 6 mm HMNP could be formed within 5 s via rapid photopolymerization. SEM showed that the height of each HMN was about 1000 μm. HMNs had distinct opening and sharp tip without the layered structure commonly associated with other 3D printing methods (**Figure 4B**).

In short, to fabricate the ideal HMNPs, the first step is to design printing pictures. For example, the sizes of the large white circle and the small black circle, which are related to the sizes of the bottom and opening of the HMNs. The relative position of the small black circle and the white circle is designed to prepare the suitable structure of HMN. The arrangement between the large white circles and the shape of the substrate determines the distribution of the microneedle array and the structure of the patch respectively. Then, according to the designed printing pictures, digital light allows the photosensitive materials to rapidly polymerize to form the HMNP

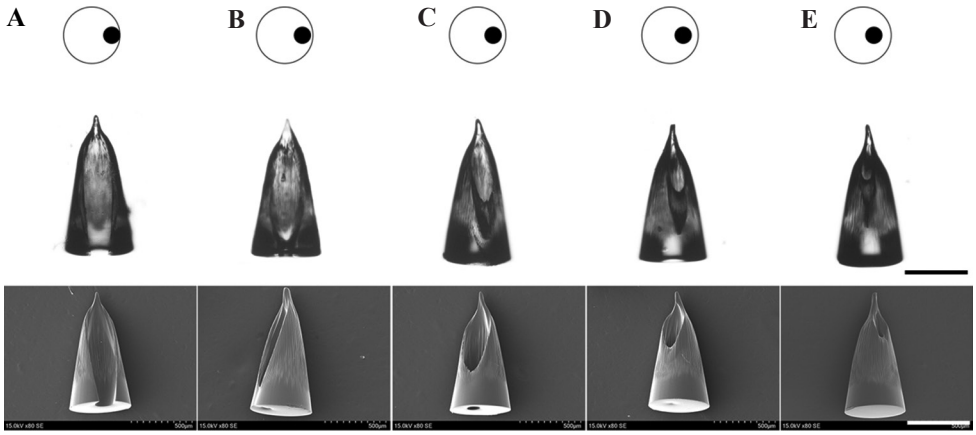


Figure 3. The morphologies of HMNs with different opening positions observed by SEM (Scale bars: 500 μm). (A-C) HMNs had holes at the bottom. (D-E) HMNs had no holes at the bottom.

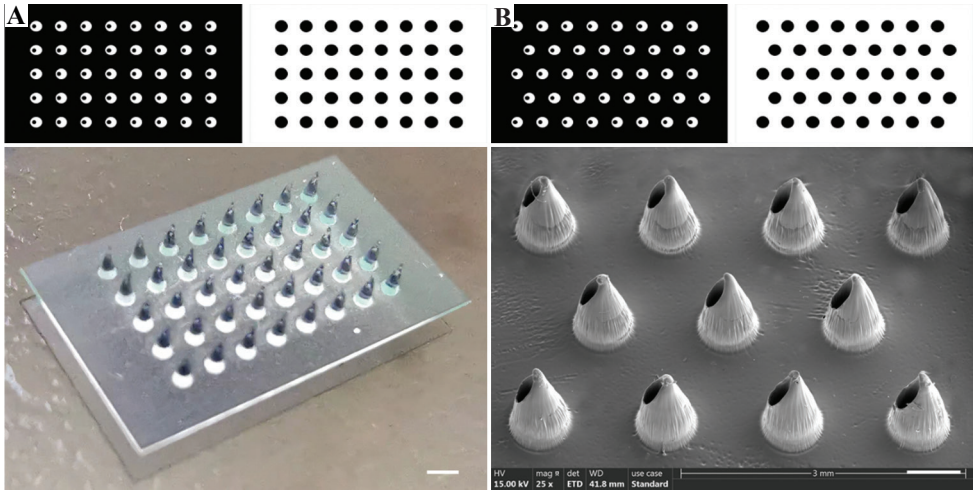


Figure 4. The printing pictures and morphologies of HMNPs. (A) A HMNP with aligned arrangement observed by camera (Scale bar: 1 mm). (B) A HMNP with dislocated arrangement observed by SEM (Scale bar: 500 μm).

without layer-by-layer structure. As a result, SOPL technology enables rapid customization of high-quality HMNPs.

3.2. *In vitro* biocompatibility of HMNPs

The safety issue of materials used in 3D printing was controversial[30] and the biocompatibility of the printing ink should be evaluated. In this study, the cytotoxicity of the extract of printing material was used to assess the *in vitro* biocompatibility of HMNP. The printed 1 cm^3 cubes were processed according to section 2.4. Post-treatment of HMNPs for the extract, and then co-incubated with HaCaT and HDF cells. The relative cell viability of cells incubated with the extract of 3D printing material had no significant difference at 24 h (1 day) and 72 h (3 days) when compared with the cells incubated with PBS (**Figure 5**). This implies that 3D-printed HMNPs have no cytotoxicity to skin cells after post-treatment.

3.3. Mechanical strength testing of HMNs

Microneedles must have enough mechanical strength to retain their intact shape when used for drug delivery. Therefore, it is necessary to test the mechanical strength of HMNs. The schematic diagram of mechanical test of a HMN is shown in **Figure 6A**. The HMN was placed on the test stage positioned vertically and a metal probe moved vertically downward at a compressive force of 2.5N/min. From the pictures of the compression process, the HMN initially remained intact, then gradually fractured (**Figure 6B**). Force-displacement curve showed the relationship between displacement and the force was almost linear at the outset. Thereafter, the HMN was broken, the curve shook suddenly, and the arrow in the figure indicated its turning point with the compression distance of about 250 μm and compression strength of about 4 N. It was reported that insertion forces of 0.1 – 3 N were sufficient to permit insertion by hand[31]. This reveals that the mechanical strength of HMNs is sufficient for skin puncture.

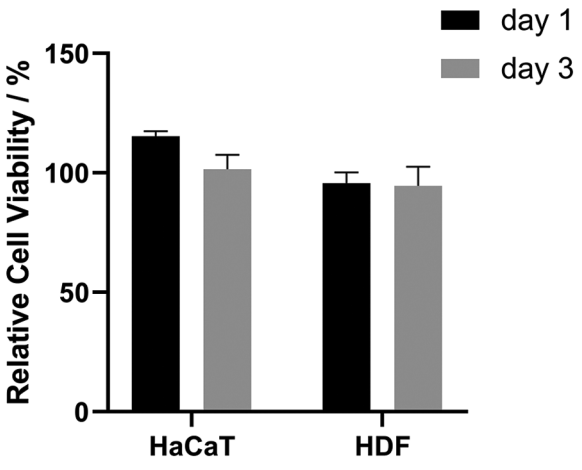


Figure 5. Relative cell viability of human adult low calcium high temperature (HaCaT) and human dermal fibroblast (HDF) cells as a percentage of their controls after 24 h and 72 h of incubation with 3D printed polymer extract. Data are mean ± standard error of the mean (n = 6).

3.4. Puncture experiment and skin healing experiment on mouse skin

Good puncture ability is critical for the microneedles to pierce stratum corneum and to assess the efficacy of transdermal drug delivery. As shown in **Figure 7A**, HMNPs efficiently penetrated the skin of mice, as evidenced by the H&E staining of tissue section with a puncture depth of about 300 μm. The pores formed by HMNs facilitated drug injection. After puncture, the skin barrier should be restored to avoid infection and other adverse reactions. **Figure 7B** showed that the micropore array on the surface of the mouse skin could be seen by naked eyes, and the shape was just the same as that of the HMNP. Then, the micropores gradually disappeared after HMNPs removal. After 120 min, the skin almost completely recovered, indicating that the skin could heal from HMNP insertion. These results show that HMNPs can be used for drug injection in a minimally invasive way.

3.5. Preparation of HMN syringes

Many drugs need to be injected subcutaneously/intracutaneously to exert their effects. HMN syringes transdermally deliver drugs in minimally invasive and painless way, showing notable advantages due to the convenient quantitative delivery. In this study, HMNPs with holes at the bottom (**Figure 3C**) were used to manufacture HMN syringes for efficient and convenient drug delivery. The HMN syringe was assembled according to the schematic diagram shown in **Figure 8A**. An HMN syringe consists of an HMNP, a 3D printed converter and a micro-syringe. After assembly, an actual picture of the HMN syringe is shown in **Figure 8B**, which was a small,

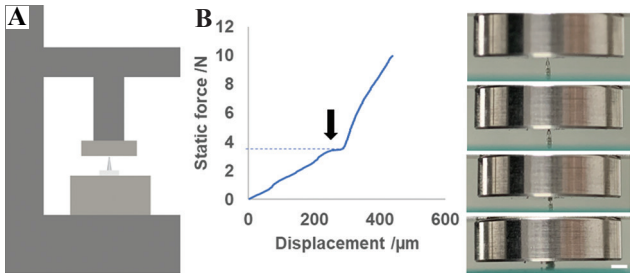


Figure 6. Mechanical strength testing of HMNs. (A) Schematic diagrams of mechanical strength testing of an HMN. (B) Force-displacement curve of a single HMN subjected to a compressive force of 2.5 N/min, and pictures for the deformation process of the HMN during compression tests (Scale bar: 1 mm).

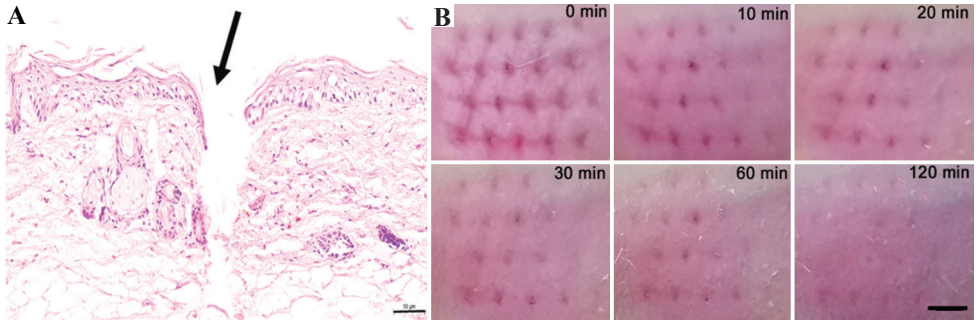


Figure 7. Puncture experiment and skin healing experiment. (A) Hematoxylin-eosin-stained cross-section of inserted skin by HMNs (Scale bar: 50 μm). (B) Skin healing images at 0 min, 10 min, 20 min, 30 min, 60 min, and 120 min after the HMNP treatment (Scale bar: 500 μm).

portable microinjection device. Based on the range and scale of syringe, injection volume and injection precision of HMN syringe can be determined, such as 0 – 10 μl, 0 – 25 μl, 0 – 50 μl, etc.

3.6. Delivery ability of HMN syringes *in vitro*

The drug delivery ability of HMN syringes needs to be first verified *in vitro*. Agarose gel is commonly used to simulate skin *in vitro*. It is a homogeneous and semi-clear material that enables the observation of the drug delivery process with an optical microscope[27]. Rhodamine is often used as a model drug for microneedle delivery. The results of multiple intermittent photographs within 0 – 1 min showed that rhodamine gradually diffused along the injection site within the agarose gel while an HMN syringe was used to perform injection (**Figure 9**). These results indicate that HMN syringes can be used for drug delivery.

3.7. Blood glucose control study in type 1 diabetic mice

People with Type 1 diabetes must inject insulin to control blood glucose. The long insulin needle causes huge physical and psychological pain to the patient. Therefore, repeated injection always causes poor compliance and unsatisfactory glycemic control. A portable HMN syringe is found to be useful for quantitative, minimally invasive, painless, and user-friendly injection, which can ease diabetic patients from needle phobia under traditional subcutaneous injection of insulin, thus improving their life quality.

In this study, our HMN syringes were used to deliver insulin for regulating blood glucose levels in diabetic mice. First, diabetic mice were successfully induced after STZ administration. The initial blood glucose level was 23 ± 5 mmol/L. Diabetic mice were then randomly divided into three groups. Diabetic mice in the commercial insulin syringe and HMN syringe group were treated with insulin (2 IU/kg). Their schematic representations of insulin injection are shown

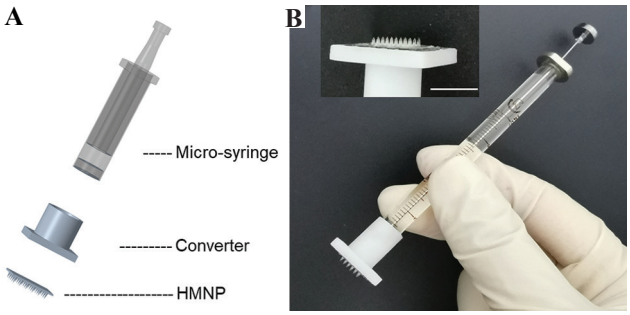


Figure 8. Preparation of the HMN syringe. (A) Schematic diagram for assembly of an HMN syringe. (B) An actual picture of an HMN syringe (Scale bar: 500 μm).

in **Figure 10A and B**. Commercial insulin needles often penetrate deep into the body, which often irritates nerves and causes pain. While the HMN with micron needles only penetrate the superficial layer of skin, which holds the advantages of minimal invasiveness and painlessness. The regulation of blood glucose levels detected at the time points of 0, 0.5, 1, 2, 4 h in the untreated group, commercial insulin syringe, and HMN syringe group are shown in **Figure 10C**. The reduction in blood glucose level in the HMN syringe group was similar to that in the commercial insulin syringe group. There was no obvious improvement in blood glucose levels in the untreated group, and the slight increase in 0.5 h might be due to stress response caused by blood sampling for monitoring blood glucose. The results indicate that the HMN syringe can be used for insulin injection to control blood glucose levels in a quantitative, minimally invasive, painless, and user-friendly way, which is beneficial for blood glucose management.

4. Discussion

Currently, HMNs have been used for drug delivery in four main forms, that is, coated HMNs with drug-impregnated outer surface and inner cavity[29], HMN-based patch-like drug delivery system combining HMNP with drug reservoir[32], microinjection devices with a complex auxiliary injection device[5,7,8,33], and HMN syringe

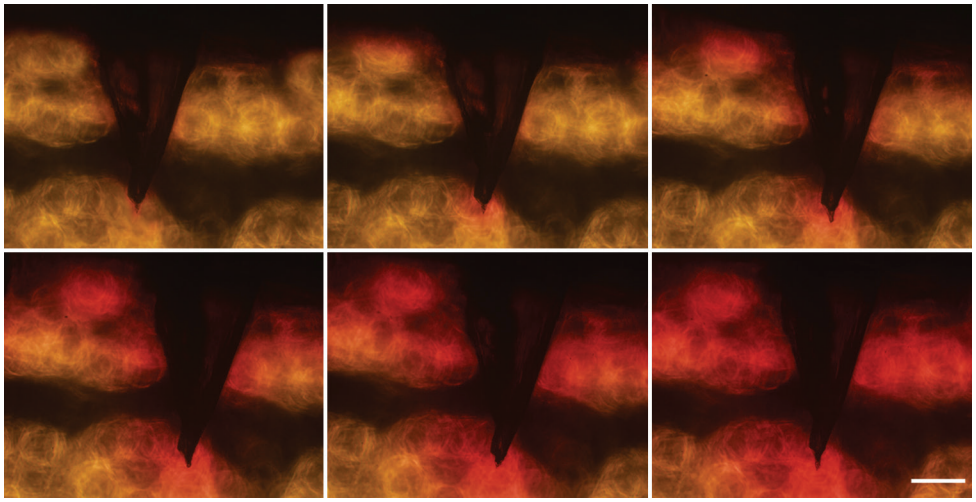


Figure 9. Delivery process of rhodamine into agarose gel by the HMN syringe (Scale bar: 200 μm).

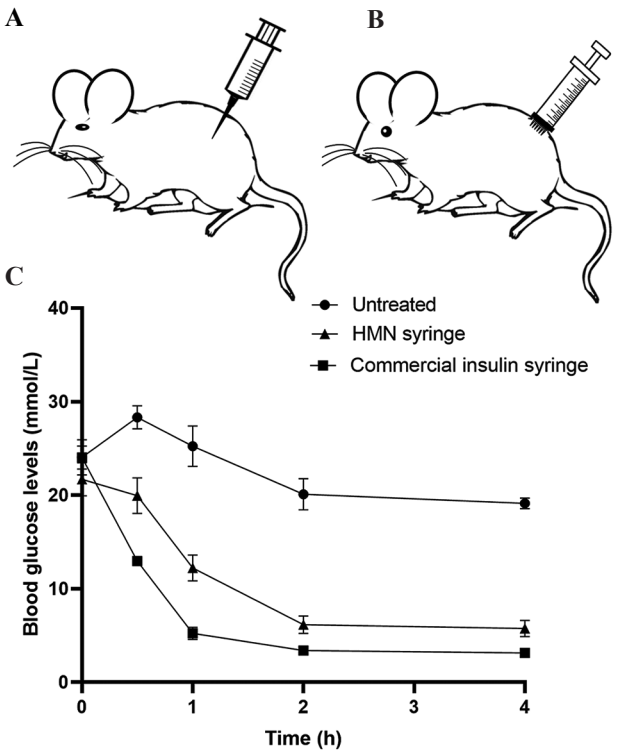


Figure 10. Blood glucose control study in type 1 diabetic mice. (A) Schematic representation of insulin injection via commercial insulin syringe. (B) Schematic representation of insulin injection via HMN syringe. (C) Comparative blood glucose levels versus time (at time point of 0, 0.5, 1, 2, 4 h) for the untreated group, commercial insulin syringe and HMN syringe group applied to diabetic mice (n = 5).

connecting HMN with a syringe[34-36]. However, coated HMNs are similar to commonly coated microneedles and hardly enable quantitative drug delivery. HMN-based patch-like drug delivery system and microinjection devices suffer from the limitation of complicated preparation and difficulty in drug dosage control. Microinjection devices need to connect the HMNs with a MEMS and injection device; therefore, the entire device has a large volume and is not conducive to portable use. In comparison, HMN syringe holds obvious advantages in the convenient quantitative delivery of drugs without complicated devices. HMN syringes have been effectively used for transdermal delivery of insulin[5,6,34,37], vaccines[7,38], immune checkpoint blockers[39], gene drugs[36], phenylephrine[40], etc. In addition, it is worth noted that HMNs are only suitable for local and small-dose drug delivery. Therefore, the insertion site and dosage of the drug administration should be carefully considered when exploiting the application of HMNs.

In this study, SOPL technology customizes an HMNP in seconds, which is the fastest speed for fabricating HMNPs at present. Meanwhile, the obtained HMNs have a smooth surface without layer-by-layer structure, improving the quality of 3D-printed HMNs. Despite the unprecedented progress in 3D printing of HMNPs, there are still several hurdles in this technology. First, because of the one-step photopolymerization of SOPL, it may be difficult to make microneedles with particularly complex structures, such as hollow surgical microneedle[41]. Second, only photopolymeric materials with certain transparency are available for preparing 3D-printed HMNPs. Third, most photopolymeric materials cannot meet the requirement of fabricating HMNs with good mechanical properties. Therefore, there is an urgent need to develop photopolymer materials with high strength, high toughness and high transparency. Finally, complicated post-treatment processes are required for the resultant HMNPs, including washing to remove residual materials, secondary photocuring to enhance HMNs and soaking into alcohol to improve biocompatibility, etc. The issue of complex post-processing can also be solved by exploiting new materials

with better properties. Collectively, SOPL, a compelling and suitable approach, overcomes the limitations of speed, volume, and quality in HMNP fabrication. With the development of materials and technology, SOPL technology could promote the effective clinical translation and commercialization of HMNP.

5. Conclusions

In summary, this study innovatively used SOPL technology for fast customization of HMNPs with high quality. An HMNP could be obtained by one-step photopolymerization within 5 s. The obtained HMNs had good biocompatibility, mechanical properties, and puncture performance. After being equipped with syringes, HMNPs could be used for minimally invasive and painless injection of insulin to control blood glucose levels. Collectively, SOPL technology is expected to provide technical support for the mass production of HMNPs and promote their widespread clinical application.

Acknowledgments

We thank H. Wang from the Analytical and Testing Center, Sichuan University, P. R. China for the SEM observation and analysis of the data. We thank Zhiyuan Gou for his help in the preparation of the HMN syringe. We also thank Xide Dai for his work in the simulation video for the visualization of the HMN formation process.

Funding

This research was funded by National Key Research and Development Program of China (2021YFF1200800), Sichuan Innovative Research Team Program for Young Scientists (2021JDTD0001), 1·3·5 project for disciplines of excellence, West China Hospital, Sichuan University (ZYJC18017, ZYYC08007).

Conflict of interest

No conflict of interest was reported by all authors.

Author contributions

The manuscript was written through contributions of all authors. All authors have given approval to the final version of the manuscript. M.G. and Xian.J. designed and supervised the project. R.L., X.L., and B.L. contributed to experiment design and results. R.L., X.L., X.Y., S.W., L.L., Xue.J. and B.L. performed experiments. R.L., X.J., X.Y., S.W., L.L. and Xue.J. wrote the manuscript.

References

1. Gao B, Guo M, Lyu K, *et al.*, 2021, Intelligent Silk Fibroin Based Microneedle Dressing (i-SMD). *Adv Funct Mater*, 31:2006839. http://doi.org/10.1002/adfm.202006839
2. Li X, Huang X, Mo J, *et al.*, 2021, A Fully Integrated Closed-Loop System Based on Mesoporous Microneedles-Iontophoresis for Diabetes Treatment. *Adv Sci* (*Weinh*), 8:e2100827. http://doi.org/10.1002/advs.202100827
3. Yao S, Wang Y, Chi J, *et al.*, 2021, Porous MOF Microneedle Array Patch with Photothermal Responsive Nitric Oxide Delivery for Wound Healing. *Adv Sci* (*Weinh*), 9:e2103449. http://doi.org/10.1002/advs.202103449
4. Sadeqi A, Kiaee G, Zeng W, *et al.*, 2022, Hard Polymeric Porous Microneedles on Stretchable Substrate for Transdermal Drug Delivery. *Sci Rep*, 12:1853. http://doi.org/10.1038/s41598-022-05912-6
5. Economidou SN, Uddin MJ, Marques MJ, *et al.*, 2021, A Novel 3D Printed Hollow Microneedle Microelectromechanical System for Controlled, Personalized Transdermal Drug Delivery. *Addit Manuf*, 38:101815. http://doi.org/10.1016/j.addma.2020.101815
6. Mishra R, Maiti TK, Bhattacharyya TK, 2019, Feasibility Studies on Nafion Membrane Actuated Micropump Integrated With Hollow Microneedles for Insulin Delivery Device. *J Microelectromech Syst*, 28:987–96. http://doi.org/10.1109/Jmems.2019.2939189
7. Niu L, Chu LY, Burton SA, *et al.*, 2019, Intradermal Delivery of Vaccine Nanoparticles Using Hollow Microneedle Array Generates Enhanced and Balanced Immune Response. *J. Control Release*, 294:268–78. http://doi.org/10.1016/j.jconrel.2018.12.026
8. van der Maaden K, Heuts J, Camps M, *et al.*, 2018, Hollow Microneedle-mediated Micro-injections of a Liposomal HPV E743-63 Synthetic Long Peptide Vaccine for Efficient Induction of Cytotoxic and T-helper Responses. *J Control Release*, 269:347–54. http://doi.org/10.1016/j.jconrel.2017.11.035
9. Gupta J, Denson DD, Felner EI, *et al.*, 2012, Rapid Local Anesthesia in Humans Using Minimally Invasive Microneedles. *Clin J Pain*, 28:129–35. http://doi.org/10.1097/AJP.0b013e318225dbe9
10. Dardano P, De Martino S, Battisti M, *et al.*, 2021, One-Shot Fabrication of Polymeric Hollow Microneedles by Standard Photolithography. *Polymers* (*Basel*), 13:520. http://doi.org/10.3390/polym13040520
11. Wang PC, Wester BA, Rajaraman S, *et al.*, 2009, Hollow Polymer Microneedle Array Fabricated by Photolithography Process Combined with Micromolding Technique. *Annu Int Conf IEEE Eng Med Biol Soc*, 2009:7026–9.

http://doi.org/10.1109/IEMBS.2009.5333317

12. Bolton CJ, Howells O, Blayney GJ, *et al.*, 2020, Hollow Silicon Microneedle Fabrication Using Advanced Plasma Etch Technologies for Applications in Transdermal Drug Delivery. *Lab Chip*, 20:2788–95. http://doi.org/10.1039/d0lc00567c
13. Li Y, Zhang H, Yang R, *et al.*, 2019, Fabrication of Sharp Silicon Hollow Microneedles by Deep-reactive Ion Etching Towards Minimally Invasive Diagnostics. *Microsyst Nanoeng*, 5:41. http://doi.org/10.1038/s41378-019-0077-y
14. Trautmann A, Roth GL, Nujiqi B, *et al.*, 2019, Towards a Versatile Point-of-care System Combining Femtosecond Laser Generated Microfluidic Channels And Direct Laser Written Microneedle Arrays. *Microsyst Nanoeng*, 5:6. http://doi.org/10.1038/s41378-019-0046-5
15. Carcamo-Martinez A, Mallon B, Dominguez-Robles J, *et al.*, 2021, Hollow Microneedles: A Perspective in Biomedical Applications. *Int J Pharm*, 599:120455. http://doi.org/10.1016/j.ijpharm.2021.120455
16. Xenikakis I, Tsongas K, Tzimtzimis EK, *et al.*, 2021, Fabrication of Hollow Microneedles Using Liquid Crystal Display (LCD) Vat Polymerization 3D Printing Technology for Transdermal Macromolecular Delivery. *Int J Pharm*, 597:120303. http://doi.org/10.1016/j.ijpharm.2021.120303
17. Yeung C, Chen S, King B, *et al.*, 2019, A 3D-Printed Microfluidic-enabled Hollow Microneedle Architecture for Transdermal Drug Delivery. *Biomicrofluidics*, 13:064125. http://doi.org/10.1063/1.5127778
18. Ovsianikov BC, Mente P, Monteiro-Riviere NA, *et al.*, 2007, Two Photon Polymerization of Polymer–Ceramic Hybrid Materials for Transdermal Drug Delivery. *Int J Appl Ceram Technol*, 4:22–9. http://doi.org/10.1111/j.1744-7402.2007.02115.x
19. Mathew E, Pitzanti G, Dos Santos AL, *et al.*, 2021, Optimization of Printing Parameters for Digital Light Processing 3D Printing of Hollow Microneedle Arrays. *Pharmaceutics*, 13:1837. http://doi.org/10.3390/pharmaceutics13111837
20. Liao C, Anderson W, Antaw F, *et al.*, 2019, Two-Photon Nanolithography of Tailored Hollow three-dimensional Microdevices for Biosystems. *ACS Omega*, 4:1401–9. http://doi.org/10.1021/acsomega.8b03164
21. Doraiswamy A, Ovsianikov A, Gittard SD, *et al.*, 2010, Fabrication of Microneedles Using Two Photon Polymerization for Transdermal Delivery of Nanomaterials. *J Nanosci Nanotechnol*, 10:6305–12. http://doi.org/10.1166/jnn.2010.2636
22. Liu X, Li R, Yuan X, *et al.*, 2021, Fast Customization of Microneedle Arrays by Static Optical Projection Lithography. *ACS Appl Mater Interfaces*, 13:60522–30. http://doi.org/10.1021/acsami.1c21489
23. Tan JY, Kim A, Kim JJ, 2021, Modeling, Characterization, and Fabrication of Bell-tip Microneedle Array by Diffraction and Self-aligned Lens Effects. *Appl Phys Lett*, 119:023501. http://doi.org/10.1063/5.0055073
24. Yang C, Yu Y, Wang X, *et al.*, 2021, Cellular Fluidic-based Vascular Networks for Tissue Engineering. *Eng Regen*, 2:171–4. http://doi.org/10.1016/j.engreg.2021.09.006
25. Use of International Standard ISO-10993-1, 2020, Biological Evaluation of Medical Devices Part 1: Evaluation and Testing within a Risk Management Process. In: US Department of Health and Human Services FDA, Center for Devices and Radiological Health, Center for Biologics Evaluation and Research.
26. Lim SH, Tiew WJ, Zhang J, *et al.*, 2020, Geometrical Optimisation of a Personalised Microneedle Eye Patch for Transdermal Delivery of Anti-wrinkle Small Peptide. *Biofabrication*, 12:035003. http://doi.org/10.1088/1758-5090/ab6d37
27. Zhang D, Das DB, Rielly CD, 2014, Microneedle Assisted Micro-Particle Delivery from Gene Guns: Experiments Using Skin-Mimicking Agarose Gel. *J Pharm Sci*, 103:613–27. http://doi.org/10.1002/jps.23835
28. Wang J, Yu J, Zhang Y, *et al.*, 2019, Charge-switchable Polymeric Complex for Glucose-responsive Insulin Delivery in Mice and Pigs. *Sci Adv*, 5:eaaw4357. http://doi.org/10.1126/sciadv.aaw4357
29. Zhou C, Tang H, Zhang L, *et al.*, 2021, Hollow Microneedle Arrays Produced by Low-Cost, High-Fidelity Replication of Hypodermic Needle Tips for High-Dose Transdermal Drug Delivery. *Adv Eng Mater*, 23:2001355. http://doi.org/10.1002/adem.202001355
30. Oskui SM, Diamante G, Liao C, *et al.*, 2016, Assessing and Reducing the Toxicity of 3D-Printed Parts. *Environ Sci Technol Lett*, 3:1–6. http://doi.org/10.1021/acs.estlett.5b00249
31. Davis SP, Landis BJ, Adams ZH, *et al.*, 2004, Insertion of Microneedles into Skin: Measurement and Prediction of Insertion Force and Needle Fracture Force. *J Biomech*, 37:1155–63. http://doi.org/10.1016/j.jbiomech.2003.12.010

32. Roxhed N, Samel B, Nordquist L, *et al.*, 2008, Painless Drug Delivery through Microneedle-based Transdermal Patches Featuring Active Infusion. *IEEE Trans Biomed Eng*, 55:1063–71. http://doi.org/10.1109/TBME.2007.906492
33. Burton SA, Ng CY, Simmers R, *et al.*, 2011, Rapid Intradermal Delivery of Liquid Formulations Using a Hollow Microstructured Array. *Pharm Res*, 28:31–40. http://doi.org/10.1007/s11095-010-0177-8
34. Ma Y, Li CG, Kim S, *et al.*, 2018, An Insulin Microneedle Pen (IMP) for Self-Subcutaneous Insulin Injection. *Adv Mater Technol*, 3:1800234. http://doi.org/10.1002/admt.201800234
35. Jung YS, Koo DH, Yang JY, *et al.*, 2018, Peri-tumor Administration of 5-fluorouracil Sol-gel Using a Hollow Microneedle for Treatment of Gastric Cancer. *Drug Deliv*, 25:872–9. http://doi.org/10.1080/10717544.2018.1455760
36. Dul M, Stefanidou M, Porta P, *et al.*, 2017, Hydrodynamic Gene Delivery in Human Skin Using a Hollow Microneedle Device. *J Control Release*, 265:120–31. http://doi.org/10.1016/j.jconrel.2017.02.028
37. Norman JJ, Brown MR, Raviele NA, *et al.*, 2013, Faster Pharmacokinetics and Increased Patient Acceptance of Intradermal Insulin Delivery Using a Single Hollow Microneedle in Children and Adolescents with Type 1 Diabetes. *Pediatr Diabetes*, 14:459–65. http://doi.org/10.1111/pedi.12031
38. Ogai N, Nonaka I, Toda Y, *et al.*, 2018, Enhanced Immunity in Intradermal Vaccination by Novel Hollow Microneedles. *Skin Res Technol*, 24:630–5. http://doi.org/10.1111/srt.12576
39. Chen G, Chen Z, Wen D, *et al.*, 2020, Transdermal Cold Atmospheric Plasma-mediated Immune Checkpoint Blockade Therapy. *Proc Natl Acad Sci U S A*, 117:3687–92. http://doi.org/10.1073/pnas.1917891117
40. Jun H, Han MR, Kang NG, *et al.*, 2015, Use of Hollow Microneedles for Targeted Delivery of Phenylephrine to Treat Fecal Incontinence. *J Control Release*, 207:1–6. http://doi.org/10.1016/j.jconrel.2015.03.031
41. Szeto B, Aksit A, Valentini C, *et al.*, 2020, Novel 3D-printed Hollow Microneedles Facilitate Safe, Reliable, and Informative Sampling of Perilymph from Guinea Pigs. *Hear Res*, 400:108141. http://doi.org/10.1016/j.heares.2020.108141

Publisher's note

Whioce Publishing remains neutral with regard to jurisdictional claims in published maps and institutional affiliations.

RESEARCH ARTICLE

Laser-Induced Forward Transfer Printing on Microneedles for Transdermal Delivery of Gemcitabine

Zoi Kanaki[1†], Chrysoula Chandrinou[2†], Ioanna-Maria Orfanou[1†], Christina Kryou[2], Jill Ziesmer[3], Georgios A. Sotiriou[3], Apostolos Klinakis[1], Constantin Tamvakopoulos[1*], Ioanna Zergioti[2*]

[1]Biomedical Research Foundation Academy of Athens, 4 Soranou Ephessiou Street, 11527, Athens, Greece
[2]Department of Physics, School of Mathematical and Physical Sciences, National Technical University of Athens, Heroon Polytehneiou 9, 15780, Athens, Greece
[3]Department of Microbiology, Tumor and Cell Biology, Karolinska Institutet, SE-171 77, Stockholm, Sweden
[†]*These authors contributed equally to this work.*

Abstract: Cancer treatment with chemotherapeutic drugs remains to be challenging to the physician due to limitations associated with lack of efficacy or high toxicities. Typically, chemotherapeutic drugs are administered intravenously, leading to high drug concentrations that drive efficacy but also lead to known side effects. Delivery of drugs through transdermal microneedles (MNs) has become an important alternative treatment approach. Such delivery options are well suited for chemotherapeutic drugs in which sustained levels would be desirable. In the context of developing a novel approach, laser-induced forward transfer (LIFT) was applied for bioprinting of gemcitabine (Gem) to coat polymethylmethacrylate MNs. Gem, a chemotherapeutic agent used to treat various types of cancer, is a good candidate for MN-assisted transdermal delivery to improve the pharmacokinetics of Gem while reducing efficiency limitations. LIFT bioprinting of Gem for coating of MNs with different drug amounts and successful transdermal delivery in mice is presented in this study. Our approach produced reproducible, accurate, and uniform coatings of the drug on MN arrays, and on in vivo transdermal application of the coated MNs in mice, dose-proportional concentrations of Gem in the plasma of mice was achieved. The developed approach may be extended to several chemotherapeutics and provide advantages for metronomic drug dosing.

Keywords: Laser-induced forward transfer bioprinting; Microneedles; Metronomic chemotherapy; Pharmacokinetics; Transdermal dosing; Sustained drug release

*Correspondence to: Ioanna Zergioti, National Technical University of Athens, Athens GR15780, zergioti@central.ntua.gr; Constantin Tamvakopoulos, Biomedical Research Foundation Academy of Athens, Athens, GR 11527; ctamvakop@bioacademy.gr

Received: December 28, 2021; **Accepted:** February 8, 2022; **Published Online:** February 8, 2022

Citation: Kanaki Z, Chandrinou C, Orfanou IM, *et al*., 2022, Laser Induced Forward Transfer Printing on Microneedles for Transdermal Delivery of Gemcitabine. *Int J Bioprint,* 8(2):554. http://doi.org/10.18063/ijb.v8i2.554

1. Introduction

In the past decades, drug delivery through microneedles (MNs) has become an important approach for treatment when compared to other transdermal methods such as hypodermic needles, topical creams, and transdermal patches. MNs have several advantages over the aforementioned methods such as deeper skin penetration, reduced pain, and increased penetration of high molecular weight drug molecules through stratum corneum, the skin's outermost layer. There are five main ways for active pharmaceutical ingredient (API) delivery[1,2]: (a) API-entrapped in soluble MNs[3-6] (b) API-coated MNs[7], (c) API applied on a patch after the skin has been pierced by solid MNs[8], (d) hollow MNs that enable a continuous fluid flow of the API, and (e) swelling MNs which swell after application and absorption of interstitial fluid, leading to drug diffusion through the swollen MNs[9]. API-coated MNs can be used for delivery of both hydrophilic and hydrophobic drugs[5,10,11]. Their ideal use is for low-dose administration of potent drugs, which are efficacious at low circulating amounts. For example, vaccines applied with MNs induce similar or better immune responses when

© 2022 Author(s). This is an Open Access article distributed under the terms of the Creative Commons Attribution License, permitting distribution and reproduction in any medium, provided the original work is properly cited.

compared to hypodermic needle injections[12]. Despite its advantages, the coating process remains challenging due to limited quantity of the drug coating, the uniformity of the coating, material waste, and the precision in drug dosing. Several technologies have been used in the past, such as dip coating[7,13], gas jet drying[14,15], and spray coating[16,17] with noted limitations[18,19].

In the last decade, three-dimensional (3D) printing technologies have emerged as promising tools for both optoelectronics, and biomedical applications[20]. Through printing methodologies, a plethora of materials can be used with various geometries to achieve a layer-by-layer building of 3D structures. The 3D printing approaches can be used to coat MNs by transferring small microdroplets of the API solution onto the MNs, thus forming uniform layers.

The most noticeable techniques among 3D printing technologies are droplet-based bioprinting (inkjet printing, thermal, piezoelectric, and electrostatic printing), extrusion bioprinting, and laser-induced forward transfer (LIFT). For the coating of MNs for transdermal applications, inkjet printing has been used before[21-23]; however, it has limitations with high viscosity materials, due to excessive force required to eject highly viscous drops. Moreover, inkjet printing is also associated with nozzle clogging[24,25]. In contrast, LIFT[26] is a digital, high-resolution, non-destructive, contactless (nozzle-free) bio-printing technique, which employs single laser pulses to propel the bioink under transfer toward the receiving substrate with high precision. Therefore, LIFT is a promising method used to improve drug coating on MNs with uniform coating layers.

Anticancer chemotherapy drugs (doxorubicin, paclitaxel, methotrexate, etoposide, cisplatin, and gemcitabine [Gem]) are typically associated with non-specific systemic toxicity that leads to patient discomfort and even treatment secession. Gem has been shown to be efficacious against colon, pancreatic, ovarian, breast, head and neck, and lung cancers, in combination with various anticancer agents[27]. However, its poor pharmacokinetics[28] creates a need for alternative approaches for Gem delivery, including encapsulation in nanocarriers (e.g., liposomes, dendrimers, carbon nanotubes, hydrogel[21]) or transdermal patches[29]. Gem's pharmacokinetic and efficacy limitations can be attributed to rapid deactivation and formation of the inactive metabolite 2′,2′-difluoro-2′-deoxyuridine (dFdU) by cytidine deaminase. As Gem is administered based on the classical maximum tolerated dose approach (MTD), initial high doses lead to efficacy. However, such high doses are associated with significant side effects. Furthermore, plasma concentrations of Gem decline rapidly. Patient recovery after treatment necessitates long intervals between doses (3 – 4 weeks, that often lead to disease progression.

Previous studies by our groups have shown that Gem's limitations can be overcome with different strategies. Initially, different targeting peptides were developed and used to generate novel targeted compounds (peptide-Gem conjugate analogs that specifically bound to receptors known to be overexpressed in cancer cells). Such analogs provided us with improved efficacy, pharmacokinetic advantages, and improved toxicity in comparison to equimolar Gem dosing[30-32].

As an extension of the peptide-drug conjugate work, another concept, the metronomic approach (MTR) based on the daily low-dose administration of Gem, was recently evaluated[33]. An oral pro-drug of Gem (OralGem) was chosen for this work in non-small cell lung cancer animal models. We showed that MTR chemotherapy resulted in low circulating and sustained levels of Gem that could potentially lead to the efficacy with less toxicity in comparison to MTD treatments. However, the continuous low-dose supplementation of Gem that is essential for MTR dosing schemes remains a challenge. For example, OralGem is a prodrug of Gem with its own toxicity and dosing limitations due to its first-pass effect[34].

In the effort to search for treatments that provide the optimum efficacy to safety window for cancer patients, a novel concept is presented in this paper. We employed LIFT bioprinting of Gem for coating polymethylmethacrylate (PMMA) MNs with different drug amounts and evaluated the transdermal delivery in mice. Our approach produced reproducible, accurate, and uniform coatings of the drug on the MN arrays, and also yielded dose-proportional concentrations of Gem in mice, following in vivo transdermal application of the coated MNs.

2. Materials and methods

2.1. Materials

Gem hydrochloride was purchased from Carbosynth Limited (Compton, Berkshire, UK). Ammonium acetate, formic acid, and glycerol (≥99.5%) were purchased from Sigma-Aldrich (Sigma-Aldrich Chemie GmbH, Munich, Germany). Acetonitrile (ACN, liquid chromatography [LC-MS] grade) was purchased from Fisher Scientific (Fisher Scientific, Loughborough, UK). Water (LC-MS grade) was purchased from Carlo Erba (Carlo Erba, Milan, Italy). Ketamin was purchased from Richter pharma ag (Austria). Xylazine was purchased from Neocell Pharmaceuticals.

2.2. Gem dispersion preparation

Gem solutions with concentrations of 10, 37.5, and 75 mg/mL were prepared by dissolving Gem in a H_2O: Glycerol solution (90:10 v: v).

Solubility feasibility experiments were conducted to identify the proper solution mixture for the described

studies, since low, medium, high concentrations of drug had to be achieved in a non-toxic solvent system that was compatible with the LIFT technology.

Since Gem is highly soluble in H_2O (>50 mg/mL), we initially tested a range of Gem concentrations (60-80 mg/mL) at 100% H_2O to find the highest soluble concentration. Subsequently, we tested a series of Gem concentrations (60-80 mg/mL) in a mixture of H_2O with a small amount of glycerol (10%). Glycerol contributes to the proper LIFT printing process. Finally, we found that 75 mg/mL was the highest soluble concentration of Gem in a H_2O: Glycerol solution (90:10 v: v).

2.3. MN array fabrication

MN arrays were produced as previously reported[6] using (PMMA, MW 120k, Sigma-Aldrich) which was dissolved at 30 w/v% in ethyl lactate (≥98%, Sigma-Aldrich) for 1.5 h at 150°C. The MN molds (Micropoint Technologies) contained 100 pyramidical cavities with base length and height of 200 μm and 600 μm, respectively. 50 mg of 30 w/v% PMMA was casted on the MN mold, centrifuged for 30 min at 3500 rpm, and left to dry overnight in the fume hood. PMMA MNs were imaged with scanning electron microscopy using a Phenom Pharos microscope (Thermo Fisher Scientific) with 5 kV beam voltage after being sputter-coated with a 5 nm thick carbon nanolayer with the Quorum Q150T (QuorumTech) (**Figure 1**).

2.4. Donor/receiver substrate materials

Quartz substrates coated with 60 nm of Ti were the donor layers and the receiver material was PMMA MNs.

2.5. LIFT process

Printing of Gem solutions was carried out by a solid-state lamp-pumped Nd: YAG (Litron Nano-L 200-10, Neodymium-doped Yttrium Aluminum Garnet, λ = 355 nm, 10 ns pulse duration, UK) and a high-power imaging micromachining system. The imaging system monitored the whole process in real-time through a customized microscope system equipped with a camera, enabling the accurate alignment of the target and substrate materials. A target holder was fixed onto a computer-controlled x–y translation stage with 1 μm positioning resolution and a LabVIEW program was used to synchronize the x–y motion with the laser. The laser beam was controlled by an attenuator while the size of the beam could be adjusted through a variable circular mask. Consequently, a ×15 plano-convex lens was used to focus the laser beam on a donor substrate. The donor substrate was a 1-inch quartz plate coated with a Ti film laser absorbing interlayer, onto which 10 μl of the three Gem solutions (100 μg, 375 μg, and 750 μg) were drop cast. By focusing the laser beam onto the donor substrate, a high-pressure vapor pocket is created in the interface between the Ti layer and the deposited API solution, due to the absorption of the laser pulse from the Ti layer of the donor. This high-pressure vapor pocket expands and propels the supernatant fluid creating a dynamic jet which drives the API solution to the receiver substrate with a high impact velocity, resulting in an nL droplet of Gem solution printed onto the MN substrates for each laser beam pulse. The distance between the donor and the receiver substrates is 700 μm. The laser transfer resulted in a continuous Gem film (5 × 5 mm) on the MNs substrate. The high-speed imaging setup, consisting of a high-speed camera (Photron Europe Limited, FASTCAM Mini-Series AX100 model, High Wycombe, UK) coupled to the system (**Figure 2**); with a maximum recording speed at 540kfps, and a standard LED (Thorlabs LEDD1B) placed opposite of the camera, for illumination purposes. **Figure 2** shows a schematic of the LIFT process for the coating of the PMMA MNs with Gem solution.

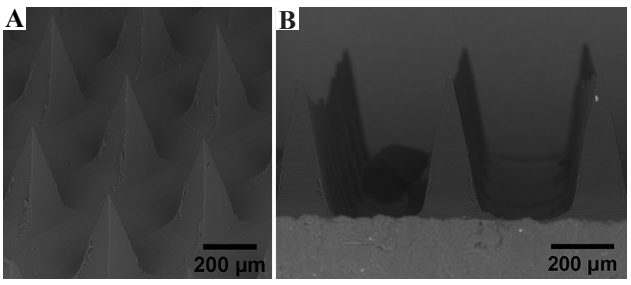


Figure 1. SEM images of PMMA MN arrays tilted at (A) 45° and (B) 90°.

2.6. Statistical analysis

Statistical analysis of the data value distribution was performed by calculating the mean and its standard deviation (SD) from at least 9 individual droplets per LIFT experiment. The results are expressed as mean ± SD. Statistical analyses were performed by the GraphPad Prism 7.0 (GraphPad Software, San Diego, CA, 41 USA).

2.7. Imaging and analysis

The PFV and ImageJ software were utilized to process the captured images.

2.8. Characterization and quantitative analysis of Gem by LC-MS mass spectrometry (MS)

The amount of Gem on the printed areas on the MNs was determined with a high-performance liquid chromatography-tandem mass spectrometry (HPLC-MS/MS). For the identification and quantification of Gem standards and samples, an LC-MS/MS method in MRM mode was developed and validated as described previously[30,31]. HPLC was performed using a Sciex Exion LC system (AB SCIEX LLC, CA, USA) equipped with two pumps, a temperature-

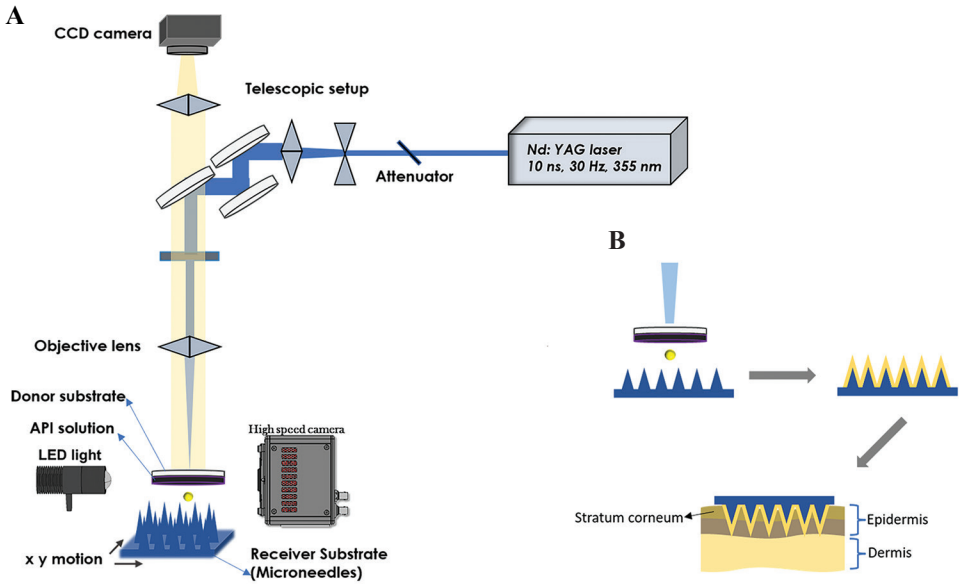


Figure 2. Schematic representation of the LIFT printing process for coating the PMMA MNs. (A) LIFT setup. (B) Coating process.

controlled column compartment, and an autosampler. A dC18 column (Water, Atlantis, 2.1 × 50 mm, 3 µM) was used at a flow rate of 300 µl/min for the separation of analytes of interest. The injection volume of the samples was 10 µl. The mobile phase consisted of A: 100% water, 2 mM ammonium acetate, and 0.1% FA and B: 90% ACN, 10% water, 2 mM ammonium acetate, and 0.1% FA. MS was performed on an API 5500 QTRAP LC-MS/MS system fitted with a Turbo Ion Spray source and a hybrid triple quadrupole/linear ion trap mass spectrometer (AB SCIEX LLC, CA, USA). The standard solutions within a concentration range of 10 – 200 ng/mL of Gem were prepared. Samples of 100, 375, and 750 µg of the initial amount of Gem printed by the LIFT technique were used for the quantification studies. The Gem standards and the laser printed samples on the MN substrates were extracted with MeOH (100%) and then centrifuged with a Speed Vac for 5 min at 16000 rpm. The obtained Gem standards and samples were resuspended in mobile phase A, followed by a 10-fold dilution, and analyzed by HPLC-MS/MS. Warfarin was used as internal standard (IS). The gradient methodology was as follows: 0 – 1.5 min: 100% A, 1.5 – 5 min: 40% A – 60% B, 5 – 10 min: 100% A. The primary MRM transitions for Gem and warfarin were: m/z 264.1→112.0 and 309.1→162.9, respectively. Gem was eluted with a retention time of 1.6 min and the IS was eluted at 5.2 min. Linearity was shown for Gem concentration range of 1–500 ng/mL with a lower on-column detection limit of 10 pg.

2.9. In vivo administration of Gem and extraction of mouse plasma Gem

Mice (C57Bl/6) were purchased from Jackson laboratories and were housed in individually ventilated cages, under specific pathogen-free conditions, in full compliance with Federation of Laboratory Animal Science Associations recommendations in the Animal House Facility of the Biomedical Research Foundation of the Academy of Athens (BRFAA, Greece). All procedures for the care and treatment of the animals were approved by the Institutional Committee on Ethics of Animal Experiments and the Attica Prefecture. No:971840/16-11-21.

Gem was administered to mice either transdermally or intraperitoneally (IP). A total of 36, 5-week-old male mice (average weight 20 g) were used in this study. Prior to the procedure, animals were anesthetized with a Ketamine: Xylazine mix (90 mg/kg Ketamine and 10 mg/kg Xylazine) as previously described[35]. For MN application onto the skin of mice, the left side just above the flank of the mouse was shaved and the MN patch was placed and pressed with the thumb for approximately 2 min and left on the skin for another 10 min without pressure. Manual insertion of MN patches by human volunteers has been reported to be approximately 20 N[4]. PMMA was chosen as the MN polymer based on previous work[6] using PMMA MN tips coated with water-dissolvable, drug-loaded layer which showed that PMMA MNs can be removed successfully from the skin after application. This may reduce toxicity concerns because nonbiodegradable polymers are removed from the tissue after the treatment.

Regarding the transdermal application of Gem, six groups of mice were generated (n≥3) and treated with MNs loaded with 100 µg, 375 µg, or 750 µg of Gem.

Four groups of mice, each composed of 4 individuals were generated to compare intraperitoneal with transdermal application. In the first two groups,

mice were treated with MNs loaded with 10 mg/mL of Gem while mice in another two groups were injected with 10 mg/mL of Gem IP; both dosing routes resulted in 100 μg dose.

Blood was collected from the mouse cheek 15 and 60 min after MN application or IP injection. Blood was placed in heparinized Eppendorf tubes, containing 10 μL heparin (5000 iu/mL), which were then placed immediately on ice and centrifuged for 10min at 3000 rpm. Plasma was then stored in a −80°C freezer prior to analysis. Mice were then euthanized.

Plasma samples (50 μL) were prepared for quantification by protein precipitation with the addition of cold ACN, centrifugation, and evaporation to dryness based on previously reported approach[31]. Gem was determined and quantified by LC-MS/MS analysis as described (see section 2.7). This methodology provided a linear calibration curve with a range of 100–5000 ng/mL for the quantification of Gem in the obtained plasma samples.

3. Results

3.1. LIFT printing of Gem solutions

The direct transfer of the API solution via LIFT printing, which relies on the high velocity and pressure that the liquid droplets have an impact with the MNs substrate, was achieved, resulting in a physical adsorption of the materials onto the substrate. Two-dimensional patterns of continuous Gem layers were printed on the MNs by adjusting the droplet-to-droplet distance to create an even film (**Figure 3**). The photo was taken before the coated material dried. After drying, the difference is not apparent to the naked eye. The purpose is to show that the liquid printed material is evenly distributed and confined within the MN area.

To test process parameters, time-resolved imaging of the printing process was performed by a high-speed camera while the distance between donor and receiver was 700 μm. Different fluences (in the range of 2 J/cm^2 and 250 mJ/cm^2) were investigated to evaluate the process and select the optimum printing conditions. LIFT did not occur at fluences below 380 mJ/cm^2 and above 1530 mJ/cm^2, where the laser energy either produced a small jet and did not transfer the material (subthreshold regime), or it produced a large jet causing a violent ejection of material leading to a disorderly transfer (splashing regime). In the duration of laser transfer, the material that forms the jet is not subjected to any mechanical stress and even though it suffers thermal stress, it only happens during the first few nanometres of bubble formation[36] which does not influence the quality of the transferred material. High-quality laser transfer of a single droplet can only happen in a narrow range of laser fluences which correspond to the optimal regime[37]. In these experiments, the optimum laser fluence was found between 390 and 450 mJ/cm^2, as presented in **Figure 4**.

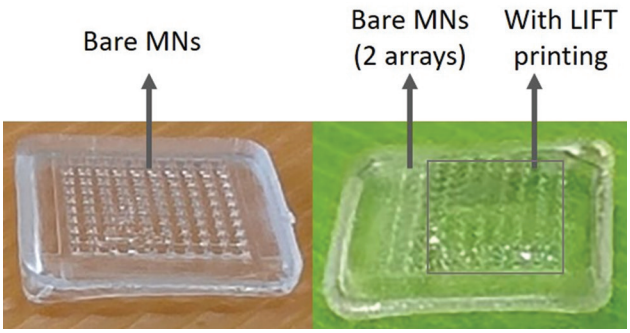


Figure 3. Photograph of the bare MNs substrate (left) and partially just printed Gem-loaded MNs substrate (right).

The impact velocity (0.8 m/s) was calculated by a linear fit of the propagation length of the jet front before impact as a function of the elapsed time of the successive frames captured from the videos. **Figure 5** presents snapshots taken during the printing process by a high-speed camera at four different fluences where successful transfer of the Gem solution occurred.

The droplet size increases with increasing fluence, while higher fluences lead to higher droplet size variation. This may lead to non-uniform deposition film causing the API not to be distributed evenly on the MN patches. It should also be noted that the LIFT technique has the ability to precisely print very small droplets[38] (< 100 pL) of liquids on each MN by adjusting the spot size and fluence for specialized applications. However, the aim of this work was to coat the MNs reproducibly and with a precise amount of Gem.

3.2. Quantification of Gem on the MNs following LIFT printing

LIFT-printed MNs from the three different drug-loaded solutions were analyzed with HPLC-MS/MS to quantify the amount of printed Gem. The results shown in **Figure 6A and B** indicate the average amount of LIFT-Gem: (i) 88 ± 11 μg, (ii) 388 ± 102 μg, and (iii) 1019 ± 100 μg. These values are in good agreement with the theoretical amounts of 100, 375, and 750 μg, suggesting that LIFT enables the precise deposition of API in a reliable and reproducible manner.

It should be noted that a higher than nominal value was observed at the 750 μg dose in comparison to the lower measurements (100 and 375 μg). A limitation of the present study is that at higher doses, solubility leads to a slight increase of the MN loading. Future studies should include more extended trials and optimization at higher doses.

It should be noted that with most conventional drug coating approaches on MNs, the amount of API used

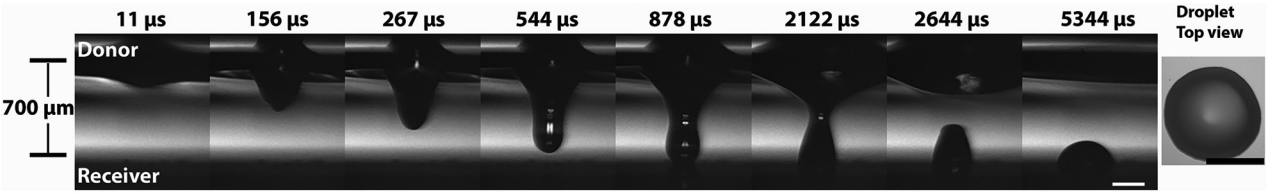


Figure 4. Still frame images extracted from high-speed video of the LIFT printing process for the Gem solution (10 mg/ml). The laser fluence is 390 mJ/cm^2 and the donor-receiver gap is fixed at 700 µm. On the right, a top view of the printed droplet from an optical microscope is shown. The scale bar is 200 µm.

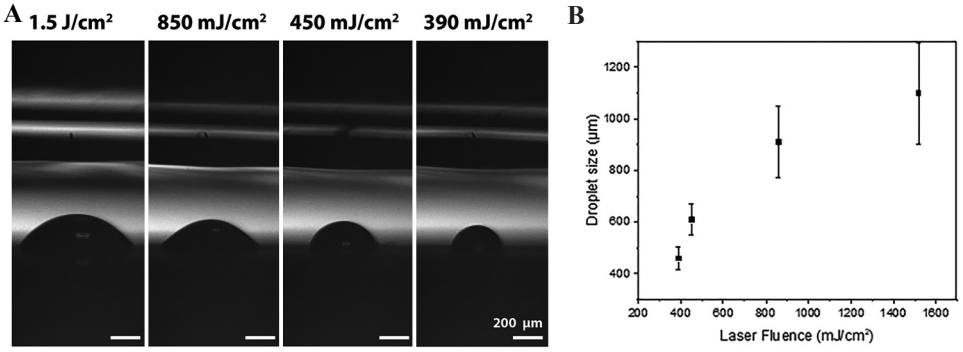


Figure 5. (A) Still frame images of the printed droplet at different fluences extracted from high-speed video. **(B)** Graph showing the relation of the droplet size to the laser fluence.

on the MNs prior to coating is not controlled rather the eventual drug loading is only calculated using loading efficiency equations after the coating is applied[29,34]. The LIFT technique is highly efficient as it only utilizes the amount that is needed for each printing, thus reducing API and solvent waste.

In a study performed by Bhatnagar *et al*.[29], Gem dissolved in phosphate buffer was coated on Zein MNs by a dip-coating technique. In this study, the maximum quantity of drug loaded on the MNs was found at 83 µg, considerably lower than the procedure described herein, where each MN patch could be loaded with up to 750 µg of Gem.

3.3. Gem quantification in mouse plasma

HPLC-MS/MS methodology was utilized to quantify Gem concentrations in the bloodstream of mice treated with MNs loaded with 100, 375, and 750 µg of Gem. A representative HPLC-MS/MS chromatogram for Gem detection in mouse plasma, 15 min after dosing mice with MNs (100 µg dose) is depicted in **Figure 7**.

The use of transdermal MN patches with increasing quantities of Gem leads to higher amounts of Gem in mouse plasma (**Figure 8**). Application of MNs with 100, 375, and 750 µg of Gem in mice led to blood Gem concentrations averaging 479, 1353, and 3067 ng/mL, respectively, at 15 min following dosing. Importantly, Gem levels were increased significantly 1 h after dosing, leading to average blood Gem concentrations of 1087, 1455, and 3803 ng/mL, respectively (**Figure 8B**). The findings from the pharmacokinetic experiments suggested that the administration of Gem through MNs can lead to prolonged systemic exposure. Furthermore, increasing amounts of loaded Gem corresponded well with those found in the bloodstream of treated mice. **Figure 8C** depicts comparative curves of Gem levels, following the increasing dosing in mice.

A comparative study between transdermal delivery and IP injection was performed to further explore the capability of transdermal administration. The IP route was selected for the comparison since it represents a common administration scheme for preclinical efficacy studies in mice. **Figure 9** shows the circulating Gem concentrations after transdermal application and IP delivery of 100 µg Gem in mice. The average amount of LIFT-Gem after 15 min and 60 min were: 479 ± 241 ng/mL and 1087 ± 558 ng/mL respectively, whereas the average amount of IP-Gem after 15 min and 60 min were: 1528 ± 442 ng/mL and 262 ± 12 ng/mL, respectively. These findings are in agreement with previous reports[33] in which 33 µg of Gem was injected IP in mice (Cmax 685 ng/mL, Tmax at 30 min, and rapid decrease within 1 h following the dose). It is important to note that, while IP injection led to decreased Gem levels after 1 h, with the MN transdermal application, a rise in circulating Gem levels was observed.

IP administration of Gem resulted in more than three-fold increase of Gem plasma concentrations 15 min after administration in comparison to the Gem plasma

A

LIFT printed API substance on microneedles	Calculated Gem concentration AVERAGE (μg) ± SD
100 μg (x4)	88 ± 11
375 μg (x4)	388 ± 102
750 μg (x2)	1019 ± 100

B

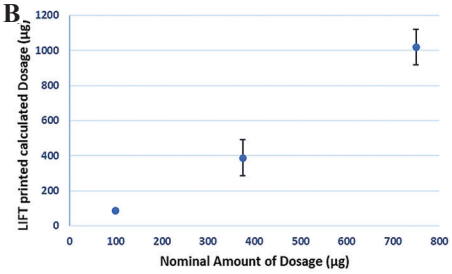


Figure 6. HPLC-MS/MS quantification of Gem on the MNs following LIFT printing. (A) Table presenting the three different Gem concentrations used, the number of repeats of LIFT printing, and the calculated amount of Gem found on the microneedle substrate. (B) Graph showing the LIFT printed calculated dosage related to the nominal amount of Gem.

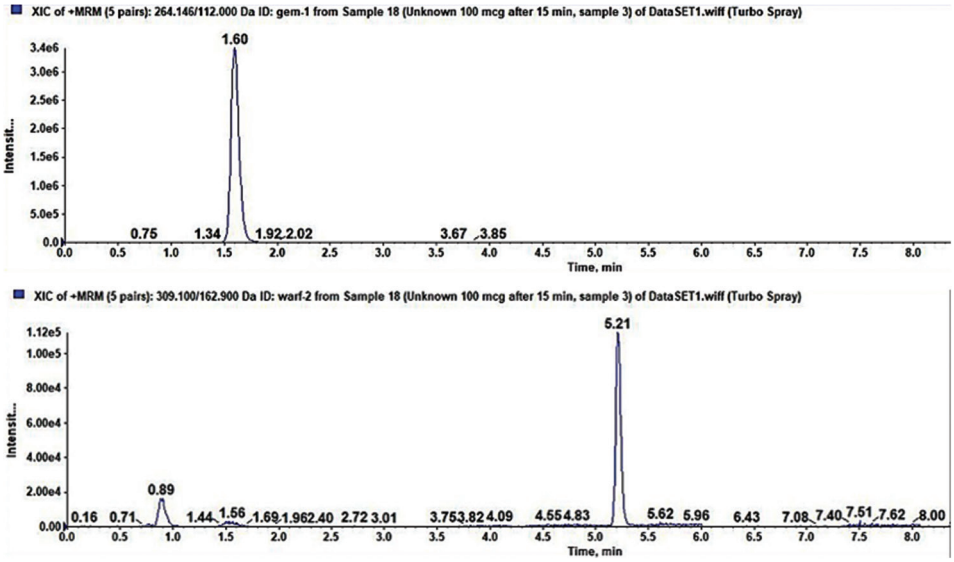


Figure 7. Representative LC-MS/MS chromatograms for Gem detected in mouse plasma, 15min after dosing mice with MNs (100 μg dose). Upper panel: For the detection of Gem, the 264.1/112.0 MRM transition was used (retention time 1.6 min). Lower panel: for the detection of Warfarin used as an internal standard, the 309.1/162.9 MRM transition was used (retention time 5.2 min).

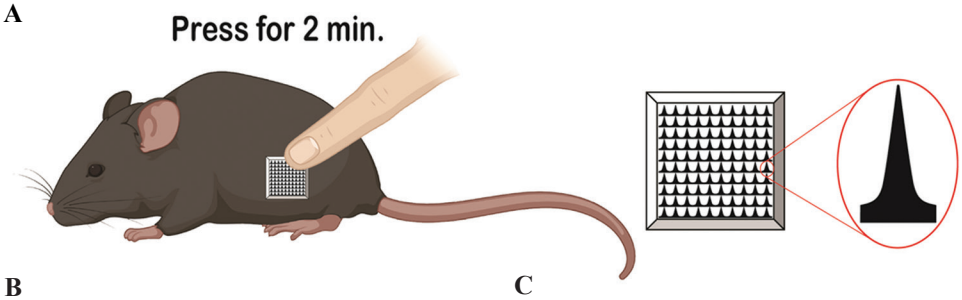
concentrations after MN application. However, within 60 min after IP administration, the Gem concentrations were significantly reduced, while MN transdermal application led to a rise of circulating Gem. This indicates that the MN administration of Gem may have reduced side effects and improved long-term pharmacokinetic profile.

Thus, a sustained release profile might be possible with smaller Gem dosages loaded onto MNs. Indeed, further experimentation is needed to investigate this possibility. Importantly, the average levels of Gem levels in the mouse plasma were found at 1.8 μM and 4.1 μM (479 and 1087 ng/mL) for the 15 and 60 min respectively, even when MNs loaded with a lower dose (100 μg) were used. These concentrations are well above the IC50 of Gem reported for several cancer cell lines (range 20 – 1000 nM[30-33]), suggesting that the efficacy can be achieved in clinically relevant cancer models with the LIFT-coated MNs.

4. Discussion

Current drug manufacturing techniques are performed in specialized factories which follow best practice protocols for mass drug production. Digital printing techniques can be used in medical facilities (i.e., hospitals, medical centers) to maximize the advantage of drug personalization. LIFT method requires a specialized equipment that includes laser, optics, translation stages, and a robot-based pipetting module (under development) for the automated loading of the pharmaceutical compound onto the donor substrate. The cost of LIFT method depends on the automation level and throughput when it comes to the mass production. It offers advantages such as the ability to use any potency and viscosity drug formulations, adaptable resolution (10 – 500 μm) for coating any kind of thin-film substrates including MN patches- as well as individual MNs- and minimal drug formulation waste.

A



B

Amount of LIFT printed Gem on microneedles	Extraction Time (min)	Gem quantification in mouse plasma AVERAGE (ng/mL) ± SD
100 µg	15	479 ± 241
	60	1087 ± 558
375 µg	15	1353 ± 283
	60	1455 ± 408
750 µg	15	3067 ± 466
	60	3803 ± 206

C

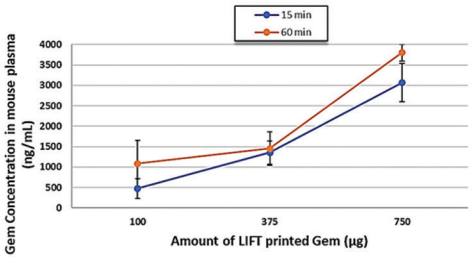


Figure 8. Gem experiments in mice. **(A)** Schematic representation of the in vivo experiment with MNs. MNs application onto the skin of the mouse, on the left side just above the flank. MNs consist of 100 pyramidical cavities with base length 200 µm. The height of each pyramidical cavity is 600 µm. **(B)** Table summarizing the Gem concentrations following dosing, the number of samples, the time point and the Gem concentration in the mouse plasma after transdermal application in mice. **(C)** Graph indicating the correlation between the amount of Gem LIFT loaded in the MNs and the concentration of Gem found in mouse plasma at 15min and 60min.

A

Samples of 100 µg Gem	Calculated Gem concentration in mouse plasma AVERAGE (ng/mL) ± SD
15 min IP (x4)	1528 ± 442
15 min LIFT/microneedles (x4)	479 ± 241
60 min IP (x4)	262 ± 12
60 min LIFT/microneedles (x4)	1087 ± 558

B

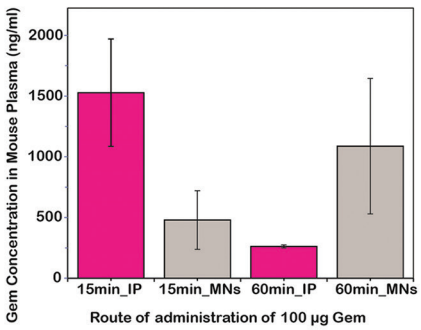


Figure 9. Gem quantification in mouse plasma: MNs versus IP. **(A)** Table presenting the calculated amount of Gem found in mouse plasma after IP injection or transdermal application of 100µg Gem, at 15- and 60-min blood extraction. **(B)** 100 µg of Gem was administered IP and the blood was collected at 15 and 60 min (15_IP, 60_IP). In parallel, the same amount of Gem was administered through MNs and the blood was collected at 15 and 60 min (15_MNs, 60_MNs).

The automated LIFT device is greatly advantageous because it can be used by medical staff offer personalized dosing after minimum training. A laboratory prototype will be built following the optimization process and the validation phase to include the appropriate automation features for the loading of drug formulations and its printing onto the selected substrate (i.e., MN patches).

LIFT printing was employed for the coating of PPMA MNs with (i) 88 µg, (ii) 388 µg, and (iii) 1019 µg of Gem, respectively, for transdermal application in mice. Quantification of the Gem-loaded MNs showed that LIFT printing achieved MN loading with satisfactory reproducibility and accuracy. Unlike most coating techniques, this methodology minimizes drug waste and allows personalized drug dosing with minimum preparation times. It is worth noting, however, that there is a limitation in the amount of drug that can be printed onto the MN patches. Higher Gem doses using the LIFT printing technique as described could not be obtained due to solubility limitations. A maximum 75 mg/mL solution of Gem was achieved in H_2O: Glycerol (90:10 v: v). In future studies, different solutions compatible with the LIFT printing process should be investigated to explore the possibility of higher dosing. Therefore, this method is more suited for potent drugs that are effective at lower dosages. In vivo transdermal application in mice

demonstrated the successful delivery of Gem in the bloodstream for all tested doses. A comparison of MN transdermal application and intraperitoneal injection of 0.1 mg of Gem in mice revealed that the transdermal approach produced similar results but at a slower release rate than the IP. It should be noted that the short half-life of Gem through IP administration as demonstrated by previous reports[33] led to the design of this study protocol by selecting the specific time points. This was also shown in our results (**Figure 9).** However, our results show that the MN approach after 1 h is beneficial, and this will be investigated further.

Although significant Gem concentrations (low μM) were achieved in mouse plasma at the lower Gem dose (100 μg), such concentrations are not expected to lead to toxicity as compared with other administration routes of chemotherapeutics Thus, in comparison with other dosing routes (IP or intravenous dosing), the MNs described here could be an ideal tool for metronomic dosing strategies. The benefits of metronomic dosing can only be achieved with appropriate dosing choices (e.g., oral) since drug administration has to be performed frequently.

The doses tested in this study were those that could be achieved (100 – 750 μg in one MN patch) based on drug solubility in the appropriate vehicle. Dosing in mice ranged from 5 – 37.5 mg/kg (the average weight of mice in the study was 20 g). In order to determine clinical relevance, Gem is dosed in humans as follows: 1000 – 1250 mg/m^2 (approximately 30 – 37.5 mg/kg) as a standard dose of intravenous infusion once a week for 3 – 4 weeks. Alternative dosing schemes for metronomic therapy include a more frequent schedule of every 3rd day with a low-dose infusion of 250 mg/m^2 (7.5 mg/kg) Gem[39]. Clinical studies of the oral availability of Gem have found very low systemic exposure due to rapid first-pass metabolism to dFdU (doses up to 8 mg, or 0.12 mg/kg), suggesting that only a pro-drug approach could be used to provide metronomic Gem with appreciable concentrations following oral dosing[33,40].

5. Conclusions

This work presents a novel approach to coat MN patches in ambient conditions using the LIFT technique. The LIFT process successfully coated PPMA MNs with (i) 88 μg, (ii) 388 μg, and (iii) 1019 μg of Gem for transdermal application in mice, in a reliable and reproducible manner. Application of MNs with the three aforementioned amounts of Gem in mice led to blood Gem concentrations averaging 479, 1353, and 3067 ng/mL respectively, at 15 min and increased considerably after 1h, suggesting that administration of Gem through MNs can lead to prolonged systemic exposure. Furthermore, a comparative study between transdermal delivery and IP injection was performed and the results suggested a sustained release profile with smaller Gem dosages loaded onto MNs and further investigations are underway to explore this possibility. Based on our findings in this study, we believe that MN dosing is a viable alternative to the oral dose. Future studies should include more extended pharmacokinetic protocols as well as their applicability to the preclinical efficacy models to further explore the benefits of the described approach.

Acknowledgments

This research has been co-financed by the European Union and Greek national funds through the Operational Program Competitiveness, Entrepreneurship and Innovation, under the call RESEARCH–CREATE–INNOVATE (project code: T1EDK-00976). G.A.S. acknowledges funding from the European Research Council (ERC) under the European Union's Horizon 2020 research and innovation program (ERC Grant agreement n° 758705). Part of **Figure 8A** has been created using Biorender.com

Conflict of interest

The authors have no conflict of interest to declare.

Author contributions

I.Z., A.K. and C.T. conceived the idea for the project. Z.K. developed the animal models and performed the animal dosing experiments and contributed to the writing of the manuscript. C.C. performed the LIFT high-speed camera experiments for the coating of the MNs, contributed to the LIFT experiments for the coating of the MNs, analyzed the LIFT process data, and also contributed to the writing of the manuscript. I-M.O developed and performed the HPLC-MS/MS quantification methodology and the pharmacokinetics analysis and contributed to the writing of the manuscript. C.K. contributed to the LIFT experiments for the coating of the MNs. J.Z. performed the MN fabrication and contributed in writing - editing. G.A.S. supervised the MN fabrication experiments, analyzed data and contributed to the writing-editing of the manuscript.

References

1. Waghule T, Singhvi G, Dubey SK, *et al*., 2019, Microneedles: A Smart Approach and Increasing Potential for Transdermal Drug Delivery System. *Biomed Pharmacother*, 109:1249–58. https://doi.org/10.1016/j.biopha.2018.10.078
2. Sirbubalo M, Tucak A, Muhamedagic K, *et al*., 2021, 3D Printing a "Touch-Button" Approach to Manufacture Microneedles for Transdermal Drug Delivery. *Pharmaceutics*, 13:924. https://doi.org/10.3390/pharmaceutics13070924

3. Kochhar JS, Quek TC, Soon WJ, *et al*., 2013, Effect of Microneedle Geometry and Supporting Substrate on Microneedle Array Penetration into Skin. *J Pharm Sci*, 102:4100–8. https://doi.org/10.1002/jps.23724
4. Larrañeta E, Moore J, Vicente-Pérez EM, *et al*., 2014, A Proposed Model Membrane and Test Method for Microneedle Insertion Studies. *Int J Pharm*, 472:65–73. https://doi.org/10.1016/j.ijpharm.2014.05.042
5. Larrañeta E, Lutton RE, Woolfson AD, *et al*., 2016, Microneedle Arrays as Transdermal and Intradermal Drug Delivery Systems: Materials Science, Manufacture and Commercial Development. *Mater Sci Eng R Rep*, 104:1–32. https://doi.org/10.1016/j.mser.2016.03.001
6. Ziesmer J, Tajpara P, Hempel NJ, *et al*., 2021, Vancomycin-Loaded Microneedle Arrays against Methicillin-Resistant Staphylococcus Aureus Skin Infections. *Adv Mater Technol*, 6:2001307. https://doi.org/10.1002/admt.202001307
7. Gill HS, Prausnitz MR, 2007, Coated Microneedles for Transdermal Delivery. *J Control Release*, 117:227–37. https://doi.org/10.1016/j.jconrel.2006.10.017
8. Yang Y, Kalluri H, Banga AK, 2011, Effects of Chemical and Physical Enhancement Techniques on Transdermal Delivery of Cyanocobalamin (Vitamin B12) *In Vitro*. *Pharmaceutics*, 3:474–484.
9. Vranic E, Tucak A, Sirbubalo J, *et al*., 2019, Microneedle-based Sensor Systems for Real-time Continuous Transdermal Monitoring of Analytes in Body Fluids. Vol. 73. Cham, Switzerland: Proceedings of the CMBEBIH 2019, IFMBE Proceedings, Springer, p167–172.
10. Pearton M, Saller V, Coulman SA, *et al*., 2012, Microneedle Delivery of Plasmid DNA to Living Human Skin: Formulation Coating, Skin Insertion and Gene Expression. *J Control Release*, 160:561–9. https://doi.org/10.1016/j.jconrel.2012.04.005
11. Zhao X, Coulman SA, Hanna SJ, *et al*., 2017, Formulation of Hydrophobic Peptides for Skin Delivery Via Coated Microneedles. *J Control Release*, 265:2–13. https://doi.org/10.1016/j.jconrel.2017.03.015
12. Tuan-Mahmood TM, McCrudden MT, Torrisi BM, *et al*., 2013, Microneedles for Intradermal and Transdermal Drug Delivery. *Eur J Pharm Sci*, 50:623–37. https://doi.org/10.1016/j.ejps.2013.05.005
13. Ameri M, Kadkhodayan M, Nguyen J, *et al*., 2014, Human Growth Hormone Delivery with a Microneedle Transdermal System: Preclinical Formulation, Stability, Delivery and PK of Therapeutically Relevant Doses. *Pharmaceutics*, 6:220–34. https://doi.org/10.3390/pharmaceutics6020220
14. Chen X, Prow TW, Crichton ML, *et al*., 2009, Dry-coated Microprojection Array Patches for Targeted Delivery of Immune-therapeutics to the Skin. *J Control Release*, 139:212–20. https://doi.org/10.1016/j.jconrel.2009.06.029
15. Chen X, Fernando GJ, Crichton ML, *et al*., 2011, Improving the Reach of Vaccines to Low-resource Regions, with a Needle-free Vaccine Delivery Device and Long-term Thermostabilization. *J Control Release*, 152:349–55. https://doi.org/10.1016/j.jconrel.2011.02.026
16. McGrath MG, Vrdoljak A, O'Mahony C, *et al*., 2011, Determination of Parameters for Successful Spray Coating of Silicon Microneedle Arrays. *Int J Pharm*, 415:140–9. https://doi.org/10.1016/j.ijpharm.2011.05.064
17. Vrdoljak A, McGrath MG, Carey JB, *et al*., 2012, Coated Microneedle Arrays for Transcutaneous Delivery of Live Virus Vaccines. *J Control Release*, 159:34–42. https://doi.org/10.1016/j.jconrel.2011.12.026
18. Bierwagen GP, 1992. Film Coating Technologies and Adhesion. *Electrochim Acta*. 37:1471–8.
19. Gill HS, Prausnitz MR, 2007, Coating Formulations for Microneedles. *Pharm Res*, 24:1369–80. https://doi.org/10.1007/s11095-007-9286-4
20. Alhnan MA, Okwuosa TC, Sadia M, *et al*., 2016, Emergence of 3D Printed Dosage Forms: Opportunities and Challenges. *Pharm Res*, 33:1817. https://doi.org/10.1007/s11095-016-1933-1
21. Uddin MJ, Scoutaris N, Klepetsanis P, *et al*., 2015, Inkjet Printing of Transdermal Microneedles for the Delivery of Anticancer Agents. *Int J Pharm*, 494:593–602. https://doi.org/10.1016/j.ijpharm.2015.01.038
22. Ross S, Scoutaris N, Lamprou D, *et al*., 2015, Inkjet Printing of Insulin Microneedles for Transdermal Delivery. *Drug Deliv Transl Res*, 5:451–61. https://doi.org/10.1007/s13346-015-0251-1
23. Uddin MJ, Scoutaris N, Economidou SN, *et al*., 2020, 3D Printed Microneedles for Anticancer Therapy of Skin Tumours. *Mater Sci Eng C Mater Biol Appl*, 107:110248. https://doi.org/10.1016/j.msec.2019.110248
24. Tarbox TN, Watts AB, Cui Z, *et al*., 2018, An Update on Coating/Manufacturing Techniques of Microneedles. *Drug Deliv Transl Res*, 8:1828–43. https://doi.org/10.1007/s13346-017-0466-4

25. Haj-Ahmad R, Khan H, Arshad MS, *et al*., 2015, Microneedle Coating Techniques for Transdermal Drug Delivery. *Pharmaceutics*, 7:486–502.
https://doi.org/10.3390/pharmaceutics7040486

26. Papazoglou S, Zergioti I, 2017, Laser Induced Forward Transfer (LIFT) of nano-micro patterns for sensor applications. *Microelectron Eng Rev*, 182:25–34.

27. Paroha S, Verma J, Dubey RD, *et al*., 2021, Recent Advances and Prospects in Gemcitabine Drug Delivery Systems. *Int J Pharm*, 592:120043.
https://doi.org/10.1016/j.ijpharm.2020.120043

28. Reid JM, Qu W, Safgren SL, *et al*., 2004. Phase I Trial and Pharmacokinetics of Gemcitabine in Children with Advanced Solid Tumors. *J Clin Oncol*, 22:2445–51.
https://doi.org/10.1200/jco.2004.10.142

29. Bhatnagar S, Kumari P, Pattarabhiran SP, *et al*., 2018, Zein Microneedles for Localized Delivery of Chemotherapeutic Agents to Treat Breast Cancer: Drug Loading, Release Behavior, and Skin Permeation Studies. *AAPS PharmSciTech*, 19:1818–26.
https://doi.org/10.1208/s12249-018-1004-5

30. Karampelas T, Argyros O, Sayyad N, *et al*., 2014. GnRH-Gemcitabine Conjugates for the Treatment of Androgen-independent Prostate Cancer: Pharmacokinetic Enhancements Combined with Targeted Drug Delivery. *Bioconjug Chem*, 25:813–23.
https://doi: 10.1021/bc500081g

31. Karampelas T, Skavatsou E, Argyros O, *et al*., 2017. Gemcitabine Based Peptide Conjugate with Improved Metabolic Properties and Dual Mode of Efficacy. *Mol Pharm*, 14:674–85.
https://doi.org/10.1021/acs.molpharmaceut.6b00961

32. Sayyad N, Vrettos EI, Karampelas T, *et al*., 2019. Development of Bioactive Gemcitabine-D-Lys6-GnRH Prodrugs with Linker-controllable Drug Release Rate and Enhanced Biopharmaceutical Profile. *Eur J Med Chem*, 166:256–66.
https://doi:10.1016/j.ejmech.2019.01.041

33. Skavatsou E, Semitekolou M, Morianos I, *et al*., 2021. Immunotherapy Combined with Metronomic Dosing: An Effective Approach for the Treatment of NSCLC. *Cancers* (*Basel*), 13:1901.
https://doi.org/10.3390/cancers13081901

34. Infante JR, Benhadji KA, Dy GK, *et al*., 2015. Phase 1b Study of the Oral Gemcitabine "Pro-drug" LY2334737 in Combination with Capecitabine in Patients with Advanced Solid Tumors. *Invest New Drugs*, 33:432–9.
https://doi.org/10.1007/s10637-015-0207-9

35. Kanaki Z, Voutsina A, Markou A, *et al*., 2021, Generation of Non-Small Cell Lung Cancer Patient-Derived Xenografts to Study Intratumor Heterogeneity. *Cancers* (*Basel*), 13:2446.
https://doi.org/10.3390/cancers13102446

36. Wang W, Chrisey DB, 2008, Study of Impact-Induced Mechanical Effects in Cell Direct. *J Manuf Sci Eng*, 130:1–10.

37. Theodorakos I, Kalaitzis A, Makrygianni M, *et al*., 2019, Laser-induced forward transfer of high viscous, non-newtonian silver nanoparticle inks: Jet dynamics and temporal evolution of the printed droplet study. *Adv Eng Mater*, 21:1900605.
https://doi.org/10.1002/adem.201900605

38. Makrygianni M, Millionis A, Kryou C, *et al*., 2018, On-Demand Laser Printing of Picoliter-Sized, Highly Viscous, Adhesive Fluids: Beyond Inkjet Limitations. *Adv Mater Interfaces*, 5:1800440.
https://doi.org/10.1002/admi.201800440

39. Pratt SE, Durland-Busbice S, Shepard RL, *et al*., 2013. Efficacy of Low-dose Oral Metronomic Dosing of the Prodrug of Gemcitabine, LY2334737, in Human Tumor Xenografts. *Mol Cancer Ther*, 12:481–90.
https://doi.org/10.1158/1535-7163.MCT-12-0654

40. Veltkamp SA, Jansen RS, Callies S, *et al*, 2008. Oral Administration of Gemcitabine in Patients with Refractory Tumors: A Clinical and Pharmacologic Study. *Clin Cancer Res*, 14:3477–86.
https://doi.org/10.1158/1078-0432.CCR-07-4521

Publisher's note

Whioce Publishing remains neutral with regard to jurisdictional claims in published maps and institutional affiliations.

REVIEW ARTICLE

Application of Bioprinting in Ophthalmology

Yanfang Wang[1,2,3†], Jiejie Wang[4†], Ziyu Ji[5†], Wei Yan[6], Hong Zhao[7], Wenhua Huang[2,3,4*], Huan Liu[8*]

[1]Key Laboratory of Biorheological Science and Technology (Chongqing University), Ministry of Education, Chongqing, 400045, China
[2]Guangdong Engineering Research Center for Translation of Medical 3D Printing Application, Guangdong Provincial Key Laboratory of Medical Biomechanics, School of Basic Medical Sciences, Southern Medical University, Guangzhou 510515, China
[3]Guangdong Innovation Platform for Translation of 3D Printing Application, The third Affiliated Hospital of Southern Medical University, Guangzhou 510630, China
[4]Department of Anatomy, School of Basic Medical Sciences, Southern Medical University, Guangzhou 510515, China
[5]College of Integrated Chinese and Western Medicine, Southwest Medical University, Lu Zhou 646000, China
[6]Department of Anatomy, Hebei Medical University, Shijiazhuang 050011, China
[7]School of Basic Medicine, Guangdong Medical University, Dongguan, Guangdong 523000, China
[8]National Traditional Chinese Medicine Clinical Research Base, The Affiliated Traditional Chinese Medicine Hospital of Southwest Medical University, Luzhou, Sichuan 646000, China
[†]*These authors contributed equally to this work.*

Abstract: Three-dimensional (3D) bioprinting is an emerging technology that is widely used in regenerative medicine. With the continuous development of the technology, it has attracted great attention and demonstrated promising prospects in ophthalmologic applications. In this paper, we review the three main types of 3D bioprinting technologies: Vat polymerization-based bioprinting, extrusion-based bioprinting, and jetting-based bioprinting. We also present in this review the analysis of the usage of both natural and synthesized hydrogels as well as the types of cells adopted for bioinks. Cornea and retina are the two main types of ocular tissues developed in bioprinting, while other device and implants were also developed for the ocular disease treatment. We also summarize the advantages and limitations as well as the future prospects of the current bioprinting technologies based on systematic reviews.

Keywords: Bioprinting; Ophthalmology; Bioinks; Biomaterials; Ocular bioprinting

*Correspondence to: Wenhua Huang, Guangdong Innovation Platform for Translation of 3D Printing Application, The third Affiliated Hospital of Southern Medical University, Guangzhou, Guangdong 510150, China; huangwenhua2009@139.com; Huan Liu, National Traditional Chinese Medicine Clinical Research Base, The Affiliated Traditional Chinese Medicine Hospital of Southwest Medical University, Luzhou, Sichuan, 646000, China; 20016040@163.com

Received: December 15, 2021; **Accepted:** February 22, 2022; **Published Online:** February 22, 2022

Citation: Wang Y, Wang J, Ji Z, *et al*., 2022, Application of Bioprinting in Ophthalmology. Int J Bioprint, 8(2):552. http://doi.org/10.18063/ijb.v8i2.552

1. Introduction

Bioprinting is an additive biofabrication method that prints target tissue engineering structures automatically by depositing bioinks in a layer-by-layer manner[1]. The technology attempts to produce original-tissue-like constructs through the precise combination of living cells, natural or synthesized biomaterials, crosslinkers, and/or other functional factors[2]. Since the emergence of the invention[3,4], bioprinting has been subject to persistent development mostly in the last decades and is used in a wide range of medical applications nowadays[5].

In ophthalmology, three-dimensional (3D) printing is utilized for diverse purposes, varying from the fabrication of preoperative eye models[6], personalized lens[7,8], glasses[9,10] and to other implants[9]. However, in tissue engineering and regenerative medicine, the use of bioprinting in fabricating ocular tissues and preserving relevant biological functions still need to be further studied.

© 2022 Author(s). This is an Open-Access article distributed under the terms of the Creative Commons Attribution License, permitting distribution and reproduction in any medium, provided the original work is properly cited.

In this article, we review the main 3D bioprinting techniques, summarize the bioinks adopted in 3D bioprinting, and discuss the applications of bioprinting in ophthalmology. We also present the advantages and limitations of bioprinting in the ocular tissue engineering as well as the future directions that will translate the technologies to personalized therapeutic and pharmaceutical tools in ophthalmology.

At present, vat polymerization (VP)-based, material extrusion-based, and material jetting-based printing strategies are the three principal printing techniques used in biological and medical applications (**Figure 1**). Due to the distinct working principles, each approach demonstrates different strengths and drawbacks.

1.1. VP-based bioprinting

The VP-based bioprinting refers to the process that fabricates the 3D structures through photo-polymerization reaction with photo-curable liquid bio-resin radiated by the light at specific wavelength[11]. The developed techniques include stereolithography (SLA), digital light processing (DLP), and two-photon polymerization (2PP) (**Figure 1A**).

As shown in **Figure 1A**, the SLA system cures the bio-resin when the laser source is refracted and scanned the materials in a vat. Depending on the position of the laser source, SLA can print the structures either in a top-down or bottom-up manner[11]. In the top-down method, the system prints the support and target structures together to form a precise designed construct. On the contrary, the bottom-up method scanned and cured the biomaterials with the light source from the bottom side. During the bottom-up printing, the build platform is raised above the vat for each peeling step between layers, thus resulting in a slower printing speed than the top-down method with continuous light scanning. To attain a successful printing, it is critical for both methods to have a good bonding between the printed structure and build-platform. Immediately after printing, the support structures need to be removed manually. The advantages of SLA techniques include the high lateral and vertical printable resolution (about 20–50 μm and 25–100 μm, respectively)[12], a wide range of printable viscosities (up to 5 Pa.s)[13], high printable cell density (could be 10^8 cells per ml), and great potential to formulate highly complex structures with the aid of support structures. However, its applications are limited in bioprinting due to the harmful effect of UV rays (shorter wavelength results in more DNA damage) and cytotoxic effect from the increased light intensity and photo-initiator concentration. To reduce DNA damage, the usage of visible light source as well as biocompatible photo-initiators is necessary.

Different from the SLA, the DLP prints the structures with the use of a digital micro-mirror device (DMD) to crosslink the photo-curable bio-resin in a vat. With the aid of DMD, DLP can speed up the printing process by crosslinking a layer of bio-resin rather than a single dot in SLA[14]. By controlling the light source power and exposure time, the cure depth of the bio-resin can be determined in the DLP system. Compared to the SLA, the DLP is more suitable in printing large-scale structures, which could be attained in micron resolutions.

The 2PP system adopts a near-infrared femtosecond laser light source (about 740 nm wavelength) and fabricates microstructures in a nanoscale resolution (up to sub-100 nm)[15]. The femtosecond laser is tightly focused to the bio-resin, and controlled the movement through an oil-immersed objective lens. The polymerization process

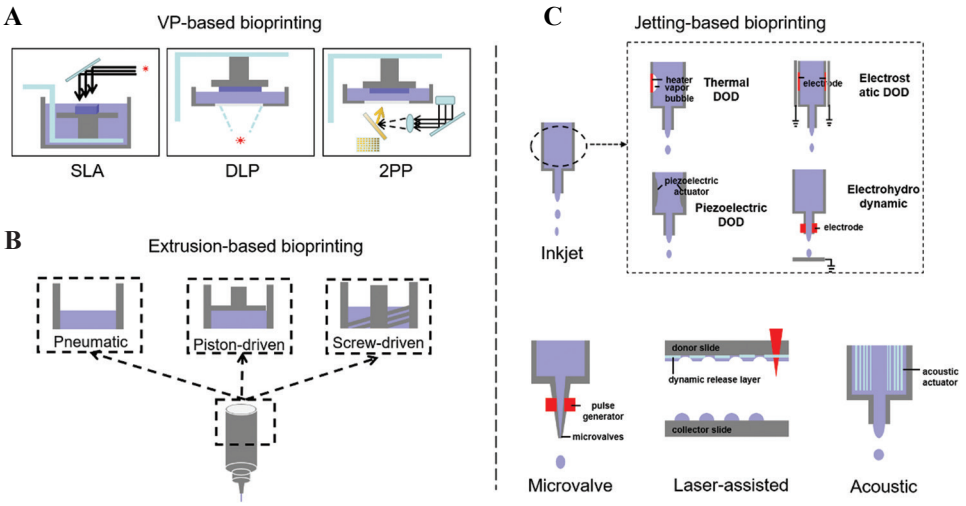


Figure 1. Three major categories of bioprinting technologies. (A) VP-based bioprinting. (B) Extrusion-based bioprinting. (C) Jetting-based bioprinting. DLP: Digital light processing; DOD: Drop-on-demand; SLA: Stereolithography; VP: Vat polymerization; 2PP: Two-photon polymerization.

in 2PP is initiated by exciting the molecules through two-photon absorption. The process can occur in an extremely short period (mm/seconds of scanning speed) and fabricate highly complex structure at any spatial position. However, the application of 2PP in bioprinting is also limited by a few drawbacks, including the material degradation caused by high laser power and bubble damage[16].

1.2. Extrusion-based bioprinting

The extrusion-based bioprinting is the most widely used technique because it has fast printing speed and can work with a broad range of printable bioinks[17]. In general, the material can be extruded from the cartridges either through pneumatic pressure or mechanical forces (piston-driven or screw-driven) (**Figure 1B**). The extrusion-based bioprinting can print bioinks with high cell densities (10^7 cells per ml) and print multiple types of cells at same time to fabricate a heterogenous structure. However, it also has limitations on the cell viability due to the damage with shear stress and nozzle clogging. To improve the performance of extrusion-based bioprinting, it is necessary to optimize the bioink design, select nozzle of suitable size, and choose suitable materials. The adjustment of printing parameters (e.g., pressure, speed, layer thickness) is required before printing to achieve a better performance.

1.3. Jetting-based bioprinting

As shown in **Figure 1C**, the jetting-based bioprinting represents a big group of techniques, including inkjet bioprinting, microvalve bioprinting, laser-assisted bioprinting, and acoustic bioprinting[18]. An advantage of the jetting-based printing technique is the drop-on-demand (DOD) patterning of different types of cells and biomaterials in a noncontact profile. Using this method, the droplets can be generated either by the heater-vapored bubbles in a thermal style[19], the deformation under the electrode pressure in an electrostatic style[20,21], the vibration of a piezoelectric actuator in piezoelectric style[22,23], or the high voltage filed energy from the nozzle electrodes in electrohydrodynamic style[24,25]. Different from the traditional continuous method, the DOD inkjet bioprinting ejects droplets only when the signal meets the demanded levels, which makes the droplet to formulate specific patterns as designed. Besides, as the diameter of inkjet nozzle is comparable to the size of a cell (50 μm), the inkjet printing could also be used for single cell printing. The high-resolution printing helps fabricate smaller tissues/organs, and the unique printing patterns could enhance the cell-cell and cell-matrix interactions. The inkjet bioprinting would contribute to cell damages by shear stress or pressure during printing or collision with the substrate after ejection. However, the damage only occurs to a low proportion of the cells; the efficiency and high-throughput features of inkjet printing still outweigh its drawbacks.

2. Bioinks

Compared with the traditional methods, bioprinting can be used to design complex 3D structures. It prints bioinks layer by layer to control the spatial distribution of cells and is used to fabricate the specific structure of tissues. The success of using bioprinting depends on printability and bioactivity of the bioinks[26]. In ophthalmology, bioinks of either cell-free hydrogel or cell-laden biomaterials were developed for different purposes.

2.1. Biomaterials

Biocompatibility, printability, and mechanical properties are the three main requirements for bioinks[27]. To formulate a highly biocompatible environment for the cells, decellularized extracellular matrix (dECM), and nature-derived or semi-synthesized hydrogels are widely used in ophthalmic applications.

(1) dECM

The ECM is important for cell nutrition, protection, and tissue function[28]. The ECM network is rich in molecules of collagen, elastin, microfibrillar proteins, adhesive glycoproteins and proteoglycans, providing support and crucial cues for cell adhesion, engraftment, and functions[29]. The dECM was developed for bioink bioprinting to mimic an optimized microenvironment for specific tissue engineering[30]; for instance, cornea- and retina-specific dECMs were developed for ocular tissue regeneration[31-33]. In corneal engineering, dECMs present great advantage in maintaining the keratocyte morphology and transparency by preventing the transdifferentiation of corneal fibroblasts[34]. To prepare the cornea-specific dECM bioink for bioprinting, Kim *et al*. decellularized the ECM from the bovine corneal stroma and lyophilized the cornea-derived dECM (Co-dECM) samples[31]. When printing, the Co-dECM powder was solubilized in acidic solutions and adjusted to form printable gel. The removal of the cells helps to reduce immune rejection response in tissue grafting. Moreover, the Co-dECM bioink has comparable levels of collagen and glycosaminoglycans as the natural cornea. The thin collagen fibrils in the bioink have a larger amount of proteoglycans, which make it possible to pass through the greater amount of light and maintain the transparency property as the native cornea. In addition, the Co-dECM bioink presented no toxicity in animal experiments and showed a good therapeutic potential in corneal diseases[35].

(2) Hydrogels

Hydrogels are structured networks of crosslinked polymers that are capable of absorbing and retaining large quantities

of water. They can be engineered to support the cellular growth, migration, and tissue formation[36,37]. Hydrogels present strong biomimetic advantages in the clinical translational applications attributed to their hydrophilic nature, good biocompatibility, biodegradability, controllable responsiveness to external stimuli, and tunable physical and chemical properties such as adhesion or low mechanical properties. Both naturally derived and synthetically derived hydrogels are widely used in bioprinting.

A series of natural hydrogels have been used for bioprinting due to their similarity to the cell microenvironment. The corneal stroma is rich in collagen, proteoglycan, and matrix metalloproteinase, which play an important role in the mechanical strength and transparency of the cornea. Due to the good biocompatibility and low immunogenicity, collagen is widely used as a bioink in 3D bioprinting[38]. However, low mechanical property of the pure collagen is the main limitation of using it as the bioink to form a stable structure. Crosslinking using different methods (e.g., chemical, physical, or biological) or a mixture with other components (e.g., fibrin, agarose, and alginate) can be performed to improve the properties of collagen bioinks[39-41]. Depending on the types of strategies selected, the bioinks can be tuned to prepare suitable low-viscosity solutions for jetting-based printing[42,43] or hydrogels with increased storage modules for extrusion-based printing[38]. In addition, synthesized peptide-based collagen is considered a good option to reduce the batch-to-batch variation effect and improve the mechanical properties in bioprinting[41].

Hyaluronic acid, which is another natural component of ECM, is abundant in the subretinal space. The hyaluronic acid hydrogel provides a biocompatible environment for the culture of retinal cells but the physiological property needs to be modified to fulfill the need of the native retina and printing requirements. Crosslinking the hydrogel with methacrylate groups could mimic the mechanical properties of retina and contributed to a good survival rate for the retinal pigment epithelial cells and differentiation of the fetal retinal progenitor cells (fRPCs)[44].

Gelatin is a type of hydrogel which shows good adhesive properties in the oculus usage and is considered a good option for cornea engineering[45]. It is biocompatible, transparent and non-toxic. Besides, it can be easily processed and has the reasonable mechanical properties to mimic the ECM. Gelatin can gain different viscoelastic and mechanical properties to facilitate the functions of oculus.

In addition to the natural hydrogels, synthetic bioinks are also widely used in bioprinting. Gelatin methacrylate (GelMA) is a photopolymerized hydrogel comprising of modified natural ECM components and can be prepared from the water-soluble gelatin. Gelatin is a temperature-sensitive polymer that transforms between the solid and liquid states when the temperature changes. With the addition of methacryloyl component, GelMA can improve the thermal stability of gelatin, demonstrating properties of both physicochemical strength and biocompatibility[46]. Both simulation of the matrix microenvironment and 3D printing of GelMA hydrogels to produce artificial matrices with high transparency, biocompatibility, and stability are the important pillars in the development of bioprinting in ophthalmology[47].

2.2. Types of cells

To facilitate their application in printing, the cells can be presented as cell-laden biomaterials, cell suspension or tissue spheroids for different printing technologies.

(1) Cell composition

The eyeball is a complex organ and composed of a variety of tissues. The cornea and retina are the two main types of tissues obtaining great attention in the ocular regenerative medicine and tissue engineering.

The cornea is located at the anterior section of the eye and formed by five layers: epithelium, bowman membrane, stroma, Descemet's membrane, and endothelium. To form the stroma equivalent, the corneal keratocytes can be isolated from the stromal cells of cadaverous human corneal tissues[48] and purified to print together with the biomaterials[49]. Besides, the corneal epithelium cells and endothelium cells also triggered the attention from the researchers to be bio-printed[50,51]. The human corneal epithelial cells and endothelial cells can be harvested from the donor corneas and made laden with matrix gel to form bioinks.

The retina is a complex stratified structure, which is located at the posterior section of the eye. It embodies more than 60 types of cells and nerve fibers that are difficult to be regenerated when damaged[52]. The cells isolated from the rat retinal tissues can be prepared as cell suspensions and printed independently with inkjet printing method onto a substrate matrix[53,54]. Besides, the fetal human retinal progenitor cells have been adopted in bioprinting, and have successfully differentiated into photoreceptors after printing[44].

(2) Stem cell induction

The latest advances in the research of induced pluripotent stem cell have paved the way for the production of patient-specific cells that are ideal for autologous cell replacement therapies in the treatment of various alternative diseases. Adipose-derived stem cells (ADSCs) are fat-derived stem cells with self-renewal, proliferation, and differentiation potentials. ADSCs can differentiate into corneal cells both *in vivo* and *in vitro*, and as reported in the previous studies, other researchers have printed differentiated ADSCs

with corneal characteristics using biomaterials, thereby successfully printing a layered corneal tissue that mimics the natural cornea[28]. In addition, the mesenchymal stem cells derived from the turbinate can also use to produce cells of keratocyte lineage that can be used for corneal regeneration[31].

3. Function and applications

In a general sense, bioprinting refers to 3D printing for medical applications, which can be divided into four stages of development[55]. Stage I is to print non-biocompatible structures that can be used as the models for surgery planning. Stage II is to print biocompatible but non-biodegradable products, such as implanted prothesis. Stage III is to print biocompatible and biodegradable products, which can be used as scaffolds to improve tissue damage repair or regeneration. Stage IV is to print biomimic 3D structures with cells. In the narrow sense, bioprinting can also be defined as cellular printing[27]. In the present review, our definition of bioprinting encompasses all four stages of development.

3.1. Treatment device and prosthesis

(1) Contact lens and scleral cover shell prothesis

Contact lens are used for vision correction or other therapeutic or cosmetic purposes. In addition, they can be incorporated with sensors for disease diagnosis and management (e.g., measure glucose composite in tears or monitor intraocular pressure for glaucoma)[56]. Through 3D printing technology, different sensor components have been designed and printed to make cost-efficient and smart contact lens[7,8,57]. The nanostructures patterned by direct laser writing help to detect the disease at early stages, while techniques still need to be further developed for commercial utilization.

The scleral cover shell prosthesis is used to correct the eye diagram in pathological conditions. It covers the corneal and adjacent scleral areas during the treatment. In the pilot study, Sanchez-Tena *et al*. printed a prosthesis with polylactic acid (PLA) using fused filament fabrication printing[58]. Further attempts using biocompatible materials to simulate the corneoscleral profile fitting are necessary.

(2) Intraocular lenses (IOLs)

IOLs are common personalized devices to treat cataract in clinic. The products mimic the shape and dimensions of crystalline lens and provide the substitute optical functions. Studies have been performed to reproduce the IOLs with a patented 3D printing technology called Print Optical. In the method, the photopolymer material (e.g., Luxexcel polymer) was deposited onto a poly(methylmethacrylate) (PMMA) substrate and cured with ultraviolet[59,60]. The printed IOLs with PMMA-like materials had a good level of transparency and showed the properties of biconvex lens, but were still limited by the surface roughness and optical performance (e.g., wavefront aberrations) in comparison to the qualified implants[59]. Similar results were also observed in the study by John *et al*., which demonstrated higher levels of surface roughness, figure errors, and wavefront deformations than the control product[60]. A better performance on the curvature radii was obtained on smaller lenses when printed. Although printing technology has great advantage over the manufacture of irregular and asymmetric products, it still has room for improvement in the future replication of IOLs. Further improvement on the surface figure is needed to make the printed lens fulfill the requirements of clinical implant.

(3) Choroidal models

The choroid is a soft membrane layer formed mainly by blood vessels between retina and sclera. It is the main blood supply for the retina and the surrounding ocular tissues. The reduction of choroidal vessels due to tumor or other ocular diseases will result in the loss or death of tissues in the supply areas. To evaluate the structural changes of choroidal vessels, Maloca *et al*. printed 3D models of choroidal vessels based on the optical coherence tomography images from normal eyes and pigmented choroidal tumors[6]. The group segmented the choroidal vessels in the interested areas by a threshold filter, and printed the 3D models with transparent resin by SLA printing or gypsum power by additive fused deposition modeling. The resolution of the models was limited to 1 mm in wall thickness, which was able to characterize the choroidal vessels in details. This helps to better understand the architecture of choroidal vessels and their interactions with the adjacent tissues and tumors.

(4) Artificial eyes

In the study by Xie *et al*., an eye model with different ametropia state was produced using 3D printing technology for the fundus viewing system[10]. The optical parameters of printed models are adjustable and the models can simulate the optical performance of human eye. The technique developed by Xie *et al*. could be a useful tool for fundus range viewing research and training for fundus examination in future. Besides, conformer shells are clear plastic lens fitted to support the shape of the eye socket and maintain the natural appearance without glasses after an enucleation/eye removal surgery. 3D printing of conformer shells makes the production of individualized shells possible.

A lot of attempts have also been pursued to generate "bionic eyes" using 3D printing technology. By printing

the semiconductive polymer onto a hemispherical surface using a customized extrusion printer, Park *et al*. fabricated the polymer-based photodetectors that can generate electricity from the light stimuli[61]. The production of electronic devices by 3D printing confirms that the design of light receptors is a more flexible and efficient method than the traditional manufacturing. Indirectly, this might facilitate the development of wearable and implantable material that can restore the vision in future.

(5) Orbital implant

3D printing is a flexible and low-cost method for designing customized complex orbital reconstruction implants[62-65]. Based on the digital images from the orbital tumor resection or fracture, the researchers can reconstruct the structure model, design the implant templates according to the orbital structure of the intact part, and print the 3D models to serve as stencil for the actual implant material[62]. The application of 3D printing technology reduces the need to adjust and manipulate the Medpor-titanium implant during the operation and could improve various surgical indicators (e.g., reduced tissue damage, shortened surgical duration, improved clinical outcomes, and cost effectiveness)[62,64]. Besides, 3D printing technology also demonstrated advantages in implant exchange or dermis fat graft secondary to the orbital implants[63]. This technique can be used to design the exact shape of the implant and center the implants in patients with recurrent implant migration.

3.2. Drug delivery systems

Due to the existence of blood-retinal barrier and blood-aqueous barrier, it is difficult to deliver the drug to the back of the eye for treatment. Chitosan is one of the hemi-synthetic, highly biocompatible, and biodegradable hydrogels considered suitable for ocular drug delivery[66-68]. Chitosan nanoparticles could prolong drug delivery, facilitate penetration through the physiological barriers, and enhance mucoadhesive properties[69,70]. Meanwhile, preparation of nanogels of personalized medication using 3D printing technology has begun to gain traction[70].

3.3. Graft tissue and organs

(1) Cornea

The cornea is the outermost protective layer of the eye and is responsible for the transmission and refraction of incident light. Although corneal diseases are the causal factor of visual impairment and blindness worldwide[71], the percentage of corneal transplantation undertaken in individuals with treatable corneal blindness is still very low (approximately 1.4%)[72]. By estimation, more than 12.7 million patients are on the waiting list of a keratoplasty[73]. The shortage of donated cornea in eye banks against the increasing cases of corneal blindness is the main driver for the development of artificial cornea. Compared with the traditional technologies for artificial cornea production, 3D bioprinting provides a fast method to reconstruct individual-specific tissues and organs with high reproducibility.

Bioprinting offers the possibility of producing artificial cornea. The human corneal scanning model is used to print artificial cornea with complex structure through bioprinting, but the tissue function of artificial cornea still needs to be further validated in clinical trials[31]. The challenge in bioprinting the cornea lies in the transparency, microporosity and specific shape properties of the structure[74,75].

The natural cornea consists of three cellular layers (epithelium, stroma and endothelium) and two acellular layers (Bowman's and Descemet's membranes) (**Figure 2**)[76]. Stroma forms the major part of the cornea, accounting for 90% of the corneal thickness (approximate 500 μm)[75]. A series of studies have presented feasible strategies to bioprint the stroma equivalents[35,49,77-79]. Among the bioprinting technologies, the extrusion-based method is the most widely used, whereas the jetting method also demonstrates some advantages (**Table 1**). With the aid of a supportive gelatin scaffold, Isaacson *et al*. successfully printed the cornea-shaped structure with optimized cell-laden collagen/alginate bioinks using pneumatic extrusion 3D bioprinter[49]. A high cell viability of corneal keratocytes was observed on both day 1 (92%)

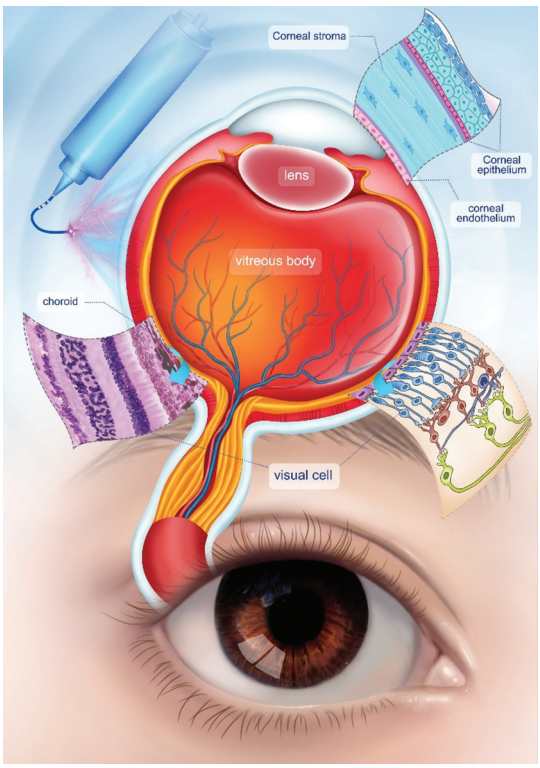


Figure 2. Roles of bioprinting in ophthalmology.

Table 1. Application of 3D bioprinting in ophthalmology

Ocular tissues	Tissue layer	Bioprinting approaches	Biomaterials	Cell types	References
Cornea	Epithelium	Extrusion	GelMa bioink/GelMA dome-shaped mold	CEpCs/LECs, Human CEpCs line	[50,86]
	Stroma	Extrusion, Inkjet, Laser-assisted, SLA	Matrigel-COL I bioink/ LN-COL IV support sheet, ALG-COL I bioink/FRESH support, COL I-AG bioink/ no support, GelMa bioink/ reinforced with PEG-PCL fibers, GelMA bioink/ no support, cornea-derived dECM bioink/no spport, ALG/GEL bioink/resin support	CSKs/LSSCs, human LECs+ADSCs, human CSKs, rat LSSCs, human TDMSCs with keratocyte induction, HCKs	[28,31,35,49,79,80,86-88]
	Endothelium	Extrusion	Gelatin-RGD bioink/amniotic membrane dECM support	CECs, human CECs	[51,86]
Retina	Retinal pigment epithelium	Laser-assisted, Microvalve jetting	HA-GM and PEG-RGDs, DMEM:F12/ALG and Pluronic	RPEs, human fetal retinal progenitor cells, ARPE-19, human retinoblastoma cell line (Y79)	[44,89]
	Retinal ganglion cells	Piezoelectric inkjet, 2PP, thermal inkjet combined with electrospinning	DMEM, ITO-coated glass, alginate and culture Medium/ PLA/HEIP and matrigel for electrospinning	Retinal granlion cell neurons, retinal glial cells, human iPSC, retinal ganglion cells	[54,83,90]

ADSCs: Adipose-derived stem cells; AG: Agarose; ALG: Alginate; CECs: Corneal endothelial cells; ARPE-19: Adult retinal pigmented epithelial cell line-19; CEpCs: Corneal epithelial cells; COL: Collagen; CSK: Corneal stromal keratocytes; dECM: Decellularized extracellular matrix; DMEM: Dubelcco's Modified Eagle's medium; FRESH: Freeform reversible embedding of suspended hydrogels; GelMA: Gelatin methacrylate; HA-GM: Hyaluronic acid with methacrylation by glycidyl-hydroxyl reaction; HCKs: Human corneal keratocytes; HEIP: Hexafluoroisopropanol; iPSC: Induced pluripotent stem cell; ITO: Indium tin oxide; LECs: Limbal epithelial cells; LN: Laminin; LSSCs: Limbal stromal stem cells; PEG-PCL: Polyethylene glycol-polycaprolactone; PEG-RGDs: Arg-Gly-Asp-Ser peptide; PLA: Polylactic acid; RPE: Retinal pigment epithelial cells; SLA: Stereolithography; TDMSCs: Turbinate-derived mesenchymal stem cells; 2PP: Two-photon polymerization

and day 7 (83%) post-printing. Without using supportive scaffold, Campos *et al*. adopted an electromagnetic micro-valve, rather than micro-extrusion, to directly print the corneal structure with collagen hydrogel in a DOD manner[77]. The transparency and optical density of the printed structure was comparable to those of the native cornea, and the keratocyte cells assumed the typical dendritic morphology on day 7 post-printing. GelMA is another good option for stroma printing; however, in GelMA-only printed structure, the keratocytes stayed in round shapes after days[35]. The specially designed alignment of collagen fibrils is critical to the transparency of the cornea. To mimic the sophisticated topological alignment of the stroma structure, Kong *et al*. fabricated the 3D construct with poly (ε-caprolactone)-poly (ethylene glycol) (PECL) microfibrous scaffold, which is a modified type of poly (ε-caprolactone) (PCL) with improved hydrophilicity, and GelMA hydrogel by direct writing[78]. The construction provided a good environment for the survival and phenotype maintenance of keratocyte cells. In another study, shear stress was induced by printing nozzles of different sizes in order to organize the printed collagen fibrils in the lattice pattern[79].

Besides, researchers also attempted to print the endothelial and epithelial components of the cornea (**Table 1**)[45]. For instance, Sorkio *et al*. printed the stratified corneal epithelium and stroma construct with the stem cell-laden laminin/collagen bioink using laser-assisted technology[28]. Jin *et al*. printed the cells of corneal epithelium using DLP technology coupled with extrusion printing[50]. Kim *et al*. printed the corneal endothelium cells using extrusion printing[51]. The results of these studies strengthened the possibility that corneal substitute can be rapidly generated. Nevertheless, further *in vitro* and *vivo* studies are still needed for clinical validation.

Hence, 3D bioprinting technologies embody a great potential and show promising prospects in the fabrication of artificial cornea. Efforts have been made to improve

the printing of corneal cells for personalized medicine. However, printing multilayers of the cornea and maintaining the physiological and mechanical properties and functions is still an immense challenge. Using natural macromolecules in the ECM, rather than synthetic materials, can reduce the risk of corneal transplantation, but the degree of immune response elicited by these constructs remains to be investigated[12,80].

(2) Retina

The retina is situated at the back of the eye and contains cells of completely different morphologies and functions arranged in a stratified and vascularized manner[52,81]. It forms distinct circuits to generate visual output; the loss of retinal neurons could lead to visual impairment or blindness. Compared with the cornea, the retina has a more complex multilayered structure (**Figure 2**). It is composed of different types of cells in nine layers, that is, the pigment epithelial cells in the retinal pigment epithelium (RPE) layer, rod, and cone photoreceptor cells in the photoreceptors layer, Müller cells in the outer nuclear layer, horizontal cells in the outer plexiform layer, bipolar cells in the inner nuclear layer, amacrine cells in the inner plexiform layer, retinal ganglion cells (RGCs) and glial cells in the ganglion cell layer and nerve fiber layer, and internal limiting membranes. Those cells interact and form circuits to work together in transmitting and converting the light signals from the environment into electrical signals in the brain. The structure is about 400 μm in thickness and contains more than 130 million cells[82].

Researchers have attempted to regenerate the retinal tissues using 3D bioprinting technologies and achieved proof of principle in certain types of cells. Lorber *et al*. was first to successfully print the RGCs and glia directly using piezoelectric inkjet printing technology[83]. The cells demonstrated a good degree of viability post-printing but were unable to form a complex cellular structure in multilayers. The challenges in creating a functional retina through printing include achieving sufficient number of cells and maintaining the cell phenotype and viability post-printing[53]. Validation of the functionalities of printed retina is also very important to create transplantable tissues, while the construction of blood vessels is critical to ensure the supply of nutrients and oxygen to the tissues. In combination with the degradable scaffold prepared with electrospinning technology, Kador *et al*. printed the RGCs together with brain-derived neurotrophic factor and ciliary neurotrophic factor onto the scaffold using the thermal inkjet printing technique[54]. The RGCs demonstrated a good degree of viability, possessed normal electrophysiological functions, and presented radial axon outgrowth on the scaffold. According to other reports, attempts have been made to print photoreceptors and RPE, which are other types of retinal cells[44,84,85]. Incorporated with the matched hyaluronic acid hydrogel, a bilayer structure of human fRPCs and RPE were printed and the fRPCs differentiated to mutant photoreceptors in 2 weeks[44].

4. Prospects

In recent years, the application of bioprinting technology has considerably expanded to the field of ophthalmology. This technology has a broad range of applications in ophthalmology, including the production of treatment device and prosthesis as well as the establishment of a system to deliver drug to transplantable tissues and organs. Further development of the technology is still needed to enhance functionalities of the printed structures to fulfill the requirements for treating ocular diseases.

Funding

This work is supported by grants from the Visiting Scholar Foundation of Key Laboratory of Biorheological Science and Technology (Chongqing University), Ministry of Education (CQKLBST-2020-003 to YW), the Sichuan Applied Basic Research Project (2018JY0402 to HL) and Luzhou Municipal People's Government-Southwest Medical University Science and Technology Strategic Cooperation Project (2018LZXNYD-ZK19 to HL), National Natural Science Foundation of China (NSFC 31972915 to WHH), the Science and Technology Project of Guangdong Province (2016B090917001to WHH), and Sanming Project of Medicine in Shenzhen (SZSM201612019 to WHH).

Conflict of interest

The authors declare that they have no conflicts of interest with the contents of this article.

Author contributions

Y.W., J.W., Z.J., W.Y., H.Z., and H.L. reviewed the literature and wrote the manuscript. Y.W., J.W., and Z.J. prepared the literature and figured. H.L. and W.H. conceived the idea of the review and revised the manuscript. All authors approved the final manuscript for publication.

References

1. Di Marzio N, Eglin D, Serra T, *et al*., 2020, Bio-Fabrication: Convergence of 3D Bioprinting and Nano-Biomaterials in Tissue Engineering and Regenerative Medicine. *Front Bioeng Biotechnol*, 8:326. https://doi.org/10.3389/fbioe.2020.00326
2. Moroni L, Burdick JA, Highley C, *et al*., 2018, Biofabrication Strategies for 3D *In Vitro* Models and Regenerative Medicine. Nature reviews. *Materials*, 3:21–37.

https://doi.org/10.1038/s41578-018-0006-y

3. Hull CW, Uvp I, 1986, Apparatus for Production of Three-dimensional Objects by Stereolithography. Patent US-6027324-A.
4. Klebe RJ, 1988, Cytoscribing: A Method for Micropositioning Cells and the Construction of Two and Three-dimensional Synthetic Tissues. *Exp Cell Res*, 179:362–73. https://doi.org/10.1016/0014-4827(88)90275-3
5. Castilho M, de Ruijter M, Beirne S, *et al.*, 2020, Multitechnology Biofabrication: A New Approach for the Manufacturing of Functional Tissue Structures? *Trends Biotechnol*, 38:1316–28. https://doi.org/10.1016/j.tibtech.2020.04.014
6. Maloca PM, Tufail A, Hasler PW, *et al.*, 2019, 3D Printing of the Choroidal Vessels and Tumours Based on Optical Coherence Tomography. *Acta Ophthalmol*, 97:e313–6. https://doi.org/10.1111/aos.13637
7. AlQattan B, Yetisen A Kand Butt H, 2018, Direct laser writing of nanophotonic structures on contact lenses. *ACS Nano*, 12:5130–40. https://doi.org/10.1021/acsnano.8b00222
8. Park J, Ahn D B, Kim J*, et al.*, 2019, Printing of Wirelessly Rechargeable Solid-state Supercapacitors for Soft, Smart Contact Lenses with Continuous Operations. *Sci Adv*, 5:eaay0764. https://doi.org/10.1126/sciadv.aay0764
9. Sommer AC, Blumenthal EZ, 2019, Implementations of 3D Printing in Ophthalmology. *Graefes Arch Clin Exp Ophthalmol*, 257:1815–22. https://doi.org/10.1007/s00417-019-04312-3
10. Xie P, Hu Z, Zhang X, *et al.*, 2014, Application of 3-dimensional Printing Technology to Construct an Eye Model for Fundus Viewing Study. *PLoS One*, 9:e109373. https://doi.org/10.1371/journal.pone.0109373
11. Ng WL, Lee JM, Zhou M, *et al.*, 2020, Vat Polymerization-based Bioprinting-Process, Materials, Applications and Regulatory Challenges. *Biofabrication*, 12:022001. https://doi.org/10.1088/1758-5090/ab6034
12. Zhao W, Qin P, Zhang D, *et al.*, 2019, Long Non-coding RNA PVT1 Encapsulated in Bone Marrow Mesenchymal Stem Cell-derived Exosomes Promotes Osteosarcoma Growth and Metastasis by Stabilizing ERG and Sponging miR-183-5p. *Aging* (*Albany NY*), 11:9581–96. https://doi.org/10.18632/aging.102406
13. Hinczewski C, Corbel S, Chartier T, 1998, Ceramic Suspensions Suitable for Stereolithography. *J Eur Ceram Soc*, 18:583–90. https://doi.org/10.1016/S0955-2219(97)00186-6
14. Zhu W, Ma X, Gou M, *et al.*, 2016, 3D Printing of Functional Biomaterials for Tissue Engineering. *Curr Opin Biotechnol*, 40:103–12. https://doi.org/10.1016/j.copbio.2016.03.014
15. Xing JF, Zheng ML, Duan XM, 2015, Two-photon Polymerization Microfabrication of Hydrogels: An Advanced 3D Printing Technology For Tissue Engineering and Drug Delivery. *Chem Soc Rev*, 44:5031–9. https://doi.org/10.1039/c5cs00278h
16. Nguyen AK, Narayan RJ, 2017, Two-photon Polymerization for Biological Applications. *Mater Today*, 20:314–22. https://doi.org/10.1016/j.mattod.2017.06.004
17. Jiang T, Munguia-Lopez JG, Flores-Torres S, *et al.*, 2019, Extrusion Bioprinting of Soft Materials: An Emerging Technique for Biological Model Fabrication. *Appl Phys Rev*, 6:011310. https://doi.org/10.1063/1.5059393
18. Li X, Liu B, Pei B, *et al.*, 2020, Inkjet Bioprinting of Biomaterials. *Chem Rev*, 120:10793–833.
19. Cui X, Boland T, D'Lima DD, *et al.*, 2012, Thermal Inkjet Printing in Tissue Engineering and Regenerative Medicine. *Recent Pat Drug Deliv Formul*, 6:149–155. https://doi.org/10.2174/187221112800672949
20. Nishiyama Y, Nakamura M, Henmi C, *et al.*, 2009, Development of a Three-dimensional Bioprinter: Construction of Cell Supporting Structures Using Hydrogel and State-of-the-art Inkjet Technology. *J Biomech Eng*, 131:035001. https://doi.org/10.1115/1.3002759
21. Nakamura M, Iwanaga S, Henmi C, *et al.*, 2010, Biomatrices and Biomaterials for Future Developments of Bioprinting and Biofabrication. *Biofabrication*, 2:0141. https://doi.org/10.1088/1758-5082/2/1/014110
22. Wijshoff H, 2010, The Dynamics of the Piezo Inkjet Printhead Operation. *Phys Rep*, 491:77–177. https://doi.org/10.1016/j.physrep.20https://doi.org/10.03.003
23. Christensen K, Xu C, Chai W, *et al.*, 2015, Freeform Inkjet Printing of Cellular Structures with Bifurcations. *Biotechnol Bioeng*, 112:1047–55. https://doi.org/10.1002/bit.25501
24. Park JU, Hardy M, Kang SJ, *et al.*, 2007, High-resolution Electrohydrodynamic Jet Printing. *Nat Mater*, 6:782–9. https://doi.org/10.1038/nmat1974
25. Poellmann MJ, Barton KL, Mishra S, *et al.*, 2011, Patterned Hydrogel Substrates for Cell Culture with Electrohydrodynamic Jet Printing. *Macromol Biosci*, 11:1164–8.

https://doi.org/10.1002/mabi.201100004

26. Dorishetty P, Dutta NK, Choudhury NR, 2020, Bioprintable Tough Hydrogels for Tissue Engineering Applications. *Adv Colloid Interface Sci*, 281:102163. https://doi.org/10.1016/j.cis.2020.102163
27. Gu Z, Fu J, Lin H, *et al.*, 2019, Development of 3D Bioprinting: From Printing Methods to Biomedical Applications. *Asian J Pharm Sci*, 15:529–557. https://doi.org/10.1016/j.ajps.2019.11.003
28. Sorkio A, Koch L, Koivusalo L, *et al.*, 2018, Human Stem Cell Based Corneal Tissue Mimicking Structures Using Laser-assisted 3D Bioprinting and Functional Bioinks. *Biomaterials*, 171:57–71. https://doi.org/10.1016/j.biomaterials.2018.04.034
29. Mecham RP, 2012, Overview of Extracellular Matrix. *Curr Protoc Cell Biol*, Chapter 10:Unit 10 11. https://doi.org/10.1002/0471143030.cb1001s57
30. Pati F, Jang J, Ha DH, *et al.*, 2014, Printing Three-dimensional Tissue Analogues with Decellularized Extracellular Matrix Bioink. *Nat Commun*, 5:3935. https://doi.org/10.1038/ncomms4935
31. Kim H, Park MN, Kim J, *et al.*, 2019, Characterization of Cornea-specific Bioink: High transparency, Improved *In Vivo* Safety. *J Tissue Eng*, 10:2041731418823382. https://doi.org/10.1177/2041731418823382
32. Maqueda M, Mosquera JL, Garcia-Arumi J, *et al.*, 2021, Repopulation of Decellularized Retinas with hiPSC-derived Retinal Pigment Epithelial and Ocular Progenitor Cells Shows Cell Engraftment, Organization and Differentiation. *Biomaterials*, 276:121049. https://doi.org/10.1016/j.biomaterials.2021.121049
33. Wang F, Shi W, Li H, *et al.*, 2020, Decellularized Porcine Cornea-derived Hydrogels for the Regeneration of Epithelium and Stroma in Focal Corneal Defects. *Ocul Surf*, 18:748–60. https://doi.org/10.1016/j.jtos.2020.07.020
34. Chameettachal S, Prasad D, Parekh Y, *et al.*, 2021, Prevention of Corneal Myofibroblastic Differentiation *In Vitro* Using a Biomimetic ECM Hydrogel for Corneal Tissue Regeneration. *ACS Appl Bio Mater*, 4:533–44. https://doi.org/10.1021/acsabm.0c01112
35. Bektas CK, Hasirci V, 2020, Cell Loaded 3D Bioprinted GelMA Hydrogels for Corneal Stroma Engineering. *Biomater Sci*, 8:438–49. https://doi.org/10.1039/C9BM01236B
36. Leijten J, Seo J, Yue K, *et al.*, 2017, Spatially and Temporally Controlled Hydrogels for Tissue Engineering. *Mater Sci Eng R Rep*, 119:1–35. https://doi.org/10.1016/j.mser.2017.07.001
37. Lee KY, Mooney DJ, 2001, Hydrogels for Tissue Engineering. *Chem Rev*, 101:1869–79. https://doi.org/10.1021/cr000108x
38. Osidak EO, Karalkin PA, Osidak MS, *et al.*, 2019, Viscoll Collagen Solution as a Novel Bioink for Direct 3D Bioprinting. *J Mater Sci Mater Med*, 30:31. https://doi.org/10.1007/s10856-019-6233-y
39. Stepanovska J, Otahal M, Hanzalek K, *et al.*, 2021, pH Modification of High-Concentrated Collagen Bioinks as a Factor Affecting Cell Viability, Mechanical Properties, and Printability. *Gels*, 7:252. https://doi.org/10.3390/gels7040252
40. Wu Z, Liu J, Lin J, *et al.*, 2022, Novel Digital Light Processing Printing Strategy Using a Collagen-Based Bioink with Prospective Cross-Linker Procyanidins. *Biomacromolecules*, 23:240–52. https://doi.org/10.1021/acs.biomac.1c01244
41. Lee JM, Suen SK, Ng WL, *et al.*, 2021, Bioprinting of Collagen: Considerations, Potentials, and Applications. *Macromol Biosci*, 21:e2000280. https://doi.org/10.1002/mabi.202000280
42. Roth EA, Xu T, Das M, *et al.*, 2004, Inkjet printing for high-throughput cell patterning. *Biomaterials*, 25:3707–15. https://doi.org/10.1016/j.biomaterials.2003.10.052
43. Ng WL, Lee JM, Yeong WY, *et al.*, 2017, Microvalve-based Bioprinting process, Bio-inks and Applications. *Biomater Sci*, 5:632–47. https://doi.org/10.1039/c6bm00861e
44. Wang P, Li X, Zhu W, *et al.*, 2018, 3D Bioprinting of Hydrogels for Retina Cell Culturing. *Bioprinting (Amsterdam, Netherlands)*, 11:e00029. https://doi.org/10.1016/j.bprint.2018.e00029
45. Khalili M, Asadi M, Kahroba H, *et al.*, 2020, Corneal Endothelium Tissue Engineering: An Evolution of Signaling Molecules, Cells, and Scaffolds toward 3D Bioprinting and Cell Sheets. *J Cell Physiol*, 236:3275–303. https://doi.org/10.1002/jcp.30085
46. Ashammakhi N, Ahadian S, Xu C, *et al.*, 2019, Bioinks and Bioprinting Technologies to Make Heterogeneous and Biomimetic Tissue Constructs. *Materials Today Bio*, 1:100008. https://doi.org/10.1016/j.mtbio.2019.100008
47. West-Mays JA, Dwivedi DJ, 2006, The Keratocyte: Corneal Stromal Cell with Variable Repair Phenotypes. *Int J Biochem Cell Biol*, 38:1625–31. https://doi.org/10.1016/j.biocel.2006.03.010

48. Gouveia RM, Connon CJ, 2013, The Effects of Retinoic Acid on Human Corneal Stromal Keratocytes Cultured *In Vitro* Under Serum-Free Conditions. *Investig Ophthalmol Visual Sci*, 54:7483–91. https://doi.org/10.1167/iovs.13-13092
49. Isaacson A, Swioklo S, Connon CJ, 2018, 3D Bioprinting of a Corneal Stroma Equivalent. *Exp Eye Res*, 173:188–93. https://doi.org/10.1016/j.exer.2018.05.010
50. Jin K, Wang S, Zhang Y, *et al.*, 2019, Long Non-coding RNA PVT1 Interacts with MYC and its Downstream Molecules to Synergistically Promote Tumorigenesis. *Cell Mol Life Sci*, 76:4275–89. https://doi.org/10.1007/s00018-019-03222-1
51. Kim KW, Lee SJ, Park SH, *et al.*, 2018, *Ex Vivo* Functionality of 3D Bioprinted Corneal Endothelium Engineered with Ribonuclease 5-Overexpressing Human Corneal Endothelial Cells. *Adv Healthc Mater*, 7:1800398. https://doi.org/10.1002/adhm.201800398
52. Masland RH, 2011, Cell Populations of the Retina: The Proctor Lecture. *Investig Ophthalmol Visual Sci*, 52:4581–91. https://doi.org/10.1167/iovs.10-7083
53. Lorber B, Hsiao WK, Martin KR, 2016, Three-dimensional Printing of the Retina. *Curr Opin Ophthalmol*, 27:262–7. https://doi.org/10.1097/ICU.0000000000000252
54. Kador KE, Grogan SP, Dorthé EW, *et al.*, 2016, Control of Retinal Ganglion Cell Positioning and Neurite Growth: Combining 3D Printing with Radial Electrospun Scaffolds. *Tissue Eng Part A*, 22:286–94. https://doi.org/10.1089/ten.TEA.2015.0373
55. Yong HE, Qing GA, Liu A, *et al*., 2019, 3D Bioprinting: From Structure to Function. *J Zhejiang Univ*, 53:407–19. https://doi.org/10.3785/j.issn.1008-973X.2019.03.001
56. Farandos NM, Yetisen AK, Monteiro MJ, *et al.*, 2015, Contact Lens Sensors in Ocular Diagnostics. *Adv Healthc Mater*, 4:792–8. https://doi.org/10.1002/adhm.201400504
57. Tang H, Alqattan B, Jackson T, *et al.*, 2020, Cost-Efficient Printing of Graphene Nanostructures on Smart Contact Lenses. *ACS Applied Materials & Interfaces*, 12(9): 10820-10828. https://doi.org/10.1021/acsami.9b21300
58. Sanchez-Tena MA, Alvarez-Peregrina C, Santos-Arias F, *et al.*, 2019, Application of 3D Printing Technology in Scleral Cover Shell Prosthesis. *J Med Syst*, 43:149. https://doi.org/10.1007/s10916-019-1280-y
59. Debellemanière G, Flores M, Montard M, *et al.*, 2016, Three-dimensional Printing of Optical Lenses and Ophthalmic Surgery: Challenges and Perspectives. *J Refract Surg* (*Thorofare NJ: 1995*), 32:201–4. https://doi.org/10.3928/1081597X-20160121-05
60. John G, Michal EP, Tomasz ST, 2017, Quantitative Evaluation of Performance of Three-dimensional Printed Lenses. *Opt Eng*, 56:1–13. https://doi.org/10.1117/1.OE.56.8.084110
61. Park SH, Su R, Jeong J, *et al.*, 2018, 3D Printed Polymer Photodetectors. *Adv Mater* (*Deerfield Beach, Fla.*), 30:e1803980. https://doi.org/10.1002/adma.201803980
62. Callahan AB, Campbell AA, Petris C, *et al.*, 2017, Low-Cost 3D Printing Orbital Implant Templates in Secondary Orbital Reconstructions. *Ophthalmic Plastic Reconstr Surg*, 33:376–80. https://doi.org/10.1097/IOP.0000000000000884
63. Dave TV, Gaur G, Chowdary N, *et al.*, 2018, Customized 3D Printing: A Novel Approach to Migrated Orbital Implant. *Saudi J Ophthalmol*, 32:330–3. https://doi.org/10.1016/j.sjopt.2018.03.003
64. Fan B, Chen H, Sun YJ, *et al.*, 2017, Clinical Effects of 3-D Printing-assisted Personalized Reconstructive Surgery for Blowout Orbital Fractures. *Graefes Arch Clin Exp Ophthalmol*, 255:2051–7. https://doi.org/10.1007/s00417-017-3766-y
65. Kang S, Kwon J, Ahn CJ, *et al.*, 2018, Generation of Customized Orbital Implant Templates Using 3-dimensional Printing for Orbital Wall Reconstruction. *Eye* (*London, England*), 32:1864–70. https://doi.org/10.1038/s41433-018-0193-1
66. Zamboulis A, Nanaki S, Michailidou G, *et al.*, 2020, Chitosan and its Derivatives for Ocular Delivery Formulations: Recent Advances and Developments. *Polymers*, 12:1519. https://doi.org/10.3390/polym12071519
67. Silva MM, Calado R, Marto J, *et al.*, 2017, Chitosan Nanoparticles as a Mucoadhesive Drug Delivery System for Ocular Administration. *Mar Drugs*, 15:370. https://doi.org/10.3390/md15120370
68. Başaran E, Yazan Y, 2012, Ocular Application of Chitosan. *Exp Opin Drug Deliv*, 9:701–12. https://doi.org/10.1517/17425247.2012.681775
69. Lynch C, Kondiah PP, Choonara YE, *et al.*, 2019, Advances in Biodegradable Nano-Sized Polymer-Based Ocular Drug Delivery. *Polymers*, 11:1371. https://doi.org/10.3390/polym11081371
70. Cho H, Jammalamadaka U, Tappa K, 2018, Nanogels for Pharmaceutical and Biomedical Applications and Their Fabrication Using 3D Printing Technologies. *Materials* (*Basel, Switzerland*), 11:302.

https://doi.org/10.3390/ma11020302

71. Flaxman SR, Bourne RR, Resnikoff S, *et al.*, 2017, Global Causes of Blindness and Distance Vision Impairment 1990–2020: A Systematic Review and meta-analysis. *Lancet Global Health*, 5:e1221–34. https://doi.org/10.1016/S2214-109X(17)30393-5
72. Mathews PM, Lindsley K, Aldave AJ, *et al.*, 2018, Etiology of Global Corneal Blindness and Current Practices of Corneal Transplantation: A Focused Review. *Cornea*, 37:1198–203. https://doi.org/10.1097/ICO.0000000000001666
73. Gain P, Jullienne R, He Z, *et al.*, 2016, Global Survey of Corneal Transplantation and Eye Banking. *JAMA Ophthalmol*, 134:167–73. https://doi.org/10.1001/jamaophthalmol.2015.4776
74. Zhang B, Xue Q, Li J, *et al.*, 2019, 3D bioprinting for Artificial Cornea: Challenges and Perspectives. *Med Eng Phys*, 71:68–78. https://doi.org/10.1016/j.medengphy.2019.05.002
75. Fuest M, Yam GH, Mehta JS, *et al.*, 2020, Prospects and Challenges of Translational Corneal Bioprinting. *Bioengineering*, 7:71. https://doi.org/10.3390/bioengineering7030071
76. Faye PA, Poumeaud F, Chazelas P, *et al.*, 2021, Focus on Cell Therapy to Treat Corneal Endothelial Diseases. *Exp Eye Res*, 204:108462. https://doi.org/10.1016/j.exer.2021.108462
77. Campos DF, Rohde M, Ross M, *et al.*, 2019, Corneal Bioprinting Utilizing Collagen-based Bioinks and Primary Human Keratocytes. *J Biomed Mater Res Part A*, 107:1945–53. https://doi.org/10.1002/jbm.a.36702
78. Kong B, Chen Y, Liu R, *et al.*, 2020, Fiber Reinforced GelMA Hydrogel to Induce the Regeneration of Corneal Stroma. *Nat Commun*, 11:1435–5. https://doi.org/10.1038/s41467-020-14887-9
79. Kim H, Jang J, Park J, *et al.*, 2019, Shear-induced Alignment of Collagen Fibrils Using 3D Cell Printing for Corneal Stroma Tissue Engineering. *Biofabrication*, 11:035017. https://doi.org/10.1088/1758-5090/ab1a8b
80. Holland G, Pandit A, Sanchez-Abella L, *et al.*, 2021, Artificial Cornea: Past, Current, and Future Directions. *Front Med* (*Lausanne*), 8:770780. https://doi.org/10.3389/fmed.2021.770780
81. Hoon M, Okawa H, Santina LD, *et al.*, 2014, Functional Architecture of the Retina: Development and Disease. *Prog Retin Eye Res*, 42:44–84. https://doi.org/10.1016/j.preteyeres.2014.06.003
82. Ruiz-Alonso S, Villate-Beitia I, Gallego I, *et al.*, 2021, Current Insights Into 3D Bioprinting: An Advanced Approach for Eye Tissue Regeneration. *Pharmaceutics*, 13:308. https://doi.org/10.3390/pharmaceutics13030308
83. Lorber B, Hsiao WK, Hutchings IM, *et al.*, 2014, Adult Rat Retinal Ganglion Cells and Glia can be Printed by Piezoelectric Inkjet Printing. *Biofabrication*, 6:015001. https://doi.org/10.1088/1758-5082/6/1/015001
84. Masaeli E, Forster V, Picaud S, *et al.*, 2020, Tissue Engineering of Retina Through High Resolution 3-Dimensional Inkjet Bioprinting. *Biofabrication*, 12:025006. https://doi.org/10.1088/1758-5090/ab4a20
85. Masaeli E, Marquette C, 2020, Direct-Write Bioprinting Approach to Construct Multilayer Cellular Tissues. *Front Bioeng Biotechnol*, 7:478. https://doi.org/10.3389/fbioe.2019.00478
86. Meek KM, Knupp C, 2015, Corneal Structure and Transparency. *Prog Retin Eye Res*, 49:1–16. https://doi.org/10.1016/j.preteyeres.2015.07.001
87. Kutlehria S, Dinh TC, Bagde A, *et al.*, 2020, High-throughput 3D Bioprinting of Corneal Stromal Equivalents. *J Biomed Mater Res B Appl Biomater*, 108:2981–94. https://doi.org/10.1002/jbm.b.34628
88. Mahdavi SS, Abdekhodaie MJ, Kumar H, *et al.*, 2020, Stereolithography 3D Bioprinting Method for Fabrication of Human Corneal Stroma Equivalent. *Ann Biomed Eng*, 48:1955–70. https://doi.org/10.1007/s10439-020-02537-6
89. Shi P, Edgar TY, Yeong WY, *et al.*, 2017, Hybrid Three-dimensional (3D) Bioprinting of Retina Equivalent for Ocular Research. *Int J Bioprint*, 3:8. https://doi.org/10.18063/IJB.2017.02.008
90. Worthington KS, Wiley LA, Kaalberg EE, *et al.*, 2017, Two-photon Polymerization for Production of Human iPSC-derived Retinal Cell Grafts. *Acta Biomater*, 55:385–95. https://doi.org/10.1016/j.actbio.2017.03.039

Publisher's note

Whioce Publishing remains neutral with regard to jurisdictional claims in published maps and institutional affiliations.

SHORT COMMUNICATION

Novel High-Speed 3D Printing Method Using Selective Oil Sintering with Thermoplastic Polyurethane Powder Printing

Jun Yi-Wu[1], Chih-Hua Hsieh[2]*, Zheng-Ying Lin[2]

[1]Department of Mechanical Engineering, Chien Hsin University of Science and Technology, No. 229, Jianxing Rd., Zhongli Dist., Taoyuan City 320312, Taiwan
[2]High Speed 3D Printing Research Center, National Taiwan University of Science and Technology, No. 43, Keelung Rd., Sec. 4, Da'an Dist., Taipei 10607, Taiwan

Abstract: Present methods used in three-dimensional (3D) printing, such as selective laser sintering (SLS) and multijet fusion (MJF), have limited applications, especially in relation to the manufacturing of biomedical products. The speed of SLS printing is too low, and high-speed 3D printing technology with MJF uses carbon black particles as a fusing agent, which cannot be removed from the completed 3D printed products. Carbon black and high-energy lasers are not suitable for biomedical applications, especially human implants. A new high-speed 3D method is therefore required. In this study, we used hot oil droplets (175°C) as a new type of fusing agent to melt the biomaterial thermoplastic polyurethane (TPU) powder particles to define the print area. This method replaces lasers and the carbon black fusing agent in high-speed 3D printing technology and is more energy efficient. In addition, this method can be used to not only print on TPU, but also on other flexible materials.

Keywords: Selective oil sintering; Fusing agent; Food oil; Powder bed; Thermoplastic polyurethane

*Correspondence to: Chih-Hua Hsieh, High Speed 3D Printing Research Center, National Taiwan University of Science and Technology, No. 43, Keelung Rd., Sec. 4, Da'an Dist., Taipei 10607, Taiwan; d9603205@mail.ntust.edu.tw

Received: November 24, 2021; **Accepted:** January 07, 2022; **Published Online:** January 7, 2022

Citation: Wu JY, Hsieh CH, Lin ZY., 2022, Novel High-Speed 3D Printing Method Using Selective Oil Sintering with Thermoplastic Polyurethane Powder Printing. *Int J Bioprint,* 8(2):521. http://doi.org/10.18063/ijb.v8i2.521

1. Introduction

Thermoplastic polyurethane (TPU) has become a key biomaterial for medical products, because it has good biocompatibility and can be used for human implants[1]. Three-dimensional (3D) printing is a new manufacturing method that can be applied to the manufacturing of customized biomedical products[2], with methods including fused deposition modeling[3], selective laser sintering (SLS)[4], direct light processing[5], and multijet fusion (MJF)[6]. SLS and MJF are types of powder bed fusion (PBF) 3D printing. Fast 3D printing can be defined as a printing process of the form "face (slice) → body"[7]. The printing process used by SLS is of the form "dot→line→surface (slice)→body"; however, the processing speed is limited by this complex procedure. Thus, only MJF constitutes a fast 3D printing method. Fast 3D printing has been recently developed, and fast 3D printing processes such as MJF accelerate the printing process. MJF uses a "2D-to-3D" process, and the printing speed is thus fundamentally higher than that of SLS. High-speed 3D printing technology uses infrared (IR) light as the energy to melt the polymer particles to obtain a 3D pattern[8]. The process is as follows: (i) Depositing a powder layer on a platform; (ii) defining the print area on the powder surface after a fusing agent is deposited; and (iii) finally, irradiating the defined powder surface using an IR lamp[9]. The fusing agent contains carbon black, which is a strong IR absorber. The powder is then sintered by exposing the entire part bed to IR radiation. However, according to reference[10], the carbon black particles are not uniformly deposited on the powder particle surface, which influences the sintering process, and the finished 3D-printed product still contains carbon

© 2022 Author(s), This is an Open Access article distributed under the terms of the Creative Commons Attribution License, permitting distribution and reproduction in any medium, provided the original work is properly cited.

black particles, which cannot be eliminated. Hewlett Packard's MJF PBF high-speed 3D printer contains a considerable amount of carbon black particles and hence cannot be used in biomedical products because of its toxicity. In addition, carbon black particles may be inhaled, causing secondary lung injury. Thus, the applications of this technology are limited. Therefore, a high-speed 3D printing method that is environmentally friendly, nontoxic, and can be manufactured in large quantities at a high speed is required. At present, no methods can print TPU, which, as a biomaterial, can be used in biomedical products and is environmentally friendly. The difference between the two types of 3D printing is that the oil droplet can directly define the printing area and heating, while the MJF needs to define the area first and then illuminate and heat it. Therefore, the oil droplet is used as a 3D printing method and only one step is required for the printing speed. SOS's 3D printing speed must be faster than MJFIn this study; we developed a novel fusing agent (i.e., food oil) that does not require photo absorbers. The oil covers the particle surface uniformly, and the heated oil droplets completely melt the powder. Moreover, when oil is used as the fusing agent, the powder can be directly fused, and the printed area can be accurately defined with heated oil droplets. Moreover, this method can print TPU.

2. Experimental methods

2.1. Materials

TPU (maximum particle size of 100) was supplied by BASF. Food oil is canola oil was purchased from a local store and used without any further purification. The boiling point of the food oil was 250°C.

2.2. 3D printing

Figure 1 presents the PBF process of melting TPU particles in a layer-by-layer manner using selective hot oil sintering technology. A commercial powder bed 3D printer (T10 3D printer, Microjet Technology Co Ltd., Taiwan) was used in this work for spreading the TPU micro powder. The hot oil droplets (175°C, droplet size of approximately 2000 μm) were ejected through a glass dropper. Using oil as a fusing agent for high-speed 3D printing technology, all printing processes can be completed in one step. The hot oil can be transformed into small droplets through the multiple glass droppers, and then through a large number of small droplets to define the pre-printed area and shape. The heat source moved along the X and Y axes of the bed to which a thin and uniform powder layer was applied. The base was then lowered based on the thickness of one layer (0.1 – 0.08 mm), and another powder layer was applied and sintered. The powder sintering steps were repeated until a 3D structure was formed. The printed objects are heated on a hot plate set at 220°C for 30 min, cooled at room temperature for 10 min, and then washed with soapy water to remove excess oil for post-processing to complete the final product. The final parts were characterized using scanning electron microscopy (SEM) and a universal tensile machine (UTM).

3. Results and discussion

Figure 2 presents the SEM images of the TPU particles fused using two different fusing agents-food oil and carbon black. As illustrated by **Figures 2A** and **C**, the energy of the hot oil was sufficient to melt the powder, leaving no porosity (red circle in **Figure 2C**). When carbon black was used (**Figures 2B** and **D**), no melt tracks were formed because carbon black does not cover the particle surfaces uniformly and the heat of the IR absorber is insufficient to melt the powder and solidify it onto the substrate. Moreover, the resulting pore size was approximately 90 in diameter (red circle in **Figure 2D**).

Differential scanning calorimetry (DSC) was used to determine the melting and crystallization temperatures of the TPU particles. A DSC8000 instrument from PerkinElmer was used at a temperature of 20 – 200°C, with a heating rate of 5°C/min. Nitrogen purge gas and 0.5-mg aluminum crucibles

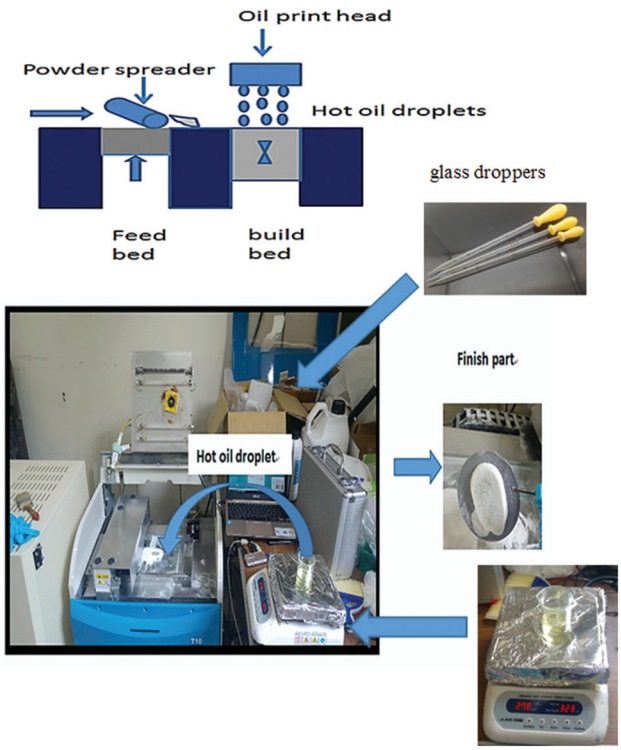


Figure 1. Selective oil sintering process.

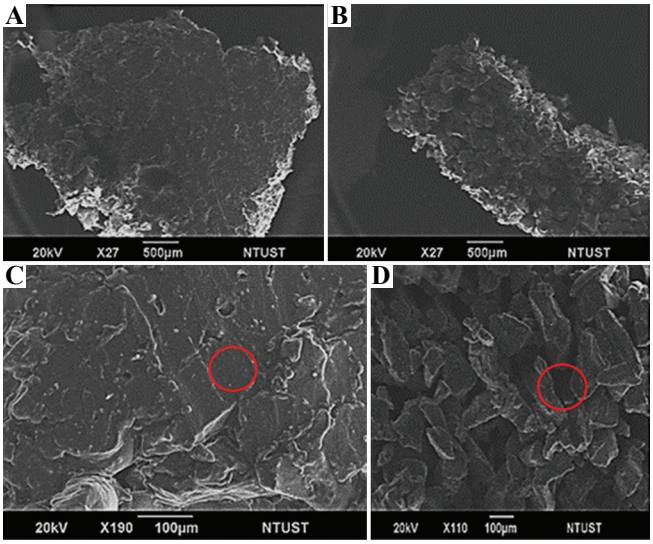


Figure 2. Morphology of the thermoplastic polyurethane particles fused using different fusing agents: (A) oil 27×, (B) carbon black 27×, (C) oil 190×, and (D) carbon black 190×.

were used in the experiments. **Figure 3A** provides an example of a DSC curve, which indicates that the TPU particles exhibited a melting temperature of approximately 160°C and a crystallization temperature of approximately 80°C.

The oil thermal decomposition profiles for the thermogravimetric analysis (TGA; **Figure 3B**) indicate an oil cracking temperature ranging from 230°C to 500°C, with no residue at 600°C. The decomposition of the food oil involves three steps — decomposition of polyunsaturated fatty acids at 230 – 380°C, decomposition of monounsaturated (MAC) fatty acids at 380 – 480°C, and decomposition of saturated (SAC) fatty acids at 480 – 500ºC. During the decomposition of MAC fatty acids, the carbon double bonds were broken, causing the triglyceride molecules in the vegetable oils to become SAC. This result indicates that food oil samples incubated at 300°C exhibit higher thermal stability. Oil at a temperature above the melting point of the TPU micropowder can be used as the TPU micropowder fusing agent.

TPU is a flexible and abrasion-resistant thermoplastic used in various manufacturing processes for both consumer and industrial use. The 3D printed samples obtained from TPU regained their original shape after compression (**Figure 4**). MJF's printed dimensional accuracies were slightly higher than SOS. This is due to the detailing agent used in the MJF process. The dimensional accuracy of the TPU printed with hot oil on the vertical direction was not as good as TPU printed with carbon black, which might be due to the excessive layer-overlapping during SOS process as a result of oil heat input.

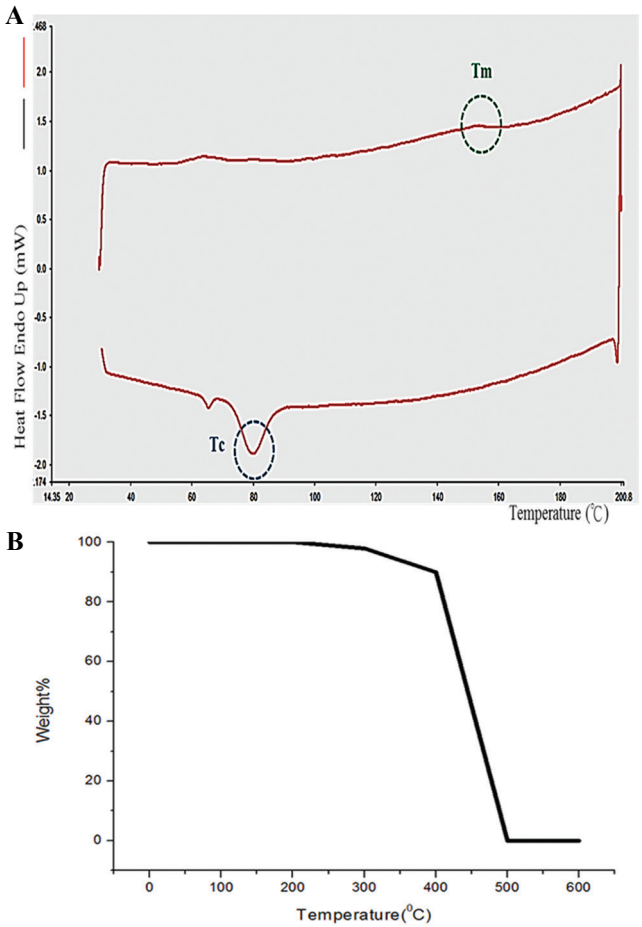


Figure 3. (A) Relationship between the peaks in the differential scanning calorimetry curve and particle melting. (B) Thermogravimetric oil curves.

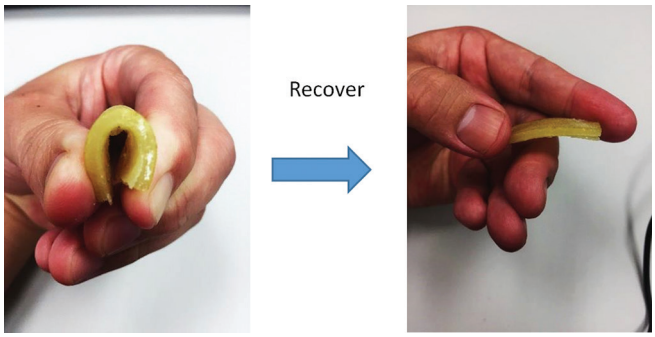


Figure 4. Compression of the thermoplastic polyurethane sample. The sample regained its original shape after compression.

The mechanical properties of the solid TPU were studied with respect to the stress-strain responses (**Figure 5**). A UTM was used to analyze the mechanical properties of the printed TPU, including its tensile strength and breaking point (**Figure 5**). The ultimate tensile strength of the pure TPU (without carbon black) reached 2.7 MPa. The break stress is 2.9 MPa. According to the literature[10,11], TPU containing carbon black will

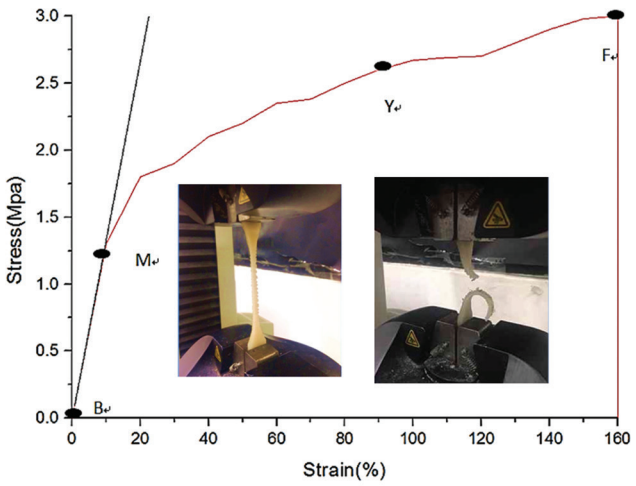


Figure 5. Stress-strain curves for the pure thermoplastic polyurethane at 20°C.

change its mechanical properties, but TPU containing carbon black will have better mechanical properties than TPU without carbon black. The stress-strain curves indicated that the pure TPU could be stretched by up to 160%. The full stress-strain curve of the pure TPU contains three regions: (i) An elastic region (0 – 20%), (ii) a plastic region (20 – 150%), and (iii) a break region (160%).

4. Conclusions

This study developed a new high-speed 3D method using food oil as a new fusing agent material. In addition, we reported the formulation of a fusion ink (food oil) for fabricating 3D structures by combining PBF and inkjet printing. The printed 3D samples exhibit high levels of repeatability and bendability. Thus, this paper describes a novel environmentally friendly fusing agent that can be used for PBF high-speed 3D printing and is suitable for manufacturing biomedical products.

Acknowledgment

This work was financially supported by the "High-Speed 3D Printing Research Center" of National Taiwan University of Science and Technology (NTUST) from The Featured Areas Research Center Program within the framework of the Higher Education Sprout Project by the Ministry of Education (MOE) in Taiwan.

Conflict of interest

The authors have no relevant conflicts of interest to declare.

Author contributions

J.Y.W. guided and supervised the project. J.Y.W. designed and supervised the experiments. J.Y.W., H.C.H. conducted experiments and contributed intellectually to the scientific design of the project. J.Y.W., H.C.H., L.Z.Y. mentored the technical part of the project.

References

1. Drupitha MP, Das B, Parameswaran R, *et al*., 2018, Hybrid Electrospun Fibers Based on TPU-PDMS and Spherical Nanohydroxyapatite for Bone Tissue Engineering. *Mater Today Commun*, 16:264–73. https://doi.org/10.1016/j.mtcomm.2018.06.013
2. Bachtiar EO, Erol O, Millrod M, *et al*., 2020, 3D Printing and Characterization of a Soft and Biostable Elastomer with High Flexibility and Strength for Biomedical Applications. *J Mech Behav Biomed Mater*, 104:103649. https://doi.org/10.1016/j.jmbbm.2020.103649
3. Lu Q, Song KY, Feng Y, *et al*., 2021, Fabrication of Suspended Uniform Polymer Microfibers by FDM 3D Printing. *CIRP J Manufa Sci Technol*, 32:179–87. https://doi.org/10.1016/j.cirpj.2020.11.005
4. Fina F, Goyanes A, Gaisford S, *et al*., 2017, Selective Laser Sintering (SLS) 3D Printing of Medicines. *Int J Pharm*, 529:285–93. https://doi.org/10.1016/j.ijpharm.2017.06.082
5. Guo J, Zeng Y, Li P, *et al*., 2019, Fine Lattice Structural Titanium Dioxide Ceramic Produced by DLP 3D Printing. *Ceram Int*, 45:23007–12. https://doi.org/10.1016/j.ceramint.2019.07.346
6. Srinivas RP, Alomarah A, Masood SH, *et al*., 2020, Mechanical Response of a Compressed Novel 3D Tetrachiral Structure Processed by MJF 3D Printing Process. *Mater Today*, 46:4776–81.
7. Xu Z, Wang Y, Wu D, *et al*., 2019, The Process and Performance Comparison of Polyamide 12 Manufactured by Multi Jet Fusion and Selective Laser Sintering. *J Manuf Process*, 47:419–26.
8. HP Development Company, 2018, L.P. Introduction of HP 3D Printers. Available form: http://www8.hp.com/uk/en/printers/3dprinters [Last accessed on 2018 Oct 23].
9. Sillania F, Kleijnena R, Vetterlia M, *et al*., 2019, Selective Laser Sintering and Multi Jet Fusion: Process-Induced Modification of the Raw Materials and Analyses of Parts Performance. *Addit Manuf*, 27:32–41. https://doi.org/10.1016/j.addma.2019.02.004

10. Espera AH Jr., Valino AD, Palaganas JO, *et al.*, 2019, 3D Printing of a Robust Polyamide-12-Carbon Black Composite via Selective Laser Sintering: Thermal and Electrical Conductivity, Macromol. *Mater Eng*, 304:1800718. https://doi.org/10.1002/mame.201800718

11. Tey WS, Cai C, Zhou K, 2021, A Comprehensive Investigation on 3D Printing of Polyamide 11 and Thermoplastic Polyurethane via Multi Jet Fusion. *Polymers,* 13:2139. https://doi.org/10.3390/polym13132139

Publisher's note

Whioce Publishing remains neutral with regard to jurisdictional claims in published maps and institutional affiliations.

SHORT COMMUNICATIONS

Deep Learning-Assisted Nephrotoxicity Testing with Bioprinted Renal Spheroids

Kevin Tröndle[1]*, Guilherme Miotto[2], Ludovica Rizzo[3], Roman Pichler[4], Fritz Koch[1], Peter Koltay[1], Roland Zengerle[1,2], Soeren S. Lienkamp[3], Sabrina Kartmann[1,2], Stefan Zimmermann[1]

[1]University of Freiburg, IMTEK - Department of Microsystems Engineering, Freiburg, 79110, Germany
[2]Hahn-Schickard, Freiburg, 79110, Germany
[3]Institute of Anatomy, University of Zurich, Zurich, Switzerland
[4]Renal Division, Department of Medicine, Faculty of Medicine and Medical Center - University of Freiburg, Freiburg, Germany

Abstract: We used arrays of bioprinted renal epithelial cell spheroids for toxicity testing with cisplatin. The concentration-dependent cell death rate was determined using a lactate dehydrogenase assay. Bioprinted spheroids showed enhanced sensitivity to the treatment in comparison to monolayers of the same cell type. The measured dose-response curves revealed an inhibitory concentration of the spheroids of $IC_{50} = 9 \pm 3$ µM in contrast to the monolayers with $IC_{50} = 17 \pm 2$ µM. Fluorescent labeling of a nephrotoxicity biomarker, kidney injury molecule 1 indicated an accumulation of the molecule in the central lumen of the spheroids. Finally, we tested an approach for an automatic readout of toxicity based on microscopic images with deep learning. Therefore, we created a dataset comprising images of single spheroids, with corresponding labels of the determined cell death rates for training. The algorithm was able to distinguish between three classes of no, mild, and severe treatment effects with a balanced accuracy of 78.7%.

Keywords: Bioprinting; Spheroids; Kidney; Nephrotoxicity; Deep learning

***Correspondence to:** Kevin Tröndle, University of Freiburg, IMTEK - Department of Microsystems Engineering, Freiburg, 79110, Germany; kevintroendle@gmail.com

Received: November 2, 2021; **Accepted:** January 19, 2022; **Published Online:** January 19, 2022

Citation: Tröndle K, Miotto G, Rizzo L, et al., 2022, Deep Learning-Assisted Nephrotoxicity Testing with Bioprinted Renal Spheroids. *Int J Bioprint,* 8(2):528. http://doi.org/10.18063/ijb.v8i2.528

1. Introduction

The development of novel three-dimensional (3D) cell culture models is motivated by their better accuracy in predicting the physiological response of a target organ *in vitro*[1]. This would be beneficial for a variety of applications, including preclinical drug testing for toxicity or personalized treatment optimizations. In this context, the kidney plays a crucial role. Many substances show nephrotoxic side effects in late stage clinical studies, which were not covered in preclinical screenings[2]. To model the kidney, specific cell types were isolated or reprogrammed to provide basic characteristics of the cells found in the functional units of the kidney, that is, the nephric tubules. These include the frequently used renal proximal tubule epithelial cells (RPTECs[3]), or the more sophisticated induced renal epithelial cells (iRECs[4]). The latter could be used prospectively to establish personalized testing, since they are derived by reprogramming fibroblasts, an accessible cell source. Besides the cell type, the structure of the cell models was found to significantly influence their functionality[1-3]. The simplest cell models are two-dimensional (2D) monolayers. On top of this, the structural complexity could be increased by embedding cells in artificial 3D scaffolds to mimic the natural extracellular matrix (ECM). In various tissue engineering studies, the embedded cells showed unique mechanisms of self-assembly and formed complex 3D structures over time, including hollow spheroids[4,5] and tubules[3], both of which recapitulated nephron tubule organization and functionality. Direct comparisons with 2D monolayers revealed an increased sensitivity to treatment with the known nephron-toxicant cisplatin, which is a common reference substance[3]. Bioprinting was established as an enabling technology for the biofabrication of 3D cell culture models

© 2022 Author(s). This is an Open Access article distributed under the terms of the Creative Commons Attribution License, permitting distribution and reproduction in any medium, provided the original work is properly cited.

by providing a high degree of automation and spatial resolution. Various bioprinting techniques were developed and applied to fabricate 3D cell models with defined size and shape by spatially controlling the cell distribution in an artificial ECM[6]. In this study, we used a drop-on-demand (DoD) bioprinting technology which was previously applied in the production, handling, and treatment of cell spheroids[7], attributed to its capability to precisely deposit low volumes of low viscous bioinks, such as spheroids or cells in suspensions. Compared to classical tissue engineering approaches, bioprinting provides increased sample reproducibility, which is one key requirement for systematic screening applications. In previous studies, we have described a scalable concept of DoD bioprinting and controlled cellular self-assembly to fabricate size-defined renal spheroids and tubules in a hydrogel scaffold[8]. These structures comprise of a hollow lumen surrounded by an organized epithelial cell layer, thereby closely mimicking the nephron tubule structure. Here, we applied this concept to fabricate 3D renal spheroids from iRECs for a head-to-head comparison with 2D monolayers of the same cell type. The sensitivity to the nephron-toxicant cisplatin was investigated with different readout methods. First, we determined the cell death rate Ψ using a lactate dehydrogenase (LDH) quantification assay. Next, we fluorescently labeled a nephrotoxicity biomarker for microscopic imaging. In the context of bioprinting, machine learning image processing could prospectively contribute to improve 3D cell model generation, fabrication, and readouts[9,10]. In the latter, microscope images of cell morphology could be used to assign biochemical values (e.g., viability) in an automated manner without requiring additional assays to be conducted for each experimental setting. This again addresses important aspects of prospective screening applications, such as automation and high throughput. Here, we present a feasibility study for an automated toxicity readout using deep learning image classification based on bioprinted renal spheroids[11,12]. We trained a convolutional neural network (CNN) through supervised learning to predict the Ψ of a spheroid from its microscopic image.

2. Materials and methods

2.1. Cell culture and hydrogels

For all sample preparations, we used iRECs[4]. A detailed description of the cell type and culture conditions can be found in previous studies[4]. The cells were cultured in Dulbecco's Modified Eagle Medium (DMEM, #41966029, Gibco), with additives of fetal bovine serum (10%) and penicillin/streptomycin (1%), for cell expansion. Matrigel (100%, #356231, Corning) was used as artificial ECM material. The 3D spheroid models were cultured in renal epithelial growth medium (REGM, #CC-3190, Lonza), without addition of additives.

2.2. DoD bioprinting

For bioprinting, we used a piezo-actuated DoD bioprinting technology (PipeJet®, Biofluidix GmbH). A detailed description of the printing process can be found in our previous study[6]. In brief, single droplets (10 nl) each containing about 150 cells were deposited onto a Matrigel substrate layer. The printed cell clusters were encapsulated with a second layer of Matrigel and incubated for subsequent incubation supporting the cellular self-assembly of one spheroid per cluster.

2.3. LDH toxicity assay

We used a colorimetric LDH Assay Kit (ab65393, Abcam) to quantify the cellular release of LDH enzyme caused by a treatment with different concentrations of cisplatin (ab141398, Abcam). The cell death rate Ψ was determined relative to a lysed control (Lysed Ctrl) obtained by sample treatments with Triton X (30 min, 37°C). The treatment was conducted by incubating the cells for 24 h and changing medium subsequently. To determine Ψ, the supernatant of treated samples was collected (10 µl) and compared to an un-lysed control (Neg. Ctrl). The measured absorbance was determined by measurements of the optical density at 450 nm wavelength (OD_{450}). A normalized solution of LDH enzyme (0.25 µg/µl, LDH Ctrl) was used to assess the assay performance.

2.4. Fluorescent image acquisition

The treated samples were imaged using a fluorescence microscope (Axio Observer.Z1/7, Carl Zeiss) with a 20-fold magnification objective (EC Plan-Neofluar 20x/0.5 M27), LED excitation, and fluorescently labeled biomarkers for nephrotoxicity. The obtained images were correlated with the treatment dose and Ψ, which was chemically determined as the relative cytotoxicity with the released LDH amount. As primary biomarker of cytotoxicity, the integrity of the cell membranes was observed, which were labeled in the cell line (iRECs) with a stable expression of membrane-localized green fluorescent protein (GFP). The kidney injury molecule 1 (KIM-1) was labeled as a specifically expressed biomarker of nephrotoxic effects[13]. For this, the protein was fluorescently labeled post-treatment with a primary antibody (Invitrogen, #PA5-79345), and a secondary antibody (Abcam, #ab6939) for the microscopic detection within spheroids. For cultivation and microscopy, the spheroid arrays were fabricated in an 8-chamber microscopy slide (µ-Slide 8 well; ibidi GmbH, #80826).

2.5. Deep learning

The code was written in Python 3.8.10 using Pytorch 1.8.1. Detailed information is listed in the Supplementary File. The dataset was made of 4974 spheroid images taken

after 3 days of treatment with different concentrations of cisplatin. The composition of this dataset is described in the **Table S1**. The network architecture and hyperparameters were chosen by automatic hyperparameter optimization. The selected architecture was a VGG11 optimized with ADAM for 90 epochs. The full list of hyperparameters is provided in the Supplementary File. The concept of automated treatment effect readout was adapted from previous studies[11,12].

3. Results and discussion

3.1. Required 3D cell count for toxicity quantification

First, the required total cell count per 3D sample was defined, which enabled the quantification of toxicity with a chemical LDH assay readout. Therefore, cell cluster arrays were fabricated, ranging from 1 to 400 spheroids (**Figure 1A**). The cell clusters self-assembled to spheroids of uniform size within 4 days of incubation[8]. Then, the spheroids were lysed (Lysed Ctrl), and the amount of released LDH was compared to the Neg. Ctrl. (**Figure 1B**). The Lysed Ctrl samples showed an increasing amount of LDH in the supernatant in relation to an increasing number of spheroids per array, as expected. In contrast, the Neg. Ctrl samples showed a constant absorbance, independent of the cell count. The positive to negative signal ratio (*SP/N* = Lysed Ctrl/Neg. Ctrl) was calculated to determine the minimum spheroid count required to distinguish the Lysed Ctrl. from the Neg. Ctrl. The desired value of *SP/N* ≥3 was achieved for arrays with at least 100 spheroids. For these, an $OD^{450_100} = 0.8 \pm 0.6$ was measured, showing a high coefficient of variation (75%). A number of 225 spheroids showed an absorbance of $OD_{450_225} = 1.3 \pm 0.4$. In addition, the lowest coefficient of variation was found for this format (30%). In addition, the value was in the range of the LDH Ctrl, which was measured to $OD_{450\ LDH\ Ctrl} = 1.6 \pm 0.3$, corresponding to 83 ± 25%. The largest array format (400 spheroids) showed an absorbance of 114 ± 47% relative to the LDH Ctrl, however, with an increased coefficient of variation. Based on these findings, spheroid arrays consisting of 225 spheroids, or 34×10^6 cells, were selected for the quantification of toxicity using an LDH assay.

3.2. 3D response time to toxic treatment

Next, a suitable time-point for the toxicity readout was determined. A schematic timeline of the experimental procedure is shown in **Figure 1C**. All samples were prepared by bioprinting 4 days before a treatment with cisplatin, a common nephrotoxic substance[14]. Two types of samples were prepared, either classical monolayers (2D) or bioprinted arrays of 225 spheroids (3D Samples). On day 4 of incubation, the medium was replaced by a cell culture medium containing a dilution of cisplatin ($c_{Cisplatin}$ = 100 μM). The treatment was conducted at 37°C for 24 h. Then, the cisplatin dilution was replaced by fresh medium. At this time point, we started the readout. During the subsequent incubation period, the supernatant was sampled at different time points (0, 12, 24, 36, 48, and 72 h post treatment), and the release of LDH was quantified. The measured LDH release curves for the 2 sample types are shown in **Figure 1D** and **E**. For 2D monolayer cultures, no significant LDH release was detected within the first 24 h (**Figure 1D**). After 36 h, the LDH release accounted for 60 ± 20% and increased to 96 ± 20% after 48 h, relative to the Lysed Ctrl. At 72 h post-treatment, the released LDH decreased to 42 ± 23%. The decrease in measured LDH could be related to the degradation of the enzyme in the culture supernatant. For the untreated control group (Neg. Ctrl), the release of LDH continuously increased over time, reaching a maximum of 10 ± 7% at 72 h. This could be explained by the fact that the 2D monolayer cultures were fully confluent. At this point, the cells in culture need to adapt to the limited growth area and nutrient deficiency, which could cause unspecific cell lysis and LDH release. The 3D spheroid arrays showed a distinct behavior compared to the 2D monolayers (**Figure 1E**). The first increase in LDH release occurred 24 h post-treatment, reaching 60 ± 32% of the Lysed Ctrl. After 48 h, the maximum was reached at 96 ± 7%. Afterward, the value declined to 79 ± 27% (72 h). Again, this decline could be explained by an impairment of the LDH activity due to the progressive incubation period. The untreated control shared a similar behavior with the 2D monolayers, with a slight and static linear increase of released LDH over time, reaching a maximum of 23 ± 1% at 72 h. This indicates again that within 3D spheroid cultures, unspecific cell lysis occurred, which was not related to a toxic treatment. This finding is in good accordance with the previously published data[15]. Taken together, from the experiments, the optimal time-point for the LDH-assay based readout was found to be at $t_{treatment}$ = 48 h. The dynamic observation of LDH release after cisplatin treatment indicated significant differences between 2D and 3D cell models. The faster onset of toxicity in 3D models could be related to a more efficient uptake of the toxin. In the case of cisplatin, the uptake occurs through transport proteins located on the basal side of the cells. This side is facing toward the cisplatin containing culture medium in the case of hydrogel embedded 3D spheroids, while in 2D monolayers it is in contact to the solid culture vessel surface.

3.3. Dose-response curves

Next, dose-dependent treatment effects were quantified to derive dose-response curves for different cell culture

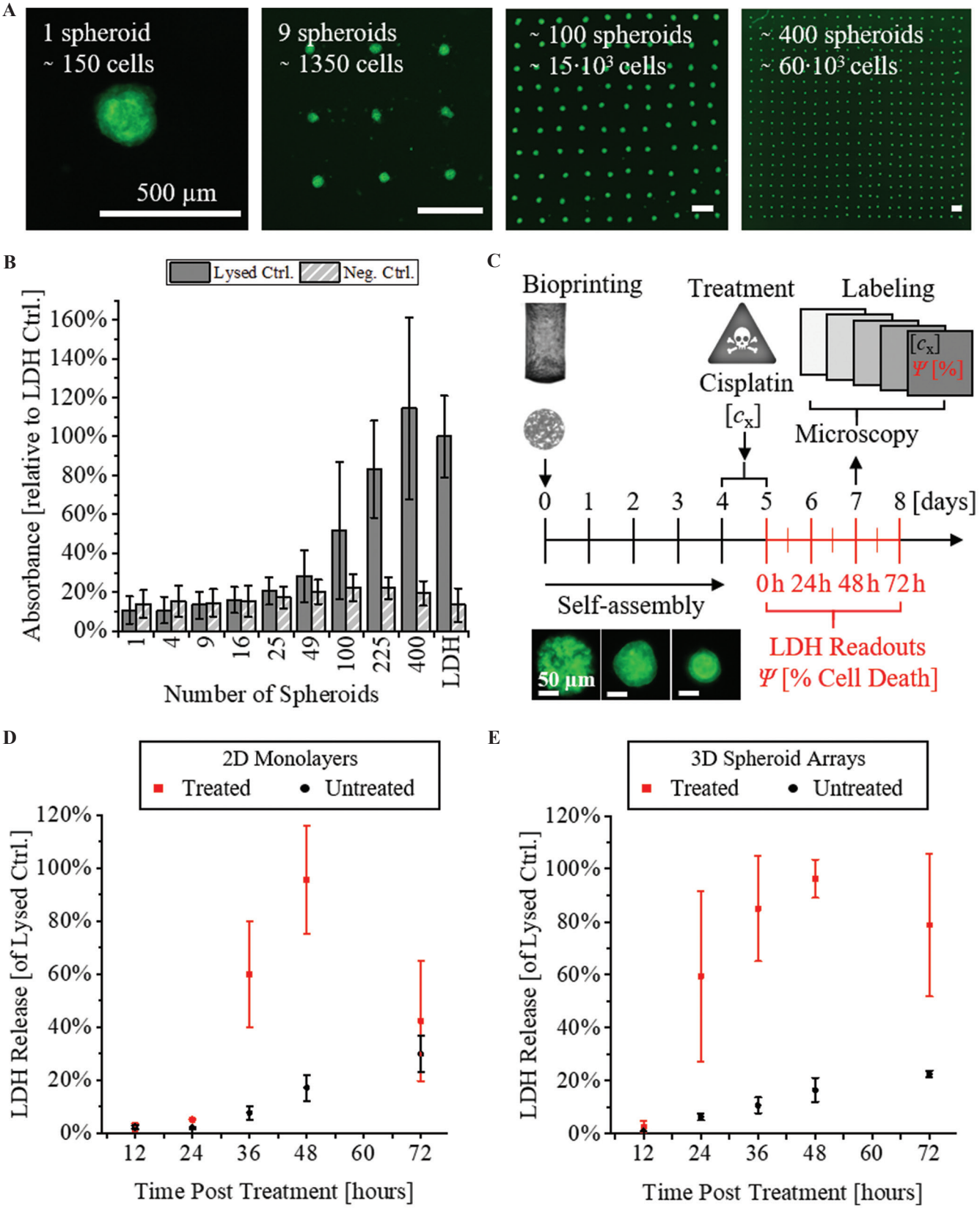


Figure 1. LDH toxicity readout with 3D renal spheroids. (A) Fluorescent microscope images of bioprinted spheroid arrays with different formats. Scale bars: 500 µm. (B) Quantification of total LDH release after lysis of different array formats. (C) Schematic timeline of sample preparation, treatment, and readout. (D and E) Time-dependent LDH release of 2D monolayers versus 3D spheroids at different time points post-treatment.

models. For head-to-head comparison, three parameters were used, including the inhibitory concentration leading to 50% cell death (IC_{50}), and the maximum and minimum response (E_{max}, E_{min}). As described in literature, clinically relevant cisplatin concentrations were in the range of 10 µM[16]. Based on this value, we prepared a dilution series ($c_{Cisplatin}$ = 0.075, 0.5, 1, 2, 4, 8, 16, 32, 64, and 128 µM) for the treatment. Representative fluorescence microscope images of each sample type are shown in **Figure 2A**. For both sample types, the mean absorbance of three replicates for each treatment condition was calculated relative to the Lysed Ctrl. The dose-response curves were derived using a pharmacological dose-response fit function (see equation (1) in Supplementary File). The 2 sample types showed distinct curves and relations to the treatment concentration (**Figure 2B**). 2D monolayers showed an $IC_{50\ 2D\ Ref.}$ = 17 ± 2 µM, with a maximum response of E_{max} = 95 ± 7% and E_{min} = 15 ± 8% relative to the Lysed Ctrl. A significant lower IC_{50} was found for treated spheroid arrays compared to 2D monolayers, with an $IC_{50\ 3D\ Spheroids}$ = 9 ± 3 µM and similar values of E_{min} and E_{max}. The determined IC_{50} values of the 3D bioprinted models were in good accordance with the previously published data. In other studies, reported values were 5.72 µM[17], between 10 and 50 µM[3], or > 30 µM[18]. It should be noted that each of the reported data was based on experiments on different cell types, treatment protocols, and readout methods. Thus, a quantitative head-to-head comparison would not be conclusive. The reported values herein indicated that the fabricated 3D models showed similar sensitivities to cisplatin treatments as reported for other 3D models. In addition, a higher sensitivity compared to a 2D cell culture of the same cell type under identical treatment conditions were found, which is consistent with previous reports[3].

3.4. Microscopic readout

In addition to the chemical readout, we investigated whether microscopic observations of the cell morphology could be used to assess toxicity effects in the 3D spheroids. With this, we aimed to achieve a higher sensitivity, compared to the chemical readout. Cytotoxic effects could become detectable before cell

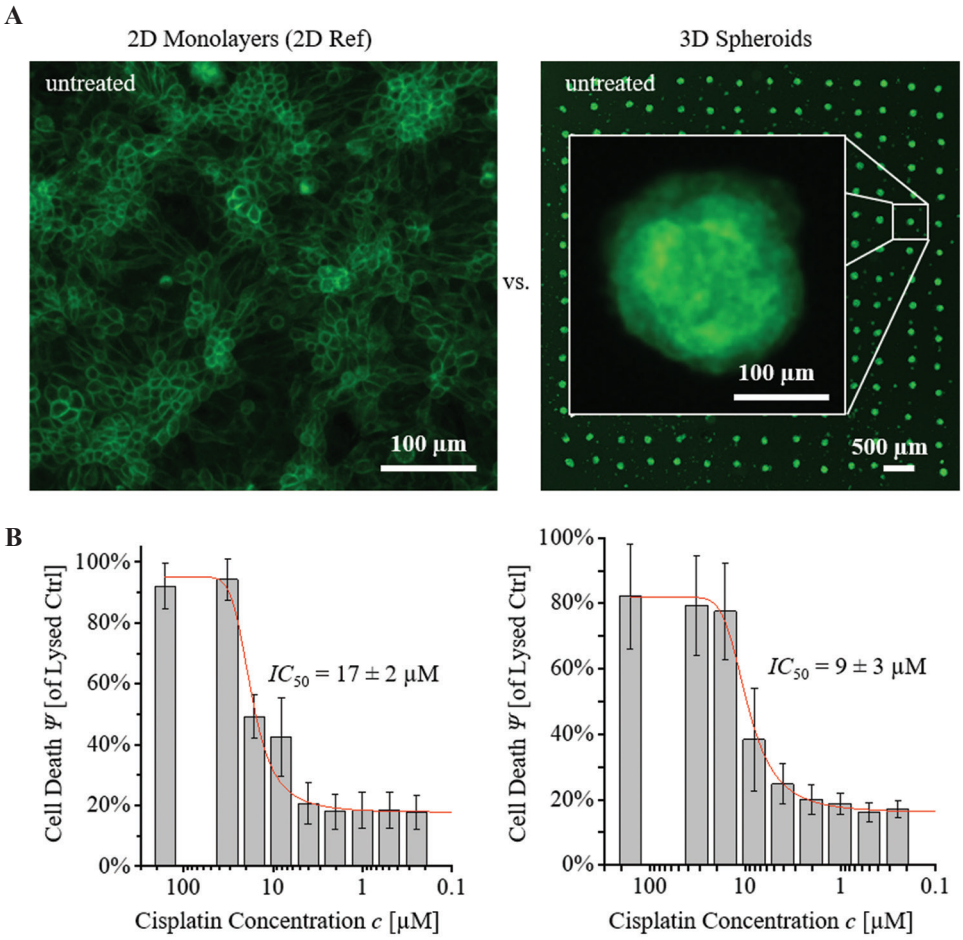


Figure 2. Head-to-head comparison. (A) 2D monolayers and 3D spheroid arrays, comprising of iREC cells. (B) Dose-response curves for a treatment with cisplatin.

membrane lysis occurs, which leads to the release of LDH. Since the lysis of the cell membrane is considered the final step of cell death, this assumption is plausible. A cisplatin serial dilution was prepared in REGM, and the treatment was conducted according to the process and timeline described in **Figure 1C**. Three replicates of each treatment condition were used for microscopic observations. For the KIM-1 nephrotoxicity marker expression assessment, samples were fixed (PFA 4%, 1 h) before immunolabeling was performed. Representative false-color images of the observed spheroid morphologies for different treatment concentrations are shown in **Figure 3**. The observations showed a disintegration of the spheroids at treatment concentrations $c_{\text{Cisplatin}} \geq 32$ µM. The outer boundary of the spheroids was found to be disrupted in the bright field and GFP channel, and no intact cell layer was outlining the spheroids. The KIM-1 signal was detected throughout the entire spheroid structures. For lower treatment concentrations ($c_{\text{Cisplatin}} \leq 16$ µM), a distinct signal distribution was detected. The KIM-1 positive signal was exclusively located at the central lumen of the spheroids. Furthermore, we observed an intact cell layer surrounding the lumen without positive KIM-1 signal. This indicated that the KIM-1 proteins were transported out of the cells and accumulated in the lumen of the spheroids. This accumulation was later found to undergo a decline with decreasing treatment concentrations. The untreated control showed very low levels of KIM-1 positive signals. The KIM-1 unlabeled samples showed no detectable KIM-1 signals, confirming the specificity of the immunolabeling process. This observation was in good accordance with physiological observations in patients, where an increase in KIM-1 signal at the apical side of the renal tubules was detected as a consequence of kidney injury. This, in turn, led to an increase of KIM-1 concentrations in the urine, indicating an active transport and release of KIM-1 into the nephron lumen[19]. Thus, the accumulation of KIM-1 molecules found here hints at a basic physiological transport mechanism within the developed spheroid models.

3.5. Deep learning

Finally, we investigated the feasibility of automatic determination of Ψ of single spheroids from their morphological appearance in microscope images. A schematic process diagram is shown in **Figure 4A**. For this purpose, we developed a deep learning system based on CNN trained via supervised learning. We used fluorescence images from the GFP channel. The images were labeled with their Ψ values, as estimated by the dose-response curves (**Figure 2**). The network was trained as a regressor that takes an image of a single spheroid as input and a scalar corresponding to its estimated Ψ as output. The hyperparameters of the training pipeline were tuned via Bayesian Optimization[20], as implemented by (Bayesian Optimization with Hyperband [BOHB][20]). The hyperparameter search space and the optimum configuration found by BOHB are shown in the **Table S2**. The following results originate from this configuration. The dataset was split for training and testing in the proportions of 80 – 20%, respectively. The images were cropped to 450 × 450 px with the spheroid positioned at the center of the image. Online data augmentation was used. At each epoch, the images were randomly transformed within the ranges as shown in the **Table S3**. Training was conducted for 90 epochs, which resulted in a test mean squared error of 7.67×10^{-3}. **Figure 4B** shows the predictions made by the network on the test dataset. It is possible to see that it performs well to differentiate spheroids with $\Psi < 30\%$ from those above 80%. Nevertheless, it fails to tell apart rates above 50%. Visual inspection of the dataset demonstrated that this was indeed a difficult task, as shown in **Figure 4C**. The accuracy of this network can be appreciated by framing the regression problem as a classification by binning the regressor outputs into discrete intervals.

We report the results of 2 classification formulations: first, a 3-class problem, where classes are divided based on death rate, that is, < 33.3%, between 33.3% and 66.6%, and more than 66.6%; second, a binary classification to distinguish 2 classes, either below or above the IC_{50}. The results are shown as confusion matrices in **Figure 4D and E**. The 3-class problem achieved a balanced accuracy (mean per-class accuracy) of 78.7%. As expected, the main issue was to correctly differentiate spheroids with intermediary death rates from those with high death rates. On the other hand, the binary classification achieves a balanced accuracy of 98.2%, which confirms that the network can differentiate extreme values of death rate. These results are encouraging for a proof-of-concept study, but in the short term, small improvements should be attempted to further increase the network's accuracy. The first step is to collect a dataset with good quality bright-field images. These images may contain vital information to improve the performance on the medium to high death rate range, where our network performed the worst. Second, the dataset should cover the intermediate death rate values better. The dataset used in this study has a uniform distribution of cisplatin concentrations (in the log scale), but due to the sigmoidal profile of the dose-response curve, this distribution translates to a sparse sampling of intermediate values of death rate. The current lack of training data for intermediate death rates is very likely to be reducing the performance of the deep learning network.

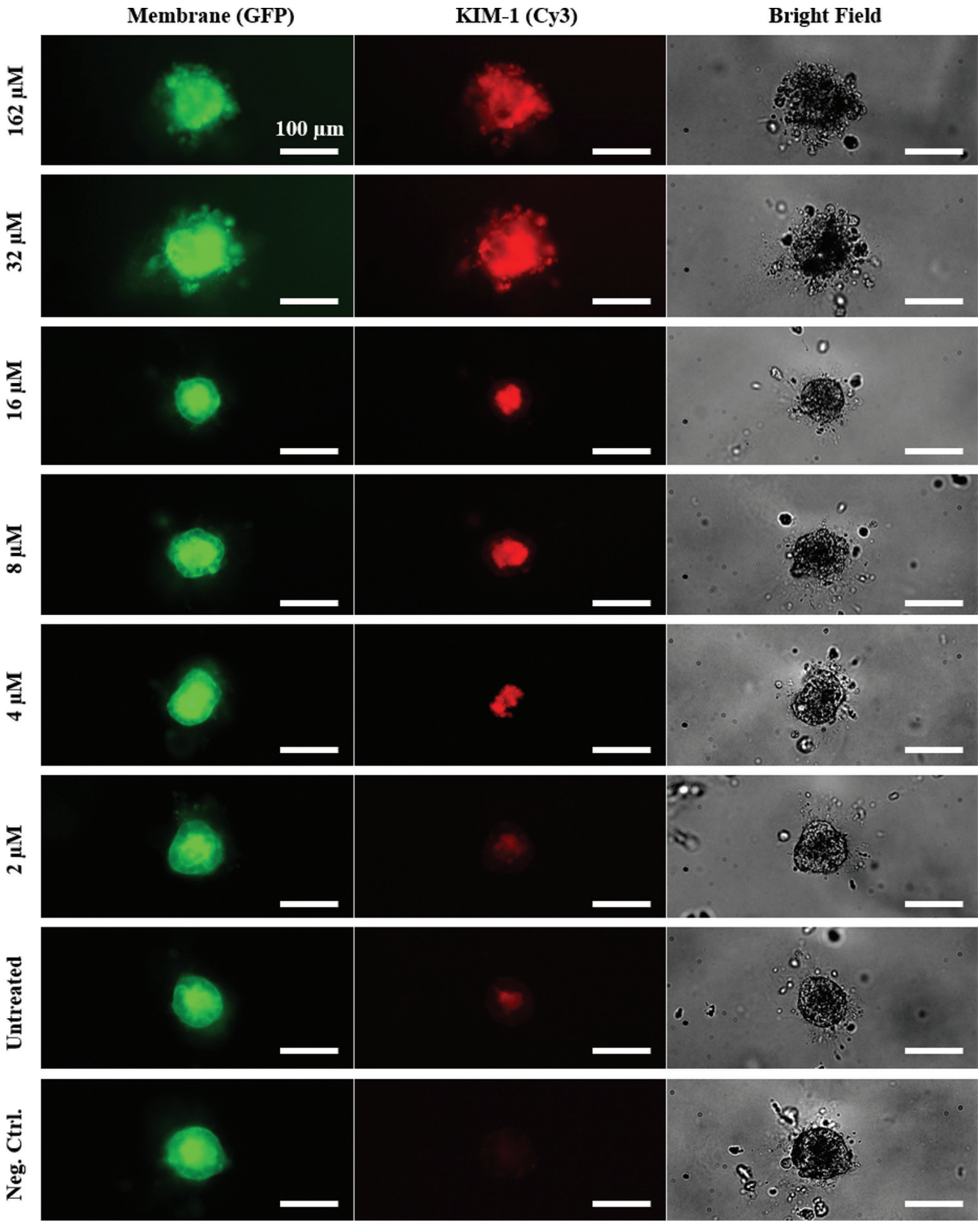


Figure 3. Fluorescence microscope images of cisplatin treated renal spheroids. The fluorescence channels show membrane-localized GFP (green) and nephrotoxicity biomarker KIM-1 (red). Scale bars: 100 µm.

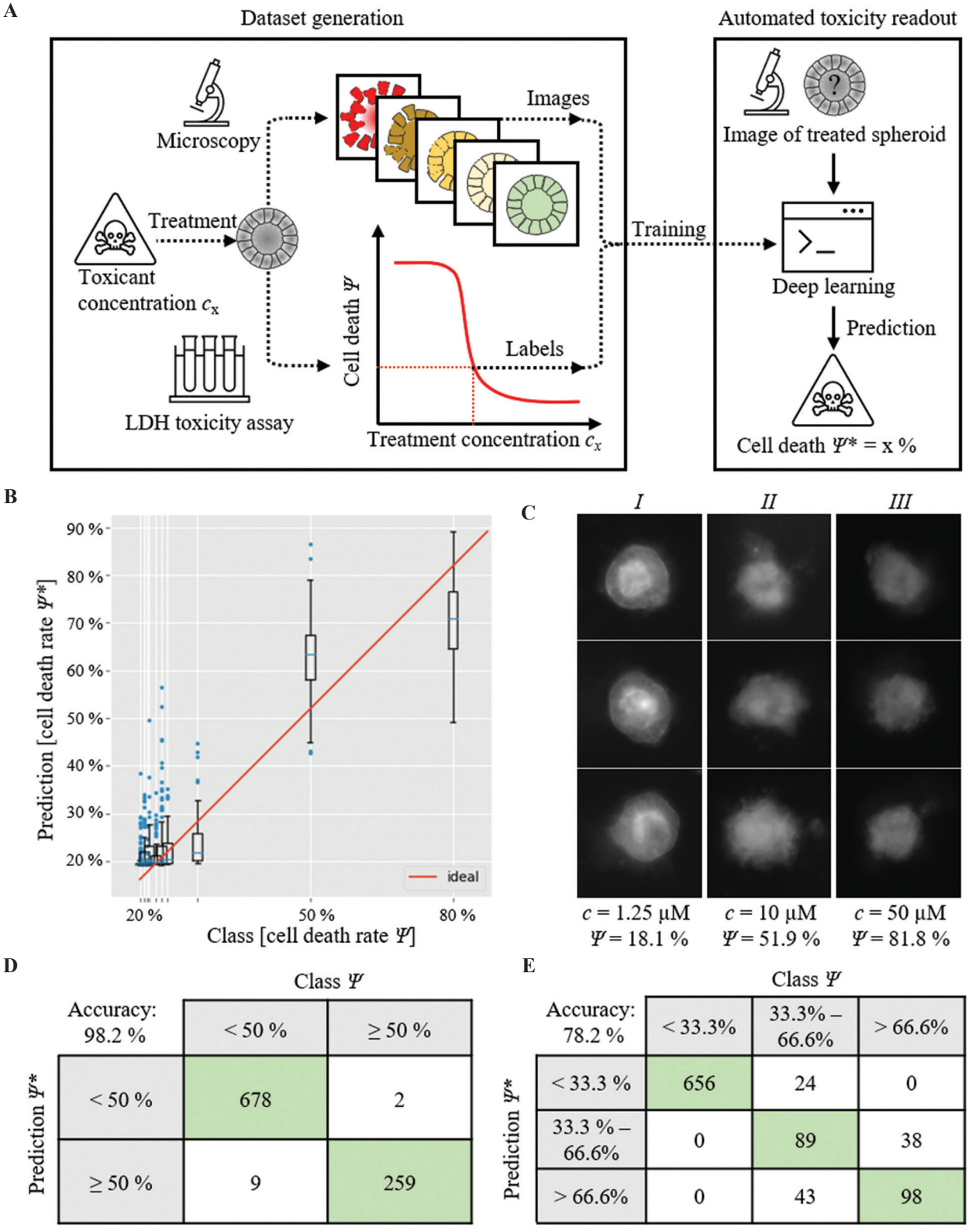


Figure 4. (A) Schematic of automatic toxicity readout. (B) Class vs. prediction box plot. (C) Fluorescent images of spheroids treated with different cisplatin concentrations *c* and corresponding cell death rates Ψ: Spheroids with low death rates (*I*) show obviously different appearances. Spheroids with intermediate (*II*) and high (*III*) death rates show similar appearances. (D and E) Confusion matrices when using the neural network as a classifier. The 2-class problem delivered a balanced accuracy: 98.2%. The 3-class problem delivered an accuracy of 78.7%.

4. Conclusion and outlook

The presented results successfully demonstrated a concept for automated toxicity testing with renal spheroids. 3D bioprinting technology enabled scalable, reproducible, and automated fabrication of renal spheroids. In a head-to-head comparison, functional differences between 2D and 3D cell models were found. Toxic treatment effects varied with time and quantity, indicating increased sensitivity to the specific toxicant. This clearly demonstrated how 3D cell models could be of increasing relevance for future applications, such as toxicity studies. Deep learning image classification enabled an automated image-based readout. Although relatively high accuracies were achieved in this study, further improvements could be implemented in the future. To improve the performance, the present dataset could be augmented with additional images of the cell morphologies. Therefore, more biomarkers[13] and cell viability assays (e.g., MTT, PrestoBlue, etc.)[21] could be applied to generate ideally multi-channel and -dimensional fluorescence images, which could then be used to train the algorithm. With this additional image information, an increased performance could potentially be achieved, which would contribute to image-based toxicity readouts with higher precision in the future.

Acknowledgments

This work was supported by the Baden-Württemberg Stiftung (Grant No IAF-3). The authors acknowledge to S.S.L. and S.Z,. and the European Research Council to S.S.L. (grant agreement No 804474, DiRECT), and the Swiss National Science Foundation to S.S.L. (NCCR Kidney.CH).

Conflict of interest

The authors have no conflicts to declare.

Author contributions

K.T., G.M., S.Z., R.Z., S.L., R.P., and S.K. provided the conceptual design. S.L. and S.Z. were responsible for formal analysis. S.K., S.Z., R.Z., P.K., and S.L. acquired funding. K.T., G.M., L.R., R.P., and F.K. conducted experiments including cell culture, bioprinting, imaging, and investigation. F.K., K.T., R.P., L.R., P.K., and S.Z. provided resources. S.Z.; R.Z. supervised the work. K.T., G.M., and S.Z. were responsible for writing and visualization.

References

1. Breslin S, O'Driscoll L, 2013, Three-dimensional Cell Culture: The Missing Link in Drug Discovery. *Drug Discov Today*, 18:240. https://doi.org/10.1016/j.drudis.2012.10.003
2. Homan KA, Kolesky DB, Skylar-Scott MA, *et al*., 2016. Bioprinting of 3D Convoluted Renal Proximal Tubules on Perfusable Chips. *Sci Rep*, 6:34845. https://doi.org/10.1038/srep34845
3. Secker PE, Luks L, Schlichenmaier N, *et al*., 2018, RPTEC/TERT1 Cells form Highly Differentiated Tubules when Cultured in a 3D Matrix. *ALTEX*, 35:223. https://doi.org/10.14573/altex.1710181
4. Kaminski MM, Tosic J, Kresbach C, *et al*., 2016. Direct Reprogramming of Fibroblasts into Renal Tubular Epithelial Cells by Defined Transcription Factors. *Nat Cell Biol*, 18:1269. https://doi.org/10.1038/ncb3437
5. Buzhor E, Harari-Steinberg O, Omer D, *et al*., 2011, Kidney Spheroids Recapitulate Tubular Organoids Leading to Enhanced Tubulogenic Potency of Human Kidney-derived Cells. *Tissue Eng Part A*, 17:2305. https://doi.org/10.1089/ten.TEA.2010.0595
6. Mota C, Camarero-Espinosa S, Baker MB, *et al*., 2020, Bioprinting: From Tissue and Organ Development to *In Vitro* Models. *Chem Rev*, 120:10547. https://doi.org/10.1021/acs.chemrev.9b00789
7. Gutzweiler L, Kartmann S, Troendle K, *et al*., 2017, Large Scale Production and Controlled Deposition of Single HUVEC Spheroids for Bioprinting Applications. *Biofabrication*, 9:25027. https://doi.org/10.1088/1758-5090/aa7218
8. Tröndle K, Rizzo L, Pichler R, *et al*., 2021, Scalable Fabrication of Renal Spheroids and Nephron-like Tubules by Bioprinting and Controlled Self-assembly of Epithelial Cells. *Biofabrication*, 13:185. https://doi.org/10.1088/1758-5090/abe185
9. Ng WL, Chan A, Ong YS, *et al*., 2020, Deep Learning for Fabrication and Maturation of 3D Bioprinted Tissues and Organs. *Virtual Phys Prototyp*, 15:340. https://doi.org/10.1080/17452759.2020.1771741
10. Yu C, Jiang J, 2020, A Perspective on Using Machine Learning in 3D Bioprinting. *Int J Bioprint*, 6:253. https://doi.org/10.18063/ijb.v6i1.253
11. Benning L, Peintner A, Finkenzeller G, *et al*., 2020, Automated Spheroid Generation, Drug Application and Efficacy Screening Using a Deep Learning Classification: A Feasibility Study. *Sci Rep*, 10:11071. https://doi.org/10.1038/s41598-020-67960-0
12. La Greca A, Pérez N, Castañeda S, *et al*., 2020, Celldeath: A Tool for Detection of Cell Death in Transmitted Light

Microscopy Images by Deep Learning-based Visual Recognition. *PLoS One*, 16:e0253666. https://doi.org/10.1101/2020.03.22.002253.

13. Kim SY, Moon A, 2012, Drug-induced Nephrotoxicity and its Biomarkers. *Biomol Ther*, 20:268. https://doi.org/10.4062/biomolther.2012.20.3.268
14. Yao X, Panichpisal K, Kurtzman N, *et al*., 2007, Cisplatin Nephrotoxicity: A Review. *Am J Med Sci*, 334:115. https://doi.org/10.1097/MAJ.0b013e31812dfe1e
15. Tröndle K, Koch F, Finkenzeller G, *et al*., 2019, Bioprinting of High Cell Density Constructs Leads to Controlled Lumen Formation with Self-assembly of Endothelial Cells. *J Tissue Eng Regen Med*, 13:1883–95. https://doi.org/10.1002/term.2939
16. Salas S, Mercier C, Ciccolini J, *et al*., 2006. Therapeutic Drug Monitoring for Dose Individualization of Cisplatin in Testicular Cancer Patients Based Upon Total Platinum Measurement in Plasma. *Ther Drug Monit*, 28:532–9. https://doi.org/10.1097/00007691-200608000-00008
17. King SM, Higgins JW, Nino CR, *et al*., 2017, 3D Proximal Tubule Tissues Recapitulate Key Aspects of Renal Physiology to Enable Nephrotoxicity Testing. *Front Physiol*, 8:123. https://doi.org/10.3389/fphys.2017.00123
18. Vormann MK, Gijzen L, Hutter S, *et al*., 2018, Nephrotoxicity and Kidney Transport Assessment on 3D Perfused Proximal Tubules. *AAPS J*, 20:90. https://doi.org/10.1208/s12248-018-0248-z
19. Han WK, Bailly V, Abichandani R, *et al*., 2002. Kidney Injury Molecule-1 (KIM-1): A Novel Biomarker for Human Renal Proximal Tubule Injury. *Kidney Int*, 62:237. https://doi.org/10.1046/j.1523-1755.2002.00433.x
20. Falkner S, Klein A, Hutter F. BOHB: Robust and Efficient Hyperparameter Optimization at Scale. 2018 International Conference on Machine Learning.
21. Boncler M, Różalski M, Krajewska U, *et al*., 2014, Comparison of PrestoBlue and MTT Assays of Cellular Viability in the Assessment of Anti-proliferative Effects of Plant Extracts on Human Endothelial Cells. *J Pharmacol Toxicol Methods*, 69:9. https://doi.org/10.1016/j.vascn.2013.09.003

Publisher's note

Whioce Publishing remains neutral with regard to jurisdictional claims in published maps and institutional affiliations.

METHODS

Computer Vision-Aided 2D Error Assessment and Correction for Helix Bioprinting

Changxi Liu[1], Jia Liu[2], Chengliang Yang[2],Yujin Tang[2]*, Zhengjie Lin[3], Long Li[4], Hai Liang[4], Weijie Lu[1], Liqiang Wang[1]*

[1]State Key Laboratory of Metal Matrix Composites, School of Material Science and Engineering, Shanghai Jiao Tong University, No. 800 Dongchuan Road, Shanghai, 200240, China
[2]Department of Orthopaedics, Affiliated Hospital of Youjiang Medical University for Nationalities, Guangxi Key Laboratory of Basic and Translational Research of Bone and Joint Degenerative Diseases, Guangxi Biomedical Materials Engineering Research Center for Bone and Joint Degenerative Diseases, Baise, 533000, Guangxi, China
[3]3D Printing Clinical Translational and Regenerative Medicine Center, Shenzhen Shekou People's Hospital
[4]Department of Stomatology, Shenzhen Shekou People's Hospital

Abstract: Bioprinting is an emerging multidisciplinary technology for organ manufacturing, tissue repair, and drug screening. The manufacture of organs in a layer-by-layer manner is a characteristic of bioprinting technology, which can also determine the accuracy of constructs confined by the printing resolution. The lack of sufficient resolution will result in defect generation during the printing process and the inability to complete the manufacture of complex organs. A computer vision-based method is proposed in this study to detect the deviation of the printed helix from the reference trajectory and calculate the modified reference trajectory through error vector compensation. The new printing helix trajectory resulting from the modified reference trajectory error is significantly reduced compared with the original helix trajectory and the correction efficiency exceeded 90%.

Keywords: Bioprinting; Computer vision; Error detection; Quality assurance; Sobel operator

*Correspondence to: Liqiang Wang, State Key Laboratory of Metal Matrix Composites, School of Material Science and Engineering, Shanghai Jiao Tong University, No. 800 Dongchuan Road, Shanghai, 200240, China; wang_liqiang@sjtu.edu.cn; Yujin Tang, Department of Orthopaedics, Affiliated Hospital of Youjiang Medical University for Nationalities, Guangxi Key Laboratory of basic and translational research of Bone and Joint Degenerative Diseases, Guangxi Biomedical Materials Engineering Research Center for Bone and Joint Degenerative Diseases, Baise, 533000, Guangxi, China; tangyujin196709@163.com.

Received: December 30, 2021; **Accepted:** February 7, 2022; **Published Online:** February 7, 2022

Citation: Liu C, Liu J, Yang C, *et al.*, 2022, Computer Vision-Aided 2D Error Assessment and Correction for Helix Bioprinting. *Int J Bioprint,* 8(2):547. http://doi.org/10.18063/ijb.v8i2.547

1. Introduction

As a novel and advanced method, bioprinting is developed based on additive manufacturing technologies and has attracted significant attention from academia and the medical sector since it may deliver a promising solution to the shortage of organ for transplantation[1-3]. Although artificial human heart was successfully produced by bioprinting technology, systematic investigations of organ bioprinting are still rare, especially on the integrity of organ and tissue regeneration[4]. Hence, the utilization of artificial bioprinted organs is still in its infancy and facing tremendous challenges[5].

At present, bioprinting is divided into extrusion-based, injection-based, droplet, and stereolithography bioprinting[6-8]. Extrusion-based bioprinting is the most popular bioprinting method with much higher efficiency than other bioprinting methods since it can support large-volume printing structures[9,10]. The power sources of extrusion-based bioprinting can be categorized into three types, that is, air pressure, rotation, and force, as shown in **Figure 1A**. These external forces push the bioink in the pipeline then the bioink is extruded from the extrusion nozzle in a layer-by-layer manner, according to a predetermined trajectory and the organ manufacturing model.

© 2022 Author(s). This is an Open-Access article distributed under the terms of the Creative Commons Attribution License, permitting distribution and reproduction in any medium, provided the original work is properly cited.

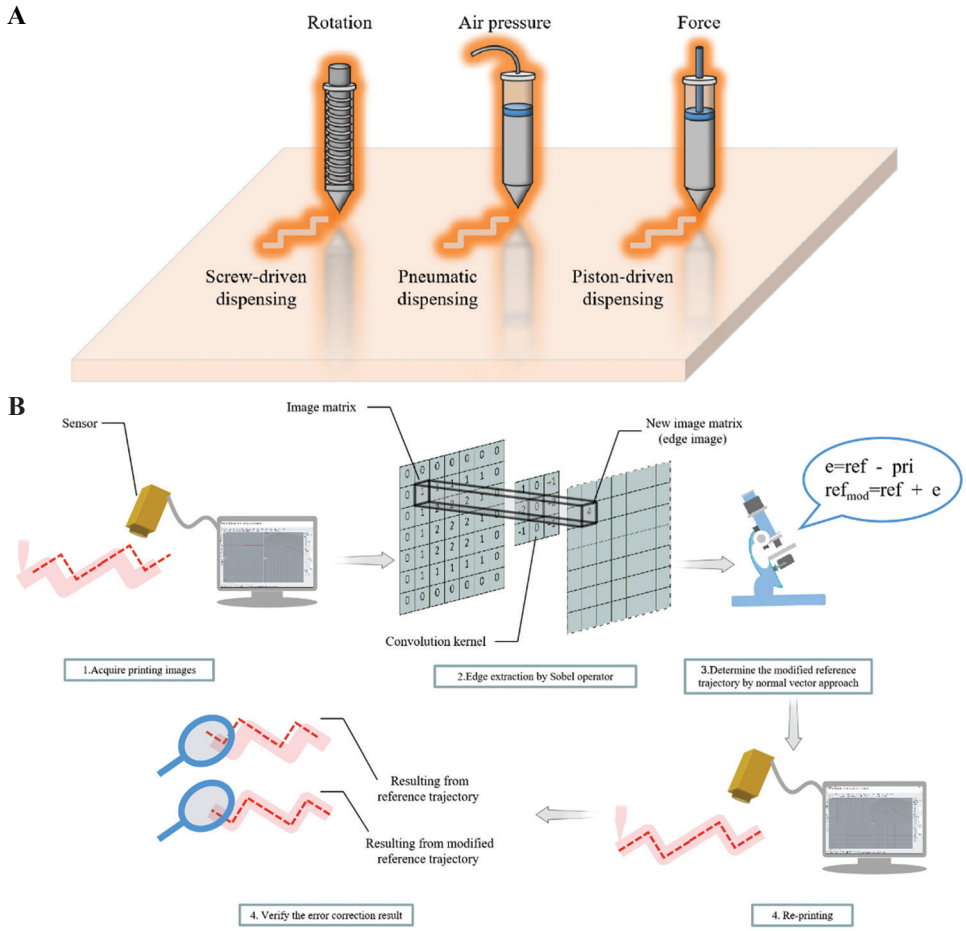


Figure 1. (A) Three sources of bioprinting power. From left to right: Rotation dispensing by screw driven, air pressure dispensing by pneumatic, and force dispensing by piston driven. (B) Schematic illustration of computer vision-aided trajectory error assessment and correction in bioprinting.

Despite the numerous advantages of bioprinting, low printing resolution is a critical issue limiting bioprinting development and utilization. It should be noted that bioprinting resolution is a decisive factor affecting the overall quality of printing[11,12]. A lower resolution substantially reduces the accuracy in the bioprinting model, thereby resulting in tremendous hidden dangers which affect treatment procedure and the overall success of organ transplantation. For instance, studies have shown that the survival rate and differentiation of osteoblasts in the lattice area are higher than those in the film area in the bioprinting experiment. In the same printing environment, the low printing resolution leads to fading and the blur between the lattice area and the film area that finally will induce ambiguity and problems in the final cell survival rate and classification status[13]. Furthermore, recent studies on the bioprinting of the human heart have indicated that the resolution of utilized bioprinting technology has a significant impact on the formation of blood vessels in the heart[4].

Poor process control and feedback during the printing by extrusion-based bioprinting devices is the principal factor of the low resolution of extrusion-based bioprinting, which is a primary limitation of this printing process[14]. The actual printing trajectory often does not reflect according to the originally designed reference trajectories, and some error remains between the designed reference trajectories. The deviation error between the actual trajectory and the reference trajectory is small during the straight-line printing scheme, while the deviation error significantly increases during the printing process of bending and curving structures[15,16].

Many organ bioprinting models, including ear bioprinting model, have been proposed in recent studies[17,18]. The ear is a typical three-dimensional (3D) organ with a curved structure. A computer vision system was never used to achieve process control in most of the studies, which means the error between the actual printing trajectory and the reference trajectory during the printing process remains and affects the final product, reducing the resolution of ears[19].

The main objective of this research is to reduce the deviation error between the printing helix trajectory and the reference trajectory to improve the printing resolution, as shown in **Figure 1B**. A process control method is proposed based on computer vision to locate the helix coordinates and ensure that the helix is extruded at the correct position. The central concept of computer vision is to use equipment and algorithm to replace the human eye to identify objects and obtain information to achieve exact object positioning, object size measurement, and defect detection[20-22]. The deviation error is difficult to distinguish by the naked eye but could be effectively detected and visualized by computer vision. The collected deviation error plays an important role in modifying the reference trajectory to readjust the position of the helix printing. Improved computer vision strategies are required to ensure that the printed structures are of high shape complexity and to improve extrusion bioprinting.

2. Method

2.1. System parameters and material design

A non-contact camera (Samsung SM-G7810) is placed above the XY printing plane to take helix images. The original helix image data are abstract and cannot be directly used for error calculation, so the helix images must be preprocessed by image algorithms. The content of the algorithm will be discussed in sections **2.3** and **2.4**.

Alginate-based hydrogel is used as the bioink material for helix printing. The core component of the alginate-based hydrogel, alginate, is a derivative of alginic acid, which has the structure of long chains of polysaccharides to maintain the state of the gel[23-26]. At present, alginate-based hydrogels are still among the mainstream substances for biological tissue engineering, including drug delivery[27], vaccine manufacturing[28], tissue regeneration[29], and bioprinting[30].

2.2. Printing helix number

To verify the universality of the proposed computer vision-based process control method, three helixes with different sizes and trajectories were put into the printing and correction system. The printing error produced by each helix will show different fluctuations degrees during the bioprinting process due to the difference in the size and curvature degree of the helix. These helix structures are designed by computer-aided design software as a printing helix reference trajectory composed of various straight and curved lines.

2.3. Process control

Process control of bioprinting is proposed to detect and reduce the possible errors between the ideal reference trajectory and the actual printing trajectory that remains in the printed helix. The overall process control can be divided into a measurement part and an execution part; these two parts are shown in **Figure 2A**. The purpose of the measurement part is to determine the error between the actual printing trajectory and the ideal reference trajectory. Next, the error correction and verification procedure will be accomplished in the execution part. MATLAB was used to calculate the deviation value between two trajectories and to obtain the new reference trajectory.

The first step of the procedure is the original bioprinting part. The extrusion-based bioprinting machine performs printing according to the original helix reference trajectory. There is no correction operation added in this step, and the error between the printed helix trajectory and the ideal reference trajectory is retained in the final helix. The second step uses a camera to take the printed helix images. The camera is horizontally fixed to the top of the printed helix and takes the entire helix trajectory images after bioprinting is finished. The captured helix images are required to be preprocessed to acquire the point cloud data; then, the point cloud data will be transmitted to the Cartesian coordinate system to facilitate the subsequent error calculations. The third step is error calculation which is the most critical part. The different vector between the actual printing helix trajectory and the reference trajectory is defined as the error value. The normal vector approach, as shown in **Figure 2B,** uses the compensation vector calculated by the error vector to obtain a new corrected reference path. First, the algorithm determines the size of the compensation vector based on the error and then compensates the original reference trajectory by mirroring to obtain a new reference trajectory[31]. The fourth step is a correction step. The new printing helix trajectory will be guided with the corrected reference trajectory of the replenishment vector obtained in the previous step. The fifth step is the verification step. The specific operation is the same as the second step, in which the new helix trajectory is put into the Cartesian coordinate system to detect the error value compared with the ideal reference trajectory.

2.4. Image algorithm

Figure 3A-G shows the steps in detail to transform abstract helix image data into coordinate data by the algorithm. Furthermore, the error between the helix and the reference trajectory is calculated based on the coordinate data of the helix; accordingly, the modification of the reference trajectory is proposed.

At first, the original images of the printed helix trajectory are collected. Then, the collected images are binarized to reduce the 3D image channel of the picture into the single channel. The purpose is to strengthen the contour edge feature of the image and facilitate subsequent image processing. In the third step, the edges

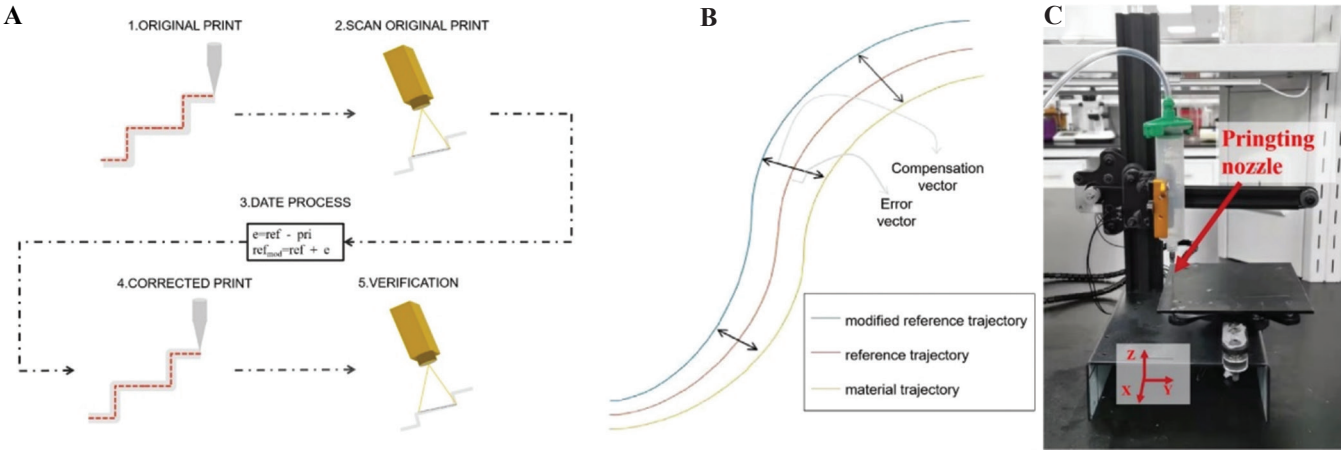


Figure 2. Schematic illustration of the process control principle for helix trajectory detection and correction. (A) Five steps from process control to identification and correction of helix trajectory. (B) Example of normal vector approach to compensate the error vector of the reference trajectory by mirroring to obtain a new modified reference trajectory. (C) Extrusion-based bioprinting machine with standard Cartesian coordinates.

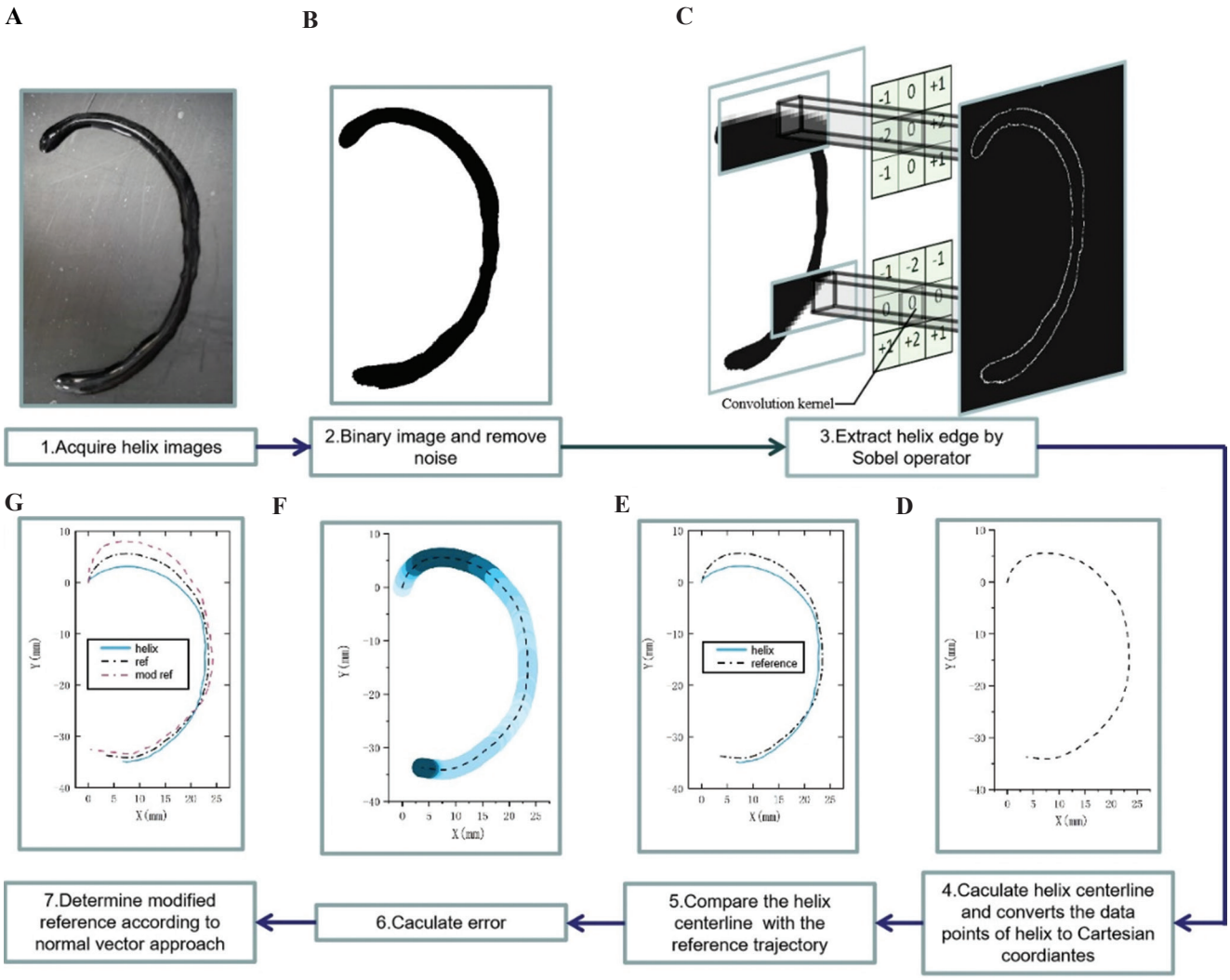


Figure 3. (A-G) The input data required for trajectory correction and seven different processing steps for the helix image. The captured helix trajectory photos cannot be directly calculated by the trajectory error since the image data are unacceptable for the error algorithm. The coordinate data converted from the image data by binarization and edge extraction processing is used for comparison with the reference trajectory, and calculation of the deviation value of the helix trajectory.

of the binarized helix are identified and extracted by the Sobel operator, as shown in **Figure 3C**, to convert the abstract image data into specific point cloud data. Object contour recognition is an emerging field of computer vision to visualize algorithms to recognize the contours of objects to quickly determine the type of objects. The convolution kernel is used to process the image matrix. Which is the most popular object contour recognition algorithm[32–35]. Two 3×3 convolution kernels are shown in **Figure 4**. Each pixel in the image matrix is convolved by the convolution kernel. The convolution kernels on the left and right in **Figure 4** have a maximum response to the vertical edge and level edge, respectively. The helix edge is obtained according to the maximum value of the two convolution kernels.

In the fourth step, the centerline estimate of the helix is calculated based on the helix contour. The centerline of the helix is defined as the helix trajectory after the bioprinting and is placed in the Cartesian coordinate system for subsequent error calculations. In the fifth step, the print helix trajectory in the Cartesian coordinate system (blue solid line) deviates from the predetermined reference trajectory (black dashed line). **Figure 3E** records the print trajectory and reference trajectory of the helix in the same Cartesian coordinate system. In the sixth step, due to the offset of the helix print trajectory (blue solid line) in the Cartesian coordinate system, the difference between each point of the helix trajectory and the reference trajectory could be calculated. **Figure 3F** illustrates the error generation in each of the trajectory segments. In the seventh step, the new reference trajectory is obtained by compensating the error vector, on the foundation of the reference trajectory.

3. Results

3.1. Original printing

The point cloud data of the printing helix trajectory after bioprinting were collected according to the algorithm introduced in Section 2.4. The printing trajectory and the reference trajectory were both established in the same Cartesian coordinate system. **Figure 5** shows the printed helix trajectory (solid flesh-colored line), the estimated value of the printing helix centerline (red dotted line), and the designed ideal reference trajectory (black dotted line).

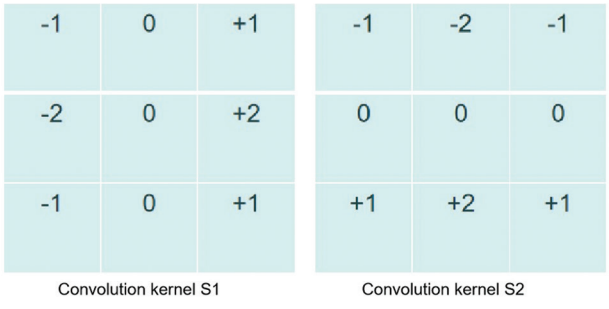


Figure 4. Sobel edge operator

3.2. Correct printing

The coordinate data of the ideal helix reference trajectory and printing helix trajectory could be collected and counted; then, the modified helix reference trajectory with error vector compensation could be determined through the normal vector approach. **Figure 6** shows the XY plane containing the printing helix trajectory resulting from the modified helix reference trajectory and the original printing helix trajectory. The white path was the original helix trajectory, and the translucent blue path was the new printing helix trajectory resulting from modified reference trajectory. The black dashed line was the pre-designed reference trajectory, which was the ideal printing result without error interference.

The deviation vector between the original printing helix trajectory and the ideal reference trajectory was defined as the bioprinting error. **Figure 7** reveals the error values of different positions for each original helix trajectory in the coordinate system by mapping the error values to the printed helix trajectory. The color depth was carried by the color column placed on the right side of the coordinate system, reflecting the error magnitude of each printing helixes. The error and its degree for each printing helix showed an increasing tendency with the color transitioning from light blue to dark blue. The error exceeded 2.4 mm which the color was between blue and black, reaching the high error range. The dashed line in **Figure 7** represents the centerline of the printing helix trajectory, and the different depths of blue color surrounding the centerline represent the error value carried by the helix at different positions, which correspond to the error color column on the right. The dark blue magnitude of error could be seen in the three-helix trajectories, illustrating that the three helixes showed a significant error, exceeding 2.4 mm.

Figure 8 presents additional data of the normal vector approach for each helix: Corrected reference trajectory and corrected printing helix trajectory. In **Figure 8A**, the original reference trajectory and the modified reference trajectory of the compensation error were compared. "Orig Ref" was a black-dashed line representing the original reference trajectory, and "Corr Ref" was a blue solid line representing the modified reference trajectory. **Figure 8B** compared two printing trajectories resulting from the original reference trajectory and the modified reference

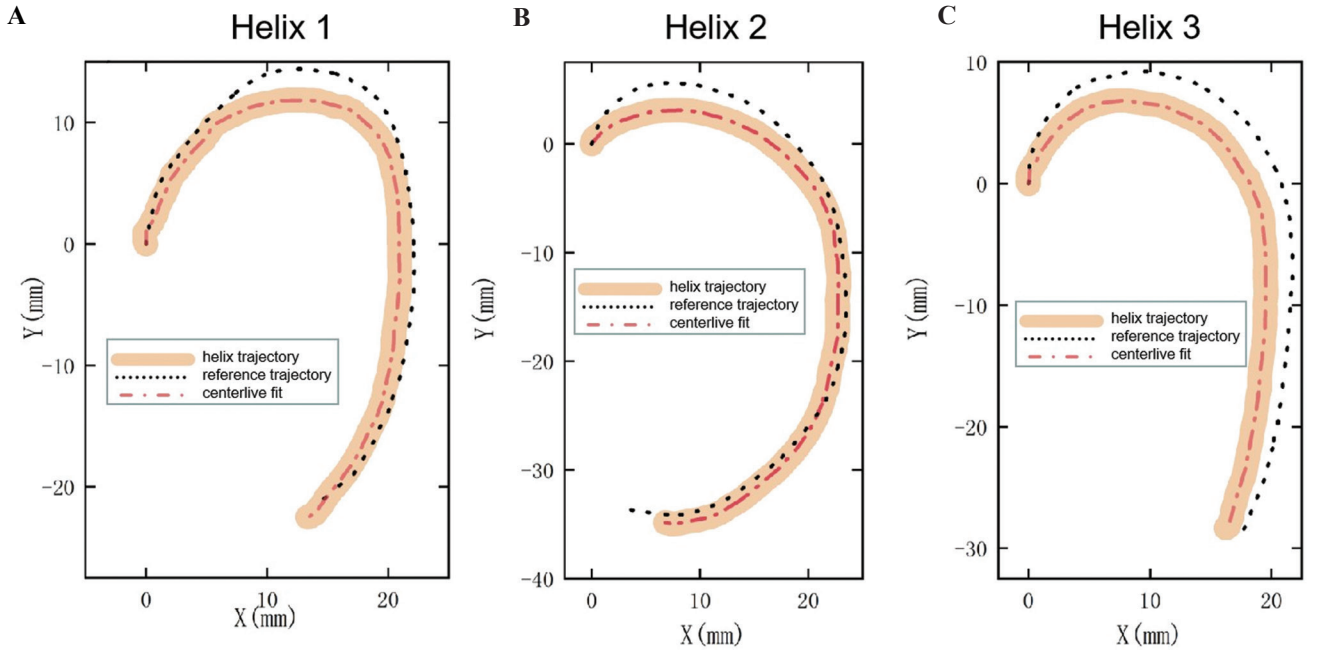


Figure 5. (A-C) The observed solid flesh-colored, black-dashed, and red-dashed lines indicated the print helix locus, reference locus, and the printed helix centerline estimation, respectively. The black-dashed line was the printing helix trajectory obtained in an ideal state, and the red-dashed line output of the algorithm represents the helix printing trajectory.

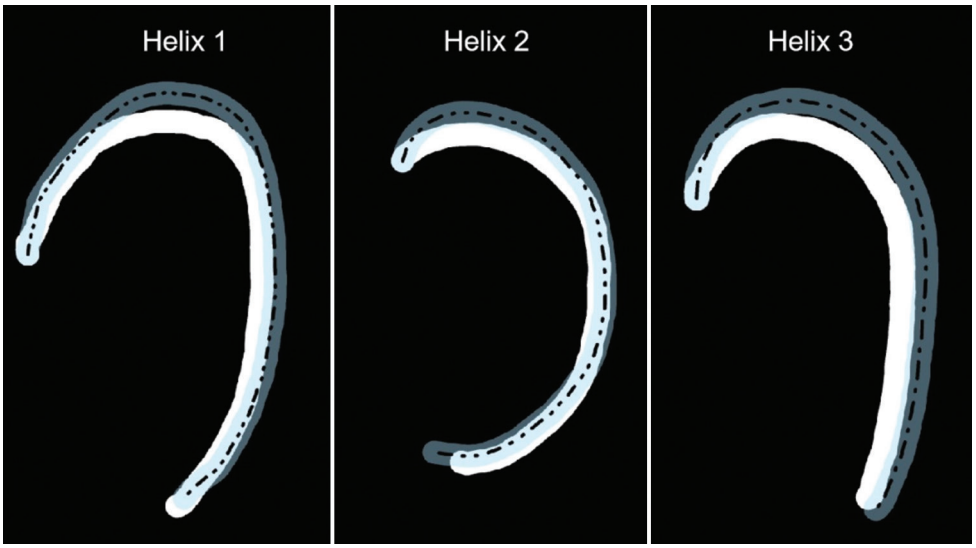


Figure 6. The original printed helix trajectory (white material), the new printed helix trajectory (translucent blue material), and the pre-designed reference trajectory (translucent blue material).

trajectory. Compared with the original printing, the printed helix trajectory resulting from the modified reference trajectory was overlapped with the ideal helix trajectory as much as possible. "Orig Ref" was a black-dashed line representing the original reference trajectory; "Orig Prt" was a blue solid line representing the printing helix trajectory that resulted from the initial reference trajectory; and "Corr Prt" was the red dashed line representing the printed helix trajectory resulting from the modified reference trajectory.

The corrected printing helix trajectory stemming from the modified reference trajectory for each helix was collected, and the error between the ideal reference trajectory and printing helix trajectory was counted, as shown in **Figure 9**. The black-dashed line represented

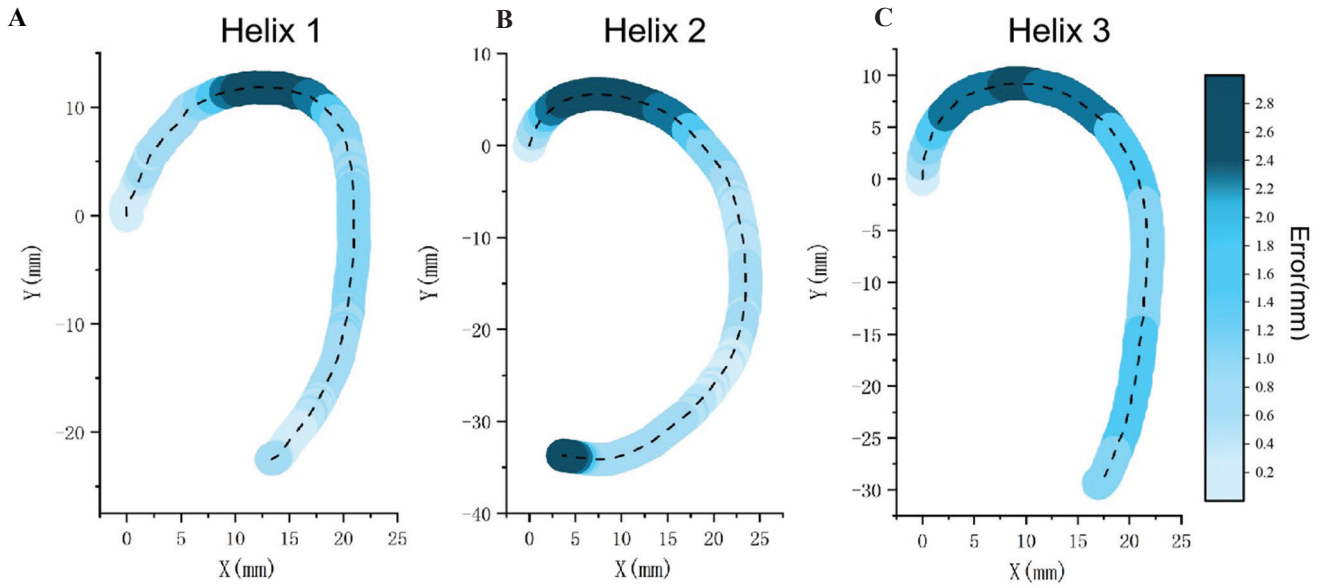


Figure 7. (A-C) The error between the printing helix trajectory and the reference trajectory was mapped to the helix trajectory; the darker blue represents higher level of error. The error value of each helix was shown in the color column on the right. Each helix model was tested 3 times repeatedly.

the correct printing helix trajectory, and the surrounding blue line mapped the errors at different positions. The depth of the color reflected the error value between the corrected printing helix trajectory and the ideal reference trajectory. The error value corresponded to the error color column on the right, which was consistent with the color column, as shown in **Figure 7**. Obviously, the error value of the corrected printing helix trajectory had been reduced dramatically by algorithm processing and a high error range represented by dark blue hues for each helix compared with the original printing helix trajectory was absent.

3.3. Repeatability

To ensure that the error statistics of the corrected helix print trajectory maintained high repeatability, three repeated corrected printing helix trajectories for each helix were tested independently. **Figure 10** illustrates the error distribution state in three printings for each helix. The value of the overall error in the low error range (light blue) was less than 1.0 mm, while there was no high error range (dark blue) in the three printing experiments of each helix.

4. Discussion

Many studies have indicated that bioprinting resolution is a crucial printing parameter. However, the number of studies aiming to improve printing resolution, including printing error detection and correction, is still limited. Most of the printing helix trajectories contain large curves, which induce much greater challenges in the error correction stage. **Figure 5** shows the deviation error between the printed helix trajectory and the ideal reference trajectory. Therefore, the significance of this study is to correct this deviation value and to improve the resolution of extrusion-based bioprinting. The error of each helix reference trajectory is compensated according to the normal vector approach, and the printed helix trajectory is overlapped with the ideal helix trajectory as much as possible. Furthermore, the printing error is reduced to an acceptable range.

Figure 7 shows that the errors are not similar at different positions between the printing helix trajectory and the ideal reference trajectory in the same Cartesian coordinate system. The dark blue area with high error is concentrated on the top curvature position for each helix, which indicates that the error value at the curvature position is higher than the error at the other positions, and the highest error reaches 2.53 mm in the second helix calculated by Euclidean norm (1)[36]. The error level shows a decreasing tendency due to the helix trajectory changes from curve to straight, which dropped to the blue and light blue middle error range. Furthermore, compared with straight trajectory, relying on single-axis control, the curved trajectory requires two axes to control the print head during the printing process, and the error level is also higher than the straight trajectory because of the low accuracy of multiple axis motion.

For the new printing helix trajectory resulting from the modified reference trajectory, the errors are all located in

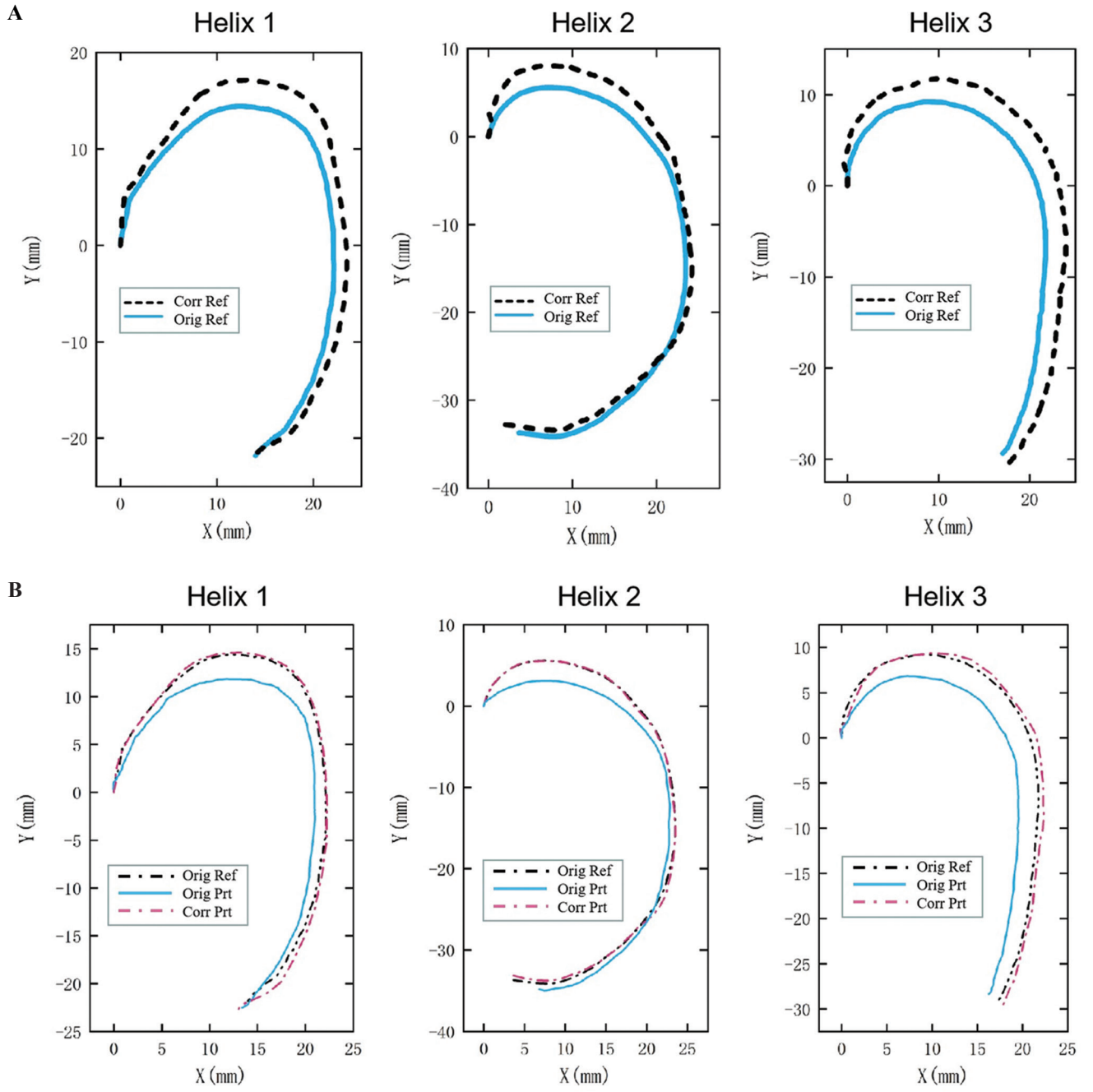


Figure 8. (A) Comparison of the original reference path (blue solid line) and the modified reference path (black-dashed line). (B) Original reference path (black-dashed line), printing helix trajectory resulting from original reference trajectory (blue solid line), and printing helix trajectory resulting from modified reference trajectory (red-dashed line).

the light blue area with low error and less than 1.0 mm. The errors higher than 1.0 mm are corrected by the algorithm and do not appear in the statistical results for each helix, as shown in **Figure 8**. Especially, the average error in the dark blue area with high error at the top curvature position calculated by Euclidean norm (1), has dropped from 2.33 mm, 2.34 mm, and 2.15 mm to 0.21 mm, 0.19 mm, 0.28 mm, respectively, and reached to efficiency rates of about 91%, 92%, and 87%, respectively in Table 1. The curve structure error has been greatly reduced, which proves that the normal vector approach algorithm has a strong correction ability in the curve structure.

$$\|x_2\| = \sqrt{\sum_{i=1}^{N} x_i^2} \tag{1}$$

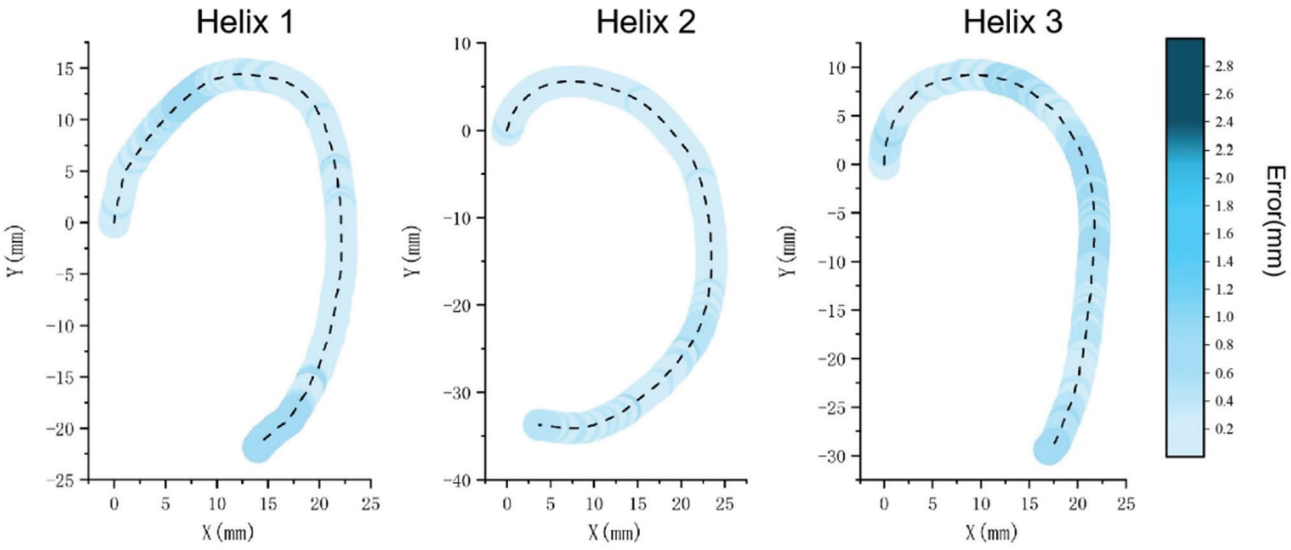


Figure 9. The error between the corrected printing helix trajectory and the reference trajectory was mapped to the helix trajectory; the darker blue represents higher level of error. The error value of each helix was shown in the color column on the right.

Table 1. Error results before and after correction for each helix

	Helix 1	Helix 2	Helix 3
Average error (mm)	1.06	1.15	1.58
Corrected error (mm)	0.36	0.25	0.48
Average error (mm) (high error range)	2.33	2.34	2.15
Corrected error (mm) (high error range)	0.21	0.19	0.25

Computer vision technology is applied to the experimental operation to obtain the point cloud data of the printing helix and realize the process control. A non-contact camera is placed directly above the printing platform and records the entire printing of the helix images during the bioprinting process. The recorded helix images will be transferred from the camera to the computer system, the edges of the helix will be identified and extracted by the Sobel operator. The estimated value of the printing helix centerline can be calculated by the edges of the helix, which represents the printing helix trajectory. In the future, computer vision will play an important role in process control with the development of computer science, including more accurate measurement of the printed components' size. More precise centerline data accurately reflect the printing helix trajectory, and the modified reference trajectory could be exactly expressed by the normal vector approach, which indirectly improves the accuracy of correction.

At present, the position of the printed helix trajectory is adjusted as much as possible to be consistent with the reference trajectory, and the helix error in the two-dimensional (2D) space has been significantly reduced with computer vision processing. In the future work, an extension of the 2D space to the entire 3D space to evaluate and correct the errors of other 3D organs should be attempted. However, the study was afflicted with a few challenges. For example, the current computer vision is beneficial in processing flat images, but in the case of a target object with a 3D image, the limitations of computer vision will be magnified. Furthermore, the error definition will also shift from 2D space to 3D space. Hence, further investigations are required on this topic.

5. Conclusions

The main limitation for high-precision bioprinting is the low resolution caused by the lack of process control, which is reflected in the printing trajectory as a deviation from the original reference trajectory. The error caused by this deviation is one of the reasons that affect the resolution of extrusion-based bioprinting. In this study, computer

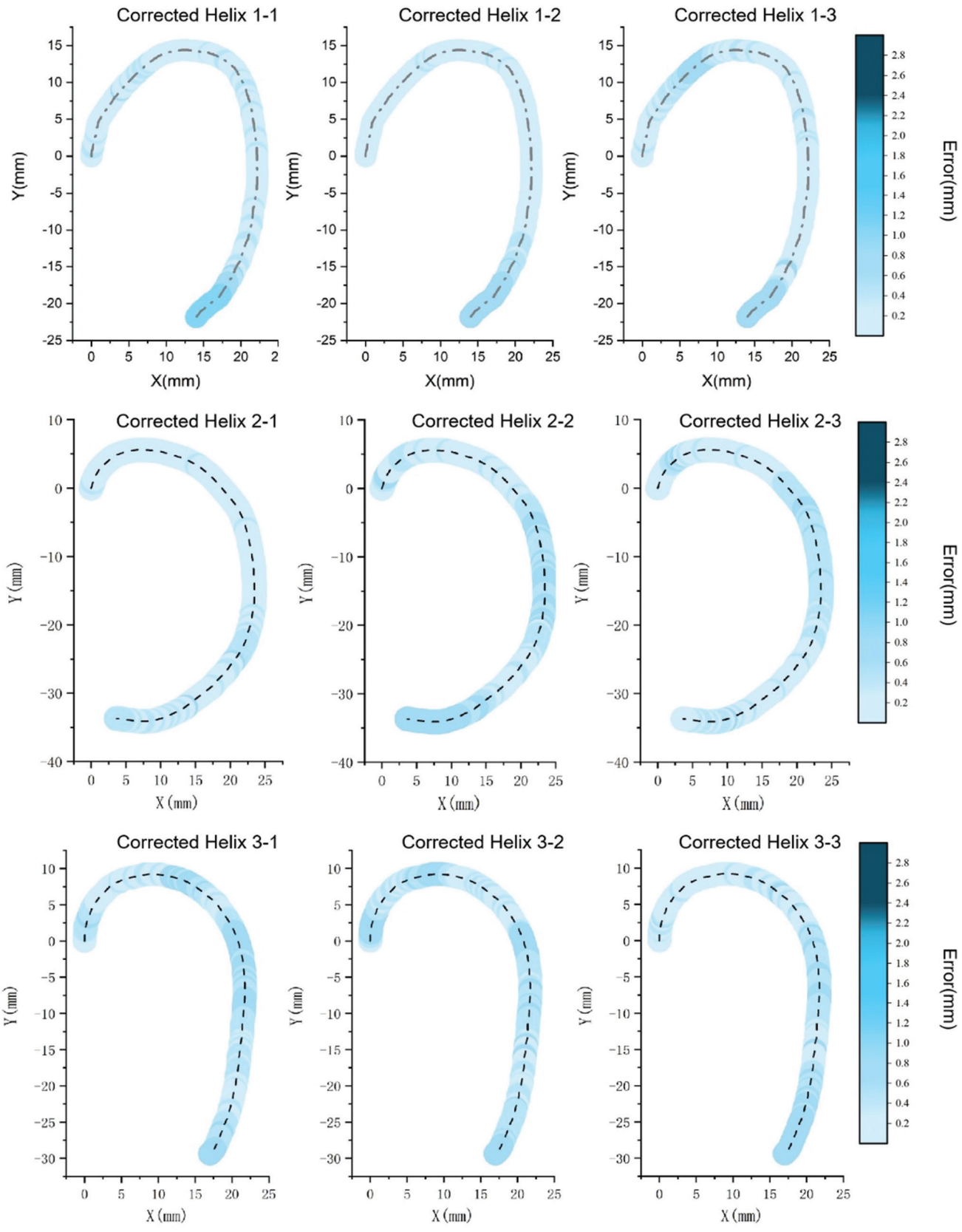


Figure 10. Printing helix trajectory resulting from modified reference trajectory was printed 3 times, and all errors of each helix were located in the low error range (light blue).

vision technology was applied to helix bioprinting to achieve process control. The average error of the three helixes has been reduced from 1.06 mm, 1.15 mm, and 1.58 mm to 0.36 mm, 0.25 mm, and 0.48mm, respectively. For the high error area of each helix, the average error has been reduced from 2.33 mm, 2.34 mm, and 2.15 mm to 0.21 mm, 0.19 mm, and 0.25mm, respectively, and the correction efficiency has reached 91%, 92%, and 87%, respectively. The resolution of bioprinting shows a great improvement, it should be noted that only the reference trajectory is modified. More intuitively, the error is significantly reduced compared with the original helix printing trajectory after correction and shows high repeatability.

This study, for the 1st time, proposes the use of a computer vision technology in bioprinting procedure to reduce the deviation values of the printing helix trajectory compared to the reference trajectory through process control. This method is applicable to the printing of other organs, in addition to the human ear, so as to reduce printing errors. Through this procedure, the bioprinting resolution can be further increased and the printing accuracy can be improved, thereby improving the areas of organ manufacturing and tissue engineering.

Acknowledgments

Guangxi Science and Technology Program: The central government guides the local science and technology development science and technology innovation base project (Guike Jizi[2020] No.198): Basic Research and Transformation Technology Innovation Base of Bone and Joint Degenerative Diseases.

Funding

The authors thankfully acknowledge the financial support listed as below: National Natural Science Foundation of China under (Grant Nos.51831011, 52011530181), Shanghai Science and Technology Commission under Grant No.20S31900100.

Conflict of interest

The authors declare no competing financial interests.

Authors' contributions

The manuscript was written through contributions of all authors. All authors have given approval to the final version of the manuscript.

References

1. Lawlor KT, Vanslambrouck JM, Higgins JW, *et al*., 2021, Cellular Extrusion Bioprinting Improves Kidney Organoid Reproducibility and Conformation. *Nat Mater*, 20:260–71. https://doi.org/10.1038/s41563-020-00853-9
2. Cui X, Breitenkamp K, Finn MG, *et al*., 2012, Direct Human Cartilage Repair Using Three-Dimensional Bioprinting Technology. *Tissue Eng A,* 18:1304–12. https://doi.org/10.1089/ten.tea.2011.0543
3. Yanez M, Rincon J, Dones A, *et al*., 2015, *In Vivo* Assessment of Printed Microvasculature in a Bilayer Skin Graft to Treat Full-Thickness Wounds. *Tissue Eng A*, 21:224–33. https://doi.org/10.1089/ten.tea.2013.0561
4. Lee A, Hudson AR, Shiwarski DJ, *et al*., 2019, 3D Bioprinting of Collagen to Rebuild Components of the Human Heart. *Science,* 365:482–7. https://doi.org/10.1126/science.aav9051
5. Daly AC, Prendergast ME, Hughes AJ, *et al*., 2021, Bioprinting for the Biologist. *Cell*, 184:18–32. https://doi.org/10.1016/j.cell.2020.12.002
6. Jose RR, Rodriguez MJ, Dixon TA, *et al*., 2016, Evolution of Bioinks and Additive Manufacturing Technologies for 3D Bioprinting. *ACS Biomater Sci Eng,* 2:1662–78. https://doi.org/10.1021/acsbiomaterials.6b00088
7. Murphy SV, Atala A, 2014, 3D Bioprinting of Tissues and Organs. *Nat Biotechnol,* 32:773–85. https://doi.org/10.1038/nbt.2958
8. Zorlutuna P, Jeong JH, Kong H, *et al*., 2011, Stereolithography-Based Hydrogel Microenvironments to Examine Cellular Interactions. *Adv Funct Mater,* 21:3642–51. https://doi.org/10.1002/adfm.201101023
9. Darwish LR, El-Wakad MT, Farag MM, 2021, Towards an Ultra-Affordable Three-Dimensional Bioprinter: A Heated Inductive-Enabled Syringe Pump Extrusion Multifunction Module for Open-Source Fused Deposition Modeling Three-Dimensional Printers. *J Manuf Sci Eng*, 143:125001. https://doi.org/10.1115/1.4050824
10. Duan B, Hockaday LA, Kang KH, *et al*., 2008, 3D Bioprinting of Heterogeneous Aortic Valve Conduits with Alginate/Gelatin Hydrogels. *Bone,* 23:1–7. https://doi.org/10.1002/jbm.a.34420.3D
11. Hinton TJ, Lee A, Feinberg AW, 2017, 3D Bioprinting from the Micrometer to Millimeter Length Scales: Size Does Matter. *Curr Opin Biomed Eng,* 1:31–7. https://doi.org/10.1016/j.cobme.2017.02.004
12. Ozbolat IT, Hospodiuk M, 2016, Current Advances and Future Perspectives in Extrusion-Based Bioprinting. *Biomaterials,* 76:321–43.

https://doi.org/10.1016/j.biomaterials.2015.10.076

13. McBeth C, Lauer J, Ottersbach M, *et al*., 2017, 3D Bioprinting of GelMA Scaffolds Triggers Mineral Deposition by Primary Human Osteoblasts. *Biofabrication*, 9:015009. https://doi.org/10.1088/1758-5090/aa53bd
14. Dababneh AB, Ozbolat IT, 2014, Bioprinting Technology: A Current State-of-the-Art Review. *J Manuf Sci Eng Trans ASME*, 136:1–11. https://doi.org/10.1115/1.4028512
15. Armstrong AA, Norato J, Alleyne AG, *et al*., 2020, Direct Process Feedback in Extrusion-Based 3D Bioprinting. *Biofabrication*, 12:015017. https://doi.org/10.1088/1758-5090/ab4d97
16. Armstrong AA, Alleyne AG, Johnson AJ, 2020, 1D and 2D Error Assessment and Correction for Extrusion-Based Bioprinting Using Process Sensing and Control Strategies. *Biofabrication*, 12:045023. https://doi.org/10.1088/1758-5090/aba8ee
17. Hockaday LA, Kang KH, Colangelo NW, *et al*., 2012, Rapid 3D Printing of Anatomically Accurate and Mechanically Heterogeneous Aortic Valve Hydrogel Scaffolds. *Biofabrication*, 4:035005. https://doi.org/10.1088/1758-5082/4/3/035005
18. Rastogi P, Kandasubramanian B, 2019, Review of Alginate-Based Hydrogel Bioprinting for Application in Tissue Engineering. *Biofabrication*, 11:042001. https://doi.org/10.1088/1758-5090/ab331e
19. Fisch P, Broguiere N, Finkielsztein S, *et al*., 2021, Bioprinting of Cartilaginous Auricular Constructs Utilizing an Enzymatically Crosslinkable Bioink. *Adv Funct Mater,* 31:1–15. https://doi.org/10.1002/adfm.202008261
20. Wibisono A, Mursanto P, 2020, Multi Region-Based Feature Connected Layer (RB-FCL) of Deep Learning Models for Bone Age Assessment. *J Big Data*, 7:67. https://doi.org/10.1186/s40537-020-00347-0
21. Qiu C, Ravi GA, Attallah MM, 2015, Microstructural Control During Direct Laser Deposition of a β-Titanium Alloy. *Materials and Design,* 81:21–30. https://doi.org/10.1016/j.matdes.2015.05.031
22. Fu G, Corradi P, Menciassi A, Dario P, 2011, An Integrated Triangulation Laser Scanner for Obstacle Detection of Miniature Mobile Robots in Indoor Environment. *IEEE/ASME Trans Mechatron,* 16:778–83. https://doi:10.1109/TMECH.2010.2084582
23. Yang JS, Xie YJ, He W, 2011, Research Progress on Chemical Modification of Alginate: A Review. *Carbohydr Polym,* 84:33–9. https://doi.org/10.1016/j.carbpol.2010.11.048
24. Wang B, Wan Y, Zheng Y, *et al*., 2019, Alginate-Based Composites for Environmental Applications: A Critical Review. *Crit Rev Environ Sci Technol,* 49:318–56. https://doi.org/10.1080/10643389.2018.1547621
25. Thakur S, Sharma B, Verma A, *et al*., 2018, Recent Progress in Sodium Alginate Based Sustainable Hydrogels for Environmental Applications. *J Clean Prod,* 198:143–59. https://doi.org/10.1016/j.jclepro.2018.06.259
26. Axpe E, Oyen ML, 2016, Applications of Alginate-Based Bioinks in 3D Bioprinting. *Int J Mol Sci*, 17:1976. https://doi.org/10.3390/ijms17121976
27. Abasalizadeh F, Moghaddam SV, Alizadeh E, *et al*., 2020, Erratum: Alginate-Based Hydrogels as Drug Delivery Vehicles in Cancer Treatment and Their Applications in Wound Dressing and 3D Bioprinting. *J Biol Eng*, 14:8 https://doi.org/10.1186/s13036-020-00239-0
28. Farjah A, Owlia P, Siadat SD, *et al*., 2015, Immunological Evaluation of an Alginate-Based Conjugate as a Vaccine Candidate Against Pseudomonas Aeruginosa. *Apmis*, 123:175–83. https://doi.org/10.1111/apm.12337
29. Rastogi P, Kandasubramanian B, 2019, Review of Alginate-Based Hydrogel Bioprinting for Application in Tissue Engineering. *Biofabrication*, 11:042001. https://doi.org/10.1088/1758-5090/ab331e
30. Reakasame S, Boccaccini AR, 2018, Oxidized Alginate-Based Hydrogels for Tissue Engineering Applications: A Review. *Biomacromolecules*, 19:3–21. https://doi.org/10.1021/acs.biomac.7b01331
31. Bandy HT, Donmez MA, Gilsinn DE, *et al*., 2001, *A Methodology for Compensating Errors Detected by Process-Intermittent Inspection*. Maryland, United States: National Institute of Standards and Technology.
32. Kanopoulos N, Vasanthavada N, Baker RL, 1988, Design of an Image Edge Detection Filter Using the Sobel Operator. *IEEE J Solid-State Circuits,* 23:358–67. https://doi.org/10.1109/4.996
33. Gao W, Yang L, Zhang X, *et al*., 2010, An Improved Sobel Edge Detection. In: *Proceedings-2010 3rd IEEE International Conference on Computer Science and Information Technology, ICCSIT No.* 5, p. 67–71.

https://doi.org/10.1109/ICCSIT.2010.5563693

34. Vairalkar MM, 2012, Edge Detection of Images Using Sobel Operator. *Int J Emerg Technol Adv Eng,* 2:291–3.
35. Perra C, Massidda F, Giusto DD, 2005, Image Blockiness Evaluation Based on Sobel Operator. In: *Proceedings-International Conference on Image Processing, ICIP No. 1*, p. 389–92. https://doi.org/10.1109/ICIP.2005.1529769
36. Celebi ME, Celiker F, Kingravi HA, 2011, On Euclidean Norm Approximations. *Pattern Recognit,* 44:278–83. https://doi.org/10.1016/j.patcog.2010.08.028

Publisher's note

Whioce Publishing remains neutral with regard to jurisdictional claims in published maps and institutional affiliations.

Author Guidelines

Before submitting for publication, please check that your manuscript has been prepared in accordance to the step-by-step instructions for submitting a manuscript to our online submission system.

Manuscript format

Your manuscript should be in MS Word. You are advised to download the **template** (https://ijb.whioce.com/public/site/Instruction_for_Typesetting_Manuscript_V1.3.docx) when preparing your submissions to this journal. All manuscripts must be written in clear, comprehensible English. Both British and American English are accepted. Usage of non-English words should be kept to a minimum and all must be italicized, with the exception of “e.g.” and “i.e.” If you have concerns about the level of English in your submission, please ensure that it is proofread before submission by a native English speaker or a scientific editing service.

Types of submission

International Journal of Bioprinting accepts original articles, reviews, letters, editorials, commentaries, perspectives and position papers. Please read this section further for the definition of each type and select the appropriate option in the submission system. Submissions exceeding the suggested requirements, such as total manuscript length, will still be processed for consideration and peer review. However, article processing charges will differ in exceptional cases (e.g. a raw text file exceeding 2MB, etc.) The article processing charge will then be determined on a case-by-case basis.

(1) Original Articles

Original Articles are scientific articles based on original, basic and applied research and/or analysis. This manuscript type typically has 5 tables and figures in total, approximately 40 references, and 7,000 words (inclusive of Abstract and References).

(2) Review Articles

A Review Article summarizes and highlights recent developments and current/future trends of the field. This manuscript type typically has 5 tables and figures in total, approximately 70 references, and 7,000 words (inclusive of Abstract and References).

(3) Short Communications

Short Communications are short articles that present original and significant findings on a particular problem or novel findings that is anticipated to have significant impact. The length of a Short Communication, including the Abstract and References, should not exceed 4,000 words. The article should contain Abstract (not more than 150 words), Background, Materials and Method, Results, Discussion, Conclusion and References, and contain no more than 5 figures and/or tables. Typically, this manuscript type has 15 references.

(4) Perspective Articles

Perspective Articles contain author's personal opinions on a subject/topic. Unlike Reviews, Perspective articles may cover a more specific, narrow part of the field. However, these are still required to uphold the spirit of academia to be objective as well as aim to initiate or further discussions and novel experimental procedures in the field. This manuscript type typically has 5 tables and figures in total, approximately 70 references, and 7,000 words (inclusive of Abstract and References).

(5) Commentaries

This type of article contains unsolicited commentaries or analysis from reader(s) targeting specific published articles in the journal. This manuscript type typically has 3 tables and figures in total, approximately 20 references, and 3,500 words (inclusive of Abstract and References).

(6) Clinical Case Studies

A Clinical Case Study presents the details and results from the clinical application of bioprinted products or equivalents on patient cases, and highlights specific instances of interesting phenomena. Submissions will be evaluated on a case-by-case basis. This manuscript type typically has 5 tables and figures in total, approximately 20 references, and 3,000 words (inclusive of Abstract and References).

(7) Methods

Methods articles present new or improved version of experimental methods, tests or procedures pertaining to the field of bioprinting. This manuscript type typically has 10 tables and figures in total, approximately 30 references, and 5,000 words (inclusive of Abstract and References).

(8) Letters to the Editor-in-Chief/Authors

Letters to the Editor-in-Chief/Authors consist of comments from reader(s) about individual articles. These letters must be constructive and contribute to the development of individual articles published or the entire journal. Letters containing new ideas, supporting data or data criticizing the article may be subjected to peer-review (determined on a case-by-case basis by the journal's editorial team). Authors should specify the intended recipient of the letters, i.e. Editor-in-Chief or specific author(s). This manuscript type typically has 2 tables and figures in total, no more than 10 references, and 2,000 words (inclusive of References). No Abstract is required.

(9) Reports

A Report summarizes the execution of a collaborative research program that is directly related to the advancement of bioprinting. Submissions are usually solicited by the editors. This manuscript type typically has 5 tables and figure in total, 20 references, and 5,000 words (inclusive of Abstract and References).

(10) Position Papers

A Position Paper reflects the official opinion of an organization (e.g. government body, funding agency, etc.). This manuscript type typically has 2 tables and figure in total, not more than 15 references, and 3,500 words (inclusive of References). An Abstract is not required in a Position Paper.

(11) Editorials

An Editorial is a solicited, concise commentary that highlights prominent topics in particular issue. Commonly, the Editorials are the official opinions of the editors of the journal or special issue. An Editorial should not exceed 1,000 words (inclusive of References). Typically, an Abstract is not required and only one figure/table is allowed.

(12) Book Reviews

Book Reviews provide an overview of new publications (books) from the area of bioprinting. Brief summary, focus, argumentation and impact of the book should be provided. A Book Review is typically of the length of 400-500 words. No Abstract, References, figures and tables are required.

(13) Extended Conference Papers

An Extended Conference Paper is the conference paper version of an original research article that presents the new findings and in-depth discussion of a certain topic. The manuscripts that do not have relevance to the Focus and Scope of *International Journal of Bioprinting* will be rejected. The requirements for Extended Conference Papers are as follows:

- The Extended Conference Paper must have at least 30% new material and include a citation to the conference paper. In addition to the 30% new material which is acquired through additional experimentation, analyses and proposal of new ideas or theories, the original content that can be found in the conference paper must be paraphrased, i.e. rewriting the sentences or changing the sentence structure. The 30% new material may also include the clarifications in response to questions raised during the presentation at the conference.
- The Extended Conference Paper must have a new title and a new abstract that are different from the corresponding title in the conference paper. Nevertheless, the new title and new abstract must retain the 'motivation, methods and conclusions' of the paper presented at the conference presentation. More data in the form of tables and figures should be added. The results should be discussed in-depth with more examples and explanations. In this regard, more references will be needed.
- The conference paper must be cited.
- The order in which the authors' names listed on the conference paper can be changed, but no new names can be added to and no existing names can be removed from the author list in the Extended Conference Paper.
- A PDF copy of the conference paper must be submitted along with the submission of the Extended Conference Paper.
- The format and style of an Extended Conference Paper is similar to the ones of an Original Article. Refer to the specific requirements of the Original Articles.

(14) Erratum

Authors should contact the editors of *International Journal of Bioprinting* (editor@whicoe.com) if certain errors made by the journal are found. The editors will evaluate the impact of the errors and decide on the appropriate course of action. Any corrections to a paper are published at the sole discretion of the editors.

(15) Corrigendum

Authors should contact the editors of *International Journal of Bioprinting* (editor@whicoe.com) if certain errors made by the authors are found. The editors will evaluate the impact of the errors and decide on the appropriate course of action. Any corrections to a paper are published at the sole discretion of the editors.

Cover letter

All submissions should include a cover letter as a separate file. The cover letter is confidential and will be read only by the editors. It will not be seen by reviewers. A cover letter should contain the following:

- a brief explanation of what was previously known, the conceptual advancement with the findings and its significance to broad readership
- any associated accession numbers or DOIs of the corresponding preprint version of the submission if it has been deposited on a preprint server
- recommendations of up to four academically qualified reviewers (including name, email address and affiliation)
- exclusion of individuals who might have conflict of interest from reviewing the work (including name, email address and affiliation)
- a statement that "neither the manuscript nor any significant part of it is under consideration for publication elsewhere or has appeared elsewhere in a manner that could be construed as a prior or duplication of the same work"
- conflict of interest statement
- a list of names and email addresses of all co-authors of the work who have already seen and approved the manuscript

Title

The title should capture the conceptual significance for a broad audience. The title should not be more than 50 words and should be able to give readers an overall view of the paper's significance. Titles should avoid using uncommon jargons, abbreviations and punctuation.

List of Authors

The names of authors must be spelled out rather than set in initials along with their affiliations. Authors should be listed according to the extent of their contribution, with the major contributor listed first. All corresponding authors should be identified with an asterisk. Affiliations should contain the following core information: department, institution, city, state, postal code, and country. For contact, email address of at least one corresponding author must be included. Please note that all authors must view and approve the final version of the manuscript before submitting.

Abstract

Articles must include an abstract containing a maximum of 200 words. The purpose of abstract is to provide sufficient information for a reader to determine whether or not to proceed to the full text of the article. After the abstract, please give 5 keywords; please avoid using the same words as those already used in the title, separate terms with a semi-colon (term1; term2; term3).

Section Headings

Please number the section headings (e.g. **1**, **2**, **3**, **4**, etc.) in boldface. Likewise, use boldface to identify subheadings too but please distinguish it from major headings using numbers (e.g. **1.1**, **1.2**, **2.1**, **2.2**, etc.) Further subsections of subheadings should be differentiated by boldface and italics font with the numbers ***(1)***, ***(2)***, ***(3)***, etc.

Introduction

The introduction should provide a background that gives a broad readership an overall outlook of the field and the research performed. It tackles a problem and states its important regarding with the significance of the study. Introduction can conclude with a brief statement of the aim of the work and a comment about whether that aim was achieved.

Materials and Methods

This section provides the general experimental design and methodologies used. The aim is to provide enough detail to for other investigators to fully replicate the results. It is also required to facilitate better understanding of the results obtained. Protocols and procedures for new methods must be included in detail for the reproducibility of the experiments. Informed consent should be obtained from patients or parents before the experiments start and should be mentioned in this section.

Ethics

Ethics information include IACUC permit numbers and/or IRB name, if applicable. This information should be included in a subheading labelled "Ethics Statement" in the "Methods" section of the manuscript file, in as much detail as possible.

Results

This section can be divided into subheadings and focuses on the results of the experiments performed.

Discussion

This section should provide the significance of the results and identify the impact of the research in a broader context. It should not be redundant or similar to the content of the results section.

Conclusion

Please use the conclusion section for interpretation only, and not to summarize information already presented in the text or abstract.

Conflict of interest

All authors are required, at the time of submission, to declare all activities that have the potential to be deemed as a source of competing (commercial) interest in relation to their submitted manuscript, as consistent with **the recommendations from the International Committee of Medical Editors (ICMJE)** (http://www.icmje.org/recommendations/). Examples of such activities could include personal or work-related relationships, events, etc. The disclosure should also include all sources of revenue paid (or promised to be paid) directly to authors or their institution on your behalf over the 36 months before submission of the relevant work. Authors who have nothing to declare are encouraged to add "No conflict of interest was reported by all authors" in this section.

During submission, the Conflict of Interest statement should be included in both the cover letter and manuscript (beneath the Acknowledgments section).

Authors will be requested to complete **ICMJE form for Disclosure of Potential Conflict of Interest** (http://www.icmje.org/disclosure-of-interest/) when they are invited to submit a revision. Failure to do return a completed form will result in a delay to editorial and peer review progress. If necessary, the initial disclosure statement provided by the authors will be subject to edits for grammar corrections by the editors. Failure to comply with the conflict of interest disclosure statement requirement may result in rejection of the submissions.

Funding

Authors should declare all financial and non-financial support that have the potential to be deemed as a source of competing interest in relations to their submitted manuscript in this section. Financial supports are generally in the form of grants, royalties, consulting fees and others. Examples of non-financial support could include the following: externally-supplied equipment/biological sources, writing assistance, administrative support, contributions from non-authors, etc.

Appendix

This section is optional and is for all materials (e.g. advanced technical details) that has been excluded from the main text but remain essential to the readers in understanding the manuscripts. This section is not for supplementary figures. Authors are advised to refer to the section on Supplementary Figures for such submissions.

Text

The text of the manuscript should be in Microsoft Word or Latex. The length of the manuscript cannot be more than 50,000 characters (inclusive of spaces), or approximately 7,000 words.

Nomenclature for genes and proteins

This journal aims to reach researchers all over the globe. Hence, for reviewers' and readers' ease in comprehension, authors are highly encouraged to use the appropriate gene and protein nomenclature. Authors may prefer to utilize resources such as http://www.ncbi.nlm.nih.gov/gene.

Figures

Authors should include all figures into the manuscript and submit it as one file. Figures include photographs, scanned images, graphs, charts and schematic diagrams. Figures submitted should avoid unnecessary decorative effects (e.g. 3D graphs), as well as should be minimally processed (e.g. changes in brightness and contrast applied uniformly for the entire figure). It should also be set against a white background. Please remember to label all figures (e.g. axis, etc.) and add captions below the figure, as required. These captions should be numbered (e.g. **Figure 1**, **Figure 2**, etc.) in boldface. All figures must have a brief title (also known as caption) that describes the entire figure without

citing specific panels, followed by a legend, defined as description of each panel. Please identify each panel with uppercase letters in parenthesis (e.g. (**A**), (**B**), (**C**), etc.)

The preferred file formats for any separately submitted figure(s) are TIFF or JPEG. All figures should be legible in print form and of optimal resolution. Optimal resolutions preferred are 300 dots per inch (dpi) for RBG coloured, 600 dpi for greyscale and 1,200 dpi for line art. Although there is no file-size limitation imposed, authors are highly encouraged to compress their figures to an ideal size without unduly affecting the legibility and resolution of figures. This will also speed up the process of uploading in the submission system, if necessary.

The Editor-in-Chief and Publisher reserve the right to request from author(s) the high-resolution files and unprocessed data and metadata files, should the need arise at any point after manuscript submission for reasons such as production, evaluation or other purposes. The file name should allow for ease in identifying the associated manuscript submitted.

Tables, lists and equations

Tables created using Microsoft Word table function are preferred. The tables should include a title at the top. Titles and footnotes/legends should be concise. These must be submitted in the manuscript. Likewise, lists and equations should be properly aligned and its meaning clear to readers. For listing items within the main body of the manuscript, please use Roman numbers in parenthesis (e.g. (i), (ii), (iii), (iv), etc.).

Supplementary files

This section is optional and contains all materials and figures that have been excluded from the entire manuscript. These materials, figures or additional information are relevant to the manuscript but remain non-essential to readers' understanding of the manuscript's main content. All supplementary information should be submitted as a separate file in Step 4 during submission. Please ensure the names of such files contain 'suppl. info'. Videos may be included in this section.

In-text citations

Reference citations in the text should be numbered consecutively in superscript square brackets. Some examples:

1. Negotiation research spans many disciplines[3,4].
2. This result was later contradicted by Becker and Seligman[5].
3. This effect has been widely studied[1–3,7].

Personal communications and unpublished works can only be used in the main text of the submission and are not to be placed in the Reference section. Authors are advised to limit such usage to the minimum. These should also be easily identifiable by stating the authors and year of such unpublished works or personal communications, and the word 'Unpublished' in parenthesis.

E.g. (Smith J, 2000, Unpublished)

References

This section is compulsory and should be placed at the end of all manuscripts. Do not use footnotes or endnotes as a substitute for a reference list. The list of references should only include works that are cited in the text and that have been published or accepted for publication. Personal communications and unpublished works should be excluded from this section. The EndNote output style of IJB can be downloaded at **here** (https://ijb.whioce.com/public/site/IJB.ens).

For the reference list, all authors must be stated. Authors being referenced are listed with their surname followed by their initials. All references should be numbered (e.g. 1, 2, 3, etc.) and sequenced according to the order they appear as the in-text citations. References should follow the following pattern: Author(s), followed by year of publication, title of publication, abbreviated journal name in italics, volume number, issue number in parenthesis and lastly, page range. If the referred article has more than three authors, list only the first three authors and abbreviate the remaining authors as the italicized '*et al*.' (meaning "and others"). If the DOI is available, please include it after the page range. Examples of references for different types of publications are as follows;

(1) Journals

Journal article (print) with one to three authors:

Younger P, 2004, Using the internet to conduct a literature search. *Nurs Stand*, 19(6): 45–51.

Journal article (print) with more than three authors:

Gamelin F X, Baquet G, Berthoin S, *et al*., 2009, Effect of high intensity intermittent training on heart rate variability in prepubescent children. *Eur J Appl Physiol,* 105(1): 731–738.

Journal article (online) with one to three authors:

Jackson D, Firtko A and Edenborough M, 2007, Personal resilience as a strategy for surviving and thriving in the face of workplace adversity: A literature review. *J Adv Nurs*, 60(1): 1–9. http://doi.org/10.1111/j.1365-2648.2007.04412.x

Journal article (online) with more than three authors:

Hargreave M, Jensen A, Nielsen T S S, *et al*., 2015, Maternal use of fertility drugs and risk of cancer in children — A nationwide population-based cohort study in Denmark. *Int J Cancer*, 136(8): 1931–1939. http://doi.org/10.1002/ijc.29235

(2) Books

Book with one to three authors:

Schneider Z, Whitehead D and Elliott D, 2007, *Nursing and Midwifery Research: Methods and Appraisal for Evidence-based Practice*, 3rd edn, Elsevier Australia, Marrickville, NSW, 112–130.

Book with more than three authors

Davis M, Charles L, Curry M J, *et al*., 2003, *Challenging Spatial Norms*, Routledge, London, 12–30.

Chapter or article in book

Knowles M S, (eds) 1986, Independent study, in *Using Learning Contracts*, Jossey-Bass, San Francisco, 89–96.

(3) Preprints

Preprint article with one to three authors:

Ulgen A, Gurkut O, Li W, 2019, Potential Predictive Factors for Breast Cancer Subtypes from a North Cyprus Cohort Analysis. *medRxiv*. https://doi.org/10.1101/19010181

Preprint article with more than three authors:

Wu S, Sun P, Li R, *et al*., 2020, Epidemiological Development of Novel Coronavirus Pneumonia in China and Its Forecast. *medRxiv*. https://doi.org/10.1101/2020.02.21.20026229

(4) Others

Proceedings of meetings and symposiums, conference papers:

Chang S S, Liaw L and Ruppenhofer J, (eds) 2000, *Proceedings of the twenty-fifth annual meeting of the Berkeley Linguistics Society, February 12–15, 1999: General session and parasession on loan word phenomena*. Berkeley Linguistics Society, Berkeley, 12–13.

Conference proceedings (from electronic database):

Wang T, Cook C and Derby B, 2009, Fabrication of a glucose biosensor by piezoelectric inkjet printing. *Proceedings of the Third International Conference on Sensor Technologies and Applications, 2009 (SENSORCOM-M'09)*, 82–85.

Online document with author names:

Este J, Warren C, Connor L, *et al*., 2008, Life in the clickstream: The future of journalism, *Media Entertainment and Arts Alliance*, viewed May 27, 2009, http://www.alliance.org.au/documents/foj_report_final.pdf

Online document without author name:

Developing an argument, n.d., viewed March 30, 2009, http://web.princeton.edu/sites/writing/Writing_Center/WCWritingResources.htm

Thesis/Dissertation:

Gale L, 2000, The relationship between leadership and employee empowerment for successful total quality management, thesis, *Australasian Digital Thesis database*, University of Western Sydney, 110–130.

Standards:

Standards Australia Online, 2006, Glass in buildings: selection and installation, AS 1288-2006, amended January 31, 2008, *SAI Global database*, viewed May 19, 2009.

Government report:

National Commission of Audit, 1996, *Report to the Commonwealth Government*, Australian Government Publishing Service, Canberra.

Government report (online):

Department of Health and Ageing, 2008, Ageing and aged care in Australia, viewed November 10, 2008, http://www.health.gov.au/internet/main/publishing.nsf/Content/ageing

No author:

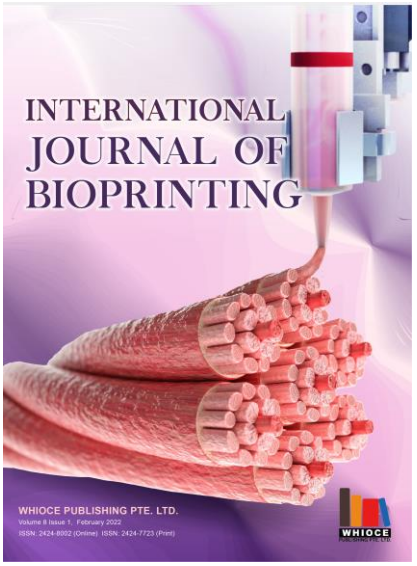
Guide to agricultural meteorological practices, 1981, 2nd edn, Secretariat of the World Meteorological Organization, Geneva, 10–20.

Note: When referencing an entry from a dictionary or an encyclopedia with no author there is no requirement to include the source in the reference list. In these cases, only cite the title and year of the source in-text. For an authored dictionary/encyclopedia, treat the source as an authored book.

International Journal of Bioprinting

Special Issue Alerts

Invitation for Special Issue Proposals



Organizing and editing for a Special Issue helps Guest Editors gain editorial experience and improve academic profile, in addition to being a part of organizing scientific communication of contemporary topics.

If you are published researcher and have an idea for a Special Issue, please write in via email to our Special Issue Commissioning Editor (felicia_wang@whioce.com). Please provide your CV, professional profile page and a topic of interest in your email. Our colleague will guide you in the process of writing a Special Issue proposal.

Current Special Issues

A selection of Special Issue titles are listed below.

Composite/Multi-component Biomaterial Inks and Bioinks
Liliang Ouyang, Yu Shrike Zhang

Mechanical Behaviours of 3D/4D Printing Biomaterials and Smart Structure
Mahdi Bodaghi, Ali Zolfagharian, Lisa-Marie Faller, Falguni Pati, Charbel Dalely Tawk

Integrated Biofabrication Technologies for Constructing Functional Tissue
Qi Gu, Jeremy M. Crook

Novel Materials and Processing for Medical 3D Printing and Bioprinting
Roger Narayan, Jinah Jang

3D Printing in Tissue Engineering
Qing Jiang, Pingqiang Cai, Yi Cao

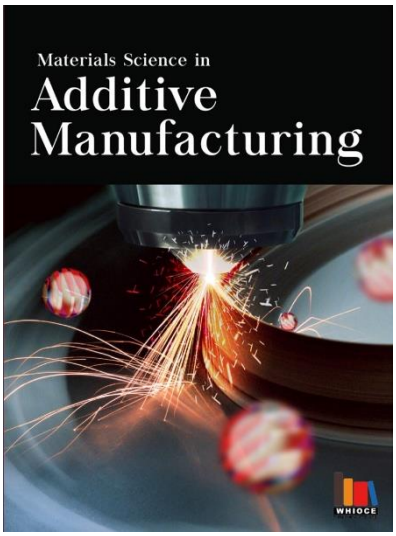
3D Bioprinting with Photocurable Bioinks
Yong He

Completed Special Issues

Congratulations to the Guest Editors who have completed guest-editing the following Special Issues.

3D Printing and Bioprinting for the Future of Healthcare
Wai Yee Yeong, Shweta Agarwala, Lifeng Kang

OUR JOURNALS

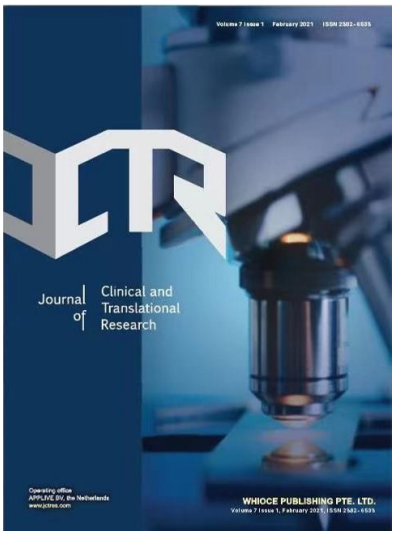


Materials Science in Additive Manufacturing aims to bridge the cutting-edge research between additive manufacturing and the entire spectrum of materials science. The journal covers all applied and fundamentals of processing, synthesis, structure, composition, properties and performance of materials designed or manipulated for additive manufacturing. The journal covers a wide scope of innovative techniques, processes, methods, and applications. Topics of particular interest include, but are not limited to:

- Theory and modelling
- Artificial intelligence
- Polymers
- Metals and alloys
- Ceramics
- Composites
- Magnetic materials
- Smart materials
- Nano-materials
- Materials for electronics
- Characterization techniques

The *Journal of Clinical and Translational Research* is an open access, peer-reviewed, multidisciplinary scientific journal that publishes studies with at least an ex vivo, in vivo, or clinical component. The published research is centered on any clearly defined clinical problem, which may comprise a disease or the basis of disease, a form of therapy or intervention, and clinical diagnostics or prognostics. Articles (original research, reviews, technical reports, medical hypotheses, commissioned articles, special issue articles, and editorials) are published continuously online. The key features of this journal are:

- Open access
- No submission or publication fees
- Reputable international editorial board
- Easy and fast submissions - no formatting rules (“your paper, your way”)
- No word count or reference restrictions
- Double blind review process to minimize bias
- Rapid online publication of articles upon acceptance
- Outlet for academic institutions and industry



Start a new journal

Write to us via email if you are interested to start a new journal with Whioce Publishing. Please attach your CV, professional profile page and a brief pitch proposal in your email. We shall inform you of our decision whether we are interested to collaborate in starting a new journal.

Contact: info@whioce.com



Whioce Publishing Pte. Ltd.
Publishing Office:
73 Upper Paya Lebar Road, #07-02B-06 Centro Bianco, Singapore 534818.

Editorial Office:
34-2B, Jalan Puteri 1/2, Bandar Puteri, 47100 Puchong, Selangor, Malaysia.

Editorial Office : editor@whioce.com
General inquiries : info@whioce.com

https://ijb.whioce.com/index.php/int-j-bioprinting

Whioce Publishing Pte. Ltd. is a company registered in Singapore (No. 201427293E)